Analytical chemistry editor's pick
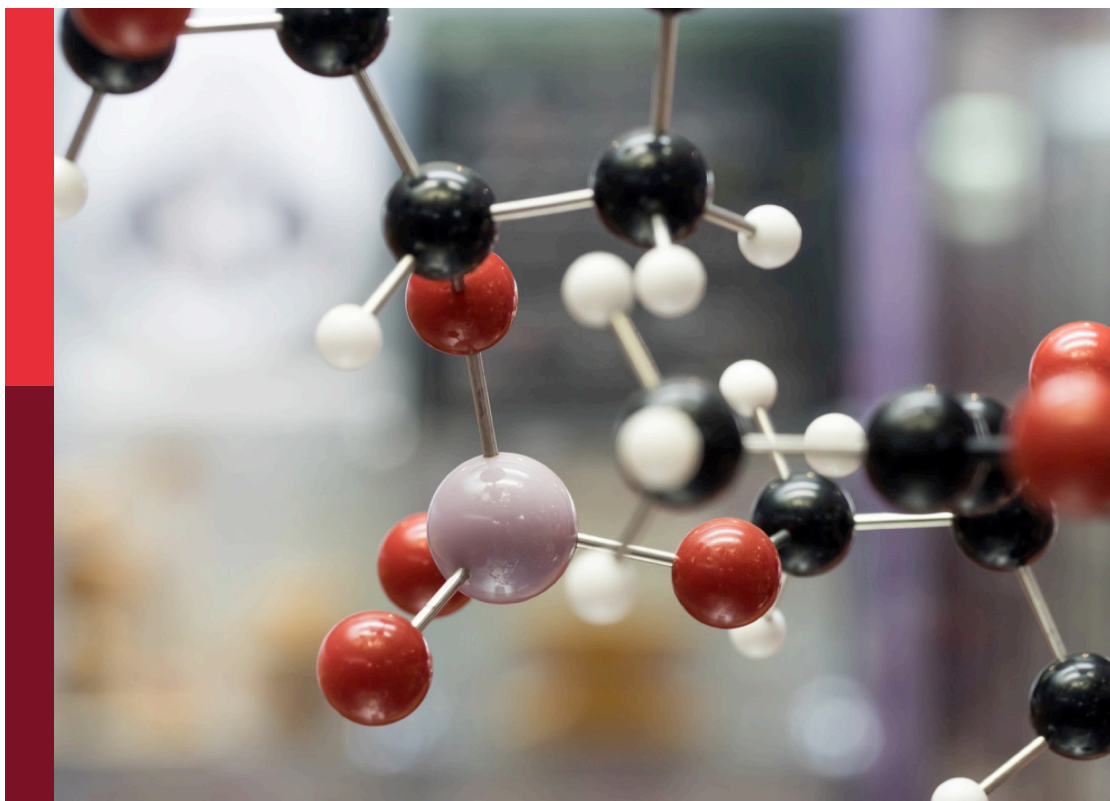## 2024

Edited by
Serge Cosnier and Huangxian Ju

Published in
Frontiers in Chemistry

About Frontiers

Frontiers is more than just an open access publisher of scholarly articles: it is a pioneering approach to the world of academia, radically improving the way scholarly research is managed. The grand vision of Frontiers is a world where all people have an equal opportunity to seek, share and generate knowledge. Frontiers provides immediate and permanent online open access to all its publications, but this alone is not enough to realize our grand goals.

Frontiers journal series

The Frontiers journal series is a multi-tier and interdisciplinary set of open-access, online journals, promising a paradigm shift from the current review, selection and dissemination processes in academic publishing. All Frontiers journals are driven by researchers for researchers; therefore, they constitute a service to the scholarly community. At the same time, the *Frontiers journal series* operates on a revolutionary invention, the tiered publishing system, initially addressing specific communities of scholars, and gradually climbing up to broader public understanding, thus serving the interests of the lay society, too.

Dedication to quality

Each Frontiers article is a landmark of the highest quality, thanks to genuinely collaborative interactions between authors and review editors, who include some of the world's best academicians. Research must be certified by peers before entering a stream of knowledge that may eventually reach the public - and shape society; therefore, Frontiers only applies the most rigorous and unbiased reviews. Frontiers revolutionizes research publishing by freely delivering the most outstanding research, evaluated with no bias from both the academic and social point of view. By applying the most advanced information technologies, Frontiers is catapulting scholarly publishing into a new generation.

What are Frontiers Research Topics?

Frontiers Research Topics are very popular trademarks of the *Frontiers journals series*: they are collections of at least ten articles, all centered on a particular subject. With their unique mix of varied contributions from Original Research to Review Articles, Frontiers Research Topics unify the most influential researchers, the latest key findings and historical advances in a hot research area.

Find out more on how to host your own Frontiers Research Topic or contribute to one as an author by contacting the Frontiers editorial office: frontiersin.org/about/contact

Analytical chemistry editor's pick 2024

Table of contents

Check for updates

Quantification of phospholipids and glycerides in human milk using ultra-performance liquid chromatography with quadrupole-time-of-flight mass spectrometry

Yan Liu[1,2], Weicang Qiao[1,2], Yanpin Liu[1,2], Junying Zhao[1,2], Qian Liu[1,2], Kai Yang[1,2], Minghui Zhang[1,2], Yaling Wang[1,2], Yan Liu[1,2] and Lijun Chen[1,2]*

[1]National Engineering Research Center of Dairy Health for Maternal and Child, Beijing Sanyuan Foods Co. Ltd., Beijing, China, [2]Beijing Engineering Research Center of Dairy, Beijing Technical Innovation Center of Human Milk Research, Beijing Sanyuan Foods Co. Ltd., Beijing, China

Human milk lipids, which are an important source of energy and affect growth and development of infants, require a comprehensive method for its qualitative and quantitative analysis. This work describes a method for the analysis of phospholipids, glycerides, free fatty acids and gangliosides in human milk by ultra-performance liquid chromatography using a C18 column with quadrupole-time-of-flight mass spectrometry (Q-TOF-MS). The lipids were extracted by liquid-liquid extraction and phospholipids were separated by solid phase extraction (SPE). The chromatographic columns with two different specifications (4.6 mm × 150 mm, and 3 mm × 50 mm) were used to detect phospholipids and glycerides in human milk, respectively. The sphingolipids and glycerides were analyzed in positive ion mode, and the glycerophospholipids and free fatty acids were analyzed in negative ion mode. Both internal and external standards were used for absolute quantification in this experiment. 483 species of lipids, including phospholipids, glycerides, free fatty acids and gangliosides, in human milk were analyzed using UPLC-Q-TOF-MS with high sensitivity and good linearity, with coefficient of correlation above 0.99, the relative standard deviation of accuracy and precision less than 10%. The results in a large number of human milk samples showed that this method was suitable for qualitative and quantitative analysis of lipids in human milk, even for other mammalian milk and infant formulae.

KEYWORDS

UPLC-Q-ToF-MS, human milk, lipids, phospholipids, glycerides, gangliosides, quantification

Abbreviations: PC, phosphatidylcholine; PE, phosphatidylethanolamine; PI, phosphatidylinositol; PG, phosphatidylglycerol; PS, phosphatidylserine; PA, phosphatidic acid; SM, sphingomyelin; Cer, ceramides; LPC, lysophosphatidylcholine; LPE, lysophosphatidylethanolamine; LPI, lysophosphatidylinositol; LPG, lysophosphatidylglycerol; LPS, lysophosphatidylserine; LPA, lysophosphatidic acid; DAG, diacylglycerols; TAG, triacylglycerols; FFA, free fatty acid; UPLC-Q-TOF-MS, Ultra-Performance Liquid Chromatography with Quadrupole-Time-of-Flight Mass Spectrometry; LLE, liquid-liquid extraction; SPE, solid phase extraction.

1 Introduction

Lipids are generally defined as a group of organic compounds in living organisms, most of which are insoluble in water but soluble in non-polar organic solvents. Lipids are one of the important nutrients that supply energy and essential fatty acids for the body. Fahy, et al. (2008) categorized lipids into eight classes: fatty acids, glycerides, glycerophospholipids, sphingolipids, sterol lipids, prenol lipids, saccharolipids and polyketides. For human milk, lipids account for 3%–5%, which are the second largest component including 98%–99% glycerides, 0.26%–0.80% phospholipids (including glycerophospholipids and sphingolipids), 0.08%– 0.40% free fatty acids, 0.25%–0.34% cholesterol and 0.001% gangliosides (Delplanque et al., 2015; Zou et al., 2017; George et al., 2018). Studies have shown that the composition of human milk lipids affects growth and development of infants and young children. As for infants and young children, 45%–55% of daily energy is provided by lipids (Caudill, 2010; Contarini and Povolo, 2013). Phospholipids are an indispensable component of cell membrane and organelle membrane, and can resist various metabolic diseases (Verardo et al., 2017). Human milk lipids also play an important role in infants' cell proliferation, small intestine cell maturation, intestinal function, nerve and brain development, immunity and resistance to pathogen invasion, signal transduction, etc., (Sánchez-Juanes et al., 2009; Gallier et al., 2010; Koletzko, 2016). Therefore, it is necessary to comprehensively profile the lipids in tissue samples.

Presently, the traditional liquid-liquid extraction (LLE) methods, including Folch method (Folch et al., 1957) and Bligh & Dyer method (Bligh and Dyer, 1959), are the commonly used methods for lipids extraction, in which chloroform and methanol are both involved. Dichloromethane is also used in some studies (Castro-Gómez et al., 2014; Claumarchirant et al., 2016; Liaw et al., 2016; Yangbo, 2016). Several classes of lipids were extracted by LLE method separately, and the all classes of lipids including phospholipids, glycerides, free fatty acids and gangliosides were extracted by different human milk sample (McJarrow et al., 2019; Liu et al., 2020; Xu et al., 2020; Song et al., 2021; Zhang et al., 2021). Recently, liquid chromatography-mass spectrometry (LC-MS) has been widely used in lipids analysis. The technology of electronic spray ionization-mass spectrometry (ESI-MS) has been widely used in the analysis of lipids for the structure information (Han and Gross, 1994; Han and Gross, 2001; Schwudke et al., 2006). Time of flight-mass spectrometry (TOF-MS) has the advantages of fast scanning speed, fast ion transfer rate and high sensitivity. With the combination of the above two technologies, the accuracy of profiling lipid in complex samples could be effectively improved (Mirsaleh-Kohan et al., 2008; Zhao et al., 2021). Presently, most of the studies extract and detect glycerides, phospholipids and gangliosides by TOF-MS, respectively (Ten-Domenech et al., 2015; Ali et al., 2017; Tu et al., 2017; Jiang C. et al., 2018; George et al., 2020; Bukowski and Picklo, 2021; Song et al., 2021).

Human milk is the gold standard for design of infant formula. Because human milk lipids are affected by maternal genes, diet, environment and other factors (Liaw et al., 2016; Vieira et al., 2018), it is necessary to establish the database of human milk lipids by profiling their representative samples. However, due to the small collection volume of human milk, especially colostrum, the establishment of a human milk lipid database relies on methods which could extracted phospholipids, glycerides, free fatty acids and gangliosides. Therefore, it is necessary to study low volume of human milk with the methods.

This study aims to separate and detect human milk lipids with a method that combines solid phase extraction (SPE), ultra-performance liquid chromatography/quadrupole-time-of-flight mass spectrometry (UPLC-Q-TOF-MS), and electrospray ionization source (ESI). This method enables qualitative and quantitative analysis of lipids, including free fatty acids (FFA), triacylglycerols (TAG), diacylglycerols (DAG), phosphatidylcholine (PC, including LPC (lysophosphatidylcholine)), phosphatidylethanolamine (PE, including LPE (lysophosphatidylethanolamine)), phosphatidylinositol (PI, including LPI (lysophosphatidylinositol)), phosphatidylserine (PS, including LPS (lysophosphatidylserine)), phosphatidylglycerol (PG, including LPG (lysophosphatidylglycerol)), phosphatidic acid (PA, including LPA (lysophosphatidic acid)), sphingomyelin (SM), ceramides (Cer) and ganglioside (GM3 and GD3). This study is intended to provide the method for the analysis of human milk lipids at molecular level and serve as a reference for the subsequent optimization of infant formulae.

2 Materials and methods

2.1 Chemicals and reagents

Methanol, acetonitrile, isopropanol, dichloromethane, chloroform and ammonium acetate were all of LC-MS grade, and purchased from Thermo Fisher Scientific (United States). The standards of phospholipids, including phosphatidylcholine (PC, 18:0/18:2 and 14:1/17:0), phosphatidylethanolamine (PE, 18:0/18:2 and 14:1/17:0), phosphatidylinositol (PI, 16:0/18:1 and 14:1/17:0), phosphatidylglycerol (PG, 16:0/18:1 and 14:1/17:0), sphingomyelin (SM, d20:1/24:0 and d17:0/18:1) and ceramide (Cer, d18:1/24:1 and d18:2/24:0), were purchased from Avanti Polar Lipids (United States). The standards of glycerides, including triacylglycerols (TAG, 16:0/18: 1/18:1 and d5-18:1/18:1/18:1), were purchased from Larodan AB (Sweden) and Shanghai ZZBIO (China), respectively. ProElut Silica (1 g/6 ml) gel bonded cartridges were purchased from Dikma Technologies (United States).

2.2 Samples collection

Human milk samples were collected from healthy Chinese women. All the volunteers provided three samples including colostrum of 0–5 d, transitional milk of 10–15 d and mature milk of 30 d. All the volunteers had normal physical indicators whose infants were delivered at full term (38–42 weeks of gestation) without congenital or genetic disease. The milk sample was collected from one breast at morning according to a standardized sample collection instruction. The collected human milk was stored at the -80°C refrigerator for later use. The study was approved by Ethics Committee of Beijing Ditan Hospital affiliated to Capital Medical University (#2015-027-01), and all the subjects signed on the informed consent form. The study was also registered at clinicaltrials.gov (with Registration No: NCT02658500).

Bovine milk, goat milk, camel milk, horse milk, and donkey milk were purchased from producers in Beijing, Dalian, Alxa, Urumqi and

Jinan, respectively. Infant formulae were purchased from a supermarket in Beijing.

2.3 Extraction of lipids from human milk

The lipid extraction procedure was established according to the Bligh & Dyer method (Bligh and Dyer, 1959) with minor modifications. The standards were dissolved to appropriate concentrations with methanol/dichloromethane (1:1, v/v) solution of 5 mM ammonium acetate. Infant formula (1.0 g) was dissolved in ultrapure water (9.0 ml) before extraction. The 200 µL of sample was mixed with the internal standards of 20 µL PC 14:1/17:0 (10.38 mg/L), 20 µL PE 14:1/17:0 (9.64 mg/L), 20 µL SM d17:0/18:1 (10.00 mg/L), 8 µL PI 14:1/17:0 (10.22 mg/L), 4 µL PG 14:1/17:0 (9.81 mg/L), 4 µL Cer d18:2/24:0 (10.00 mg/L) and 20 µL d5-TAG 18:1/18:1/18:1 (4000 mg/L).

First LLE: The mixture mixed with 200 µL ultrapure water, 2 ml methanol and 900 µL dichloromethane were subjected to vortex mixing for seconds, and then 200 µL ultrapure water and 900 µL dichloromethane were added and vortex mixed again. The mixture was centrifuged at 6000 rpm for 15 min to separate the organic phase and aqueous phases.

Second LLE: The aqueous phase extracted by first LLE was mixed with 1.8 ml dichloromethane and centrifuged at 6000 rpm for 15 min to separate the organic phase and aqueous phases.

Third LLE: The organic phase extracted by first LLE was mixed with 1 ml ultrapure water, 2.2 ml methanol and 600 µL dichloromethane and centrifuged at 3000×g for 10 min to separate the organic phase and aqueous phase.

The organic phases obtained from the second and third LLE, as well as the aqueous phase obtained from the second and third LLE were then combined and blown to dry with nitrogen, respectively. The samples from the dried aqueous phase were redissolved in 200 µL methanol/ultrapure water (4:1, v/v) solution for gangliosides detection. And the samples from the dried organic phase were redissolved in 1 ml of methanol/dichloromethane (1:1, v/v) solution of 5 mM ammonium acetate. 50 µL reconstitution sample were diluted 200 times with methanol/dichloromethane (1:1, v/v) solution of 5 mM ammonium acetate for direct detection of glycerides. The other 950 µL reconstitution sample were extracted by solid phase to obtain polar lipids (Ali et al., 2017) as the following.

Firstly, the solid phase (silica cartridges) was activated with 3 ml n-hexane, then 950 µL reconstitution sample was poured into the cartridges, and kept still for 5 min. The non-polar lipids were eluted by 3 ml of hexane/diethyl-ether (8:2, v/v) and 3 ml of hexane/diethyl-ether (1:1, v/v). The polar lipids were eluted with 4 ml of methanol and 4 ml of chloroform/methanol/ultrapure water (3:15:2, v/v/v). The eluted liquid were blown to dry with nitrogen, and redissolved in 190 µL methanol/dichloromethane (1:1, v/v) solution of 5 mM ammonium acetate for the analysis of phospholipids.

2.4 Separation conditions by liquid chromatography

The human milk phospholipids were separated on a Kinetex C18 column (Phenomenex, 4.6 mm × 150 mm, 2.6 µm). The injection volume of 2 µL, and the column temperature of 30°C were adopted as the chromatographic conditions. The water/methanol/acetonitrile (v/v/v, 1:1:1) solution of 5 mM ammonium acetate was used as mobile phase A, and the isopropanol solution of 5 mM ammonium acetate was used as mobile phase B. The flow rate was 0.8 ml/min within a total run time of 20 min. The elution gradient was as follows: 0 min, 50% B; 1.0 min, 98% B; 10.0 min,98% B; 15.0 min, 50% B; 20 min, 50% B.

The human milk glycerides were separated on a Kinetex C18 column (Phenomenex, 3 mm × 50 mm, 2.6 µm). The injection volume of 2 µL, and the column temperature of 50°C were adopted as the chromatographic conditions. The water/methanol/acetonitrile (v:v:v, 1:1:1) solution of 5 mM ammonium acetate was used as mobile phase A, and the isopropanol solution of 5 mM ammonium acetate was used as mobile phase B. The flow rate was 0.3 ml/min within a total run time of 10 min. The elution gradient was as follows: 0 min, 50% B; 5.0 min, 98% B; 8.0 min,98% B; 8.01 min, 50% B; 10 min, 50% B.

The human milk gangliosides were separated on a BEH C18 column (Waters, 2.1 mm × 100 mm, 1.7 µm). The injection volume of 10 µL, and the column temperature of 50°C were adopted as the chromatographic conditions. The methanol/water (v/v, 1:9) solution of 1 mM ammonium acetate was used as mobile phase A, and the methanol solution of 1 mM ammonium acetate was used as mobile phase B. The flow rate was 0.3 ml/min within a total run time of 14 min. The elution gradient was as follows: 0 min, 90% B; 0.13 min, 90% B; 3.13 min, 95% B; 4.13 min, 95% B; 6.27 min, 100% B; 12.27 min, 100% B; 12.40 min, 90% B; 14.00 min, 90% B.

2.5 Detection conditions of Q-TOF mass spectrometry

The Triple TOF 6600 instrument of AB SCIEX Company was used for detection of human milk phospholipids, glycerides and free fatty acids with ESI source in positive and negative ion modes. MS and MS/MS data were scanned in the range of 50–1300 m/z. The spray voltage of ion source was 5500 V, the declustering potential was 80 V, and the collision energy was 10 V in positive ion mode. And the spray voltage of ion source was −4500 V, the declustering potential was −80 V, and the collision energy was −10 V in negative ion mode. The gas pressure of ion source was 60 psi, the curtain gas pressure was 35 psi and the temperature of ion source was 650°C in both positive and negative ion modes.

The Q-TOF-MS instrument was used for detection of human milk gangliosides with ESI source in negative ion modes. MS and MS/MS data were scanned in the range of 100–2000 m/z. The spray voltage of ion source was −4500 V, the declustering potential was −40 V, and the collision energy was −40 V. The gas pressure of ion source was 40 psi, the curtain gas pressure was 15 psi and the temperature of ion source was 400°C.

2.6 Data analysis

The data collected by the Analyst 1.7.1 software were qualitatively analyzed by PeakView 2.2 software according to the fragments of lipids and were quantitatively analyzed by MultiQuant 3.0.2.

The methods for both internal and external standards were used for accurate quantification of phospholipids and glycerides in this experiment. Calibration curves were plotted with the gradient external standards as the abscissa and the ratio between the corresponding areas of external and internal standards as the ordinate. The peak areas of the internal standards, human milk phospholipids and human milk glycerides were integrated from extracted ion chromatograms (EICs). Each lipid class was quantified by one corresponded pair internal-external standard The final concentrations of lipids were expressed in mean ± standard deviations (mg/L).

2.7 Method validation

Human milk, and external and internal standards of lipids were used to determine the accuracy, precision, sensitivity, and linearity of the method to validate the method. The limit of detection (LOD) and the linear range of phospholipids and glycerides were determined using internal and external standards. The sensitivity was measured using LOD for each lipid from triplicate measurements. A series of eight dilutions were prepared for phospholipids and glycerides. A gradient series of external and internal standards from 0.001 to 5 mg/L were analyzed in triplicate to evaluate the linearity.

The sample without external standards was set as matrix and the recovery of added external standards was studied at the content similar to the sample. All of the samples need to spike internal standard whose concentrations were written on 2.3.1 and six parallel samples were determined. Three specific concentration levels of external standards of each lipid were as follows: PC, PE: 5 mg/L, 2.5 mg/L, 1.25 mg/L, PI: 0.8 mg/L, 0.4 mg/L, 0.2 mg/L, PG, Cer: 0.4 mg/L, 0.2 mg/L, 0.1 mg/L, SM: 2 mg/L, 1 mg/L, 0.5 mg/L, OPO: 8000 mg/L, 4000 mg/L, 2000 mg/L. The accuracy was evaluated from recovery rate (%). Accordingly, the recovery rate was calculated from the peak area obtained. The precision was estimated by determining low, medium, and high concentrations of external standards of lipids, which was calculated as the relative standard deviation (RSD) of each lipid from six injections. The repeatability of the method was determined by repeated analysis of human milk quality control samples in each batch of analysis carried out on different days over the course of this study. Three parallel samples were prepared for the investigation of repeatability among 3 days.

3 Results

3.1 Optimization of extracting solvents of lipids

Traditional lipid extraction method is mostly based on LLE introduced by Folch et al. (1957) and modified by Bligh and Dyer (Bligh and Dyer, 1959; Garwolinska et al., 2017), which requires substantially large volumes of toxic organic solvents such as chloroform. In this method, lipids was extract from human milk with dichloromethane instead of chloroform, because dichloromethane was less toxic than chloroform (Wernke and Schell, 2004).

The extraction procedure used in the current study was selected by comparing the results in the species number of extracted lipids. Different lipid extraction solvents were tested in the experiment,

TABLE 1 Species numbers of human milk lipids extracted by different extraction solvents.

	Dichloromethane	Chloroform
PC	14 (including 1 LPC)	6 (including 3 LPC)
PE	25 (including 4 LPE)	12 (including 5 LPE)
PI	11	5 (including 1 LPI)
PS	13 (including 1 LPS)	1
PG	7 (including 1 LPG)	4 (including 2 LPG)
PA	3	6 (including 2 LPA)
SM	14	24
Cer	5	5
DAG	17	16
TAG	107	92
FFA	23	18
Total	239	189

and each assay was performed in triplicate. Table 1 shows the species number of lipids in human milk extracted by dichloromethane and chloroform, respectively. Compared with chloroform, dichloromethane could extract more species of human milk lipids.

In terms of the number of lipid species, dichloromethane could extract more species of phospholipids (except PA), glycerides and free fatty acids, while chloroform was good at extracting lysophospholipids and sphingolipids. Chloroform only extracted three unsaturated phospholipids, which accounted for 8.8% in the species amount of total glycerophospholipids. High-content glycerophospholipids such as PC 36:2, PE 36:2 and PI 36:2 (Zhao et al., 2021) were not extracted by chloroform. Unsaturated fatty acids, especially polyunsaturated fatty acids, play a crucial role in infant growth, and the development of brain and vision (Glaser et al., 2015; Kevin et al., 2016). Most of the phospholipids in human milk contain unsaturated fatty acids (Lee et al., 2011; Ali et al., 2017; Ingvordsen Lindahl et al., 2019). If a few species of unsaturated phospholipids can be detected by chloroform, it will affect the qualitative and quantitative analysis of phospholipids in human milk. As an extraction solvent, dichloromethane not only can extract more species of lipids, but also has lower toxicity than chloroform. Therefore, dichloromethane is chosen to extract lipids from human milk.

3.2 Identification of lipids

Various informative fragments in MS/MS mode can be used to differentiate lipid classes and species. Due to the structural diversity of lipids, it is necessary to combine positive and negative ion modes to achieve a comprehensive and clear identification. The optimum instrument detection conditions of human milk phospholipids were decided by MS/MS fragment. Figure 1 shows the mass to charge ratios and retention time range of each lipid class in human milk.

tThe glycerides were identified in positive ion mode with the adduct ion of "+NH$_4$", and the produced fragments included [M − R$_1$]$^+$, [M −
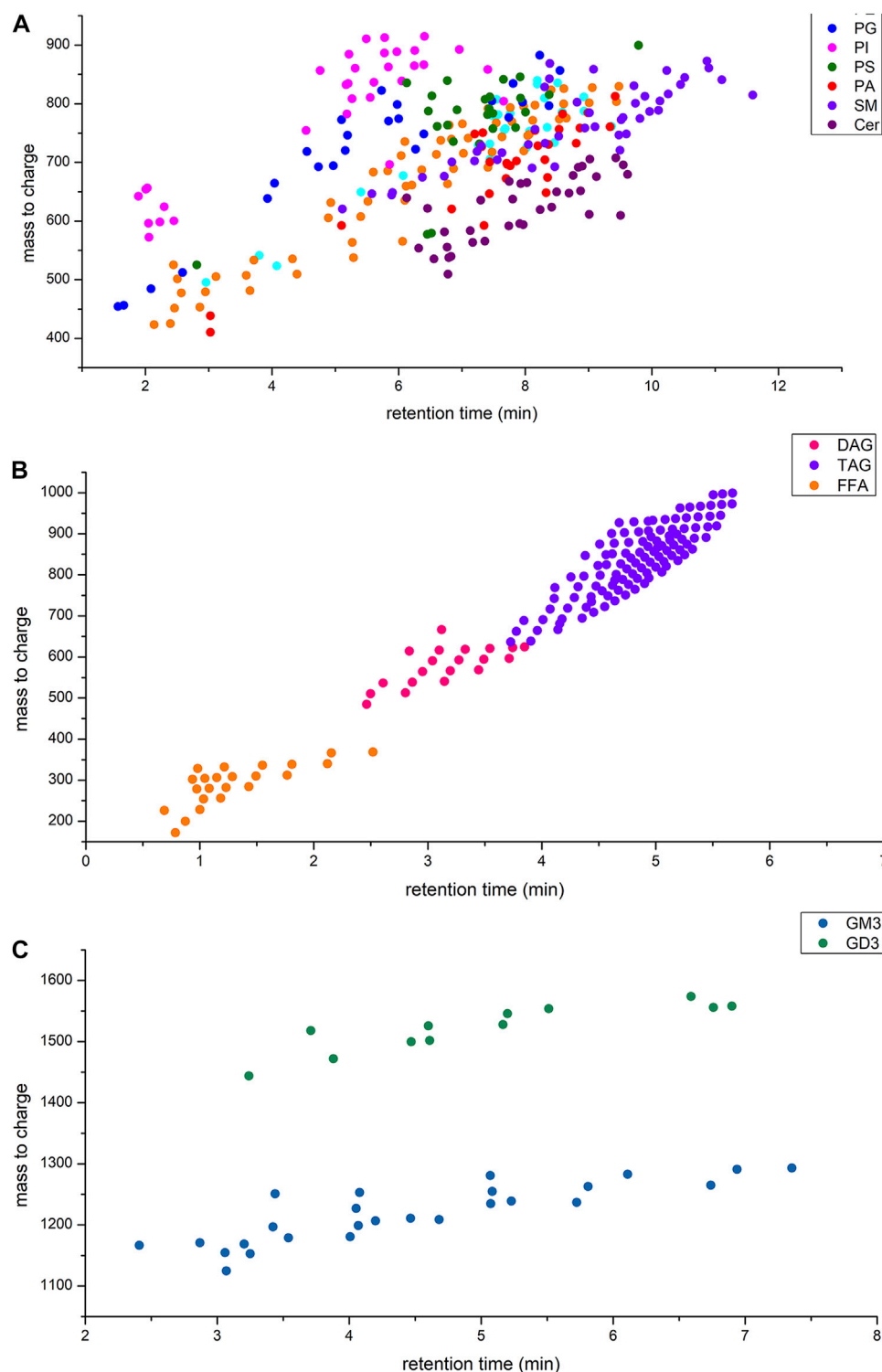
FIGURE 1
(A) Retention time and mass to charge ratios of phospholipids in human milk; **(B)** Retention time and mass to charge ratios of glycerides and free fatty acids in human milk; **(C)** Retention time and mass to charge ratios of gangliosides in human milk.

R_2]+and [M − R_3]+in MS/MS. For DAG, one fatty acyl was replaced by oxhydryl. The fatty acyl composition could be calculated by subtracting the fragments from glycerides, respectively (Supplementary Figure S1). Free fatty acid could be directly identified under negative ion mode with [M − H] $^-$ fragment (Supplementary Figure S1). Under the negative ion

mode, the adduct ion of PE, PG, PI, PS and PA was "-H$^+$" and that of PC was "+CH3COO$^-$". The adduct ion of sphingolipids was "+H$^+$" under positive ion mode (Table 2). For PE and PS, the fragment of fatty acyl was produced under negative ion mode and the fragment of phospholipids residue losing a head group was identified in positive

TABLE 2 Characteristic fragments of lipids by UPLC-Q-TOF-MS.

Lipid	Mode	Precursor Ion	Characteristic Fragment
PC	ESI⁻	[M + CH3COO]⁻	[R$_1$-H]⁻ [R$_2$-H]⁻
PE	ESI⁻	[M-H]⁻	[R$_1$-H]⁻ [R$_2$-H]⁻
PI	ESI⁻	[M-H]⁻	[R$_1$-H]⁻ [R$_2$-H]⁻
PS	ESI⁻	[M-H]⁻	[R$_1$-H]⁻ [R$_2$-H]⁻
PG	ESI⁻	[M-H]⁻	[R$_1$-H]⁻ [R$_2$-H]⁻
PA	ESI⁻	[M-H]⁻	[R$_1$-H]⁻ [R$_2$-H]⁻
SM	ESI⁺	[M + H]⁻	184.07
Cer	ESI⁺	[M + H]⁻	264.26/266.28
DAG	ESI⁺	[M + NH4]⁺	[M-R$_1$]+[M-R$_2$]⁺
TAG	ESI⁺	[M + NH4]⁺	[M- R$_1$]+[M- R$_2$]+[M- R$_3$]⁺
FFA	ESI⁻	[M-H]⁻	[M-H]⁻
GM3	ESI⁻	[M-H]⁻	290.08
GD3	ESI⁻	[M-2H]²⁻	290.08

ion mode (Supplementary Figures S2, S3). MS/MS spectra of PI, PG, PA demonstrated abundant ions corresponding to the loss of fatty acyl [R$_1$]- and [R$_2$]-under negative ion mode but no characteristic fragment under positive ion mode (Supplementary Figures S4–6). Therefore, PE, PG, PI, PS and PA were identified under negative ion mode so that the fatty acids composition could be identified easily. For PC and SM containing choline, the phosphocholine fragment ion m/z 184 was produced under positive ion mode (Supplementary Figures S7, S8). Under negative ion mode, the characteristic fragments of PC lost fatty acyl [R$_1$]-and [R$_2$] ⁻, however, no characteristic fragment of SM was observed. The LCB-2H$_2$O (long chain base) ion in positive ion mode (+H⁺) and [R$_1$]-in negative ion mode (-H⁺) was allowed for the characterization of detailed structure of Cer (Supplementary Figure S9). The extracted ion chromatogram (XIC) had better base line and chromatographic peak in negative mode, but the fatty acid anions intensity is low. The characteristic fragment ion m/z 264 or 266 showed that the corresponding LCB-2H$_2$O included oleic acid (C18:1) or stearic acid (C18:0), respectively.

For phospholipids, the characteristic fragments of sphingolipids and glycerophospholipids need to be collected in positive and negative ion mode, respectively. Thus, the chromatographic method was established based on two consecutive separations of phospholipids by LC. The method was used in the positive ion mode for the first run followed by a data dependent MS-MS analysis, and then the same chromatography method was used for reanalysis in the negative ion mode for the second run. Glycerides (positive ion mode) and free fatty acids (negative ion mode) were detected in the same way as phospholipids.

The gangliosides were identified in negative ion mode, the adduct ion of GM3 was "-H" and GD3 was "-2H ²⁻". And sialic acid fragment ion m/z 290 was produced as the characteristic fragment of GM3 and GD3 (Supplementary Figure S10).

All in all, lipids qualitative analysis used m/z with adduct ion to extract secondary mass spectra from TIC and the corresponding characteristic fragments were used to identified lipids species. The typical extracted ion chromatogram of lipids were shown in

Supplementary Figure S11. The characteristic fragments of each class of lipids were shown in Table 2. Although some lipids that mass to charge were similar (Figure 1), they have the different headgroup or fatty acids composition. Thus, this qualitative analysis method could distinguish lipids species clearly and ensure the reliability of results.

3.3 Method validation

According to the contents of various lipids in human milk, the external standards of different concentrations were prepared, a gradient series of external and internal standards were analyzed in triplicate to evaluate the linearity. The standard curves were plotted with the gradient concentration of external standards as the abscissa and the corresponding area ratio between external and internal standards as the ordinate. The regression equations and coefficient of determination R^2 are shown in Table 3. Among the concentration range of phospholipids and glycerides, the correlation coefficients are all above 0.99 within the working range. LOD is defined as the smallest amount of a lipid that could be identified from the characteristic fragments required for qualitative analysis. The LODs for most lipids were well below 0.001 mg/L (Table 3), demonstrating high sensitivity of this method.

Human milk sample was used as a matrix in the experiment to measure recovery. It was determined that the spiked samples of three-level standards were within the working range. Three specific concentration levels of external standards of each lipid were determined 6 times. The average recovery rate of various lipids was 79.21%–117.98%. The experimental results (Table 4) showed that the analytical method could meet the quantitative detection requirements. The precision of the method was evaluated using the mixed lipid standards. Mixed lipid standards were prepared and determined 6 times during the day and night, respectively. The relative standard deviation (RSD) of the lipids concentration was 1.98%–9.80%. It could be known from the result shown in Table 4 that the instrument method had good precision. Through the detection of the same human milk sample for 3 days, it could be seen that the RSD of this method was 6.35%–12.89%, which was less than 15% and could meet the requirement of mass spectrometry repeatability.

3.4 Application of the method in human milk, other mammalian milk, and infant formulae

Figure 2; Figure 3 showed the result of 57 human milk samples, including colostrum, transitional milk and mature milk. The species of phospholipids, glycerides, free fatty acids and gangliosides were qualitatively analyzed, and the concentrations of phospholipids, glycerides were absolutely quantitatively analyzed by internal standard method.

In the human milk, there were totally 483 species of lipids, including 21 species of PC, 60 species of PE, 18 species of PI, 21 species of PS, 20 species of PG, 24 species of PA, 46 species of SM, 35 species of Cer, 29 species of DAG, 148 species of TAG, 23 species of FFA, 26 species of GM3 and 12 species of GD3. The list of lipids identified in human milk were shown in Supplementary Tables S1–3. In the transitional milk, the species of total lipids were the most abundant. Among three lactation stages, the species number of

TABLE 3 LOD, LOQ, linearity of lipid standards and corresponding internal standards.

Standard	Internal standard	LOD (mg/L)	Calibration equations	R^2	Range (mg/L)
PC (18:0/18:2)	PC (14:1/17:0)	0.0006	Y = 1.0891X+0.0064	0.9995	0.0025–5
PE (18:0/18:2)	PE (14:1/17:0)	0.0005	Y = 1.7927X-0.0274	0.9993	0.0025–5
PI (16:0/18:1)	PI (14:1/17:0)	0.0005	Y = 6.0527X-0.3599	0.9986	0.001–1
PG (16:0/18:1)	PG (14:1/17:0)	0.0003	Y = 7.9927X-0.1704	0.9995	0.001–1
SM (d18:1/24:0)	SM (d18:1/17:0)	0.0005	Y = 0.6395X-0.0018	0.9980	0.0025–5
Cer (d18:1/24:1)	Cer (d18:2/24:0)	0.0008	Y = 3.7307X-0.0617	0.9927	0.001–1
TAG (16:0/18:1/18:1)	TAG (16:0/18:1/18:1 (d5))	0.0001	Y = 7.5236X+0.1681	0.9993	0.0025–5

TABLE 4 Repeatability (RSD, %) of standards and sample.

Standard	Internal standard	Standard addition concentration	Recovery%	Repeatability%	RSD% (day)	RSD% (night)
PC (18:0/18:2)	PC (14:1/17:0)	5	97.1	9.39	2.86	3.57
		2.5	93.17		4.31	7.63
		1.25	113.55		7.20	9.43
PE (18:0/18:2)	PE (14:1/17:0)	5	102.1	6.35	8.92	7.07
		2.5	90.38		5.13	2.02
		1.25	117.98		7.47	3.76
PI (16:0/18:1)	PI (14:1/17:0)	0.8	95.3	8.88	7.58	6.85
		0.4	84.79		5.41	4.62
		0.2	102.53		8.91	4.28
PG (16:0/18:1)	PG (14:1/17:0)	0.4	102.6	10.68	6.46	1.98
		0.2	86.32		7.68	2.45
		0.1	108.35		6.58	2.19
SM (d18:1/24:0)	SM (d18:1/17:0)	2	91.1	11.51	7.46	9.26
		1	79.21		7.05	7.05
		0.5	115.07		8.46	8.10
Cer (d18:1/24:1)	Cer (d18:2/24:0)	0.4	94.7	12.89	7.03	6.24
		0.2	82.65		9.80	8.96
		0.1	80.04		9.21	6.39
TAG (16:0/18:1/18:1)	TAG (16:0/18:1/18:1 (d5))	8000	94.5	10.87	5.51	4.66
		4000	81.51		5.68	5.83
		2000	104.54		7.84	9.21

glycerides in mature milk was the most, the species number of PC, PE, PI, and PA in transition milk was the most, the species number of PG, SM, and Cer in colostrum milk was the most, and the species number of PS was basically stable in three lactation stages. The species of DAG in transitional milk and mature milk were significantly higher than those in colostrum, and the species of PA in transitional milk were significantly lower than those in colostrum and mature milk. There was no significant difference between the species of Cer in transitional milk and those in mature milk, but the species of Cer in colostrum were significantly higher than those in mature milk.

The internal standards of PS, PA, FFA, GD3 and GM3 were not added; therefore, they were not accurately quantified in this study. The concentrations of TAG were higher than those of other lipids in human milk, it accounted for more than 98% of the lipids measured, with concentration significantly increased from 15441.6 mg/L in colostrum to 35996.3 mg/L in mature milk. Meanwhile, the
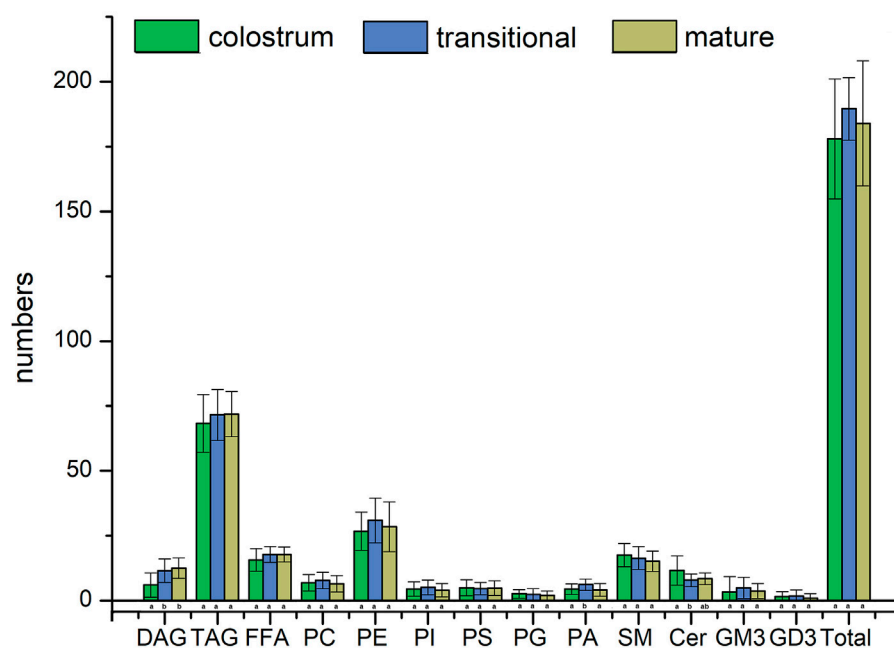
FIGURE 2
Species number of human milk lipids at different lactation stages.
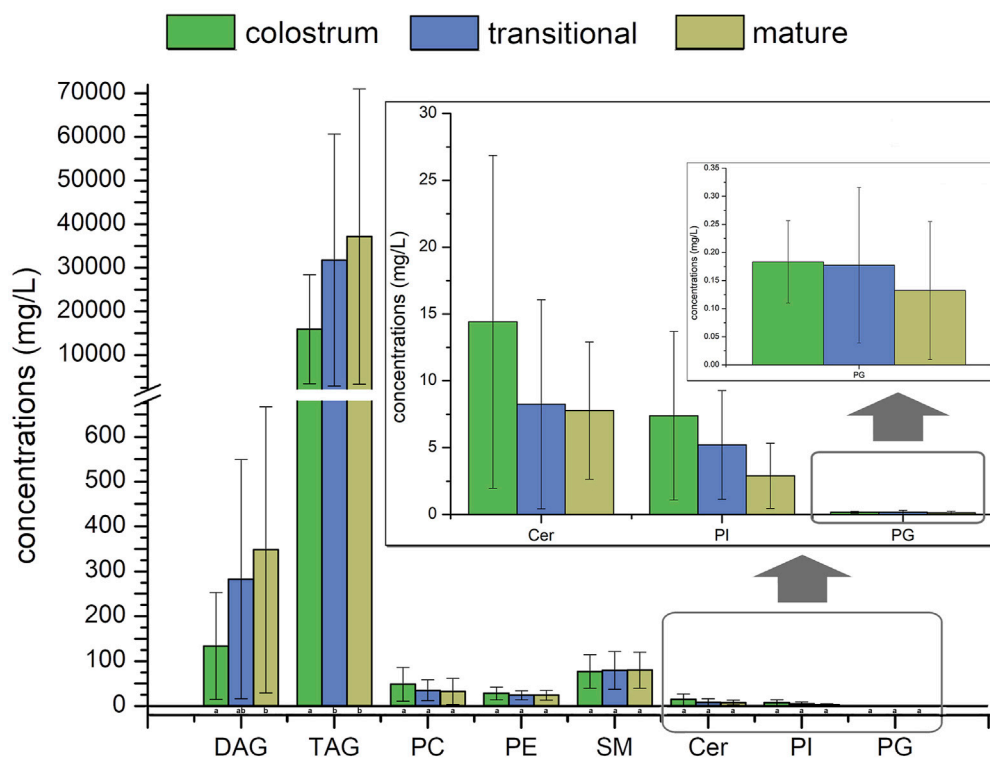
FIGURE 3
Concentrations of human milk lipids at different lactation stages.

concentrations of SM were higher than that of other phospholipids in human milk, accounting for more than 44% of the phospholipids measured, with concentration increased from 76.9 mg/L in colostrum to 79.7 mg/L in mature milk. In addition, the concentrations of DAG increased with the lactation phase, and the concentrations of other phospholipids decreased with the lactation phase.
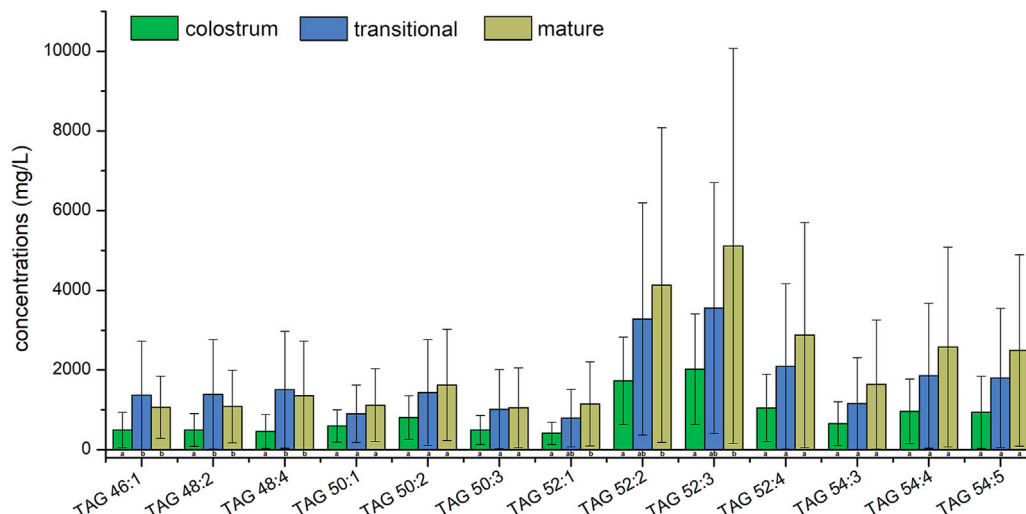
FIGURE 4
Average concentrations of top ten human milk glycerides at different lactation stages.
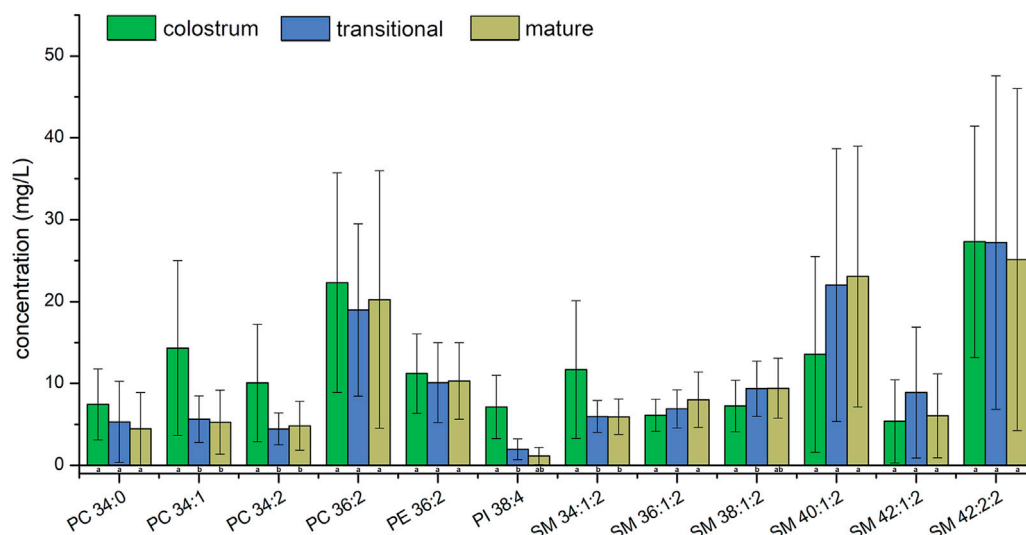
FIGURE 5
Average concentrations of top ten human milk phospholipids at different lactation stages.

Top ten lipids of average concentration in three stages were shown in Figure 4; Figure 5, the species of top ten glycerides and phospholipids were a bit different among three stages. Only four TAGs, including TAG 48:4, TAG 50:2, TAG 52:2, and TAG 54:4 was detected in all of the human milk samples. The glycerides of TAG52:3, TAG52:2, TAG 52:4, and TAG 54:4 had the highest concentrations which totally accounted for more than 31.6% in all glycerides and increased gradually among three stages. The concentrations of TAG 46:1, TAG 48:2, and TAG 48:4 in transitional milk and mature milk were significantly higher than those in colostrum. There was no significant difference between the concentrations of TAG 52:1, TAG 52:2, and TAG 54:4 in mature milk and those in transitional

milk, but the concentration of those in mature milk were significantly higher than those in colostrum.

The concentrations of PC 36:2, PE 36:2 and SM 42:2;2 were the highest among all PC, PE and SM in three stages, respectively. Although the concentrations of PI 38:4 was highest among PIs molecular species in colostrum, it was the second highest in transitional milk and mature milk while that of PI 36:2 was the highest. Only SM 34:1;2 and SM 42:2;2 were detected in all of the human milk samples. The phospholipids of SM 42:2;2 had the highest concentration which accounted for more than 11.1% in all phospholipids among three stages and the proportion of the top ten lipids in total lipids gradually increased. The concentrations of

TABLE 5 The total species number of lipids in other mammalian milk and infant formula.

Lipids	Human milk	Bovine milk	Goat milk	Camel milk	Horse milk	Donkey milk	Infant formula
PC	21	13	8	10	10	4	13
PE	60	27	29	28	34	17	25
PI	18	17	12	12	15	7	17
PS	21	8	7	9	5	2	6
PG	20	8	3	7	8	0	6
PA	24	8	6	7	7	1	5
SM	46	25	17	17	15	21	25
Cer	35	7	7	9	5	6	8
DAG	29	10	3	4	2	0	13
TAG	148	117	97	92	94	57	115
FFA	23	8	11	8	9	9	5
GM3	26	0	1	7	0	0	0
GD3	12	9	3	0	0	0	5
Total	483	249	204	209	204	124	243

PC 34:1, PC 34:2, and SM 34:1;2 in transitional milk and mature milk were significantly lower than those in colostrum. There was no significant difference between the concentrations of PI 38:4 and SM 38:1;2 in mature milk and those in transitional milk, but the concentrations of those in transitional milk were significantly lower than those in colostrum.

Among the top ten concentration PIs, PI 38:4 is rich in arachidonic acid (AA, C20:4), which is more abundant in colostrum. AA is critical for growth, brain development, and health of infants (Kevin et al., 2016), therefore, PI 38:4 may be an important source of AA in phospholipids from human milk. Linoleic acid (C18:2) is an essential fatty acid existing in TAG 50:3, TAG 52:3, TAG 52:4, TAG 54:4, TAG 54:5, PC 34:2, PC 36:2, and PE 36:2 with high concentration.

The species number of lipids in human milk were more abundant than that in other mammalian milk and infant formula (Table 5). Other mammalian milk and infant formula had more than 200 species of lipids, including phospholipids, glycerides, free fatty acids and gangliosides. However, there were only 124 species of lipids in donkey milk.

For human milk, other mammalian milk and infant formula, totally 556 species of lipids were detected, including 29 species of PC, 61 species of PE, 27 species of PI, 32 species of PS, 25 species of PG, 28 species of PA, 46 species of SM, 35 species of Cer, 30 species of DAG, 176 species of TAG, 23 species of FFA, 26 species of GM3 and 18 species of GD3. 68 species of lipids existing in other mammalian milk or infant formulae were not detected in human milk. Total concentrations of phospholipids and total glycerides in human milk, other mammalian milk and infant formula were shown in Figure 6. Compared with those in the majority of other mammalian milk and infant formula, the concentration of total phospholipids and total glycerides were present in greater amounts in human milk. The concentration of total phospholipids in camel milk were highest among these samples while those of total phospholipids and total glycerides in donkey milk were lowest.

4 Discussion

Human milk lipids provide energy for the growth and development of infants (Tingting, 2008). Different molecular components of glycerides and phospholipids in human milk are closely related to their physiological functions (Huang et al., 2013; Zhao et al., 2021). Therefore, an accurate and reliable method is essential for a comprehensive identification and absolute quantitation of lipids at molecular level. The extraction, separation, identification and quantification methods of lipids from human milk and dairy products are shown in Table 6.

LLE technique was used to separate lipids by their relative solubilities in different immiscible liquids (George et al., 2018). Extracting solvents and process were key to obtain lipids from samples. In the Folch (Folch et al., 1957) and Bligh–Dyer(Bligh and Dyer, 1959) method, chloroform was commonly used to extract lipids from human milk or dairy products (Sala Vila et al., 2003; Ten-Domenech et al., 2015; Claumarchirant et al., 2016; Tang et al., 2021). When chloroform is exposed to light, it could react with oxygen in the air and is gradually decomposed to produce the highly toxic phosgene, which has anesthetic effect on heart, liver and kidney. The data analysis of human milk lipids requires to process a large number of samples and it might be harmful to the health of the operators who have been engaged in the detection for a long time. Therefore, safety solvents are beneficial for the health of the operator and it is necessary to establish safer and more reliable methods. We extracted lipids for 3 times with dichloromethane instead of chloroform in this study, and obtained aqueous phase containing gangliosides and organic phase containing glycerides and phospholipids. In contrast, most of studies used twice extraction (Jiang C. et al., 2018; Alexandre-Gouabau et al., 2018; Tavazzi et al., 2018; Moloney et al., 2020) or once extraction (Sokol et al., 2015; Li et al., 2017; Liu et al., 2020; Song et al., 2021). However, fewer
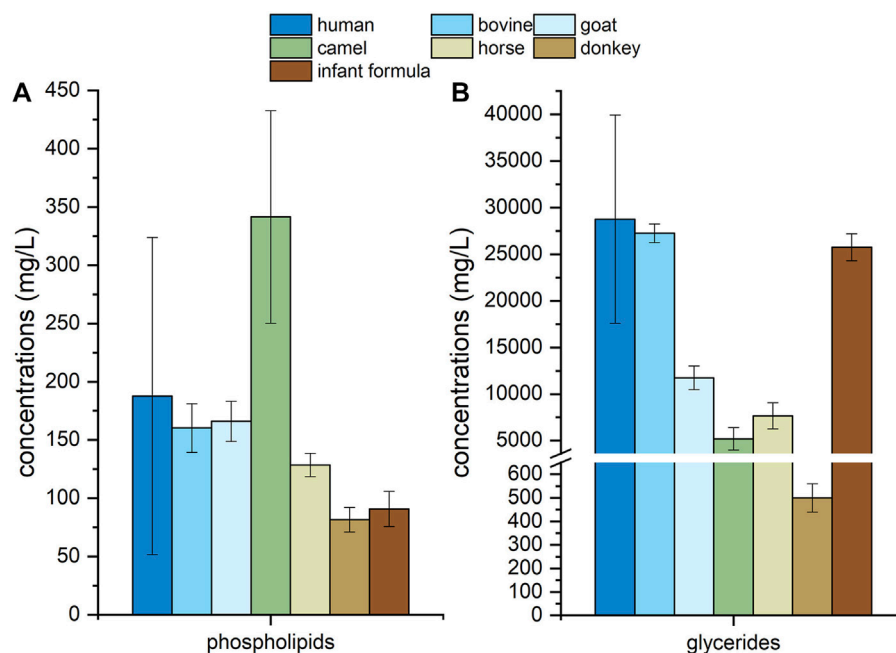
FIGURE 6
Concentrations of phospholipids **(A)** and glycerides **(B)** in human milk, mammalian milk and infant formula.

species of glycerides and phospholipids were obtained and ganglioside was not enriched.

The concentrations of glycerides and phospholipids accounted for about 98% and 0.8% in human milk lipids, respectively (Delplanque et al., 2015; Zou et al., 2017; George et al., 2018), leading to the wide concentration range of different lipid subclasses in human milk. If all lipid classes were quantified simultaneously in one analytical cycle, the MS signal of main glycerides could become saturated, which would not only influence quantitative results, but also contaminate the instrument. Meanwhile, the MS signals for phospholipid and ganglioside classes were very low. Therefore, the organic phase needs to be further processed with solid phase extraction to obtain phospholipids. The silica SPE column, which was usually applied in the separation of polar and non-polar lipids and showed good accuracy (Contarini and Povolo, 2013; Verardo et al., 2017), was used in this method. The obtained phospholipids could be detected without dilution and with high signal intensity.

This method not only reduced the use of hazardous chloroform solvent, but also extracted phospholipids, glycerides and free fatty acids, even gangliosides in an individual process. In contrast, only a few of methods could extract two or more classes of lipids among phospholipids, glycerides, free fatty acids and gangliosides in human milk through one preparation process (Sokol et al., 2015; Garwolinska et al., 2017; Alexandre-Gouabau et al., 2018; Wang et al., 2020). In published studies, gangliosides only could be extracted from human milk individually or together with phospholipids that used more than 250 μL human milk (McJarrow et al., 2019; Liu et al., 2020). Other lipid extraction methods usually extract glycerides, phospholipids and gangliosides, respectively (Zou et al., 2013; Wei et al., 2019a; Wei et al., 2019b), which require more solvents, human milk samples, and long and complex extraction process.

In the present study, glycerophospholipids and sphingolipids were detected in negative mode and positive mode, respectively. In contrast, many studies detected glycerophospholipids and sphingolipids in the same ion mode (Garwolinska et al., 2017; Jiang C. et al., 2018; Song et al., 2018; Ingvordsen Lindahl et al., 2019; Mitina et al., 2020; Garwolinska et al., 2021). Some studies only identified headgroup of glycerophospholipids, the number of carbon atoms and double bonds in total fatty acyls through fragment, without fatty acyls moieties (Garwolinska et al., 2017; Tavazzi et al., 2018). Meanwhile, most studies identified glycerophospholipids through the residue losing a fatty acyl (Donato et al., 2011; Ali et al., 2017; Jiang C. et al., 2018; Liu et al., 2020) for qualitative analysis of glycerophospholipids. In contract, this study could identify the fatty acid composition of glycerophospholipids more easily according to m/z of fragment. Cer and gangliosides could also be detected in negative ion mode, and more lipids classed (HexCer, Hex2Cer) and fatty acid composition were identified by MS/MS and MS³ (Calvano et al., 2019). Meanwhile, milk sphingolipids, including (SM and Cer), were detected in positive mode in most of the literature (Liu et al., 2020; Wang et al., 2020; Zhao et al., 2021) and the comparison results of this method shows that the characteristic fragment ion m/z 264 or 266 directly indicates the ceramides long-chain base including C18:1 or C18:0, respectively. In negative mode, although XIC had better chromatographic peak, the characteristic fragment ([R1]⁻) intensity was too low (Supplementary Figure S9) that may influence the accuracy of qualitative analysis, especially for those low concentration Cer. In some studies, Cer species detected in negative mode were less than that in positive mode (Liu et al., 2020; Wang et al., 2020), while some of Cer also was higher level in human milk phospholipids (Alexandre-Gouabau et al., 2018; Zhao et al., 2021). Thus, the positive mode was finally chosen for the detection of Cer.

TABLE 6 Comparison of extraction and analytical methods used for lipids in milk and dairy products.

Sample	Extraction Method	Instrumentation	Lipids Identified	Number of Lipids	Quantification	References
Human milk	LLE, chloroform/methanol (2:1, v/v), 1 times extraction	UPLC-Q-TOF-MS	PC, PE, PI, PS, SM, TAG	136	Relative quantification	Sokol et al. (2015)
Human milk	LLE, dichloromethane/methanol (2:1, v/v), 3 times extraction	UPLC-APCI- MS	TAG	42	Relative quantification	Ten-Domenech et al. (2015)
Human milk, formula milk, bovine milk	SPME, methanol: H_2O (5:1, v/v)	UPLC-ESI-Q-TOF-MS	PC, PE, PI, PS, PG, PA, SM, Cer, DAG, TAG, FFA, PR, ST	764	Cannot quantification	Garwolinska et al. (2017)
Bovine milk, goat milk, soymilk	LLE, chloroform/methanol (2:1, v/v), 1 times extraction	UPLC-Q-Exactive Orbitrap MS	PC, PE, PI, PS, PG, PA, SM, Cer, DAG, TAG, FFA	462	Absolute quantification	Li et al. (2017)
Human milk	LLE, n-hexane, 1 times extraction	SFC-Q-TOF-MS	DAG, TAG	95	Relative quantification	Tu et al. (2017)
Human milk, infant formula, butter milk powder	LLE, chloroform/methanol (2:1, v/v), 2 times extraction	HPLC-ESI-MS	PC, PE, PI, Cer	62	Absolute quantification	Tavazzi et al. (2018)
Human milk, infant formula	LLE, chloroform/methanol (2:1, v/v), 2 times extraction	HPLC-ESI-IT-TOF-MS	PC, PE, PI, PS, PG, PA, SM	161	Absolute quantification	Jiang C. et al. (2018)
Bovine milk	LLE, MTBE: methanol (5:1, v/v), 3 times extraction	UPLC-ESI-Q-TOF-MS	PC, PE, PI, PS, PG, PA, SM, Cer, DAG, TAG, HexCer, Hex2Cer, CL	335	Absolute quantification	Li et al. (2020)
Bovine milk	LLE, chloroform/methanol (2:1, v/v), 1 times extraction	UPLC-HESI-Q Exactive-MS	PC, PE, PI, PS, PG, PA, PC-P, PE-P, SM, Cer, GluCer, LacCer, GD3, GM3	524	Absolute quantification	Liu et al. (2020)
Infant formula, growing up milk powders, raw materials	PLs: LLE, chloroform/methanol (9/1, v/v), 2 times extraction	PLs: HPLC-ELSD	PC, PE, PI, PS, SM, GD3, GM3	No mentioned	Absolute quantification	Moloney et al. (2020)
	GAs: LLE & SPE, chloroform/methanol, 2 times extraction	GAs: UPLC-Q-TOF-MS				
Human milk, bovine milk, caprine milk	LLE, MTBE/methanol (5:1, v/v), 3 times extraction	UPLC-ESI-Q-TOF-MS	PC, PE, PI, PS, PG, PA, SM, Cer, DAG, TAG, HexCer, Hex2Cer, CL	348	Relative quantification	Wang et al. (2020)
Human milk	LLE, chloroform/methanol (2:1, v/v), 1 times extraction	UPLC-ESI-IT-TOF-MS	PC, PE, PS, PI, PG, PA, SM	258	Absolute quantification	Song et al. (2021)
Human milk, infant formulae, other mammalian milk	LLE & SPE, dichloromethane/methanol (1:2, v/v), 3 times extraction	UPLC-ESI-Q-TOF-MS	PC, PE, PI, PS, PG, PA, SM, Cer, DAG, TAG, FFA, GD3, GM3	556	Absolute quantification	This study

Methyl-tert-butyl ether (MTBE).

High-resolution mass spectrum was good at qualitative analysis, while it was a bit instable in quantification. So, if internal standards were not added, the intraassay results of recovery and the reproducibility would be poor. Adding internal standards with similar structure to the existing lipids in human milk is an effective way to eliminate the impact of poor instrument stability for quantitative analysis. Except for d5-TAG 18:1/18:1/18:1, the internal standards of other phospholipids were not deuterated. Meanwhile, PC 14:1/17:0, PE 14:1/17:0, SM d17:0/18:1, PI 14:1/17:0, PG 14:1/17:0, and Cer d18:2/24:0 was not detected in human milk, indicating that the addition of internal standard will not influence the content of the lipids in human milk. The addition of internal standards could ensure the accuracy of quantitative results and the comparability between the corresponding batches.

Due to the high resolution of TOF, the number of lipids species, including phospholipids, glycerides, free fatty acids and gangliosides, in human milk reported in this study were higher compared with that in

most previous researches (Li et al., 2017; Wang et al., 2020; Song et al., 2021). It was shown that this method had good performance in the characterization of human milk lipids. Meanwhile, this method could be used for absolute quantification of each species of phospholipids and glycerides, which was beneficial for the omni-directional analysis of the composition and content of lipids in human milk.

Human milk is the golden standard for the development of infant formula. In most infant formulae, other mammalian milk, especially bovine milk, is mixed with vegetable oils in order to mimic the fatty acid profile of human milk (Tu et al., 2017; Jiang T. et al., 2018). It is necessary to profile the lipids in human milk, other mammalian milk and infant formula with the same extraction and detection method. Table 5 showed that infant formula and other mammalian milk had some difference in lipid composition from human milk, while the species number of lipids in the former was all lower than that in human milk. And no gangliosides were detected in horse milk and donkey milk. The concentrations of phospholipids in bovine milk and

goat milk were similar to that in human milk. Meanwhile, the concentration of phospholipids in camel milk was higher than that in human milk and infant formula, those of horse milk and donkey milk was lower. The concentration of glycerides in bovine milk, infant formula and human milk were similar, the glycerides concentration of other mammalian milk was much lower. These results suggested that the present method would also be a reliable tool for the profiling of lipids in other mammalian milk and infant formula.

5 Conclusion

In this study, a qualitative and quantitative method was established and validated for profiling phospholipids and glycerides in human milk using UPLC-Q-TOF-MS with LLE and SPE. This method could extract a variety of lipids including phospholipids, glycerides, free fatty acids and gangliosides from a small volume of human milk after one series of pretreatment. We applied the established method to analyze a large number of human milk samples and detected 245 species of phospholipids, 177 species of glycerides, 23 species of free fatty acids and 38 species of gangliosides. Meanwhile, the use of internal standard allowed quantitative analysis of lipids and also corrected the loss of analyte during sample preparation and detection. The applicability of this method was validated by analyzing lipids in human milk, other mammalian milk and infant formula.

Data availability statement

The data presented in the study are deposited in Figshare repository, accession DOI: 10.6084/m9.figshare.21785891.v1.

Ethics statement

The studies involving human participants were reviewed and approved by Ethics Committee of Beijing Ditan Hospital affiliated to Capital Medical University (#2015-027-01). The patients/participants provided their written informed consent to participate in this study.

Author contributions

YL (1st author): Visualization, Investigation, Data curation, Formal analysis, Methodology, Writing–original draft, Writing–review and editing. WQ: Project administration. YL: Project administration. JZ: Conceptualization, Methodology, Software, Writing–review and editing. QL: Data curation, Formal analysis. KY: Writing–review and editing. MZ: Resources. YW: Resources. YL (9th author): Formal analysis. LC: Conceptualization, Methodology, Project administration, Supervision, Funding acquisition.

Funding

Conflict of interest

Authors YL, WQ, YL, JZ, QL, KY, MZ, YW, YL, and LC were employed by the company Beijing Sanyuan Foods Co., Ltd.

The authors declare that this study received funding from Beijing Sanyuan Foods Co., Ltd. The funder had the following involvement in the study: Maternal and Infant Nutriomics Cohort Study.

Publisher's note

All claims expressed in this article are solely those of the authors and do not necessarily represent those of their affiliated organizations, or those of the publisher, the editors and the reviewers. Any product that may be evaluated in this article, or claim that may be made by its manufacturer, is not guaranteed or endorsed by the publisher.

Supplementary material

The Supplementary Material for this article can be found online at: https://www.frontiersin.org/articles/10.3389/fchem.2022.1101557/full#supplementary-material

SUPPLEMENTARY FIGURE S1
(A) MS/MS fragments of TAG 52:3 acquired in positive ion mode; **(B)** MS/MS fragments of DAG 34:2 acquired in negative ion mode; **(C)** MS/MS fragments of FFA 18:1 acquired in negative ion mode. **(A)** MS/MS fragments of PE 36:2 acquired in positive ion mode; **(B)** MS/MS fragments of PE 36:2 acquired in negative ion mode.

SUPPLEMENTARY FIGURE S2
(A) MS/MS fragments of PE 36:2 acquired in positive ion mode; **(B)** MS/MS fragments of PE 36:2 acquired in negative ion mode.

SUPPLEMENTARY FIGURE S3
(A) MS/MS fragments of PS 36:0 acquired in positive ion mode; **(B)** MS/MS fragments of PS 36:0 acquired in negative ion mode.

SUPPLEMENTARY FIGURE S4
(A) MS/MS fragments of PI 34:1 acquired in positive ion mode; **(B)** MS/MS fragments of PI 34:1 acquired in negative ion mode.

SUPPLEMENTARY FIGURE S5
(A) MS/MS fragments of PG 38:5 acquired in positive ion mode; **(B)** MS/MS fragments of PG 38:5 acquired in negative ion mode.

SUPPLEMENTARY FIGURE S6
(A) MS/MS fragments of PA 34:1 acquired in positive ion mode; **(B)** MS/MS fragments of PA 34:1 acquired in negative ion mode.

SUPPLEMENTARY FIGURE S7
(A) MS/MS fragments of PC 36:2 acquired in positive ion mode; **(B)** MS/MS fragments of PC 36:2 acquired in negative ion mode.

SUPPLEMENTARY FIGURE S8
(A) MS/MS fragments of SM 38:1;2 acquired in positive ion mode; **(B)** MS/MS fragments of SM 38:1;2 acquired in negative ion mode.

SUPPLEMENTARY FIGURE S9
(A) MS/MS fragments of Cer 42:2;2 acquired in positive ion mode; **(B)** MS/MS fragments of Cer 42:2;2 acquired in negative ion mode.

SUPPLEMENTARY FIGURE S10
(A) MS/MS fragments of GM3 36:1;2 acquired in negative ion mode; **(B)** MS/MS fragments of GD3 34:1;2 acquired in negative ion mode.

SUPPLEMENTARY FIGURE S11
(A) Extracted ion chromatogram of SM 38:1;2 acquired in positive ion mode; **(B)** Extracted ion chromatogram of PE 36:2 acquired in negative ion mode; **(C)** Extracted ion chromatogram of TAG 52:3 acquired in positive ion mode; **(D)** Extracted ion chromatogram of FFA 18:1 acquired in negative ion mode; **(E)** Extracted ion chromatogram of GM3 36:1;2 acquired in negative ion mode.

SUPPLEMENTARY TABLE S1
List of identified phospholipids in human milk detected by UPLC-Q-TOF-MS.

SUPPLEMENTARY TABLE S2
List of identified glycerides and free fatty acids in human milk detected by UPLC-Q-TOF-MS.

SUPPLEMENTARY TABLE S3
List of identified gangliosides in human milk detected by UPLC-Q-TOF-MS.

References

Alexandre-Gouabau, M. C., Moyon, T., Cariou, V., Antignac, J. P., Qannari, E. M., Croyal, M., et al. (2018). Breast milk lipidome is associated with early growth trajectory in preterm infants. *Nutrients* 10 (2), 164. doi:10.3390/nu10020164

Ali, A. H., Zou, X., Huang, J., Abed, S. M., Tao, G., Jin, Q., et al. (2017). Profiling of phospholipids molecular species from different mammalian milk powders by using ultra-performance liquid chromatography-electrospray ionization-quadrupole-time of flight-mass spectrometry. *J. Food Compos. Anal.* 62, 143–154. doi:10.1016/j.jfca.2017.05.007

Bligh, E. G., and Dyer, W. J. (1959). A rapid method of total lipid extraction and purification. *Can. J. Biochem. Physiol.* 37 (8), 911–917. doi:10.1139/o59-099

Bukowski, M. R., and Picklo, M. J. (2021). Simple, rapid lipidomic analysis of triacylglycerols in bovine milk by infusion-electrospray mass spectrometry. *Lipids* 56 (2), 243–255. doi:10.1002/lipd.12292

Calvano, C. D., Ventura, G., Sardanelli, A. M., Losito, I., Palmisano, F., and Cataldi, T. R. I. (2019). Identification of neutral and acidic glycosphingolipids in the human dermal fibroblasts. *Anal. Biochem.* 581, 113348. doi:10.1016/j.ab.2019.113348

Castro-Gómez, M. P., Rodriguez-Alcalá, L. M., Calvo, M. V., Romero, J., Mendiola, J. A., Ibañez, E., et al. (2014). Total milk fat extraction and quantification of polar and neutral lipids of cow, goat, and Ewe milk by using a pressurized liquid system and chromatographic techniques. *J. Dairy Sci.* 97 (11), 6719–6728. doi:10.3168/jds.2014-8128

Caudill, M. A. (2010). Pre- and postnatal health: Evidence of increased choline needs. *J. Am. Dietetic Assoc.* 110 (8), 1198–1206. doi:10.1016/j.jada.2010.05.009

Claumarchirant, L., Cilla, A., Matencio, E., Sanchez-Siles, L. M., Castro-Gomez, P., Fontecha, J., et al. (2016). Addition of milk fat globule membrane as an ingredient of infant formulas for resembling the polar lipids of human milk. *Int. Dairy J.* 61, 228–238. doi:10.1016/j.idairyj.2016.06.005

Contarini, G., and Povolo, M. (2013). Phospholipids in milk fat: Composition, biological and technological significance, and analytical strategies. *Int. J. Mol. Sci.* 14 (2), 2808–2831. doi:10.3390/ijms14022808

Delplanque, B., Gibson, R., Koletzko, B., Lapillonne, A., and Strandvik, B. (2015). Lipid quality in infant nutrition: Current knowledge and future opportunities. *J. Pediatr. Gastroenterol. Nutr.* 61 (1), 8–17. doi:10.1097/MPG.0000000000000818

Donato, P., Cacciola, F., Cichello, F., Russo, M., Dugo, P., and Mondello, L. (2011). Determination of phospholipids in milk samples by means of hydrophilic interaction liquid chromatography coupled to evaporative light scattering and mass spectrometry detection. *J. Chromatogr. A* 1218 (37), 6476–6482. doi:10.1016/j.chroma.2011.07.036

Fahy, E., Subramaniam, S., Murphy, R. C., Nishijima, M., Raetz, C. R. H., Shimizu, T., et al. (2008). Update of the LIPID MAPS comprehensive classification system for lipids. *J. Lipid Res.* 50, S9–S14. doi:10.1194/jlr.R800095-JLR200

Folch, J., Less, .M., and Sloane Stanley, G. H. (1957). A simple method for the isolation and purification of total lipides from animal tissues. *J. Biol. Chem.* 226, 497–509. doi:10.1016/S0021-9258(18)64849-5,

Gallier, S., Gragson, D., Cabral, C., Jiménez-Flores, R., and Everett, D. W. (2010). Composition and fatty acid distribution of bovine milk phospholipids from processed milk products. *J. Agric. Food Chem.* 58 (19), 10503–10511. doi:10.1021/jf101878d

Garwolinska, D., Hewelt-Belka, W., Namiesnik, J., and Kot-Wasik, A. (2017). Rapid characterization of the human breast milk lipidome using a solid-phase microextraction and liquid chromatography-mass spectrometry-based approach. *Proteome Res.* 16 (9), 3200–3208. doi:10.1021/acs.jproteome.7b00195

Garwolinska, D., Mlynarczyk, M., Kot-Wasik, A., and Hewelt-Belka, W. (2021). The influence of storage on human milk lipidome stability for lipidomic studies. *J. Proteome Res.* 21, 438–446. doi:10.1021/acs.jproteome.1c00760

George, A. D., Gay, M. C. L., Trengove, R. D., and Geddes, D. T. (2018). Human milk lipidomics: Current techniques and methodologies. *Nutrients* 10 (9), 1169. doi:10.3390/nu10091169

George, A. D., Gay, M. C. L., Wlodek, M. E., Trengove, R. D., Murray, K., and Geddes, D. T. (2020). Untargeted lipidomics using liquid chromatography-ion mobility-mass spectrometry reveals novel triacylglycerides in human milk. *Sci. Rep.* 10 (1), 9255. doi:10.1038/s41598-020-66235-y

Glaser, C., Lattka, E., Rzehak, P., Steer, C., Koletzko, B., Maternal, J., et al. (2015). Genetic variation in polyunsaturated fatty acid metabolism and its potential relevance for human development and health. *Matern. Child. Nutr.* 7, 27–40. doi:10.1111/j.1740-8709.2011.00319.x

Han, X., and Gross, R. W. (1994). Electrospray ionization mass spectroscopic analysis of human erythrocyte plasma membrane phospholipids. *Proc. Natl. Acad. Sci. U. S. A.* 91 (22), 10635–10639. doi:10.1073/pnas.91.22.10635

Han, X., and Gross, R. W. (2001). Quantitative analysis and molecular species fingerprinting of triacylglyceride molecular species directly from lipid extracts of biological samples by electrospray ionization tandem mass spectrometry. *Anal. Biochem.* 295 (1), 88–100. doi:10.1006/abio.2001.5178

Huang, H.-L., Chuang, L.-T., Li, H.-H., Lin, C.-P., and Glew, R. H. (2013). Docosahaexaenoic acid in maternal and neonatal plasma phospholipids and milk lipids of Taiwanese women in Kinmen; fatty acid composition of maternal blood, neonatal blood and breast milk. *Lipids Health Dis.* 12, 27. doi:10.1186/1476-511X-12-27

Ingvordsen Lindahl, I., Artegoitia, V., Downey, E., O'Mahony, J., O'Shea, C.-A., Ryan, C., et al. (2019). Quantification of human milk phospholipids: The effect of gestational and lactational age on phospholipid composition. *Nutrients* 11 (2), 222. doi:10.3390/nu11020222

Jiang, C., Ma, B., Song, S., Lai, O.-M., and Cheong, L.-Z. (2018). Fingerprinting of phospholipid molecular species from human milk and infant formula using HILIC-ESI-IT-TOF-MS and discriminatory analysis by principal component analysis. *J. Agric. Food Chem.* 66 (27), 7131–7138. doi:10.1021/acs.jafc.8b01393

Jiang, T., Liu, B., Li, J., Dong, X., Lin, M., Zhang, M., et al. (2018). Association between sn-2 fatty acid profiles of breast milk and development of the infant intestinal microbiome. *Food Funct.* 9 (2), 1028–1037. doi:10.1039/c7fo00088j

Kevin, H., Alan, R., Stewart, F., Sheila, G., and Norman, S. (2016). The essentiality of arachidonic acid in infant development. *J. Nutr.* 8 (4), 216. doi:10.3390/nu8040216

Koletzko, B. (2016). Human milk lipids. *Ann. Nutr. Metab.* 69 (2), 27–40. doi:10.1159/000452819

Lee, J. Y., Min, H. K., and Moon, M. H. (2011). Simultaneous profiling of lysophospholipids and phospholipids from human plasma by nanoflow liquid chromatography-tandem mass spectrometry. *Anal. Bioanal. Chem.* 400 (9), 2953–2961. doi:10.1007/s00216-011-4958-7

Li, M., Li, Q., Kang, S., Cao, X., Zheng, Y., Wu, J., et al. (2020). Characterization and comparison of lipids in bovine colostrum and mature milk based on UHPLC-QTOF-MS lipidomics. *Food Res. Int.* 136, 109490. doi:10.1016/j.foodres.2020.109490

Li, Q., Zhao, Y., Zhu, D., Pang, X., Liu, Y., Frew, R., et al. (2017). Lipidomics profiling of goat milk, soymilk and bovine milk by UPLC-Q-Exactive Orbitrap Mass Spectrometry. *Food Chem.* 224, 302–309. doi:10.1016/j.foodchem.2016.12.083

Liaw, L., Prudovsky, I., Koza, R. A., Anunciado-Koza, R. V., Siviski, M. E., Lindner, V., et al. (2016). Lipid profiling of *in vitro* cell models of adipogenic differentiation: Relationships with mouse adipose tissues. *J. Cell. Biochem.* 117 (9), 2182–2193. doi:10.1002/jcb.25522

Liu, Z., Li, C., Pryce, J., and Rochfort, S. (2020). Comprehensive characterization of bovine milk lipids: Phospholipids, sphingolipids, glycolipids, and ceramides. *J. Agric. Food Chem.* 68 (24), 6726–6738. doi:10.1021/acs.jafc.0c01604

McJarrow, P., Radwan, H., Ma, L., MacGibbon, A. K. H., Hashim, M., Hasan, H., et al. (2019). Human milk oligosaccharide, phospholipid, and ganglioside concentrations in breast milk from united Arab emirates mothers: Results from the MISC cohort. *Nutrients* 11 (10), 2400. doi:10.3390/nu11102400

Mirsaleh-Kohan, N., Robertson, W. D., and Compton, R. N. (2008). Electron ionization time-of-flight mass spectrometry: Historical review and current applications. *Mass Spectrom. Rev.* 27 (3), 237–285. doi:10.1002/mas.20162

Mitina, A., Mazin, P., Vanyushkina, A., Anikanov, N., Mair, W., Guo, S., et al. (2020). Lipidome analysis of milk composition in humans, monkeys, bovids, and pigs. *BMC Evol. Biol.* 20 (1), 70. doi:10.1186/s12862-020-01637-0

Moloney, C., O'Connor, D., and O'Regan, J. (2020). Polar lipid, ganglioside and cholesterol contents of infant formulae and growing up milks produced with an alpha lactalbumin-enriched whey protein concentrate. *Int. Dairy J.* 107, 104716. doi:10.1016/j.idairyj.2020.104716

Sala Vila, A., Castellote-Bargalló, A. I., Rodrı´guez-Palmero-Seuma, M., and López-Sabater, M. C. (2003). High-performance liquid chromatography with evaporative light-scattering detection for the determination of phospholipid classes in human milk, infant

formulas and phospholipid sources of long-chain polyunsaturated fatty acids. *J. Chromatogr. A* 1008 (1), 73–80. doi:10.1016/s0021-9673(03)00989-0

Sánchez-Juanes, F., Alonso, J. M., Zancada, L., and Hueso, P. (2009). Distribution and fatty acid content of phospholipids from bovine milk and bovine milk fat globule membranes. *Int. Dairy J.* 19 (5), 273–278. doi:10.1016/j.idairyj.2008.11.006

Schwudke, D., Oegema, J., Burton, L., Entchev, E., Hannich, J. T., Ejsing, C. S., et al. (2006). Lipid profiling by multiple precursor and neutral loss scanning driven by the data-dependent acquisition. *Anal. Chem.* 78 (2), 585–595. doi:10.1021/ac051605m

Sokol, E., Ulven, T., Faergeman, N. J., and Ejsing, C. S. (2015). Comprehensive and quantitative profiling of lipid species in human milk, cow milk and a phospholipid-enriched milk formula by GC and MS/MSALL. *Eur. J. Lipid Sci. Technol.* 117 (6), 751–759. doi:10.1002/ejlt.201400575

Song, S., Cheong, L. Z., Man, Q. Q., Pang, S. J., Li, Y. Q., Ren, B., et al. (2018). Characterization of potential plasma biomarkers related to cognitive impairment by untargeted profiling of phospholipids using the HILIC-ESI-IT-TOF-MS system. *Anal. Bioanal. Chem.* 410 (12), 2937–2948. doi:10.1007/s00216-018-0975-0

Song, S., Liu, T. T., Liang, X., Liu, Z. Y., Yishake, D., Lu, X. T., et al. (2021). Profiling of phospholipid molecular species in human breast milk of Chinese mothers and comprehensive analysis of phospholipidomic characteristics at different lactation stages. *Food Chem.* 348, 129091. doi:10.1016/j.foodchem.2021.129091

Tang, Y., Ali, M. M., Sun, X., Debrah, A. A., Wang, M., Hou, H., et al. (2021). Development of a high-throughput method for the comprehensive lipid analysis in milk using ultra-high performance supercritical fluid chromatography combined with quadrupole time-of-flight mass spectrometry. *J. Chromatogr. A* 1658, 462606. doi:10.1016/j.chroma.2021.462606

Tavazzi, I., Fontannaz, P., Lee, L. Y., and Giuffrida, F. (2018). Quantification of glycerophospholipids and sphingomyelin in human milk and infant formula by high performance liquid chromatography coupled with mass spectrometer detector. *J. Chromatogr. B* 1072, 235–243. doi:10.1016/j.jchromb.2017.10.067

Ten-Domenech, I., Beltran-Iturat, E., Herrero-Martinez, J. M., Sancho-Llopis, J. V., and Simo-Alfonso, E. F. (2015). Triacylglycerol analysis in human milk and other mammalian species: Small-scale sample preparation, characterization, and statistical classification using HPLC-ELSD profiles. *J. Agric. Food Chem.* 63 (24), 5761–5770. doi:10.1021/acs.jafc.5b01158

Tingting, Z. (2008). *The effect of maternal diet during pregnancy and lactation on FA composition of breast milk and infants' blood as well as infants' growth and development.* [Master's Degree]. Shanghai: Fudan University.

Tu, A., Ma, Q., Bai, H., and Du, Z. (2017). A comparative study of triacylglycerol composition in Chinese human milk within different lactation stages and imported infant formula by SFC coupled with Q-TOF-MS. *Food Chem.* 221, 555–567. doi:10.1016/j.foodchem.2016.11.139

Verardo, V., Gómez-Caravaca, A., Arráez-Román, D., and Hettinga, K. (2017). Recent advances in phospholipids from colostrum, milk and dairy by-products. *Int. J. Mol. Sci.* 18 (1), 173. doi:10.3390/ijms18010173

Vieira, A. M., Guiomar, D. A. B., PolianaFerreira, M. S., Mateus, K., Figueiredo, M. S., Lisboa, P. C., et al. (2018). Maternal soybean diet during lactation alters breast milk composition and programs the lipid profile in adult male rat offspring. *Endocrine* 60, 272–281. doi:10.1007/s12020-018-1572-x

Wang, L., Li, X., Liu, L., da Zhang, H., Zhang, Y., Hao Chang, Y., et al. (2020). Comparative lipidomics analysis of human, bovine and caprine milk by UHPLC-Q-TOF-MS. *Food Chem.* 310, 125865. doi:10.1016/j.foodchem.2019.125865

Wei, W., Sun, C., Jiang, W., Zhang, X., Hong, Y., Jin, Q., et al. (2019a). Triacylglycerols fingerprint of edible vegetable oils by ultra-performance liquid chromatography-Q-ToF-MS. *Lwt* 112, 108261. doi:10.1016/j.lwt.2019.108261

Wei, W., Yang, J., Yang, D., Wang, X., Yang, Z., Jin, Q., et al. (2019b). Phospholipid composition and fat globule structure I: Comparison of human milk fat from different gestational ages, lactation stages, and infant formulas. *J. Agric. Food Chem.* 67 (50), 13922–13928. doi:10.1021/acs.jafc.9b04247

Wernke, M. J., and Schell, J. D. (2004). Solvents and malignancy. *Clin. Occup. Environ. Med.* 4 (3), 513–527, vii. doi:10.1016/j.coem.2004.03.008

Xu, L., Chen, W., Wang, X., Yu, Z., and Han, S. (2020). Comparative lipidomic analyses reveal different protections in preterm and term breast milk for infants. *Front. Pediatr.* 8, 590. doi:10.3389/fped.2020.00590

Yangbo, H. (2016). *The phospholipidomics and analysis of fatty acids in the human milk of Chinese han nationality.* [Master's Degree]. Harbin: Northeast Agricultural University.

Zhang, X., Wei, W., Tao, G., Jin, Q., and Wang, X. (2021). Identification and quantification of triacylglycerols using ultraperformance supercritical fluid chromatography and quadrupole time-of-flight mass spectrometry: Comparison of human milk, infant formula, other mammalian milk, and plant oil. *J. Agric. Food Chem.* 69 (32), 8991–9003. doi:10.1021/acs.jafc.0c07312

Zhao, J., Liu, Q., Liu, Y., Qiao, W., Yang, K., Jiang, T., et al. (2021). Quantitative profiling of glycerides, glycerophosphatides and sphingolipids in Chinese human milk with ultra-performance liquid chromatography/quadrupole-time-of-flight mass spectrometry. *Food Chem.* 346, 128857. doi:10.1016/j.foodchem.2020.128857

Zou, X., Ali, A. H., Abed, S. M., and Guo, Z. (2017). Current knowledge of lipids in human milk and recent innovations in infant formulas. *Curr. Opin. Food Sci.* 16, 28–39. doi:10.1016/j.cofs.2017.06.010

Zou, X., Huang, J., Jin, Q., Guo, Z., Liu, Y., Cheong, L., et al. (2013). Lipid composition analysis of milk fats from different mammalian species: potential for use as human milk fat substitutes. *J. Agric. Food Chem.* 61 (29), 7070–7080. doi:10.1021/jf401452y

Development of the DNA-based voltammetric biosensor for detection of vincristine as anticancer drug

Mahmoud Abbasi[1], Fahad Alsaikhan[2], Rasha Fadhel Obaid[3], Shohreh Jahani[4]*, Saeed Biroudian[5], Maziar Oveisee[6], Mohammad Reza Arab[7], Zahra Aramesh-Boroujeni[8] and Mohammad Mehdi Foroughi[9]

[1]Medical Ethics and Law Research Center, Shahid Beheshti University of Medical Sciences, Tehran, Iran, [2]College of Pharmacy, Prince Sattam Bin Abdulaziz University, Alkharj, Saudi Arabia, [3]Department of Biomedical Engineering, Al-Mustaqbal University College, Babylon, Iraq, [4]Noncommunicable Diseases Research Center, Bam University of Medical Sciences, Bam, Iran, [5]Department of Medical Ethics, Medical School, Iran University of Medical Sciences, Tehran, Iran, [6]Orthopedic Department, Bam University of Medical Sciences, Bam, Iran, [7]Department of Medical, Bam University of Medical Sciences, Bam, Iran, [8]Department of Chemistry, University of Isfahan, Isfahan, Iran, [9]Department of Chemistry, Kerman Branch, Islamic Azad University, Kerman, Iran

In the article presented herein, a deoxyribonucleic acid (DNA) biosensor is introduced for Vincristine determination in pharmaceutical preparations based on the modification of screen printed electrode (SPE) with double-stranded DNA (ds-DNA), polypyrrole (PP), peony-like CuO:Tb^{3+} nanostructure (P-L CuO: Tb^{3+} NS). The developed sensor indicated a wide linear response to Vincristine concentration ranged from 1.0 nM to 400.0 μM with a limit of detection as low as .21 nM. The intercalation of Vincristine with DNA guanine led to the response. The optimized parameters for the biosensor performance were ds-DNA/ Vincristine interaction time, DNA concentration and type of buffer solution. The docking investigation confirm the minor groove interaction between guanine base at surface of or ds-DNA/PP/P-L CuO:Tb^{3+} NS/SPE and Vincristine. The proposed sensor could successfully determine Vincristine in Vincristine injections and biological fluids, with acceptable obtains.

1 Introduction

Vincristine (Figure 1) is placed in a class of drugs called the vinca alkaloids, which is extracted from *Catharanthus roseus*, and used as a chemotherapy drug (Khan et al., 2022). Vincristine is applied for treating a various type of cancers such as acute lymphocytic leukemia, acute myeloid leukemia, neuroblastoma, Hodgkin's disease, rhabdomyosarcoma, Wilms' tumor and small cell lung cancer (Li et al., 2021; Filippi-Chiela et al., 2022). Some VCR-caused complications are headaches, hair loss, difficulty in
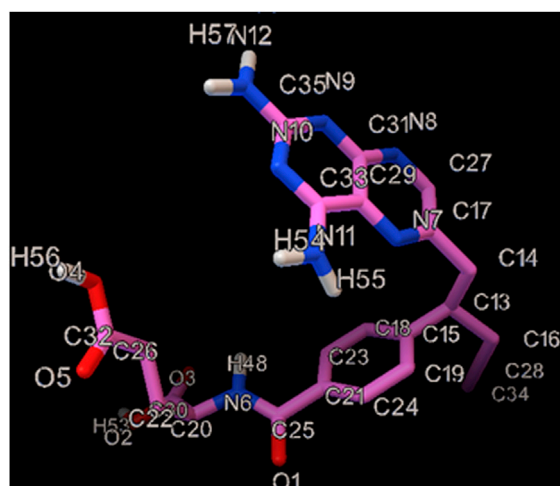
walking, constipation, change in sensation, neuropathic pain, lung damage and lowered white blood cells (Childress et al., 2022; Mujib et al., 2022). Therefore, it is essential to quantify the VCR in the biological specimens like urine and plasma. There are diverse analytical methods in this regard, including liquid chromatography together with electrochemical or ultraviolet determination, liquid chromatography-mass spectrometry and LC–MS/MS (Gupta et al., 2005; Amila Jeewantha et al., 2017; Kiani et al., 2018; Jin et al., 2021).

Among these, the electrochemical biosensors have some merits like selectivity, sensitivity, cost-effectiveness, rapidity and simplicity (Foroughi and Jahani, 2021; Zhang et al., 2022). The screen printed electrode (SPE) can be used to produce a disposable equipment (Núñez et al., 2021). Deoxyribonucleic acid (DNA) biochemical biosensors concentrate molecules with affinity for nucleic acids to assess the electronic surface using the DNA layer selectivity. Alterations in the redox attributes of DNA (in the guanine oxidation) are examined to study the interactions between DNA and analytes in these biosensors (Moarefdoust et al., 2022a; Cao et al., 2022; Fang et al., 2022).

The electrode surface modification can boost the function of the electrode to establish a suitable substrate for the stabilization of biomolecules and to decrease the charge transfer resistance on the sensor surface (Li et al., 2016; Zhou et al., 2018; Farvardin et al., 2020; Iftikhar et al., 2021a; Gao et al., 2022; Jahani et al., 2022; Jia et al., 2022). The sensors can be produced by a majority of metals, metal oxides and alloys (Fathi et al., 2020; Vakili Fathabadi et al., 2020; Ejaz et al., 2021; Anqi et al., 2022; Chen et al., 2022; Duan et al., 2022; Iftikhar et al., 2022). Several materials are
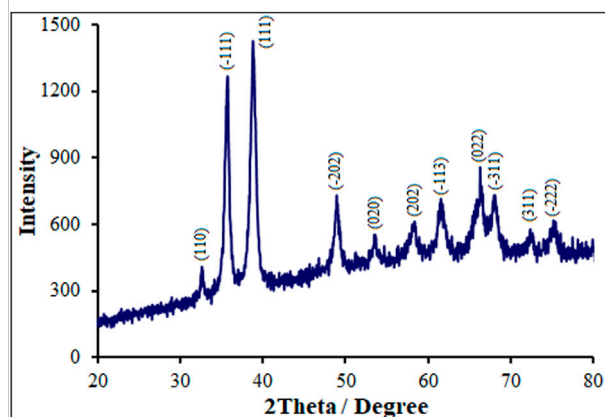
noble metals or toxic metals, others with slow kinetics and negligible selectivity (Zhang et al., 2016a; Yang et al., 2017; Iftikhar et al., 2021b; Foroughi et al., 2021; Moarefdoust et al., 2022b; Kumar et al., 2022). Copper oxide (CuO) is a p-type semiconductor, has a 1.2-eV bandgap and can be utilized in the structure of batteries, catalysis, biosensors and gas sensors (Park et al., 2014; Yang et al., 2014; Hu and Liu, 2015). The merits of CuO for sensor applications can be attributed to non-toxicity, cost-effectiveness, easy fabrication, specific capacitances and facile storage (Yang et al., 2012). The electrocatalytic traits of CuO can be reinforced through the combination of CuO with highly conductive materials like rare Earth metals, gold (Au), silver (Ag), carbon nanotubes (CNTs) and graphene to generate composite materials (Dung et al., 2013; Zheng et al., 2014; Dong et al., 2015; Tian et al., 2015).

The current attempt was made to fabricate a selective and sensitive method to determine the Vincristine. The literature review revealed that there is no study so far evaluating determination of Vincristine based on electrochemical DNA. The sensor was modified with double-stranded DNA (ds-DNA), polypyrrole (PP) and peony-like CuO:Tb^{3+} nanostructure (P-L CuO:Tb^{3+} NS) to determine nano-molar Vincristine. The practical potential of the proposed ds-DNA/PP/P-L CuO:Tb^{3+} NS/SPE sensor was verified by determining Vincristine in urine, blood serum and injection. We found outstanding advantages for our biosensor, including an impressive sensitivity, cost-effective, admirable reproducibility fast response, and narrow limit of detection in spite of the presence of various interferants. In addition, the findings of this study are significant because ds-DNA/PP/P-L CuO:Tb^{3+} NS/SPE provided appreciable analytical behavior and sensitivity when comparing with counterpart electrochemical and non-electrochemical methods previously introduced for Vincristine determining.
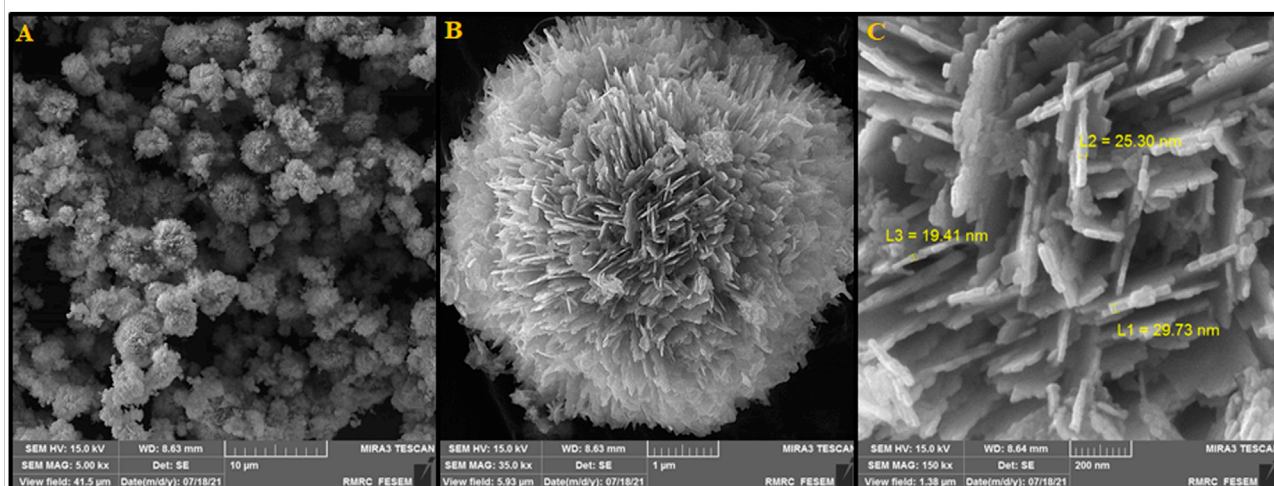
FIGURE 3
(A) FESEM image, **(B)** and **(C)** High resolution FESEM image of P-L CuO:Tb³⁺ NS.

2 Experimental

2.1 Chemicals and devices

Vincristine (>99.0%), sodium nitrate (NaNO$_3$, = 99.0%), copper nitrate trihydrate (Cu(NO$_3$)$_2$.3H$_2$O, >99.0%), absolute ethanol (=99.8%), NaOH (>97%), 28% ammonia and terbium chloride hexahydrate (TbCl$_3$.6H$_2$O, >99.0%) belonged to Sigma–Aldrich Company (Germany). All solutions were freshly prepared by double distilled water (DDW). To obtain 1.0 mM Vincristine stock solution, Vincristine (824.96 mg) was dissolved in water solution. The freshly prepared human blood serum and urine samples were from Pasteur Bam Hospital (Bam, Iran). The 1-mg/ml Vincristine ampoule was from Nanodaru Pajuhan Pardis Co. (Tehran; Iran). All measurements of electrochemical impedance spectroscopy (EIS), voltammetry were performed by a SAMA 500 Electro-analyzer (Isfahan; Iran). The three-electrode cell system contained one working electrode (SPE), one axillary electrode (platinum wire) and one reference electrode (SCE). All pH values were measured by a digital ELICO LI 120 pH meter. All X-ray powder diffraction (XRD) findings belonged to a Philips PC-APD X-ray diffractometer (the Netherlands). EM 3200 SEM and KYKY Scanning Electron Microscopy-Energy Dispersive Spectroscopy (SEM-EDS; China) characterized the modifier.

2.2 Production of peony-like CuO:Tb³⁺ nanostructure (P-L CuO:Tb³⁺ NS)

A simple hydrothermal protocol was applied to construct the P-L CuO:Tb³⁺ NS. Thus, 1.2 g of copper nitrate trihydrate and

.1 g of terbium chloride hexahydrate were poured in 100 ml of ethanol. Then, the solution was added with 25 ml of 28% ammonia and 20 ml of 1.0 M NaOH as dropwise, followed by appending 10 g of NaNO$_3$. Next, the solution was autoclaved in a 250-ml Teflon-lined stainless steel device. After that, the mix was heated in an electric oven at 140°C for 24 h, the result of which was a black product that was gathered by washing with water, performing centrifugation and drying at 80°C.

2.3 Modification of electrode surface

The bare SPE (BSPE) was exposed to Piranha solution (H$_2$SO$_4$:H$_2$O$_2$, 3:1 as v/v) and ultra-sonicated for 15 s. Next, 1 mg of P-L CuO:Tb³⁺ NS was dispersed to 1 ml of DDW and ultra-sonicated for 1 hour, followed by adding .1 M pyrrole to the obtained solution. The pyrrole electro-polymerization on the SPE surface was carried out using the cyclic voltammetry (CV) (30 potential cycles between .0 and .8 V at 100 mV/s scan rate) (Foroughi and Jahani, 2021). To prepare the dsDNA solution, 90.0 mg of fish sperm DNA was dissolved in 1 L of DDW in ultrasonic bath to obtain a homogeneous solution. Afterwards, a certain amount of produced solution (5 µL) was casted on the PP/P-L CuO:Tb³⁺ NS/SPE (Moarefdoust et al., 2022b).

2.4 Sample treatment and detection

Vincristine was electroanalytically detected in the real pharmaceutical formulations and human blood serum and urine samples. 1 ml of Vincristine Sulfate (1 mg/ml solution)
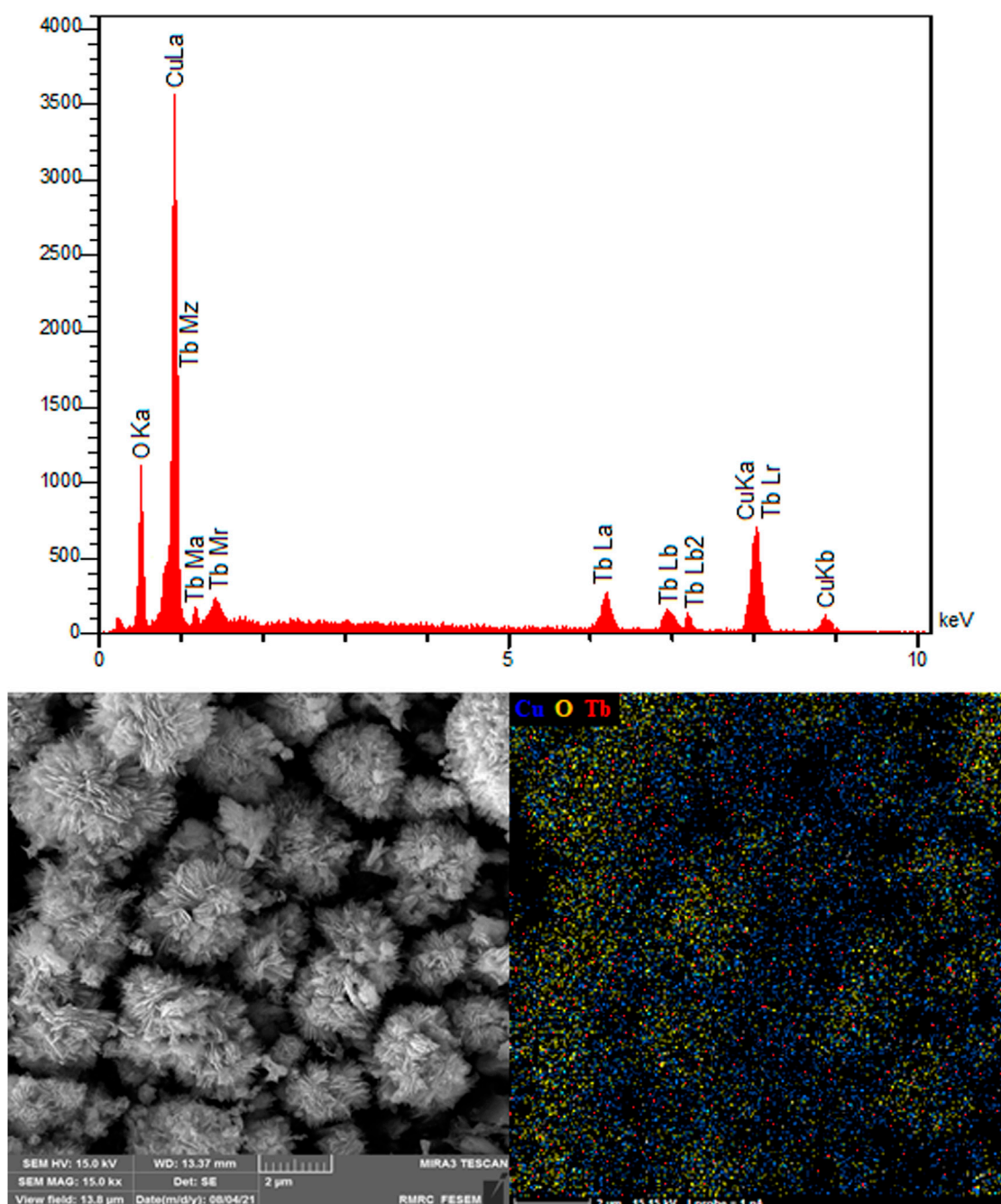
FIGURE 4
EDS spectra and elemental mapping of P-L CuO:Tb³⁺ NS.

for injection diluted to 100 ml in acetate buffer solution at the pH value of 4.8. The standard solutions of Vincristine was spiked in the pharmaceutical formulations to perform the recovery tests of their determination. No pretreatment step was conducted for the detection of Vincristine in the refrigerated human blood serum and urine samples collected from a Pasteur Bam Hospital (Bam, Iran).

2.5 Molecular docking study

A molecular docking investigation was conducted as part of a biological assay to predict the mode of binding of vincristine anticancer drug inside the DNA receptor. From the Brook haven protein data bank, the crystal structures of DNA duplex (entry codes 1BNA and with sequence d (CGCGAATTCGCG)$_2$ dodecamer) was downloaded.
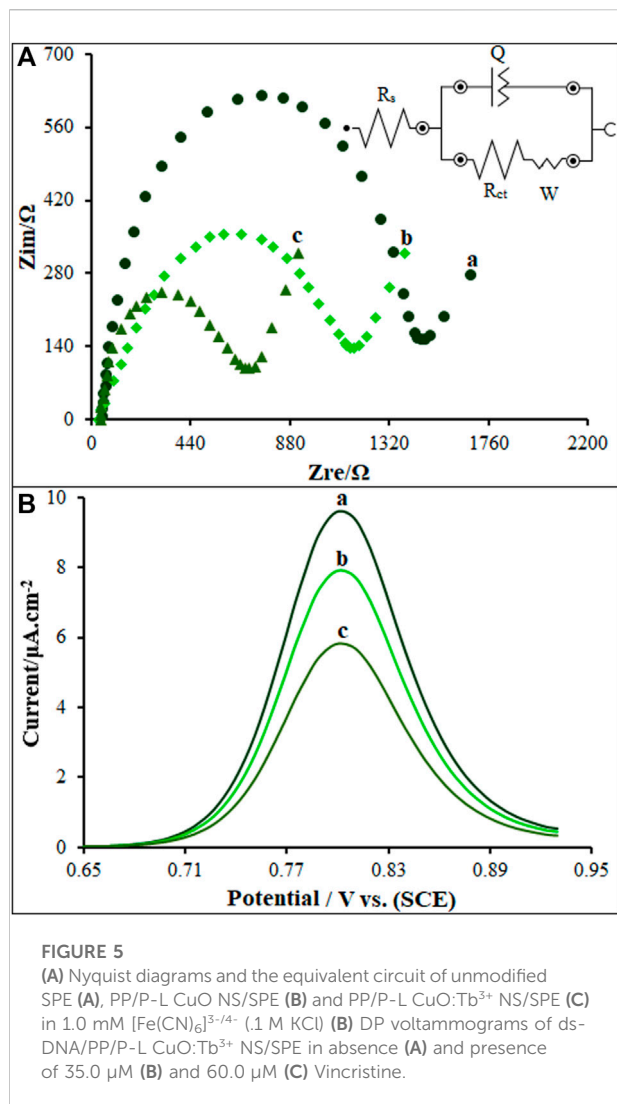
FIGURE 5
(A) Nyquist diagrams and the equivalent circuit of unmodified SPE **(A)**, PP/P-L CuO NS/SPE **(B)** and PP/P-L CuO:Tb³⁺ NS/SPE **(C)** in 1.0 mM [Fe(CN)₆]³⁻/⁴⁻ (.1 M KCl) **(B)** DP voltammograms of ds-DNA/PP/P-L CuO:Tb³⁺ NS/SPE in absence **(A)** and presence of 35.0 µM **(B)** and 60.0 µM **(C)** Vincristine.

3 Result and discussion

3.1 Characterization of P-L CuO:Tb³⁺ NS

Figure 2 illustrates the XRD spectra obtained from pure and Tb-doped CuO nanostructures. The XRD spectra for all specimens are similar to those for monoclinic CuO nanostructures, JCPDS:895,898 (Uma Maheswari et al., 2018). The diffraction peaks at 2θ for monoclinic CuO include (−222), (311), (−311), (022), (−113), (202), (020), (−202), (111), (−111) and (110) corresponding to 75.36°,72.68°, 68.12°, 66.24°, 61.52°, 58.44°, 53.68°, 48.92°, 38.76°, 35.72° and 32.56°, sequentially. Higher degree switch is there for P-L CuO:Tb³⁺ NS at peaks (−202), (022) and (−311), probably because of Tb incorporation in CuO that imposes internal stress owing to its larger atomic radii (175 p.m.) when comparing with that for Cu (128 p.m.). It rendered also for the formation of defects. Replacing dopants of a lower atomic radius in the host lattice results

in a greater angle peak shift. In our study, paradoxically, the peak angle shift is higher and the end of distance d is less observed for dopants that their atomic radius is larger than that of host copper, which may be related to further internal tensile stress caused by dopants and defects in the network, probably resulting in an abnormal shift in the greater angle peak and lower end of distance d found in XRD (Jansi Rani et al., 2020). The XRD had no secondary peaks related to dopant, confirming the fabrication of single-phase CuO NSs. According to the XRD patterns, the appeared diffraction peaks are related only to CuO formation. There were no other peaks related to Tb oxides. The lower shift of angle peaks related to greater atomic radii of dopant ion has been evaluated in detail.

Figure 3 depicts SEM images exhibiting the morphology and size of fabricated P-L CuO:Tb³⁺ NS. As shown in Figure 3A, a uniform peony-like morphology can be observed for these 5-µm fabricated nanoflowers regularly stacked by CuO:Tb³⁺ sheets. Figures 3B, C, with greater magnification, shows clearer shape of CuO:Tb³⁺ NS. Images show a unique hierarchical flower-like architecture containing ultra-thin nano-sheets with a mean thickness of 20 nm. The images show the uniform distribution of the nano-sheets along the radius throughout the sample, which resulted in the formation of a flower-like structure with abundant spaces between the petals. This structure, due to its larger specific surface area, can promise the construction of catalysts with unique applications.

Figure 4 verifies the elements of as-synthesized NSs and exhibits the electrocatalyst purities. The existence of Cu, Tb and O is evident. The EDS patterns display the production of NSs without any impurity and with high quality, probably supporting the statement of sample purity in the XRD spectrum. The EDS mapping analysis was also applied to determine the spatial dispersion of Cu, Tb and O. Figure 4 illustrates entire dispersion of Tb (red zone), Cu (blue zone) and O (yellow zone) throughout the area, indicating evident reasons for uniform dispersion in the P-L CuO:Tb³⁺ NS.

3.2 Electrochemical behaviors of modified electrode

The modified electrode was assessed for the electrochemical behaviors by the EIS (Figure 5A) in 1.0 mmol/L [Fe(CN)₆]³⁻/⁴⁻/0.1 M KCl electrolyte, in comparison to unmodified SPE, PP/P-L CuO NS/SPE and PP/P-L CuO:Tb³⁺ NS/SPE. The charge-transfer resistance (Rct) was estimated at approximately 1,482 Ω for the SPE according to Nyquist diagram. In the identical experimental circumstances, there was a reduction in the semicircle diameter on the PP/P-L CuO:Tb³⁺ NS/SPE and PP/P-L CuO NS/SPE, with the Rct values of approximately 660 and 1,143 Ω. Anchoring PP/P-L CuO:Tb³⁺ NS on the SPE surface caused an increase in electrical conductivity of electrode surface and a decrease in mass-transfer resistance during the redox process.
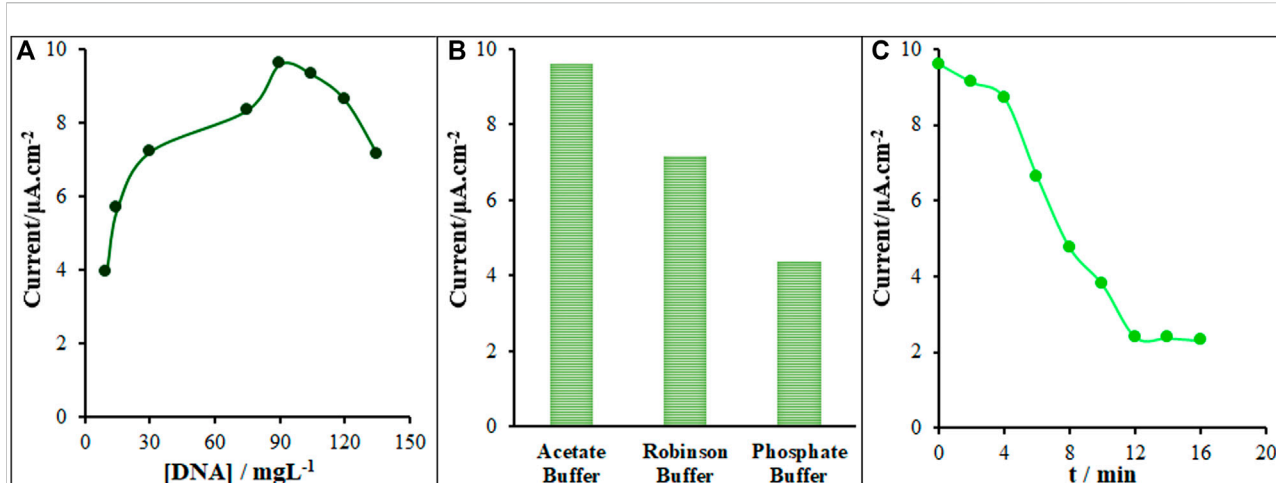
FIGURE 6
(A) Current *versus* ds-DNA concentration (10.0, 15.0, 30.0, 75.0, 90.0, 105.0, 120.0 and 135.0 mg/L) plot **(B)** Current recorded on ds-DNA/PP/P-L CuO:Tb^{3+} NS/SPE vs type of buffer at optimum condition (90.0 mg/L ds-DNA) **(C)** Effect of the time duration of 350.0 µM Vincristine on the guanine oxidation signal recorded on ds-DNA/PP/P-L CuO:Tb^{3+} NS/SPE (*n* = 5).

3.3 Intercalation of ds-DNA and vincristine

The differential pulse voltammetry's (DPVs) were recorded for as-fabricated sensor under inclusion and exclusion of the Vincristine for the exploration of its intercalation with ds-DNA on the ds-DNA/PP/P-L CuO:Tb^{3+} NS/SPE surface (Figure 5B). As seen in Figure 5B (curve a), the Vincristine exclusion created an oxidation signal at 805 mV with an oxidation current of 9.6 µA in .5 M acetate buffer solution (pH 4.8). In the inclusion of 35.0 and 60.0 µM of Vincristine (in Tris-HCl buffer; pH 7.4), the ds-DNA/PP/P-L CuO:Tb^{3+} NS/SPE was placed in the solution and then stirred for 12 min. Next, .5 M acetate buffer solution (pH 4.8) was replaced by Tris-HCl, followed by recording the DPV for ds-DNA/PP/P-L CuO:Tb^{3+} NS/SPE. According to data in Figure 5B (curves b and c), the 35.0 and 60.0 µM Vincristine solutions had the oxidation currents of 7.9 and 5.8 µA, respectively. Vincristine declined the oxidation signal of ds-DNA on the ds-DNA/PP/P-L CuO:Tb^{3+} NS/SPE surface. Therefore, the intercalation of Vincristine with ds-DNA was validated on as-fabricated sensor surface.

3.4 Optimization of determinants

The determining parameters in the optimization of biosensor activity were ds-DNA concentration, intercalation time and type of buffer solution. Variable ds-DNA contents were applied to construct the ds-DNA/PP/P-L CuO:Tb^{3+} NS/SPE according to Section 2.3. As seen in Figure 6A, there was an increase in the guanine oxidation current with increasing ds-DNA content on

the ds-DNA/PP/P-L CuO:Tb^{3+} NS/SPE surface. The highest oxidation current was related to starting ds-DNA concentration of 90.0 mg/L, as shown in Figure 6A. At higher concentrations, the oxidation signal of guanine was stable compared to ds-DNA, which means the PP/P-L CuO:Tb^{3+} NS/SPE surface was saturated by being occupied with ds-DNA molecules. Hence, the optimized starting concentration was selected to be 90.0 mg/L in the fabrication of ds-DNA/PP/P-L CuO:Tb^{3+} NS/SPE. Then, the signal of ds-DNA guanine was recorded at different buffer solutions of Britton–Robinson, acetate and phosphate buffer solutions with the pH 4.8. Figure 6B shows the oxidation currents of 7.15, 9.60 and 4.36 µA recorded for ds-DNA/PP/P-L CuO:Tb^{3+} NS/SPE in Britton–Robinson acetate, and phosphate buffer solutions, successively. As seen, the maximum sensitivity was found in the acetate buffer, thereby it was the solution selected for next testing. The last optimization step was related to the incubation time of the sensor. Thus, the modified electrode was exposed to the Vincristine solution while stirring for variable times. Finally, the interaction of ds-DNA with Vincristine on the ds-DNA/PP/P-L CuO:Tb^{3+} NS/SPE surface was completed during 12 min, and so this time was selected to be optimal for next testing (Figure 6C).

3.5 Analytical experiments

A general, pulse techniques, such as DPV, are more sensitive than the linear sweep methods because there is minimization of the capacitive current. In turn, CV is most commonly used for exploratory purposes. In DPV, small

FIGURE 7
(A) DP voltammograms of ds-DNA/PP/P-L CuO:Tb^{3+} NS/SPE in the presence of increasing concentrations (.0, .001; 1.0; 5.0; 10.0; 20.0; 30.0; 40.0; 50.0; 60.0; 70.0; 80.0; 90.0; 100.0; 200.0, 300.0 and 400.0; μM) of Vincristine **(B)** ΔI *vs.* Vincristine concentration (*n* = 5) plot.

FIGURE 8
Current responses of Vincristine (50.0 μM) Five modified electrode fabricated **(B)** DPVs of modified electrode **(A)** (containing 50.0 μM of Vincristine) and **(B)** after 5 Weeks.

TABLE 1 Comparison of major characteristics of various methods for the determination of Vincristine.

Method	Dynamic ranges	Detection limits	Ref
High-performance liquid chromatography	.25–25.0 μg/ml	8.0 μg/ml	Gupta et al. (2005)
Spectrophotometric	5.0–50.0 μg/ml	2.108 μg/ml	Amila Jeewantha et al. (2017)
Liquid chromatography-tandem mass spectrometry	2.5–250.0 ng/ml	2.5 ng/ml	Jin et al. (2021)
High-performance liquid chromatography-UV detection	.05–5.0 mg/L	.15 mg/L	Kiani et al. (2018)
Voltammetry	.01–.2 μM	7.0 nM	Yong et al. (2004)
Voltammetry	.05–5.0 μM	.26 μM	Zhang et al. (2016b)
Voltammetry	.2–50.0 nM	.08 nM	Saify Nabiabad and Amini, (2020)
Amperometry	2.0–.1 μM	1.1 nM	Babkina and Ulakhovich, (2011)
Voltammetry	.01–400.0 μM	.21 nM and 2.39 nM	This work

TABLE 2 The selectivity test of ds-DNA/PP/P-L CuO:Tb^{3+} NS/SPE for the determination of Vincristine.

Species	Species tolerant limits (Winterference/W vincristine)
K$^+$, Na$^+$, Li$^+$, F$^-$, Ca^{2+}	1,000
Alanine, Glycine, valine, Dopamin, Uric acid, Ascorbic acid	800

amplitude, short pulses are superimposed on a linear ramp. Current is measured before the application of the pulse and at the end of each pulse, and the difference between the currents is calculated. This procedure effectively reduces the background current due to the direct current (DC) ramp, and thus this procedure results in a Faradaic current free of most capacitive current. The major advantage of DPV is low capacitive current, which leads to high sensitivity. In inclusion and exclusion of Vincristine at variable concentrations, the DPVs were obtained for ds-DNA/PP/P-L CuO:Tb^{3+} NS/SPE (Figure 7A). In order to achieve the higher analytical response (anodic current), the optimal conditions for DPV measurements were as follow: ABS, pH 4.8, modulation amplitude of .02505 V, modulation time of 30 ms, interval time of 200 ms, step potential of 10 mV, initial potential = 680 mV and end potential of 930 mV. The net oxidation current of guanine in relation to ds-DNA on the ds-DNA/PP/P-L CuO:Tb^{3+} NS/SPE surface (net current refers to a difference between oxidation current in exposure or non-exposure to drug) had two linear regression equation is demonstrated by y = .0584x + .2586 from .001 μM to 100.0 μM linear range with R^2 = .9995 while the other linear range (100.0–400.0 μM) represents linear regression equation of y = .0048x + 5.61 (R^2 = .999) for Vincristine concentration. The limit of detections (LOD) as low as .21 nM and 2.39 nM (LOD = 3S$_b$/m; where, S$_b$ refers to the standard deviation of blank (n = 5) and m means the slope of linear dynamic range (LDR)), as seen in Figure 7B. According to the result, the high slope of the curve at low concentrations indicates the fact that

the electrode provides enough active sites for vincristine. Whereas, the low slope value of the curve at high concentrations highlights relatively limited active sites for concentrated vincristine.

3.6 Comparison of proposed biosensor with other reported analytical methods for the determination of vincristine

The comparison of analytical efficacy between as-fabricated electrode and other non-electrochemical and electrochemical methods was performed for Vincristine (Table 1) (Yong et al., 2004; Gupta et al., 2005; Babkina and Ulakhovich, 2011; Zhang et al., 2016b; Amila Jeewantha et al., 2017; Kiani et al., 2018; Saify Nabiabad and Amini, 2020; Jin et al., 2021). Based on Table 1, the detection limit and linear range of as-fabricated sensor were better than those of non-electrochemical methods (Gupta et al., 2005; Amila Jeewantha et al., 2017; Kiani et al., 2018; Jin et al., 2021). When comparing with electrochemical methods, the HPLC/MS and HPLC are expensive, sophisticated and multi-process techniques, with the need for sample preparation, pre-filtration and extraction as well as temperature monitoring. In addition, the performance of our proposed DNA biosensor for sensing Vincristine displayed a comparable linear range and better detection limit and sensitivity when comparing with the other electrochemical methods. The detection limit of only Ref (Saify Nabiabad and Amini, 2020). developed for detection of Vincristine was superior to our sensor. The strength of our work than Ref (Saify Nabiabad and Amini, 2020). was the use of non-destructive, non-toxic and cost-effective modifiers (ds-DNA/PP/P-L CuO:Tb^{3+} NS) when comparing with Au nanoparticles, carbon nanotubes, monoclonal antibody. We also achieved lower limit of detection and broader linear range than others (Table 1). Accordingly, as-fabricated biosensor is potentially able to determine the trace amount of Vincristine in various media. Moreover, the electrode used for the sensor fabrication is a SPE that has various advantages like cost-effectiveness, facile modification, admirable accessibility and lower background

TABLE 3 Determination of Vincristine in injection, serum and urine samples using ds-DNA/PP/P-L CuO:Tb^{3+} NS/SPE (n = 5).

Sample	Detected (μM)	Added (μM)	Found (μM)[a]	Recovery (%)
Vincristine injection	3.6	5.0	8.8 ± 2.1	102.3
		10.0	13.7 ± 2.7	100.7
Human Blood Serum	ND[b]	10.0	9.9 ± 3.6	99.0
		15.0	15.5 ± 1.9	103.3
Urine	ND[b]	20.0	20.1 ± 2.3	100.5
		25.0	24.9 ± 2.9	99.6

[a]Mean ± standard deviation for n = 5.
[b]Not detected.
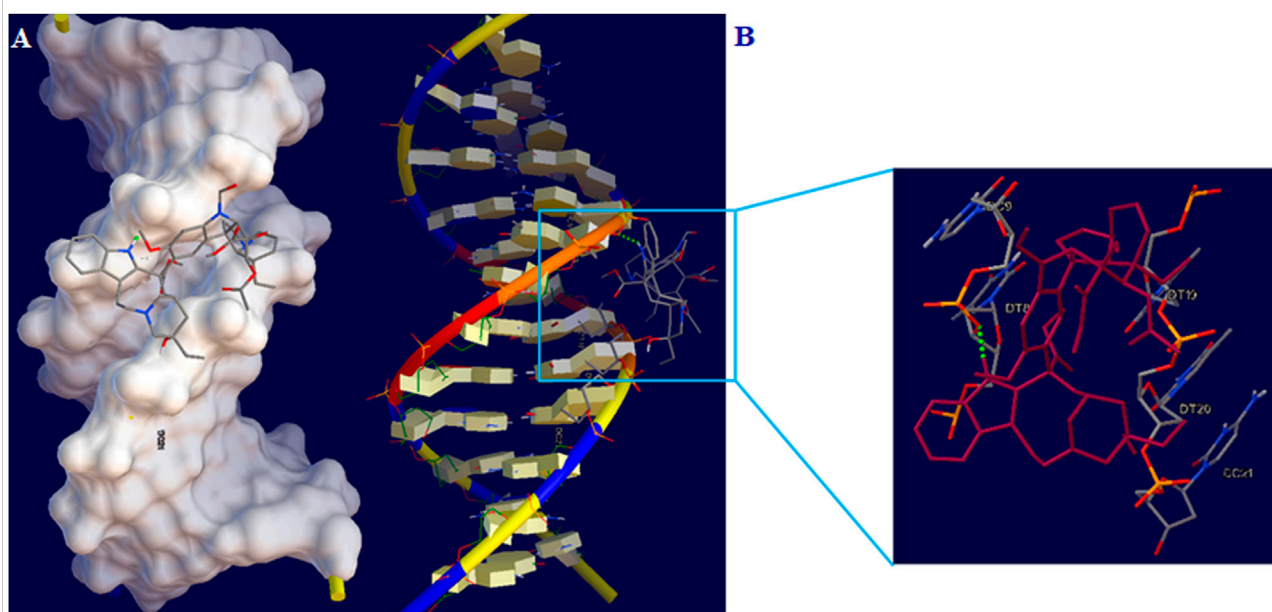
FIGURE 9
(A) Vincristine-DNA minor groove interaction **(B)** Geometrical disposition of vincristine in DNA minor groove.

current when comparing with other electrodes. As seen in Tables 1, the electrode as-fabricated for electrochemically bio-sensing Vincristine generally showed admirable properties for measurement speed, sensitivity, detection limit, linear range and sensitivity when compared to other methods reported in literature.

3.7 Reproducibility, stability and interference analysis

The peak currents of three study Vincristine was measured to determine the ds-DNA/PP/P-L CuO:Tb^{3+} NS/SPE reproducibility using five different sensors fabricated in the identical conditions (n = 5), the results of which showed the relative standard deviation (RSD) of 2.1% that means successful reproducibility of sensor (Figure 8A). The sensor was stored at 4°C for five consecutive weeks to determine the ds-DNA/PP/P-L CuO:Tb^{3+} NS/SPE stability, the results of which showed the maintenance of the peak current of 98.7% of its primary value that means successful stability of sensor (Figure 8B). The modified electrode was stored in ABS (pH 4.8) for Vincristine to test its stability for 10 days, followed by recording the DPVs and then comparing to pre-immersion DPVs. Based on the findings, the peak current was slightly reduced 99.2%, highlighting impressive stability of the sensor.

The interference determinations were carried out under the optimized conditions, consisting of metal ions and organic compounds. The tolerance limit for interferants was the highest concentration presenting a relative error of ˂±5.0% at the Vincristine concentration of 5.0 μM. The alanine, glycine, valine, dopamin, uric acid, ascorbic acid were the most abundant compounds in serum specimens along with Vincristine. According to the results these analytes separately (800-fold, 4.0 mM) could not interfere with the determination of Vincristine. In addition, the Ip values of Vincristine were not affected by 1000-fold concentrations (5.0 mM) of K$^+$, Na$^+$, Li$^+$, F$^-$, Ca^{2+} (Table 2). Accordingly, it can be claimed that none of the tested common interferants had a significant influence on the detection of Vincristine in the real study specimens using the as-fabricated ds-DNA/PP/P-L CuO:Tb^{3+} NS/SPE sensor.

3.8 Real sample analysis

The practical potential of ds-DNA/PP/P-L CuO:Tb^{3+} NS/SPE was evaluated by sensing Vincristine in injection, human blood serum and urine samples using standard addition protocol. According to data (Table 3), the recovery rates were as satisfactory as 99.0%–103.3% that means the successful applicability of our Vincristine sensor. Moreover, the relative standard deviation (RSD) was lower than 4%, indicating a good precision of this method which can meet the requirement of nanoanalysis. Therefore, the developed electrochemical method is applicable to the determination of Vincristine.

3.9 Intercalation docking

Docking study was done to investigate the ideal interaction site and best compounds conformation on the DNA with the lowest energy. The lowest binding energy and Ki for the interaction of DNA with vincristine were obtained to be −6.08 kcal/mol and 35.18 μM, respectively. Studies indicated stabilization of vincristine at the DNA minor groove across one hydrogen bond with the nucleotides and hydrophobic interactions (Figure 9). Hydrogen (H) one bonds to nitrogen 48 of vincristine interacted with O3' from thymine 8 (DT8). Moreover, the major contribution of hydrogen bond has been demonstrated in interacting between vincristine and DNA. According to the results of docking, vincristine can interact effectively with bases in the minor groove of DNA.

4 Conclusion

The P-L CuO:Tb^{3+} NS was prepared by the simple hydrothermal method. The physical characterization and structural properties are confirmed by the XRD, SEM and EDS analysis and discussed well. In addition, new DNA biosensor was designed using ds-DNA immobilization on the surface of PP/P-L CuO:Tb^{3+} NS/SPE. The DPV method was used to detect dsDNA-Vincristine interaction on the modified ds-DNA/PP/P-L CuO:Tb^{3+} NS/SPE surface. The factors affecting the performance of the biosensor such as DNA concentration (90 mg/ml), type of buffer solution (acetate buffer), and ds-DNA/ Vincristine interaction time (12 min)) were optimized. In the analytical investigation of Vincristine using DPV, the modified electrode exhibited two linear responses in concentration ranges of .001–100.0 μM and 100.0–400.0 μM with detection limits of .021 and 2.39 nM, respectively. The experimental results and docking indicated that the binding mode of Vincristine and ds-DNA was minor groove. The practical potential of ds-DNA/PP/ P-L CuO:Tb^{3+} NS/SPE was evaluated by sensing Vincristine in Vincristine injection, human blood serum and urine samples.

Data availability statement

The original contributions presented in the study are included in the article/supplementary material, further inquiries can be directed to the corresponding author.

Ethics statement

The studies involving human participants were reviewed and approved by Ethics committee of Bam University of Medical Sciences. The patients/participants provided their written informed consent to participate in this study.

Author contributions

All authors listed have made a substantial, direct, and intellectual contribution to the work and approved it for publication.

Conflict of interest

The authors declare that the research was conducted in the absence of any commercial or financial relationships that could be construed as a potential conflict of interest.

Publisher's note

All claims expressed in this article are solely those of the authors and do not necessarily represent those of their affiliated organizations, or those of the publisher, the editors and the reviewers. Any product that may be evaluated in this article, or claim that may be made by its manufacturer, is not guaranteed or endorsed by the publisher.

References

Amila Jeewantha, H., Aleksei Ivanovich, S., and Pavel Mihailovich, K. (2017). Validated spectrophotometric method for the estimation of vincristine and vinblastine. *Int. J. Pharm. Pharm. Sci.* 9, 78–86. doi:10.22159/ijpps.2017v9i4.16577

Anqi, E. A., Li, C., Dhahad, H. A., Sharma, K., Attia, E. A., and Abdelrahman, A. (2022). Effect of combined air cooling and nano enhanced phase change materials on thermal management of lithium-ion batteries. *J. Energy Storage* 52, 104906. doi:10.1016/j.est.2022.104906

Babkina, S. S., and Ulakhovich, N. A. (2011). Determination of pharmaceuticals based on indole alkaloids with amperometric DNA-sensors and enzyme immunoassay test-system. *Anal. Lett.* 44, 837–849. doi:10.1080/00032711003789975

Cao, C., Wang, J., Kwok, D., Zhang, Z., Cui, F., and Zhao, D. (2022). webTWAS: a resource for disease candidate susceptibility genes identified by transcriptome-wide association study. *Nucleic Acids Res.* 50, D1123–D1130. doi:10.1093/nar/gkab957

Chen, C., Wang, C., Zhao, P., Zhang, J., Ma, D., and Fei, J. (2022). Determination of dopamine based on a temperature-sensitive PMEO2MA and Au@rGO-MWCNT nanocomposite-modified electrode. *Analyst* 147, 303–311. doi:10.1039/d1an02134f

Childress, M. Q., Christian, J. A., Ramos-Vara, J. A., Rosen, N. K., and Ruple, A. (2022). Greater baseline serum C-reactive protein concentrations are associated with reduced survival in dogs receiving cyclophosphamide, doxorubicin, vincristine, and prednisone chemotherapy for primary nodal diffuse large B-cell lymphoma. *Vet. J.* 289, 105911. doi:10.1016/j.tvjl.2022.105911

Dong, J., Ren, L., Zhang, Y., Cui, X., Hu, P., and Xu, J. (2015). Direct electrodeposition of cable-like CuO@Cu nanowires array for non-enzymatic sensing. *Talanta* 132, 719–726. doi:10.1016/j.talanta.2014.10.027

Duan, Z., Li, C., Zhang, Y., Yang, M., Gao, T., and Liu, X. (2022). Cryogenic minimum quantity lubrication machining: From mechanism to application. *Front. Mech. Eng.* 16, 649–697. doi:10.1007/s11465-021-0654-2

Dung, N. Q., Patil, D., Jung, H., and Kim, D. (2013). A high-performance nonenzymatic glucose sensor made of CuO–SWCNT nanocomposites. *Biosens. Bioelectron.* 42, 280–286. doi:10.1016/j.bios.2012.10.044

Ejaz, A., Babar, H., Ali, H. M., Jamil, F., Janjua, M. M., and Fattah, I. R. (2021). Concentrated photovoltaics as light harvesters: Outlook, recent progress, and challenges. *Sustain. Energy Technol. Assess.* 46, 101199. doi:10.1016/j.seta.2021.101199

Fang, Q., Liu, X., Zeng, K., Zhang, X., Zhou, M., and Du, J. (2022). Centrifuge modelling of tunnelling below existing twin tunnels with different types of support. *Undergr. space* 7, 1125–1138. doi:10.1016/j.undsp.2022.02.007

Farvardin, N., Jahani, Sh., Kazemipour, M., and Foroughi, M. M. (2020). The synthesis and characterization of 3D mesoporous CeO_2 hollow spheres as a modifier for the simultaneous determination of amlodipine, hydrochlorothiazide and valsartan. *Anal. Methods* 12, 1767–1778. doi:10.1039/d0ay00022a

Fathi, Z., Jahani, Sh., Shahidi Zandi, M., and Foroughi, M. M. (2020). Synthesis of bifunctional cabbage flower–like Ho^{3+}/NiO nanostructures as a modifier for simultaneous determination of methotrexate and carbamazepine. *Anal. Bioanal. Chem.* 412, 1011–1024. doi:10.1007/s00216-019-02326-8

Filippi-Chiela, E. C., Eduardo Vargas, J., Bueno e Silva, M. M., Thome, M. P., and Lenz, G. (2022). Vincristine promotes differential levels of apoptosis, mitotic catastrophe, and senescence depending on the genetic background of glioblastoma cells. *Toxicol. Vitro* 85, 105472. doi:10.1016/j.tiv.2022.105472

Foroughi, M. M., Jahani, Sh., Aramesh-Boroujeni, Z., Vakili Fathabadi, M., Hashemipour Rafsanjani, H., and Rostaminasab Dolatabad, M. (2021). Template-free synthesis of ZnO/Fe_3O_4/Carbon magnetic nanocomposite: Nanotubes with hexagonal cross sections and their electrocatalytic property for simultaneous determination of oxymorphone and heroin. *Michrochem. J.* 170, 106679. doi:10.1016/j.microc.2021.106679

Foroughi, M. M., and Jahani, S. (2021). Investigation of a high-sensitive electrochemical DNA biosensor for determination of Idarubicin and studies of DNA-binding properties. *Microchim. J.* 179, 107546. doi:10.1016/j.microc.2022.107546

Gao, T., Li, C., Wang, Y., Liu, X., An, Q., and Li, H. N. (2022). Carbon fiber reinforced polymer in drilling: From damage mechanisms to suppression. *Compos. Struct.* 286, 115232. doi:10.1016/j.compstruct.2022.115232

Gupta, M. M., Singh, D. V., Tripathi, A. K., Pandey, R., Verma, R. K., and Singh, S. (2005). Simultaneous determination of vincristine, vinblastine, catharanthine, and vindoline in leaves of catharanthus roseus by high-performance liquid chromatography. *J. Chromatogr. Sci.* 43, 450–453. doi:10.1093/chromsci/43.9.450

Hu, Z., and Liu, H. (2015). Three-dimensional CuO microflowers as anode materials for Li-ion batteries. *Ceram. Int.* 41, 8257–8260. doi:10.1016/j.ceramint.2015.03.010

Iftikhar, T., Asif, M., Aziz, A., Ashraf, G., Jun, S., and Li, G. (2021). Topical advances in nanomaterials based electrochemical sensors for resorcinol detection. *Trends Environ. Anal. Chem.* 31, e00138. doi:10.1016/j.teac.2021.e00138

Iftikhar, T., Aziz, A., Ashraf, G., Xu, Y., Li, G., and Zhang, T. (2022). Engineering MOFs derived metal oxide nanohybrids: Towards electrochemical sensing of catechol in tea samples. *Food Chem.* 395, 133642. doi:10.1016/j.foodchem.2022.133642

Iftikhar, T., Xu, Y., Aziz, A., Ashraf, G., Li, G., and Asif, M. (2021). Tuning electrocatalytic aptitude by incorporating α-MnO2 nanorods in Cu-MOF/rGO/CuO hybrids: Electrochemical sensing of resorcinol for practical applications. *ACS Appl. Mat. Interfaces* 13, 31462–31473. doi:10.1021/acsami.1c07067

Jahani, Sh., Sedighi, A., Toolabi, A., and Foroughi, M. M. (2022). Development and characterization of La_2O_3 nanoparticles@snowflake-like Cu_2S nanostructure composite modified electrode and application for simultaneous detection of catechol, hydroquinone and resorcinol as an electrochemical sensor. *Electrochim. Acta* 416, 140261. doi:10.1016/j.electacta.2022.140261

Jansi Rani, B., Ravi, G., Yuvakkumar, R., Hasan, Zinab M., Ravichandran, S., and Hong, S. I. (2020). Binder free, robust and scalable CuO@GCE modified electrodes for efficient electrochemical water oxidation. *Mat. Chem. Phys.* 239, 122321. doi:10.1016/j.matchemphys.2019.122321

Jia, D., Zhang, Y., Li, C., Yang, M., Gao, T., and Said, Z. (2022). Lubrication-enhanced mechanisms of titanium alloy grinding using lecithin biolubricant. *Tribol. Int.* 169, 107461. doi:10.1016/j.triboint.2022.107461

Jin, Y., Li, Y., Uddin, M. E., Sparreboom, A., and Hu, S. (2021). Rapid quantification of vincristine in mouse plasma using ESI-LC-MS/MS: Application to pharmacokinetic studies. *J. Chromatogr. B* 1168, 122591. doi:10.1016/j.jchromb.2021.122591

Khan, J., Ali, G., Khurshid, A., Saeed, A., Ahmad, S., and Ullah, N. (2022). Mechanistic efficacy assessment of selected novel methanimine derivatives against vincristine induced neuropathy: *In-vivo*, *ex-vivo* and in-silico correlates. *Int. Immunopharmacol.* 112, 109246. doi:10.1016/j.intimp.2022.109246

Kiani, M., Qomi, M., Hashemian, F., and Rajabi, M. (2018). Multivariate optimization of solvent bar microextraction combined with HPLC-UV for determination of trace amounts of vincristine in biological fluids. *J. Chromatogr. B* 1072, 397–404. doi:10.1016/j.jchromb.2017.10.054

Kumar, R., Ranjan, N., Kumar, V., Kumar, R., Singh Chohan, J., and Piyush, A. Y. (2022). Characterization of friction stir-welded polylactic acid/aluminum composite primed through fused filament fabrication. *J. Mat. Eng. Perform.* 31, 2391–2409. doi:10.1007/s11665-021-06329-4

Li, A. L., Crystal, J. D., Lai, Y. Y., Sajdyk, T. J., Renbarger, J. L., and Hohmann, A. G. (2021). An adolescent rat model of vincristine-induced peripheral neuropathy. *Neurobiol. Pain* 10, 100077. doi:10.1016/j.ynpai.2021.100077

Li, B., Li, C., Zhang, Y., Wang, Y., Jia, D., and Yang, M. (2016). Grinding temperature and energy ratio coefficient in MQL grinding of high-temperature nickel-base alloy by using different vegetable oils as base oil. *Chin. J. Aeronaut.* 29, 1084–1095. doi:10.1016/j.cja.2015.10.012

Moarefdoust, M. M., Jahani, Sh., Moradalizadeh, M., Motaghi, M. M., and Foroughi, M. M. (2022). A DNA biosensor based on a raspberry-like hierarchical nano-structure for the determination of the anticancer drug nilotinib. *ChemistrySelect* 11, e202100261. doi:10.1002/open.202100261

Moarefdoust, M. M., Jahani, Sh., Moradalizadeh, M., Motaghi, M. M., and Foroughi, M. M. (2022). A DNA biosensor based on a raspberry-like hierarchical nano-structure for the determination of the anticancer drug nilotinib. *ChemistryOpen* 11, e202100261. doi:10.1002/open.202100261

Mujib, A., Fatima, S., and Malik, M. Q. (2022). Cryo-derived plants through embryogenesis showed same levels of vinblastine and vincristine (anticancer) in Catharanthus roseus and had normal genome size. *Sci. Rep.* 12, 16635. doi:10.1038/s41598-022-20993-z

Núñez, C., Triviño, J. J., and Arancibia, V. (2021). A electrochemical biosensor for As(III) detection based on the catalytic activity of Alcaligenes faecalis immobilized on a gold nanoparticle–modified screen–printed carbon electrode. *Talanta* 223, 121702. doi:10.1016/j.talanta.2020.121702

Park, H. J., Choi, N.-J., Kang, H., Jung, M. Y., Park, J. W., and Park, K. H. (2014). A ppb-level formaldehyde gas sensor based on CuO nanocubes prepared using a polyol process. *Sensors Actuators B Chem.* 203, 282–288. doi:10.1016/j.snb.2014.06.118

Saify Nabiabad, H., and Amini, M. (2020). Fabrication of an impedimetric immunosensor for screening and determination of vincristine in biological samples. *J. Anal. Chem.* 75, 1094–1101. doi:10.1134/s1061934820080092

Tian, Y., Yu, L., Wang, W. P., Zhang, X., and Peng, W. (2015). CuO nanoparticles on sulfur-doped graphene for nonenzymatic glucose sensing. *Electrochim. Acta* 156, 244–251. doi:10.1016/j.electacta.2015.01.016

Uma Maheswari, R., Jansi Rani, B., Ravi, G., Yuvakkumar, R., Ameen, F., and Al-Sabri, A. (2018). Structural, morphological, optical and antibacterial properties of pentagon CuO nanoplatelets. *J. Sol-Gel Sci. Tech.* 87, 515–527. doi:10.1007/s10971-018-4773-0

Vakili Fathabadi, M., Hashemipour Rafsanjani, H., Foroughi, M. M., Jahani, Sh., and Arefi Nia, S. (2020). Synthesis of magnetic ordered mesoporous carbons (OMC) as an electrochemical platform for ultrasensitive and simultaneous detection of thebaine and papaverine. *J. Electrochem. Soc.* 167, 027509. doi:10.1149/1945-7111/ab6446

Yang, C., Wang, J., Xiao, F., and Xintai, S. (2014). Microwave hydrothermal disassembly for evolution from CuO dendrites to nanosheets and their applications in catalysis and photo-catalysis. *Powder Technol.* 264, 36–42. doi:10.1016/j.powtec.2014.05.012

Yang, M., Li, C., Zhang, Y., Wang, Y., Li, B., and Jia, D. (2017). Research on microscale skull grinding temperature field under different cooling conditions. *Appl. Therm. Eng.* 126, 525–537. doi:10.1016/j.applthermaleng.2017.07.183

Yang, Z., Feng, J., Qiao, J., Yan, Y., Yu, Q., and Sun, K. (2012). Copper oxide nanoleaves decorated multi-walled carbon nanotube as platform for glucose sensing. *Anal. Methods* 4, 1924. doi:10.1039/c2ay25283j

Yong, Y., Jing-Bo, H., Jun, S., and Qi-Long, L. (2004). Study on the electrochemical behaviors of vincristine and the interaction of vincristine with tubulin. *Acta Chim. Sin.* 62, 137–141.

Zhang, H., Zou, Q., Ju, Y., Song, C., and Chen, D. (2022). Distance-based support vector machine to predict DNA N6-methyladenine modification. *Curr. Bioinform.* 17, 473–482. doi:10.2174/1574893617666220404145517

Zhang, Y. B., Li, C. H., Yang, M., Jia, D. Z., Wang, Y., and Li, B. (2016). Experimental evaluation of cooling performance by friction coefficient and specific friction energy in nanofluid minimum quantity lubrication grinding with different types of vegetable oil. *J. Clean. Prod.* 139, 685–705. doi:10.1016/j.jclepro.2016.08.073

Zhang, Y., Zheng, J., and Guo, M. (2016). Preparation of molecularly imprinted electrochemical sensor for detection of vincristine based on reduced graphene oxide/gold nanoparticle composite film. *Chin. J. Chem.* 34, 1268–1276. doi:10.1002/cjoc.201600582

Zheng, B., Liu, G., Yao, A., Xiao, Y., Juan, D., and Guo, Y. (2014). A sensitive AgNPs/CuO nanofibers non-enzymatic glucose sensor based on electrospinning technology. *Sensors Actuators B* 195, 431–438. doi:10.1016/j.snb.2014.01.046

Zhou, Q., Umar, A., Sodki, E. M., Amine, A., Xu, L., and Gui, Y. (2018). Fabrication and characterization of highly sensitive and selective sensors based on porous NiO nanodisks. *Sens. Actuators B* 259, 604–615. doi:10.1016/j.snb.2017.12.050

Probe-integrated electrochemical immunosensor based on electrostatic nanocage array for reagentless and sensitive detection of tumor biomarker

Dong Chen[1], Xuan Luo[2] and Fengna Xi[2]*

[1]General Surgery Department, Shanxi Bethune Hospital, Taiyuan, China, [2]Department of Chemistry, Zhejiang Sci-Tech University, Hangzhou, China

Sensitive detection of tumor biomarkers is crucial for early diagnosis and prognosis evaluation of cancer. Owing to no need of labelled antibody, formation of sandwich immunocomplexes and additional solution-based probe, probe-integrated electrochemical immunosensor for reagentless detection of tumor biomarkers is highly desirable. In this work, sensitive and reagentless detection of a tumor biomarker is realized based on fabrication of a probe-integrated immunosensor by confining redox probe in electrostatic nanocage array modified electrode. Indium tin oxide (ITO) electrode is employed as the supporting electrode because it is cheap and easily available. The silica nanochannel array consisted of two layers with opposite charges or different pore diameters was designated as bipolar films (bp-SNA). In this work, Electrostatic nanocage array is equipped on ITO electrode by growth of bp-SNA with two layered nanochannel array having different charge properties including a negatively charged silica nanochannel array (n-SNA) and a positively charged amino-modified SNA (p-SNA). Each SNA can be easily grown with 15 s using electrochemical assisted self-assembly method (EASA). Methylene blue (MB) is applied as the model electrochemical probe with positive charge to be confined in electrostatic nanocage array with stirring. The combination of the electrostatic attraction from n-SNA and the electrostatic repulsion from p-SNA endows MB with highly stable electrochemical signal during continuous scanning. When the amino groups of p-SNA are modified using the bifunctional glutaraldehyde (GA) to introduce aldehydes, the recognitive antibody (Ab) of the most commonly used tumor biomarker, carcinoembryonic antigen (CEA), can be covalently immobilized. After the non-specific sites are blocked, the immunosensor is successfully fabricated. As the formation of antigen-antibody complex decreases electrochemical signal, the immunosensor can achieve reagentless detection of CEA ranged from 10 pg/mL to 100 ng/mL with a low limit of detection (LOD, 4 pg/mL). Determination of CEA in human serum samples is realized with high accuracy.

1 Introduction

Cancer, malignant tumor, is a serious threat to human health. As known, early screening and diagnosis of cancer is the key to reduce mortality. Tumor biomarkers are substances secreted by tumor cells or produced by the body to resist tumors in the process of tumor formation and growth (Fumet et al., 2020; Jones et al., 2021; Liu et al., 2022) Their appearance can precede the morphological and biological changes of cells or tissues. Thus, tumor biomarkers play an important role in the pathological diagnosis, accurate classification, clinical diagnosis and treatment, observation of curative effect, and prognosis evaluation of cancer. For example, carcinoembryonic antigen (CEA) is one of the most important tumor biomarkers related to colon cancer, lung cancer and ovarian cancer (Tan et al., 2009; Grunnet and Sorensen, 2012; Sorensen et al., 2016) CEA is usually produced in gastrointestinal tissues during fetal development, but it stops after birth. Commonly, CEA exists in the blood of healthy adults at a very low level (usually below 5.0 ng/mL). However, it increases significantly in cancer patients. Therefore, rapid and sensitive determination of CEA is of great significance.

At present, methods based on enzyme linked immunosorbent assay (ELISA) (Arnab et al., 2014) chemiluminescence (Hou et al., 2022) fluorescence (Wu et al., 2021) surface plasmon resonance (SPR) (Liu et al., 2016) and quartz crystal microbalance (QCM) (Chi et al., 2020) have been used for CEA detection. However, these methods commonly suffer from low operation speed, unsatisfied sensitivity, expensive instruments, and special reagents. Electrochemical (EC) immunosensors are attractive because of simple instrument, easy operation, high sensitivity and great potential for integration and miniaturization (Lin et al., 2020; Zhang et al., 2022a) In addition, electrochemical sensors can achieve high sensitivity or even ultra-high sensitivity in combination with nanomaterial-based signal amplification (Ayl´ en et al., 2022; Zheng et al., 2022a) These merits of characteristics exhibit great potential in fast and sensitive detection of tumor biomarkers in biological samples. Usually, EC detection is based on the electrochemical signal of the analyte or redox probe (Gong et al., 2022a; Zheng et al., 2022b) As tumor biomarkers are proteins with no electrochemical activity, electrochemical detection of tumor markers is mainly realized based on the change of the electrochemical signal of redox probes (Chen et al., 2022) Therefore, effective signal probes are the key to detect tumor biomarkers in EC immunoassay. Compared with the detection based on free probes in solution, the probe-integrated (reagentless) immunosensors based on the immobilization of redox probes on the electrode surface can realize convenient and rapid detection (Gong et al., 2022b) In comparison with the sandwich immunoassay, these label-free immunosensors without label of antibody also greatly reduce the cost of detection and simplify the operation steps. Thus, the development of simple and reliable probe-integrated electrochemical immunosensors is highly desirable.

The introduction of nanomaterials to efficiently immobilize signal probes is the key to build probe-integrated immunosensors with high sensitivity. Recent studies have proven that silica nanochannel array film (SNA), also vertically-ordered silica nanochannels film (VMSF), is attractive as a matrix to enrich electrochemical or electrochemiluminescence probes (Liang et al., 2021; Ma et al., 2022a) SNA is a nanoscale ultrathin film (20–200 nm) with high pore density (~7.5 × 10^{12} pores/cm^2), ultrasmall (2–3 nm) nanochannel array (Walcarius, 2021; Yan et al., 2021) These unique structures endow SNA modified electrodes with significant advantages in electrochemical sensing applications (Ma et al., 2022b; Huang et al., 2022; Zou et al., 2022) For instance, ultrasmall nanochannels have screening capabilities on molecular level. On the one hand, the large substances in complex matrices cannot enter the nanochannels, leading to high anti-fouling of the electrodes (Zhou et al., 2022a; Zhou et al., 2022b; Deng et al., 2023) On the other hand, the dissociation of silanol groups (Si-OH, pK_a~2) in SNA makes the surface of nanochannel negatively charged, which can enrich positively charged molecules through electrostatic interaction (Zheng et al., 2022c; Wang et al., 2022; Huang et al., 2023) The charge of SNA can also be reversed by introducing functional groups. Thus, functional nanostructures, e.g., electrostatic nanocage arrays, can be flexibly designed by growing multilayer of SNA (Gong et al., 2022b; Gong et al., 2022c) Secondly, SNA with confined probe can generate gating signal when biomacromolecules are detected. As known, the SiO$_2$ structure of SNA is an electrical insulator. As antibodies cannot enter the nanochannels of SNA, they can only be immobilized on the outer surface of SNA. When tumor biomarkers bind with the recognitive antibodies, the entrance of some nanochannels will be blocked, decreasing the signal of immobilized electrochemical probes resulting from the increased interface resistance of electrode (Gong et al., 2022b) Therefore, in combination of high specific surface area, SNA-based electrodes exhibit great potential for the construction of probe-integrated electrochemical immunosensors.

In this work, a probe-integrated electrochemical immunosensor is fabricated based on confinement of electrochemical probe in electrostatic nanocage array prepared by double-layered bipolar SNA (bp-SNA), which enables sensitive and reagentless detection of tumor marker carcinoembryonic antigen (CEA). The cheap and easily available indium tin oxide (ITO) electrode is applied as the supporting electrode to successively grow the negatively charged SAN (n-SNA) and the positively charged SNA with rich amine groups (p-SNA). Owing to the asymmetric surface charge, n-SNA and p-SNA constitute bp-SNA with electrostatic nanocage array. The electrochemical probe, methylene blue (MB), is electrostatically confined in the nanocage array to achieve high loading and good stability (MB@ bp-SNA/ITO). After the amine groups of p-SNA is modified to produce aldehyde surface, CEA recognitive antibody (Ab) are covalently immobilized on the outer surface of bp-SNA followed by blocking non-specific sites to fabricate the immunosensor interface. The constructed probe-integrated immunoassay system is also employed to achieve rapid and highly sensitive detection of CEA. The developed probe-integrated electrochemical immunosensor has advantages of simple fabrication and easy operation because of no need labelled antibody, formation of sandwich immunocomplexes and additional solution-based probe. In addition, stable enrichment of electrochemical probe in electrostatic nanocage array leads to reagentless detection of tumor biomarkers with high sensitivity and good stability.

2 Materials and methods

2.1 Chemicals and materials

Tetraethyl orthosilicate (TEOS), hexadecyl trimethyl ammonium bromide (CTAB), sodium phosphate dibasic dodecahydrate ($Na_2HPO_4 \cdot 12H_2O$), methylene blue trihydrate (MB), glutaraldehyde (GA) and tripyridine ruthenium chloride hexahydrate ($Ru(bpy)_3Cl_2 \cdot 6H_2O$) were purchased from Aladdin Chemistry Co., Ltd. (Shanghai, China). Sodium dihydrogen phosphate dehydrate ($NaH_2PO_4 \cdot 2H_2O$), 3-aminopropyltriethoxysilane (APTES) and potassium hydrogen phthalate (KHP) were purchased from Macklin (Shanghai, China). Ethanol (EtOH) and hydrochloric acid (HCl) was obtained from Hangzhou Gaojing Chemistry Co., Ltd. (Hangzhou, China). Sodium nitrate ($NaNO_3$) were purchased from the Wuxi Zhang Wang Chemical Industry (Wuxi, China). Carbohydrate antigen 199 (CA199), carcinoembryonic antigen (CEA), CEA antibody, prostate specific antigen (PSA), carcinoma antigen 125 (CA125) and alphafetoprotein (AFP) were purchased from Beijing KEY-BIO Biotech Co., Ltd. (Beijing, China). ITO coated glasses (<17 Ω/square, thickness: 100 $\pm$ 20 nm) were purchased from Zhuhai Kaivo Optoelectronic Technology (Shenzhen, China). To get a clean surface, ITO was immersed in NaOH solution (1 M) overnight and then sonicated in acetone, ethanol, and ultrapure water, respectively. All aqueous solutions were prepared with ultrapure water (18.2 MΩ cm) in this work.

2.2 Measurements and instrumentations

The morphology of bp-SNA modified electrode were investigated using field-emission scanning electron microscope (SEM, S-4800, Hitachi, Japan) and transmission electron microscope (TEM, Hitachi, HT7700, Japan), respectively. The acceleration voltage of TEM is 100 kV. The TEM sample was prepared by peeling the bp-SNA from the ITO electrode surface. After being dispersed in ethanol (200 μL) and sonicated, the obtained solution was dropped onto a copper grid. An Autolab PGSTAT302N electrochemical workstation (Metrohm, Switzerland) was used to perform all electrochemical measurements including cyclic voltammetry (CV), electrochemical impedance spectroscopy (EIS) and differential pulse voltammetry (DPV). A traditional three-electrode system was used with bare or modified ITO as working electrode, Ag/AgCl (saturated KCl solution) as reference electrode and Pt wire electrode as counter electrode. The applied DPV parameters including step modulation amplitude (0.005 V), modulation time (0.05 s) and interval time (0.2 s).

2.3 Preparation of MB@bp-SNA/ITO

The n-SNA was firstly grown on bare ITO electrode (1 cm $\times$ 0.5 cm) by EASA method (Zhang et al., 2022b; Yang et al., 2022) Briefly, a mixture consisting of $NaNO_3$ aqueous solution (20 mL, 0.1 M, pH = 2.6), ethanol (20 mL), TEOS (3.050 mL), and CTAB (1.585 g) were prepared. After stirring for 2.5 h to pre-hydrolyze

TEOS, the precursor for the growth of n-SNA was obtained. Then, bare ITO electrode was immersed into the precursor solution and applied a constant current density (-0.70 mA cm^{-2}) for 10 s. After being quickly rinsed with ultrapure water and aged at 120℃ overnight, the modified electrode containing surfactant micelles (SM) inside the nanochannels was obtained and termed as SM@n-SNA/ITO. The bp-SNA/ITO electrode was then obtained after p-SNA was grown on n-SNA/ITO electrode by EASA method. Typically, a solution consisting of $NaNO_3$ aqueous solution (20 mL, 0.1 M, pH = 2.6), ethanol (20 mL), TEOS (2.732 mL), APTES (0.318 mL) and CTAB (1.585 g) were mixed and stirred for 2.5 h to obtain the precursor solution. Before the growth of p-SNA, the possible silica spheres on SM@n-SNA/ITO electrode were removed by scotch tape. SM could be removed by immersing the SM@n-SNA/ITO electrode in HCl-ethanol solution (0.1 M) and stirring for 5 min. Subsequently, the n-SNA/ITO was placed in the above precursor solution and a constant current density (-0.70 mA cm^{-2}) was applied to the electrode for 15 s. After rinsed with a large amount of ultrapure water and aged overnight at 120℃, the SM@bp-SNA/ITO electrode was obtained. Finally, silica spheres on the surface of bp-SNA/ITO electrode were removed by Scotch tape. SM was removed using HCl-ethanol solution (0.1 M) to get an electrode with electrostatic nanocage array, that was termed as bp-SNA/ITO. Then, MB was confined in electrostatic nanocage array. Briefly, bp-SNA/ITO was immersed in a PBS (0.01 M, pH = 7.4) solution containing MB (1 mM) under stirring for 6 min. After thorough rise, electrode with confined probe was obtained and denoted as MB@bp-SNA/ITO.

2.4 Fabrication of immunosensor

To fabricate the immuno-recognitive interface, glutaraldehyde (GA) was chosen as the bifunctional linker to introduce aldehyde groups on the outer surface of p-SNA. Briefly, the MB@bp-SNA/ITO electrode was immersed in GA (1%, pH = 7.4) solution for 1 h at 37℃ in the dark. After removing the residual GA, CEA antibody (50 μL, 10 μg/mL) was dropped on the surface of GA/MB@bp-SNA/ITO electrode and incubated at 37℃ for 1 h. The unbounded CEA antibody was rinsed with PBS and the obtained electrode (Ab/GA/MB@bp-SNA/ITO) was immersed in BSA (1 mg/mL in 0.01 M PBS, pH 7.4) at 37℃ for 1 h to block non-specific sites. Finally, the immunosensor, BSA/Ab/GA/MB@bp-SNA/ITO electrode, was obtained.

2.5 Electrochemical detection of CEA

For the detection of CEA, each BSA/Ab/GA/MB@bp-SNA/ITO electrode was incubated with different concentrations of CEA at 37℃ for 0.5 h. PBS (0.01 M, pH = 7.4) was used as the detection electrolyte and the electrochemical signals of MB in absence and presence of CEA were measured by DPV. For the analysis of real sample, human serum (healthy woman) was diluted by a factor of 50 using PBS (0.01 M, pH 7.4).
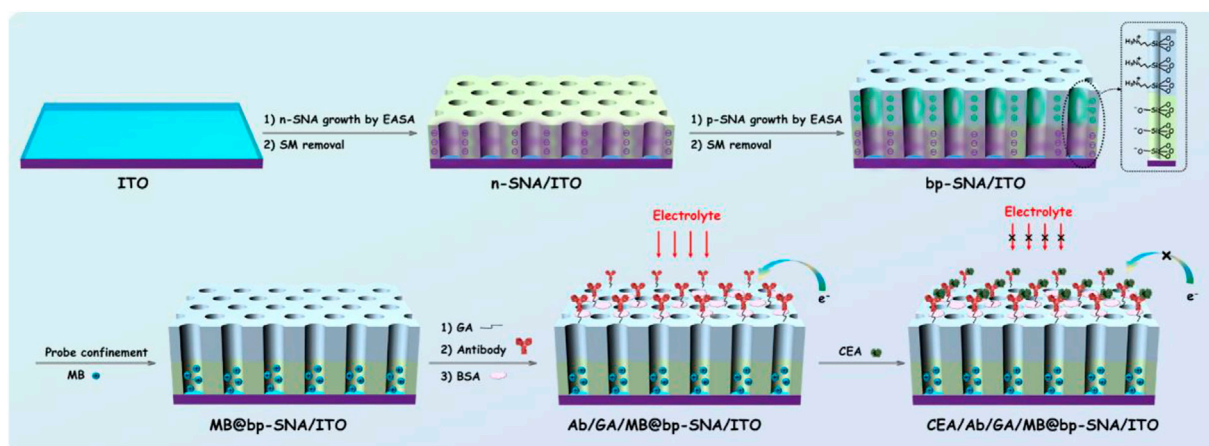
FIGURE 1
Schematic illustration for the fabrication of probe-integrated immunosensor based on MB confinement in bp-SNA and the electrochemical detection of CEA.

3 Results and discussion

3.1 Fabrication of probe-integrated immunosensor based on confinement of redox probe on electrostatic nanocage array

Electrochemical detection has the advantages of fast detection speed, easy miniaturization and integration. In addition, high sensitivity can be achieved by combining nanomaterial for signal amplification. As the electrode is easy to be contaminated by the complex matrix of real sample, the current electrochemical immunoassay mostly uses sandwich immune complexes with the labeling signal on the second antibody (Ab_2) for detection. However, antibody labeling and sandwich immunoassay mode increase the operation complexity and detection cost. Electrochemical immunoassay without the label of antibody remains challenges. In this work, a probe-integrated electrochemical immunosensor is constructed for highly sensitive detection of CEA by confinement redox probe on electrostatic nanocage array. Figure 1 illustrates the fabrication of probe-integerated immunosensor based on confinement of redox probe on electrostatic nanocage array. As shown, the cheap ITO electrode is used as the support electrode and SNA with negative charge (n-SNA) can be rapidly grown on ITO surface within 10 s by electrochemical assisted self-assembly method (EASA). Using the negative surface charge and high specific surface area of n-SNA, small molecule probes with opposite charges (MB) can be immobilized in large quantities through electrostatic interaction. However, the probes are easy to run off during use, thus reducing the detection accuracy of immunoassay. In this work, positive SNA (p-SNA) is further grown on the surface of n-SNA, and a bipolar film (bp-SNA) is prepared by using the above double-layered SNA with asymmetric surface charge. As shown, bp-SNA is consisted of electrostatic nanocage array. Based on the electrostatic attraction of the inner n-SNA layer and the electrostatic repulsion of the outer p-SNA layer, the electrostatic nanocage array can achieve high loading and high stability confinement of the positive electrochemical probe MB (MB@bp-SNA/ITO).

Using functional siloxane, SNA with reactive groups (e.g., amino group, epoxy group, etc.) can be introduced. Herein, amino containing siloxanes (3-aminopropyl-triethoxysilane, APTES) is employed to grow p-SNA with rich amino groups on n-SNA. After the amino group on the outer surface of p-SNA reacts with glutaraldehyde (GA/MB@bp-SNA/ITO), the introduced aldehyde group can be applied to covalently immobilize the recognitive antibody of CEA. After the non-specific sites are blocked by bovine serum albumin (BSA), the immunosensor can be fabricated and donated as BSA/Ab/GA/MB@bp-SNA/ITO. When CEA specifically binds to the Ab on the immune recognitive interface, the formed antigen-antibody complex increases the interface resistance of the electrode, resulting in the reduction of the electrochemical signal of MB. Based on this mechanism, the electrochemical detection of CEA can be realized.

3.2 Morphology of bp-SNA

Transmission electron microscope (TEM) and scanning electron microscope (SEM) are applied to characterize the morphology of bp-SNA. From the top-view TEM images at different magnification, it can be seen that the bp-SNA has nanochannel array evenly arranged in hexagonal shape. No obvious defects are observed and the diameter of each channel is 2.3 ± 0.3 nm ($n = 11$) (Figure 2A). The cross-sectional SEM image reveals p-SNA layer, n-SNA layer, ITO layer and glass from top to bottom (Figure 2B). The thicknesses of p-SNA layer and n-SNA are 103 ± 1 nm ($n = 3$) and 111 ± 1 nm ($n = 3$), respectively. The silica spheres adhered on the surface can be easily removed by adhesive tap.

3.3 Stable confinement of MB in bp-SNA

The standard electrochemical probe ($Ru(bpy)_3^{2+}$) was used to investigate the changes of electrode surface during the electrode
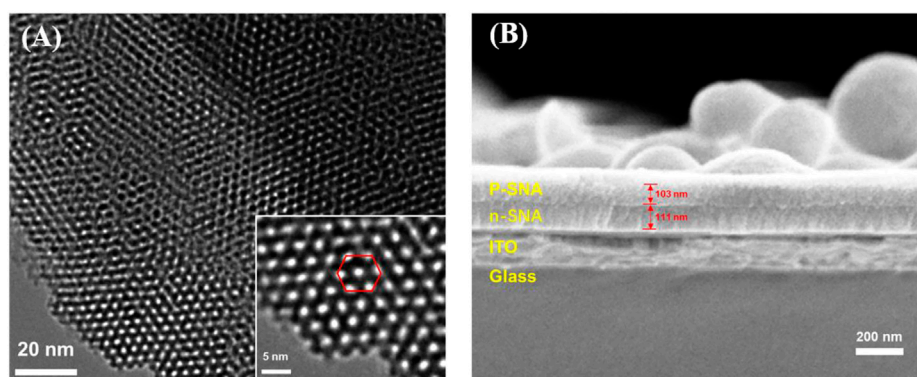
FIGURE 2
(A) Top-view TEM images of bp-SNA at different magnification. **(B)** Cross-sectional SEM image of bp-SNA/ITO.
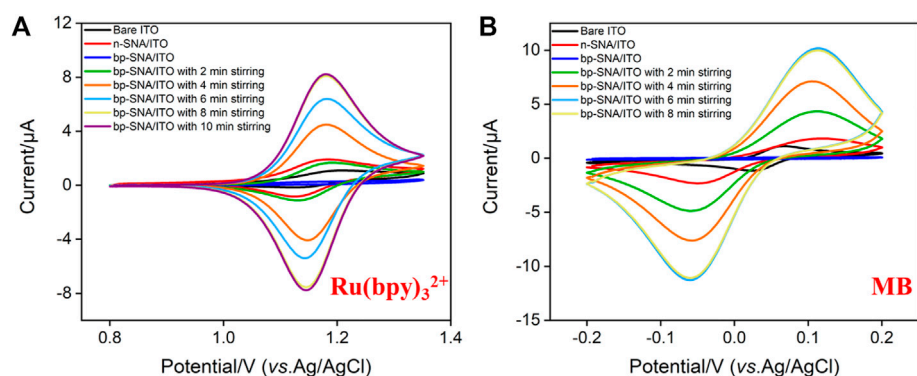
FIGURE 3
CV curves obtained on bare ITO, n-SNA/ITO, bp-SNA/ITO electrodes in KHP (0.05 M, pH = 4) containing 10 μM Ru(bpy)$_3$$^{2+}$ **(A)** or MB **(B)** solution.

modification. As shown in Figure 3A, the redox signal of Ru(bpy)$_3$$^{2+}$ can be observed on bare ITO electrode. When n-SNA was grown on ITO surface, a significantly increased redox peak was observed. This is due to the negative charge generated by the ionization of silanol group (pK_a~2) in n-SNA, which can attract Ru(bpy)$_3$$^{2+}$ electrostatically, thus generating high redox signal. However, there is no obvious redox peak on bp-SNA/ITO after further growth of p-SNA, which is attributed to the electrostatic repulse from the positively charged sites generated after the protonation of amino groups in p-SNA. When bp-SNA/ITO is stirred in Ru(bpy)$_3$$^{2+}$ solution, the redox peak current of Ru(bpy)$_3$$^{2+}$ increases with the increase of stirring time. After stirring for 8 min, the redox peak current reaches the maximum value. In addition, the peak current is significantly higher than that of n-SNA/ITO electrode. This shows that the positive probe can break through the electrostatic repulsion of the outer p-SNA in the stirring process. The probed can be enriched by the inner n-SNA, generating a high redox signal. Supplementary Figure S1 (SI) compares cyclic voltammetry curves obtained from bare ITO, n-SNA or bp-SNA modified ITO electrodes in KHP containing Fe(CN)$_6$$^{3-}$. As seen, the peak current
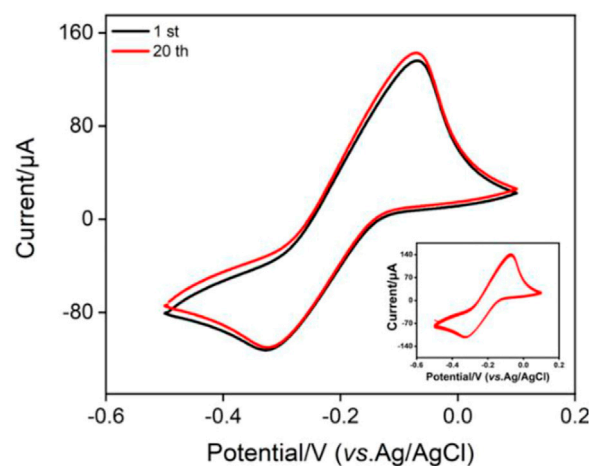
FIGURE 4
CV curves obtained on MB@bp-SNA/ITO in PBS (0.01 M, pH = 7.4). The inset is the CV curves obtained in successive scanning.
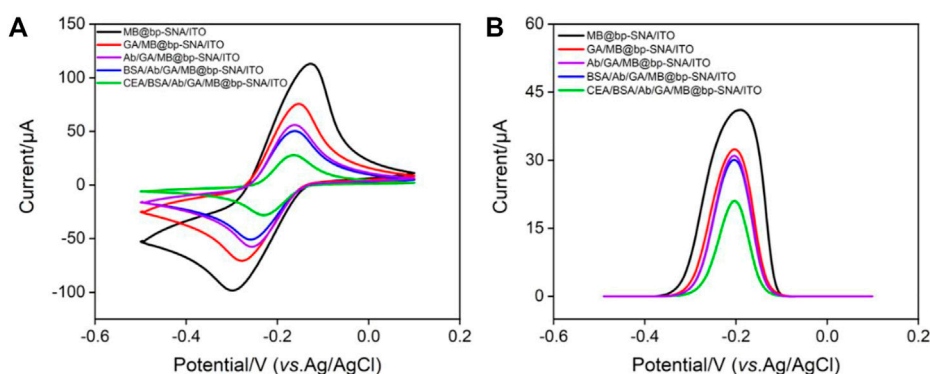
FIGURE 5
(A) CV curves and **(B)** DPV curves obtained on different modified electrode in PBS (0.01 M, pH = 7.4).

obtained on n-SNA/ITO electrode decreased resulting from the permselective towards anionic $Fe(CN)_6^{3-}$. After the growth of bp-SNA, $Fe(CN)_6^{3-}$ is attracted by the electrostatic attraction of the external p-SNA layer and repelled by the electrostatic repulsion of the internal n-SNA layer. Thus, an increased current for $Fe(CN)_6^{3-}$ was observed at the bp-SNA/ITO compared with the n-SNA/ITO. However, the electrochemical signal of $Fe(CN)_6^{3-}$ displays almost no change after stirring for 30 min, indicating no effect on the enrichment of negative probes.

The electrochemical probe, methylene blue (MB), is chosen to be confined in the nanocage array in this work. In case of the positively charged MB, its electrochemical signals on ITO, n-SNA/ITO, bp-SNA/ITO electrodes exhibit a consistent trend with that of $Ru(bpy)_3^{2+}$. In the stirring state, MB can also break through the electrostatic repulsion of the outer p-SNA layer and be enriched by the negatively charged n-SNA. The enrichment equilibrium time was 6 min (Figure 3B).

The inset in Figure 4 shows the CV curves when the electrode with fixed MB probe (MB/bp-SNA/ITO) is placed in buffer solution for continuous scanning. As seen, the peak currents do not significantly change when the electrode is continuously scanned. The peak currents obtained on the 1st and 20th scanning cycles are basically the same (Figure 4), indicating high stability of MB. This phenomenon is unlike the single-layered n-SNA modified electrode which only concentrates MB by electrostatic attraction. When MB is entrapped in electrostatic nanocage array in bp-SNA, the electrostatic attraction of the inner n-SNA and the electrostatic repulsion of the outer layer p-SNA makes MB stably confined in bp-SNA/ITO electrode.

3.4 Fabrication of the immunosensor

CV, DPV and EIS are used to observe the changes of electrode surface during the construction of immunosensor. When MB/bp-SNA/ITO is modified with GA derivatization (GA/MB/bp-SNA/ITO), immobilization of antibodies and blocking of non-specific sites (BSA/Ab/GA/MB/bp-SNA/ITO), the electrode surface resistance gradually increases, leading to gradually decreased redox peak current of MB (Figure 5A). The DPV curves in

Figure 5B also proves the same result. When the fabricated immunosensor was incubated with CEA, decreased peak currents are observed resulting from the formation of antigen-antibody complex. Supplementary Figure S2 shows the EIS responses of each electrode to 2.5 mM $Fe(CN)_6^{3-/4-}$. As seen, the charge transfer resistance was increased after each modification, which was consistent with the current variation of CV and DPV responses.

3.5 Reagentless electrochemical detection of CEA using the constructed immunosensor

The fabricated immunosensor, BSA/Ab/GA/MB/bp-SNA/ITO, is employed to detect CEA. Figure 6A shows the DPV curves obtained in presence of different concentrations of CEA. As shown, the peak current gradually decreases with the increase of CEA concentration because the formation of antigen-antibody complex hindered the electrochemical process of confined MB. The peak current (I, μA) is linear proportional to the logarithm of concentration of CEA ($\log C_{CEA}$, ng/mL) in the range from 10 pg/mL to 100 ng/mL ($I = -3.79 \log C_{CEA} + 18.0$, $R^2 = 0.995$, Figure 6B). The limit of detection (LOD) of 4 pg/mL is obtained at a signal-to-noise ratio of 3. The developed immunosensor has advantages of simple operation because of no need of antibody labeling or fabrication of sandwich immunocomplex. However, it cannot be applied under strong alkaline solutions owing to the possible hydrolysis of silica nanochannels.

The selectivity of immunosensor for the detection of CEA was investigated using tumor biomarkers including CA125, PSA, CA199, or AFP as possible interfering substances. Figure 7 shows the DPV peak current (I) obtained on the immunosensor in absence or presence of different interfering substances or their mixture. As seen, the peak current only decreases in the presence of CEA or mixture containing CEA, proving that the sensor has good detection selectivity. The immunosensor remains 92% of initial signal after 20-day storage period at 4°C, indicating high stability of the immunosensor.
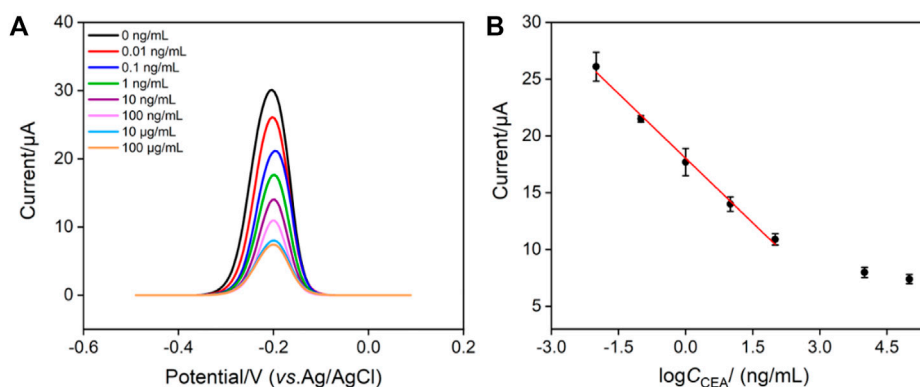
FIGURE 6
(A) DPV response of the immunosensor to different concentrations of CEA from 0.01 ng/mL to 100 µg/mL. **(B)** Calibration curve of the proposed EC immunosensor. Error bars represent the relative standard deviation (RSD) of three measurements.
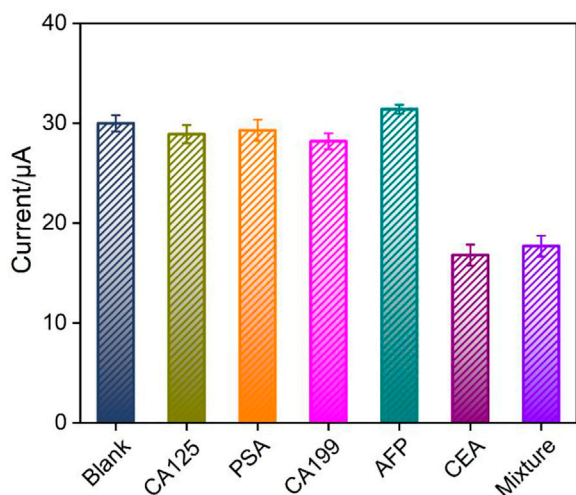
FIGURE 7
The peak current (*I*) obtained on the immunosensor in absence or presence of different interfering substances or their mixture. Error bars represent the RSD of three measurements.

3.6 Real sample analysis

The reliability of the fabricated immunosensor is evaluated by detection of CEA in real serum sample. The concentration of CEA in a healthy human serum (woman) detected by the constructed immunosensor is 1.92 ± 0.03 ng/mL (mean ± SD, $n = 3$), which is quite closed to that obtained using the commonly electrochemiluminescence (ECL) analyzer (1.95 ± 0.04 ng/mL). The obtained F-value (2.45) was lower than the critical F-value (19.00), suggesting no significant difference between these two data. To investigated the anti-interference or anti-fouling performance in complex biological media, the concentration of CEA in human serum is also detected by standard addition method. As shown in Supplementary Table S1 (SI), the recovery rate is between 97.7%–102% with low relative standard deviation (RSD, less than 4.0%). These results confirm high anti-interference or anti-fouling performance in complex biological media, suggesting good accuracy in CEA determination in real samples.

4 Conclusion

In summary, a probe-integrated electrochemical immunosensor is conveniently constructed for reagentless and sensitive detection of a tumor marker, carcinoembryonic antigen (CEA). To avoid adding any solution-based electrochemical probes, the redox probe, methylene blue (MB), is confined to the electrostatic nanocage array on the electrode surface. Electrostatic nanocage array is prepared by successive growing a layer of negatively charged nanochannel array film (n-SNA) and then a layer of positively charged amino-modified SNA (p-SNA). These two SNA layers with opposite charges form a bipolar film (bp-SNA) with electrostatic nanocage array to immobilize MB. When MB is confined, it is attracted by n-SNA and repelled by p-SNA, leading to high stability. The immunosensor can be constructed after the antibody is covalently immobilized followed with blocking the non-specific sites using bovine serum albumin (BSA). Electrochemical determination of CEA is realized by the reduced electrochemical signal of MB resulting from the formation of antigen-antibody complex and the increased surface resistance of the electrode. Although SNA has been widely used in electrochemiluminescence (ECL) systems because of high sensitivity. SNA-based electrochemical biosensors have advantages of simple instrument, low probe cost, easy integration and miniaturization for portable and real-time detection. The probe-integrated immunosensor has advantages of simple fabrication, no need of labelled antibody and formation of sandwich immunocomplexes, showing great potential in bioanalysis of tumor markers.

Data availability statement

Author contributions

Funding

Conflict of interest

Publisher's note

Supplementary material

References

Arnab, D., Subhasis, B., Saptak, B., Anamika, B., Koustav, S., Jaydip, B., et al. (2014). A monoclonal antibody against neem leaf glycoprotein recognizes carcinoembryonic antigen (CEA) and restricts CEA expressing tumor growth. *J. Immunother.* 37, 394–406. doi:10.1097/cji.0000000000000050

Ayl´en, D., Gabriela, V., Gabriel, L., Andr´es, G., María, A., H´ector, F., et al. (2022). Development of an electrochemical immunosensor for the determination of molinate by using phages labeled with CdS nanocrystals as a novel strategy to signal amplification. *Sens. Actuators B Chem.* 367, 132136.

Chen, H., Huang, J., Zhang, R., and Yan, F. (2022). Dual-mode electrochemiluminescence and electrochemical sensor for alpha-fetoprotein detection in human serum based on vertically ordered mesoporous silica films. *Front. Chem.* 10, 1023998. doi:10.3389/fchem.2022.1023998

Chi, L., Xu, C., Li, S., Wang, X., Tang, D., and Xue, F. (2020). *In situ* amplified QCM immunoassay for carcinoembryonic antigen with colorectal cancer using horseradish peroxidase nanospheres and enzymatic biocatalytic precipitation. *Analyst* 145, 6111–6118. doi:10.1039/d0an01399d

Deng, X., Lin, X., Zhou, H., Liu, J., and Tang, H. (2023). Equipment of vertically-ordered mesoporous silica film on electrochemically pretreated three-dimensional graphene electrodes for sensitive detection of methidazine in urine. *Nanomaterials* 12, 239. doi:10.3390/nano13020239

Fumet, J., Truntzer, C., Yarchoan, M., and Ghiringhelli, F. (2020). Tumour mutational burden as a biomarker for immunotherapy: Current Data and emerging concepts. *Eur. J. Cancer* 131, 40–50. doi:10.1016/j.ejca.2020.02.038

Gong, J., Tang, H., Wang, M., Lin, X., Wang, K., and Liu, J. (2022). Novel three-dimensional graphene nanomesh prepared by facile electro-etching for improved electroanalytical performance for small biomolecules. *Mater. Des.* 215, 110506. doi:10.1016/j.matdes.2022.110506

Gong, J., Zhang, T., Chen, P., Yan, F., and Liu, J. (2022). Bipolar silica nanochannel array for dual-mode electrochemiluminescence and electrochemical immunosensing platform. *Sens. Actuators B: Chem.* 368, 132086. doi:10.1016/j.snb.2022.132086

Gong, J., Zhang, T., Luo, T., Luo, X., Yan, F., Tang, W., et al. (2022). Bipolar silica nanochannel array confined electrochemiluminescence for ultrasensitive detection of SARS-CoV-2 antibody. *Biosens. Bioelectron.* 215, 114563. doi:10.1016/j.bios.2022.114563

Grunnet, M., and Sorensen, J. (2012). Carcinoembryonic antigen (cea) as tumor marker in lung cancer. *Lung Cancer* 76, 138–143. doi:10.1016/j.lungcan.2011.11.012

Hou, Y., Wang, J., Liu, S., Sun, Y., Dai, Y., Luo, C., et al. (2022). A novel flower-shaped Ag@ZIF-67 chemiluminescence sensor for sensitive detection of CEA. *Talanta* 253, 123938. doi:10.1016/j.talanta.2022.123938

Huang, J., Zhang, T., Dong, G., Zhu, S., Yan, F., and Liu, J. (2022). Direct and sensitive electrochemical detection of bisphenol A in complex environmental samples using a simple and convenient nanochannel-modified electrode. *Front. Chem.* 10, 900282. doi:10.3389/fchem.2022.900282

Huang, J., Zhang, T., Zheng, Y., and Liu, J. (2023). Dual-mode sensing platform for cancer antigen 15-3 determination based on a silica nanochannel array using electrochemiluminescence and electrochemistry. *Biosensors* 13, 317. doi:10.3390/bios13030317

Jones, R., Pugh, S., Graham, J., Primrose, J., and Barriuso, J. (2021). Circulating tumour dna as a biomarker in resectable and irresectable stage IV colorectal cancer; A systematic review and meta-analysis. *Eur. J. Cancer* 144, 368–381. doi:10.1016/j.ejca.2020.11.025

Liang, R., Jiang, J., Zheng, Y., Sailjoi, A., Chen, J., Liu, J., et al. (2021). Vertically oriented mesoporous silica film modified fluorine-doped tin oxide electrode for enhanced electrochemiluminescence detection of lidocaine in serum. *RSC Adv.* 11, 34669–34675. doi:10.1039/d1ra06375h

Lin, J., Li, K., Wang, M., Chen, X., Liu, J., and Tang, H. (2020). Reagentless and sensitive determination of carcinoembryonic antigen based on a stable prussian blue modified electrode. *RSC Adv.* 10, 38316–38322. doi:10.1039/d0ra06751b

Liu, C., Wang, X., Xu, J., and Chen, Y. (2016). Chemical strategy to stepwise amplification of signals in surface plasmon resonance imaging detection of saccharides and glycoconjugates. *Anal. Chem.* 88, 10011–10018. doi:10.1021/acs.analchem.6b02184

Liu, Q., Ma, Z., Cao, Q., Zhao, H., Guo, Y., Liu, T., et al. (2022). Perineural invasion-associated biomarkers for tumor development. *Pharmacother* 155, 113691. doi:10.1016/j.biopha.2022.113691

Ma, K., Yang, L., Liu, J., and Liu, J. (2022). Electrochemical sensor nanoarchitectonics for sensitive detection of uric acid in human whole blood based on screen-printed carbon electrode equipped with vertically-ordered mesoporous silica-nanochannel film. *Nanomaterials* 12, 1157. doi:10.3390/nano12071157

Ma, K., Zheng, Y., An, L., and Liu, J. (2022). Ultrasensitive immunosensor for prostate-specific antigen based on enhanced electrochemiluminescence by vertically ordered mesoporous silica-nanochannel film. *Front. Chem.* 10, 851178. doi:10.3389/fchem.2022.851178

Sorensen, C., Karlsson, W., Pommergaard, H., Burcharth, J., and Rosenberg, J. (2016). The diagnostic accuracy of carcinoembryonic antigen to detect colorectal cancer recurrence - a systematic review. *Int. J. Surg.* 25, 134–144. doi:10.1016/j.ijsu.2015.11.065

Tan, E., Gouvas, N., Nicholls, R., Ziprin, P., Xynos, E., and Tekkis, P. (2009). Diagnostic precision of carcinoembryonic antigen in the detection of recurrence of colorectal cancer. *Surg. Oncol.* 18, 15–24. doi:10.1016/j.suronc.2008.05.008

Walcarius, A. (2021). Electroinduced surfactant self-assembly driven to vertical growth of oriented mesoporous films. *Acc. Chem. Res.* 54, 3563–3575. doi:10.1021/acs.accounts.1c00233

Wang, K., Yang, L., Huang, H., Lv, N., Liu, J., and Liu, Y. (2022). Nanochannel array on electrochemically polarized screen printed carbon electrode for rapid and sensitive electrochemical determination of clozapine in human whole blood. *Molecules* 27, 2739. doi:10.3390/molecules27092739

Wu, Y., Chen, X., Luo, X., Yang, M., Hou, C., and Huo, D. (2021). Bimetallic organic framework Cu/Uio-66 mediated "fluorescence turn-on" method for ultrasensitive and

rapid detection of carcinoembryonic antigen (CEA). *Anal. Chim. Acta.* 1183, 339000. doi:10.1016/j.aca.2021.339000

Yan, F., Luo, T., Jin, Q., Zhou, H., Sailjoi, A., Dong, G., et al. (2021). Tailoring molecular permeability of vertically-ordered mesoporous silica-nanochannel films on graphene for selectively enhanced determination of dihydroxybenzene isomers in environmental water samples. *J. Hazard. Mater.* 410, 124636. doi:10.1016/j.jhazmat.2020.124636

Yang, L., Zhang, T., Zhou, H., Yan, F., and Liu, Y. (2022). Silica nanochannels boosting Ru(bpy)$_3^{2+}$-Mediated electrochemical sensor for the detection of guanine in beer and pharmaceutical samples. *Front. Nutr.* 9, 987442. doi:10.3389/fnut.2022.987442

Zhang, J., Yang, L., Pei, J., Tian, Y., and Liu, J. (2022). A reagentless electrochemical immunosensor for sensitive detection of carcinoembryonic antigen based on the interface with redox probe-modified electron transfer wires and effectively immobilized antibody. *Front. Chem.* 10, 939736. doi:10.3389/fchem.2022.939736

Zhang, J., Zou, Y., Zhou, X., Yan, F., and Ding, Z. (2022). Vertically-ordered mesoporous silica films for electrochemical detection of Hg(II) ion in pharmaceuticals and soil samples. *Front. Chem.* 10, 952936. doi:10.3389/fchem.2022.952936

Zheng, W., Zhu, D., Wang, W., Liu, J., Thng, S. T. G., and Chen, P. (2022). A silk-microneedle patch to detect glucose in the interstitial fluid of skin or plant tissue. *Sens. Actuat. B-Chem.* 372, 132626. doi:10.1016/j.snb.2022.132626

Zheng, W., Su, R., Lin, X., and Liu, J. (2022). Nanochannel array modified three-dimensional graphene electrode for sensitive electrochemical detection of 2,4,6-trichlorophenol and prochloraz. *Front. Chem.* 10, 954802. doi:10.3389/fchem.2022.954802

Zheng, W., Su, R., Yu, G., Liu, L., and Yan, F. (2022). Highly sensitive electrochemical detection of paraquat in environmental water samples using a vertically ordered mesoporous silica film and a nanocarbon composite. *Nanomaterials* 12, 3632. doi:10.3390/nano12203632

Zhou, H., Dong, G., Sailjoi, A., and Liu, J. (2022). Facile pretreatment of three-dimensional graphene through electrochemical polarization for improved electrocatalytic performance and simultaneous electrochemical detection of catechol and hydroquinone. *Nanomaterials* 12, 65. doi:10.3390/nano12010065

Zhou, H., Ma, X., Sailjoi, A., Zou, Y., Lin, X., Yan, F., et al. (2022). Vertical silica nanochannels supported by nanocarbon composite for simultaneous detection of serotonin and melatonin in biological fluids. *Sens. Actuators B Chem.* 353, 131101. doi:10.1016/j.snb.2021.131101

Zou, Y., Zhou, X., Xie, L., Tang, H., and Yan, F. (2022). Vertically-ordered mesoporous silica films grown on boron nitride-graphene composite modified electrodes for rapid and sensitive detection of carbendazim in real samples. *Front. Chem.* 10, 939510. doi:10.3389/fchem.2022.939510

Check for updates

Authenticity and species identification of Fritillariae cirrhosae: a data fusion method combining electronic nose, electronic tongue, electronic eye and near infrared spectroscopy

Xin-Jing Gui[1,2,3,4,5†], Han Li[1†], Rui Ma[1], Liang-Yu Tian[6], Fu-Guo Hou[1], Hai-Yang Li[1], Xue-Hua Fan[1], Yan-Li Wang[2,3,4,5], Jing Yao[2,3,4,5], Jun-Han Shi[2,3,4,5], Lu Zhang[2,3,4,5], Xue-Lin Li[2,3,4,5]* and Rui-Xin Liu[2,3,4,5,7]*

[1]School of Pharmacy, Henan University of Chinese Medicine, Zhengzhou, China, [2]Department of Pharmacy, The First Affiliated Hospital of Henan University of Chinese Medicine, Zhengzhou, China, [3]Henan Province Engineering Research Center for Clinical Application, Evaluation and Transformation of Traditional Chinese Medicine, Zhengzhou, China, [4]Co-Construction Collaborative Innovation Center for Chinese Medicine and Respiratory Diseases by Henan and Education Ministry of China, Henan University of Chinese Medicine, Zhengzhou, China, [5]Henan Provincial Key Laboratory for Clinical Pharmacy of Traditional Chinese Medicine, Zhengzhou, China, [6]Zhengzhou Traditional Chinese Hospital of Orthopedics, Zhengzhou, China, [7]Engineering Research Center for Pharmaceutics of Chinese Materia Medica and New Drug Development, Ministry of Education, Beijing, China

This paper focuses on determining the authenticity and identifying the species of *Fritillariae cirrhosae* using electronic nose, electronic tongue, and electronic eye sensors, near infrared and mid-level data fusion. 80 batches of *Fritillariae cirrhosae* and its counterfeits (including several batches of *Fritillaria unibracteata* Hsiao et K.C. Hsia, *Fritillaria przewalskii* Maxim, *Fritillaria delavayi* Franch and *Fritillaria ussuriensis* Maxim) were initially identified by Chinese medicine specialists and by criteria in the 2020 edition of *Chinese Pharmacopoeia*. After obtaining the information from several sensors we constructed single-source PLS-DA models for authenticity identification and single-source PCA-DA models for species identification. We selected variables of interest by VIP value and Wilk's lambda value, and we subsequently constructed the three-source fusion model of intelligent senses and the four-source fusion model of intelligent senses and near-infrared spectroscopy. We then explained and analyzed the four-source fusion models based on the sensitive substances detected by key sensors. The accuracies of single-source authenticity PLS-DA identification models based on electronic nose, electronic eye, electronic tongue sensors and near-infrared were respectively 96.25%, 91.25%, 97.50% and 97.50%. The accuracies of single-source PCA-DA species identification models were respectively 85%, 71.25%, 97.50% and 97.50%. After three-source data fusion, the accuracy of the authenticity identification of the PLS-DA identification model was 97.50% and the accuracy of the species identification of the PCA-DA model was 95%. After four-source data fusion, the accuracy of the authenticity of the PLS-DA identification model was 98.75% and the accuracy of the species identification of the PCA-DA model was 97.50%. In terms of authenticity identification, four-source data fusion can improve the performance of the model, while for the identification of the

species the four-source data fusion failed to optimize the performance of the model. We conclude that electronic nose, electronic tongue, electronic eye data and near-infrared spectroscopy combined with data fusion and chemometrics methods can identify the authenticity and determine the species of *Fritillariae cirrhosae*. Our model explanation and analysis can help other researchers identify key quality factors for sample identification. This study aims to provide a reference method for the quality evaluation of Chinese herbs.

1 Introduction

Fritillariae cirrhosae is an herb used both in traditional Chinese medicine and as food. *Fritillaria cirrhosae* is used in the treatment of cough, it eliminates phlegm, relieves asthma, reduces blood pressure, has analgesic effects, prevents ulcers, and has antibacterial and anti-inflammatory properties (Zhong et al., 2019; Chen et al., 2020). The sources of *Fritillariae cirrhosae* recorded in the 2020 edition of *Chinese Pharmacopoeia* include *Fritillariae cirrhosae*, *Fritillaria unibracteata*, *Fritillaria przewalskii*, *Fritillaria delavayi*, *Fritillaria taipaiensis*, *Fritillaria unibracteata*. These are named songbei, qingbei, lubei, *etc.*, based on different characteristics. The Fritillaria genus includes other related plants such as *Fritillaria thunbergii*, and *Fritillaria ussuriensis*. Because of the scarcity of *Fritillariae Cirrhosae* and the difficulties in cultivating it, it is common to find other plants sold as *Fritillaria cirrhosae* especially the cheap and easy to obtain *Fritillaria ussuriensis*. The presence of the market of plants sold as *Fritillariae Cirrhosae* would weaken the safety, efficacy and stability of clinical application of *Fritillariae Cirrhosae* decoctions. Therefore, efficient, rapid and sensitive authenticity and species identification technology is of great significance to ensure the quality of *Fritillariae Cirrhosae* decoction pieces (Xin et al., 2014; Hua et al., 2021).

Chinese herb medicines are traditionally identified by integrating a variety of human senses to determine their quality. This method is fast but subjective and difficult to quantify. The development of modern analytical techniques, chemical and biological detection techniques such as chromatography, spectroscopy, and molecular biology has played a key role in the identification and quality evaluation of TCM decoction pieces (Moon et al., 2018; Qi et al., 2018; Pu et al., 2019; Zhang Y. et al., 2021). Detection methods based on modern analytical techniques such as chromatographic methods have high accuracy, but the sample pretreatment is complex, time-consuming and costly. Artificial intelligence sensory technology can imitate human sensory systems, quantifying information and providing fast and accurate comprehensive information on the samples. Such methods are widely used in the detection and analysis of drugs and food (Buratti et al., 2018; Orlandi et al., 2019; Xu et al., 2019; Zhang X. et al., 2021).

Data fusion strategy consists in merging complementary information to obtain more data points; this strategy has been gradually applied to trace the origin of Chinese medicine (Shen et al., 2019; Wang et al., 2019; Jing et al., 2022), identify its quality (Ying et al., 2017; Dai et al., 2018; Sun et al., 2020) and analyze

pharmaceutical processes (Wang et al., 2021; Zhang et al., 2022). Data fusion includes low, medium and high-level fusion. In low-level data fusion, the original data are directly combined into a new matrix. In mid-level data fusion, features are firstly extracted from the original data and then features are fused. It is worth noting that the removal of redundant information can improve the efficiency of the algorithm. In high-level data fusion, single data sources are firstly identified and chosen, and the final result is obtained based on the recognition results of each data source (Borràs et al., 2015). The flowchart of data fusion in this article is shown in Supplementary Data Sheet 1. The compositions of traditional Chinese medicine decoction pieces are complex, and the data measured by a single technology are not sufficient to accurately determine the authenticity and identify the species of the samples. Similar to what humans do, data fusion strategies can complement different sensory information to improve the identification accuracy. Previous studies have found that data fusion of observations made by artificial intelligence senses, such as electronic noses, electronic tongues and electronic eyes, can be successfully used to differentiate the two botanical origins of Magnolia Officinalis Cortex (Jing et al., 2022), evaluate the quality of Xiaochaihu granules (Zhang X. et al., 2021), identify products made with Curcuma (Lan et al., 2020), and identify and classify medicinal materials based on their smell and taste (Lan et al., 2020; Jing et al., 2022).

Principal Component Analysis-Discriminant Analysis (PCA-DA) and Partial Least Squares-Discriminant Analysis (PLS-DA) are two methods based respectively on principal component regression and partial least squares regression. The PCA-DA algorithm applies discriminant analysis (DA) based on principal component analysis (PCA), using the principle of principal component analysis to further compress high-dimensional data by maximizing the ratio of within-class variance and minimizing the ratio of between-class variance, thus exploring the combination of variables that can explain the main trends of the dataset (Chua et al., 2011; Wong et al., 2014). PCA-DA can simplify overlapping sample information in multi-dimensional data, and is more suitable for multi-class classification. PLS-DA can reduce the dimension of original data and simplify sample information. The mechanism of this technique is to search for linear combinations of the original variables (latent variables) that display maximum covariance with the Y-variables (classes) for classification prediction (Borraz-Martínez et al., 2019). A discriminator, or threshold is created to separate the different classes. The classification model is established by using known categories as a training set and then is used to predict the unknown samples. PLS-DA can determine whether the

samples belong to a predefined category (Ballabio and Consonni, 2013; Yao et al., 2018; Borraz-Martínez et al., 2019). PLS-DA is generally used to deal with binary classification problems, but the PLS algorithm can deal with multi-column dependent variable Y, so PLS-DA can be used for multi-class classification in some cases.

In this study, we used a mid-level data fusion strategy to verify the authenticity and determine the species of *Fritillariae Cirrhosae*. Firstly, we analyzed the NIR spectra and the sample responses of electronic nose, electronic tongue and electronic eye. Based on four kinds of single source data (electronic nose, electronic eye electronic tongue and NIR), we then constructed PLS-DA models to determine the authenticity of the samples, and PCA-DA models to identify the species of the samples. Secondly, we selected the original variables (electronic sensors) respectively based on Variable Importance in Projection (VIP) and wilk's lambda value, and the NIR characteristic spectral bands based on Competitive Adaptive Reweighted Sampling (CARS). And the selected variables from three intelligent sensors were fused for three-source data fusion, the selected variables from four kinds of single source data were fused for four-source data fusion. Finally, based on the fusion variables data matrix, we verified the authenticity and identified the species of the samples. Also, we determined the optimal model based on the accuracies of models and analyzed it in combination with the sensor response signals. This study aims to provide a reference for the quality evaluation of *Fritillariae Cirrhosae* and other traditional Chinese medicine decoction pieces.

2 Materials and methods

2.1 Samples

80 batches (20 of *Fritillaria unibracteata* (FU), 20 of *Fritillaria przewalskii* (FP), 20 of *Fritillaria delavayi* (FD), and 20 of *Fritillaria ussuriensis* (FUS)) were collected from either the Zhengzhou traditional Chinese medicine hospital, the Zhengzhou Chinese medicine market, the first affiliated hospital of Henan University of Chinese medicine or the Bozhou Chinese medicine market. Each batch consisted of 100 g of material. Samples plot is shown in Figure 1.

2.2 Sample identification

2.2.1 Human experience: Specialist identification

Experts with a wealth of experience in identifying TCM decoction pieces (over 15 years work experience in the production, processing and preparation of TCM decoctions), affiliated with different organizations (universities, industries, hospitals, etc.), and with different backgrounds (covering the cultivation, processing, circulation and use of TCM decoction pieces), were invited to identify the samples. A total of 8 experts from the Henan province identified the samples.

2.2.2 Physicochemical identification based on pharmacopoeia

The samples were identified based on their appearance, by microscopic identification, thin-layer chromatography (TLC),

moisture content, ash content and other detection methods as described in the *Fritillariae Cirrhosae* section in the 2020 edition of Chinese Pharmacopoeia.

2.3 Electronic sensory signal acquisition and preprocessing

2.3.1 Electronic nose

Olfactory information collection was acquired by ten types of metal oxide sensors (W1C, W5S, W3C, W6S, W5C, W1S, W1W, W2S, W2W, and W3S) from German PEN3 electronic nose (PEN3 portable electronic nose by the German AIRSENSE company). 2 g powder were taken from samples 1 to 80 and 3 replicates per sample, marked as A-1, A-2, A-3. Based on our pre-experimental results, the samples were tested after 15 min. The experiment was carried out at 20°C and 60% humidity. The sampling conditions were the following: sampling time (the time the sample was exposed to the sensors), 120 s; cleaning time, 100 s; sampling interval, 1 s; air intaking flow rate, 150 mL·s⁻¹. An olfactory information matrix $X1$ (80×10) was obtained, and the data was used to establish the model.

2.3.2 Electronic eye

The IRIS VA400 electronic eye (France Alpha MOS company) was used to collect visual information on the samples. An area of about 8×8 cm^2 was randomly selected from each sample and placed on watch glass. Top lighting conditions were selected based on pre-experimental results, and a 24-color color correction plate was used for color correction. A 5 mm aperture was used and the upper and lower backlights were simultaneously turned on to eliminate the background. Images from each sample were collected three times after changing the position of the samples. A visual information matrix $X2$ (80×65) was obtained by 65 sensors, and the data was used to establish the model.

2.3.3 Electronic tongue

Taste information was collected using the TS-5000Z Insent electronic tongue (Ensoul Technology LTD.). The C00, AN0, BT0 and AE1 sensors were used. The principle of the electronic nose is to use sample gas to interact with the sensor to change the conductivity of the active material of the sensor, thus generating the response value. 5 g of each sample were weighed and crushed in an electric homogenizer for 15 s. The sample powder was then placed in 100 mL of artificial saliva to be ultrasonically processed. The samples were subsequently filtered, sterilized and poured into a special cup to be tested by the electronic tongue. The electronic tongue sensor was cleaned in a cleaning solution for 90 s, in a reference solution for 120 s, and in a different reference solution for 120 s. The sensor started to collect sample information after the response value stabilized at 0 for 30s. The acquisition time of the beforetaste value of each sample was 30 s, the sensors were then cleaned for 3 s in the two reference solutions. Finally, the sensors were inserted into the new reference solution to collect data for 30 s and the aftertaste value was exported. This cycle was repeated four times, data from the first cycle was removed, and the average data of the last three cycles was calculated. Liquid used for cleaning, balancing and aftertaste-testing were placed in different sample cups. A six sensor

taste information matrix $X3$ (80 × 6) was obtained and the original data were used to establish the model.

2.3.4 NIR spectra acquisition and spectra selection

(1) NIR spectra acquisition: NIR spectra were acquired by the Nicolet6700 Fourier transform near-infrared spectrometer (InGaAs detector). Sampling mode was set to diffuse reflection. The samples were dried in an oven at 60°C for 6 h and then crushed and sieved with the No.4 Pharmacopoeia sieve (250 ± 9.9 μm). The parameters of the NIR spectrometer were the following: reference: air; temperature: 25°C ± 2°C; relative humidity: 50 %–60%; resolution: 8cm^{-1}; number of scans: 64; scanning range: 12,000 cm^{-1}-4,000 cm^{-1}; number of gratings: 9–11. Each sample was placed in a quartz sample pool and scanned three times. The spectrum information was collected at room temperature by the opus spectrum acquisition software (Bruker company) and the average spectra were calculated. A NIR spectral information matrix $X4$ (80 × 2075) was obtained.

(2) Spectra selection: The Competitive Adaptive Reweighted Sampling (CARS) method was used to eliminate redundant information in the NIR spectra and to select the characteristic spectra related to the structure of the tested compounds. CARS uses Monte Carlo sampling to establish a Partial Least Squares (PLS) model and simulates the principle of survival of the fittest to eliminate variables by exponential decay function, so that the wavelength variables with smaller absolute values of regression coefficients in the PLS model are removed and the wavelength points with larger weights are screened out through adaptive reweighted sampling technology. An optimal variable wavelength subset was selected based on Root Mean Squares Error of Cross-Validation (RMSECV) of the PLS model (Li et al., 2009; Wang et al., 2017). When using CARS, the number of iterations of Monte Carlo was set to 100, and the pretreatment method of NIR spectra data was "mean centering".

2.4 Construction of authenticity and species identification model based on single source data

PLS-DA was used to establish the authenticity identification models of *Fritillariae cirrhosae* based on data from electronic nose, electronic tongue, electronic eye, and NIR spectra. The performance of the four models based on each type of sensor was evaluated with leave-one-out cross-validation. Because PLS-DA has unclassified cases in multi-classification (Rui-xin et al., 2020; Wen-hao and Shi, 2021), PCA-DA was then chosen to establish the species identification models of *Fritillariae cirrhosae* based on electronic nose, electronic tongue, electronic eye and NIR spectra. The performance of the models was evaluated by the model's accuracy (the ratio of the number of correctly classified samples to the total number of samples) after leave-one-out cross-validation.

2.5 Variable selection

Variable Importance in Projection (VIP) of each sensor in the authenticity identification model was obtained with the PLS-DA algorithm. VIP can explain the contribution extent of independent variables to dependent variables. The larger the VIP is, the greater the contribution of independent variables compared to dependent variables is. VIP >1 indicates a significant contribution of independent variables to dependent variables. In the identification of authenticity, the original variables with VIP greater than 1 were selected from electronic nose, electronic tongue and electronic eye. Wilk's lambda value represented the ratio of within-group variation to between-group variation in the training set (Huan-ran et al., 2019). The smaller one variable's wilk's lambda value is, the stronger the discriminant ability of this variable is. In species identification, by gradually eliminating the variables with the largest Wilk's lambda value in the PCA-DA model, we selected characteristic variables from electronic nose, electronic tongue and electronic eye sensors according to the change of model's accuracy after removal of different variables. Key wavelengths selected by CARS were used as NIR characteristic variables.

2.6 Construction of authenticity and species identification model based on fusion data

Based on the sample identification results, we constructed an authenticity PLS-DA model and a species PCA-DA model using the fusion of three-source intelligent sensors and three-source intelligent sensors and NIR (based on the variables selected in 2.5). The performance of the model was evaluated considering the accuracy of the model after leave-one-out cross validation.

2.7 Model explanation and analysis

Based on the VIP and Wilk's lambda value of the optimal discriminant model, we identified the sensors that most contributed to the classification. We analyzed the characteristic component and key quality factors affecting the authenticity and species identification of *Fritillariae cirrhosae*.

3. Results and discussion

3.1 Sample identification

The results of the specialist identification are shown in Supplementary Table S1. When the identification results of 8 specialists are inconsistent, we determined the final specialist identification result of each sample by judging that the number of specialists was whether larger than or equal to 3/4 of the total specialists or not.

The identification results of *Fritillariae cirrhosae* based on the 2020 edition of Chinese Pharmacopoeia were the following.

- Appearance characteristics: S23, S24, S43 and S61-S80 did not meet the requirements;
- Microscopic identification: S71, S74 and S78 did not contain spiral vessel, while all other samples met the requirements of the pharmacopeia to be identified as F. cirrhosae;
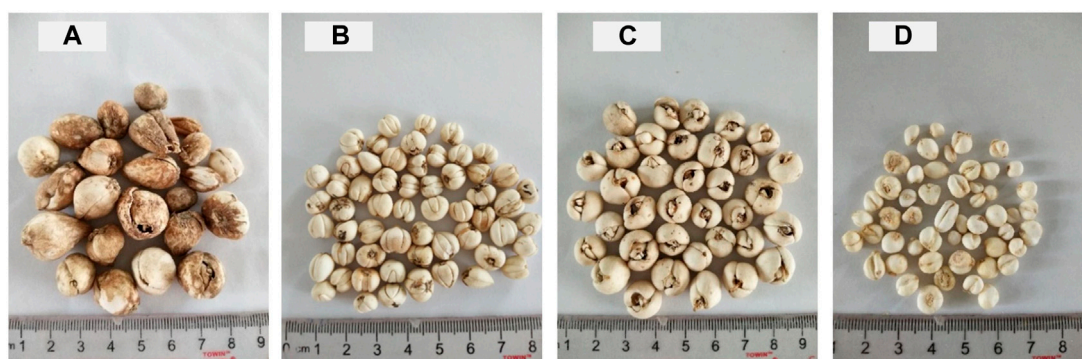
FIGURE 1
Samples plot: sample15, FU **(A)**; sample38, FP **(B)**; sample50, FD **(C)**; sample73, FUS **(D)**.

- Thin-Layer Chromatography identification: S23 and S24 did not contain peiminine and therefore were not identified as F. cirrhosae, while TLC of S61-S80 showed the same color spots corresponding to the reference medicinal materials of *Fritillariae cirrhosae*;
- The results of moisture and ash content for all 80 samples were in line with the requirements of the pharmacopeia for the identification of F. cirrhosae.

After combining the identification results of the specialist identification and the test results based on the 2020 edition of the Chinese Pharmacopoeia, (if the results of artificial experience identification and the pharmacopeia test were in disagreement, we carried out a retest to avoid identification errors), the final results of our identification were: S1-S20, FU; S21-S22, S25-S40, FP; S41-S42, S44-S60, FD; S23, S24, S43, S61-S80, FUS.

3.2 Signal response of electronic senses

Based on the response of the electronic sensors, it can be seen that in the electronic nose test (Figure 2A) most samples had the largest response value on W1W sensor, followed by W1S and W2W, while sample S69 had the largest response value for the W1W, W2W and W5S sensors. All samples had small response values on the W5C, W3C and W1C sensors, which are sensitive to aromatic compounds. In the electronic tongue test (Figure 2B), samples had the largest response value at the B-bitterness2 sensor, which is related to the alkaloid components contained in the samples. The NIR spectra (Figure 2C) showed that the samples had more abundant information at wavelengths 4,000–7,000 cm^{-1}. In the electronic eye test (Figure 2D), the samples had the largest response at color number values of 4,095, 4,093, 4,094, 4,092 and 4,075, which are related to white surfaces characteristics of *Fritillariae cirrhosae* and *Fritillaria taipaiensis*.

3.3 Selection of NIR spectra

The full NIR spectra data for the 80 samples were selected by CARS. After 81 iterations, the Root Mean Square Error of Cross-

Validation (RMSECV) of the PLS model was the smallest. Eight key wavelengths were eventually selected. The number of wavelengths decreased significantly from 2075 to 8. The eight key wavelengths of the NIR spectra were 4,188 cm^{-1}, 5,102 cm^{-1}, 5,970 cm^{-1}, 6,900 cm^{-1}, 9,754 cm^{-1}, 10,884 cm^{-1}, 11,254 cm^{-1}, and 11,678 cm^{-1}.

As shown in Figure 3A, there were two operation stages of CARS: fast selection (sampling times 0–30) and refined selection (sampling times 30–80). In the fast selection stage, the exponentially decreasing function filters out the wavenumbers with little or no information, thus effectively simplifying the spectral data (Li et al., 2009; Ma Hui et al., 2021).

As shown in Figure 3B, the RMSECV remains unchanged in the rapid selection stage, while in the initial stage of refined selection it changes from the maximum to the minimum due to the removal of key variables during the iteration process. As shown in L1 and L2 of Figure 3, when the variables marked L1 were filtered and removed, the regression coefficient of one variable was also immediately reduced to 0 under this sampling number, indicating CARS removed variables that played a key role in the PLS model as part of the sampling operation, so that there was a sharp decline in model's stability. This phenomenon can also be seen in L2. Therefore, the variables selected by CARS are called "key variables".

3.4 Authenticity identification

3.4.1 Electronic nose

PLS-DA was used to establish a qualitative identification model to identify 60 batches of *Fritillariae cirrhosae* and 20 batches of *Fritillaria taipaiensis* based on data collected by electronic nose. Five latent variables, which explain 96.4% of the total variation in the X data among the samples, can be used to establish a PLS-DA model. As shown in Figure 4A, the two types of samples displayed obvious cluster characteristics, while sample S69 was significantly far from all other counterfeit samples. The electronic nose test was then repeated and its results showed a considerable difference in three-times sensory data for S69, this may have been the result of differences in the decoction due to its complex sources.

Near the separation line, under the first two latent variables, S24 and S43 were misclassified as authentic FC, this can be explained

FIGURE 2
response values **(A)** electronic nose, **(B)** electronic tongue, **(C)** NIR spectra, **(D)** electronic eye.

from the results of previous human experience of specialist identification and the pharmacopeia detection: in the identification and detection results of S24, four experts had identified it as counterfeit, one expert identified it as authentic, and three other experts failed to identify it. And the results of TLC and appearance test from the pharmacopeia both showed that S24 could not be identified.

In the identification and detection results of S43, three experts had identified it as authentic and five experts had failed to identify it.

The pharmacopeia detection results showed that S43 was counterfeit. S21, S22 and S40 of FP were identified as counterfeits, so it was speculated that the misclassified samples were caused by differences in geographical sources. The accuracy of this model was 96.25%, and the sensitivity (*Se*), specificity (*Sp*) after cross-validation were 0.9825 and 0.8696. These parameters indicate that the electronic nose can identify both FC and FUS.

3.4.2 Electronic tongue

The first three latent variables were used to establish a better PLS-DA qualitative analysis model, which could explain 82.55% of the total variation in the samples. The distribution of counterfeit samples was relatively scattered, indicating that the counterfeits have larger internal differences in terms of intelligent taste information. As shown in Figure 4B, using the first two latent variables S24 was misclassified as again, and so were S79 and S80, while S1, S2, S4 and S45 were misclassified as counterfeits. In the specialist identification of S79, only three experts had identified it as FUS, suggesting it was a difficult sample to identify. S1, S2 and S4 were in line with regulations in the pharmacopeia of FC and the detection indexes of S80 were in accordance with the standards of FUS, while these samples were still mis-classified under the first two latent variables. We speculated that the internal material of the samples had changed because of variations in the environmental temperature and humidity during storage and transportation. The appearance detection of S45 from the pharmacopeia identification did not meet the requirements, and the TLC results were not obviously colored. We speculated that these differences caused its misclassification. The accuracy of the PLS-DA model established by the electronic tongue sensors was 91.25%, and *Se* and *Sp* after cross-validation were 0.9649 and 0.7826. These parameters indicate that the model performance needs to improve to be able to use electronic tongue sensors to identify FC and FUS.

3.4.3 Electronic eye

After leave-one-out cross-validation, the qualitative analysis model established by the first three latent variables had the best performance. The first three latent variables could explain 74.63% of the total sample variation. From Figure 4C, the cluster characteristics of authentic and counterfeit samples are not obvious. Samples S4, S45, S43 and S79 were misclassified as in the previous tests, indicating that the response value of these samples was significantly different from other samples. Although there were some mis-classified samples using the first two latent variables, when the number of latent variables in the model is three, the accuracy of the model reaches 97.50%, and the model parameters *Se* and *Sp* are 1,0.8696 and 0.9750. These parameters indicate that the electronic eye can identify the two types of samples.

3.4.4 NIR spectra

When the first six latent variables were selected for modeling, the model performance was the best. The first six latent variables can explain 99.80% of the total variation among the samples. From Figure 4D it can be seen that the cluster characteristics of counterfeit samples were not obvious. In addition to the samples that have been misclassified, S23, S25 and S61 were also misclassified under the first two latent variables.

FIGURE 3
The changing trend of the ratio of retained variables **(A)**, 10-fold RMSECV values **(B)** and regression coefficients of each variable **(C)** with the increasing of sampling runs.

Two experts had identified S23 as counterfeit, one expert had identified it as authentic and five experts had failed to identify it, while the results of the extract test from the pharmacopeia and appearance detection showed that S23 was unqualified. The pharmacopeia detection indexes of S25 and S61 were in line with the regulations respectively of FC and FUS. The overall classification results of the model were determined by the six latent variables. The accuracy of this model was 97.50%. *Se* and *Sp* were 1 and 0.8696. These parameters indicate that the full spectra, combined with the PLS-DA algorithm, can accurately identify the samples.

3.4.5 Variable selection of authenticity identification model

Original variables with VIP >1 in the four single-source PLS-DA models are shown in Table 1.

3.4.6 Three-source data fusion

The original variables (sensors) with VIP >1 in each single-source intelligent sensory data model were fused to explore and analyze the discriminant ability of the fused data in identifying the samples. When the first four latent variables were selected for modeling, the model performance was the best: the first four
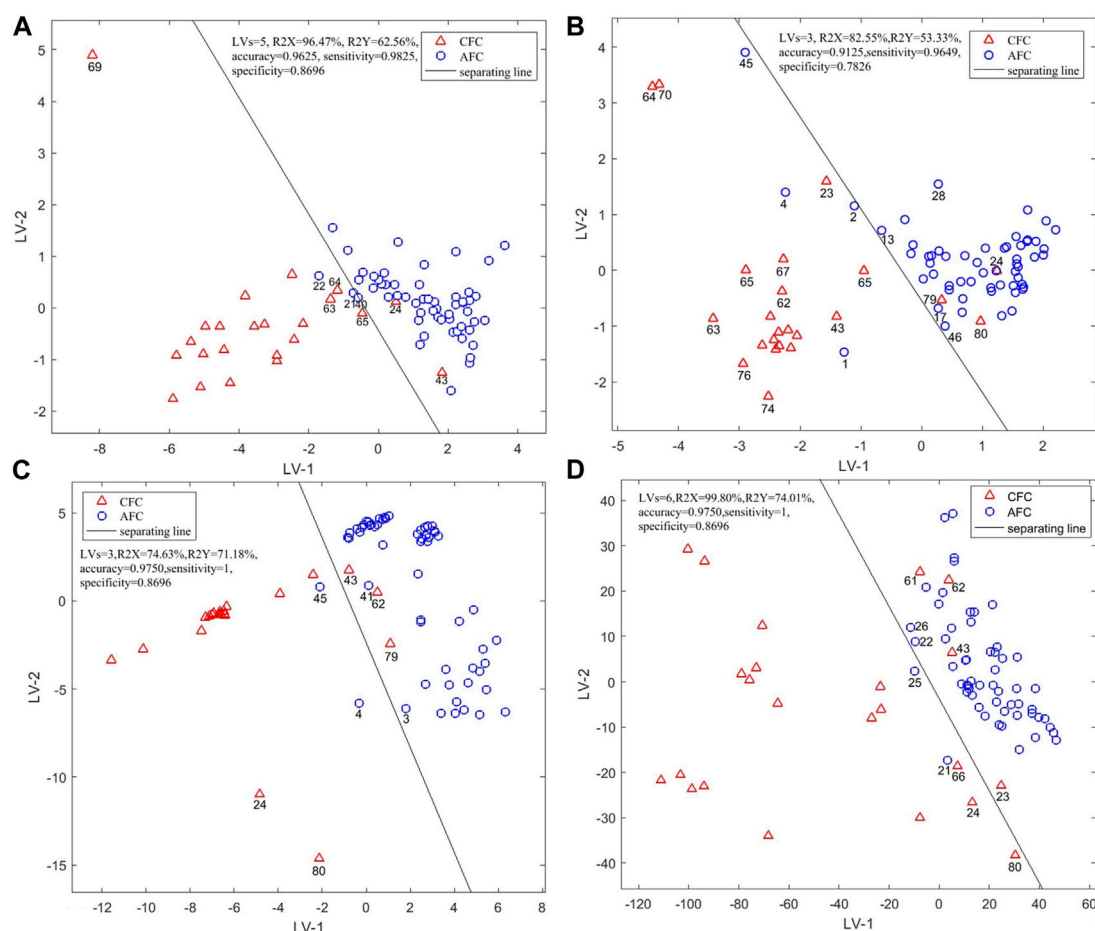
FIGURE 4
Scores Plot of Single-Source PLS-DA authenticity and counterfeit identification model based on **(A)** electronic nose, **(B)** electronic tongue, **(C)** electronic eye and **(D)** NIR spectra.

TABLE 1 Original variables with VIP >1.

Data Source	Original Variables
electronic nose	W1C, W3C, W5C, W1S, W2S
electronic tongue	Aftertaste-A, H-bitterness,Bitterness, Astringency
electronic eye	Color number value 2,712、 2,985、 3,257、 3,258、 3,273、 3,513、 3,529、 3,530、 3,545、 3,783、 3,786、 3,800、 3,802、 3,803、 3,818、 4,056、 4,057、 4,059、 4,073、 4,074、 4,076、 4,090、 4,091、 4,094、 4,095
NIR	Wavenumber 4188.696、5102.804、5970.628、6900.164、9754.34、10884.44、11254.71、11678.98

latent variables explain 80.84% of the total variation among the samples. As in Figure 5A, the cluster characteristics of two types are more obvious than those in single-source data analysis, and only S4 was misclassified as FUS on the first two latent variables. The rate of correct results of the model after three-source fusion was 97.50%. Although the accuracy is the same as using the electronic eye sensor or NIR alone, the accuracy is greater than using the electronic tongue or the electronic nose alone. The classification results on the first two latent variables were also better than that when using single-

source electronic sensory data alone. The model parameters, *Se* and *Sp*, were 1 and 0.9130.

These results show that data fusion can obtain multi-dimensional information of samples, and the fusion of original variables will contribute to sample classification.

3.4.7 Four-source data fusion

The sample information obtained by the fusion data is richer, and the model's classification performance is improved. We therefore explored the result of the fusion of NIR feature spectra
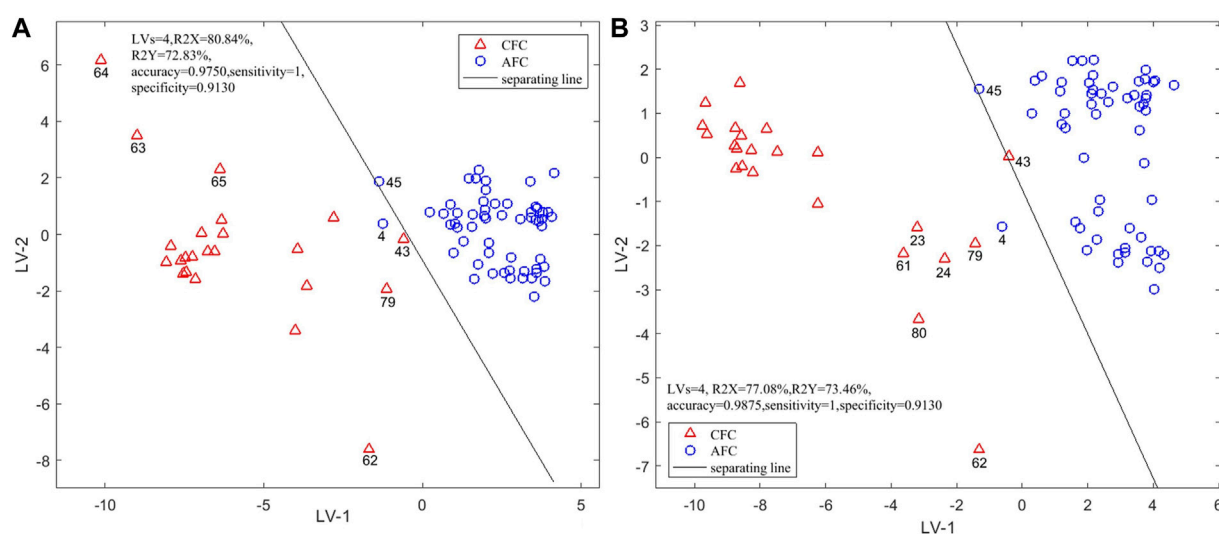
FIGURE 5
Scores Plot of PLS-DA authenticity and counterfeit identification model based on three-source fusion **(A)** (EN + ET + EE) and four-source fusion **(B)** (EN + ET + EE + NIR).
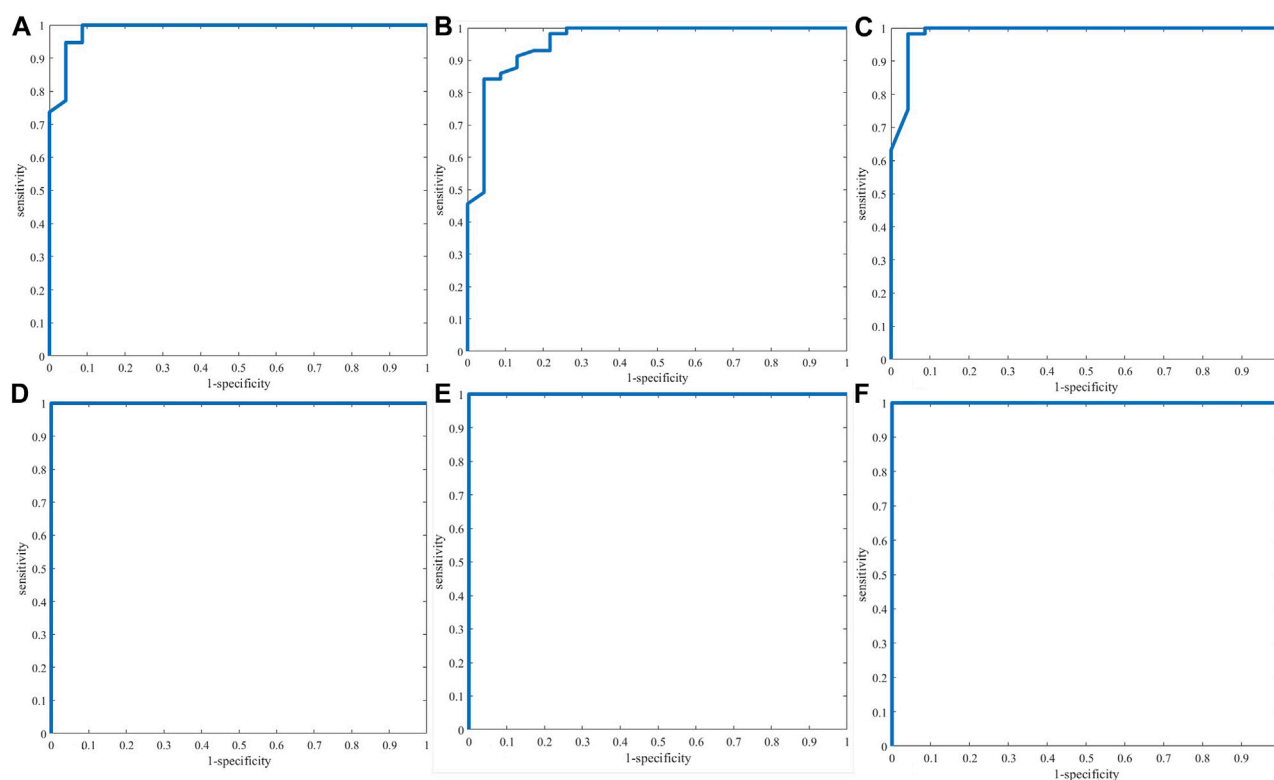
FIGURE 6
ROC curves of single-source PLS-DA authenticity and counterfeit identification model based on electronic nose **(A)**, electronic tongue **(B)**, electronic eye **(C)** and NIR spectra **(D)** and three-source fusion **(E)** (EN + ET + EE) and four-source fusion **(F)** (EN + ET + EE + NIR).

and data from three electronic sensors. After leave-one-out cross-validation, the model established by the first four latent variables had the best performance. These four latent variables explained 77.08% of the variation among samples. In Figure 5B it can be seen that the classification situation after four-source data fusion is similar to that after three-source data fusion. Although S4 and S43 were
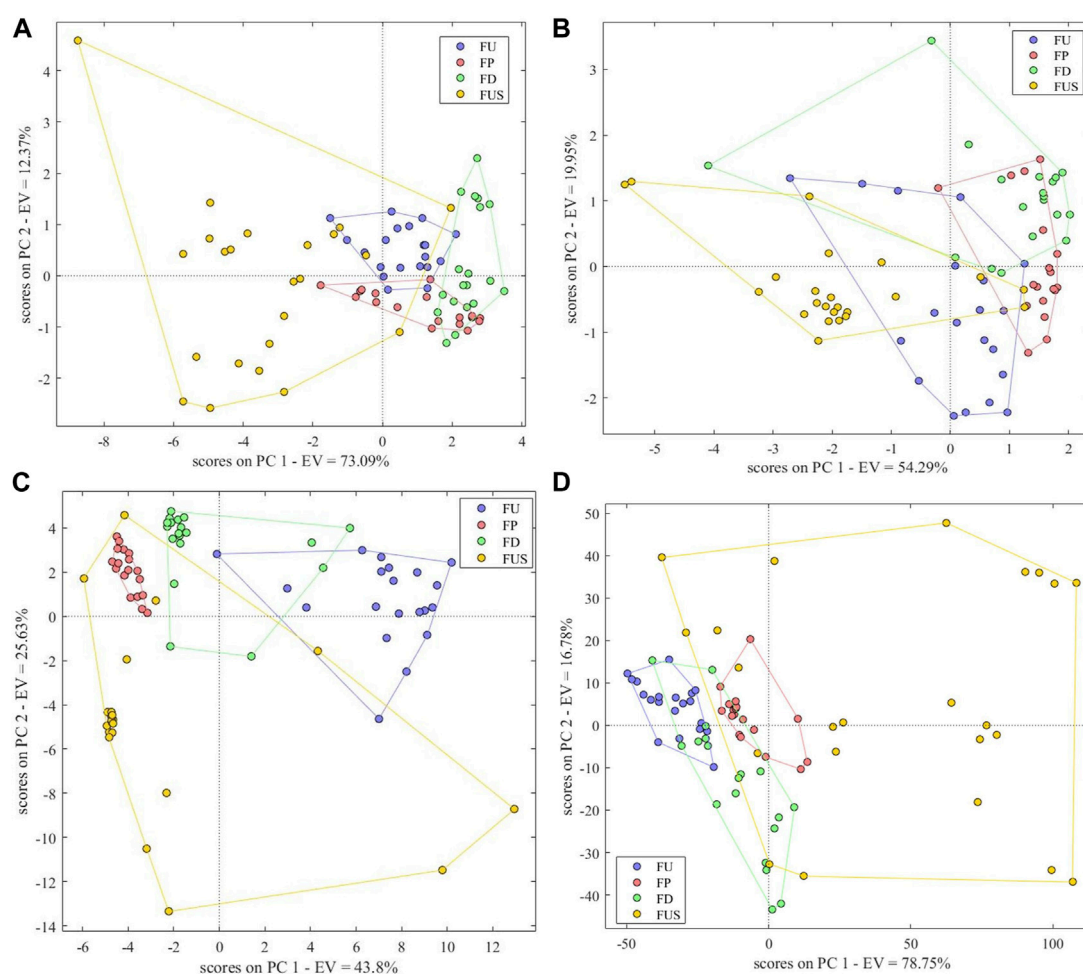
FIGURE 7
Scores Plot of Single-Source PCA-DA species identification model based on **(A)** electronic nose, **(B)** electronic tongue, **(C)** electronic eye and **(D)** NIR spectra.

misclassified under the first two latent variables, the model performance was determined by the first four latent variables and the accuracy of the model constructed with the first four latent variables was 98.75%, which is higher than when using any single source. The model parameters Se and Sp were 1 and 0.913. The PLS-DA model constructed with four-source data fusion has therefore the best performance and achieved the best classification.

ROC curves (Figure 6) showed that PLS-DA authenticity and counterfeit identification models based on NIR and three-source data fusion and four-source data fusion have better performance and the AUC of the three models is 1 while the classification performance of PLS-DA model based on electronic tongue (AUC:0.9573) is not very well in comparison with the other five models.

3.5 Species identification

3.5.1 Electronic nose

The accuracy of the PCA-DA model based on electronic nose data was 85%, and there were no unclassified samples. The model

parameters Se, Sp and Pre were respectively 0.85, 0.98 and 0.94. The classification results showed that 3 FU were misclassified as FD, 3 FP were misclassified as FD, 1 FP was misclassified as FUS, 1 FD was misclassified as FP, 1 FUS was misclassified as FU, 2 FUS were misclassified as FP and 1 FUS was misclassified as FD. There was no obvious difference between different FC and FUS samples based on electronic nose data, resulting in a number of misclassified samples (Figure 7A). As shown in the scores plot, on the variation information represented by the first two principal components, FU and FD samples could be distinguished easily and the clusters of FU, FP and FD samples were clear, while counterfeit samples had a wide range of differences and appeared scattered.

3.5.2 Electronic tongue

The correct rate of the PCA-DA model based on electronic tongue data was 71.25%, with no unclassified samples. The model parameters Se, Sp and Pre were respectively 0.65, 0.92 and 0.72. There were 7 FU samples misclassified, 6 FP, 5FD, and 5 FUS, indicating that electronic tongue data showed little differences between different FC and FUS samples. It can be also seen that the cluster distribution of the four types of samples was not obvious

TABLE 2 Selected variables for electronic nose, electronic tongue and electronic eye.

| Data Source	Original Variables
electronic nose	W1C, W3C, W6S, W5C, W1S, W1W, W2S, W2W, W3S
electronic tongue	H-bitterness,Bitterness, Astringency
electronic eye	Color number value 1911,2167,2183,2184,2438,2439,2694,2710,2711,2712,2966, 2967,2982,2983,2984,2985,3239,3240,3255,3256,3257,3258,3512, 3513,3529,3530,3531,3785,3786,3800,3802,3803,3818,4073,4074, 4075,4076,4090,4091,4092,4093,4094,4095
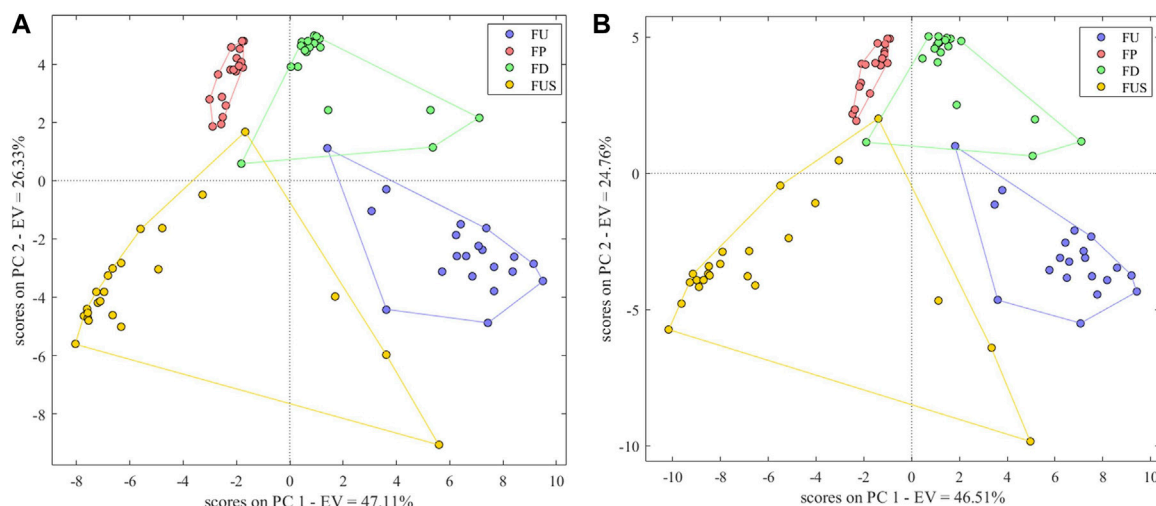
FIGURE 8
Scores Plot of PCA-DA species identification model based on three-source fusion **(A)** (EN + ET + EE) and four-source fusion **(B)** (EN + ET + EE + NIR).

in the variation information represented by the first two principal components, and there were overlaps between the four types (Figure 7B). We conclude that the performance of the species identification model based on electronic tongue data is not good.

3.5.3 Electronic eye

The PCA-DA model based on electronic eye data could effectively distinguish the four species of samples, and the correct identification rate we observed was 97.5%. The model parameters *Se*, *Sp*, and *Pre* were respectively 1.00, 0.98, and 0.95. All FU and FP samples were correctly classified, and there was only one misclassified sample in FD and one in FUS. As shown in Figure 7C, the cluster of FP samples was the clearest, followed by the FD and FU samples. On the contrary, there were some scattered samples in FUS, indicating that the traits of these samples were significantly different from other samples.

3.5.4 NIR spectra

The PCA-DA model based on NIR spectra could also distinguish between the four types of samples. The correct identification rate was 97.5%, and parameters *Se*, *Sp*, and *Pre* were respectively 1.00, 0.98, and 0.95. FU, FP, and FD samples were all correctly classified. One FUS sample was misclassified as FU and another was misclassified as FD. The scores plot (Figure 7D)

shows clearer clusters for FU and FP samples, while FD and FUS samples appear more dispersed in comparison.

3.5.5 Variable selection of the species identification model

The variables from single-source data were selected based on the Wilk's lambda value of the model. We proceeded by gradually removing variables with larger Wilk's lambda values and stopped the removal at the point at which removing a variable resulted in the correct identification rate decreasing. The variables remaining were selected. Table 2 shows the variables selected for each intelligent sensor.

3.5.6 Three-source data fusion

Fusing data obtained from electronic nose, electronic tongue and electronic eye, the correct identification rate of the model was 95%, higher than that of the models using either only electronic nose data or only electronic tongue data. The model parameters *Se*, *Sp* and *Pre* were respectively 0.95, 0.98, and 0.90. The principal component score plot (Figure 8A) shows the cluster of FP samples is more concentrated than other samples. FU, FD and FUS clusters could be better together except for several samples. S2 was misclassified as FD; S45 was misclassified as FP; S43 was misclassified as FP and S79 was misclassified as FU. These samples were also misclassified in the authenticity and counterfeit identification. All other samples were correctly identified. The

TABLE 3 Model parameters of single-source data and multi-source data (EN: electronic nose; ET: electronic tongue; EE: electronic eye) (the bold values means the parameters of optimal PCA-DA and PLS-DA models).

Model		parameters		
		Sp	Se	Ac
PLS-DA authenticity and counterfeit identification	EN	0.8696	0.9825	0.9625
	ET	0.7826	0.9649	0.9125
	EE	0.8696	1.0000	0.9750
	NIR	0.8696	1.0000	0.9750
	EN + ET + EE	0.9130	1.0000	0.9750
	EN + ET + EE + NIR	**0.9130**	**1.0000**	**0.9875**
PCA-DA species identification	EN	0.9800	0.8500	0.8500
	ET	0.9200	0.6500	0.7125
	EE	**0.9800**	**1.0000**	**0.9750**
	NIR	**0.9800**	**1.0000**	**0.9750**
	EN + ET + EE	0.9800	0.9500	0.9500
	EN + ET + EE + NIR	**1.0000**	**1.0000**	**0.9750**

FIGURE 9
VIP value of each variable in the four-source fusion PLS-DA model (cnv: color number value).
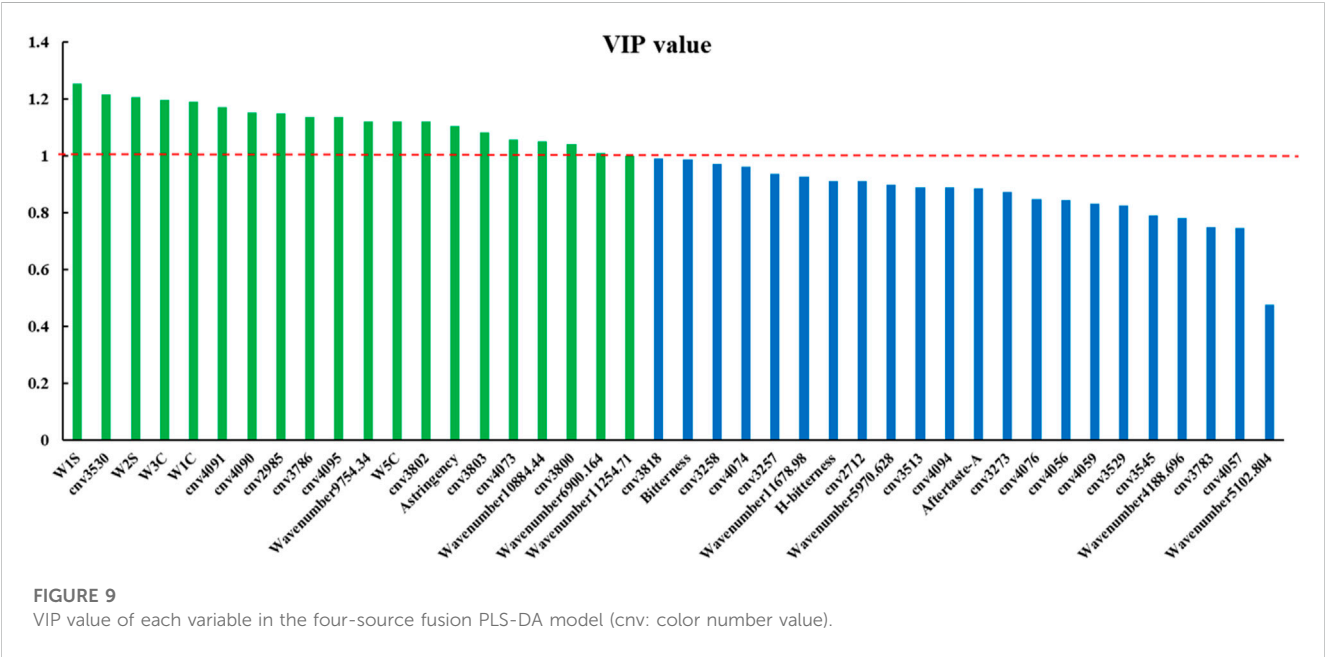
positive identification rate of the model based on fusion data was lower than that of the model based on electronic eye data alone, which we hypothesized could be explained by the removal of key variables during the process of variable selection. This suggests that the increase in the number of variables in data fusion does not necessarily improve the performance of the model, while it is crucial to focus on the choice of the variables.

3.5.7 Four-source data fusion

After fusing the data of electronic nose, electronic tongue, electronic eye and near infrared, the correct identification rate of

the model was 97.50%, and the model parameters Se, Sp and Pre were 1.00, 1.00, and 0.95. The principal component scores plot (Figure 8B) was similar to the scores plot of the three-source fusion data model. S43 was misclassified as FP and S79 was misclassified as FU, suggesting that the fusion of NIR spectra features and intelligent senses didn't significantly improve the model performance and it can only reach the same classification ability of electronic eye and NIR.

Comparing the model parameters of single-source data and multi-source data model (Table 3), we observed that the parameters of the model after data fusion were equal to or better than in the single-source data models. In the authenticity and counterfeit identification model,

TABLE 4 Response substances (information) of variables with VIP >1.

Variables	Response substances (information)
W1S	alkane
Color number value 3,530	L: 81.324, a:2.059, b:18.207
W2S	Alcohols, part of aromatic compounds
W3C	Ammonia, aromatic molecules
W1C	aromatic hydrocarbons
Color number value 4,091	L: 96.445, a: 7.26, b:30.891
Color number value 4,090	L: 96.225, a: 8.707, b:38.525
Color number value 2,985	L: 69.923, a: 4.012, b:10.507
Color number value 3,786	L: 82.772, a: 8.202, b:20.463
Color number value 4,095	L: 97.579, a: 0, b:0
W5C	alkene, aromatic compounds, polar molecules
Color number value 3,802	L: 86.778, a: 0.367, b:25.861
Astringency	astringency
Color number value 3,803	L: 87.04, a: 1.983, b:17.941
Color number value 4,073	L: 91.97 a: 2.515, b:40.97
Color number value 3,800	L: 86.343 a: 2.375, b:41.459

the positive identification rate in the four-source fusion model was higher than that of each single-source data model. While in the species identification model, the parameters of the fusion model were only better than the single-source models based on data from either electronic nose or electronic tongue, but equal to the single-source model constructed from electronic eye sensors and NIR spectra. We believe this may be due to the fact that the accuracy of the identification model based on these two instruments was already high.

3.6 Explanation and analysis of the models

3.6.1 Explanation and analysis of the models based on VIP

We identified the optimal discriminant model as the model based on four-source data fusion, based on its accuracy. VIPs of each variable in this model are displayed in Figure 9. There were 20 variables with VIP >1, contributing to the classification of samples. Among these, the five sensors that played a key role in the classification based on electronic nose single-source data contributed greatly to the classification of authentic and counterfeit samples after data fusion. Among the eight NIR wavelengths selected by CARS, four of them had a greater contribution to sample classification after data fusion. There were 25 sensors that played an important role in the classification of electronic eye single-source data, while only 10 played a crucial role in authenticity and counterfeit classification after data fusion. Among the four sensors which contributed to the classification based on electronic tongue, only the "Astringency" sensor had VIP>1. We therefore concluded that the four instruments played different and complementary roles in the classification of sample authenticity and counterfeit.

The sensor with highest response in the electronic tongue was B-bitterness2, but its contribution to sample classification was relatively small. Although the sensor Astringency had a small response, it contributed greatly to sample classification.

We performed a T-test on the response values of the Astringency sensor for authentic and counterfeit samples and found there was a significant difference between the two types of samples ($p < 0.05$).

Among the sensors of the electronic nose, W1S, W2S, W3C, W1C and W5C contributed the most to the classification of authentic and counterfeit samples. The response values of all other sensors except W1S were small. In addition, sensors with larger response values (W1W, W2W and W5S) showed little contribution to the classification of samples. The response values
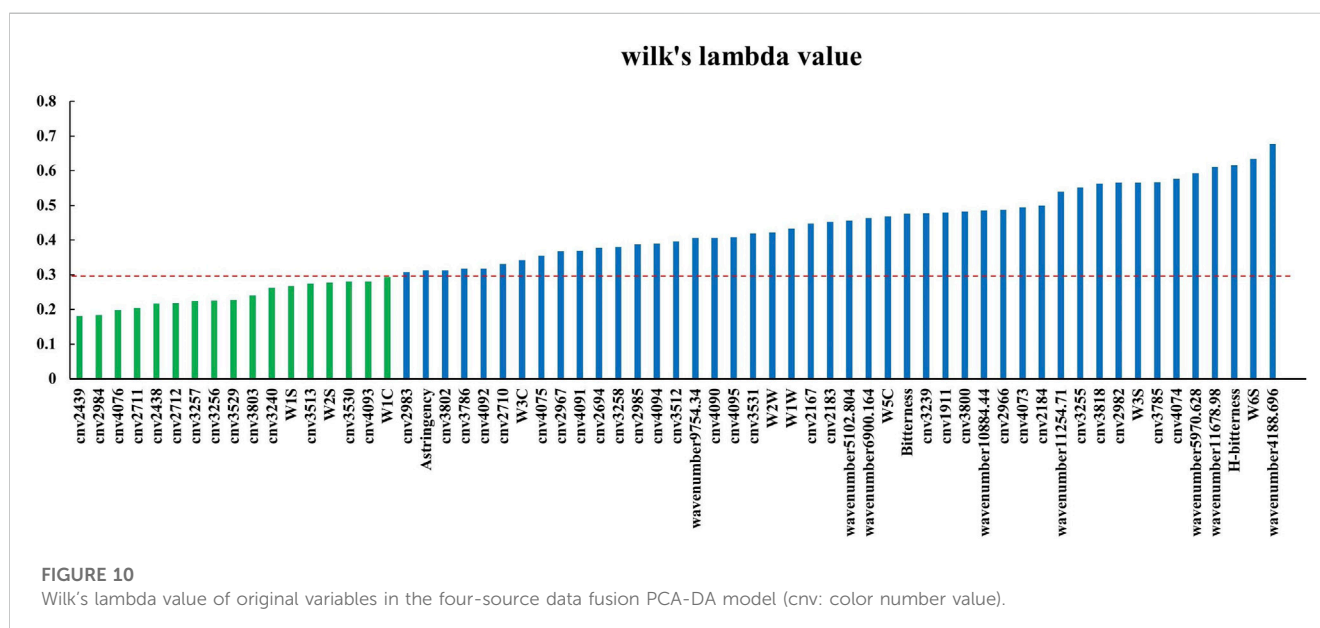

FIGURE 10
Wilk's lambda value of original variables in the four-source data fusion PCA-DA model (cnv: color number value).

TABLE 5 Variables selected based on Wilk's lambda values and their response substances.

Variables	Response substances (information)
Color number value 2,439	L: 57.822, a: 4.244, b: 10.942
Color number value 2,984	L:69.632, a:2.25, b:18.817
Color number value 4,076	L: 92.679, a: 1.916, b: 17.697
Color number value 2,711	L:63.64, a:2.371, b:19.17
Color number value 2,438	L:57.535, a:2.516, b:19.565
Color number value 2,712	L:63.929, a:4.119, b:10.712
Color number value 3,257	L:75.524, a:2.147, b:18.497
Color number value 3,256	L:75.268, a:0.568, b:26.636
Color number value 3,529	L:81.065, a:0.459, b:26.233
Color number value 3,803	L:87.04, a:1.983, b:17.941
Color number value 3,240	L:71.156, a:8.649, b:21.178
W1S	alkane
Color number value 3,513	L:77.007, a:8.412, b:20.803
W2S	Alcohols, part of aromatic compounds
Color number value 3,530	L:81.324, a:2.059, b:18.207
Color number value 4,093	L:96.96, a: 3.919, b:15.452
W1C	aromatic hydrocarbons

of authentic and counterfeit samples were significantly different ($p < 0.05$) on W1S, W2S, W3C, W1C and W5C sensors.

Among the ten color number values that played an important role in the classification based on electronic eye data, the response values of the samples were all small for all values except 4,095, 3,802 and 3,803. The response values of the two types of samples were significantly different ($p < 0.05$). We found that the sensors that contributed the most to the sample classification were not necessarily the sensors with the highest response values. Some components had a smaller response value on the sensors, but, as the content of these components was significantly different in authentic and counterfeit samples, they played a key role in classification of the samples. This kind of component can be defined as "intelligent sensory information with high identification contribution".

The response substances of sensors with VIP >1 are shown in Table 4, which indicates that their response values had a great influence on the classification of authentic and counterfeit FC. The response substances of these sensors can be used as key index components to determine the authenticity of FC.

3.6.2 Explanation and analysis of the models based on Wilk's lambda

The variables that contributed the most to the classification of samples were selected if Wilk's lambda value <0.3. We selected a total of 17 variables. The selected variables are shown in Figure 10, and the information they represent are listed in Table 5, which shows the contribution to the discrimination of authentic FC samples is significant.

By selecting variables based on the Wilk's lambda value, we identified 14 among the 43 original variables of electronic eye data that contributed greatly to the classification of fusion data. Except for color number values 4,076, 2,711, 3,256, 3,529 and 3,803, the response values of the remaining 9 color number values were small. Among the 9 original variables of electronic nose data, 3 variables (W1S, W2S and W1C) showed a large contribution to the classification results in the data fusion model. Yet the W1S sensor had the largest response value, showing once again that the sensors that contribute the most to sample classification are not necessarily the ones with a high response value.

None of the electronic tongue sensors had a significant contribution to the classification results in fusion data.

We performed a t-test on the original data collected by the sensors with large contributions. On color number values 2,712 and 3,257 of the electronic eye, the four types of samples were significantly different ($p < 0.05$), while on the remaining 12 color number values there was no significant difference.

In the original data of four types of samples, FT and FU showed no significant difference on W1S and W2S, and FU and FD showed no significant difference on W1C. Yet, the model identification results were not based on a single sensor, but on the comprehensive results from multiple sensors.

4 Conclusion

We established a functional and effective method to determine the authenticity and identify the species of *Fritillariae cirrhosae* samples based on electronic nose, electronic tongue, and electronic eye sensors, NIR spectra, and mid-level data fusion technology. We proved the established PLS-DA model can accurately identify authentic and counterfeit FC samples. The identification model with the best performance was the four-source data fusion model (based on the fusion of electronic nose, electronic tongue, electronic eye data and NIR spectra). The positive identification rate of the model was as high as 98.75%.

In addition, the established PCA-DA model could effectively discriminate between species related to FC. The species identification model with optimal performance was based on electronic eye or on NIR spectra data or on four-source data fusion and its positive discriminant rate was 97.50% in three cases. The model explanation and analysis showed that the information collected by W1S, W2S and W1C sensors in the electronic nose, the Astringency sensor in electronic tongue, color number values 3,530 and 4,091 in the electronic eye and eight NIR characteristic wavelengths selected by CARS were the key quality information for the model to distinguish between the authentic and counterfeit FC samples and identify their species. Being able to extract such information from FC samples makes it possible to achieve a rapid evaluation of the quality of FC decoctions. We believe this study provides reference methods for the rapid evaluation of the quality of FC, as well as for the evaluation and control of the quality of other herbal samples.

Data availability statement

The original contributions presented in the study are included in the article/Supplementary Material, further inquiries can be directed to the corresponding authors.

Author contributions

R-XL and X-LL conceived the original idea and directed the work. X-JG and HL took the lead in developing the experiment and writing the manuscript. RM, L-YT, and F-GH analyzed the data and revised the manuscript. H-YL and X-HF provided samples and materials. Y-LW, JY, J-HS, and LZ developed the experiment. All authors contributed to the article and approved the submitted version.

Funding

Conflict of interest

The authors declare that the research was conducted in the absence of any commercial or financial relationships that could be construed as a potential conflict of interest.

Publisher's note

All claims expressed in this article are solely those of the authors and do not necessarily represent those of their affiliated organizations, or those of the publisher, the editors and the reviewers. Any product that may be evaluated in this article, or claim that may be made by its manufacturer, is not guaranteed or endorsed by the publisher.

Supplementary material

The Supplementary Material for this article can be found online at: https://www.frontiersin.org/articles/10.3389/fchem.2023.1179039/full#supplementary-material

References

Ballabio, D., and Consonni, V. (2013). Classification tools in chemistry. Part 1: Linear models. PLS-DA. *Anal. Methods* 5 (16), 3790–3798. doi:10.1039/c3ay40582f

Borràs, E., Ferré, J., Boqué, R., Mestres, M., Aceña, L., and Busto, O. (2015). Data fusion methodologies for food and beverage authentication and quality assessment - a review. *Anal. Chim. Acta* 891, 1–14. doi:10.1016/j.aca.2015.04.042

Borraz-Martínez, S., Boqué, R., Simó, J., Mestre, M., and Gras, A. (2019). Development of a methodology to analyze leaves from Prunus dulcis varieties using near infrared spectroscopy. *Talanta* 204, 320–328. doi:10.1016/j.talanta.2019.05.105

Buratti, S., Malegori, C., Benedetti, S., Oliveri, P., and Giovanelli, G. (2018). E-Nose, e-tongue and e-eye for edible olive oil characterization and shelf life assessment: A powerful data fusion approach. *Talanta* 182, 131–141. doi:10.1016/j.talanta.2018.01.096

Chen, T., Zhong, F., Yao, C., Chen, J., Xiang, Y., Dong, J., et al. (2020). A systematic review on traditional uses, sources, phytochemistry, pharmacology, pharmacokinetics, and toxicity of Fritillariae cirrhosae bulbus. *Evid. Based Complement. Altern. Med.* 2020, 1–26. doi:10.1155/2020/1536534

Chua, L. S., Latiff, N. A., Lee, S. Y., Lee, C. T., Sarmidi, M. R., and Aziz, R. A. (2011). Flavonoids and phenolic acids from labisia pumila (kacip fatimah). *Food Chem.* 127 (3), 1186–1192. doi:10.1016/j.foodchem.2011.01.122

Dai, S., Lin, Z., Xu, B., Wang, Y., Shi, X., and Qiao, Y., (2018). Metabolomics data fusion between near infrared spectroscopy and high resolution mass spectrometry: A synergetic approach to boost performance or induce confusion. *Talanta* 189, 641–648. doi:10.1016/j.talanta.2018.07.030

Hua, D. A., Wc, A., Yl, A., Fl, A., Hl, A., Wei, D. B., et al. (2021). Discrimination of authenticity of Fritillariae Cirrhosae Bulbus based on terahertz spectroscopy and chemometric analysis. *Microchem. J.* 168, 106440. doi:10.1016/j.microc.2021.106440

Huan-ran, Y., Mao-Song, L., and Wang, C. (2019). Maize drought statistic discriminant model based on color and texture features. *J. Agric. Sci. Technol.* 21, 62–73.

Jing, W., Zhao, X., Li, M., Hu, X., Cheng, X., Ma, S., et al. (2022). Application of multiple-source data fusion for the discrimination of two botanical origins of Magnolia Officinalis Cortex based on E-nose measurements, E-tongue measurements, and chemical analysis. *Molecules* 27 (12), 3892. doi:10.3390/molecules27123892

Lan, Z., Zhang, Y., Sun, Y., Ji, D., Wang, S., Lu, T., et al. (2020). A mid-level data fusion approach for evaluating the internal and external changes determined by FT-NIR, electronic nose and colorimeter in Curcumae Rhizoma processing. *J. Pharm. Biomed. Anal.* 188, 113387. doi:10.1016/j.jpba.2020.113387

Li, H., Liang, Y., Xu, Q., and Cao, D. (2009). Key wavelengths screening using competitive adaptive reweighted sampling method for multivariate calibration. *Anal. Chim. Acta* 648 (1), 77–84. doi:10.1016/j.aca.2009.06.046

Ma Hui, Z. W., Chen-chen, H., and Kim-Chen, A. (2021). Rapid determination of baicalin content in multi-section of Scutellaria baicalensis Georgi by near infrared spectroscopy combined with chemometrics algorithm. *Lishizhen Med. Materia Medica Res.* 32, 2091–2094.

Moon, B. C., Kim, W. J., Park, I., Sung, G. H., and Noh, P. (2018). Establishment of a PCR assay for the detection and discrimination of authentic cordyceps and adulterant species in food and herbal medicines. *Molecules* 23 (8), 1932. doi:10.3390/molecules23081932

Orlandi, G., Calvini, R., Foca, G., Pigani, L., Vasile Simone, G., and Ulrici, A. (2019). Data fusion of electronic eye and electronic tongue signals to monitor grape ripening. *Talanta* 195, 181–189. doi:10.1016/j.talanta.2018.11.046

Pu, Z. J., Yue, S. J., Zhou, G. S., Yan, H., Shi, X. Q., Zhu, Z. H., et al. (2019). The comprehensive evaluation of safflowers in different producing areas by combined analysis of color, chemical compounds, and biological activity. *Molecules* 24 (18), 3381. doi:10.3390/molecules24183381

Qi, L., Ma, Y., Zhong, F., and Shen, C. (2018). Comprehensive quality assessment for Rhizoma Coptidis based on quantitative and qualitative metabolic profiles using high performance liquid chromatography, Fourier transform near-infrared and Fourier transform mid-infrared combined with multivariate statistical analysis. *J. Pharm. Biomed. Anal.* 161, 436–443. doi:10.1016/j.jpba.2018.09.012

Rui-xin, L., Xiao-jia, H., Zhang, H., Zhang, L., Gui, X. J., Lin, Z. Z., et al. (2020). A rapid identification of authenticity and specifications of Chinese medicine Fritillariae Cirrhosae Bulbus based on E-eye technology. *Chin. J. Chin. Mater Med.* 45, 3441–3451. doi:10.19540/j.cnki.cjcmm.20200601.301

Shen, T., Yu, H., and Wang, Y. Z. (2019). Assessing geographical origin of Gentiana rigescens using untargeted chromatographic fingerprint, data fusion and chemometrics. *Molecules* 24 (14), 2562. doi:10.3390/molecules24142562

Sun, F., Chen, Y., Wang, K. Y., Wang, S. M., and Liang, S. W. (2020). Identification of genuine and adulterated pinellia ternata by mid-infrared (MIR) and near-infrared (NIR) spectroscopy with partial least squares - discriminant analysis (PLS-DA). *Anal. Lett.* 53, 937–959. doi:10.1080/00032719.2019.1687507

Wang, Q. Q., Huang, H. Y., and Wang, Y. Z. (2019). Geographical authentication of macrohyporia cocos by a data fusion method combining ultra-fast liquid chromatography and fourier transform infrared spectroscopy. *Molecules* 24 (7), 1320. doi:10.3390/molecules24071320

Wang, Y., Jiang, F., Gupta, B. B., Rho, S., Liu, Q., Hou, H., et al. (2017). Variable selection and optimization in rapid detection of soybean straw biomass based on CARS. *IEEE Access* 6, 5290–5299. doi:10.1109/access.2017.2763596

Wang, Z., Cao, J., Li, W., Wang, Y., Luo, G., Qiao, Y., et al. (2021). Using a material database and data fusion method to accelerate the process model development of high shear wet granulation. *Sci. Rep.* 11 (1), 16514. doi:10.1038/s41598-021-96097-x

Wen-hao, T. L., and Shi, J. (2021). Analysis on feasibility of electronic nose technology for identification of Fritillariae cirrhosae bulbus from authenticity and specifications. *Chin. J. Exp. Tradit. Med. Form.* 27, 108–118.

Wong, K. H., Razmovski-Naumovski, V., Li, K. M., Li, G. Q., and Chan, K. (2014). Differentiating puerariae lobatae radix and puerariae thomsonii radix using HPTLC coupled with multivariate classification analyses. *J. Pharm. Biomed. Anal.* 95, 11–19. doi:10.1016/j.jpba.2014.02.007

Xin, G. Z., Lam, Y. C., Maiwulanjiang, M., Chan, G. K., Zhu, K. Y., Tang, W. L., et al. (2014). Authentication of bulbus Fritillariae cirrhosae by RAPD-derived DNA markers. *Molecules* 19 (3), 3450–3459. doi:10.3390/molecules19033450

Xu, M., Wang, J., and Zhu, L. (2019). The qualitative and quantitative assessment of tea quality based on E-nose, E-tongue and E-eye combined with chemometrics. *Food Chem.* 289, 482–489. doi:10.1016/j.foodchem.2019.03.080

Yao, S., Li, T., Liu, H., Li, J., and Wang, Y. (2018). Traceability of Boletaceae mushrooms using data fusion of UV-visible and FTIR combined with chemometrics methods. *J. Sci. Food Agric.* 98 (6), 2215–2222. doi:10.1002/jsfa.8707

Ying, G., Ding, X., and Ni, Y. (2017). The combination of NIR spectroscopy and HPLC chromatography for differentiating lotus seed cultivars and quantitative prediction of four main constituents in lotus with the aid of chemometrics. *Anal. Methods* 9, 6420–6429. doi:10.1039/c7ay02021j

Zhang, J., Xu, X., Li, L., Li, H., Gao, L., Yuan, X., et al. (2022). Multi critical quality attributes monitoring of Chinese oral liquid extraction process with a spectral sensor fusion strategy. *Spectrochim. Acta A Mol. Biomol. Spectrosc.* 278, 121317. doi:10.1016/j.saa.2022.121317

Zhang, X., Wu, H., Lin, L., Du, X., Tang, S., Liu, H., et al. (2021a). The qualitative and quantitative assessment of xiaochaihu granules based on e-eye, e-nose, e-tongue and chemometrics. *J. Pharm. Biomed. Anal.* 205, 114298. doi:10.1016/j.jpba.2021.114298

Zhang, Y., Wu, M., Xi, J., Pan, C., Xu, Z., Xia, W., et al. (2021b). Multiple-fingerprint analysis of Poria cocos polysaccharide by HPLC combined with chemometrics methods. *J. Pharm. Biomed. Anal.* 198, 114012. doi:10.1016/j.jpba.2021.114012

Zhong, Y., Wang, H., Wei, Q., Cao, R., Zhang, H., He, Y., et al. (2019). Combining DNA barcoding and HPLC fingerprints to trace species of an important traditional Chinese medicine Fritillariae bulbus. *Molecules* 24 (18), 3269. doi:10.3390/molecules24183269

Frontiers | Frontiers in Chemistry

Detection of sulfur mustard simulants using the microwave atmospheric pressure plasma optical emission spectroscopy method

Dexin Xu[1], Cong Li[1], Liu Yang[1], Wenchao Zhu[1]*,
Bangdou Huang[2]*, Cheng Zhang[2,3] and Tao Shao[2,3]

[1]State Key Laboratory of NBC Protection for Civilian, Beijing, China, [2]Beijing International S&T Cooperation Base for Plasma Science and Energy Conversion, Institute of Electrical Engineering, Chinese Academy of Sciences, Beijing, China, [3]University of Chinese Academy of Sciences, Beijing, China

Sulfur mustard (SM) is one kind of highly toxic chemical warfare agent and easy to spread, while existing detection methods cannot fulfill the requirement of rapid response, good portability, and cost competitiveness at the same time. In this work, the microwave atmospheric pressure plasma optical emission spectroscopy (MW-APP-OES) method, taking the advantage of non-thermal equilibrium, high reactivity, and high purity of MW plasma, is developed to detect three kinds of SM simulants, i.e., 2-chloroethyl ethyl sulfide, dipropyl disulfide, and ethanethiol. Characteristic OES from both atom lines (C I and Cl I) and radical bands (CS, CH, and C_2) is identified, confirming MW-APP-OES can preserve more information about target agents without full atomization. Gas flow rate and MW power are optimized to achieve the best analytical results. Good linearity is obtained from the calibration curve for the CS band (linear coefficients $R^2 > 0.995$) over a wide range of concentrations, and a limit of detection down to sub-ppm is achieved with response time on the order of second. With SM simulants as examples, the analytical results in this work indicate that MW-APP-OES is a promising method for real-time and in-site detection of chemical warfare agents.

KEYWORDS

atmospheric pressure plasma, optical emission spectroscopy, microwave plasma, toxic agents, trace detection

1 Introduction

Even though the Convention on the Banning of Chemical Weapons (CWC) came into effect in 1997 (The Chemical Weapons Convention CWC, 1997), there still exists the risk of chemical warfare agents (CWAs) due to terrorist attack or leakage. Sulfur mustard (SM) is one kind of highly toxic blister CWA, and the maximum safe concentration–time (*Ct*) of SM vapor is 5 mg/min/m³ with a latency of 0–6 h (McNutt et al., 2020). SM has been widely spread over the world in war and induced millions of casualties in history (Szinicz, 2005; Tang and Loke, 2012). With a simple structure, SM is also relatively easy to synthesize, threatening social security (Devi, 2016).

As the most probable dispersion route of SM is via aerosol or vapor (Young et al., 2020), it is desirable to explore a sensitive and on-line gas-phase detection method with rapid response, good portability, and cost competitiveness. Nevertheless, existing traditional

methods, including flame photometric detector (FID), ion mobility spectrometry (IMS), and gas chromatography–mass spectrometry (GC–MS), cannot fulfil these requirements at the same time (Cordell et al., 2007; Harris et al., 2011; McKelvie and Thurbide, 2019). Recently, numerous innovative strategies have been investigated and developed, such as surface-enhanced Raman spectroscopy (Xu et al., 2021), fluorescent probe (Feng et al., 2021), quantum dot sensor (Alev et al., 2022), quartz crystal microbalance (Lee et al., 2019), and atmospheric pressure plasma optical emission spectroscopy (APP-OES) (Broekaert and Siemens, 2004; Karanassios, 2004; Niu et al., 2021).

Among these emerging methods, APP-OES is based on the dissociation of target agents and excitation of fragments under the reactive APP environment, and OES is collected during radiative transition (de-excitation) processes (Niu et al., 2021). Distinguished from the traditional inductively coupled plasma (ICP) OES method, where plasma is at a nearly thermal equilibrium condition and the target agents are fully atomized, APP can be generated with non-equilibrium, called non-thermal APP (Shao et al., 2018). This indicates that the mean energy or temperature of mobile electrons with a small inertia is much higher than that of the background gas (Zhu et al., 2008). Benefitting from these characteristics, the target agents could be partially dissociated by non-thermal APP under a relatively low gas temperature, reserving more structure information about agents. Therefore, OES from both characteristic elements and radicals can be efficiently excited by high-energy electrons (Huang et al., 2023). It is also found that the OES intensity ratio of different radicals can be used to distinguish agents with similar element components, which further extends the discriminating ability of APP-OES (Yuan et al., 2012).

Up to now, many types of APP sources have been developed and used for the trace analysis, including (but not limited to) dielectric barrier discharge (DBD) (Meyer et al., 2012; Jiang et al., 2016; Han et al., 2018), glow discharge (Meng and Duan, 2015; Zhu et al., 2018), electrolyte cathode discharge (Yuan et al., 2021), mini-point discharge (Li et al., 2018; Yang et al., 2021), and microwave (MW) discharge (Pohl et al., 2008; Yuan et al., 2016; Borowska et al., 2019; Jung et al., 2019; Williams et al., 2019; Müller et al., 2020; Akhdhar et al., 2021). Compared with other APP sources, MW discharge has a relatively high power density (i.e., a strong dissociation ability) and a large reaction region (i.e., a long residence time for agents), and a highly purified reaction environment, eliminating any contamination due to the metal electrode, could be obtained, showing a promising future for trace detection of WCAs. It should be noted that, even though most MW sources engage rare gases or nitrogen as the carrier gas, an MW plasma source-based ¼-wavelength resonator with only ambient air as the carrier gas has been developed (Yu et al., 2023).

In our previous work, the OES characteristic of different APP excitation sources has been compared (Yang et al., 2022), and the analytical performance of the microwave atmospheric pressure plasma optical emission spectroscopy (MW-APP-OES) method for WCA simulants containing phosphorus and chlorine has been investigated (Li et al., 2022). In this work, the MW-APP-OES method is extended to detect three kinds of SM simulants, 2-chloroethyl ethyl sulfide (2-CEES), dipropyl disulfide, and ethanethiol. Characteristic OES from the C atom, CS radical, and Cl atom is identified. Good linearity is obtained from the calibration

curve ($R^2 > 0.995$ for CS band), and a limit of detection (LOD) down to sub-ppm is achieved.

2 Materials and methods

2.1 Chemicals and reagents

SM simulants engaged in this work are 2-CEES (C_4H_9ClS, 97%, Macklin), dipropyl disulfide ($C_6H_{14}S_2$, 99%, Innochem), and ethanethiol (C_2H_6S, 98%, Macklin). Original SM simulants are used in the experiment without any pre-treatment. High-purity argon (99.999%, Jinghui Gas, China) is used as the carrier gas for MW-APP.

2.2 MW-APP-OES system

Figure 1 shows an illustrative diagram of the MW-APP-OES system used in this work. An MW power source (WSPS-2450-200M, Wattsine, China) with a frequency of 2.45 GHz and a maximum power up to 200 W is used to generate MW-APP. A customized MW surfatron device is adapted to couple MW from the power source to plasma (Moisan and Nowakowska, 2018). Gas breakdown is induced at the slit of the surfatron, where MW electric field is locally intensified, and extended plasma is generated in a quartz tube with an inner diameter (ID) of 1.5 mm and an outer diameter (OD) of 3 mm. There are two tuning knobs in the MW surfatron, by rotating which the MW reflection from the plasma to power source can be reduced to below 5%.

A flow controller (G300C-5000sccm-P-24, Gas Tool Instrument, China) is used to control the rate of the carrier gas (argon). The gas line is heated, and its temperature is regulated using a temperature controller (AI-208FGL0, Udian, China). The SM simulants are injected into the gas line using a micro syringe (10 µL, Agilent), which is driven by a high-accuracy syringe pump (Pump 11 Elite, Harvard).

OES from MW-APP at around the middle position of the plasma column is collected by a fiber and is transferred to a three-channel spectrometer (PG2000-PRO-3, Ideaoptics, China), which covers a wavelength range of 196.79–1,039.58 nm (channel 1: 196.79–420.58 nm, channel 2: 406.59–623.60 nm, and channel 3: 604.89–1,039.58 nm) and provides a spectral resolution of about 0.1–0.2 nm.

2.3 Analysis procedure

When performing the MW-APP-OES analysis, the gas line is heated to a stable temperature of 180°C, which guarantees the full vaporization of SM simulants (in liquid phase at room temperature). The injection rate of SM simulants (F_s) is controlled from 50–500 nL/min, via which their concentrations in the plasma environment are modulated. The flow rate of the carrier gas (F_{Ar}) can be varied from 0.5–3.5 L/min, and the MW power can be varied from 50–120 W. The accumulation time of the spectrometer is fixed at 500 ms for channel 1, 200 ms for channel 2, and 100 ms for channel 3 in all measurements of this work.
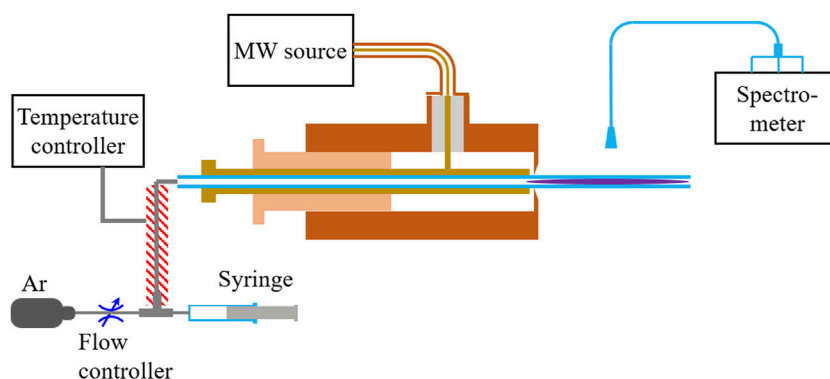
FIGURE 1
An illustrative diagram of the experimental setup.

As the gas line is heated to a relatively high temperature (180°C) and the injection rate of the target agent is very low, the vapor pressure of the target agent in the gas flow is much lower than its saturated value under the given temperature, and it is safe to assume the target agent is fully vaporized before arriving at the MW-APP region. Therefore, the concentration of target agent C_s (mg/m³) can be obtained from the ratio of the injection rate to the flow rate of the carrier gas (Li et al., 2022),

$$C_s = F_s \cdot \rho_s / F_{Ar}, \qquad (1)$$

and its volume concentration C_s^V (ppm) is given by the following formula:

$$C_s^V = \left(F_s \cdot \rho_s / M_s\right) / \left(F_{Ar}/V_m\right). \qquad (2)$$

Here, ρ_s and M_s are the density (g/cm³) and molar mass (g/mol) of the agent, respectively. V_m is the gas molar volume at STP (22.4 L).

3 Results and discussion

3.1 Characteristic OES of SM simulants

Figure 2 shows MW-APP-OES for the blank and 2-CEES with an injection rate of 150 nL/min.

By comparing these two groups of OES and looking into database (Gaydon and Pearse, 1963; NIST, 2022), it can be identified that the emerging OES after 2-CEES injection includes the C I line at 247.8 nm, CS band around 257.6 nm, CH C→X around 314 nm, C_2 c→b band around 385 and 360 nm, and C_2 A→X band around 516, 474, and 564 nm. These lines/bands can be clearly distinguished from the background. Furthermore, the Cl I line at 894.8 nm can also be identified, which is on the wind of argon lines, while most of other Cl I lines are overlapped with argon lines.

Based on the aforementioned observations, it can be analyzed that 2-CEES is partially dissociated in MW-APP, generating both atoms (C and Cl) and radials (CS, CH, and C_2). As OES from C, CH, and C_2 can be frequently observed in regular hydrocarbons (Meng and Duan, 2015), OES from CS and Cl should be particularly concerned when detecting 2-CEES. It should be noted that the

CS band can also be frequently observed when detecting volatile organic sulfur compounds using OES excited by gas discharge (Li et al., 2018). Therefore, the Cl I line can be further involved to identify the agent. The characteristic OES from dipropyl disulfide and ethanethiol is similar to that of 2-CEES, except for the absence of Cl I, which will not be repeated here.

It is worth noting that the real samples containing target analytes can be mixed with interfering compounds at different concentrations producing similar or the same OES in the MW-APP. In this case, the target analyte cannot be identified and quantitatively analyzed solo by characteristic OES. To solve this challenge, coupling with a small gas chromatograph or ion mobility spectrometer as a front-end separation technique is one efficient way for this method to be applied in practical detection scenarios, which can solve the OES interference currently faced and the carrier gas issues.

3.2 Optimization of MW-APP-OES analysis

In order to obtain the best analytical results in MW-APP-OES quantitative analysis, plasma parameters, including gas flow rate and MW power, should be optimized.

Figures 3A–C show the effect of the gas flow rate on the signal-to-noise ratio (SNR) of the characteristic OES from 2-CEES, dipropyl disulfide, and ethanethiol, respectively. It should be noted that the injection rate of SM simulants is adjusted proportionally to the gas flow rate to maintain a constant concentration in the MW-APP environment. It can be observed that there is a peak for the relationship between SNR of the characteristic OES of all three SM simulants and the gas flow rate at around 3 SLM, which is chosen in the quantitative analysis below. This phenomenon is explained as follows: when the gas flow rate is small, the MW heating is not well taken away by the gas flow (i.e., overheating), which introduces instability for the MW plasma. On the contrary, when the gas flow rate is large, the gas flow in the quartz tube turns from laminar to turbulent, the latter of which also results in instability (Arnoult et al., 2008).

The effect of MW power on SNR is also explored for these three SM simulants (see Figures 3D–F). It can be seen that there is a peak
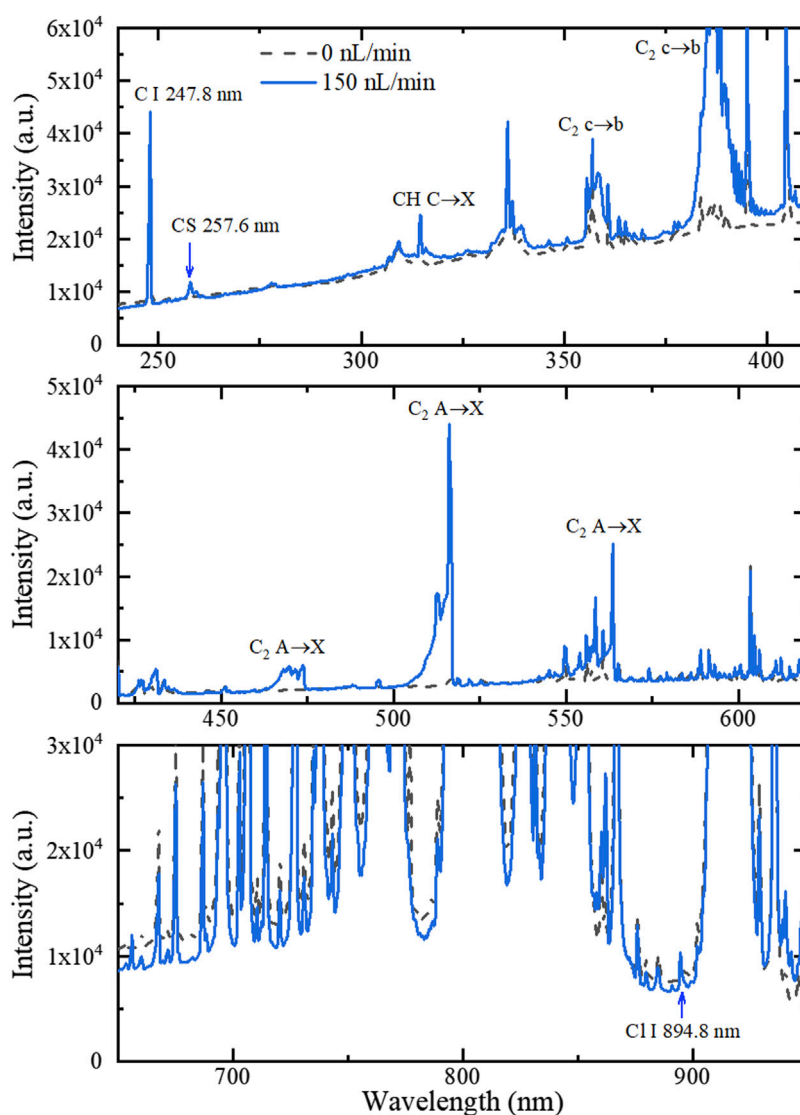
FIGURE 2
MW-APP-OES within different wavelength ranges for the blank and 2-CEES with an injection rate of 150 nL/min.

for dipropyl disulfide and ethanethiol at around 80–90 W, which is not observed for 2-CEES. It should be noted that based on our previous investigation (Li et al., 2022), the OES intensity will increase almost linearly with MW power, while the signal-to-background ratio is nearly constant with MW power. In practice, one should balance the power consumption and OES intensity. In the quantitative analysis below, the MW power is set at 80 W.

3.3 Quantitative analysis and calibration curves

Figure 4 shows the temporal trace of MW-APP-OES of three SM simulations, and the corresponding calibration curves with the analytical results are shown in Table 1.

It can be seen that there is a clear square-wave feature on the temporal evolution of the OES intensity from characteristic line/

band when the pulse injection of SM simulations is performed. The rising edge of OES intensity is as short as 1 s, indicating the rapid time response of the MW-APP-OES method in this work.

The intensity of CS 257.6 nm has a good linear relationship with the concentration of all three simulations from ~20 to 140 mg/m^3 (linear coefficients R^2 > 0.995). However, the intensity of C I 247.8 nm and Cl I 894.8 nm deviates from linearity when the concentration of 2-CEES is larger than ~80 mg/m^3. A similar phenomenon is also observed for dipropyl disulfide but does not exist for ethanethiol. The non-linearity at high concentrations is related to the partial dissociation and excitation processes of SM simulations in the MW-APP environment, and OES from radial bands shows better linearity compared with atom lines.

In order to quantify the analytical performance of the MW-APP-OES method, the LODs for three SM simulations are estimated by Shi et al. (2014)

$$\text{LOD} = 3\sigma_B/k. \qquad (3)$$
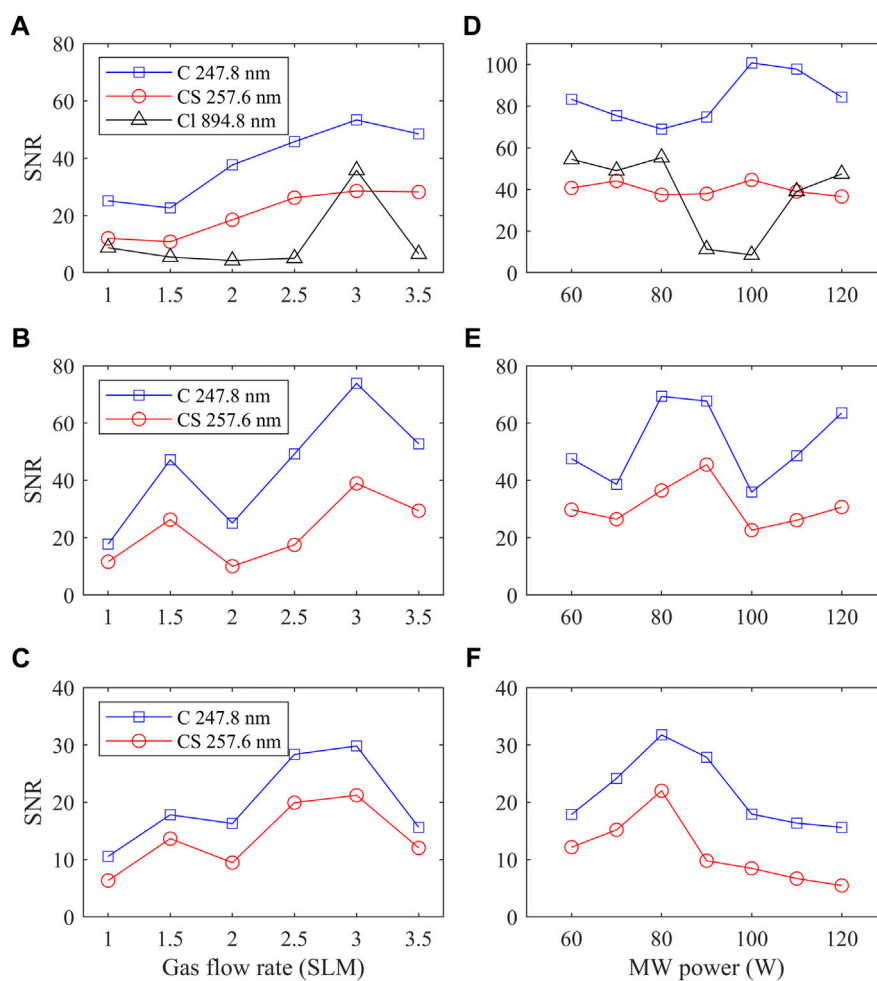
FIGURE 3
Optimization of the MW-APP-OES condition. The effect of the gas flow rate on the signal-to-noise ratio of the characteristic OES from **(A)** 2-CEES, **(B)** dipropyl disulfide, and **(C)** ethanethiol. **(D–F)** Effect of power on SNR for corresponding SM simulants.

Here, σ_B is the standard deviation of characteristic OES intensity from 200 replicated blank cases, and k is the slope of the calibration curve. When the CS 257.6 nm band is used as the characteristic OES, the LODs of three SM simulations can reach a level as low as ~ 1–2 mg/m³ (sub-ppm level).

In principle, the system developed in this work is tested using vapor of SM simulants. SM simulants are injected into the plasma environment with the carrier gas (argon) via the heated gas line for vaporization, and the characteristic OES is identified and analyzed. At the current stage, this system does not include a sampling scheme for gases (such as air) as the analyte.

Under actual testing conditions, the analytes are typically aerosols or vapors in the air. It would be necessary to develop an injection method to achieve carrier gas replacement, which can be achieved by collecting air samples with a given gas flow rate, adsorbing with active carbon, and desorbing the analytes using certain solvents and carrier gas, as has been performed by Jiang et al. (2016).

When carrier gas replacement is involved, the true LOD will be strongly influenced by the efficiency of adsorption and desorption processes and their time duration, i.e., how much analyte is gathered

and released. As the current system only needs an analyte amount of several nL, based on the rise time of OES trace (i.e., response time) and injection rate, it may be safe to argue that when actual analytes in air are considered, an LOD similar to that using argon carrier gas (~ppm) can still be obtained, and the LOD can further be extended with a longer adsorption time, sacrificing the response time.

The relative standard deviation (RSD) of the characteristic OES from three SM simulations is generally below ~5%, obtained from the temporal trace of OES intensity during sample injection. Repeated experiments are also performed, and the reproducibility of the characteristic OES intensity from three SM simulations is generally better (~10%) for concentrations larger than 50 mg/m³.

The recovery of the MW-APP-OES method is evaluated to confirm its accuracy. As there is no standard sample with known concentration for SM simulations, a recovery experiment is also performed using the original sample of SM simulants, and the concentration is controlled with the injection rate. A concentration of ~50 mg/m³ is selected as the baseline, and more samples are added into the MW-APP environment. The CS 257.6 nm band is used as the characteristic OES, and the results are shown in Table 2. It can be seen that recoveries of this method for
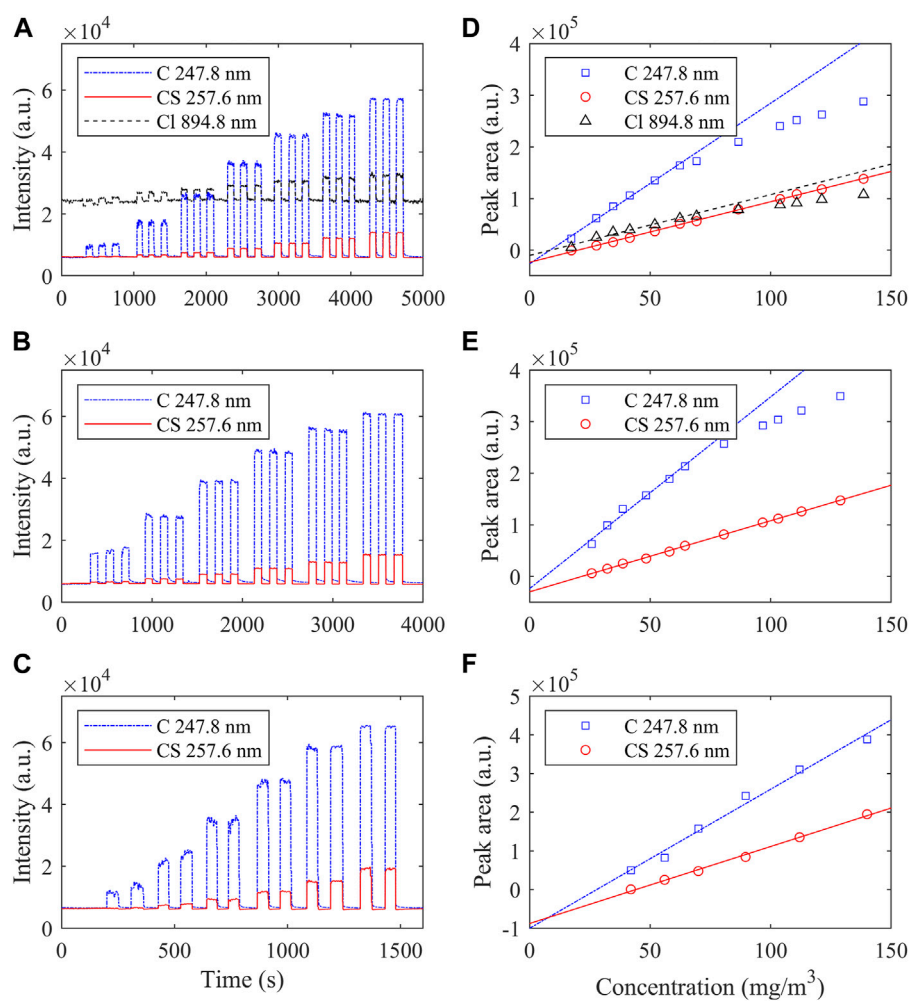
FIGURE 4
Temporal trace of MW-APP-OES of three SM simulations. **(A)** 2-CEES (C_s ~ 17.3, 27.7, 41.6, 62.3, 86.6, 110.8, and 138.5 mg/m³), **(B)** dipropyl disulfide (C_s ~ 25.8, 38.7, 58.0, 80.6, 103.1, and 128.9 mg/m³), and **(C)** ethanethiol (C_s ~ 42.0, 50.3, 69.9, 89.5, 111.9, and 139.8 mg/m³). **(D–F)** Corresponding calibration curves.

TABLE 1 Analytical results of SM simulants by the MW-APP-OES method in this work.

SM simulant	Characteristic line/band	Fitting curve	R^2	LOD (mg/m³, ppm)	RSD (%)	Reproducibility (%)
2-CEES	C I 247.8 nm	$y = 3.1 \times 10^3 x - 2.6 \times 10^4$	0.995	0.3, 0.05	1.9	4
	CS 257.6 nm	$y = 1.2 \times 10^3 x - 2.4 \times 10^4$	0.999	1.5, 0.3	3.5	7
	Cl I 894.8 nm	$y = 2.4 \times 10^2 x - 2.1 \times 10^3$	0.97	4.2, 0.8	2.9	7
Dipropyl disulfide	C I 247.8 nm	$y = 3.7 \times 10^3 x - 2.3 \times 10^4$	0.986	0.3, 0.04	1.4	3
	CS 257.6 nm	$y = 1.4 \times 10^3 x - 3.0 \times 10^4$	0.999	2.1, 0.3	2.6	6
Ethanethiol	C I 247.8 nm	$y = 3.6 \times 10^3 x - 1.0 \times 10^4$	0.987	0.3, 0.1	3.4	2
	CS 257.6 nm	$y = 2.0 \times 10^3 x - 8.8 \times 10^4$	0.996	1, 0.4	4.7	4

three SM simulations at different concentration levels are within the range of 80%–110%, indicating the utility of the current MW-APP-OES method.

Table 3 shows a comparison of the LOD and response time of different detection methods for 2-CEES. It can be seen that compared with the surface-enhanced Raman spectroscopy and

TABLE 2 Recoveries of three SM simulants.

SM simulant	Added (mg/m³)	Found (mg/m³)	Recovery (%)
2-CEES	10.4	8.9	86
	17.3	13.9	80
	52.0	54.3	104
Dipropyl disulfide	9.7	8.6	89
	16.1	15.0	93
	48.4	50.0	103
Ethanethiol	14.0	14.3	102
	33.6	34.8	104
	83.9	90.6	108

TABLE 3 Comparison of the LOD and response time of different methods.

Method	Analyte	LOD	Response time	Reference
Surface-enhanced Raman spectroscopy	2-CEES	0.01 ppm	10 min	Xu et al. (2021)
Fluorescent probes	2-CEES	0.2 ppm	<4 min	Feng et al. (2021)
Quartz crystal microbalance	2-CEES	0.76 ppm	~10 min	Alev et al. (2022)
Quantum dot sensor	2-CEES	0.5 ppm	3 s	Lee et al. (2019)
Liquid chromatography + DBD-OES + MW hydrolysis	Dithiocarbamate	0.1 μg/mL	>400 s	Han et al. (2018)
Photochemical vapor generation + miniaturized point discharge OES	Methylmercury	0.1 μg/L	~10 s	Yang et al. (2021)
Dielectric barrier microhollow cathode discharge OES	Hydrochlorofluorocarbon	27 ppb	<1 s	Meyer et al. (2012)
DBD-OES	Dichloromethane	2 ng/mL	<1 s (15 min collection)	Jiang et al. (2016)
MW-APP-OES	2-CEES	1.5 mg/m³ or 0.3 ppm	1 s	This work

fluorescent probe methods, which have a lower LOD, the MW-APP-OES method in this work has a much faster response time. Furthermore, expensive light sources in the former two methods are avoided in MW-APP-OES. Compared with the quartz crystal microbalance and quantum dot sensor methods, MW-APP-OES shows advantages in both LOD and response time.

Table 3 also gives a comparison of the analytical performances of other APPs with the presenting method. As the target analyte, phase of the analyte (gas or liquid), and carrier gas in each APP are different, it is safe not to judge their performances simply. Compatibility with different carrier gases should be a key point in further investigations.

4 Conclusion

SM is one kind of highly toxic CWA and is easy to spread, threatening social security. However, existing traditional detection methods (FID, IMS, and GC-MC) cannot fulfil the requirement of rapid response, good portability, and cost competitiveness at the same time. In this work, the MW-APP-OES method is developed to

detect three kinds of SM simulants, 2-CEES, dipropyl disulfide, and ethanethiol, taking the advantage of non-thermal equilibrium, high reactivity, and high purity of MW plasma. Characteristic OES from both atom lines (C I and Cl I) and radical bands (CS, CH, and C_2) is identified, confirming MW-APP-OES can preserve more information about target agents without full atomization. The gas flow rate and MW power are optimized to achieve the best detection results. Good linearity is obtained from the calibration curve for the CS band ($R^2 > 0.995$) over a wide range of concentrations of SM simulations. A LOD down to sub-ppm is achieved with a response time on the order of second, showing competitiveness compared with other innovative detection methods to some extent. With SM simulants as examples, the analytical results in this work indicate that MW-APP-OES is a promising method for real-time and in-site detection of CWAs.

Data availability statement

The raw data supporting the conclusion of this article will be made available by the authors, without undue reservation.

Author contributions

WZ, BH, and TS contributed to the conception and design of the study. DX, CL, and LY contributed to the acquisition and analysis of data for the work. BH wrote the first draft of the manuscript. WZ and CZ wrote sections of the manuscript. WZ and TS provided approval for publication of the manuscript. All authors contributed to the article and approved the submitted version.

Conflict of interest

The authors declare that the research was conducted in the absence of any commercial or financial relationships that could be construed as a potential conflict of interest.

Publisher's note

All claims expressed in this article are solely those of the authors and do not necessarily represent those of their affiliated organizations, or those of the publisher, the editors, and the reviewers. Any product that may be evaluated in this article, or claim that may be made by its manufacturer, is not guaranteed or endorsed by the publisher.

References

Akhdhar, A., Schneider, M., Hellmann, S., Orme, A., Carasek, E., Krupp, E. M., et al. (2021). The use of microwave-induced plasma optical emission spectrometry for fluorine determination and its application to tea infusions. *Talanta* 227, 122190. doi:10.1016/j.talanta.2021.122190

Alev, O., Özdemir, O., Goldenberg, E., Arslan, L. C., Büyükköse, S., and Öztürk, Z. Z. (2022). WS2 thin film based quartz crystal microbalance gas sensor for dimethyl methylphosphonate detection at room temperature. *Thin Solid Films* 745, 139097. doi:10.1016/j.tsf.2022.139097

Arnoult, G., Cardoso, R. P., Belmonte, T., and Henrion, G. (2008). Flow transition in a small scale microwave plasma jet at atmospheric pressure. *Appl. Phys. Lett.* 93, 191507. doi:10.1063/1.3025564

Borowska, M., Giersz, J., and Jankowski, K. (2019). Determination of nanopowders using microwave plasma optical emission spectrometry operating in a single particle mode. *Anal. Chim. Acta* 1089, 25–31. doi:10.1016/j.aca.2019.08.053

Broekaert, J. A. C., and Siemens, V. (2004). Some trends in the development of microplasmas for spectrochemical analysis. *Anal. Bioanal. Chem.* 380, 185–189. doi:10.1007/s00216-004-2635-9

Cordell, R. L., Willis, K. A., Wyche, K. P., Blake, R. S., Ellis, A. M., and Monks, P. S. (2007). Detection of chemical weapon agents and simulants using chemical ionization reaction time-of-flight mass spectrometry. *Anal. Chem.* 79, 8359–8366. doi:10.1021/ac071193c

Devi, S. (2016). Syria's health crisis: 5 years on. *Lancet* 387, 1042–1043. doi:10.1016/s0140-6736(16)00690-5

Feng, W., Li, H., Xue, M. J., Zhang, Q. L., Liu, S. L., and Song, Q. H. (2021). Quinoline-2-thione-based fluorescent probes for selective and sensitive detections of mustard gas and its analogues. *Anal. Chim. Acta* 1159, 338440. doi:10.1016/j.aca.2021.338440

Gaydon, A. G., and Pearse, R. W. B. (1963). *The identification of molecular spectra*. 3rd ed. London: Chapman & Hall LTD.

Han, B. J., Li, Y., Qian, B., He, Y., Peng, L. X., and Yu, H. M. (2018). A novel liquid chromatography detector based on a dielectric barrier discharge molecular emission spectrometer with online microwave-assisted hydrolysis for determination of dithiocarbamates. *Analyst* 143, 2790–2798. doi:10.1039/c8an00613j

Harris, G. A., Kwasnik, M., and Fernandez, F. M. (2011). Direct analysis in real time coupled to multiplexed drift tube ion mobility spectrometry for detecting toxic chemicals. *Anal. Chem.* 83, 1908–1915. doi:10.1021/ac102246h

Huang, B. D., Zhang, C., Zhang, C. S., and Shao, T. (2023). Accumulation effect of active species in atmospheric-pressure plasma jet driven by nanosecond high-voltage pulses with MHz pulse repetition rate. *J. Phys. D. Appl. Phys.* 56, 095201. doi:10.1088/1361-6463/acb71d

Jiang, X., Hua, Z. M., He, H. W., Luo, J., Tian, Y. F., and Hou, X. D. (2016). A two-dimensional sensor based on dielectric barrier discharge molecular optical emission and chemiluminescence for discrimination analysis of volatile halohydrocarbons. *Microchem. J.* 129, 16–22. doi:10.1016/j.microc.2016.05.018

Jung, M. Y., Kang, J. H., Choi, Y. S., Lee, D. Y., Lee, J. Y., and Park, J. S. (2019). Analytical features of microwave plasma-atomic emission spectrometry (MP-AES) for the quantitation of manganese (Mn) in wild grape (Vitis coignetiae) red wines: Comparison with inductively coupled plasma-optical emission spectrometry (ICP-OES). *Food Chem.* 274, 20–25. doi:10.1016/j.foodchem.2018.08.114

Karanassios, V. (2004). Microplasmas for chemical analysis: Analytical tools or research toys? *Spectrochim. Acta Part B* 59, 909–928. doi:10.1016/j.sab.2004.04.005

Lee, J. H., Jung, H. B., Yoo, R., Park, Y. J., Lee, H. S., Choe, Y. S., et al. (2019). Real-time selective detection of 2-chloroethyl ethyl sulfide (2-CEES) using an Al-doped ZnO quantum dot sensor coupled with a packed column for gas chromatography. *Sensors Actuators B. Chem.* 284, 444–450. doi:10.1016/j.snb.2018.12.144

Li, C., Yang, J. C., Wang, K. Q., Zhu, W. C., Ding, Z. J., Huang, B. D., et al. (2022). Detection of toxic simulant phosphorus and chlorine by atmospheric pressure microwave plasma optical emission spectrometry. *Chin. J. Anal. Chem.* 50, 1425–1434.

Li, M. T., Huang, S. X., Xu, K. L., Jiang, X. M., and Hou, X. D. (2018). Miniaturized point discharge-radical optical emission spectrometer: A multichannel optical detector for discriminant analysis of volatile organic sulfur compounds. *Talanta* 188, 378–384. doi:10.1016/j.talanta.2018.05.082

McKelvie, K. H., and Thurbide, K. B. (2019). Micro-flame photometric detection in miniature gas chromatography on a titanium tile. *Chromatographia* 82, 935–942. doi:10.1007/s10337-019-03723-y

McNutt, P. M., Hamilton, T. A., Lyman, M. E., and Nelson, M. R. (2020). "Ocular toxicity of chemical warfare agents," in *Handbook of toxicology of chemical warfare agents*. Editor R. C. Gupta (Boston: Academic Press), 567–588.

Meng, F. Y., and Duan, Y. X. (2015). Nitrogen microplasma generated in chip-based ingroove glow discharge device for detection of organic fragments by optical emission spectrometry. *Anal. Chem.* 87, 1882–1888. doi:10.1021/ac504035q

Meyer, C., Demecz, D., Gurevich, E. L., Marggraf, U., Jestel, G., and Franzke, J. (2012). Development of a novel dielectric barrier microhollow cathode discharge for gaseous atomic emission spectroscopy. *J. Anal. At. Spectrom.* 27, 677. doi:10.1039/c2ja10225k

Moisan, M., and Nowakowska, H. (2018). Contribution of surface-wave (SW) sustained plasma columns to the modeling of RF and microwave discharges with new insight into some of their features. A survey of other types of SW discharges. *Plasma Sources Sci. Technol.* 27, 073001. doi:10.1088/1361-6595/aac528

Müller, A., Pozebon, D., and ValderiDressler, L. V. L. (2020). Advances of nitrogen microwave plasma for optical emission spectrometry and applications in elemental analysis: A review. *J. Anal. At. Spectrom.* 35, 2113–2131. doi:10.1039/d0ja00272k

NIST (2022). NIST standard reference database 78. Version 5.10. doi:10.18434/T4W30F

Niu, G. H., Knodel, A., Burhenn, S., Brandt, S., and Franzke, J. (2021). Review: Miniature dielectric barrier discharge (DBD) in analytical atomic spectrometry. *Anal. Chim. Acta* 1147, 211–239. doi:10.1016/j.aca.2020.11.034

Pohl, P., Zapata, I. J., Amberger, M. A., Bings, N. H., and Broekaert, J. A. C. (2008). Characterization of a microwave microstrip helium plasma with gas-phase sample introduction for the optical emission spectrometric determination of bromine, chlorine, sulfur and carbon using a miniaturized optical fiber spectrometer. *Spectrochim. Acta Part B* 63, 415–421. doi:10.1016/j.sab.2007.12.005

Shao, T., Wang, R. X., Zhang, C., and Yan, P. (2018). Atmospheric-pressure pulsed discharges and plasmas: Mechanism, characteristics and applications. *High. Volt.* 3, 14–20. doi:10.1049/hve.2016.0014

Shi, Q., Niu, G. H., Lin, Q. Y., Wang, X., Wang, J., Bian, F., et al. (2014). Exploration of a 3D nano-channel porous membrane material combined with laser-induced breakdown spectrometry for fast and sensitive heavy metal detection of solution samples. *J. Anal. At. Spectrom.* 29, 2302–2308. doi:10.1039/c4ja00220b

Szinicz, L. (2005). History of chemical and biological warfare agents. *Toxicology* 214, 167–181. doi:10.1016/j.tox.2005.06.011

Tang, F. R., and Loke, W. K. (2012). Sulfur mustard and respiratory diseases. *Crit. Rev. Toxicol.* 42, 688–702. doi:10.3109/10408444.2012.698405

The Chemical Weapons Convention (CWC) (1997). *Convention on the prohibition of the development, production, stockpiling and use of chemical Weapons and on their destruction.* The Hague: Technical Secretariat of the Organisation for Prohibition of Chemical Weapons.

Williams, C. B., Amais, R. S., Fontoura, B. M., Jones, B. T., Nóbrega, J. A., and Donati, G. L. (2019). Recent developments in microwave-induced plasma optical emission spectrometry and applications of a commercial Hammer-cavity instrument. *Trends Anal. Chem.* 116, 151–157. doi:10.1016/j.trac.2019.05.007

Xu, W. S., Bao, H. M., Zhang, H. W., Fu, H., Zhao, Q., Li, Y., et al. (2021). Ultrasensitive surface-enhanced Raman spectroscopy detection of gaseous sulfur-mustard simulant based on thin oxide-coated gold nanocone arrays. *J. Hazard. Mater.* 420, 126668. doi:10.1016/j.jhazmat.2021.126668

Yang, J. C., An, J. L., Li, C., Zhu, W. C., Huang, B. D., Zhang, C., et al. (2022). Study on detecting method of toxic agent containing phosphorus (simulation agent) by optical emission spectroscopy of atmospheric pressure low temperature plasma. *Spectrosc. Spectr. Anal.* 42, 1728–1734.

Yang, J. H., Lin, Y., He, L. B., Su, Y. B., Hou, X. D., Deng, Y. R., et al. (2021). Three-Dimensional printed dual-mode chemical vapor generation point discharge optical emission spectrometer for field speciation analyses of mercury and inorganic selenium. *Anal. Chem.* 93, 14923–14928. doi:10.1021/acs.analchem.1c02023

Young, R. A., and Bast, C. B. (2020). "Blister agents," in *Handbook of toxicology of chemical warfare agents.* Editor R. C. Gupta (Waltham: Elsevier), 149–169.

Yu, J. C., Liu, Y. S., Huang, B. D., Xia, L. Z., Kong, F., Zhang, C., et al. (2023). Rapid hydrophobicity recovery of contaminated silicone rubber using low-power microwave plasma in ambient air. *Chem. Eng. J.* 465, 142921. doi:10.1016/j.cej.2023.142921

Yuan, H., Zhou, X. F., Nie, Y., Li, Y., Liang, J. P., Yang, D. Z., et al. (2021). Temporal resolved atomic emission spectroscopy on a pulsed electrolyte cathode discharge for improving the detection sensitivity of Cu. *Spectrochim. Acta Part B At. Spectrosc.* 177, 106072. doi:10.1016/j.sab.2021.106072

Yuan, X., Ding, X. L., Zhao, Z. J., Zhan, X. F., and Duan, Y. X. (2012). Performance evaluation of a newly designed DC microplasma for direct organic compound detection through molecular emission spectrometry. *J. Anal. At. Spectrom.* 27, 2094. doi:10.1039/c2ja30246b

Yuan, X., Zhan, X. F., Li, X. M., Zhao, Z. J., and Duan, Y. X. (2016). Matrix-Assisted plasma atomization emission spectrometry for surface sampling elemental analysis. *Sci. Rep.* 6, 19417. doi:10.1038/srep19417

Zhu, X. M., Chen, W. C., and Pu, Y. K. (2008). Gas temperature, electron density and electron temperature measurement in a microwave excited microplasma. *J. Phys. D. Appl. Phys.* 41, 105212. doi:10.1088/0022-3727/41/10/105212

Zhu, Z. L., Guan, X. D., Zheng, H. T., Yang, C., Xing, Z., and Hu, S. H. (2018). Determination of nitrate and ammonium ions in water samples by atmospheric pressure glow discharge microplasma molecular emission spectrometry coupled with chemical vapour generation. *J. Anal. At. Spectrom.* 33, 2153–2159. doi:10.1039/c8ja00287h

Check for updates

Noninvasive drug adherence monitoring of antipsychotic patients via finger sweat testing

K. Longman[1], C. Frampas[1], H. Lewis[1], C. Costa[2], R. Nilforooshan[3,4],
M. Chambers[4] and M. Bailey[1]*

[1]School of Chemistry and Chemical Engineering, University of Surrey, Guildford, United Kingdom, [2]Surrey
Ion Beam Centre, University of Surrey, Guildford, United Kingdom, [3]Abraham Cowley Unit, St Peter's
Hospital, Surrey and Borders Partnership NHS Foundation Trust, Chertsey, United Kingdom, [4]Faculty of
Health and Medical Sciences, University of Surrey, Guildford, United Kingdom

Collection of finger sweat is explored here as a rapid and convenient way of monitoring patient adherence to antipsychotic drugs. Finger sweat samples (*n* = 426) collected from patients receiving treatment with clozapine, quetiapine and olanzapine were analysed by liquid chromatography mass spectrometry, including a subgroup of patients with paired plasma samples. Finger sweat samples were also analysed from a negative control group and patients who had handled antipsychotic medication only. The finger sweat test (based on the detection of parent drug in one donated sample) was 100% effective in monitoring adherence within commonly prescribed dosing ranges. In comparison to participants who handled the medication only, the test could distinguish between contact and administration through monitoring of the drug metabolite, or the level of parent drug. Additionally, in a subgroup of patients prescribed clozapine, a statistically significant correlation was observed between the mass of parent drug in finger sweat and plasma concentration. The finger sweat technology shows promise as a dignified, noninvasive method to monitor treatment adherence in patients taking antipsychotics.

1 Introduction

One of the greatest challenges in the treatment of psychotic disorders is nonadherence to antipsychotic medication, where approximately half of patients do not adhere to their prescribed regime (García et al., 2016). Poor compliance is consistently associated with a high rate of relapse and unfortunate patient outcomes, including increased risk of rehospitalization and suicide (Higashi et al., 2013). Such consequences extend beyond patient welfare, where greater use of emergency services, longer hospital stays and societal effects from violent or criminal behavior incur increased costs to society and healthcare systems.

Atypical antipsychotics such as clozapine (CLZ), quetiapine (QTP) and olanzapine (OLZ) are commonly prescribed for the treatment of schizophrenia and other psychotic and affective disorders. Reportedly more effective than their predecessors, particularly in respect to the negative or depressive symptoms of psychosis, these second-generation medications are less likely to produce extrapyramidal side effects (Gründer et al., 2009). Whilst better tolerated, several adverse effects, most notably metabolic disruption (Pillinger et al., 2020)

are associated with these medications, especially at higher dosages (Haddad and Sharma, 2012). Despite the associated risks, antipsychotic medications are considered the primary tool for the alleviation and management of psychotic symptoms.

Various objective (observed administration, electronic pill dispensers and drug measurements) and subjective (self-reporting, clinicians' opinion) methods have been used to monitor antipsychotic adherence (Velligan et al., 2006; Haddad et al., 2014). Objective methods are considered to provide more accurate measurements than subjective methods. Measurement of antipsychotic drugs and metabolites in biofluids can inform dose adjustment and reduce the risk of adverse effects or toxicity (Skogh et al., 2002; Qi and Liu, 2021), as well as provide information relating to adherence. Traditionally such measurements are performed using serum or plasma (Aravagiri and Marder, 2001; Zhou et al., 2004; Cao et al., 2020; Qi and Liu, 2021). However, analytical methods have been developed for the evaluation of antipsychotics in hair (Weinmann et al., 2002; Günther et al., 2018; 2020), oral (Fisher et al., 2013), and cerebrospinal fluid (Josefsson et al., 2010).

Fingerprints, or finger sweat, offer a noninvasive alternative for drug monitoring. Sample collection is quick, convenient and does not require any specialist materials or training. Storage and transportation of sweat samples is much simpler than more traditional matrices as the samples are not biohazardous. The detection of drugs and their metabolites in fingerprint sweat has been reported previously for both illicit (Jacob et al., 2008; Bailey et al., 2015; Costa et al., 2017; Hudson et al., 2018; Ismail et al., 2018; Czerwinska et al., 2020; Jang et al., 2020) and therapeutic drugs (Goucher et al., 2009; Costa et al., 2021; Ismail et al., 2022). Finger sweat from unwashed hands comprises eccrine sweat, as well as substances handled by a participant. In contrast, finger sweat samples provided after handwashing are understood to be more reflective of eccrine sweat (Jang et al., 2020).

Our previous work (Costa et al., 2021) has shown that QTP was detected in the fingerprints of two patients, but to our knowledge, the presence of other antipsychotic drugs in finger sweat, and the significance of detecting them, has never been reported. Here we seek to explore the prevalence of antipsychotic medication in finger sweat and assess the significance of a 'Positive' result for the first time.

In this work, we describe a method for the determination of CLZ, QTP and OLZ in finger sweat by liquid chromatography coupled to tandem mass spectrometry (LC-MS/MS). We assess the ability of the method to detect the parent drug and metabolite in finger sweat with respect to administered dose. To test whether a patient can falsify the test, we compare these results to participants who have handled the drug only, along with a negative control group. Finally, to assess the quantitative potential of the finger sweat test, we explore the relationship between CLZ and its metabolite, N-desmethylclozapine (NDMC) in finger sweat and paired plasma samples.

2 Methods

2.1 Sample collection

Favorable ethical opinion was obtained from the National Research Ethics Service (NRES-REC reference 18/NE/0071) for the collection of finger sweat and plasma samples from patients at Surrey and Borders Partnership NHS Trust and Sussex Partnership NHS Foundation Trust. Prior to sampling, all patients provided written informed consent for collection and subsequent analysis for drug level determination. Informed consent for study participation included provision for the collection of basic metadata parameters (including treatment regime and time of last dose–see Supplementary Table S1) alongside biological sampling.

The study primarily focused on collection of finger sweat samples from patients receiving treatment with either CLZ (n = 33 patients; 198 samples), QTP (n = 7 patients; 42 samples) or OLZ (n = 20 patients; 120 samples). An additional sub study was performed where patients (n = 11) receiving CLZ also provided paired (time-matched) plasma for comparison to finger sweat. For patients receiving CLZ and QTP, oral administration was prescribed in the range 25—550 and 100—500 mg/day, respectively. For OLZ, the prescribed treatment regime was a combination of oral administration in the range 2.5—20 mg/day and monthly injection in the range 300—420 mg. Information relating to dose and time of last administration included within this study was self-reported by patients. We have therefore assumed truthful reporting and adherence to prescribed medication.

Additional finger sweat samples were collected from a drug naive negative control group (n = 30) as well as participants whose only association with an assigned antipsychotic drug was through touch. To mimic events which may lead to a false positive result, either accidental or intentional, these "contact only" participants (n = 6) were asked to handle antipsychotic medication. The participants were asked to handle whole tablets with their right hand and to touch crushed tablets with the left hand before donating samples from both hands.

2.1.1 Finger sweat collection

Finger sweat collection devices were prepared by mounting a paper substrate (Whatman 1-Chr-grade) atop a glass microscopy slide.

Finger sweat samples were collected from patients receiving antipsychotic medication before and after a hand washing procedure, hereby described as "as presented" and "after washing" respectively. Unless otherwise specified, finger sweat samples were collected from the index, middle and ring fingers of the right hand. After hand washing with soap and tap water to remove external contamination, patients were required to wear nitrile gloves for a period of 10 min to induce sweating before collection of after washing samples (Figure 1).

Finger sweat samples from a drug naive control group (n = 30) were collected from the right index finger only. Collection of samples within drug contact study were collected from both hands after handling of medication. To avoid contact between the two hands, the fingertips were washed separately by a gloved third party.

All samples were collected onto the porous paper substrate using controlled deposition time and pressure, 30 s at a pressure of 800–1,200 g (measured using a generic kitchen scale). Samples were transported at ambient temperature in microscope storage boxes before transfer to—80°C for long-term storage until analysis.

FIGURE 1
Sample collection procedure. Finger sweat samples collected (1) "as presented" and (2) "after washing". Created using Biorender.com.
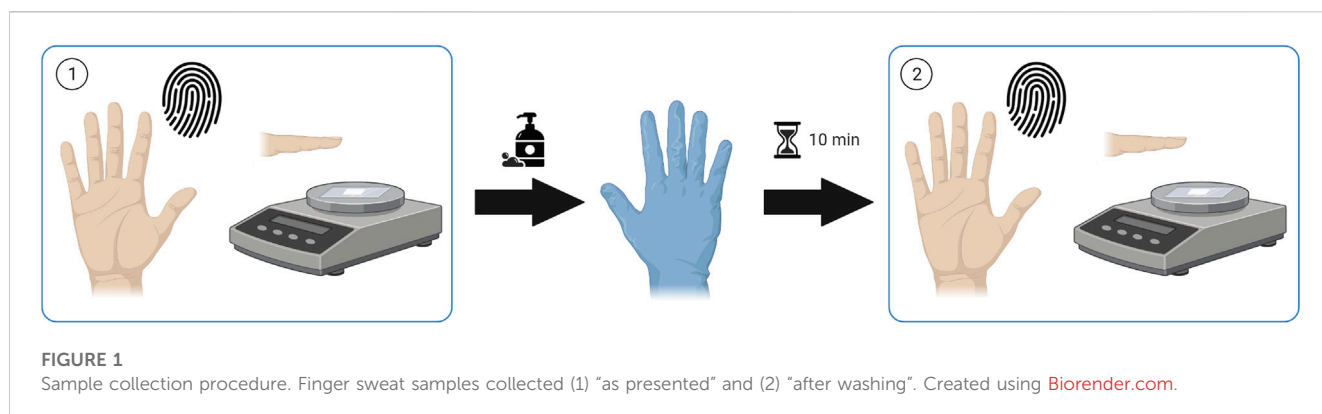
2.1.2 Plasma sample collection

Paired plasma samples were also collected from subgroup of patients (n = 11) receiving treatment with CLZ. Venous blood samples were collected into 3 mL heparinized vials. All samples were centrifuged at 4°C for 10 min (1725 ×g) and the resultant plasma was stored at—80 °C until analysis.

2.2 Chemicals and reagents

Certified reference materials of antipsychotic drugs (CLZ, QTP, OLZ) their respective metabolites (NDMC, norquetiapine (NQTP), *N*-desmethylolanzapine (DMO)) and deuterated internal standards (IS) (CLZ-d4, QTP-d8, OLZ-d8) were obtained from Sigma Aldrich. Optima™ LC/MS grade acetonitrile (ACN), formic acid (FA), methanol and water were obtained from Fisher Scientific.

2.3 Standard curve samples

2.3.1 Finger sweat methodology

A typical standard curve consisted of six standard levels prepared in water and spiked in fixed volume (10 μL) onto chromatography paper (Whatman 1-Chr-grade, 2 × 2 cm) as well as blank papers. Each level was freshly prepared in triplicate before drying at ambient temperature for 1 hour prior to extraction from paper as described in section 2.4.1. Based on proof-of-concept data, standard curve and quality control (QC) samples were prepared using this procedure but at different concentrations depending on analyte. Standards ranged from 60—360 pg for CLZ/NDMC, 30—180 pg for QTP/NQTP and 100—600 pg for OLZ/DMO. Internal standards (IS) were 200 pg, 100 pg and 350 pg, respectively. For assessment of method performance, three QC levels were prepared on paper for each analyte, reflective of lower, middle and upper of the working range. These were 90, 200 and 330 pg for CLZ/NDMC; 40, 100 and 160 pg for QTP/NQTP; and 150, 350 and 550 pg for OLZ/DMO.

For patients with matched plasma samples, the working range was extended to 100—600 pg (IS = 350 pg) for CLZ and NDMC. Three QC levels (150, 350 and 550 pg) were selected to assess the performance of the extended range.

2.3.2 Plasma methodology

For measurement of CLZ and NDMC only, standard curve samples were prepared by spiking pooled plasma in the range of 25—1,500 ng/mL. Three QC levels (75, 500 and 1,200 ng/mL) were prepared in pooled plasma for verification of method performance. An IS solution (100 ng/mL CLZ-d4) was prepared in methanol.

2.4 Sample preparation

2.4.1 Finger sweat samples

Prior to extraction, samples prepared on paper (i.e., standard curve or QC samples) or collected onto paper (i.e., finger sweat from patients or drug naïve controls) were spiked with an IS solution (exact mass of IS described in Section 2.3.1) and allowed to dry at ambient temperature for 1 hour. Using sterile tweezers, the papers were transferred into 2 mL centrifuge tubes with 1.5 mL of methanol. The tubes were then centrifuged at 9,500 ×g for 2 min. The paper substrate was discarded using sterilized tweezers, and the resultant solvent extract was evaporated to dryness using nitrogen. Samples were reconstituted in 100 μL 50:50 mobile phase A (10 mM ammonium acetate adjusted to pH 4.6 using FA) and mobile phase B (ACN +0.1% FA (v/v)) for analysis.

2.4.2 Plasma samples

All standard, QC and patient plasma samples were prepared using an existing extraction procedure (Qi and Liu, 2021). 50 μL aliquots of plasma were defrosted and prepared by protein precipitation with ACN. To each sample, 150 μL of ACN and 20 μL of IS solution were added and vortexed for 5 min. The mixtures were subjected to refrigerated (4°C) centrifugation at 15,000 rpm for 8 min 40 μL of the resultant supernatant was removed and immersed in 200 μL of water, vortexed for a further minute and transferred into vials for analysis.

2.5 Instrumentation and sample analysis

Chromatographic separation was performed using a Thermo Scientific™ Ultimate 3,000 ultra-high-performance liquid chromatography (UHPLC) system equipped with a Kinetex XB-C18 column (100 × 2.1 mm, 5 μm, Phenomenex). The 3-min gradient separation was operated at 30°C with a flow rate of

0.25 mL/min. The starting mobile phase comprised 95% A and 5% B which linearly increased to 80% B at 2 min, held constant for 0.5 min, before returning to the initial composition.

The UHPLC system was coupled to a Thermo Scientific Q Exactive™ Plus Hybrid Quadrupole-Orbitrap™ Mass Spectrometer (MS). The MS was used to scan for all analytes using high resolution full scan (HRFS). MS/MS analysis was performed using data dependent acquisition mode (dd-MS^2). The operating conditions of both the HRFS and dd-MS^2 are defined in Supplementary Table S2.

Data acquisition and processing was completed using Thermo Scientific TraceFinder™ software (version 5.0). Statistical analysis was performed using IBM SPSS Statistics software (version 28.0).

2.6 Method performance

Method performance was evaluated using the Food and Drug Administration guidelines to determine selectivity, linearity, intra- and inter-day accuracy and precision, limit of detection (LOD) and lower limit of quantification (LLOQ), matrix effect and recovery (finger sweat only), carryover and stability (U.S. Department of Health and Human Services and Food and Drug Administration, 2018). Full details of method performance are provided within the Supplementary Material.

In brief, a linear response was obtained for all drugs and metabolites with R^2 values of >0.973 when extracted from paper (Supplementary Table S3). Using the initially selected working ranges for qualitative assessment of antipsychotics in finger sweat only, the method was repeatable for analytes extracted on the same day (intra-day relative standard deviation (RSD) < 20%) (Supplementary Table S4). However, for OLZ/DMO, the method showed poor reproducibility when comparing QC samples extracted from paper on non-consecutive days. Therefore, clinical finger sweat samples were run in batches determined by drug type with standard curves extracted on each day of analysis.

Method performance experiments were repeated to assess the performance of the finger sweat method at the higher working range selected for the subset of patients with paired finger sweat and plasma samples. The intra- and inter-day accuracy and precision of CLZ/NDMC extracted from paper and in plasma was assessed using relative error (RE) and RSD. The three QC levels indicated acceptable accuracy and precision (RE and RSD <15%) for both biological matrices (Supplementary Tables S5, S6).

3 Results

Chromatograms of drug and metabolite standards are displayed in Supplementary Figure S1. No significant interference with the antipsychotic drugs and metabolites were observed within the paper only blanks. Proof of concept through successful detection and confirmation by dd-MS^2 was achieved for each of the parent drugs and their metabolites within human samples (see Supplementary Figure S2). All antipsychotics were below the LOD for samples collected from the negative control group (see Supplementary Figure S3).

3.1 Detection of antipsychotics in finger sweat

The detection rate of the parent drug and metabolite in all finger sweat samples *versus* per participant is summarized in Table 1. Samples and/or patients are classified as "positive" where the analyte is detected.

3.1.1 Clozapine

CLZ performed most reliably of the three antipsychotics. In patients prescribed 100 mg/day or higher, detection rate of the parent drug was 100% in samples collected both *as presented* and *after washing*. Across all participants, successful detection of CLZ correlated with daily dose, where only one sample was CLZ negative. This sample was collected *after washing* from participant AP-109, prescribed the lowest dose of 25 mg/day. These results indicate that the fingerprint test has sufficient sensitivity for medical application, for example, in the treatment of schizophrenia, where a low dose of clozapine is 150—300 mg/day (Subramanian et al., 2017). Using presence of parent drug in at least one finger *after washing* as indication of drug administration, the finger sweat test was 100% effective in monitoring CLZ adherence in all patients, including those prescribed below the typical dose range.

Presence of NDMC within patient samples was less prevalent and did not correlate with prescribed dose. Although not detected in any samples from AP-109, other patients also did not exhibit the metabolite in any samples *after washing*, namely, AP-127 and AP-118, prescribed 140 and 500 mg/day. It is possible that these results are related to quality of sample, as previous studies in finger sweat have shown that poor deposition of sample can generate false negative results (Ismail et al., 2022). Using presence of the metabolite in at least one finger as indication of adherence in patients prescribed 100 mg/day or higher, the test was 94% effective using samples *as presented* or 88% effective *after washing*.

3.1.2 Quetiapine

Both QTP and NQTP were detected in all samples collected *as presented* and *after washing*. Therefore, the test was 100% effective in monitoring QTP adherence. Although only a small number of patients were recruited, these results suggest the test is sufficiently sensitive to monitor typical doses prescribed in the treatment of bipolar disorder and schizophrenia which range 400—800 mg/day by oral administration (Muneer, 2015) compared to 100—500 mg/day prescribed to patients included in this study.

3.1.3 Olanzapine

OLZ and its metabolite performed most inconsistently of the three groups. Whilst OLZ was detected in 75% of samples *after washing*, DMO was rarely detected and only observed in *as presented* samples. This is likely due to the higher LOD (100 pg) and low doses of drug in comparison to others within this study. Inspection of the data per participant showed that 100% (n = 20) could be classified as '*Positive*' based on detection of OLZ in at least one finger *as presented* or 80% *after washing*. Detection of OLZ was found to be more consistent in patients who were administered medication by monthly injection, with 100% detection of OLZ in all fingers both before and after washing.

TABLE 1 Detection of antipsychotic drugs and metabolites in finger sweat only participants, collected "as presented" and "after washing", defined in all samples and per participant.

Target analyte	Detection in samples, % (n) [a]		Detection in participants, % (N) [b]	
	As presented	After washing	As presented	After washing
CLZ [c]	100 (96)	100 (96)	100 (33)	100 (32)
NDMC [c]	86 (83)	80 (77)	94 (30)	88 (28)
QTP	100 (21)	100 (21)	100 (7)	100 (7)
NQTP	100 (21)	100 (21)	100 (7)	100 (7)
OLZ	88 (53)	75 (45)	100 (20)	80 (16)
DMO	10 (6)	0 (0)	15 (3)	0 (0)

[a]"n" defined as the total number of samples per drug.
[b]"N" defined as the total number of participants per drug where positive detection requires analyte presence in at least one finger.
[c]Samples from participants prescribed ≥100 mg/day.
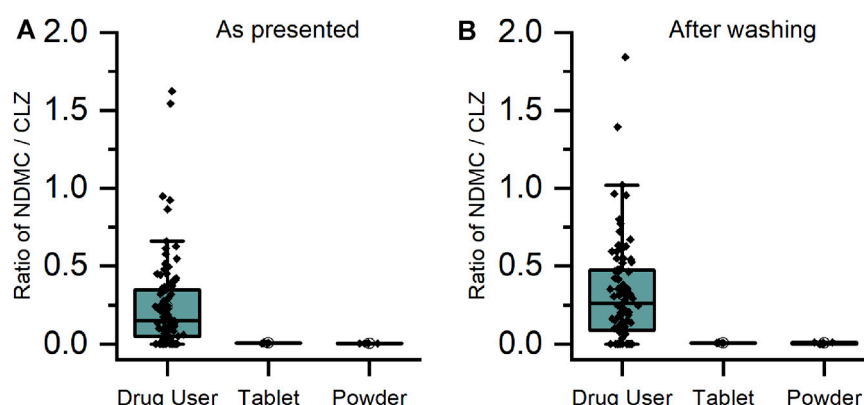
FIGURE 2
Ratio of metabolite/parent drug in finger sweat samples collected (A) "as presented" and (B) "after washing" for clozapine users prescribed ≥100 mg/day (n = 32 participants, labelled "drug user") and volunteers (N = 2) which held antipsychotic tablet in right hand (labelled "tablet") and rubbed crushed tablet in left hand (labelled "powder").

3.2 Drug contact versus administration

To explore the possibility of using the test to monitor adherence to antipsychotic medication, we assessed the feasibility of using the test to distinguish between contact and ingestion of a given drug. It is possible that false positive results could arise from both innocent handling of a tablet, as well as a deliberate attempt to cheat the test. Therefore, finger sweat samples were collected from volunteers who were asked to handle whole tablets with their right hand to mimic administration and to rub the powder crushed tablets across the tips of the left fingers to simulate intentional doctoring of a result.

For CLZ and QTP, contact-only participants were distinguished from drug users by lower levels or lack of metabolite within their sweat samples. Through plotting the ratio of metabolite to parent drug, a visually and statistically significant ($p < 0.001$, 2-tailed Mann Whitney U-test) distinction between the two populations was observed both before and after hand washing (Figures 2, 3).

As DMO was rarely detected in either the drug user or the contact only samples, it was not possible to adopt the same approach as for CLZ and QTP. Comparison of the mass of parent drug showed

a statistically significant ($p < 0.001$, 2-tailed Mann Whitney U-test) difference between the two populations for OLZ (see Supplementary Figure S4). This result was repeatable for CLZ and QTP also, suggesting that high levels of parent drug could indicate a false positive result originating from contact with medication.

3.3 Comparison of plasma and finger sweat

Paired plasma and finger sweat samples were collected from a subgroup of patients prescribed CLZ. Daily dose was matched to the previous analysis, ranging 25—550 mg/day. Given that many of the first batch of samples exhibited analyte levels above the calibration range, the linear range was extended to provide quantitative measurements of drug and metabolite in finger sweat.

Finger sweat was found to be 100% effective in monitoring adherence, where both CLZ and NDMC were detected in at least one finger either as presented and after washing. Only one participant (PS-005) provided any negative finger sweat samples. In this case, the parent drug was detected in two fingers as presented and a single
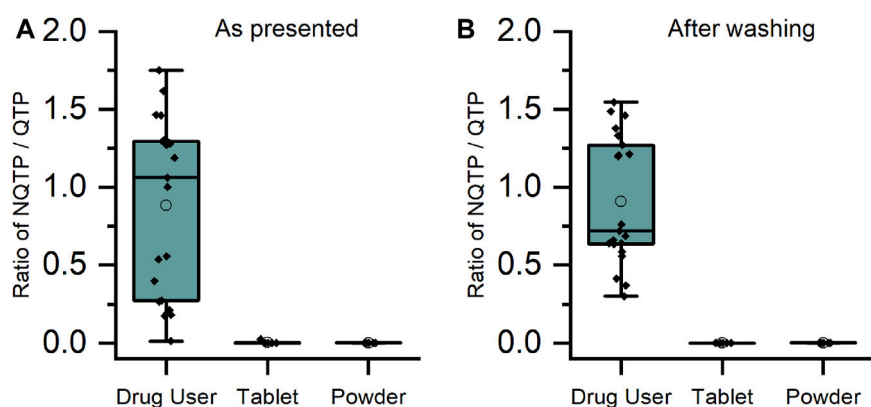
FIGURE 3
Ratio of metabolite/parent drug in finger sweat samples collected **(A)** "as presented" and **(B)** "after washing" for quetiapine users (n = 7 participants, labelled "drug user") and volunteers (N = 2) which held antipsychotic tablet in right hand (labelled "tablet") and rubbed crushed tablet in left hand (labelled "powder").
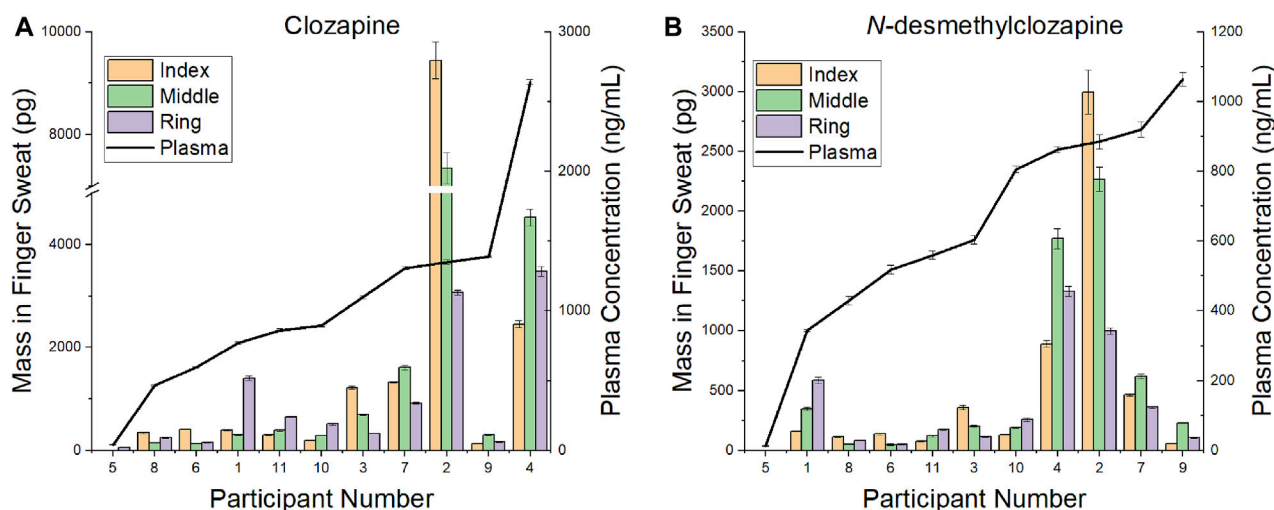
FIGURE 4
Comparison of mass in finger sweat collected "after washing" *versus* plasma concentration for **(A)** clozapine and **(B)** *N*-desmethylclozapine.

finger *after washing*, whereas NDMC was detected in the index finger *as presented* only. This could be due to several factors: including the sub-therapeutic dose of CLZ (25 mg/day), the short duration of treatment (approximately 1 week) and poor deposition of sample. It should also be noted that this patient was difficult to bleed, suggestive of dehydration, resulting in insufficient whole blood for plasma separation. In such cases, where an indication of patient adherence is required but collection of blood has failed, finger sweat provides a simplistic opportunity to assess adherence in the absence of sufficient plasma for drug analysis.

A comparison of CLZ and NDMC in *after washing* samples *versus* concentration in plasma is displayed in Figure 4. The ratio of metabolite to parent drug in sweat was 0.42 ± 0.19 compared to 0.65 ± 0.22 in plasma. Visually, the mass of analyte in finger sweat was found to mirror the concentration in plasma. The correlation of average mass per finger *versus* plasma concentration yields a Pearson correlation

coefficient (r) of 0.56 ($p < 0.04$, 1-tailed) and 0.45 ($p < 0.09$, 1-tailed) for CLZ and NDMC. Inspection of CLZ correlation per finger showed that the middle and ring finger correlated most strongly, with Pearson's r values of 0.62 ($p < 0.02$, 1-tailed) and 0.75 ($p < 0.01$, 1-tailed) (Figure 5). This suggests that sampling of middle and ring fingers is preferable for best representation of plasma level.

4 Discussion

Antipsychotic medication is considered to be the main course of treatment of psychotic disorders. Despite the extreme consequences associated with nonadherence and consequent relapse, patient adherence is often assessed by subjective means (Velligan et al., 2006). The introduction of a simple and dignified method of monitoring patients could improve patient experience and outcomes. Collection of finger

FIGURE 5
Pearson correlation coefficient (r) and p-value (P) (1-tailed) for the mass of clozapine in finger sweat collected "after washing" from the middle and ring fingers and clozapine concentration in paired plasma samples.
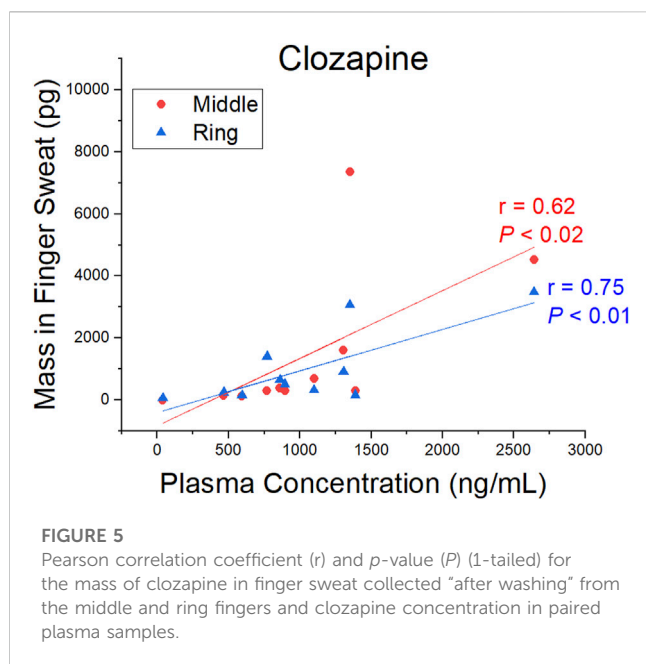
sweat is quick, convenient and does not require any specialist training or equipment. Targeted analysis of finger sweat samples offers a more accurate alternative to subjective adherence monitoring methods without the invasive procedures required for blood collection. With further development, finger sweat based diagnostics has the potential to inform clinicians on dose efficacy and toxicity.

In this work, three common antipsychotic drugs (CLZ, QTP, OLZ) and their metabolites were successfully detected in finger sweat using LC-MS/MS. Our results demonstrate that a test based on the detection of the parent drug in at least 1 of 3 samples collected *as presented* was 100% effective in monitoring patient adherence. Using participants who had handled antipsychotic medication only, we were able to distinguish between contact and administration of a given drug where potential false positive results were characterized either by a lack of metabolite, or by exceedingly high levels of parent drug. Similarly, no interferences were found in the negative control group. A limitation of the finger sweat sampling method used within this study was additional time required for handwashing and collection of *after washing* samples. These results suggest that for qualitative assessment of adherence using finger sweat, the addition of the hand washing step is not necessary. This would simplify the test for use by a layperson, as well as further speed the collection process.

To our knowledge, this is also the first study describing the relationship of CLZ and its metabolite in finger sweat and plasma. Although inter-finger levels varied, the test was sufficiently sensitive to detect the typical dosing range of CLZ prescribed in the treatment of psychotic disorders such as schizophrenia. The middle and ring fingers were found to reflect the plasma concentrations most strongly, where a statistically significant correlation between CLZ plasma concentration and mass per finger *after washing* was observed. These data provide a foundation for further exploration of the relationship between the two biological matrices. Opportunities include the implementation of a standardization procedure, such as that described by (Goucher et al., 2009) whereby creatinine was used to smooth the elimination profile of lorazepam in ten overlayed fingerprints from the same donor or by

(Ismail et al., 2022) who employed taurine to reduce the coefficient of variation of acetyl isoniazid (the main metabolite of a key anti-tuberculosis drug) between multiple fingerprint samples collected simultaneously from the same donor. Identification and implementation of similar small molecule metabolites within the antipsychotic finger sweat workflow could account for intra-donor variability and allow for more reliable quantitative measurements in future analyses.

In conclusion, a sensitive, convenient, and non-invasive method for monitoring adherence in antipsychotic patients has been developed. Analysis of human finger sweat samples from drug users has shown the method to be 100% effective at detecting commonly prescribed doses of antipsychotic medication, given the test criteria (detection of parent drug in 1 of 3 samples). Using these criteria, the test can distinguish drug administration from drug contact, and non-drug users. The finger sweat technology has broader opportunities in clinical environment, in quantitative monitoring antipsychotic medication or monitoring adherence to other treatment regimes.

Data availability statement

The raw data supporting the conclusion of this article will be made available by the authors, without undue reservation.

Ethics statement

The studies involving humans were approved by Health Research Authority's National Research Ethics Service. The studies were conducted in accordance with the local legislation and institutional requirements. The participants provided their written informed consent to participate in this study.

Author contributions

KL, CF, CC, RN, and MB contributed to conceptualization of this study. KL and CF performed methodology development and validation experiments. KL was responsible for management of clinical study and, with HL and CF, completed the analysis of collected samples. MB was responsible for group supervision and funding acquisition. KL processed the raw data and wrote the original draft of the manuscript. All authors contributed to the article and approved the submitted version.

Funding

Acknowledgments

The authors would like to thank Joshua Cudworth and the staff at Surrey and Borders NHS Partnership Trust, as well as Evelin Vogel and the staff at Sussex Partnership NHS Foundation Trust, for assistance in collection of the samples used within this study.

Conflict of interest

The authors declare that the research was conducted in the absence of any commercial or financial relationships that could be construed as a potential conflict of interest.

Publisher's note

All claims expressed in this article are solely those of the authors and do not necessarily represent those of their affiliated organizations, or those of the publisher, the editors and the reviewers. Any product that may be evaluated in this article, or claim that may be made by its manufacturer, is not guaranteed or endorsed by the publisher.

Supplementary material

The Supplementary Material for this article can be found online at: https://www.frontiersin.org/articles/10.3389/fchem.2023.1245089/full#supplementary-material

References

Aravagiri, M., and Marder, S. R. (2001). Simultaneous determination of clozapine and its N-desmethyl and N-oxide metabolites in plasma by liquid chromatography/electrospray tandem mass spectrometry and its application to plasma level monitoring in schizophrenic patients. *J. Pharm. Biomed. Anal.* 26, 301–311. doi:10.1016/S0731-7085(0100410-1)

Bailey, M. J., Bradshaw, R., Francese, S., Salter, T. L., Costa, C., Ismail, M., et al. (2015). Rapid detection of cocaine, benzoylecgonine and methylecgonine in fingerprints using surface mass spectrometry. *Analyst* 140, 6254–6259. doi:10.1039/c5an00112a

Cao, Y., Zhao, F., Chen, J., Huang, T., Zeng, J., Wang, L., et al. (2020). A simple and rapid LC-MS/MS method for the simultaneous determination of eight antipsychotics in human serum, and its application to therapeutic drug monitoring. *J. Chromatogr. B Anal. Technol. Biomed. Life Sci.* 1147, 122129. doi:10.1016/j.jchromb.2020.122129

Costa, C., Frampas, C., Longman, K. A., Palitsin, V., Ismail, M., Sears, P., et al. (2021). Paper spray screening and liquid chromatography/mass spectrometry confirmation for medication adherence testing: a two-step process. *Rapid Commun. Mass Spectrom.* 35, e8553. doi:10.1002/rcm.8553

Costa, C., Webb, R., Palitsin, V., Ismail, M., De Puit, M., Atkinson, S., et al. (2017). Rapid, secure drug testing using fingerprint development and paper spray mass spectrometry. *Clin. Chem.*, 63 (11):1745–1752. doi:10.1373/clinchem.2017.275578

Czerwinska, J., Jang, M., Costa, C., Parkin, M. C., George, C., Kicman, A. T., et al. (2020). Detection of mephedrone and its metabolites in fingerprints from a controlled human administration study by liquid chromatography-tandem mass spectrometry and paper spray-mass spectrometry. *Analyst* 145, 3038–3048. doi:10.1039/C9AN02477H

Fisher, D. S., Partridge, S. J., Handley, S. A., Couchman, L., Morgan, P. E., and Flanagan, R. J. (2013). LC–MS/MS of some atypical antipsychotics in human plasma, serum, oral fluid and haemolysed whole blood. *Forensic Sci. Int.* 229, 145–150. doi:10.1016/J.FORSCIINT.2013.02.010

García, S., Martínez-Cengotitabengoa, M., López-Zurbano, S., Zorrilla, I., López, P., Vieta, E., et al. (2016). Adherence to antipsychotic medication in bipolar disorder and schizophrenic patients: a systematic review. *J. Clin. Psychopharmacol.* 36, 355–371. doi:10.1097/JCP.0000000000000523

Goucher, E., Kicman, A., Smith, N., and Jickells, S. (2009). The detection and quantification of lorazepam and its 3-O-glucuronide in fingerprint deposits by LC-MS/MS. *J. Sep. Sci.* 32, 2266–2272. doi:10.1002/jssc.200900097

Gründer, G., Hippius, H., and Carlsson, A. (2009). The "atypicality" of antipsychotics: a concept re-examined and re-defined. *Nat. Rev. Drug Discov.* 8:3, 197–202. doi:10.1038/nrd2806

Günther, K. N., Banner, J., Linnet, K., and Johansen, S. S. (2020). Segmental hair analysis of olanzapine and N-desmethyl-olanzapine in postmortem hair from mentally ill patients by LC-MS/MS. *J. Pharm. Biomed. Anal.* 190, 113510. doi:10.1016/J.JPBA.2020.113510

Günther, K. N., Johansen, S. S., Nielsen, M. K. K., Wictor, P., Banner, J., and Linnet, K. (2018). Post-mortem quetiapine concentrations in hair segments of psychiatric patients - correlation between hair concentration, dose and concentration in blood. *Forensic Sci. Int.* 285, 58–64. doi:10.1016/J.FORSCIINT.2018.01.020

Haddad, P. M., Brain, C., and Scott, J. (2014). Nonadherence with antipsychotic medication in schizophrenia: challenges and management strategies. *Patient Relat. Outcome Meas.* 5, 43–62. doi:10.2147/PROM.S42735

Haddad, P. M., and Sharma, S. G. (2012). Adverse effects of atypical antipsychotics. *CNS Drugs* 21 (11), 911–936. doi:10.2165/00023210-200721110-00004

Higashi, K., Medic, G., Littlewood, K. J., Diez, T., Granström, O., and De Hert, M. (2013). Medication adherence in schizophrenia: factors influencing adherence and consequences of nonadherence, a systematic literature review. *Ther. Adv. Psychopharmacol.* 3, 200–218. doi:10.1177/2045125312474019

Hudson, M., Stuchinskaya, T., Ramma, S., Patel, J., Sievers, C., Goetz, S., et al. (2018). Drug screening using the sweat of a fingerprint: lateral flow detection of d9-tetrahydrocannabinol, cocaine, opiates and amphetamine. *J. Anal. Toxicol.* 43, 88–95. doi:10.1093/jat/bky068

Ismail, M., Costa, C., Longman, K., Chambers, M. A., Menzies, S., and Bailey, M. J. (2022). Potential to use fingerprints for monitoring therapeutic levels of isoniazid and treatment adherence. *ACS Omega* 7, 15167–15173. doi:10.1021/acsomega.2c01257

Ismail, M., Stevenson, D., Costa, C., Webb, R., De Puit, M., and Bailey, M. (2018). *Noninvasive detection of cocaine and heroin use with single fingerprints: Determination of an environmental cutoff*. doi:10.1373/clinchem.2017.281469

Jacob, S., Jickells, S., Wolff, K., and Smith, N. (2008). Drug testing by chemical analysis of fingerprint deposits from methadone- maintained opioid dependent patients using UPLC-MS/MS. *Drug Metab. Lett.* 2, 245–247. doi:10.2174/187231208786734094

Jang, M., Costa, C., Bunch, J., Gibson, B., Ismail, M., Palitsin, V., et al. (2020). On the relevance of cocaine detection in a fingerprint. *Sci. Rep.* 10, 1974. doi:10.1038/s41598-020-58856-0

Josefsson, M., Roman, M., Skogh, E., and Dahl, M. L. (2010). Liquid chromatography/tandem mass spectrometry method for determination of olanzapine and N-desmethylolanzapine in human serum and cerebrospinal fluid. *J. Pharm. Biomed. Anal.* 53, 576–582. doi:10.1016/J.JPBA.2010.03.040

Muneer, A. (2015). Pharmacotherapy of bipolar disorder with quetiapine: a recent literature review and an update. *Clin. Psychopharmacol. Neurosci.* 13, 25–35. doi:10.9758/CPN.2015.13.1.25

Pillinger, T., McCutcheon, R. A., Vano, L., Mizuno, Y., Arumuham, A., Hindley, G., et al. (2020). Comparative effects of 18 antipsychotics on metabolic function in patients with schizophrenia, predictors of metabolic dysregulation, and association with psychopathology: a systematic review and network meta-analysis. *Lancet Psychiatry* 7, 64–77. doi:10.1016/S2215-0366(19)30416-X

Qi, Y., and Liu, G. (2021). Ultra-performance liquid chromatography-tandem mass spectrometry for simultaneous determination of antipsychotic drugs in human plasma and its application in therapeutic drug monitoring. *Drug Des. Devel Ther.* 15, 463–479. doi:10.2147/DDDT.S290963

Skogh, E., Reis, M., Dahl, M. L., Lundmark, J., and Bengtsson, F. (2002). Therapeutic drug monitoring data on olanzapine and its N-demethyl metabolite in the naturalistic clinical setting. *Ther. Drug Monit.* 24, 518–526. doi:10.1097/00007691-200208000-00010

Subramanian, S., Völlm, B. A., and Huband, N. (2017). Clozapine dose for schizophrenia. *Cochrane Database Syst. Rev.* 2017. doi:10.1002/14651858.CD009555.PUB2

U.S. Department of Health and Human Services, and Food and Drug Administration (2018). Bioanalytical method validation guidance for industry. Available at: http://www.fda.gov/Drugs/GuidanceComplianceRegulatoryInformation/Guidances/default.htmand/orhttp://www.fda.gov/AnimalVeterinary/GuidanceComplianceEnforcement/GuidanceforIndustry/default.htm (Accessed January 18, 2023).

Velligan, D. I., Lam, Y. W. F., Glahn, D. C., Barrett, J. A., Maples, N. J., Ereshefsky, L., et al. (2006). Defining and assessing adherence to oral antipsychotics: a review of the literature. *Schizophr. Bull.* 32, 724–742. doi:10.1093/SCHBUL/SBJ075

Weinmann, W., Müller, C., Vogt, S., and Frei, A. (2002). LC-MS-MS analysis of the neuroleptics clozapine, flupentixol, haloperidol, penfluridol, thioridazine, and zuclopenthixol in hair obtained from psychiatric patients. *J. Anal. Toxicol.* 26, 303–307. doi:10.1093/JAT/26.5.303

Zhou, Z., Li, X., Li, K., Xie, Z., Cheng, Z., Peng, W., et al. (2004). Simultaneous determination of clozapine, olanzapine, risperidone and quetiapine in plasma by high-performance liquid chromatography–electrospray ionization mass spectrometry. *J. Chromatogr. B* 802, 257–262. doi:10.1016/J.JCHROMB.2003.11.037

Check for updates

Portable NIR spectroscopy: the route to green analytical chemistry

G. Gullifa[1], L. Barone[1], E. Papa[1], A. Giuffrida[2], S. Materazzi[1]* and R. Risoluti[1]*

[1]Department of Chemistry, "Sapienza" Università di Roma, Rome, Italy, [2]Department of Chemical Sciences, University of Catania, Catania, Italy

There is a growing interest for cost-effective and nondestructive analytical techniques in both research and application fields. The growing approach by near-infrared spectroscopy (NIRs) pushes to develop handheld devices devoted to be easily applied for *in situ* determinations. Consequently, portable NIR spectrometers actually result definitively recognized as powerful instruments, able to perform nondestructive, online, or *in situ* analyses, and useful tools characterized by increasingly smaller size, lower cost, higher robustness, easy-to-use by operator, portable and with ergonomic profile. Chemometrics play a fundamental role to obtain useful and meaningful results from NIR spectra. In this review, portable NIRs applications, published in the period 2019–2022, have been selected to indicate starting references. These publications have been chosen among the many examples of the most recent applications to demonstrate the potential of this analytical approach which, not having the need for extraction processes or any other pre-treatment of the sample under examination, can be considered the "true green analytical chemistry" which allows the analysis where the sample to be characterized is located. In the case of industrial processes or plant or animal samples, it is even possible to follow the variation or evolution of fundamental parameters over time. Publications of specific applications in this field continuously appear in the literature, often in unfamiliar journal or in dedicated special issues. This review aims to give starting references, sometimes not easy to be found.

KEYWORDS

NIR, portable NIR, handheld NIR, near infrared spectroscopy, chemometrics

1 Introduction

In the past 20 years, the interest to the potential of near-infrared spectroscopy (NIRs) pushed the development of portable devices devoted to new applications, since several advantages make the technique a powerful analytical tool:

Abbreviations: NIRs, Near Infrared spectroscopy; PCA, Principal Component Analysis; PLSR, Partial least square regression; PLS-DA, Partial Least Squares—Discriminant Analysis; SIMCA, Soft Independent Modelling of Class Analogies.

- The spectroscopic approach is a non-destructive characterization, which allows to have immediate analytical answers that can be correlated to other following characterizations on the same identical sample or its representative portion
- NIR spectroscopy coupled to chemometrics allows targeted or untargeted analysis since the multivariate statistical evaluation of the results allows to develop prediction models
- Results can be reported both as qualitative and quantitative output by means of simple plots that are easily readable even by non-experts in chemometrics or by numerical quantification of the single analyte
- The possibility to perform *in-situ* and online analysis favors industrial applications since spectroscopy can be easily automated and connected to an IoT (Internet of Things) system for direct management of process output
- Increasingly smaller size, lower cost, higher robustness, easy-to-use by operator, portable and with ergonomic profile make NIRs a useful tool for routine characterization.

Chemometrics play a fundamental role to obtain useful and meaningful results from NIR spectra, since prediction models allow to obtain qualitative and quantitative analytical results.

As a consequence, publications of specific applications in this field continuously appear in the literature, often in unfamiliar journal or in dedicated special issues. To have an idea of the scientific interest, inserting "NIR applications" in a search engine like Scopus or Web of Science, more than 13,000 results are listed limiting the search to the last 5 years.

Consequently, to help readers in the search for updated useful starting references, sometimes difficult to locate, in this review have been selected NIRs applications published in the period 2019–2022.

2 Portable NIR spectrometers

Miniaturized and portable NIR spectrometers have enhanced the applications of near infrared technology, nowadays evermore frequently applied in on-site and in-field analyses. Originally used by military, handheld NIR was suddenly discovered by industry for on-site fast quality check. Law enforcement, environmental analyses and food quality control fully recognize the potential of portable spectrometers.

Fast and reliable classification and characterizations for safety or authenticity can be easily performed by trained users, not necessarily scientists (Sorak et al., 2012; Rodionova et al., 2016; Crocombe, 2018; Pomerantsev and Rodionova, 2021). The main goal when the miniaturization is carried out for an analytical instrument is to verify that performance is not affected. Portable NIR actually ensure comparable analytical results to laboratory benchtop devices, in both qualitative and quantitative aspects. Weight is a fundamental parameter for portable instruments: compared to 1 kg of Raman and MIR spectrometers, NIR handheld weight is about 100 g and the close future is the integration into cellular phones (Reinig et al., 2018).

NIR spectroscopy is mainly based on overtone bands and combination vibrations of C-H, O-H, N-H, C=O, and C=C bonds (Workman and Weyer, 2012; Siesler et al., 2016).

Although the signal occurs about ten to one hundred times lower as intensity with respect to medium infrared, the chemometric prediction models make handheld NIR an useful qualitative and quantitative characterization approach in analyses.

Basically, a portable NIR device is very similar to a laboratory benchtop instrument. Miniaturization involves Micro-Electro-Mechanical or Micro-Opto-Electro-Mechanical optical systems. Two main detectors are usually found: array or single detector. Indium gallium arsenide (InGaAs) is the most used material for detectors because of the lower price.

The following main solutions are actually recognized:

(a) Linear-variable filter instruments (array detector).
(b) MEMS-based FT-NIR instruments (opto-electro-mechanical).
(c) Micro-mirror device (DMD™) (wavelength selector).
(d) Fabry-Perot tunable wavelength filter.
(e) NIR grating.

In Table 1 several examples are reported.

Recent publications critically report detector differences (Bec et al., 2021), showing that the signal-to-noise ratio of modern instruments compensates narrower NIR wavelength range.

The sample measurement is highly simplified and makes very easy-to-use the portable NIR spectrometers: by direct contact (but also placing at short distance) it is possible to record characteristic spectra in diffuse reflection.

Figure 1 collects several different portable NIR solutions, commercially available. Simplified principles and parameters are briefly described.

2.1 Instrument improvements

To improve the stability of handheld near infrared spectrometers, a reference correction was proposed by Wang et al. On the basis of the measurement method, it was designed a contrast sampling mechanism to obtain a reference beam from light source. This configuration ensured that reference beam and light source drift in the same trend. An innovative NIR spectrometer for reference correction was consequently developed. According to the experimental results, the stability of the newly designed spectrometer achieved substantial improvement (Wang et al., 2021).

Phosphor-converted light-emitting diodes (pc-LEDs) are employed in handheld spectrosmeters. A high-performance NIR pc-LED was proposed and results demonstrated that the energy transfer can be used for developing new NIR phosphors (Basore et al., 2021). He et al. proposed an innovative pc-LED device, able to scan in a 5-cm-thick chicken breast so to identify characteristic differences in the spectra. The results indicated that biological tissue penetration can be diagnostic (He et al., 2022). To identify affected chicken breasts, de Cavalho et al. proposed handheld NIR spectroscopy. From the experimental results it was shown that myopathies in meat is correlated to the age of slaughter and handheld NIR can be used as a specific tool (de Carvalho et al., 2020).

Soil texture characterization is usually carried on manually, being consequently time-consuming. Vis-NIR handheld spectroscopy is preferred as sensor to predict soil characteristics

TABLE 1 Examples of portable NIR spectrometers available in the market and their monochromator/detector principles.

TrinamiX GmbH, Ludwigshafen, Germany	Linear variable filter instruments
VIAVI Solutions Inc., Santa Rosa, CA, United States	
Texas Instruments, Dallas, TX, United States	Digital micro-mirror device spectrometers
Innospectra Corp., Xinzhu, Taiwan, China	
Spectral Engines, Helsinki, Finland	Fabry Perot tunable filter instrument
Si-Ware Systems, Cairo, Egypt	MEMS FT-NIR spectrometers
Hamamatsu Photonics, Hamamatsu city, Japan	
Southnest Technology, Hefei, Anhui, China	
Insion GmbH, Obersulm,	grating microspectrometers
Germany; OrO Photonics, Xinzhu, Taiwan, China	
Senorics GmbH, Dresden, Germany	NIR scanner with 16 solar cell detectors

(Bene et al., 2020; Benedet et al., 2020; Pham et al., 2021; Andrade et al., 2022; Naimi et al., 2022; Peng et al., 2022; Shrestha et al., 2022; Teixeira et al., 2022; Vohland et al., 2022).

Goi et al. evaluated the possibility of a micro NIR instrument to predict quality parameters in beef. Moisture, fat and protein contents were monitored by a modified PLS analysis. Results proved that the portable instrumentation ensure good levels of prediction (Goi et al., 2022). Grass-fed and grain-fed beef were differentiated by Coombs et al. using NIR spectroscopy with the aim to aid retail and consumer confidence (Coombs et al., 2021).

Yu et al. (2022) prepared innovative OPDs with broad bandwidth, improved responsivity and frequency.

For decades, NIRs demonstrated its potential in industrial process monitoring and quality insurance. Ou et al. (2022). tested a portable NIR in the 850–1700 nm wavelength range. The results from his study demonstrated that the spectrometer, although limited in NIR spectral band detection, can be used in several different sensing applications. Paiva et al. (2022) described the application of diffuse reflectance to liquid and gas samples, enhancing that does not require adaptations. Biodiesel and vegetable oil in diesel blends were determined by comparing benchtop and portable FT-NIR spectrometers.

Bertinetto et al. (2022) investigated the influence of unexpert operator actions in the interpretation of spectra of pig feed.

Miniaturization made possible to develop handheld instruments, so lowering the price of point-of-use analysis. Baumann et al. developed a cheap, handheld DLP-Nano-NIRscan associated to a smartphone for the storage of data. A specific app was developed according to a software design standard. Baumann and coworkers demonstrated the usefulness for plant tissues to determine total nitrogen content (Baumann et al., 2020).

Wang and Liu published a review where they provided a brief summary for the factors that need to be considered in the design of broadband NIR phosphors. Authors expected this review to offer useful guidelines for the development of advanced NIR pc-LEDs (Wang and Liu, 2022).

As a consequence of handheld NIR development, dedicated apps become fundamental tools. Ren and Jia used samples of four drugs as validation objects to test the data classification model, that showed satisficing accuracy and the possibility to overcome internal storage limitations and operating speed (Ren and Jia, 2023).

(Zhou et al., 2022a) used a handheld NIR instrument for powdered sample characterization. The device showed high potentiality in powder analysis and comparative characterization.

Among easy-to-use and cheap analytical instruments, optical multisensor luminescence devices were proposed by Surkova et al. (2022) to determine fat content and adulteration in milk samples.

Applications in the Internet of Things (IoT) have been developed. Classic analytical methods, like mass spectrometry and chromatography, are not compatibles with IoT. NIR devices, having no moving parts, are ideal for IoT applications. Applications in industrial and agricultural field have been reported (Wang et al., 2021).

A critical review collected NIR applications, published between January 2019 and July 2020, focused on advantages of this handheld, cheap and robust analytical technique with non-destructive properties. These characteristics insure fast quality control on food products, raw materials, and ingredients (Bwambok et al., 2020). Applications in quality analysis and authentication of nutraceuticals using NIRs was also published in a review by Nagy et al. (Nagy et al., 2022). Reviewed innovation in handheld NIR and summarized and compared their characteristics (Zhu et al., 2022).

3 Applications to food quality characterization and adulterations

Food quality (and consequently food fraud) is often related to profit: the higher is the quality, the higher can be the prize in the market. Frauds or adulterations can result in illicit but important money gain. However, sometimes food fraud can impact the health of customers and consumers. Fraud detection is a challenge to help consumers and to punish food fraudsters.

On the other hand, quality is often a complicated mix of factors not easy to specifically determine or to quantify. NIR spectroscopy creates a specific profile that is the sum of all the specific parameters and can be a fundamental analytical tool. The possibility of managing a "profile" instead of individual analytes allows the NIRs/chemometrics approach to provide an untargeted result that takes into account all the parameters that characterize the sample
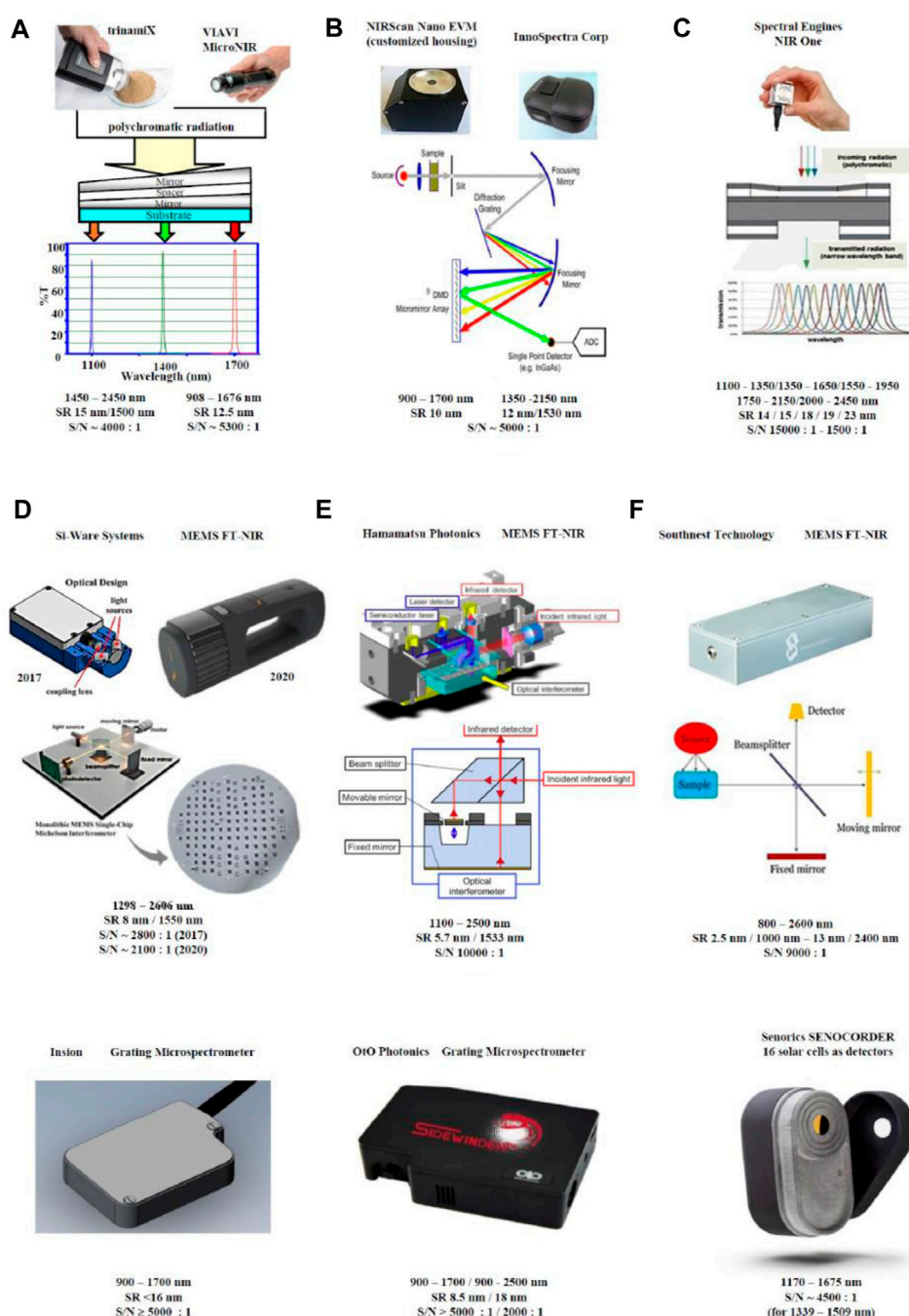
FIGURE 1
Handheld NIR spectrometers with different monochromator/detector principles and their performance parameters: **(A)** linear variable filter instruments (trinamiX GmbH, Ludwigshafen, Germany; VIAVI Solutions Inc., Santa Rosa, CA, United States); **(B)** digital micro-mirror device (DMD™) spectrometers (Texas Instruments, Dallas, TX, United States; Innospectra Corp., Xinzhu, Taiwan, China); **(C)** Fabry Perot tunable filter instrument (Spectral Engines, Helsinki, Finland); **(D)** MEMS FT-NIR spectrometers (Si-Ware Systems, Cairo, Egypt; Hamamatsu Photonics, Hamamatsu city, Japan; Southnest Technology, Hefei, Anhui, China); **(E)** grating microspectrometers (Insion GmbH, Obersulm, Germany; OrO Photonics, Xinzhu, Taiwan, China) **(F)** NIR scanner with 16 solar cell detectors (Senorics GmbH, Dresden, Germany). Reproduced (CC-BY 4.0 license) from (Bec et al., 2021).

under examination and guarantees, in the case of food, to characterize a "profile" of quality as a reference even in case of fraud investigation.

Combining NIR spectroscopy and machine intelligence is a nondestructive tool for powdery food evaluation. Zhou et al. presented a handheld device ("NIR-spoon") for simultaneous evaluation of multi-mixture powdery food. Each mixed powdered sample was analyzed by a "NIR-Spoon" and software was consequently dedicated to the "NIR-Spoon" that resulted in a good accuracy with the possibility of a mobile app (Zhou et al., 2022b). An OPLS-DA model, based on the data from the handheld NIR, showed 84.85% and 86.96% correct classification (Srinuttrakul et al., 2021).

The determination of green pea and peanut adulterations in pistachio by handheld FT-MIR and FT-NIR spectroscopy was proposed by Aykas and Menevseoglu. Pistachio adulteration derives from its high value. A fast FT-NIR methodology to check adulteration was proposed and provided advantages over FT-MIR, being more precise (Aykas and Menevseoglu, 2021). Cashew nut adulteration with Brazilian nut, pecan nut, macadamia nut and peanut was proposed, based on the development of a one-class SIMCA model (Rovira et al., 2023). Zhu et al. evaluated quality traits of oats to support breeding selection (Zhu et al., 2022).

Prediction of meat quality in fresh cut was reported by (An et al., 2022), while after treatment in the abattoir was reported by (Savoia et al., 2020; Savoia et al., 2021). Li et al. proposed a rapid and nondestructive simultaneous characterization of different types of sheep meat cut (Li et al., 2021).

Extra virgin olive oil is among the most known quality made in Italy product. Violino et al. (2022) evaluated the performance of a handheld VIS–NIR system to determine 203 oil samples quality. Ciaccheri et al. reported a bluetooth-connected pocket NIR spectrometer for the analysis of olive oils of different qualities (Ciaccheri et al., 2022) and a similar study was published by Santos and coworkers (Borghi et al., 2020; Santos et al., 2020; Santos et al., 2022).

Escuredo et al. (2021a). proposed a simple portable spectroscopic approach to predict the properties in honeys by multivariate data processing.

Maraphum et al. used a portable NIR spectrometer to determine starch and dry matter amount in fresh cassava tubers. Results suggested that the method can be useful when monitoring the quality of cassava tubers "*in field*" by breeders, with save of time and costs (Maraphum et al., 2020; Maraphum et al., 2022). In coriander oil can be found about the 70% of petroselinic acid, with anti-inflammatory and anti-aging properties. The authenticity of coriander oil and modifications by means of commercial oils was tested by handheld NIR and PLS regression models (Kaufmann et al., 2022). Edible oils are usually adulterated with sesame oil to save production costs. Portable FT-NIR, FT-MIR, and Raman spectrometers were proposed as rapid, simple, and non-invasive method to detect adulteration (Menevseoglu, 2021).

Truffles are well known and very expensive edible mushroom. Black truffles can be however found at lower prices. It is not easy to distinguish truffles without experience and often frauds occur. Kappacher et al. analyzed truffle samples of different species by 4 NIR devices: of these, 3 were miniaturized devices (Risoluti et al., 2020a). The resulting published paper compared the predicting performances of portable vs. benchtop NIR instruments, suggesting a fast, non-destructive and cheap tool (Kappacher et al., 2022).

The raspberry characterization is a procedure laborious and expensive, due to several chemical tests to use. By a NIRs approach, the prediction of raspberry quality was proposed by Gales and coworkers. Anthocyanins and solid soluble concentrations in whole fresh raspberries were easily predicted (Gales et al., 2021).

Sripaurya et al. (2021) designed and implemented a 6-digital-channel portable NIR instrument to determine the quality and the maturity of Gros Michel bananas. Portable NIR to in-field determine "Valencia" orange fruit maturity and avocado was reported by

Ncama and coworkers (Ncama et al., 2020a; Ncama et al., 2020b). The evaluation of portable spectrometers performance to characterize table grape and peach quality attributes non-invasively, was proposed by (Donis-González et al., 2020), by (Rouxinol et al., 2022), by (Zhang et al., 2021), by (Ferrara et al., 2022) and by (Beltrame et al., 2021).

Almonds, easy to adulterate to have higher profits because of the lower production costs, were characterized by a developed method for identification of almond flour adulteration by comparing three different portable NIR instruments and SIMCA as classification method (Netto et al., 2023). Bitter almonds contamination in sweet almonds was determined by by the potential of portable NIR (Torres et al., 2021). Wang et al. realized a handheld Vis/NIR prototype to discriminate different origin apples (Wang et al., 2022).

Manuelian et al. evaluated cheese total nitrogen, soluble nitrogen, ripening index, major minerals, and fatty acids by a pocket-size NIR spectrometer. When comparing the accuracy with a benchtop instrument, however, no substantial difference in accuracy resulted. The NIR miniaturization can consequently be an opportunity in dairy industry (Manuelian et al., 2022). Bittante et al. published an invited review with focus on VIS and NIR spectroscopies to predict the cheese chemical composition (Bittante et al., 2022).

Omega-3 supplements are sold at elevated prices and their quality has to be assessed. Hespanhol et al. evaluated the performance of a cheap NIR assisted by a chemometric model to determine the concentration of omega-3 in supplements. This simple, fast and inexpensive approach determined the quality of the supplements and to identify frauds or non-conformities of the market (Hespanhol et al., 2020).

Durum wheat semolina is the raw material for pasta production and, when cooking, are fundamental the protein content to obtain the gluten strength. Cecchini et al. compared two technologies (both non-destructive and rapid), i.e. a low-cost sensor and a handheld NIR spectrometer, to determine semolina quality. Experimental evidence enhanced the possibilities of a small and low cost sensor, easy to use in contact with the sample more than by a laboratory instruments (Cecchini et al., 2021).

Intrinsic and extrinsic properties of rice were studied to give the consumer a rice quality identification. Spectra were collected by a handheld NIR to develop a predictive model (Rizwana and Hazarika, 2020). Jiang and coworkers reported a fatty acid surveillance during the storage of the rice by a handheld near infrared system (Jiang et al., 2020).

Insects are well known as possible human food. Riu and coworkers studied the possibility to classify insect powder by handheld NIR spectrometer. Experimental evidences confirmed this instrumental approach to be a trusted tool of analysis, able to predict macronutrients (Riu et al., 2022).

The moisture content deeply influences the dehydration process to prevent microbial growth and to preserve nutrients and quality of fruits and vegetables. The results of a study proposed by Malvandi showed how a handheld NIR is able to monitor the moisture content (Malvandi et al., 2022a). Pesticide residues determination was presented by Ngo et al. on leafy vegetables using a handheld VIS/NIR instrument. Vegetable samples, like lettuce, oriental mustard, and bok choy, were analyzed. Results showed that

pesticide residues on leafy vegetables can be easily detected (Ngo et al., 2022). Recently, handheld and smartphone-based NIR devices have been widely used in agri-food industries as food-scanners, based on their predictive potential and compared with destructive approaches (Goisser et al., 2021). Integrated soluble solid and nitrate content assessment of spinach plants using portable NIRS sensors along the supply chain was also reported by (Torres et al., 2020)

Mishra and Woltering used an innovative approach that was tested to predict moisture and total soluble solids in pear and kiwi fruit (Mishra et al., 2021; Mishra and Woltering, 2021).

Anyidoho et al. (2022). used NIR/Chemometrics for rapid determination of fermentation duration, fermentation index and moisture content of cocoa beans.

The watermelons maturity was determined by two handheld new generation NIR spectrometers were compared in determining soluble solid content, a parameter that proves full watermelon maturity. The results obtained by different pre-processing methods showed the possibility to predict watermelon maturity (Vega-Castellote et al., 2022). Qi et al. discriminated the different varieties of red Jujube (Risoluti et al., 2019a; Qi et al., 2022).

Lycopene ia a red colored carotenoid in tomatoes that shows health benefits in scavenging free radicals. Instead of traditional in laboratory extraction process followed by HPLC analysis, Goisser et al. compared Vis/NIR spectra obtained by three portable Vis/NIR instruments defined food-scanners (Goisser et al., 2020a; Goisser et al., 2020b). The commercialization of fresh tomatoes is based on the soluble solid content as quality parameter. A handheld Vis-NIR spectrometer in interactance geometry discriminated low from high values soluble contents (Brito et al., 2021). Food waste has to be reduced as much as possible. Emsley et al. assessed the NIR potentiality to prove tomato stability during storage. Resulting informations indicated the possibility to predict tomatoes time-after-harvest (Emsley et al., 2022). Arruda de Brito et al. also proposed the possibility to determine important parameters (color, dry matter, etc) by NIR spectroscopy (Arruda de Brito et al., 2022). Handheld NIR for in-field fresh tomato quality control analysis was reported by (Borba et al., 2021) and by (de Oliveira Aguiar et al., 2022).

Gatti and coworkers investigated by handheld NIR milk chocolate, white chocolate and other different percent cocoa chocolates subjected to high temperatures. Good sensibility, specificity, and accuracy values were determined to establish thermal treatments (Gatti et al., 2021).

To assess fishery products authenticity it is fundamental an instrumentation able to give rapid, eco-friendly, cost-effective and easy answer. Varrà et al. verified the possibility to determine the geographic origin of two octopus species by a handeld-ultra-compact NIR. The results suggested the possibility to in-site or on-line monitoring fishery products (Moon et al., 2020; Varrà et al., 2022). Non-destructive characterization of salmon and tuna freshness was proposed by (Cui and Cui, 2021). Fish identification is not easy neither for consumers nor for inspectors, especially when prepared as fillets. To develop fast detectors, Cavallini et al. distinguished very similar fish species by comparing handheld SCiO (Consumer Physics), MicroNIR (VIAVI) with benchtop MPA (Bruker). (Risoluti et al., 2015; Pennisi et al., 2021; Cavallini et al., 2022). Handheld NIR spectroscopy was proposed as discrimination tool between wild and farmed sea bass by (Esposito et al., 2022). Yakes et al. (2021)

reported the analysis of two fish species and compared the performance of handheld NIR devices. Currò et al. (2021) proposed handheld NIR instrument as a fast and green method to check the origin of cuttlefish. Yu et al. (2020) assessed by rapid and nondestructive application of handeld NIRs the freshness of tilapia fillets.

By means of a calibrated image analysis, (Tugnolo et al., 2021) and by (Grassi et al., 2021) evaluated the maturation of olives. Comparative analysis was reported by optical fiber probe/benchtop NIR device. Considering the vis/NIR model good performance, an algorithm was applied.

Butteroil has sensory characteristics, economic importance, and because of the high value it can be replaed by other cheaper fats. The potential of handheld NIR spectroscopy to detect butteroil adulterations was suggested to help producers and inspectors in the supply chain (da Silva Medeiros et al., 2023).

Pepper spice adulteration is a growing problem. Evidences from analyses by a handheld NIR demonstrated that adulteration of white pepper can be easily identified (Chen et al., 2022). Oliveira and coworkers proposed PLS-DA and PLSR models (based on handheld NIR spectra) as adulteration identifiers of Paprika powder (Oliveira et al., 2020).

Ouyang and coworkers proved the possibility to predict by handheld NIR spectroscopy the total nitrogen content in pork meat (Kucha and Ngadi, 2020) or frozen pork meat (Ouyang et al., 2020). Portable NIR and machine learning was proposed by (van Kollenburg et al., 2020) and by Parastar and coworkers (Parastar et al., 2020) to determine the authenticity of chicken fillet. Beef, pork, and chicken quantification in ground meat was reported by (Silva et al., 2020).

Milk quality can be evaluated by the content of fats, proteins, lactose and total solids. Adulteration of goat milk by cow milk was proposed by (dos Santos et al., 2021) and by Muniz and Cuevas-Valdés (Muñiz et al., 2020). To authenticate milk geographical origin, Zhang et al. proposed the use of portable NIR spectroscopy to correctly and rapidly detect the adulteration (Zhang T. et al., 2022). To rapidly and conveniently detect the compositions of milk, a handheld detector was developed by Yang et al. 120 raw samples helped to set up the PLSR model to predict the main composition (Yang et al., 2020). A review on the recent advances in NIR portable spectrometers and the applications to milk, cheese and dairy powders was published by (Pu et al., 2021). That is widely supplied in the market has three main active ingredients, including. Ashie and coworkers determined, by portable NIR spectroscopy, active ingredients like silybin, silychristin and silydianin, and isosilybin in milk thistle extract because of their valuable functions for the human body. Results showed that SNV and first derivative discriminate silybin and isosilybin (Ashie et al., 2021). Water adulteration in raw milk of bovine was detected by Ehsani et al. (Ehsani et al., 2022) and by (Riu et al., 2020) who applied classification and regression techniques to spectra from handheld near infrared spectroscopy for facile and rapid detection. Risoluti et al. (Scala et al., 2018) and (Galvan et al., 2022) demonstrated that low-cost handheld NIRs and EDXRF spectrometry coupled to chemometrics can differentiate authentic cow and goat milks from whey mixed ones.

Human milk banks recently expanded because of the newborns growing need. However, human milk composition analyses are far

from routine possibility. Jorge dos Santos and coworkers developed a comparative spectroscopic approach by a portable MicroNIR to compare composition of human milk (Jorge dos Santos et al., 2021) and its conservation (dos Santos et al., 2022). Melendreras et al. (2022) characterized breast milk composition along the lactation period. The results proved the richness of near infrared spectra, and specific bands provided excellent quantitative models.

Lanza et al. (2021) compared benchtop with handheld NIR characterization to discriminate refrigeration periods of chicken breast. PLS-DA indicated correct shelf-life prediction.

A fast online estimation of quail eggs freshness was proposed by (Brasil et al., 2022) and by (Cruz-Tirado et al., 2021).

Alcohol content is essential for the quality control of beers. To this aim, a new rapid and direct multivariate method was proposed and validated using a portable NIR spectrometer and PLS regression, supported by a parallel GC-FID method (da Costa Fulgêncio et al., 2022). Foam parameters are related to beer quality and depend on the protein amount. Viejo et al. used machine learning to predict 54 proteins. Fifteen parameters with handheld NIR assessed significant correlations to physical parameters (Viejo et al., 2020).

Escuredo et al. (2021b) determined quality parameters for potatoes by a MicroNIR device, such as dry matter and reducing sugars. PCA and modified PLS models demonstrated to be useful for potato processors. $NaSO_3$ acts as browning inhibitor when storing potato slices. However, sulfur dioxide residues can be formed, very dangerous to health. NIR hyperspectral imaging was demonstrated to be able to classify SO_2 residues (Bai et al., 2020).

Technicians and producers of dairy farm forage need rapid and reliable equipment to control the quality, better if in unexpensive and easy-to-use way. Rego and coworkers presented a portable-NIR-based procedure to analyze the nutritional values of dairy farm forage. By means of Internet of Things (IoT) tools, spectra can be sent to cloud to be processed and accessible to any device. A chemometric model was developed and validated (Rego et al., 2020).

Productivity and wellness of animals can be improved by precision nutritional composition forage. Near infrared spectroscopy demonstrated to be a very useful tool to determine the nutritional content of forage (Rukundo et al., 2021a; Rukundo et al., 2021b).

Bec´ et al. (2022) published a thematic review to collect the applications of food-analysis miniaturized NIRs, enhancing challenges and perspectives.

4 Applications to drugs

The surveillance of medicines is of fundamental importance to guarantee and protect the consumer, especially when the medicines are life-saving or have a strong impact on the patient's therapy. Consequently, the surveillance of medicine devices is fundamental. NIR spectroscopy plays an extremely interesting role, given the possibility of checking the product without necessarily taking sample aliquots. The ability to carry out analyses, for example, directly inside the packaging blister is now known. Several authors have published interesting scientific applications to drug surveillance and characterization.

Caillet et al. tested six devices' utility and usability in detecting substandard and falsified medicines: four handheld spectrometers

(two near infrared and two Raman), one portable MIR spectrometer and a single-use paper analytical device (Caillet et al., 2021; Greco et al., 2023a; Greco et al., 2023b). Laboratory evaluation of twelve portable devices for medicine quality screening was proposed by Zambrzycki and coworkers, including portable instruments (Zambrzycki et al., 2021).

Illicit-drug seizures are a growing problem since the forensic drug identification is not easy to perform, especially in case of new psychoactive substances. Kranenburg and coworkers (Kranenburg et al., 2022a; Kranenburg et al., 2022b; Kranenburg et al., 2022c) and Awotunde and coworkers (Awotunde et al., 2022) introduced a handheld NIR with a 1,300–2,600 nm range. A specific chemometric model was developed for forensic samples. Authors report that it only requires few reference spectra for training the model, thus eliminating the need of extensive training sets including mixtures. The early detection of emerging street drugs by near infrared spectroscopy and chemometrics was extensively studied by Risoluti and coworkers (Risoluti et al., 2016; Materazzi et al., 2017a; Risoluti et al., 2019b; Risoluti et al., 2019d; Risoluti et al., 2020f).

An innovative screening platform was realized and validated for the detection of cannabinoids on-site in hemp seed oil, aimed to food safety control in market products. This completely automated tool is based on a miniaturized NIR in wireless mode that allows rapid and accurate sample processing and the early detection of residual cannabinoids in oils, including CBD, Δ9-THC and the Δ9-THCA (Risoluti et al., 2019c; Risoluti et al., 2019d; Risoluti et al., 2020b; Risoluti et al., 2020c; Risoluti et al., 2020d) and amphetamine (Risoluti et al., 2020e).

A discrimination of falsified Amoxicillin capsules using heterogeneous NIR spectroscopic devices for training and testing of a support vector machine (Hattori et al., 2021). A handheld NIR spectrometer was employed to quantify heroin was described by Hattori et al. samples by PLS regression and applied to determin heroin casework samples in the concentration range 4.49%–88.05% (w/w). The approach showed good results as repeatability and precision and the results demonstrated an acceptable model performance as on-site heroin detection instrument (Chen et al., 2021).

When considering a pharmaceutical manufacturing process, the ensurance of quality is needed either in the final product or in intermediates. A Raman probe and a portable NIR were applied at the blending process exit. Both the predictive models were tested for accuracy, precision, operating range, measurement frequency, placement, reliability, robustness (Panikar et al., 2021). Hattori et al. (2022). improved algorithms to screen falsified or substandard amoxicillin capsules. FT-NIR and portable wavelength dispersive NIR spectrometers validated the proposed approach. Zhong et al. (2022) proposed the handhelded NIR spectroscopy for the evaluation of coating uniformity of digestion-aid tablets.

A specific review was proposed by Usman et al. to resume the different applications of portable or miniaturized medium-IR, near-IR and Raman instruments for efficient control of quality in pharmaceutical products. These portable spectrometers demonstrated to be a powerful tool to identify of counterfeits, adulterated, fraudulent, falsified, and substandard pharmaceutical capsules or drops (Usman et al., 2020).

The possibility to evaluate Low-Cost Optical Spectrometers to detect falsified medicines is a growing need. Medicines are often counterfeit and is fundamental to warrant rapid, sensible and nondestructive methodologies for the characterization of products. Handheld NIR was proposed by (Wang et al., 2020) and by Assi et al. to authenticate branded or generic antibiotics. The resulting NIR spectra showed characteristic spectra for the main component(s) (Assi et al., 2021). Three-dimensional printing is a revolutionary technology in pharmaceuticals, enabling the personalisation of flexible-dose drug products and 3D printed polypills (polyprintlets). Polyprintlets were non-destructively characterized using a handheld NIR and calibration models were proposed by (Trenfield et al., 2020).

There is a market of seized controlled substances in combination with drug-of-abuse in which new substances psychoactive have to be identified by rapid and reliable presumptive drug testing, better if on-site. Spectroscopic techniques show several advantages because spectra are specific and non-invasive analyses are possible. NIRs is a promising technique for forensic drug detection directly "on-scene". Several portable spectrometers were sold in the past years. Kranenburg et al. realized a dataset of spectra with 430 samples, including illicit-drugs, NPS, adulterants, bulking-agents and excipients. By this dataset, illicit-drugs spectra were usable by institutes that not easily get access to controlled substances and can be of help in developing chemometric models to detect illicit-drugs (Kranenburg et al., 2022d; Kranenburg et al., 2022e).

Since 2019, COVID-19 has exploded as a global pandemy. The possibility to have false vaccines gave illusion of security, highering the exposure to the virus, and increasing the risk of infection. Assi et al. proposed a non-destructive handheld NIR approach for verification of COVID-19 vaccines. Bands corresponding to the mRNA active ingredient were detected by NIR. PCA allowed the validation of COVID-19 vaccines (Assi et al., 2022). As a parallel security procedure, alcohol-based hand sanitizers were recommended as a strategy to minimize contamination. By handheld NIR with PLS-DA, models were realized to check for conformity of commercial hand sanitizing products, while PCA was proposed to test a exploratory study. Results indicated that NIR spectroscopy with chemometrics are a promising tool to discriminate hand sanitizers and able to detect the right ethanol concentrations (Pasquini et al., 2020; Silva et al., 2021).

Aerial parts of Cannabis spp. can be easily purchased; however, in the cannabis not only is present cannabidiol, but Δ9-tetrahydrocannabinol can also be detected and its psychotropic effects are well known and its presence in high concentration is illegal in almost all the European countries. Officers need to test the Δ9-tetrahydrocannabinol concentration in questioned samples. In addition, a portable equipment is of sure interest for farmers to control the THC content in time. Duchateau et al. analyzed hemp flowers and compared results from benchtop or portable NIR devices. A GC-FID analysis determined in parallel the related THC concentration. The proposed models clearly discriminated legal and illegal cannabis samples on the base of European and Swiss laws (Duchateau et al., 2020).

Women use medroxyprogesterone when hormonal therapy is needed. In case of falsification, health risk could result for consumers. A handheld spectrometer with open-sourced software was tested by Eady and coworkers to evaluate vials of Medroxyprogesterone acetate injectable suspensions from different suppliers and results were validated (Ead et al., 2021).

Anti-leishmanial pentamidine bioconjugates based on PLGA-PEG and hyaluronic acid were described by Scala et al. (Ca et al., 2018).

5 Applications in medical diagnostic

NIR spectroscopy demonstrated to be a very helpful tool in medical diagnostic. The non-invasive spectral characterizations, with the fundamental help of chemiometric evaluation and machine learning, have been scientifically proved to be a fast and sensitive preliminary approach for a preliminary health check. Several publications can be found in recent literature.

Traumatic brain injury can lead to hematomas or edemas inside the cerebral tissue. To this end, low-cost, portable and easy-to-handle devices can be fundamental in continuous monitoring. NIR based techniques have been proposed as good solution. Vera et al. used time resolved Monte Carlo simulations in a handheld NIR study. Results showed that mean partial pathlengths, photon measurement density functions and time dependent contrasts are influenced by lesions, proving to be robust means for diagnose or monitoring (Vera et al., 2022). For the strict control of solid oral preparations, Zhang et al. (2022) studied how to determine the content of active pharmaceutical ingredient by a portable NIR sensor in the production line.

Hafiz and coworkers proposed a new hand-held camera for retinal imaging including white or NIR-LED adjacent to each other, able to illuminate by NIR without additional beam-splitters or filters. The camera was adapted to be interfaced to Android-based smartphones to determine ocular safety analysis (Hafiz et al., 2022).

Bhattacharya et al. presented the development of a NIR-portable instrument to detect acute ischemia stroke by means of albumin in human blood serum. The test on human blood samples showed good linearity to determine the concentration of albumin in human blood (Bhattacharya et al., 2022). Similar studies related to the detection of hematologic pathologies were reported by Gullifa et al. (Risoluti et al., 2019e; Risoluti et al., 2020f; Risoluti et al., 2020g; Gullifa and Risoluti, 2021). The dynamic control of lymphatic and vascular systems was published by (Wang et al., 2022).

An unusual study was proposed by Ni and coworkers, who evaluated handheld-NIR possibility to in vivo analyze healthy tissues and to correlate the results with age. Partial Least Square regression showed that vibrational spectroscopy non-destructive techniques can be used as useful tools to relate interactions between physiology and nutrition (Ni et al., 2022a). Ni et al. also evaluated the ability of an handheld NIR to relate spectral informations to food and energy intake, satiation, and satiety data. Results showed the potentiality of in-vivo NIR spectroscopy to differentiate tissues (Ni et al., 2022b). Clemson et al. (2022) proposed a portable and non-contact system for skin surveillance.

Diabetes is a life-threatening disease and needs constant monitoring of blood glucose levels. Yu and coworkers proposed a mobile application for handheld NIR useful to non-professional users. The experimental results showed that the portable and light NIR spectrometer can be easily used (Yu et al., 2021a). A NIR-LEDs-Based detection system was also proposed by Badriah et al. to measure blood sugar levels on diabetic care (Badriah et al., 2022).

Belay et al. (2020) presented a three-segment grating spectrometer, aimed to help in cancer diagnosis. The results experimentally proved

that this solution significantly improves the spectrometer signal. With the same view, Bonapace et al. (2021) described how to determine methylglyoxal adducts content by portable handheld NIR. MicroNIR/chemometrics determination of hydroxyurea occupational exposure was also proposed as a new tool in work-surveillance and prevention (Risoluti and Materazzi, 2018).

In a review published by Huang et al., a smartphone-based NIR fluorescent imaging technology was proposed. Smartphones can improve diagnoses being a tool for real-time diagnosis, even in remote regions (Huang et al., 2021). Hasan et al. proposed a state of the art review, collecting the predictive and non-invasive techniques of hemoglobin level (Hasan et al., 2021).

6 Applications to agriculture

Portable systems can be of fundamental usefulness for in-site material characterization and quality analysis in agricultural. Miniaturized NIRs were proposed in material-sensing applications. To validate the performance, several classification algorithms were compared (Behera et al., 2020).

B1 and B2 fumonisin rapid detection in corn was described by Shen and coworkers by smartphone-based handheld NIRs/chemometrics (Shen et al., 2022).

ESI(±)FT-ICR MS and portable microNIR were proposed as a new analytical tool to characterize Robusta coffees. A published study confirmed that both can be efficiently applied to coffee quality control, with many advantages such as speed and analytical reliability (Correia et al., 2020). Baqueta and coworkers directly evaluated cupping profiles in coffee blends via portable NIR and PLS-DA model. Results were presented as industrially interesting and the method could help coffee professionals in cup evaluation (Baqueta et al., 2021). A one-class classification method was proposed to control agroforestry-grown coffees by (Manuel et al., 2022).

Forage analysis by NIR spectroscopy had many advancements since 1970. Due to instrumentation, computers and chemometric algorithms improvements, it is actually the most used approach for the routine analysis by forage producers, plant breeders, animal nutritionists, cattle farmers, and feed companies. Berzaghi et al. (2021) reported a comparison among three different portable instruments and a benchtop lab instrumentation, using many forage samples.

Phenotyping information is fundamental for sugar industry. Gaci and coworkers proposed a micro-, low-cost, portable narrow VIS-NIR instrument to get a PLS predictive model (Gaci et al., 2022). Henrique da Silva Melo and coworkers evaluated portable spectroscopy for the quantification of brix and pol in a sugar production plant (Henrique da Silva Melo et al., 2022).

Edible oils, modified lipids, industrial oils, and biofuels can be produced by Brassica. Analytical methods based on Portable NIRs and NIR-Hyperspectral Imaging were applied to characterize seeds species (da Silva Medeiros et al., 2022). Jiang et al. (2022) and (Bilal et al., 2020) proposed a fast way to determine peanuts acidity index. Yu and coworkers classified the high oleic acid peanuts by comparing portable and benchtop NIRs. The accuracy of distinction was 100% with both the instruments (Yu et al., 2020). Jiang et al. (2021) and (Giussani et al., 2021) used a handheld NIR device to analyze the acid values during the storage of edible oils. Grossi et al. (2020) proposed a procedure to determine solid fat by single-wavelength NIRs.

Yao et al. developed a rapid NIR authentication procedure for exhaust oils used in frying potato chips. A miniaturized NIR sensor showed how handheld vibrational spectrometers can provide a rapid *in-situ* identification of oil type and could be a surveillance tool of the products (Yao et al., 2021).

Data from three different NIRs were analyzed to compare coriander seeds. Three instruments were compared in their prediction ability. 200 authentic coriander seeds spectra were compared with 90 adulterated samples (McVey et al., 2021). Often consumers of seedlings or fruits have troubles to recognize if that product really is what is indicated by the merchant. Consequently, it becomes particularly crucial to evaluate the marketing process. Vinhandelli et al. used PC-LDA or PLS-DA algorithms to test the ability of NIR spectroscopy to discriminate cultivars (Vinhandelli et al., 2023). Nitrogen assessment in strawberries by handheld FT-NIR was also proposed by Wu and coworkers (Wu et al., 2020).

A cost-effective and fast analysis of nutrient content in cotton leaves by handheld NIR spectroscopy was reported by (Prananto et al., 2021).

Quantitative assay of Aflatoxin B1 in maize was proposed by Deng et al. Their NIR system was realized and employed to characterize maize samples with different mildew degrees (Deng et al., 2022). High-quality production of tobacco leaves needs identification of deep green infection. Janqiang et al. proposed an identification methodology for deep green tobacco infections using a portable NIR (Jianqiang et al., 2020).

Detecting of apple valsa cancer is useful to prevent diseases and to check apples yield and quality. Zhao et al. proposed portable NIRs and Raman scattering spectrometers in reflection mode using machine learning to predict infection degrees (Zhao et al., 2021). Qiao and coworkers proposed apple sugar content determination by handheld tool connected to a cellular phone (Qiao et al., 2020). Apple hardness can be determined by non-destructive, as proposed by (Malvandi et al., 2022b) and by (Ma et al., 2021a).

The citrus industry is always searching for instrumental methods able to determine in real time and *in situ* the modifications of fruit development or storage, with a special focus on vitamin C. A NIR-based model was proposed to vuate the ripeness (Santos et al., 2021). Jahani et al. (2020) proposed a miniaturized handheld NIR as a preliminary test of adulterasin in lime juices coupled with classification methodologies.

The current practice by potato growers for tissue testing is based on petiole chemical analysis rather than leaf analysis. AbuKmeil and Al-Mallahi estimated nutrients in potato intact fresh leaves by a portable Vis-NIR spectrophotometer and the parallel chemical analyses were done on petioles following the official methods of the AOAC. The Lasso models showed a fair distribution of nitrogen, phosphorus, potassium, calcium, magnesium, and zinc with coefficient of determination values above 0.5 and acceptable to excellent RPD values (abuKmeil and Al-Mallahi, 2022).

Wang and coworkers (Wang et al., 2020; Wang et al., 2020; Sun et al., 2020; Wang et al., 2021; Jin et al., 2021; Ren et al., 2022) developed a handheld tool to check the freshness of tea.

The contamination of bee pollen by pyrrolizidine alkaloids is actually determined by LC-MS. De Jesus Inacio and coworkers suggested the use of fast NIR spectroscopy as alternative and accurate approach (De Jesus Inacio et al., 2020).

In the livestock and poultry breeding industry, the slurry is a mixture of urine, feces, flushing water, and disinfectant. The composition varies

greatly when returning to the field, due to several different influencing interferences. Liang et al. developed a NIR method to *in-situ* determine the slurry characteristics (Liang et al., 2022).

7 Applications to forensics

The use of portable NIR devices in forensic analysis has recently undergone an important boost as it makes it possible to acquire fundamental information directly at the crime scene, before starting the currently necessary sampling, custody and pre-treatment procedures. In addition, these characterizations are not destructive, nor do they modify the analyzed sample. These two aspects are peculiar in forensic investigations as they make it possible to ensure the objectivity of the experimental evidence even by non-specialized, but simply trained, personnel. Traces of human blood are among the most important evidences in criminal investigations. Blood samples have to be identified and collected immediately without contamination in the crime scene. Fonseca and coworkers evaluated the possibility to unambiguously identify human blood in stains found in floor tiles by handheld NIR spectroscopy. Authors reported that hierarchical models result in a significant scientific improvement useful for the identification of human blood stains at crime scenes (Fonseca et al., 2022).

Criminals often use common household cleaners, that are strong corrosive solutions, such as, in order to stun the victim. NIR handheld spectrometer was demonstrated to determine corrosive solutions through plastic bottles. Morillas and Frascione evaluated corrosive and harmless substances, to test the real NIR performance. Each predictive model identified the corrosive substances, enhancing the ability of this technique to pre-screen corrosive substances (Morillas and Frascione, 2022).

A modular handheld Vis-NIR spectrophotometer collected spectra from ink signatures by different ball-point pens, as a non invasive tool for ink identification in forensics (Ristova et al., 2022). As new approach in forensic chemistry, NIR/Chemometrics was proposed for the characterization of toners when questioned documents examination is requested (Materazzi et al., 2017b; Risoluti et al., 2018a).

It was proposed to solve illicit drug analysis by an ultra–portable NIR linked to a mobile application, demonstrating the possibility to display the result within 5 seconds (Coppey et al., 2020).

Determination of explosives was reported by Risoluti et al. on human hands using handheld MicroNIR (Risoluti et al., 2018b) and by Santonocito et al. using an optical array (Santonocito et al., 2022).

8 Applications to textiles

Textiles are daily used by all the people in the world. Especially in high fashion, quality and price can greatly change and often it is not easy to identify genuine products only by visualization. The possibility to easily characterize textiles allows to warrant consumers. Textiles are characterized by obvious differences in raw materials (wool, cotton, synthetics) but often small differences (blended versus pure filaments or the optimization of the appearance of polyester versus cotton) can result in significant quality assurance issues. NIR spectroscopy has demonstrated considerable potential in component characterization and feature differentiation.

Handheld NIR was proposed as good solution to textile authentication and identification by Yan et al. who demonstrated to be simply the comparison with reference spectra. PCA combined with SIMCA resulted the best discrimination models (Yan and Siesler, 2018).

Silk is a precious textile not only because of its physical and chemical properties, but also for its beauty. Cotton or polyester are the mainly mixed fibers to optimize the best look (Kumagai et al., 2004). Being not easy the distinction of silk blends from pure silk, portable NIR was tested for a fast characterization of dress composition, including a quantitative answer (Liu et al., 2013; Guifang et al., 2015). The silk was also blended with polyester and fully characterized by PLS calibration (Yan et al., 2020).

Identification of ancient textile fibers becomes fundamental for conservation of textile relics. Fiber identification methods require sampling and slicing cultural relics for observation under an optical microscope or a scanning electron microscope. Handheld NIR was applied to the identification of fibers from four Qing Dynasty textile relics, and resulted in a good spectral comparison (Li et al., 2021; Ding et al., 2021).

9 Applications to materials

Benchtop and handheld molecular spectrometers have been successfully applied in material identification. Compared to FT-MIR spectra, near infrared profiles allow to complete informations and often solve problems by simply comparing characteristic profiles instead of single band interpretation and assignment.

"To recycle" will be a must for the next generations. Great impulse is actually given to recycle the most common polymers. Handheld NIR was demonstrated to be a very easy-to-use tool to classify them with the aim of a safe recycle (Xiong et al., 2016).

Eder and coworkers described and discussed the possibility to use and transfer analytical techniques, including NIR, for in-field characterization of photovoltaic modules. Polymeric compounds of the photovoltaic modules were analyzed and characterized without modules dismantling, transporting into the lab, cutting and analyzing in conventional bench-top spectrometers (Eder et al., 2020). Catauro et al. characterized bioactive ferrous citrate–silica hybrid materials obtained by a sol–gel synthesis.

10 Applications to wood, cellulose, lignin and lignite

Wood species can be identified by Vis-NIR spectroscopy: this approach is based on light absorption scattering due to the wood characteristics. However, innovative methodologies based on diffuse reflectance demonstrated the possibility to classify many different woods and portable NIR instruments can be easily used for in-field characterizations.

A handheld Vis-NIR system was realized and, to simplify the interpretation of the spectra, wood classification was obtained by PCA scores (Ma et al., 2021b). The development of a low-cost handheld spectrometer to detect wood defects was proposed by (Sandak et al., 2020).

Characterizations from a standing tree minimize and optimize the time requested since eliminate the transport, the transformation in powder and the storage. Ramadevi et al. (2022) estimated the yield of Kraft pulp by portable NIR spectrometer. A fast characterization of holocellulose and lignin in wood by Kernel extreme learning machine was proposed by (Yang et al., 2020).

Off-line determination of diverse wood quality aspects by a portable NIR sensor was demonstrated by Sandak et al. in glue-laminated timber. The chemometric model specifically developed was demonstrated to be helpful in prediction of the total delamination and detailed delamination length (Sandak et al., 2021).

Three moisture predicting models in Para rubber timber were proposed by Noypitak et al. The handheld NIR spectrometer coupled to a smartphone facilitated the quantification of real-time moisture content. An android application was specifically settled up to manage the instrument. Unknown samples allowed to validate the rsults from the predictive equation (Noypitak et al., 2022). A similar approach was proposed by Puttipipatkajorn (Puttipipatkajorn and Puttipipatkajorn, 2020).

Lim et al. proposed to determine the densities of cross linking in latex by an innovative method based on portable NIR (Lim et al., 2021).

11 Applications to natural extracts

Natural extracts can result in complex mixtures with unknown composition if by-products or contaminations are not monitored and eventually eliminated through subsequent purifications. Consumer protection therefore becomes fundamental both for the bodies in charge of surveillance and for the producer who, in self-protection, controls his own product. Zhuang et al. proposed a quantitative model to monitor active components in Radix Astragali extract. The quantitative model was stressed by comparing a usual FT-NIR with a portable NIR. PLSR models indicated that the calibration model can significantly improve the adaptability to new samples (Zhuang et al., 2022).

The market of Turmeric is increasing since curcuminoids are recognized to give health benefits. Spectroscopic methods with chemometrics are able to quantify turmeric to control food quality and allow analysis speed, versatility, portability and no need of any pretreatments. Khongkaew et al. published a study with 5 calibration models for the quantification of curcuminoids in turmeric both by benchtop and portable instrument. The results indicated benchtop and portable methods in good agreement, confirming the suitability of portable devices in food quality control by analyses in situ (Khongkaew et al., 2022).

Menevseoglu proposed portable FT-NIR, FT-MIR, and Raman spectrometers to identify adulterations in black seed oil by. SIMCA and PLSR models were applied to predict the adulterant levels (Menevseoglu, 2022).

12 Other applications

12.1 Applications to cultural heritage

Cultural heritage is the field with the greatest application interest as the non-invasive and portability characteristics of spectroscopy fully embrace the needs of conservation and respect for works that continue over time to bear witness to the excellence of the past. For example, wall paintings are art works based on ancient technologies and materials typical of civilizations from the past. Imaging instrumentation allows the study of the materials and the characterization of pigments.

Asscher and Halevi presented comparative results by stationary or portable modified digital camera, showing the strong environmental influence on the image (Asscher and Halevi, 2022).

In the project "Leonardesque Artists beyond the Visible", non-invasive portable imaging and spectroscopic-based approach were proposed to obtain useful informations like the description of pigments composition, binder preparation and painters' technique identification. Results underlined a specific painting technique in each author (Galli et al., 2021).

12.2 Applications to geology

The characterization of mafic and ultramafic rocks is important to determine relationships with specific. Adams et al. demonstrated that the X-ray accurate determination can be completed by handheld VIS and NIR analysis (Adams et al., 2021).

12.3 Applications to waste materials

Plastic waste classification is fundamental to set the right recycle Diffuse reflectance spectra of several reference and commercial polymers allowed to give fast, nondestructive, in-site characterizations by applying different pretreatments. The results proved that PCA allows to separate different plastic materials (Yang et al., 2020).

12.4 Aquaphotomics

The spectrum of the water in aqueous systems gives information on covalent OH and hydrogen bonds since they are deeply influenced. In water NIR spectra, the information results as a function of internal and external factors. Aquaphotomics evaluates by near infrared spectra the groundwaters, not influenced by other factors like temperature or humidity.

Results published by Kovacs and coworkers demonstrated that groundwater samples give specific fingerprint and unicity of the spectroscopic profile that can be used as an indicator of water changes (Kovacs et al., 2022).

Soil-to-water ratios were calculated by Vis-NIR spectra to predict the electrical conductivity by (Gozukara et al., 2022)

A special issue, dedicated to aquaphotomics, was published in the open-access journal Molecules (Muncan and Tsenkova, 2023).

12.5 Applications to fuels

Systematic adulterations of gasoline, ethanol and diesel make fundamental the possibility to have analyitical tools,

able to determine fuel integrity. Tosato et al. (2020) characterized 115 seized fuels and proved the efficiency of portable near infrared spectrometers assiste by chemometrics. Diesel quality can be evaluated by the "condensation point". In-field fast determination of condensation point could minimize the costs. Wan et al. (2021) collected representative spectra using a handheld NIR to setup a prediction model.

Motor and crude oil can be improperly mixed, as found in Brazil by companies of energy sector. Santos and coworkers showed the possibility of handheld NIR spectroscopy to detect these frauds. Discrimination potential resulted in 100% of specificity and precision (Santos et al., 2021).

Environment protection pushes to renewable energies like bioenergy. Fuel surveillance to meet the european rules is consequently needed. Hand-held near spectroscopy was tested on wood chip samples. Results showed a satisfactory reliability because each measure is acquired in seconds and the non-destructive analysis allows to efficiently control fuel quality (Toscano et al., 2022). Pellet recently was studied because of its storage cost and combustion efficiency. The possibility to trace pellet quality is important, since fraud behaviors could impact consumers' health. Usual pellet analyses are costly and time-consuming Mancini and coworkers defined a handheld-NIRs approach to propose a fast and automatic classification of pellet (Mancini et al., 2020).

12.6 Applications to micro- and nano-materials

Orsi et al. setted up and calibrated a handheld NIR method to determine ROS, because of its impact in Photodynamic therapies. The approach is based on the fluorescence emission in the near-infrared spectral range at λ = 1,270 nm. Several nanostructures have been proposed as able to produce reactive oxygen species voted to medicine therapies (tumours in deep tissue) (Orsi et al., 2022).

Microplastics residues are a growing environmental problem. A review proposed by Tirkey and Upadhyay collected and highlighted innovative approaches in microplastics sampling and identification, including NIR (Tirkey and Upadhyay, 2021).

12.7 Applications to asphalt

Modern asphalts are often the result of modifiers inclusions. These modifiers increase sustainability, lower rutting and low-temperature cracking. To this end, a portable molecular sensing technology was proposed, consisting in a pocket-sized near-infrared molecular sensor, able to detect recycled materials. It was demonstrated that the resulting fingerprint of the bituminous materials helps the classification (Jahangiri et al., 2021). The same authors proposed a smartphone-based approach (Barri et al., 2020).

13 Chemometrics

Private companies always more ask for on-site analysis by portable instruments, better if spectroscopic devices. Schoot et al. presented a new prediction model from portable NIR data to predict protein content in pig feed (Schoot et al., 2022).

With increasing availability of handheld NIR spectrometers, is of interest the possibility to transfer calibration model from benchtop to portable NIR. Rukundo and coworkers calibrated a benchtop NIR and transferred calibrations to a benchtop and portable instruments. Model transferring however was not direct and required data treatments (Rukundo et al., 2022).

Advantages in milk analysis by NIR spectrometers was proposed by (Said et al., 2022).

Various preprocessing techniques and their combinations were comparatively proposed by Sarkar et al. to quantify soluble solids in kiwi fruits (Sarkar et al., 2020). The content of dry matter when harvesting was proved to have correlation with soluble solids in Kakadu plum samples (Bobasa et al., 2021). De Freitas and coworkers (de Freitas et al., 2022) and Wokadala and coworkers (Wokadala et al., 2020) determined the fruit dry matter content at harvest in Brazil, while the detection of internal physiological disorders was determined by (Mogollón et al., 2020). Portable optical instruments were specifically studied to determine fruit ripeness (Abasi et al., 2021), even directly on the by McCormick and Biegert (McCormick and Biegert, 2021). Pissar et al. (2021), (Zhang et al., 2022; Zhang et al., 2022), (Guo et al., 2020) and (Fan et al., 2020) described the usefulness of a portable NIR to determine apple quality.

Yang et al. (2022) and (Yu et al., 2021b) determined soluble solids content in pears based on VIS-NIR and model analysis and variable selection. Wu et al. (2021). settled up a non-destructive characterization of pears by a home-made NIR and a chemometric prediction model. Mulisa Bobasa and coworkers evaluated 4 different positions to achieve NIR spectra of Kakadu plum fruits, thus monitoring fruit chemical composition (Mulisa Bobasa et al., 2020). The nonlinear optical properties of monodispersed diphenylpolyynes were also studied by (Fazio et al., 2014).

Xiao and Chen presented an innovative research on NIR data analysis by using Machine Learning algorithms to study *in-vivo* the human skin characteristics. NIR showed sure potential to develop a cheap, handheld and powerful, skin characterization tool (Ca et al., 2018; Scala et al., 2018; Risoluti et al., 2020h; Xiao and Chen, 2022).

Author contributions

SM and RR wrote the manuscript. GG, LB, and EP searched for references. AG supervised the search. All authors contributed to the article and approved the submitted version.

Conflict of interest

The authors declare that the research was conducted in the absence of any commercial or financial relationships that could be construed as a potential conflict of interest.

Publisher's note

All claims expressed in this article are solely those of the authors and do not necessarily represent those of their affiliated organizations, or those of the publisher, the editors and the reviewers. Any product that may be evaluated in this article, or claim that may be made by its manufacturer, is not guaranteed or endorsed by the publisher.

References

Abasi, S., Minaei, S., Jamshidi, B., and Fathi, D. (2021). Development of an optical smart portable instrument for fruit quality detection. *IEEE Trans. Instrum. Meas.* 70, 1–9. doi:10.1109/TIM.2020.3011334

abuKmeil, R., and Al-Mallahi, A. (2022). "Detecting nutrients in potato plants based on visible/near infrared in-field spectral measurements," in *Proceedings of the 2022* (ASABE Annual International Meeting).

Adams, C., Dentith, M., and Fiorentini, M. (2021). Characterization of altered mafic and ultramafic rocks using portable xrf geochemistry and portable vis-nir spectrometry. *Geochem. Explor. Environ. Anal.* 21. doi:10.1144/geochem2020-065

An, J., Li, Y., Zhang, C., and Zhang, D. (2022). Rapid nondestructive prediction of multiple quality attributes for different commercial meat cut types using optical system. *Food Sci. Anim. Resour.* 42, 655–671. doi:10.5851/kosfa.2022.e28

Andrade, R., Mancini, M., Teixeira, A. F. D. S., Silva, S. H. G., Weindorf, D. C., Chakraborty, S., et al. (2022). Proximal sensor data fusion and auxiliary information for tropical soil property prediction: Soil texture. *Geoderma* 422, 115936. doi:10.1016/j.geoderma.2022.115936

Anyidoho, E. K., Teye, E., Agbemafle, R., Amuah, C. L. Y., and Boadu, V. G. (2021). Application of portable near infrared spectroscopy for classifying and quantifying cocoa bean quality parameters. *J. Food Process. Preserv.* 45. doi:10.1111/jfpp.15445

Arruda de Brito, A., Campos, F., dos Reis Nascimento, A., Damiani, C., Alves da Silva, F., de Almeida Teixeira, G. H., et al. (2022). Non-destructive determination of color, titratable acidity, and dry matter in intact tomatoes using a portable vis-NIR spectrometer. *J. Food Compos. Anal.* 107, 104288. doi:10.1016/j.jfca.2021.104288

Ashie, A., Lei, H., Han, B., Xiong, M., and Yan, H. (2021). Fast determination of three components in milk thistle extract with a hand-held NIR spectrometer and chemometrics tools. *Infrared Phys. Technol.* 113, 103629. doi:10.1016/j.infrared.2021.103629

Asscher, Y., and Halevi, S. (2022). Characterizing the pigments in wall paintings: Comparing portable and stationary multiband remote sensing imaging systems. *Springer Proc. Mater.* 16, 71–82. doi:10.1007/978-3-031-03795-5_14

Assi, S., Arafat, B., Abbas, I., and Evans, K. (2022). Evaluation of portable near-infrared spectroscopy for authentication of MRNA based COVID-19 vaccines. *PLoS ONE* 17, e0267214. doi:10.1371/journal.pone.0267214

Assi, S., Arafat, B., Lawson-Wood, K., and Robertson, I. (2021). Authentication of antibiotics using portable near-infrared spectroscopy and multivariate data analysis. *Appl. Spectrosc.* 75, 434–444. doi:10.1177/0003702820958081

Awotunde, O., Roseboom, N., Cai, J., Hayes, K., Rajane, R., Chen, R., et al. (2022). Discrimination of substandard and falsified formulations from genuine pharmaceuticals using NIR spectra and machine learning. *Anal. Chem.* 94, 12586–12594. doi:10.1021/acs.analchem.2c00998

Aykas, D. P., and Menevseoglu, A. (2021). A rapid method to detect green pea and peanut adulteration in pistachio by using portable FT-MIR and FT-NIR spectroscopy combined with chemometrics. *Food control.* 121, 107670. doi:10.1016/j.foodcont.2020.107670

Badriah, S., Bahtiar, Y., and Andang, A. (2022). Near infrared LEDs-based non-invasive blood sugar testing for detecting blood sugar levels on diabetic care. *J. Biomim. Biomater. Biomed. Eng.* 55, 183–191. doi:10.4028/p-vthp40

Bai, X., Xiao, Q., Zhou, L., Tang, Y., and He, Y. (2020). Detection of sulfite dioxide residue on the surface of fresh-cut potato slices using near-infrared hyperspectral imaging system and portable near-infrared spectrometer. *Molecules* 25, 1651. doi:10.3390/molecules25071651

Baqueta, M. R., Coqueiro, A., Março, P. H., and Valderrama, P. (2021). Multivariate classification for the direct determination of cup profile in coffee blends via handheld near-infrared spectroscopy. *Talanta* 222, 121526. doi:10.1016/j.talanta.2020.121526

Barri, K., Jahangiri, B., Davami, O., Buttlar, W. G., and Alavi, A. H. (2020). Smartphone-based molecular sensing for advanced characterization of asphalt concrete materials. *Meas. J. Int. Meas. Confed.* 151, 107212. doi:10.1016/j.measurement.2019.107212

Basore, E. T., Wu, H., Xiao, W., Zheng, G., Liu, X., and Qiu, J. (2021). High-power broadband NIR LEDs enabled by highly efficient blue-to-NIR conversion. *Adv. Opt. Mater.* 9, 1660. doi:10.1002/adom.202001660

Baumann, L., Librelotto, M., Pappis, C., Helfer, G. A., Santos, R. O., dos Santos, R. B., et al. (2020). NanoMetrix: An app for chemometric analysis from near infrared spectra. *J. Chemom.* 34, 3281. doi:10.1002/cem.3281

Beć, K. B., Grabska, J., and Huck, C. W. (2022). Miniaturized NIR spectroscopy in food analysis and quality control: Promises, challenges, and perspectives. *Foods* 11, 1465. doi:10.3390/foods11101465

Bec, K. B., Grabska, J., and Huck, C. W. (2021). Principles and applications of miniaturized near-infrared (NIR) spectrometers. *Chem. Eur. J.* 27, 1514–1532. doi:10.1002/chem.202002838

Behera, A. R., Kumar, A., Suresh, H., Pratap, M., Selvaraja, S. K., and Pratap, R. (2020). An ultra-portable vis-NIR spectrometer with an integrated light source for chemometric applications. *J. Electrochem. Soc.* 167, 167515. doi:10.1149/1945-7111/abc7e8

Belay, G. Y., Hoving, W., Van Der Put, A., Van Erps, J., Vervaeke, M., Thienpont, H., et al. (2020). "Design and prototyping of a multi-segment grating for a broadband and miniaturized spectrometer," in *Proc. Proc. SPIE Int. Soc. Opt. Eng* (USA: SPIE).

Beltrame, K. K., Gonçalves, T. R., Março, P. H., Gomes, S. T. M., Matsushita, M., and Valderrama, P. (2021). Pseudo-univariate calibration based on NIR spectroscopy in the determination of anthocyanins and antioxidant activity in grape juices. *J. Braz. Chem. Soc.* 32, 1131–1136. doi:10.21577/0103-5053.20210007

Benedet, L., Faria, W. M., Silva, S. H. G., Mancini, M., Guilherme, L. R. G., Demattê, J. A. M., et al. (2020). Soil subgroup prediction via portable X-ray fluorescence and visible near-infrared spectroscopy. *Geoderma* 365, 114212. doi:10.1016/j.geoderma.2020.114212

Benedet, L., Faria, W. M., Silva, S. H. G., Mancini, M., Demattê, J. A. M., Guilherme, L. R. G., et al. (2020). Soil texture prediction using portable X-ray fluorescence spectrometry and visible near-infrared diffuse reflectance spectroscopy. *Geoderma* 376, 114553. doi:10.1016/j.geoderma.2020.114553

Bertinetto, C. G., Schoot, M., Dingemans, M., Meeuwsen, W., Buydens, L. M. C., and Jansen, J. J. (2022). Influence of measurement procedure on the use of a handheld NIR spectrophotometer. *Food Res. Int.* 161, 111836. doi:10.1016/j.foodres.2022.111836

Berzaghi, P., Cherney, J. H., and Casler, M. D. (2021). Prediction performance of portable near infrared reflectance instruments using preprocessed dried, ground forage samples. *Comput. Electron. Agric.* 182, 106013. doi:10.1016/j.compag.2021.106013

Bhattacharya, R., Ahirwar, D., Biswas, B., Bhutani, G., and Chowdhury, S. R. (2022). A NIRS based device for identification of acute ischemic stroke by using a novel organic dye in the human blood serum. *Lect. Notes Electr. Eng.* 886, 43–53. doi:10.1007/978-3-030-98886-9_4

Bilal, M., Xiaobo, Z., Arslan, M., Tahir, H. E., Azam, M., Junjun, Z., et al. (2020). Rapid determination of the chemical compositions of peanut seed (Arachis hypogaea.) using portable near-infrared spectroscopy. *Vib. Spectrosc.* 110, 103138. doi:10.1016/j.vibspec.2020.103138

Bittante, G., Patel, N., Cecchinato, A., and Berzaghi, P. (2022). Invited review: A comprehensive review of visible and near-infrared spectroscopy for predicting the chemical composition of cheese. *J. Dairy Sci.* 105, 1817–1836. doi:10.3168/jds.2021-20640

Bobasa, E. M., Netzel, M. E., Cozzolino, D., Phan, A. D. T., and Sultanbawa, Y. (2021). Measurement of total soluble solids and moisture in puree and dry powder of Kakadu plum (Terminalia ferdinandiana) samples using hand-held near infrared spectroscopy. *J. Infrared Spectrosc.* 29, 201–206. doi:10.1177/0967033520982361

Bonapace, G., Gentile, F., Coppedé, N., Coluccio, M. L., Garo, V., Vismara, M. F. M., et al. (2021). Methylglyoxal adducts levels in blood measured on dried spot by portable near-infrared spectroscopy. *Nanomaterials* 11, 2432. doi:10.3390/nano11092432

Borba, K. R., Aykas, D. P., Milani, M. I., Colnago, L. A., Ferreira, M. D., and Rodriguez-Saona, L. E. (2021). Portable near infrared spectroscopy as a tool for fresh tomato quality control analysis in the field. *Appl. Sci. Switz.* 11, 3209. doi:10.3390/app11073209

Borghi, F. T., Santos, P. C., Santos, F. D., Nascimento, M. H. C., Corrêa, T., Cesconetto, M., et al. (2020). Quantification and classification of vegetable oils in extra virgin olive oil samples using a portable near-infrared spectrometer associated with chemometrics. *Microchem. J.* 159, 105544. doi:10.1016/j.microc.2020.105544

Brasil, Y. L., Cruz-Tirado, J. P., and Barbin, D. F. (2022). Fast online estimation of quail eggs freshness using portable NIR spectrometer and machine learning. *Food control.* 131, 108418. doi:10.1016/j.foodcont.2021.108418

Brito, A. A. D., Campos, F., Nascimento, A. D. R., Corrêa, G. D. C., Silva, F. A. D., Teixeira, G. H. D. A., et al. (2021). Determination of soluble solid content in market tomatoes using near-infrared spectroscopy. *Food control.* 126, 108068. doi:10.1016/j.foodcont.2021.108068

Bwambok, D. K., Siraj, N., Macchi, S., Larm, N. E., Baker, G. A., Pérez, R. L., et al. (2020). Qcm sensor arrays, electroanalytical techniques and nir spectroscopy coupled to multivariate analysis for quality assessment of food products, raw materials, ingredients and foodborne pathogen detection: Challenges and breakthroughs. *Sens. Switz.* 20, 6982–7042. doi:10.3390/s20236982

Catauro, M., Naviglio, D., Risoluti, R., and Vecchio Ciprioti, S. (2018). Sol–gel synthesis and thermal behavior of bioactive ferrous citrate–silica hybrid materials. *J. Therm. Anal. Calorim.* 133, 1085–1092. doi:10.1007/s10973-018-7137-7

Caillet, C., Vickers, S., Zambrzycki, S., Fernández, F. M., Vidhamaly, V., Boutsamay, K., et al. (2021). A comparative field evaluation of six medicine quality screening devices in Laos. *PLoS Negl. Trop. Dis.* 15, e0009674. doi:10.1371/journal.pntd.0009674

Cavallini, N., Pennisi, F., Giraudo, A., Pezzolato, M., Esposito, G., Gavoci, G., et al. (2022). Chemometric differentiation of sole and plaice fish fillets using three near-infrared instruments. *Foods* 11, 1643. doi:10.3390/foods11111643

Cecchini, C., Antonucci, F., Costa, C., Marti, A., and Menesatti, P. (2021). Application of near-infrared handheld spectrometers to predict semolina quality. *J. Sci. Food Agric.* 101, 151–157. doi:10.1002/jsfa.10625

Chen, R., Mei, J., Du, G., Shi, Y., and Huang, Y. (2022). Convenient detection of white pepper adulteration by portable NIRS and spectral imaging with chemometrics. *Microchem. J.* 182, 107925. doi:10.1016/j.microc.2022.107925

Chen, Y., Liu, S., Yang, Y., Qian, Z., Wang, B., An, C., et al. (2021). On-site determination of heroin by portable near-infrared spectrometer. *Aust. J. Forensic Sci.* 53, 40–49. doi:10.1080/00450618.2019.1653370

Ciaccheri, L., Adinolfi, B., Mencaglia, A. A., and Mignani, A. G. (2022). Bluetooth-connected pocket spectrometer and chemometrics for olive oil applications. *Foods* 11, 2265. doi:10.3390/foods11152265

Clemson, B., Mrsan, M., and Vishwanath, K. (2022). "Development of a portable, non-contact diffuse reflectance system for tissue spectroscopy," in *Proc. Prog. Biomed. Opt. Imaging - Proc* (USA: SPIE).

Coombs, C. E. O., Liddle, R. R., and González, L. A. (2021). Portable vibrational spectroscopic methods can discriminate between grass-fed and grain-fed beef. *J. Infrared Spectrosc.* 29, 321–329. doi:10.1177/09670335211049506

Coppey, F., Bécue, A., Sacré, P.-Y., Ziemons, E. M., Hubert, P., and Esseiva, P. (2020). Providing illicit drugs results in five seconds using ultra-portable NIR technology: An opportunity for forensic laboratories to cope with the trend toward the decentralization of forensic capabilities. *Forensic Sci. Int.* 317, 110498. doi:10.1016/j.forsciint.2020.110498

Correia, R. M., Andrade, R., Tosato, F., Nascimento, M. T., Pereira, L. L., Araújo, J. B. S., et al. (2020). Analysis of Robusta coffee cultivated in agroforestry systems (AFS) by ESI-FT-ICR MS and portable NIR associated with sensory analysis. *J. Food Compos. Anal.* 94, 103637. doi:10.1016/j.jfca.2020.103637

Crocombe, R. A. (2018). Portable spectroscopy. *Appl. Spectrosc.* 72, 1701–1751. doi:10.1177/0003702818809719

Cruz-Tirado, J. P., Lucimar da Silva Medeiros, M., and Barbin, D. F. (2021). On-line monitoring of egg freshness using a portable NIR spectrometer in tandem with machine learning. *J. Food Eng.* 306, 110643. doi:10.1016/j.jfoodeng.2021.110643

Cui, J., and Cui, C. (2021). Non-destructive evaluation of salmon and tuna freshness in a room-temperature incubation environment using a portable visible/near-infrared imaging spectrometer. *Trans. ASABE* 64, 521–527. doi:10.13031/trans.13858

Currò, S., Balzan, S., Serva, L., Boffo, L., Ferlito, J. C., Novelli, E., et al. (2021). Fast and green method to control frauds of geographical origin in traded cuttlefish using a portable infrared reflective instrument. *Foods* 10, 1678. doi:10.3390/foods10081678

da Costa Fulgêncio, A. C., Resende, G. A. P., Teixeira, M. C. F., Botelho, B. G., and Sena, M. M. (2022). Determination of alcohol content in beers of different styles based on portable near-infrared spectroscopy and multivariate calibration. *Food Anal. Methods* 15, 307–316. doi:10.1007/s12161-021-02126-w

da Silva Medeiros, M. L., Brasil, Y. L., Cruz-Tirado, L. J. P., Lima, A. F., Godoy, H. T., and Barbin, D. F. (2023). Portable NIR spectrometer and chemometric tools for predicting quality attributes and adulteration levels in butteroil. *Food control.* 144, 109349. doi:10.1016/j.foodcont.2022.109349

da Silva Medeiros, M. L., Cruz-Tirado, J. P., Lima, A. F., de Souza Netto, J. M., Ribeiro, A. P. B., Bassegio, D., et al. (2022). Assessment oil composition and species discrimination of brassicas seeds based on hyperspectral imaging and portable near infrared (NIR) spectroscopy tools and chemometrics. *J. Food Compos. Anal.* 107, 104403. doi:10.1016/j.jfca.2022.104403

de Carvalho, L. M., Madruga, M. S., Estévez, M., Badaró, A. T., and Barbin, D. F. (2020). Occurrence of wooden breast and white striping in Brazilian slaughtering plants and use of near-infrared spectroscopy and multivariate analysis to identify affected chicken breasts. *J. Food Sci.* 85, 3102–3112. doi:10.1111/1750-3841.15465

de Freitas, S. T., Guimarães, Í. T., Vilvert, J. C., do Amaral, M. H. P., Brecht, J. K., and Marques, A. T. B. (2022). Mango dry matter content at harvest to achieve high consumer quality of different cultivars in different growing seasons. *Postharvest Biol. Technol.* 189, 111917. doi:10.1016/j.postharvbio.2022.111917

De Jesus Inacio, L., Lanza, I., Merlanti, R., Contiero, B., Lucatello, L., Serva, L., et al. (2020). Discriminant analysis of pyrrolizidine alkaloid contamination in bee pollen

based on near-infrared data from lab-stationary and portable spectrometers. *Eur. Food Res. Technol.* 246, 2471–2483. doi:10.1007/s00217-020-03590-0

de Oliveira Aguiar, F. C., Dias Guariglia, B. A., de Brito, A. A., Cardoso Campos, L. F., dos Reis Nascimento, A., de Carvalho Corrêa, G., et al. (2022). Validação prática de modelos de infravermelho próximo para tomate: Sólidos solúveis e acidez. *Rev. Cienc. Agrovet.* 21, 114–122. doi:10.5965/223811712122022114

Deng, J., Jiang, H., and Chen, Q. (2022). Characteristic wavelengths optimization improved the predictive performance of near-infrared spectroscopy models for determination of Aflatoxin B1 in maize. *J. Cereal Sci.* 105, 103474. doi:10.1016/j.jcs.2022.103474

Ding, L., Gong, T., Wang, B., Yang, Q., Liu, W., Pemo, R., et al. (2021). Non-invasive study of natural dyes in textiles of the qing dynasty using fiber optic reflectance spectroscopy. *J. Cult. Herit.* 47, 69–78. doi:10.1016/j.culher.2020.10.013

Donis-González, I. R., Valero, C., Momin, M. A., Kaur, A., and Slaughter, D. C. (2020). Performance evaluation of two commercially available portable spectrometers to non-invasively determine table grape and peach quality attributes. *Agronomy* 10, 148. doi:10.3390/agronomy10010148

dos Santos Pereira, E. V., de Sousa Fernandes, D. D., de Araújo, M. C. U., Diniz, P. H. G. D., and Maciel, M. I. S. (2021). *In-situ* authentication of goat milk in terms of its adulteration with cow milk using a low-cost portable NIR spectrophotometer. *Microchem. J.* 163, 105885. doi:10.1016/j.microc.2020.105885

dos Santos, V. J., Baqueta, M. R., Março, P. H., Valderrama, P., and Visentainer, J. V. (2022). Proof-of-Concept on the effect of human milk storage time: Lipid degradation and spectroscopic characterization using portable near-infrared spectrometer and chemometrics. *Food Chem.* 368, 130675. doi:10.1016/j.foodchem.2021.130675

Duchateau, C., Kauffmann, J.-M., Canfyn, M., Stévigny, C., De Braekeleer, K., and Deconinck, E. (2020). Discrimination of legal and illegal cannabis spp. According to European legislation using near infrared spectroscopy and chemometrics. *Drug Test. Anal.* 12, 1309–1319. doi:10.1002/dta.2865

Eady, M., Payne, M., Sortijas, S., Bethea, E., and Jenkins, D. (2021). A low-cost and portable near-infrared spectrometer using open-source multivariate data analysis software for rapid discriminatory quality assessment of medroxyprogesterone acetate injectables. *Spectrochim. Acta - Part Mol. Biomol. Spectrosc.* 259, 119917. doi:10.1016/j.saa.2021.119917

Eder, G. C., Lin, Y., Voronko, Y., and Spoljaric-Lukacic, L. (2020). On-site identification of the material composition of PV modules with mobile spectroscopic devices. *Energies* 13, 1903. doi:10.3390/en13081903

Ehsani, S., Dastgerdy, E. M., Yazdanpanah, H., and Parastar, H. (2022). Ensemble classification and regression techniques combined with portable near infrared spectroscopy for facile and rapid detection of water adulteration in bovine raw milk. *J. Chemom.* 37, 3395. doi:10.1002/cem.3395

Emsley, N. E. M., Holden, C. A., Guo, S., Bevan, R. S., Rees, C., McAinsh, M. R., et al. (2022). Machine learning approach using a handheld near-infrared (NIR) device to predict the effect of storage conditions on tomato biomarkers. *ACS Food Sci. Technol.* 2, 187–194. doi:10.1021/acsfoodscitech.1c00420

Escuredo, O., Meno, L., Rodríguez-Flores, M. S., and Seijo, M. C. (2021b). Rapid estimation of potato quality parameters by a portable near-infrared spectroscopy device. *Sensors* 21, 8222. doi:10.3390/s21248222

Escuredo, O., Rodríguez-Flores, M. S., Meno, L., and Seijo, M. C. (2021a). Prediction of physicochemical properties in honeys with portable near-infrared (micronir) spectroscopy combined with multivariate data processing. *Foods* 10, 317. doi:10.3390/foods10020317

Esposito, G., Sciuto, S., Guglielmetti, C., Pastorino, P., Ingravalle, F., Ru, G., et al. (2022). Discrimination between wild and farmed sea bass by using new spectrometry and spectroscopy methods. *Foods* 11, 1673. doi:10.3390/foods11121673

Fan, S., Wang, Q., Tian, X., Yang, G., Xia, Y., Li, J., et al. (2020). Non-destructive evaluation of soluble solids content of apples using a developed portable vis/NIR device. *Biosyst. Eng.* 193, 138–148. doi:10.1016/j.biosystemseng.2020.02.017

Fazio, E., Durso, L., Consiglio, G., Giuffrida, A., Compagnini, G., Puglisi, O., et al. (2014). Nonlinear scattering and absorption effects in size-selected diphenylpolyynes. *J. Phys. Chem. C* 118, 28812–28819. doi:10.1021/jp509666x

Ferrara, G., Marcotuli, V., Didonna, A., Stellacci, A. M., Palasciano, M., and Mazzeo, A. (2022). Ripeness prediction in table grape cultivars by using a portable NIR device. *Horticulturae* 8, 613. doi:10.3390/horticulturae8070613

Fonseca, A. C. S., Pereira, J. F. Q., Honorato, R. S., Bro, R., and Pimentel, M. F. (2022). Hierarchical classification models and handheld NIR spectrometer to human blood stains identification on different floor tiles. *Spectrochim. Acta - Part Mol. Biomol. Spectrosc.* 267, 120533. doi:10.1016/j.saa.2021.120533

Gaci, B., Mas Garcia, S., Abdelghafour, F., Adrian, J., Maupas, F., and Roger, J.-M. (2022). Assessing the potential of a handheld visible-near infrared microspectrometer for sugar beet phenotyping. *J. Infrared Spectrosc.* 30, 122–129. doi:10.1177/09670335221083448

Gales, O., Rodemann, T., Jones, J., and Swarts, N. (2021). Application of near infra-red spectroscopy as an instantaneous and simultaneous prediction tool for anthocyanins and sugar in whole fresh raspberry. *J. Sci. Food Agric.* 101, 2449–2454. doi:10.1002/jsfa.10869

Galli, A., Gargano, M., Bonizzoni, L., Bruni, S., Interlenghi, M., Longoni, M., et al. (2021). Imaging and spectroscopic data combined to disclose the painting techniques and materials in the fifteenth century leonardo atelier in milan. *Dyes Pigments* 187, 109112. doi:10.1016/j.dyepig.2020.109112

Galvan, D., Lelis, C. A., Effting, L., Melquiades, F. L., Bona, E., and Conte-Junior, C. A. (2022). Low-cost spectroscopic devices with multivariate analysis applied to milk authenticity. *Microchem. J.* 181, 107746. doi:10.1016/j.microc.2022.107746

Gatti, R. F., Poppi, R. J., and Ferreira, D. S. (2021). Portable NIR spectrometer for quick identification of fat bloom in chocolates. *Food Chem.* 342, 128267. doi:10.1016/j.foodchem.2020.128267

Giussani, B., Escalante-Quiceno, A. T., Boqué, R., and Riu, J. (2021). Measurement strategies for the classification of edible oils using low-cost miniaturised portable nir instruments. *Foods* 10, 2856. doi:10.3390/foods10112856

Goi, A., Hocquette, J.-F., Pellattiero, E., and De Marchi, M. (2022). Handheld near-infrared spectrometer allows on-line prediction of beef quality traits. *Meat Sci.* 184, 108694. doi:10.1016/j.meatsci.2021.108694

Goisser, S., Fernandes, M., Wittmann, S., Ulrichs, C., and Mempel, H. (2020b). Evaluating the practicability of commercial food-scanners for non-destructive quality assessment of tomato fruit. *J. Appl. Bot. Food Qual.* 93, 204–214. doi:10.5073/JABFQ.2020.093.025

Goisser, S., Wittmann, S., Fernandes, M., Mempel, H., and Ulrichs, C. (2020a). Comparison of colorimeter and different portable food-scanners for non-destructive prediction of lycopene content in tomato fruit. *Postharvest Biol. Technol.* 167, 111232. doi:10.1016/j.postharvbio.2020.111232

Goisser, S., Wittmann, S., and Mempel, H. (2021). Food-scanner applications in the fruit and vegetable sector. *Landtechnik* 76, 52–67. doi:10.15150/lt.2021.3264

Gozukara, G., Altunbas, S., Dengiz, O., and Adak, A. (2022). Assessing the effect of soil to water ratios and sampling strategies on the prediction of EC and PH using PXRF and vis-NIR spectra. *Comput. Electron. Agric.* 203, 107459. doi:10.1016/j.compag.2022.107459

Grassi, S., Jolayemi, O. S., Giovenzana, V., Tugnolo, A., Squeo, G., Conte, P., et al. (2021). Near infrared spectroscopy as a green technology for the quality prediction of intact olives. *Foods* 10, 1042. doi:10.3390/foods10051042

Greco, V., Giuffrida, A., Locatelli, M., Savini, F., de Grazia, U., Ciriolo, L., et al. (2023a). Emerging trends in pharmacotoxicological and forensic sample treatment procedures. *Appl. Sci. Switz.* 13, 2836. doi:10.3390/app13052836

Greco, V., Locatelli, M., Savini, F., Grazia, U. D., Montanaro, O., Rosato, E., et al. (2023b). New challenges in (Bio)Analytical sample treatment procedures for clinical applications. *Separations* 10, 62. doi:10.3390/separations10010062

Grossi, M., Valli, E., Glicerina, V. T., Rocculi, P., Toschi, T. G., and Ricco, B. (2020). Practical determination of solid fat content in fats and oils by single-wavelength near-infrared analysis. *IEEE Trans. Instrum. Meas.* 69, 585–592. doi:10.1109/TIM.2019.2901605

Guifang, W., Hai, M., and Xin, P. (2015). "Identification of varieties of natural textile fiber based on Vis/NIR spectroscopy technology," in Proceedings of the 2015 IEEE Advanced Information Technology, Electronic and Automation Control Conference (IAEAC), Chongqing, China, 19–20 December 2015 (IEEE), 585–589.

Gullifa, G., and Risoluti, R. (2021). Innovative miniaturized approach by MicroNIR and chemometrics for the monitoring of the occupational exposure of workers. *Proc. J. Phys. Conf. Ser.* 1960, 012008. doi:10.1088/1742-6596/1960/1/012008

Guo, Z., Wang, M., Shujat, A., Wu, J., El-Seedi, H. R., Shi, J., et al. (2020). Nondestructive monitoring storage quality of apples at different temperatures by near-infrared transmittance spectroscopy. *Food Sci. Nutr.* 8, 3793–3805. doi:10.1002/fsn3.1669

Hafiz, F., Chalakkal, R. J., Hong, S. C., Linde, G., Hu, R., O'Keeffe, B., et al. (2022). A new approach to non-mydriatic portable fundus imaging. *Expert Rev. Med. Devices* 19, 303–314. doi:10.1080/17434440.2022.2070004

Hasan, M. K., Aziz, M. H., Zarif, M. I. I., Hasan, M., Hashem, M. M. A., Guha, S., et al. (2021). Noninvasive hemoglobin level prediction in a mobile phone environment: State of the art review and recommendations. *JMIR MHealth UHealth* 9, e16806. doi:10.2196/16806

Hattori, Y., Hoshi, Y., Hashimoto, N., Ichimura, Y., Sugiura, Y., and Otsuka, M. (2022). Algorithm and hyperparameter optimizations for hetero-device classification by near-infrared spectra of falsified and substandard amoxicillin capsules. *Anal. Sci.* 38, 1261–1268. doi:10.1007/s44211-022-00142-2

Hattori, Y., Hoshi, Y., Ichimura, Y., Sugiura, Y., and Otsuka, M. (2021). Device-independent discrimination of falsified amoxicillin capsules using heterogeneous near-infrared spectroscopic devices for training and testing of a support vector machine. *Appl. Spectrosc.* 75, 1251–1261. doi:10.1177/0003702821999659

He, S., Li, P., Ren, Y., Wei, G., Wang, Y., Yang, Y., et al. (2022). Near-infrared broadband ZnTa2O6:Cr3+Phosphor for pc-LEDs and its application to nondestructive testing. *Inorg. Chem.* 61, 11284–11292. doi:10.1021/acs.inorgchem.2c01403

Henrique da Silva Melo, B., Figueiredo Sales, R., da Silva Bastos Filho, L., Souza Povoas da Silva, J., Gabrielle Carolino de Almeida Sousa, A., Maria Camará Peixoto, D., et al. (2022). Handheld near infrared spectrometer and machine learning methods applied to the monitoring of multiple process stages in industrial sugar production. *Food Chem.* 369, 130919. doi:10.1016/j.foodchem.2021.130919

Hespanhol, M. C., Souza, J. C., and Pasquini, C. (2020). Feasibility of a portable, low-cost near-infrared spectrophotometer for the quality screening of omega-3 dietary supplements. *J. Pharm. Biomed. Anal.* 189, 113436. doi:10.1016/j.jpba.2020.113436

Huang, W., Luo, S., Yang, D., and Zhang, S. (2021). Applications of smartphone-based near-infrared (NIR) imaging, measurement, and spectroscopy technologies to point-of-care (POC) diagnostics [基于智能手机的近红外成像、测量和光谱技术在护理点诊断中的应用]. *J. Zhejiang Univ. Sci. B* 22, 171–189. doi:10.1631/jzus.B2000388

Jahangiri, B., Barri, K., Alavi, A. H., and Buttlar, W. G. (2021). A molecular sensing method integrated with support vector machines to characterize asphalt mixtures. *Meas. J. Int. Meas. Confed.* 179, 109528. doi:10.1016/j.measurement.2021.109528

Jahani, R., Yazdanpanah, H., van Ruth, S. M., Kobarfard, F., Alewijn, M., Mahboubi, A., et al. (2020). Novel application of near-infrared spectroscopy and chemometrics approach for detection of lime juice adulteration. *Iran. J. Pharm. Res.* 19, 34–44. doi:10.22037/ijpr.2019.112328.13686

Jiang, H., He, Y., and Chen, Q. (2021). Determination of acid value during edible oil storage using a portable NIR spectroscopy system combined with variable selection algorithms based on an MPA-based strategy. *J. Sci. Food Agric.* 101, 3328–3335. doi:10.1002/jsfa.10962

Jiang, H., Liu, L., and Chen, Q. (2022). Rapid determination of acidity index of peanuts by near-infrared spectroscopy technology: Comparing the performance of different near-infrared spectral models. *Infrared Phys. Technol.* 125, 104308. doi:10.1016/j.infrared.2022.104308

Jiang, H., Liu, T., and Chen, Q. (2020). Dynamic monitoring of fatty acid value in rice storage based on a portable near-infrared spectroscopy system. *Spectrochim. Acta - Part Mol. Biomol. Spectrosc.* 240, 118620. doi:10.1016/j.saa.2020.118620

Jianqiang, Z., Yan, L., Yufeng, H., Gangyi, H., and Nannan, B. (2020). Characterization of deep green infection in tobacco leaves using a hand-held digital light projection based near-infrared spectrometer and an extreme learning machine algorithm. *Anal. Lett.* 53, 2266–2277. doi:10.1080/00032719.2020.1738452

Jin, G., Wang, Y.-J., Li, M., Li, T., Huang, W.-J., Li, L., et al. (2021). Rapid and real-time detection of black tea fermentation quality by using an inexpensive data fusion system. *Food Chem.* 358, 129815. doi:10.1016/j.foodchem.2021.129815

Jorge dos Santos, V., Baqueta, M. R., Neia, V. J. C., Magalhães de Souza, P., Março, P. H., Valderrama, P., et al. (2021). MicroNIR spectroscopy and multivariate calibration in the proximal composition determination of human milk. *LWT* 147, 111645. doi:10.1016/j.lwt.2021.111645

Kappacher, C., Trübenbacher, B., Losso, K., Rainer, M., Bonn, G. K., and Huck, C. W. (2022). Portable vs. Benchtop NIR-sensor technology for classification and quality evaluation of black truffle. *Molecules* 27, 589. doi:10.3390/molecules27030589

Kaufmann, K. C., Sampaio, K. A., García-Martín, J. F., and Barbin, D. F. (2022). Identification of coriander oil adulteration using a portable NIR spectrometer. *Food control.* 132, 108536. doi:10.1016/j.foodcont.2021.108536

Khongkaew, P., Cruz, J., Bertotto, J. P., Cárdenas, V., Alcalà, M., Nuchtavorn, N., et al. (2022). A comparative study of benchtop and portable NIR and Raman spectroscopic methods for the quantitative determination of curcuminoids in turmeric powder. *Foods* 11, 2187. doi:10.3390/foods11152187

Kovacs, Z., Muncan, J., Veleva, P., Oshima, M., Shigeoka, S., and Tsenkova, R. (2022). Aquaphotomics for monitoring of groundwater using short-wavelength near-infrared spectroscopy. *Spectrochim. Acta - Part Mol. Biomol. Spectrosc.* 279, 121378. doi:10.1016/j.saa.2022.121378

Kranenburg, R. F., Ou, F., Sevo, P., Petruzzella, M., de Ridder, R., van Klinken, A., et al. (2022c). On-site illicit-drug detection with an integrated near-infrared spectral sensor: A proof of concept. *Talanta* 245, 123441. doi:10.1016/j.talanta.2022.123441

Kranenburg, R. F., Ramaker, H.-J., Sap, S., and van Asten, A. C. (2022a). A calibration friendly approach to identify drugs of abuse mixtures with a portable near-infrared analyzer. *Drug Test. Anal.* 14, 1089–1101. doi:10.1002/dta.3231

Kranenburg, R. F., Ramaker, H.-J., and van Asten, A. C. (2022b). On-site forensic analysis of colored seized materials: Detection of Brown heroin and MDMA-tablets by a portable NIR spectrometer. *Drug Test. Anal.* 14, 1762–1772. doi:10.1002/dta.3356

Kranenburg, R. F., Ramaker, H. J., Asten, V., and Portable, A. C. (2022e). Portable near infrared spectroscopy for the isomeric differentiation of new psychoactive substances. *Forensic Sci. Int.* 341, 111467. doi:10.1016/j.forsciint.2022.111467

Kranenburg, R. F., Weesepoel, Y., Alewijn, M., Sap, S., Arisz, P. W. F., van Esch, A., et al. (2022d). Dataset of near-infrared spectral data of illicit-drugs and forensic casework samples analyzed by five portable spectrometers operating in different wavelength ranges. *Data Brief.* 45, 108660. doi:10.1016/j.dib.2022.108660

Kucha, C. T., and Ngadi, M. O. (2020). Rapid assessment of pork freshness using miniaturized NIR spectroscopy. *J. Food Meas. Charact.* 14, 1105–1115. doi:10.1007/s11694-019-00360-9

Kumagai, M., Matsuura, N., Li, H., Ohisa, N., Amano, T., and Ogawa, N. (2004). Application of a portable near infrared spectrometer for the manufacturing of noodle products. *J. Near Infrared Spectrosc.* 12, 127–131. doi:10.1255/jnirs.417

Lanza, I., Conficoni, D., Balzan, S., Cullere, M., Fasolato, L., Serva, L., et al. (2021). Assessment of chicken breast shelf life based on bench-top and portable near-infrared spectroscopy tools coupled with chemometrics. *Food Qual. Saf.* 5, 32. doi:10.1093/fqsafe/fyaa032

Li, D., Tianyi, G., Qin, Y., Wei, L., Na, W., Bo, W., et al. (2021b). Non-destructive fiber type identification in ancient textiles using portable near-infrared fiber optic reflectance spectroscopy [便携式近红外光纤光谱在纺织品文物纤维 无损检测中的应用]. *Sci. Conserv. Archaeol.* 33, 128–138.

Li, Y., Zheng, X., Zhang, D., Li, X., Fang, F., and Chen, L. (2021a). Rapid nondestructive simultaneous detection for physicochemical properties of different types of sheep meat cut using portable vis/NIR reflectance spectroscopy system. *Foods* 10, 1975. doi:10.3390/foods10091975

Liang, H., Shi, Z., Fan, Y., Ren, Z., Yuan, T., Huang, Y., et al. (2022). Micro NIR on-site and rapid detection system for cow manure slurry based on cloud sharing of calibration model [基于定标模型云共享的奶牛粪水微型 NIR 现场速测系统]. *Nongye Gongcheng XuebaoTransactions Chin. Soc. Agric. Eng.* 38, 208–215. doi:10.11975/j.issn.1002-6819.2022.10.025

Lim, C. H., and Sirisomboon, P. (2021). Measurement of cross link densities of prevulcanized natural rubber latex and latex products using low-cost near infrared spectrometer. *Ind. Crops Prod.* 159, 113016. doi:10.1016/j.indcrop.2020.113016

Liu, L., Yan, L., Xie, Y., and Xu, J. (2013). Determination of fiber contents in blended textiles by NIR combined with BP neural network. *ISRN Text.* 2013, 546481–546485. doi:10.1155/2013/546481

Ma, T., Inagaki, T., and Tsuchikawa, S. (2021b). Demonstration of the applicability of visible and near-infrared spatially resolved spectroscopy for rapid and nondestructive wood classification. *Holzforschung* 75, 419–427. doi:10.1515/hf-2020-0074

Ma, T., Xia, Y., Inagaki, T., and Tsuchikawa, S. (2021a). Rapid and nondestructive evaluation of soluble solids content (SSC) and firmness in apple using vis–NIR spatially resolved spectroscopy. *Postharvest Biol. Technol.* 173, 111417. doi:10.1016/j.postharvbio.2020.111417

Malvandi, A., Feng, H., and Kamruzzaman, M. (2022a). Application of NIR spectroscopy and multivariate analysis for non-destructive evaluation of apple moisture content during ultrasonic drying. *Spectrochim. Acta - Part Mol. Biomol. Spectrosc.* 269, 120733. doi:10.1016/j.saa.2021.120733

Malvandi, A., Kapoor, R., Feng, H., and Kamruzzaman, M. (2022b). Non-destructive measurement and real-time monitoring of apple hardness during ultrasonic contact drying via portable NIR spectroscopy and machine learning. *Infrared Phys. Technol.* 122, 104077. doi:10.1016/j.infrared.2022.104077

Mancini, M., Mircoli, A., Potena, D., Diamantini, C., Duca, D., and Toscano, G. (2020). Prediction of pellet quality through machine learning techniques and near-infrared spectroscopy. *Comput. Ind. Eng.* 147, 106566. doi:10.1016/j.cie.2020.106566

Manuel, M. N. B., da Silva, A. C., Lopes, G. S., and Ribeiro, L. P. D. (2022). One-class classification of special agroforestry Brazilian coffee using NIR spectrometry and chemometric tools. *Food Chem.* 366, 130480. doi:10.1016/j.foodchem.2021.130480

Manuelian, C. L., Ghetti, M., De Lorenzi, C., Pozza, M., Franzoi, M., and De Marchi, M. (2022). Feasibility of pocket-sized near-infrared spectrometer for the prediction of cheese quality traits. *J. Food Compos. Anal.* 105, 104245. doi:10.1016/j.jfca.2021.104245

Maraphum, K., Saengprachatanarug, K., Wongpichet, S., Phuphaphud, A., and Posom, J. (2020). In-field measurement of starch content of cassava tubers using handheld vis-near infrared spectroscopy implemented for breeding programmes. *Comput. Electron. Agric.* 175, 105607. doi:10.1016/j.compag.2020.105607

Maraphum, K., Saengprachatanarug, K., Wongpichet, S., Phuphuphud, A., and Posom, J. (2022). Achieving robustness across different ages and cultivars for an NIRS-PLSR model of fresh cassava root starch and dry matter content. *Comput. Electron. Agric.* 196, 106872. doi:10.1016/j.compag.2022.106872

Materazzi, S., Peluso, G., Ripani, L., and Risoluti, R. (2017a). High-throughput prediction of AKB48 in emerging illicit products by NIR spectroscopy and chemometrics. *Microchem. J.* 134, 277–283. doi:10.1016/j.microc.2017.06.014

Materazzi, S., Risoluti, R., Pinci, S., and Saverio Romolo, F. (2017b). New insights in forensic chemistry: NIR/Chemometrics analysis of toners for questioned documents examination. *Talanta* 174, 673–678. doi:10.1016/j.talanta.2017.06.044

McCormick, R., and Biegert, K. (2021). Non-destructive vis/NIR time-series to model apple fruit maturation on the tree. *Acta Hortic.* 1311, 131–140. doi:10.17660/ActaHortic.2021.1311.17

McVey, C., Gordon, U., Haughey, S. A., and Elliott, C. T. (2021). Assessment of the analytical performance of three near-infrared spectroscopy instruments (benchtop, handheld and portable) through the investigation of coriander seed authenticity. *Foods* 10, 956. doi:10.3390/foods10050956

Melendreras, C., Forcada, S., Fernández-sánchez, M. L., Fernández-colomer, B., Costa-fernández, J. M., López, A., et al. (2022). Near-infrared sensors for onsite and noninvasive quantification of macronutrients in breast milk. *Sensors* 22, 1311. doi:10.3390/s22041311

Menevseoglu, A. (2022). Evaluation of portable vibrational spectroscopy sensors as a tool to detect black cumin oil adulteration. *Processes* 10, 503. doi:10.3390/pr10030503

Menevseoglu, A. (2021). Non-destructive detection of sesame oil adulteration by portable FTNIR, FT-MIR, and Raman spectrometers combined with chemometrics. *J. Turk. Chem. Soc. Sect. Chem.* 8, 775–786. doi:10.18596/jotcsa.940424

Mishra, P., Marini, F., Brouwer, B., Roger, J. M., Biancolillo, A., Woltering, E., et al. (2021). Sequential fusion of information from two portable spectrometers for improved prediction of moisture and soluble solids content in pear fruit. *Talanta* 223, 121733. doi:10.1016/j.talanta.2020.121733

Mishra, P., and Woltering, E. (2021). Handling batch-to-batch variability in portable spectroscopy of fresh fruit with minimal parameter adjustment. *Anal. Chim. Acta* 1177, 338771. doi:10.1016/j.aca.2021.338771

Mogollón, R., Contreras, C., da Silva Neta, M. L., Marques, E. J. N., Zoffoli, J. P., and de Freitas, S. T. (2020). Non-destructive prediction and detection of internal physiological disorders in "keitt" mango using a hand-held vis-NIR spectrometer. *Postharvest Biol. Technol.* 167, 111251. doi:10.1016/j.postharvbio.2020.111251

Moon, E. J., Kim, Y., Xu, Y., Na, Y., Giaccia, A. J., and Lee, J. H. (2020). Evaluation of salmon, tuna, and beef freshness using a portable spectrometer. *Sens. Switz.* 20, 4299–4312. doi:10.3390/s20154299

Morillas, A. V., and Frascione, N. (2022). Portable near-infrared spectroscopy as a screening test of corrosive solutions concealed in plastic containers. *Appl. Sci. Switz.* 12, 2770. doi:10.3390/app12062770

Mulisa Bobasa, E., Dao Thi Phan, A., Manolis, C., Netzel, M., Smyth, H., Cozzolino, D., et al. (2020). Effect of sample presentation on the near infrared spectra of wild harvest Kakadu plum fruits (Terminalia ferdinandiana). *Infrared Phys. Technol.* 111, 103560. doi:10.1016/j.infrared.2020.103560

Muncan, J., and Tsenkova, R. (2023). Aquaphotomics—exploring water molecular systems in nature. *Molecules* 28, 2630. doi:10.3390/molecules28062630

Muñiz, R., Cuevas-Valdés, M., and de la Roza-Delgado, B. (2020). Milk quality control requirement evaluation using a handheld near infrared reflectance spectrophotometer and a bespoke mobile application. *J. Food Compos. Anal.* 86, 103388. doi:10.1016/j.jfca.2019.103388

Nagy, M. M., Wang, S., and Farag, M. A. (2022). Quality analysis and authentication of nutraceuticals using near ir (NIR) spectroscopy: A comprehensive review of novel trends and applications. *Trends Food Sci. Technol.* 123, 290–309. doi:10.1016/j.tifs.2022.03.005

Naimi, S., Ayoubi, S., Di Raimo, L. A. D. L., and Dematte, J. A. M. (2022). Quantification of some intrinsic soil properties using proximal sensing in arid lands: Application of vis-NIR, MIR, and PXRF spectroscopy. *Geoderma Reg.* 28, e00484. doi:10.1016/j.geodrs.2022.e00484

Ncama, K., Magwaza, L. S., Tesfay, S. Z., Mditshwa, A., and Mbili, N. C. (2020a). In-field application of portable NIR to assess 'valencia' orange fruit maturity. *Acta Hortic.* 1275, 61–68. doi:10.17660/ActaHortic.2020.1275.9

Ncama, K., Magwaza, L. S., Tesfay, S. Z., Mditshwa, A., and Mbili, N. (2020b). *In-situ* assessment of harvest maturity of 'hass' avocado (persea americana) using portable vis-NIR spectrometer. *Acta Hortic.* 1299, 339–346. doi:10.17660/ActaHortic.2020.1299.51

Netto, J. M., Honorato, F. A., Celso, P. G., and Pimentel, M. F. (2023). Authenticity of almond flour using handheld near infrared instruments and one class classifiers. *J. Food Compos. Anal.* 115, 104981. doi:10.1016/j.jfca.2022.104981

Ngo, V.-D., Hoang, L.-T.-A., Pham, V.-C., Ngo, V.-H., and Tran, P.-H. (2022). Estimation of pesticide residues on leafy vegetables using a developed handheld spectrometer. *Biointerface Res. Appl. Chem.* 12, 8163–8173. doi:10.33263/BRIAC126.81638173

Ni, D., Smyth, H. E., Gidley, M. J., and Cozzolino, D. (2022a). A preliminary study on the utilisation of near infrared spectroscopy to predict age and *in vivo* human metabolism. *Spectrochim. Acta - Part Mol. Biomol. Spectrosc.* 265, 120312. doi:10.1016/j.saa.2021.120312

Ni, D., Smyth, H. E., Gidley, M. J., and Cozzolino, D. (2022b). Shedding light on human tissue (*in vivo*) to predict satiation, satiety, and food intake using near infrared reflectance spectroscopy: A preliminary study. *Innov. Food Sci. Emerg. Technol.* 78, 103033. doi:10.1016/j.ifset.2022.103033

Noypitak, S., Puttipipatkajorn, A., Ruangkhasap, S., Terdwongworakul, A., and Puttipipatkajorn, A. (2022). Application of a portable near-infrared spectrometer for rapid, non-destructive evaluation of moisture content in para rubber timber. *Wood Sci. Technol.* 56, 285–303. doi:10.1007/s00226-021-01354-x

Oliveira, M. M., Cruz-Tirado, J. P., Roque, J. V., Teófilo, R. F., and Barbin, D. F. (2020). Portable near-infrared spectroscopy for rapid authentication of adulterated Paprika powder. *J. Food Compos. Anal.* 87, 103403. doi:10.1016/j.jfca.2019.103403

Orsi, D., Vaccari, M., Baraldi, A., and Cristofolini, L. (2022). A portable NIR fluorimeter directly quantifies singlet oxygen generated by nanostructures for photodynamic therapy. *Spectrochim. Acta - Part Mol. Biomol. Spectrosc.* 265, 120357. doi:10.1016/j.saa.2021.120357

Ou, F., van Klinken, A., Ševo, P., Petruzzella, M., Li, C., van Elst, D. M. J., et al. (2022). Handheld NIR spectral sensor module based on a fully-integrated detector array. *Sensors* 22, 7027. doi:10.3390/s22187027

Ouyang, Q., Wang, L., Zareef, M., Chen, Q., Guo, Z., and Li, H. (2020). A feasibility of nondestructive rapid detection of total volatile basic nitrogen content in frozen pork based on portable near-infrared spectroscopy. *Microchem. J.* 157, 105020. doi:10.1016/j.microc.2020.105020

Paiva, E. M., Ribessi, R. L., and Rohwedder, J. J. R. (2022). Near-infrared spectra of liquid and gas samples by diffuse reflectance employing benchtop and handheld

spectrophotometers. *Spectrochim. Acta - Part Mol. Biomol. Spectrosc.* 264, 120302. doi:10.1016/j.saa.2021.120302

Panikar, S., Li, J., Rane, V., Gillam, S., Callegari, G., Kurtyka, B., et al. (2021). Integrating sensors for monitoring blend content in a pharmaceutical continuous manufacturing plant. *Int. J. Pharm.* 606, 120085. doi:10.1016/j.ijpharm.2020.120085

Parastar, H., van Kollenburg, G., Weesepoel, Y., van den Doel, A., Buydens, L., and Jansen, J. (2020). Integration of handheld NIR and machine learning to "measure & monitor" chicken meat authenticity. *Food control.* 112, 107149. doi:10.1016/j.foodcont. 2020.107149

Pasquini, C., Hespanhol, M. C., Cruz, K. A. M. L., and Pereira, A. F. (2020). Monitoring the quality of ethanol-based hand sanitizers by low-cost near-infrared spectroscopy. *Microchem. J.* 159, 105421. doi:10.1016/j.microc.2020.105421

Peng, J., Li, S., Makar, R. S., Li, H., Feng, C., Luo, D., et al. (2022). Proximal soil sensing of low salinity in southern xinjiang, China. *Remote Sens.* 14, 4448. doi:10.3390/rs14184448

Pennisi, F., Giraudo, A., Cavallini, N., Esposito, G., Merlo, G., Geobaldo, F., et al. (2021). Differentiation between fresh and thawed cephalopods using nir spectroscopy and multivariate data analysis. *Foods* 10, 528. doi:10.3390/foods10030528

Pham, V., Weindorf, D. C., and Dang, T. (2021). Soil profile analysis using interactive visualizations, machine learning, and deep learning. *Comput. Electron. Agric.* 191, 106539. doi:10.1016/j.compag.2021.106539

Pissard, A., Marques, E. J. N., Dardenne, P., Lateur, M., Pasquini, C., Pimentel, M. F., et al. (2021). Evaluation of a handheld ultra-compact NIR spectrometer for rapid and non-destructive determination of apple fruit quality. *Postharvest Biol. Technol.* 172, 111375. doi:10.1016/j.postharvbio.2020.111375

Pomerantsev, A. L., and Rodionova, O. Y. (2021). New trends in qualitative analysis: Performance, optimization, and validation of multi-class and soft models. *Trac. Trends Anal. Chem.* 143, 116372. doi:10.1016/j.trac.2021.116372

Pranato, J. A., Minasny, B., and Weaver, T. (2021). Rapid and cost-effective nutrient content analysis of cotton leaves using near-infrared spectroscopy (NIRS). *PeerJ* 9, e11042. doi:10.7717/peerj.11042

Pu, Y., Pérez-Marín, D., O'shea, N., and Garrido-Varo, A. (2021). Recent advances in portable and handheld NIR spectrometers and applications in milk, cheese and dairy powders. *Foods* 10, 2377. doi:10.3390/foods10102377

Puttipipatkajorn, A., and Puttipipatkajorn, A. (2020). Development of calibration models for rapid determination of moisture content in rubber sheets using portable near-infrared spectrometers. *J. Innov. Opt. Health Sci.* 13, 91. doi:10.1142/S1793545820500091

Qi, Z., Wu, X., Yang, Y., Wu, B., and Fu, H. (2022). Discrimination of the red Jujube varieties using a portable NIR spectrometer and fuzzy improved linear discriminant analysis. *Foods* 11, 763. doi:10.3390/foods11050763

Qiao, X., Peng, Y., Wang, Y., Li, L., Zhuang, Q., and Tian, W. (2020). Design of portable device for testing sugar content of apples combined with mobile phones [手机联用的苹果糖度便携式检测装置设计与试验]. *Nongye Jixie XuebaoTransactions Chin. Soc. Agric. Mach.* 51, 491–498. doi:10.6041/j.issn.1000-1298.2020.S2.061

Ramadevi, P., Kamalakannan, R., Suraj, G. P., V Hegde, D., and Varghese, M. (2022). Evaluation of Kraft pulp yield and syringyl/guaiacyl ratio from standing trees (Eucalyptus camaldulensis, E. Urophylla, leucaena leucocephala and Casuarina junghuhniana) using portable near infrared spectroscopy. *J. Infrared Spectrosc.* 30, 40–47. doi:10.1177/09670335211063634

Rego, G., Ferrero, F., Valledor, M., Campo, J. C., Forcada, S., Royo, L. J., et al. (2020). A portable IoT NIR spectroscopic system to analyze the quality of dairy farm forage. *Comput. Electron. Agric.* 175, 105578. doi:10.1016/j.compag.2020.105578

Reinig, P., Grüger, H., Knobbe, J., Pügner, T., and Meyer, S. (2018). "Bringing NIR spectrometers into mobile phones," in *MOEMS and miniaturized systems XVII* (Bellingham,WA, USA: SPIE), 97–104.

Ren, G., Zhang, X., Wu, R., Zhang, X., Xie, T., and Zhang, Z. (2022). Digital depiction of the quality of dianhong black tea based on pocket-sized near infrared spectroscopy. *Infrared Phys. Technol.* 127, 104418. doi:10.1016/j.infrared.2022.104418

Ren, S., and Jia, Y. (2023). Near-infrared data classification at phone terminal based on the combination of PCA and CS-rbfsvc algorithms. *Spectrochim. Acta - Part Mol. Biomol. Spectrosc.* 287, 122080. doi:10.1016/j.saa.2022.122080

Risoluti, R., Canepari, S., Frati, P., Fineschi, V., and Materazzi, S. (2019a). "2^n analytical platform" to update procedures in thanatochemistry: Estimation of post mortem interval in vitreous humor. *Anal. Chem.* 91, 7025–7031. doi:10.1021/acs.analchem.9b01443

Risoluti, R., Caprari, P., Gullifa, G., Massimi, S., Maffei, L., Sorrentino, F., et al. (2020f). An innovative multilevel test for hemoglobinopathies: TGA/Chemometrics simultaneously identifies and classifies sickle cell disease from thalassemia. *Front. Mol. Biosci.* 7, 141. doi:10.3389/fmolb.2020.00141

Risoluti, R., Caprari, P., Gullifa, G., Massimi, S., Sorrentino, F., Buiarelli, F., et al. (2019e). New methods for thalassemia screening: TGA/Chemometrics test is not influenced by the aging of blood samples. *Microchem. J.* 146, 374–380. doi:10.1016/j.microc.2019.01.008

Risoluti, R., Caprari, P., Gullifa, G., Massimi, S., Sorrentino, F., Maffei, L., et al. (2020g). Innovative screening test for the early detection of sickle cell anemia. *Talanta* 219, 121243. doi:10.1016/j.talanta.2020.121243

Risoluti, R., Gregori, A., Schiavone, S., and Materazzi, S. (2018b). Click and screen technology for the detection of explosives on human hands by a portable MicroNIR-chemometrics platform. *Anal. Chem.* 90, 4288–4292. doi:10.1021/acs.analchem.7b03661

Risoluti, R., Gullifa, G., Battistini, A., and Materazzi, S. (2020b). Development of a "single-click" analytical platform for the detection of cannabinoids in hemp seed oil. *RSC Adv.* 10, 43394–43399. doi:10.1039/d0ra07142k

Risoluti, R., Gullifa, G., Battistini, A., and Materazzi, S. (2019c). Lab-on-Click detection of illicit drugs in oral fluids by MicroNIR-chemometrics. *Anal. Chem.* 91, 6435–6439. doi:10.1021/acs.analchem.9b00197

Risoluti, R., Gullifa, G., Battistini, A., and Materazzi, S. (2019d). MicroNIR/chemometrics: A new analytical platform for fast and accurate detection of δ9-tetrahydrocannabinol (THC) in oral fluids. *Drug Alcohol Depend.* 205, 107578. doi:10.1016/j.drugalcdep.2019.107578

Risoluti, R., Gullifa, G., Battistini, A., and Materazzi, S. (2020d). Monitoring of cannabinoids in hemp flours by MicroNIR/chemometrics. *Talanta* 211, 120672. doi:10.1016/j.talanta.2019.120672

Risoluti, R., Gullifa, G., Battistini, A., and Materazzi, S. (2020c). The detection of cannabinoids in veterinary feeds by MicroNIR/chemometrics: A new analytical platform. *Analyst* 145, 1777–1782. doi:10.1039/c9an01854a

Risoluti, R., Gullifa, G., Buiarelli, F., and Materazzi, S. (2020e). Real time detection of amphetamine in oral fluids by MicroNIR/chemometrics. *Talanta* 208, 120456. doi:10.1016/j.talanta.2019.120456

Risoluti, R., Gullifa, G., Carcassi, E., Masotti, A., and Materazzi, S. (2020a). TGA/Chemometrics addressing innovative preparation strategies for functionalized carbon nanotubes. *J. Pharm. Anal.* 10, 351–355. doi:10.1016/j.jpha.2020.02.009

Risoluti, R., Gullifa, G., Fabiano, M. A., and Materazzi, S. (2015). Biomimetic complexes of Co(II), Mn(II), and Ni(II) with 2-propyl-4,5-imidazoledicarboxylic acid. EGA-MS characterization of the thermally induced decomposition. *Russ. J. Gen. Chem.* 85, 2374–2377. doi:10.1134/S1070363215100242

Risoluti, R., Gullifa, G., and Materazi, S. (2020h). Assessing the quality of milk using a multicomponent analytical platform MicroNIR/chemometric. *Front. Chem.* 8, 614718. doi:10.3389/fchem.2020.614718

Risoluti, R., Materazzi, S., Gregori, A., and Ripani, L. (2016). Early detection of emerging street drugs by near infrared spectroscopy and chemometrics. *Talanta* 153, 407–413. doi:10.1016/j.talanta.2016.02.044

Risoluti, R., and Materazzi, S. (2018). MicroNIR/chemometrics assessement of occupational exposure to hydroxyurea. *Front. Chem.* 6, 228. doi:10.3389/fchem.2018.00228

Risoluti, R., Materazzi, S., Tau, F., Russo, A., and Romolo, F. S. (2018a). Towards innovation in paper dating: A MicroNIR analytical platform and chemometrics. *Analyst* 143, 4394–4399. doi:10.1039/c8an00871j

Risoluti, R., Pichini, S., Pacifici, R., and Materazzi, S. (2019b). Miniaturized analytical platform for cocaine detection in oral fluids by MicroNIR/chemometrics. *Talanta* 202, 546–553. doi:10.1016/j.talanta.2019.04.081

Ristova, M., Skenderovska, M., and Jovkovski, T. (2022). Nondestructive vis-NIR reflectance spectroscopy as a forensic tool for ink characterization: A preliminary study. *J. Appl. Spectrosc.* 89, 967–973. doi:10.1007/s10812-022-01455-w

Riu, J., Gorla, G., Chakif, D., Boqué, R., and Giussani, B. (2020). Rapid analysis of milk using low-cost pocket-size NIR spectrometers and multivariate analysis. *Foods* 9, 1090. doi:10.3390/foods9081090

Riu, J., Vega, A., Boqué, R., and Giussani, B. (2022). Exploring the analytical complexities in insect powder analysis using miniaturized NIR spectroscopy. *Foods* 11, 3524. doi:10.3390/foods11213524

Rizwana, S., and Hazarika, M. K. (2020). Application of near-infrared spectroscopy for rice characterization using machine learning. *J. Inst. Eng. India Ser. A* 101, 579–587. doi:10.1007/s40030-020-00459-z

Rodionova, O. Y., Titova, A. V., and Pomerantsev, A. L. (2016). Discriminant analysis is an inappropriate method of authentication. *Trac. Trends Anal. Chem.* 78, 17–22. doi:10.1016/j.trac.2016.01.010

Rouxinol, M. I., Martins, M. R., Murta, G. C., Barroso, J. M., and Rato, A. E. (2022). Quality assessment of red wine grapes through NIR spectroscopy. *Agronomy* 12, 637. doi:10.3390/agronomy12030637

Rovira, G., Miaw, C. S. W., Martins, M. L. C., Sena, M. M., de Souza, S. V. C., Callao, M. P., et al. (2023). One-class model with two decision thresholds for the rapid detection of cashew nuts adulteration by other nuts. *Talanta* 253, 123916. doi:10.1016/j.talanta.2022.123916

Rukundo, I. R., Danao, M.-G. C., MacDonald, J. C., Wehling, R. L., and Weller, C. L. (2021b). Performance of two handheld NIR spectrometers to quantify crude protein of composite animal forage and feedstuff. *AIMS Agric. Food* 6, 462–477. doi:10.3934/agrfood.2021027

Rukundo, I. R., Danao, M.-G. C., Mitchell, R. B., Masterson, S. D., and Weller, C. L. (2021a). Comparing the use of handheld and benchtop NIR spectrometers in predicting nutritional value of forage. *Appl. Eng. Agric.* 37, 171–181. doi:10.13031/AEA.14157

Rukundo, I. R., Danao, M.-G. C., Mitchell, R. B., and Weller, C. L. (2022). Evaluation of predictive performance of PLS regression models after being transferred from benchtop to handheld NIR spectrometers. *Biosyst. Eng.* 218, 245–255. doi:10.1016/j.biosystemseng.2022.04.014

Said, M., Wahba, A., and Khalil, D. (2022). Semi-supervised deep learning framework for milk analysis using NIR spectrometers. *Chemom. Intell. Lab. Syst.* 228, 104619. doi:10.1016/j.chemolab.2022.104619

Sandak, J., Niemz, P., Hänsel, A., Mai, J., and Sandak, A. (2021). Feasibility of portable NIR spectrometer for quality assurance in glue-laminated timber production. *Constr. Build. Mater.* 308, 125026. doi:10.1016/j.conbuildmat.2021.125026

Sandak, J., Sandak, A., Zitek, A., Hintestoisser, B., and Picchi, G. (2020). Development of low-cost portable spectrometers for detection of wood defects. *Sens. Switz.* 20, 545. doi:10.3390/s20020545

Santonocito, R., Tuccitto, N., Cantaro, V., Carbonaro, A. B., Pappalardo, A., Greco, V., et al. (2022). Smartphone-assisted sensing of trinitrotoluene by optical array. *ACS Omega* 7, 37122–37132. doi:10.1021/acsomega.2c02958

Santos, C. S. P., Cruz, R., Gonçalves, D. B., Queirós, R., Bloore, M., Kovács, Z., et al. (2021a). Non-destructive measurement of the internal quality of citrus fruits using a portable NIR device. *J. AOAC Int.* 104, 61–67. doi:10.1093/jaoacint/qsaa115

Santos, F. D., Santos, L. P., Cunha, P. H. P., Borghi, F. T., Romão, W., de Castro, E. V. R., et al. (2021b). Discrimination of oils and fuels using a portable NIR spectrometer. *Fuel* 283, 118854. doi:10.1016/j.fuel.2020.118854

Santos, F. D., Vianna, S. G. T., Cunha, P. H. P., Folli, G. S., de Paulo, E. H., Moro, M. K., et al. (2022). Characterization of crude oils with a portable NIR spectrometer. *Microchem. J.* 181, 107696. doi:10.1016/j.microc.2022.107696

Santos, P. C., Tosato, F., Cesconetto, M., Corrêa, T., Santos, F. D., Pires, A. A., et al. (2020). Determinação da autenticidade de amostras de azeite comerciais apreendidas no estado do espírito santo usando um espectrofotômetro portátil na região do NIR. *Quimica Nova* 43, 891–900. doi:10.21577/0100-4042.20170550

Sarkar, S., Basak, J. K., Moon, B. E., and Kim, H. T. (2020). A comparative study of PLSR and SVM-R with various preprocessing techniques for the quantitative determination of soluble solids content of hardy kiwi fruit by a portable vis/NIR spectrometer. *Foods* 9, 1078. doi:10.3390/foods9081078

Savoia, S., Albera, A., Brugiapaglia, A., Di Stasio, L., Cecchinato, A., and Bittante, G. (2021). Prediction of meat quality traits in the abattoir using portable near-infrared spectrometers: Heritability of predicted traits and genetic correlations with laboratory-measured traits. *J. Anim. Sci. Biotechnol.* 12, 29. doi:10.1186/s40104-021-00555-5

Savoia, S., Albera, A., Brugiapaglia, A., Di Stasio, L., Ferragina, A., Cecchinato, A., et al. (2020). Prediction of meat quality traits in the abattoir using portable and hand-held near-infrared spectrometers. *Meat Sci.* 161, 108017. doi:10.1016/j.meatsci.2019.108017

Scala, A., Piperno, A., Micale, N., Mineo, P. G., Abbadessa, A., Risoluti, R., et al. (2018). Click on PLGA-PEG and hyaluronic acid: Gaining access to anti-leishmanial pentamidine bioconjugates. *J. Biomed. Mater. Res. Part B Appl. Biomater.* 106, 2778–2785. doi:10.1002/jbm.b.34058

Schoot, M., Alewijn, M., Weesepoel, Y., Mueller-Maatsch, J., Kapper, C., Postma, G., et al. (2022). Predicting the performance of handheld near-infrared photonic sensors from a master benchtop device. *Anal. Chim. Acta* 1203, 339707. doi:10.1016/j.aca.2022.339707

Shen, G., Kang, X., Su, J., Qiu, J., Liu, X., Xu, J., et al. (2022). Rapid detection of fumonisin B1 and B2 in ground corn samples using smartphone-controlled portable near-infrared spectrometry and chemometrics. *Food Chem.* 384, 132487. doi:10.1016/j.foodchem.2022.132487

Shrestha, G., Calvelo-Pereira, R., Roudier, P., Martin, A. P., Turnbull, R. E., Kereszturi, G., et al. (2022). Quantification of multiple soil trace elements by combining portable X-ray fluorescence and reflectance spectroscopy. *Geoderma* 409, 115649. doi:10.1016/j.geoderma.2021.115649

Siesler, H. W. (2016). "Near infrared spectra, interpretation," in *Encyclopedia of spectroscopy and spectrometry*. Editors J. C. Lindon, G. E. Tranter, and D. W. Koppenaal (Oxford, UK: Academic Press), 30–39.

Silva, A. C. D., Ribeiro, L. P. D., Vidal, R. M. B., Matos, W. O., and Lopes, G. S. (2021). A fast and low-cost approach to quality control of alcohol-based hand sanitizer using a portable near infrared spectrometer and chemometrics. *J. Infrared Spectrosc.* 29, 119–127. doi:10.1177/0967033520987315

Silva, L. C. R., Folli, G. S., Santos, L. P., Barros, I. H. A. S., Oliveira, B. G., Borghi, F. T., et al. (2020). Quantification of beef, pork, and chicken in ground meat using a portable NIR spectrometer. *Vib. Spectrosc.* 111, 103158. doi:10.1016/j.vibspec.2020.103158

Sorak, D., Herberholz, L., Iwascek, S., Altinpinar, S., Pfeifer, F., and Siesler, H. W. (2012). New developments and applications of handheld Raman, mid-infrared, and near-infrared spectrometers. *Appl. Spectrosc. Rev.* 47, 83–115. doi:10.1080/05704928.2011.625748

Srinuttrakul, W., Mihailova, A., Islam, M. D., Liebisch, B., Maxwell, F., Kelly, S. D., et al. (2021). Geographical differentiation of hom Mali rice cultivated in different regions of Thailand using ftir-atr and nir spectroscopy. *Foods* 10, 1951. doi:10.3390/foods10081951

Sripaurya, T., Sengchuai, K., Booranawong, A., and Chetpattananondh, K. (2021). Gros Michel banana soluble solids content evaluation and maturity classification using a developed portable 6 channel NIR device measurement. *Meas. J. Int. Meas. Confed.* 173, 108615. doi:10.1016/j.measurement.2020.108615

Sun, Y., Wang, Y., Huang, J., Ren, G., Ning, J., Deng, W., et al. (2020). Quality assessment of instant green tea using portable NIR spectrometer. *Spectrochim. Acta - Part Mol. Biomol. Spectrosc.* 240, 118576. doi:10.1016/j.saa.2020.118576

Surkova, A., Bogomolov, A., Paderina, A., Khistiaeva, V., Boichenko, E., Grachova, E., et al. (2022). Optical multisensor system based on lanthanide(III) complexes as near-infrared light sources for analysis of milk. *Chemosensors* 10, 288. doi:10.3390/chemosensors10070288

Teixeira, A. F. D. S., Andrade, R., Mancini, M., Silva, S. H. G., Weindorf, D. C., Chakraborty, S., et al. (2022). Proximal sensor data fusion for tropical soil property prediction: Soil fertility properties. *J. South Am. Earth Sci.* 116, 103873. doi:10.1016/j.jsames.2022.103873

Tirkey, A., and Upadhyay, L. S. B. (2021). Microplastics: An overview on separation, identification and characterization of microplastics. *Mar. Pollut. Bull.* 170, 112604. doi:10.1016/j.marpolbul.2021.112604

Torres, I., Sánchez, M.-T., and Pérez-Marín, D. (2020). Integrated soluble solid and nitrate content assessment of spinach plants using portable NIRS sensors along the supply chain. *Postharvest Biol. Technol.* 168, 111273. doi:10.1016/j.postharvbio.2020.111273

Torres, I., Sánchez, M.-T., Vega-Castellote, M., and Pérez-Marín, D. (2021). Fraud detection in batches of sweet almonds by portable near-infrared spectral devices. *Foods* 10, 1221. doi:10.3390/foods10061221

Tosato, F., Barros, E. V., Cunha, D. A., Santos, F. D., Corrêa, T., Nunes, A., et al. (2020). Análise de amOStras de combustíveis por fotometria, NIR portátil E rmn de 1 H – UMA comparação com OS resultadOS encontradOS por técnicas normatizadas. *Quimica Nova* 43, 155–167. doi:10.21577/0100-4042.20170473

Toscano, G., Leoni, E., Gasperini, T., and Picchi, G. (2022). Performance of a portable NIR spectrometer for the determination of moisture content of industrial wood chips fuel. *Fuel* 320, 123948. doi:10.1016/j.fuel.2022.123948

Trenfield, S. J., Tan, H. X., Goyanes, A., Wilsdon, D., Rowland, M., Gaisford, S., et al. (2020). Non-destructive dose verification of two drugs within 3D printed polyprintlets. *Int. J. Pharm.* 577, 119066. doi:10.1016/j.ijpharm.2020.119066

Tugnolo, A., Giovenzana, V., Beghi, R., Grassi, S., Alamprese, C., Casson, A., et al. (2021). A diagnostic visible/near infrared tool for a fully automated olive ripeness evaluation in a view of a simplified optical system. *Comput. Electron. Agric.* 180, 105887. doi:10.1016/j.compag.2020.105887

Usman, A. G., Ghali, U. M., and Işik, S. (2020). Applications of miniaturized and portable near infrared (NIR), fourier transform infrared (FT-IR) and Raman spectrometers for the inspection and control of pharmaceutical products. *Ank. Univ. Eczacilik Fak. Derg.* 44, 188–203. doi:10.33483/jfpau.599077

van Kollenburg, G., Weesepoel, Y., Parastar, H., van den Doel, A., Buydens, L., and Jansen, J. (2020). Dataset of the application of handheld NIR and machine learning for chicken fillet authenticity study. *Data Brief.* 29, 105357. doi:10.1016/j.dib.2020.105357

Varrà, M. O., Ghidini, S., Fabrile, M. P., Ianieri, A., and Zanardi, E. (2022). Country of origin label monitoring of musky and common Octopuses (eledone spp. and Octopus vulgaris) by means of a portable near-infrared spectroscopic device. *Food control.* 138, 109052. doi:10.1016/j.foodcont.2022.109052

Vega-Castellote, M., Sánchez, M.-T., Torres, I., de la Haba, M.-J., and Pérez-Marín, D. (2022). Assessment of watermelon maturity using portable new generation NIR spectrophotometers. *Sci. Hortic.* 304, 111328. doi:10.1016/j.scienta.2022.111328

Vera, D. A., García, H. A., Victoria Waks Serra, M., Baez, G. R., Iriarte, D. I., and Pomarico, J. A. (2022). A Monte Carlo study of near infrared light propagation in the human head with lesions-a time-resolved approach. *Biomed. Phys. Eng. Express* 8, 035005. doi:10.1088/2057-1976/ac59f3

Viejo, C. G., Caboche, C. H., Kerr, E. D., Pegg, C. L., Schulz, B. L., Howell, K., et al. (2020). Development of a rapid method to assess beer foamability based on relative protein content using robobeer and machine learning modeling. *Beverages* 6, 1–11. doi:10.3390/beverages6020028

Vinhandelli, A. R., De Brito, A. A., de Faria, R. C., Campos, L. F. C., Goulart, G. A. S., de Almeida Teixeira, G. H., et al. (2023). Near infrared spectroscopy as a tool for agricultural expertise: Identification of tomato seedlings. *Acta Sci. - Technol.* 45, e61270. doi:10.4025/actascitechnol.v45i1.61270

Violino, S., Taiti, C., Ortenzi, L., Marone, E., Pallottino, F., and Costa, C. (2022). A ready-to-use portable VIS–NIR spectroscopy device to assess superior EVOO quality. *Eur. Food Res. Technol.* 248, 1011–1019. doi:10.1007/s00217-021-03941-5

Vohland, M., Ludwig, B., Seidel, M., and Hutengs, C. (2022). Quantification of soil organic carbon at regional scale: Benefits of fusing vis-NIR and MIR diffuse reflectance data are greater for *in situ* than for laboratory-based modelling approaches. *Geoderma* 405, 115426. doi:10.1016/j.geoderma.2021.115426

Wan, S.-K., Lü, B., Zhang, H.-M., He, L., Fu, J., Ji, H.-J., et al. (2021). Quick measurement method of condensation point of diesel based on temperature-compensation model [基于温度修正模型的柴油凝点快速检测方法]. *Guang Pu*

Xue Yu Guang Pu Fen XiSpectroscopy Spectr. Anal. 41, 3111–3116. doi:10.3964/j.issn. 1000-0593(2021)10-3111-06

Wang, F., Zhao, C., Xu, B., Xu, Z., Li, Z., Yang, H., et al. (2020b). Development of a portable detection device for the quality of fresh tea leaves using spectral technology [便 携式茶鲜叶品质光谱检测装置研制]. *Nongye Gongcheng XuebaoTransactions Chin. Soc. Agric. Eng.* 36, 273–277. doi:10.3760/cma.j.issn.1673-0860.2020.03.018

Wang, H., and Liu, X. (2022). Recent developments on broadband near-infrared luminescent materials activated by 3d transition metal ions [3d过渡金属离子激活的 宽带近红外发光材料研究进展]. *Kuei Suan Jen. Hsueh PaoJournal Chin. Ceram. Soc.* 50, 2567–2578. doi:10.14062/j.issn.0454-5648.22020297

Wang, J., Guo, Z., Zou, C., Jiang, S., El-Seedi, H. R., and Zou, X. (2022a). General model of multi-quality detection for apple from different origins by vis/NIR transmittance spectroscopy. *J. Food Meas. Charact.* 16, 2582–2595. doi:10.1007/ s11694-022-01375-5

Wang, W., Keller, M. D., Baughman, T., and Wilson, B. K. (2020a). Evaluating low-cost optical spectrometers for the detection of simulated substandard and falsified medicines. *Appl. Spectrosc.* 74, 323–333. doi:10.1177/0003702819877422

Wang, X., Wang, L., and Fang, J. (2021b). Research and application progresses of near-infrared spectral sensing Internet of Things [近红外光谱传感物联网研究与应 用进展]. *Zhongguo JiguangChinese J. Lasers* 48. doi:10.3788/CJL202148.1210001

Wang, Y.-J., Li, T.-H., Li, L.-Q., Ning, J.-M., and Zhang, Z.-Z. (2020c). Micro-NIR spectrometer for quality assessment of tea: Comparison of local and global models. *Spectrochim. Acta - Part Mol. Biomol. Spectrosc.* 237, 118403. doi:10.1016/j.saa.2020. 118403

Wang, Y., Li, M., Li, L., Ning, J., and Zhang, Z. (2021c). Green analytical assay for the quality assessment of tea by using pocket-sized NIR spectrometer. *Food Chem.* 345, 128816. doi:10.1016/j.foodchem.2020.128816

Wang, Z. H., Sun, P. Y., Wang, Y. Z., Wei, T. Z., and Liu, J. (2021a). A measurement method in near infrared spectroscopy for reference correction with the homologous optical beams. *J. Instrum.* 16, P10019. doi:10.1088/1748-0221/16/10/P10019

Wang, Z., Yu, Y., Wu, Y., Gao, S., Hu, L., Jian, C., et al. (2022b). Dynamically monitoring lymphatic and vascular systems in physiological and pathological conditions of a swine model via a portable NIR-II imaging system with ICG. *Int. J. Med. Sci.* 19, 1864–1874. doi:10.7150/ijms.71956

Wokadala, O. C., Human, C., Willemse, S., and Emmambux, N. M. (2020). Rapid non-destructive moisture content monitoring using a handheld portable vis–NIR spectrophotometer during solar drying of mangoes (mangifera indica L.). *J. Food Meas. Charact.* 14, 790–798. doi:10.1007/s11694-019-00327-w

Workman, J., and Weyer, L. (2012). *Practical guide and spectral atlas for interpretive near-infrared.* Boca Raton, FL, USA: CRC.

Wu, G., Jiang, Q., Bai, Y., Tian, C., Pan, W., Jin, X., et al. (2020). Nitrogen status assessment for multiple cultivars of strawberries using portable FT-NIR spectrometers combined with cultivar recognition and multivariate analysis. *IEEE Access* 8, 126039–126050. doi:10.1109/ACCESS.2020.3007862

Wu, X., Li, G., and He, F. (2021). Nondestructive analysis of internal quality in pears with a self-made near-infrared spectrum detector combined with multivariate data processing. *Foods* 10, 1315. doi:10.3390/foods10061315

Xiao, P., and Chen, D. (2022). Near infrared spectra data analysis by using machine learning algorithms. *Lect. Notes Netw. Syst.* 506, 532–544. doi:10.1007/978-3-031-10461-9_36

Xiong, Z., Pfeifer, F., and Siesler, H. W. (2016). Evaluating the molecular interaction of organic liquid mixtures using near-infrared spectroscopy. *Appl. Spectrosc.* 70, 635–644. doi:10.1177/0003702816631301

Yakes, B. J., Ellsworth, Z., Karunathilaka, S. R., and Crump, E. (2021). Evaluation of portable sensor and spectroscopic devices for seafood decomposition determination. *Food Anal. Methods* 14, 2346–2356. doi:10.1007/s12161-021-02064-7

Yan, H., Shen, Y., and Siesler, H. W. (2020). Nah-Infrarot-Spektrometer für Alltagsanwendungen. *GIT Labor Fachz* 10, 1–4.

Yan, H., and Siesler, H. W. (2018). Identification of textiles by handheld near infrared spectroscopy: Protecting customers against product counterfeiting. *J. Near Infrared Spectrosc.* 26, 311–321. doi:10.1177/0967033518796669

Yang, B., Zhu, Z., Gao, M., Yan, X., Zhu, X., and Guo, W. (2020a). A portable detector on main compositions of raw and homogenized milk. *Comput. Electron. Agric.* 177, 105668. doi:10.1016/j.compag.2020.105668

Yang, H., Liu, Y., Xiong, Z., and Liang, L. (2020b). Rapid determination of holocellulose and lignin in wood by near infrared spectroscopy and Kernel extreme learning machine. *Anal. Lett.* 53, 1140–1154. doi:10.1080/00032719.2019.1700267

Yang, X., Zhu, L., Huang, X., Zhang, Q., Li, S., Chen, Q., et al. (2022). Determination of the soluble solids content in korla fragrant pears based on visible and near-infrared

spectroscopy combined with model analysis and variable selection. *Front. Plant Sci.* 13, 938162. doi:10.3389/fpls.2022.938162

Yang, Y., Zhang, X., Yin, J., and Yu, X. (2020c). Rapid and nondestructive on-site classification method for consumer-grade plastics based on portable NIR spectrometer and machine learning. *J. Spectrosc.* 2020, 1–8. doi:10.1155/2020/6631234

Yao, S., Aykas, D. P., and Rodriguez-Saona, L. (2021). Rapid authentication of potato chip oil by vibrational spectroscopy combined with pattern recognition analysis. *Foods* 10, 42. doi:10.3390/foods10010042

Yu, H.-D., Zuo, S.-M., Xia, G., Liu, X., Yun, Y.-H., and Zhang, C. (2020a). Rapid and nondestructive freshness determination of Tilapia fillets by a portable near-infrared spectrometer combined with chemometrics methods. *Food Anal. Methods* 13, 1918–1928. doi:10.1007/s12161-020-01816-1

Yu, H., Liu, H., Wang, Q., and van Ruth, S. (2020b). Evaluation of portable and benchtop NIR for classification of high oleic acid peanuts and fatty acid quantitation. *LWT* 128, 109398. doi:10.1016/j.lwt.2020.109398

Yu, Y.-Y., Peng, Y.-C., Chiu, Y.-C., Liu, S.-J., and Chen, C.-P. (2022). Realizing broadband NIR photodetection and ultrahigh responsivity with ternary blend organic photodetector. *Nanomaterials* 12, 1378. doi:10.3390/nano12081378

Yu, Y., Huang, J., Zhu, J., and Liang, S. (2021a). An accurate noninvasive blood glucose measurement system using portable near-infrared spectrometer and transfer learning framework. *IEEE Sens. J.* 21, 1–3519. doi:10.1109/JSEN.2020.3025826

Yu, Y., Zhang, Q., Huang, J., Zhu, J., and Liu, J. (2021b). Nondestructive determination of SSC in korla fragrant pear using a portable near-infrared spectroscopy system. *Infrared Phys. Technol.* 116, 103785. doi:10.1016/j.infrared. 2021.103785

Zambrzycki, S. C., Caillet, C., Vickers, S., Bouza, M., Donndelinger, D. V., Geben, L. C., et al. (2021). Laboratory evaluation of twelve portable devices for medicine quality screening. *PLoS Negl. Trop. Dis.* 15, e0009360. doi:10.1371/journal.pntd.0009360

Zhang, J., Xu, Y., Jiang, Y.-W., Zheng, C.-Y., Zhou, J., and Han, C.-J. (2021a). Recent advances in application of near-infrared spectroscopy for quality detections of grapes and grape products [近红外光谱技术在葡萄及其制品品质检测中的应用研究进 展]. *Guang Pu Xue Yu Guang Pu Fen XiSpectroscopy Spectr. Anal.* 41, 3653–3659. doi:10.3964/j.issn.1000-0593(2021)12-3653-07

Zhang, K., Wang, H., Zhong, L., Liu, L., Huang, R., Zhang, H., et al. (2021b). Evaluation and monitoring of the API content of a portable near infrared instrument combined with chemometrics based on fluidized bed mixing process. *J. Pharm. Innov.* 17, 1136–1147. doi:10.1007/s12247-021-09581-2

Zhang, M., Shen, M., Pu, Y., Li, H., Zhang, B., Zhang, Z., et al. (2022c). Rapid identification of apple maturity based on multispectral sensor combined with spectral shape features. *Horticulturae* 8, 361. doi:10.3390/horticulturae8050361

Zhang, T., Wu, X., Wu, B., Dai, C., and Fu, H. (2022a). Rapid authentication of the geographical origin of milk using portable near-infrared spectrometer and fuzzy uncorrelated discriminant transformation. *J. Food Process Eng.* 45, 40. doi:10.1111/ jfpe.14040

Zhang, Y., Huang, J., Zhang, Q., Liu, J., Meng, Y., and Yu, Y. (2022b). Nondestructive determination of SSC in an apple by using a portable near-infrared spectroscopy system. *Appl. Opt.* 61, 3419–3428. doi:10.1364/AO.455024

Zhao, Y., Fang, S., Ye, Y., and Yu, K. (2021). Chemometric Development Using Portable Molecular Vibrational Spectrometers for Rapid Evaluation of AVC (Valsa Mali Miyabe et Yamada) Infection of Apple Trees. *Vib. Spectrosc.* 114, 103231. doi:10.1016/j. vibspec.2021.103231

Zhong, Z., Liu, X., Luo, X., Zhu, Y., Wang, S., and Huang, Y. (2022). Evaluation of coating uniformity for the digestion-aid tablets by portable near-infrared spectroscopy. *Int. J. Pharm.* 622, 121833. doi:10.1016/j.ijpharm.2022.121833

Zhou, L., Tan, L., Zhang, C., Zhao, N., He, Y., and Qiu, Z. (2022b). A portable NIR-system for mixture powdery food analysis using deep learning. *LWT* 153, 112456. doi:10.1016/j.lwt.2021.112456

Zhou, L., Wang, X., Zhang, C., Zhao, N., Taha, M. F., He, Y., et al. (2022a). Powdery food identification using NIR spectroscopy and extensible deep learning model. *Food Bioprocess Technol.* 15, 2354–2362. doi:10.1007/s11947-022-02866-5

Zhu, C., Fu, X., Zhang, J., Qin, K., and Wu, C. (2022a). Review of portable near infrared spectrometers: Current status and new techniques. *J. Infrared Spectrosc.* 30, 51–66. doi:10.1177/09670335211030617

Zhu, K., Aykas, D. P., Anderson, N., Ball, C., Plans, M., and Rodriguez-Saona, L. (2022b). Nutritional quality screening of oat groats by vibrational spectroscopy using field-portable instruments. *J. Cereal Sci.* 107, 103520. doi:10.1016/j.jcs.2022.103520

Zhuang, X., Su, M., Sun, Y., Yuan, M., Wang, L., Zhang, Z., et al. (2022). A calibration method based on model updating strategy for the quantitative model of Radix Astragali extract. *Microchem. J.* 181, 107690. doi:10.1016/j.microc.2022.107690

Highly sensitive electrochemical immunosensor based on electrodeposited platinum nanostructures confined in silica nanochannels for the detection of the carcinoembryonic antigen

Qinping Guo[1], Xue Fan[2], Fei Yan[2]* and Yinquan Wang[1]*

[1]Shanxi Bethune Hospital, Shanxi Academy of Medical Sciences, Tongji Shanxi Hospital, Third Hospital of Shanxi Medical University, Taiyuan, China, [2]Key Laboratory of Surface and Interface Science of Polymer Materials of Zhejiang Province, Department of Chemistry, Zhejiang Sci-Tech University, Hangzhou, China

In this study, we report a highly sensitive electrochemical immunosensor for carcinoembryonic antigen (CEA) detection based on the electrodeposited platinum nanoparticles (Pt NPs) confined in the ultrasmall nanochannels of vertically ordered mesoporous silica film (VMSF). VMSF bearing amine groups (NH$_2$-VMSF) can be prepared on the indium tin oxide electrode surface via a one-step co-condensation route using an electrochemically assisted self-assembly method, which renders a strong electrostatic effect for [PtCl$_6$]$^{2-}$ and leads to the spatial confinement of Pt NPs inside the silica nanochannels after electrodeposition. The external surface of NH$_2$-VMSF is functionalized with CEA antibodies using glutaraldehyde as a coupling agent, resulting in an electrochemical immunosensing interface with good specificity for CEA detection. Under optimal experimental conditions, high affinity between the CEA antibody and CEA produces a steric hindrance effect for the accessibility of the electrochemical probe ([Fe(CN)$_6$]$^{3-}$) in the bulk solution to the underlying indium tin oxide surface, eventually resulting in the attenuated electrochemical signal and enabling the detection of the CEA with a wide linear range of 0.01 pg/mL~10 ng/mL and a pretty low limit of detection of 0.30 fg/mL. Owing to the signal amplification ability of Pt NPs and the anti-biofouling property of NH$_2$-VMSF, the as-prepared electrochemical immunosensor based on the Pt NPs@NH$_2$-VMSF displays an accurate analysis of the CEA in human serum samples, holding significant promise for health monitoring and clinical diagnosis.

KEYWORDS

platinum nanoparticles, silica nanochannel films, electrochemical immunosensor, carcinoembryonic antigen, anti-fouling detection

1 Introduction

Nanomaterials usually exhibit a large specific surface area and unique magnetic/optical/electrochemical properties that can improve the sensitivity and selectivity of various chemo/biosensors (Mao et al., 2019; Xi et al., 2019; Qiu et al., 2021; Zheng et al., 2021; Huang Y. et al., 2023; Xu et al., 2023; Zhu et al., 2023). Among them, noble metal nanoparticles (NPs) with nanosized structures have garnered significant attention due to their unique physicochemical

properties and large specific surface area compared to their bulk materials, which have been widely used in electroanalytical applications (Lin et al., 2020; Zhao et al., 2020). Platinum (Pt) NPs are a kind of commonly used noble metal NP but unstable and will aggregate because of their high surface energy, resulting in the disappearance of specific desired features at the ultrasmall nanoscale. To control Pt NPs at the nanoscale, organic ligands or particular supported materials are introduced in the preparation procedure (White et al., 2009).

Recently, nanoporous materials have gained significant attention due to their high specific surface area, adjustable structure, and pore size and have exhibited considerable potential in applications such as adsorption/separation, sensing, catalysis, and energy storage applications (Cui et al., 2020; 2021; Zhao et al., 2020; Gong et al., 2022a; Liu et al., 2022). Vertically ordered mesoporous silica films (VMSFs) are a kind of solid nanoporous materials composed of highly ordered and uniform silica nanochannels (2–3 nm in diameter and tens to a hundred nanometers in length) and high porosity (Walcarius, 2021; Huang J. et al., 2023; Deng et al., 2023). In the past decades, an increasing number of electrochemical and electrochemiluminescence sensors have been designed using VMSF as the electrode-modified material (Liang et al., 2021; Su et al., 2022; Wei et al., 2022; Zhou et al., 2022). Although VMSF has unique insulating properties, it has been extensively utilized as an electrode protective layer for the direct and highly sensitive anti-biofouling analysis of complicated media (Wang et al., 2022; Zheng et al., 2022; Zhu et al., 2022). On the one hand, VMSFs bearing a large amount of silanol groups (pK_a = 2–3) display pronounced permselective effects toward targets or probes and simultaneously have excellent molecular sieving capability for them (Luo et al., 2022; Lv et al., 2022). On the other hand, they offer a lot of tiny confined spaces for the synthesis of metal NPs (e.g., gold (Ding et al., 2014a; Huang L. et al., 2023), Pt (Ding and Su, 2015; Li et al., 2020), and nickel (Ding et al., 2020)), polymers (Ding et al., 2014b), and graphene quantum dots (Zhang C. et al., 2023). The Su group employed two methods (namely, direct electrodeposition and chemical reduction) to achieve Pt NPs in silica nanochannels (Ding and Su, 2015; Li et al., 2020). The latter one needs first confinement of polyaniline polymer inside the nanochannels, generating the secondary and tertiary imines for easy complex with $PtCl_6^{2-}$ and subsequently suffering from chemical reduction *in situ*. To the best of our knowledge, simple modification of VMSF with functional groups for adequate incorporation of $PtCl_6^{2-}$ and further electrodeposited growth of Pt NPs has not yet been reported. Moreover, VMSF with functional groups renders the binding site for immobilization of specific recognition elements, exhibiting promising ability for the development of various sensitive and selective electrochemical sensors (Gong et al., 2022b; Ma et al., 2022b; Zhang T. et al., 2023; Chen et al., 2023).

Screening of tumor markers in human serum, especially the level of the carcinoembryonic antigen (CEA), is particularly valuable for the early auxiliary diagnosis and prognosis of various cancers (Zhang et al., 2022; Zhou et al., 2023). CEA concentration in the blood serum of healthy individuals is generally below 5 ng/mL, whereas cancer patients may exhibit levels exceeding 20 ng/mL (Lin et al., 2021). Several strategies have been developed for CEA detection, such as the enzyme-linked immunosorbent assay (Song et al., 2017), electrochemiluminescence method (Zhang et al., 2017),

immunohistochemical method (Zeng et al., 1993), radioimmunoassay (Edgington et al., 1976), fluoroimmunoassay (Huang et al., 2018), and electrochemical immunoassay (Tang et al., 2007; Yan et al., 2023). Among them, electrochemical immunoassay has many advantages because of its low cost, rapid response, high selectivity, easy operation, and portability. Therefore, the development of electrochemical sensors with high sensitivity and anti-fouling capacity for direct detection of the CEA in human serum is highly desirable.

In this work, we demonstrate the use of amino group-functionalized VMSF (NH_2-VMSF) for the confined synthesis of Pt NPs and the design of a highly sensitive electrochemical immunosensor for the CEA. NH_2-VMSF-carrying amino groups provide a strong electrostatic effect for $[PtCl_6]^{2-}$ and lead to the well confinement of Pt NPs after electrodeposition. Such obtained Pt NPs confined in ultrasmall nanochannels of NH_2-VMSF (termed as Pt NPs@NH_2-VMSF) can be obtained in several seconds using a simple and controllable electrochemical method. The external surface of NH_2-VMSF is immobilized with CEA antibodies using glutaraldehyde as a coupling agent, giving rise to an electrochemical immunosensing interface with good specificity for CEA detection. Due to the high affinity between the CEA antibody and CEA on the sensing interface, the steric hindrance effect is enhanced for the accessibility of the electrochemical probe ($[Fe(CN)_6]^{3-}$) in the bulk solution to the underlying ITO surface, ultimately yielding the relationship between the attenuated electrochemical signal and CEA concentration. Benefiting from the signal amplification ability of Pt NPs and the anti-biofouling property of NH_2-VMSF, the developed electrochemical immunosensor based on Pt NPs@NH_2-VMSF can be applied to sensitively and selectively detect CEA in human serum.

2 Materials and methods

2.1 Chemicals and materials

The CEA antigen and anti-CEA antibody, prostate-specific antigen (PSA), and alpha-fetoprotein (AFP) were purchased from Beijing Key-Bio Biotech Co., Ltd. (Beijing, China). S100 calcium-binding protein β was bought from Proteintech (Wuhan, China). C-reactive protein (CRP) was ordered from Nanjing Okay Biotechnology Co., Ltd. (Nanjing, China). Hexadecyl trimethyl ammonium bromide (CTAB), silicon tetraacetate (TEOS), potassium ferricyanide ($K_3[Fe(CN)_6]$, 99.5%), potassium ferrocyanide ($K_4[Fe(CN)_6]$, 99.5%), sodium dihydrogen phosphate dihydrate ($NaH_2PO_4 \cdot 2H_2O$), sodium phosphate dibasic dodecahydrate ($Na_2HPO_4 \cdot 12H_2O$), glutaraldehyde (GA), and chloroplatinic acid hexahydrate ($H_2PtCl_6 \cdot 6H_2O$) were received from Aladdin Biochemical Technology Co., Ltd. (Shanghai, China). 3-Aminopropyltriethoxysilane (APTES) and potassium hydrogen phthalate (KHP) were purchased from Shanghai Macklin Biochemical Co., Ltd. (Shanghai, China). Sodium nitrate ($NaNO_3$), sodium hydroxide (NaOH), and ethanol (99.8%) were purchased from Hangzhou Gaojing Fine Chemical Co., Ltd. (Hangzhou, China). Concentrated hydrochloric acid (HCl) and concentrated sulfuric acid (H_2SO_4) were obtained from Shuanglin Inorganic Chemical Plant

(Hangzhou, China). Phosphate buffer solution (PBS) was prepared by mixing Na_2HPO_4 and NaH_2PO_4.

ITO-coated glasses (<17 Ω/square, thickness: 100 ± 20 nm) were purchased from Zhuhai Kaivo Optoelectronic Technology Co., Ltd. (China). To get a clean surface, the ITO electrode was immersed in 1 M NaOH solution overnight and then successively sonicated in acetone, ethanol, and ultrapure water. Ultrapure water (18.2 MΩ cm) used in the experiments was prepared by using the Milli-Q system (Millipore Company).

2.2 Measurements and instrumentations

Transmission electron microscopy (TEM) images were captured using a transmission electron microscope (JEM-2100, JEOL, Japan). Field-emission scanning electron microscopy (SEM) images and energy dispersive X-ray mapping spectroscopy (EDS mapping) data were analyzed using a scanning electron microscope (Sigma500, Zeiss, Germany). The X-ray photoelectron spectroscopy (XPS) data were collected on a PHI5300 electron spectrometer using 250 W, 14 kV, and Mg Kα radiation (PE Ltd., United States). All electrochemical measurements, including cyclic voltammetry (CV), electrochemical impedance spectroscopy (EIS), and differential pulse voltammetry (DPV), were conducted on a conventional three-compartment electrochemical cell by Autolab (PGSTAT302N) electrochemical workstation (Metrohm, Switzerland), with the modified ITO electrode, an Ag/AgCl electrode, and a platinum wire electrode as the working, reference, and counter electrodes, respectively. The scan rate for CV tests was 50 mV/s. The parameters for DPV measurements included step potential (0.005 V), pulse amplitude (0.05 V), pulse time (0.05 s), and interval time (0.2 s).

2.3 Preparation of SM@NH₂-VMSF/ITO and GA/Pt NPs@NH₂-VMSF/ITO electrodes

The NH_2-VMSF/ITO could be grown on the bare ITO electrode (1 cm × 0.5 cm) by the electrochemically assisted self-assembly (EASA) method within 10 s (Etienne et al., 2009; Ma et al., 2022a; Ma N. et al., 2022). In brief, CTAB (1.585 g) was first dissolved in a mixture solution consisting of 0.1 M $NaNO_3$ aqueous solution (20 mL, pH 2.6) and ethanol (20 mL). After the addition of APTES (0.318 mL), the pH of the mixed solution was adjusted to 2.97 using 6 M HCl. Subsequently, TEOS (2.372 mL) was added, and the obtained precursor solution was stirred at room temperature for 2.5 h. VMSF-bearing amino groups (NH_2-VMSF) were prepared on the bare ITO electrode surface by immersing the clean ITO electrode in the aforementioned aged solution and applying a constant current density (-0.70 mA·cm^{-2}) for 10 s. Then, the finally obtained electrode was rapidly washed with ultrapure water and aged for 12 h at 120°C. As for the directly as-prepared modified electrode, surfactant micelles (SMs) made up of CTAB were positioned inside the nanospace of silica nanochannels, designated as SM@NH_2-VMSF/ITO.

GA-functionalized SM@NH_2-VMSF/ITO, termed GA/SM@NH_2-VMSF/ITO, was obtained using a simple drop-casting procedure, which could act as a cross-linking agent for further covalent immobilization of specifically recognized antibodies. Specifically, 5% GA (50 μL) was dropped onto the SM@NH_2-VMSF/ITO electrode surface and incubated at 37°C for 30 min in a dark place. Then, the GA/SM@NH_2-VMSF/ITO electrode was placed into a 0.1 M HCl/ethanol solution under stirring for 5 min to remove the SM, generating open channels for mass transport. Such resulting electrode was denoted as GA/NH_2-VMSF/ITO. Pt nanoparticles were electrodeposited inside NH_2-VMSF using chronoamperometry, and the growth of Pt NPs can be well controlled when applying a constant potential of -0.2 V for different durations. 3.86 mM of $H_2PtCl_6·6H_2O$ electrodeposition solution was composed of 100 mg/mL $H_2PtCl_6·6H_2O$ (1 mL) and 0.1 M H_2SO_4 (49 mL). In short, the GA/NH_2-VMSF/ITO electrode was immersed in the aforementioned electrodeposition solution and applied a constant potential of -0.2 V for 2 s, finally achieving the Pt NPs confined into the nanochannels of NH_2-VMSF, designated as GA/Pt NPs@NH_2-VMSF/ITO.

2.4 Preparation of the electrochemical immunosensor based on the GA/Pt NPs@ NH₂-VMSF/ITO electrode and electrochemical determination of CEA

An electrochemical immunosensor for CEA detection was prepared by immersing the GA/Pt NPs@NH_2-VMSF/ITO electrode in a 10 μg/mL antibody-CEA (50 μL) solution and incubating at 4°C for 1 h. After being rinsed with the residual antibody-CEA with 0.01 M PBS (pH 7.4), the immunosensing interface was eventually obtained, named the Ab/GA/Pt NPs@ NH_2-VMSF/ITO electrode.

CEA solution (50 μL) with various concentrations was dropped onto the Ab/GA/Pt NPs@NH_2-VMSF/ITO electrochemical immunosensor and incubated at 4°C for 1 h. Then, the residual CEA solution was washed off using 0.01 M PBS (pH 7.4). DPV was utilized to measure the electrochemical signal of $[Fe(CN)_6]^{3-}$ before and after the interaction between Ab/ GA/Pt NPs@NH_2-VMSF/ITO and CEA. Moreover, the standard addition method was used for the determination of CEA in fetal bovine serum to prove the reliability of the constructed Ab/GA/Pt NPs@NH_2-VMSF/ITO immunosensor in real samples. The fetal bovine serum was diluted by a factor of 50 using 0.01 M PBS (pH 7.4), and the CEA with a known concentration was added to the serum sample. Finally, the same detection procedure was conducted on the CEA detection in the serum sample using the Ab/GA/Pt NPs@NH_2-VMSF/ITO electrochemical immunosensor.

3 Results and discussion

3.1 Preparation of a Pt NPs@NH₂-VMSF/ITO-based immunosensor and its sensing mechanism for CEA

Scheme 1 reveals the fabrication process of the ITO electrode decorated with NH_2-VMSF, containing Pt nanostructures inside
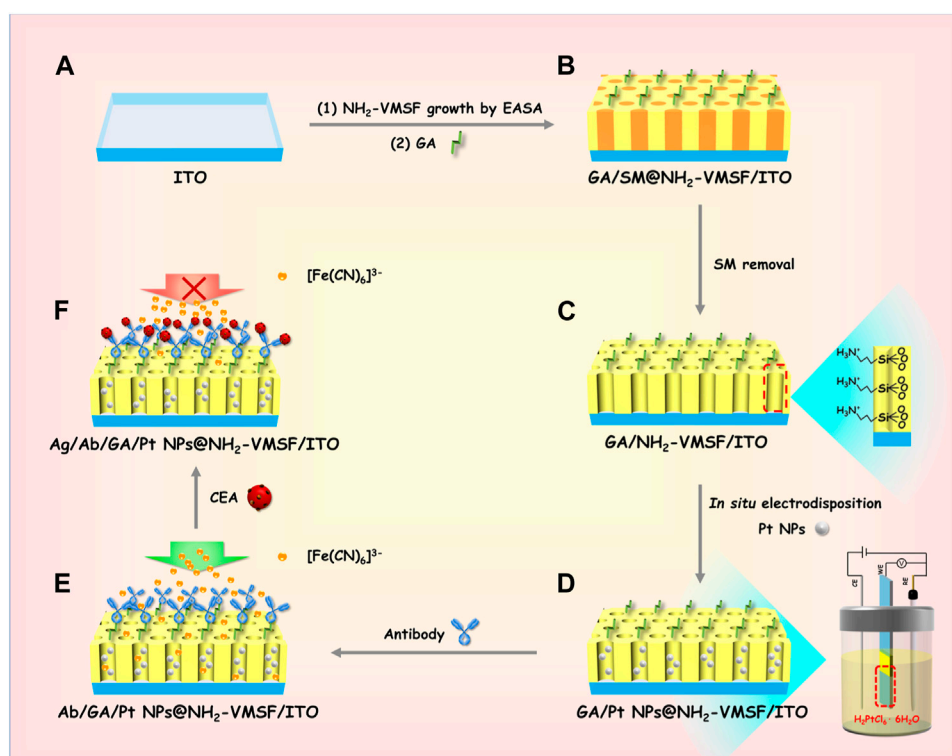
SCHEME 1
Schematic illustration of the preparation of the Ab/GA/Pt NPs@NH$_2$-VMSF/ITO electrode **(A–E)** and its sensing mechanism for the CEA **(A–F)**.

the inner nanochannels, while simultaneously modifying the anti-CEA antibody on the outmost surface using a convenient and controllable electrochemical method. The resulting electrode is termed as Ab/GA/Pt NPs@NH$_2$-VMSF/ITO, combining the electrocatalyst effect of Pt NPs and the specific recognition capacity of the anti-CEA antibody. The growth of NH$_2$-VMSF on the ITO electrode surface is accomplished by the EASA approach. Due to the presence of amine groups on both the inner silica walls and external surface, NH$_2$-VMSF-encased surfactant micelles inside the nanochannels are used to functionalize with a linker agent (glutaraldehyde, GA) (denoted as GA/SM@NH$_2$-VMSF/ITO, as shown in Scheme 1B), which can guarantee further modification of the anti-CEA antibody on the external surface of NH$_2$-VMSF. After exclusion of SMs, NH$_2$-VMSF possesses opened nanochannels and protonated amino groups on the silica walls, designated as GA/NH$_2$-VMSF/ITO (Scheme 1C), which renders the active sites for electrosynthesis of Pt NPs *in situ* to obtain GA/Pt NPs@NH$_2$-VMSF/ITO (Scheme 1D). Finally, the anti-CEA antibody is anchored to the external surface of NH$_2$-VMSF through GA, achieving the Ab/GA/Pt NPs@NH$_2$-VMSF/ITO sensor (Scheme 1E). The target CEA can be specially recognized on the Ab/GA/Pt NPs@NH$_2$-VMSF/ITO sensing interface, resulting in the hampered mass transport of the [Fe(CN)$_6$]$^{3-}$ probe in the bulk solution to the underlying ITO electrode surface through the silica nanochannels of NH$_2$-VMSF (Scheme 1F). Therefore, the decreased electrochemical current signal of [Fe(CN)$_6$]$^{3-}$ is associated with the CEA concentration,

leading to the quantitative analytical method of detection of the CEA.

3.2 Characterization of NH$_2$-VMSF/ITO and Pt NPs@NH$_2$-VMSF/ITO electrodes

Figure 1 depicts the transmission electron microscopy and electrochemical characterization of NH$_2$-VMSF. A top-view TEM image of NH$_2$-VMSF displays a crack-free structure with numerous uniform pores of nanometer-sized diameter (ca. 2–3 nm) (Figure 1A). As shown in Figure 1B, the nanochannel of the NH$_2$-VMSF is homogeneous and its length is 79 nm. Figure 1C shows the CV curves of ITO, SM@NH$_2$-VMSF/ITO, and NH$_2$-VMSF/ITO electrodes in 0.05 M KHP containing 0.5 mM K$_3$[Fe(CN)$_6$]. The ITO electrode exhibits obvious redox peaks originating from the redox reaction of [Fe(CN)$_6$]$^{3-}$. However, the CV curve measured by the SM@NH$_2$-VMSF/ITO electrode shows no obvious redox peak, which is attributed to the hydrophobic environment consisting of CTAB SM and leads to the obstructed transport of hydrophilic [Fe(CN)$_6$]$^{3-}$ within nanochannels. The NH$_2$-VMSF/ITO electrode without SM inside the nanochannels not only has an open channel for free diffusion of [Fe(CN)$_6$]$^{3-}$ but also displays electrostatic attraction for negatively charged [Fe(CN)$_6$]$^{3-}$, eventually giving rise to amplified redox signals compared to those at the ITO. These results indicate that NH$_2$-VMSF on the ITO electrode is intact without cracks, and the
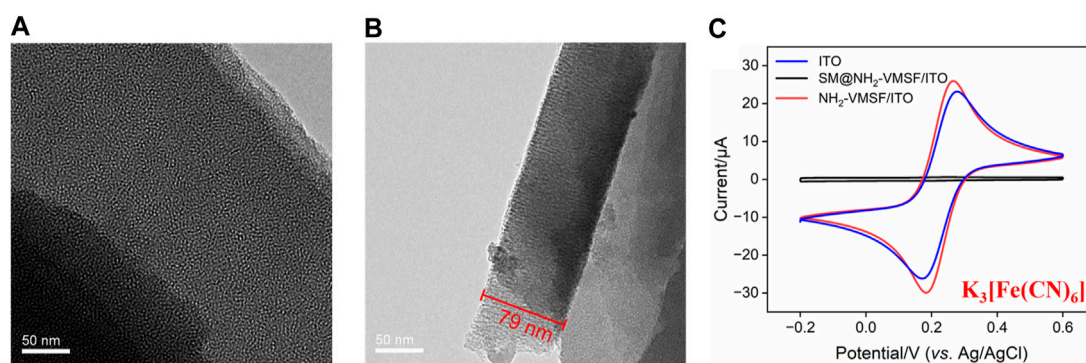
FIGURE 1
(A) Top-view TEM image of NH_2-VMSF. **(B)** Cross-sectional TEM image of NH_2-VMSF. **(C)** CV curves of the ITO, SM@NH_2-VMSF/ITO, and NH_2-VMSF/ITO electrodes in 0.05 M KHP containing 0.5 mM $K_3[Fe(CN)_6]$.
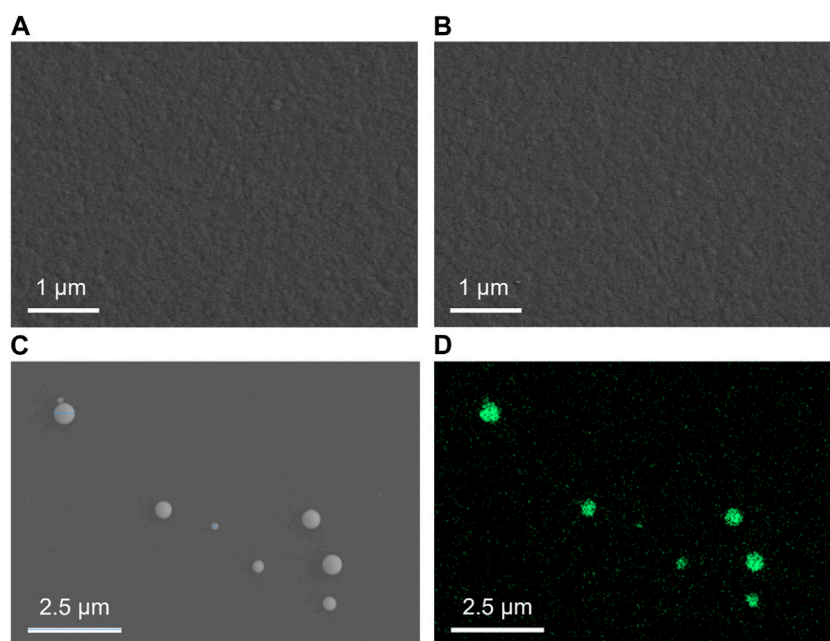
FIGURE 2
Top-view SEM images of NH_2-VMSF/ITO **(A)** and Pt NPs@NH_2-VMSF/ITO before **(B)** and after **(C)** the dissolution of NH_2-VMSF. **(D)** EDS elemental mapping of Pt NPs at the Pt NPs@NH_2-VMSF/ITO electrode after the dissolution of NH_2-VMSF.

electrochemical response of $[Fe(CN)_6]^{3-}$ at the NH_2-VMSF/ITO electrode can be enlarged, showing the significant potential of NH_2-VMSF/ITO for the design of gated-controlled electrochemical sensors.

Top-view SEM images in Figures 2A, B show the surface of the NH_2-VMSF/ITO electrode before and after the electrodeposition of Pt NPs. Both surfaces appear relatively smooth without obvious differences between NH_2-VMSF/ITO and Pt NPs@NH_2-VMSF/ITO, indicating that Pt NPs are confined inside the nanochannels. Figures 2C, D display the top-view SEM image and EDS elemental mapping of Pt NPs after dissolution of NH_2-VMSF by 0.1 M NaOH (50 μL). As seen, Pt NPs distributed on the surface of the electrode have sizes ranging from 160 to 260 nm, which is

probably due to the aggregation of Pt NPs after losing the protection of NH_2-VMSF and also confirms the successful electrodeposition of Pt NPs within the nanochannels of NH_2-VMSF.

To further verify the successful electrodeposition of Pt NPs into the nanochannels of NH_2-VMSF, XPS analysis was conducted, as shown in Figure 3. As demonstrated, the presence of N and Pt in XPS data is derived from amino groups of NH_2-VMSF and electrodeposited Pt NPs, respectively. In addition, C, O, and Si elements are from the NH_2-VMSF structure. All the aforementioned results confirm the successful preparation of the Pt NPs@NH_2-VMSF/ITO electrode.
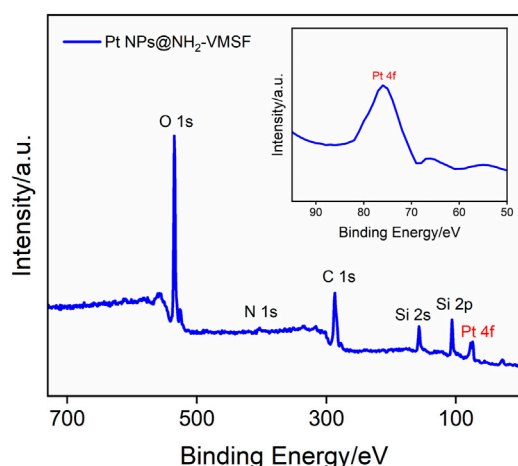
FIGURE 3
XPS survey spectra of Pt NPs@NH$_2$-VMSF/ITO.

3.3 Characterization of the Pt NPs@NH$_2$-VMSF/ITO-based electrochemical immunosensor

CV and EIS were used as electrochemical methods to investigate the interfacial state changes during the construction of the Ab/GA/Pt NPs@NH$_2$-VMSF/ITO sensor. Figure 4 displays the CV (A) and EIS (B) curves of NH$_2$-VMSF/ITO, GA/NH$_2$-VMSF/ITO, Pt NPs@NH$_2$-VMSF/ITO, GA/Pt NPs@NH$_2$-VMSF/ITO, Ab/GA/Pt NPs@NH$_2$-VMSF/ITO, and Ag/Ab/GA/Pt NPs@NH$_2$-VMSF/ITO electrodes in 50 mM KHP containing 0.5 mM [Fe(CN)$_6$]$^{3-}$. The cross-linking of GA with amino groups at the entrance of the silica nanochannels causes a decrease in redox peak current values of [Fe(CN)$_6$]$^{3-}$ at the GA/NH$_2$-VMSF/ITO and GA/Pt NPs@NH$_2$-VMSF/ITO, in comparison with those obtained at the NH$_2$-VMSF/ITO and Pt NPs@NH$_2$-VMSF/ITO (Figure 4A). After the successful electrodeposition of Pt NPs into the nanochannels of

NH$_2$-VMSF, the magnitude of redox peak currents significantly increased due to the signal amplification capacity of Pt NPs. The redox peak currents further decrease after covalently attaching Ab to the GA/Pt NPs@NH$_2$-VMSF/ITO surface, which is attributed to the insulating property of proteins hindering the mass transfer of electrons on the electrode surface. Upon immobilization of CEA, the redox current values remarkably decrease, confirming the successful formation of the antibody–antigen immunocomplex at the sensing interface. EIS plots shown in Figure 4B consist of a semicircle part in the high-frequency region and a linear part in the low-frequency region, which are associated with the electron transfer and diffusion processes, respectively. Electron transfer resistance (R_{ct}) can be extracted from the magnitude of the semicircle diameter, showing the electron transfer variation between different electrodes. EIS measurements in Figure 4B reveal R_{ct} of the same electrodes shown in Figure 4A. Similar variation is observed, and GA/Pt NPs@NH$_2$-VMSF/ITO exhibits lower R_{ct} compared to GA/NH$_2$-VMSF/ITO, indicating that Pt NPs, as a kind of excellent electronic conductivity material, improve electron transfer ability on the electrode interface. Moreover, R_{ct} significantly increases after immobilization of the anti-CEA antibody and target CEA, demonstrating that the formed antibody–antigen immunocomplex indeed obstructs the diffusion of electrons and further proving the feasible detection capacity of the developed Ab/GA/Pt NPs@NH$_2$-VMSF/ITO.

3.4 Optimization of experimental conditions

There are several factors that affect the analytical performance of the Ab/GA/Pt NPs@NH$_2$-VMSF/ITO sensor, including the electrodeposition time of Pt NPs and the incubation time of the anti-CEA antibody or CEA. First, we studied the performance of the developed sensor with various electrodeposition times of Pt NPs ranging from 1 s to 10 s (Figure 5A). When the electrodeposition time increases from 1 s to 2 s, the obtained DPV signal for CEA increases due to the increased amount of Pt NPs and reaches its
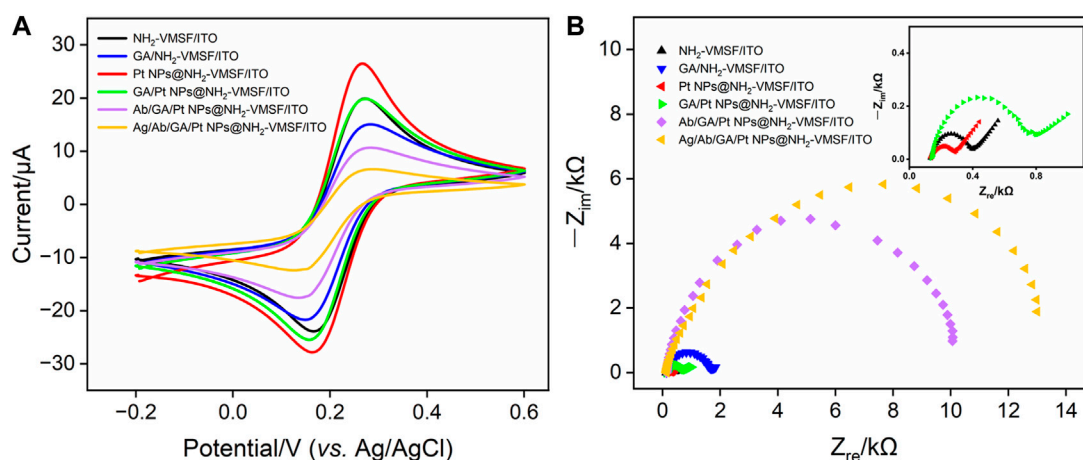
FIGURE 4
(A) CV curves of different electrodes in 50 mM KHP containing 0.5 mM K$_3$[Fe(CN)$_6$] and **(B)** EIS curves of different electrodes in 0.1 M KCl containing 2.5 mM [Fe(CN)$_6$]$^{3-}$/[Fe(CN)$_6$]$^{4-}$.
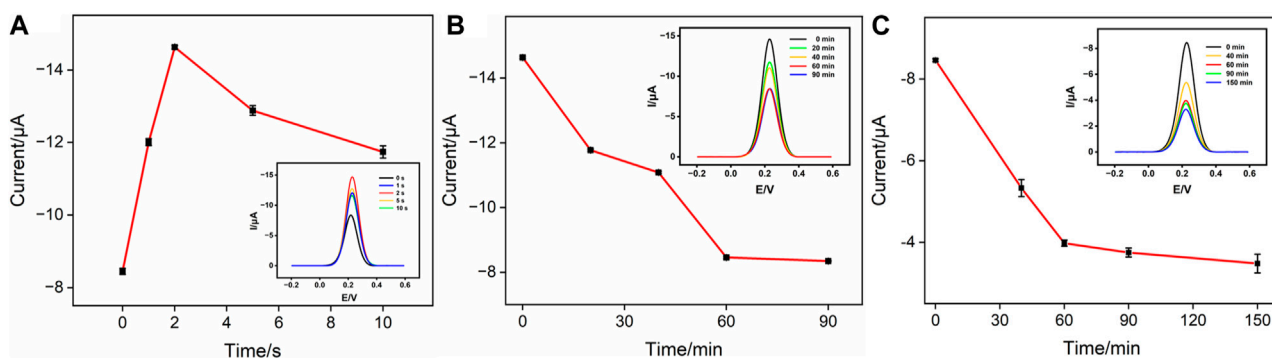
FIGURE 5
(A) Cathodic peak currents measured at the GA/Pt NPs@NH$_2$-VMSF/ITO in 50 mM KHP containing 0.5 mM K$_3$[Fe(CN)$_6$] at different deposition times of Pt NPs. The inset shows its corresponding DPV curves. **(B)** Cathodic peak currents measured at the Ab/GA/Pt NPs@NH$_2$-VMSF/ITO in 50 mM KHP containing 0.5 mM K$_3$[Fe(CN)$_6$] at different incubation times for the anti-CEA antibody. The inset shows its corresponding DPV curves. **(C)** Cathodic peak currents measured at the Ag/Ab/GA/Pt NPs@NH$_2$-VMSF/ITO in 50 mM KHP containing 0.5 mM K$_3$[Fe(CN)$_6$] at different incubation times for the CEA. The inset shows its corresponding DPV curves.
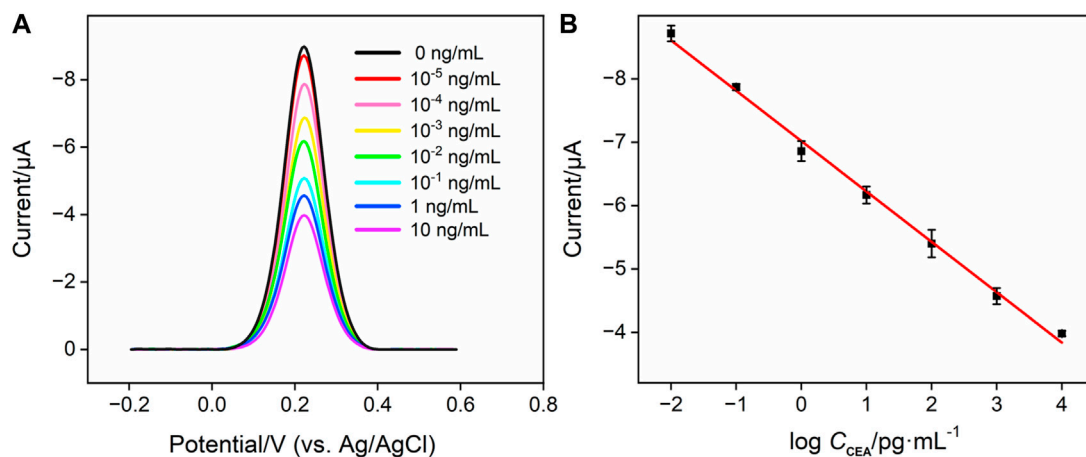
FIGURE 6
(A) DPV responses of the Ag/Ab/GA/Pt NPs@NH$_2$-VMSF electrode to various concentrations of CEA in 0.01 M PBS (pH 7.4). **(B)** Corresponding calibration curves. Error bars refer to the standard deviations of three measurements.

maximum when the deposition time is set to 2 s. When the electrodeposition time further increases from 2 s to 10 s, the signal gradually decreases. This decrease can be attributed to the reduced effective space of NH$_2$-VMSF's nanochannels for accessible transport of the [Fe(CN)$_6$]$^{3-}$ probe in the bulk solution. Subsequently, we investigated the incubation time of the anti-CEA antibody. As displayed in Figure 5B, it could be found that the peak current intensity decreases as the incubation time increases up to 60 min. This is because the amount of anti-CEA immobilized on the electrode is approaching saturation. Similarly, the effect of incubation time for the CEA on the electrochemical response is shown in Figure 5C. It is evident that as the incubation time increases, the peak current signal gradually decreases. After incubation for more than 60 min, the signal changes become minimal, indicating that the immunocomplex formed between the CEA and anti-CEA antibody has reached saturation. Therefore, 60 min is determined to be the optimal incubation time.

3.5 Quantitative determination of CEA using the fabricated Ab/GA/Pt NPs@NH$_2$-VMSF/ITO immunosensor

To evaluate the analytical performance of the Ab/GA/Pt NPs@ NH$_2$-VMSF/ITO sensor, we tested it in detecting the CEA with various concentrations under optimized conditions using the DPV technique. As shown in Figure 6A, the cathodic peak current decreased progressively with the increase in the concentration of the CEA due to the continuous formation of the antibody–antigen complex at the sensing interface. A good linear relationship is displayed between the DPV signal (I_{DPV}) and the logarithm of the CEA concentration (C_{CEA}) in the range of 0.01 pg/mL to 10 ng/mL (Figure 6B), yielding a linear regression equation of I_{DPV} (μA) = 0.796 logC_{CEA}-7.02 (R^2 = 0.996). Furthermore, the limit of detection (LOD) calculated is 0.3 fg/mL at the signal-to-noise ratio of 3 (S/N = 3). We compare the related analytical parameters and construction

TABLE 1 Comparison of the analytical performances of different methods for the determination of the CEA.

Sensing platform	Method	Detection range (ng/mL)	LOD (pg/mL)	Step	Construction time (h)	Reference
BSA/Ab/Pd@Pt/MoS$_2$-Gr/GCE	EC	0.00001–100	0.005	13	39	Lin et al. (2021)
CuO NPs/Ag/BSA/Ab/MB	Colorimetry	0.05–100	26	8	5	Li et al. (2017)
PdCu-Ab$_2$/Ag/Ab$_1$/BSA/AuNPs/GCE	EC	0.0001–10	0.08	7	16	Jiao et al. (2017)
GO-PEI-Ru-AuNPs-Ab$_2$/Ag/Ab$_1$/AuNFs/pL-Cys/GCE	ECL	0.0001–80	0.045	12	37	Yuan et al. (2018)
CEA aptamer/ZnS-CdS/MoS$_2$/GCE	ECL	0.05–20	30	8	60	Wang et al. (2016)
Ab/AuNPs@nafion/FC@CHIT/GCE	EC	0.03–100	10	9	8	Shi and Ma (2011)
Ab/GA/Pt NPs@NH$_2$-VMSF/ITO	EC	0.0001–10	0.0003	7	5	This work

BSA, bovine serum albumin; Ab, the antibody of the CEA; MoS$_2$, molybdenum disulfide; Gr, graphene; GCE, glassy carbon electrode; CuO NPs, copper oxide nanoparticle; Ag, carcinoembryonic antigen; MB, magnetic bead; PdCu, porous PdCu nanoparticles; AuNPs, gold nanoparticles; GO, graphene oxide; PEI, polyethylenimine; Ru, the luminophor tris (4,40-dicarboxylicacid-2, 20-bipyridyl) ruthenium (II) dichloride (Ru(dcbpy)$_3$$^{2+}$); AuNFs, flower-like gold nanoparticles; pL-Cys, polyamino acid L-cysteine; ZnS–CdS, ZnS–CdS nanoparticle; FC: K$_3$ [Fe(CN)$_6$]; CHIT, chitosan.
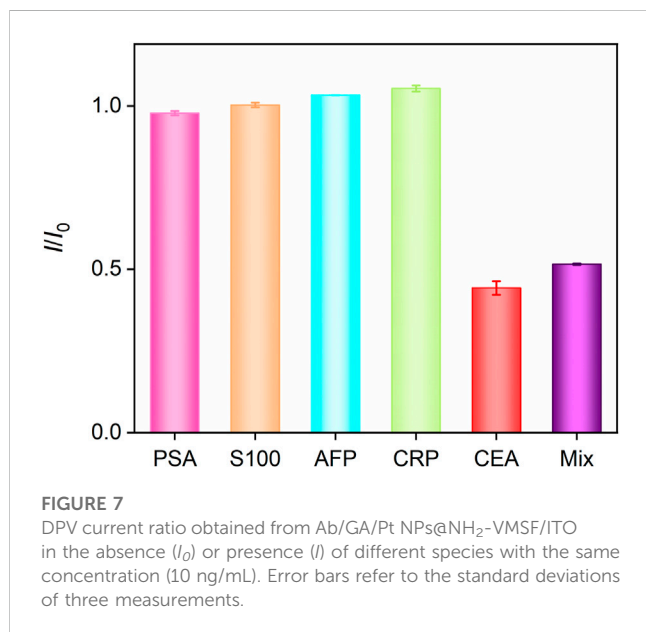
FIGURE 7
DPV current ratio obtained from Ab/GA/Pt NPs@NH$_2$-VMSF/ITO in the absence (I_0) or presence (I) of different species with the same concentration (10 ng/mL). Error bars refer to the standard deviations of three measurements.

strategy of the Ab/GA/Pt NPs@NH$_2$-VMSF/ITO sensor with the other reported sensors. As shown in Table 1, our fabricated Ab/GA/Pt NPs@NH$_2$-VMSF/ITO strategy has a low LOD and simple preparation steps. Moreover, the developed sensor not only achieves dual signal amplification through the electrocatalysis ability of Pt NPs and the electrostatic enrichment effect of VMSF at the electrode interface but also has the advantage of a shorter construction time.

3.6 Selectivity of the fabricated Ab/GA/Pt NPs@NH$_2$-VMSF/ITO immunosensor

The selectivity of the fabricated Ab/GA/Pt NPs@NH$_2$-VMSF/ITO sensor were studied by multiple potential interfering substances, including the PSA, S100 calcium-binding protein β, AFP, and CRP. As shown in Figure 7, the Ab/GA/Pt NPs@NH$_2$-VMSF/ITO immunosensor demonstrates excellent signal response to the CEA and a mixture of the aforementioned substances containing the CEA while showing almost no response to other interfering substances. This indicates that our sensing platform has high selectivity to the CEA, resulting from the specific binding of the anti-CEA antibody and CEA complex.

3.7 Detection of CEA in real samples

To validate the reliability and accuracy of the developed Ab/GA/Pt NPs@NH$_2$-VMSF/ITO sensor, we conducted real sample testing by detecting the CEA amount in fetal bovine serum using the standard addition method. After diluting the fetal bovine serum by a factor of 50 using 0.01 M PBS (pH 7.4), we added 0.1 pg/mL, 10 pg/mL, and 1000 pg/mL of CEA and measured the electrochemical signals by DPV. The added known and tested concentrations of the CEA are designated as "C_{added}" and "C_{found}". In addition, the recovery is defined as the concentration ratio ((C_{added}/C_{found})×100%), which is used to evaluate the detection performance of the fabricated Ab/GA/Pt NPs@NH$_2$-VMSF/ITO in real samples. Generally, recovery ranging from 90.0% to 110% is considered for high accuracy. The relative standard deviation (RSD) value represents the deviation of three measurements disseminated around the average value, which is expressed as the ratio of the standard deviation to the average value. The lower the RSD, the closer the measured values are to the average value, indicating good precision. As shown in Table 2, the recoveries of the CEA obtained in the aforementioned fetal bovine serum samples range from 104.5% to 107.4% with low RSD values (<5.7%). These results demonstrate the promising potential of the proposed Ab/GA/Pt NPs@NH$_2$-VMSF/ITO sensor for sensitive detection of the CEA in clinical applications.

TABLE 2 Recoveries of the CEA in the fetal bovine serum sample (n = 3).

Sample	C_{Added} (pg·mL^{-1})	C_{Found} (pg·mL^{-1})	Recovery (%)	RSD (%)
Serum	0.1000	0.1060	106.0	3.1
	10.00	10.45	104.5	5.7
	1000	1074	107.4	2.8

4 Conclusion

In summary, Pt NPs confined in the silica nanochannels of NH$_2$-VMSF without any protecting ligands have been successfully synthesized on the ITO electrode surface using a simple electrochemical method. The CEA antibody covalently modified on the external surface of NH$_2$-VMSF endows the sensor with good specificity for CEA detection. With the help of the [Fe(CN)$_6$]$^{3-}$ probe in the bulk solution, the high affinity between the CEA antibody and CEA on the sensing interface forms the steric hindrance effect for the accessibility of [Fe(CN)$_6$]$^{3-}$ to the underlying ITO surface, resulting in an attenuated electrochemical signal and allowing the detection of the CEA with a wide linear range of 0.01 pg/mL~10 ng/mL and a pretty low limit of detection of 0.30 fg/mL. Combining the signal amplification ability of Pt NPs and the anti-biofouling property of NH$_2$-VMSF, the presented sensing strategy can be directly applied in detecting the CEA in human serum samples, which is helpful for the analysis of tumor-related biomarkers in clinical diagnosis.

Data availability statement

The original contributions presented in the study are included in the article/Supplementary material; further inquiries can be directed to the corresponding authors.

Author contributions

QG: data curation, formal analysis, methodology, and writing–original draft. XF: formal analysis, methodology, validation, and writing–original draft. FY: project administration, supervision, and writing–review and editing. YW: conceptualization, supervision, and writing–review and editing.

Funding

Conflict of interest

The authors declare that the research was conducted in the absence of any commercial or financial relationships that could be construed as a potential conflict of interest.

Publisher's note

All claims expressed in this article are solely those of the authors and do not necessarily represent those of their affiliated organizations, or those of the publisher, the editors, and the reviewers. Any product that may be evaluated in this article, or claim that may be made by its manufacturer, is not guaranteed or endorsed by the publisher.

References

Chen, D., Luo, X., and Xi, F. (2023). Probe-integrated electrochemical immunosensor based on electrostatic nanocage array for reagentless and sensitive detection of tumor biomarker. *Front. Chem.* 11, 1121450. doi:10.3389/fchem.2023.1121450

Cui, Y., Duan, W., Jin, Y., Wo, F., Xi, F., and Wu, J. (2021). Graphene quantum dot-decorated luminescent porous silicon dressing for theranostics of diabetic wounds. *Acta Biomater.* 131, 544–554. doi:10.1016/j.actbio.2021.07.018

Cui, Y., Duan, W., Jin, Y., Wo, F., Xi, F., and Wu, J. (2020). Ratiometric fluorescent nanohybrid for noninvasive and visual monitoring of sweat glucose. *ACS Sens.* 5, 2096–2105. doi:10.1021/acssensors.0c00718

Deng, X., Lin, X., Zhou, H., Liu, J., and Tang, H. (2023). Equipment of vertically-ordered mesoporous silica film on electrochemically pretreated three-dimensional graphene electrodes for sensitive detection of methidazine in urine. *Nanomaterials* 13, 239. doi:10.3390/nano13020239

Ding, J., Li, X., Zhou, L., Yang, R., Yan, F., and Su, B. (2020). Electrodeposition of nickel nanostructures using silica nanochannels as confinement for low-fouling enzyme-free glucose detection. *J. Mat. Chem. B* 8, 3616–3622. doi:10.1039/c9tb02472g

Ding, L., Li, W., Sun, Q., He, Y., and Su, B. (2014a). Gold nanoparticles confined in vertically aligned silica nanochannels and their electrocatalytic activity toward ascorbic acid. *Chem.-Eur. J.* 20, 12777–12780. doi:10.1002/chem.201403426

Ding, L., Li, W., Wang, Q., Sun, Q., He, Y., and Su, B. (2014b). Vertically oriented silica mesochannels as the template for electrodeposition of polyaniline nanostructures and their electrocatalytic and electroanalytical applications. *Chem.-Eur. J.* 20, 1829–1833. doi:10.1002/chem.201303807

Ding, L., and Su, B. (2015). A non-enzymatic hydrogen peroxide sensor based on platinum nanoparticle-polyaniline nanocomposites hosted in mesoporous silica film. *J. Electroanal. Chem.* 736, 83–87. doi:10.1016/j.jelechem.2014.11.001

Edgington, T. S., Plow, E. F., Chavkin, C. I., Deheer, D. T., and Nakamura, R. M. (1976). The influence of CEA-S from different tumors and of CEA as 125I ligands on the specificity of the CEA-S radioimmunoassay. *B. Cancer* 63, 673–688.

Etienne, M., Goux, A., Sibottier, E., and Walcarius, A. (2009). Oriented mesoporous organosilica films on electrode: a new class of nanomaterials for sensing. *J. Nanosci. Nanotechno.* 9, 2398–2406. doi:10.1166/jnn.2009.se39

Gong, J., Tang, H., Wang, M., Lin, X., Wang, K., and Liu, J. (2022a). Novel three-dimensional graphene nanomesh prepared by facile electro-etching for improved

electroanalytical performance for small biomolecules. *Mat. Des.* 215, 110506. doi:10.1016/j.matdes.2022.110506

Gong, J., Zhang, T., Luo, T., Luo, X., Yan, F., Tang, W., et al. (2022b). Bipolar silica nanochannel array confined electrochemiluminescence for ultrasensitive detection of SARS-CoV-2 antibody. *Biosens. Bioelectron.* 215, 114563. doi:10.1016/j.bios.2022.114563

Huang, J., Zhang, T., Zheng, Y., and Liu, J. (2023a). Dual-mode sensing platform for cancer antigen 15-3 determination based on a silica nanochannel array using electrochemiluminescence and electrochemistry. *Biosensors* 13, 317. doi:10.3390/bios13030317

Huang, L., Su, R., and Xi, F. (2023b). Sensitive detection of noradrenaline in human whole blood based on Au nanoparticles embedded vertically-ordered silica nanochannels modified pre-activated glassy carbon electrodes. *Front. Chem.* 11, 1126213. doi:10.3389/fchem.2023.1126213

Huang, Y., Ding, Z., Li, Y., Xi, F., and Liu, J. (2023c). Magnetic nanozyme based on loading nitrogen-doped carbon dots on mesoporous Fe$_3$O$_4$ nanoparticles for the colorimetric detection of glucose. *Molecules* 28, 4573. doi:10.3390/molecules28124573

Huang, Z., Zhai, X. M., Wang, H., Deng, Q. T., Li, K., Liu, B. S., et al. (2018). Simultaneous quantitation of carbohydrate antigen 125 and carcinoembryonic antigen in human serum via time-resolved fluoroimmunoassay. *Clin. Chim. Acta.* 483, 222–226. doi:10.1016/j.cca.2018.05.003

Jiao, L., Zhang, L., Du, W., Liu, S., Wei, Q., and Li, H. (2017). Robust enzyme-free electrochemical immunoassay of CEA enhanced by porous PdCu nanoparticles. *Electrochim. Acta.* 252, 374–380. doi:10.1016/j.electacta.2017.08.188

Li, B., Lai, G., Zhang, H., Hu, S., and Yu, A. (2017). Copper chromogenic reaction based colorimetric immunoassay for rapid and sensitive detection of a tumor biomarker. *Anal. Chim. Acta.* 963, 106–111. doi:10.1016/j.aca.2017.01.030

Li, X., Zhou, L., Ding, J., Sun, L., and Su, B. (2020). Platinized silica nanoporous membrane electrodes for low-fouling hydrogen peroxide detection. *ChemElectroChem* 7, 2081–2086. doi:10.1002/celc.202000321

Liang, R., Jiang, J., Zheng, Y., Sailjoi, A., Chen, J., Liu, J., et al. (2021). Vertically oriented mesoporous silica film modified fluorine-doped tin oxide electrode for enhanced electrochemiluminescence detection of lidocaine in serum. *RSC Adv.* 11, 34669–34675. doi:10.1039/d1ra06375h

Lin, J., Li, K., Wang, M., Chen, X., Liu, J., and Tang, H. (2020). Reagentless and sensitive determination of carcinoembryonic antigen based on a stable Prussian blue modified electrode. *RSC Adv.* 10, 38316–38322. doi:10.1039/d0ra06751b

Lin, Y., Xiong, C., Shi, J., Zhang, J., and Wang, X. (2021). Electrochemical immunosensor based on Pd@Pt/MoS$_2$-Gr for the sensitive detection of CEA. *J. Solid State Electrochem.* 25, 2075–2085. doi:10.1007/s10008-021-04978-y

Liu, X., Chen, Z., Wang, T., Jiang, X., Qu, X., Duan, W., et al. (2022). Tissue imprinting on 2D nanoflakes-capped silicon nanowires for lipidomic mass spectrometry imaging and cancer diagnosis. *ACS Nano* 16, 6916–6928. doi:10.1021/acsnano.2c02616

Luo, X., Zhang, T., Tang, H., and Liu, J. (2022). Novel electrochemical and electrochemiluminescence dual-modality sensing platform for sensitive determination of antimicrobial peptides based on probe encapsulated liposome and nanochannel array electrode. *Front. Nutr.* 9, 962736. doi:10.3389/fnut.2022.962736

Lv, N., Qiu, X., Han, Q., Xi, F., Wang, Y., and Chen, J. (2022). Anti-biofouling electrochemical sensor based on the binary nanocomposite of silica nanochannel array and graphene for doxorubicin detection in human serum and urine samples. *Molecules* 27, 8640. doi:10.3390/molecules27248640

Ma, K., Yang, L., Liu, J., and Liu, J. (2022a). Electrochemical sensor nanoarchitectonics for sensitive detection of uric acid in human whole blood based on screen-printed carbon electrode equipped with vertically-ordered mesoporous silica-nanochannel film. *Nanomaterials* 12, 1157. doi:10.3390/nano12071157

Ma, K., Zheng, Y., An, L., and Liu, J. (2022b). Ultrasensitive immunosensor for prostate-specific antigen based on enhanced electrochemiluminescence by vertically ordered mesoporous silica-nanochannel film. *Front. Chem.* 10, 851178. doi:10.3389/fchem.2022.851178

Ma, N., Luo, X., Wu, W., and Liu, J. (2022c). Fabrication of a disposable electrochemical immunosensor based on nanochannel array modified electrodes and gated electrochemical signals for sensitive determination of C-reactive protein. *Nanomaterials* 12, 3981. doi:10.3390/nano12223981

Mao, Y., Zhao, C., Ge, S., Luo, T., Chen, J., Liu, J., et al. (2019). Gram-scale synthesis of nitrogen doped graphene quantum dots for sensitive detection of mercury ions and l-cysteine. *RSC Adv.* 9, 32977–32983. doi:10.1039/c9ra06113d

Qiu, G., Han, Y., Zhu, X., Gong, J., Luo, T., Zhao, C., et al. (2021). Sensitive detection of sulfide ion based on fluorescent ionic liquid-graphene quantum dots nanocomposite. *Front. Chem.* 9, 658045. doi:10.3389/fchem.2021.658045

Shi, W., and Ma, Z. (2011). A novel label-free amperometric immunosensor for carcinoembryonic antigen based on redox membrane. *Biosens. Bioelectron.* 26, 3068–3071. doi:10.1016/j.bios.2010.11.048

Song, G., Zhou, H., Gu, J., Liu, Q., Zhang, W., Su, H., et al. (2017). Tumor marker detection using surface enhanced Raman spectroscopy on 3D Au butterfly wings. *J. Mat. Chem. B* 5, 1594–1600. doi:10.1039/c6tb03026b

Su, R., Tang, H., and Xi, F. (2022). Sensitive electrochemical detection of p-nitrophenol by pre-activated glassy carbon electrode integrated with silica nanochannel array film. *Front. Chem.* 10, 954748. doi:10.3389/fchem.2022.954748

Tang, H., Chen, J., Nie, L., Kuang, Y., and Yao, S. (2007). A label-free electrochemical immunoassay for carcinoembryonic antigen (CEA) based on gold nanoparticles (AuNPs) and nonconductive polymer film. *Biosens. Bioelectron.* 22, 1061–1067. doi:10.1016/j.bios.2006.04.027

Walcarius, A. (2021). Electroinduced surfactant self-assembly driven to vertical growth of oriented mesoporous films. *Acc. Chem. Res.* 54, 3563–3575. doi:10.1021/acs.accounts.1c00233

Wang, K., Yang, L., Huang, H., Lv, N., Liu, J., and Liu, Y. (2022). Nanochannel array on electrochemically polarized screen printed carbon electrode for rapid and sensitive electrochemical determination of clozapine in human whole blood. *Molecules* 27, 2739. doi:10.3390/molecules27092739

Wang, Y. L., Cao, J. T., Chen, Y. H., and Liu, Y. M. (2016). A label-free electrochemiluminescence aptasensor for carcinoembryonic antigen detection based on electrodeposited ZnS–CdS on MoS$_2$ decorated electrode. *Anal. Methods* 8, 5242–5247. doi:10.1039/c6ay01114d

Wei, X., Luo, X., Xu, S., Xi, F., and Zhao, T. (2022). A flexible electrochemiluminescence sensor equipped with vertically ordered mesoporous silica nanochannel film for sensitive detection of clindamycin. *Front. Chem.* 10, 872582. doi:10.3389/fchem.2022.872582

White, R. J., Luque, R., Budarin, V. L., Clark, J. H., and Macquarrie, D. J. (2009). Supported metal nanoparticles on porous materials. Methods and applications. *Chem. Soc. Rev.* 38, 481–494. doi:10.1039/b802654h

Xi, F., Zhao, J., Shen, C., He, J., Chen, J., Yan, Y., et al. (2019). Amphiphilic graphene quantum dots as a new class of surfactants. *Carbon* 153, 127–135. doi:10.1016/j.carbon.2019.07.014

Xu, S., Zhang, S., Li, Y., and Liu, J. (2023). Facile synthesis of iron and nitrogen Co-doped carbon dot nanozyme as highly efficient peroxidase mimics for visualized detection of metabolites. *Molecules* 28, 6064. doi:10.3390/molecules28166064

Yan, Z., Zhang, S., Liu, J., and Xing, J. (2023). Homogeneous electrochemical aptamer sensor based on two-dimensional nanocomposite probe and nanochannel modified electrode for sensitive detection of carcinoembryonic antigen. *Molecules* 28, 5186. doi:10.3390/molecules28135186

Yuan, Y., Zhang, L., Wang, H., Chai, Y., and Yuan, R. (2018). Self-enhanced PEI-Ru(II) complex with polyamino acid as booster to construct ultrasensitive electrochemiluminescence immunosensor for carcinoembryonic antigen detection. *Anal. Chim. Acta.* 1001, 112–118. doi:10.1016/j.aca.2017.11.035

Zeng, Z., Cohen, A. M., and Urmacher, C. (1993). Usefulness of carcinoembryonic antigen monitoring despite normal preoperative values in node-positive colon cancer patients. *Dis. Colon. Rectum* 36, 1063–1068. doi:10.1007/bf02047301

Zhang, A., Huang, C., Shi, H., Guo, W., Zhang, X., Xiang, H., et al. (2017). Electrochemiluminescence immunosensor for sensitive determination of tumor biomarker CEA based on multifunctionalized Flower-like Au@BSA nanoparticles. *Sens. Actuators. B Chem.* 238, 24–31. doi:10.1016/j.snb.2016.07.009

Zhang, C., Zhou, X., Yan, F., and Lin, J. (2023a). N-doped graphene quantum dots confined within silica nanochannels for enhanced electrochemical detection of doxorubicin. *Molecules* 28, 6443. doi:10.3390/molecules28186443

Zhang, J., Yang, L., Pei, J., Tian, Y., and Liu, J. (2022). A reagentless electrochemical immunosensor for sensitive detection of carcinoembryonic antigen based on the interface with redox probe-modified electron transfer wires and effectively immobilized antibody. *Front. Chem.* 10, 939736. doi:10.3389/fchem.2022.939736

Zhang, T., Xu, S., Lin, X., Liu, J., and Wang, K. (2023b). Label-free electrochemical aptasensor based on the vertically-aligned mesoporous silica films for determination of aflatoxin B1. *Biosensors* 13, 661. doi:10.3390/bios13060661

Zhao, X., Zhao, H., Yan, L., Li, N., Shi, J., and Jiang, C. (2020). Recent developments in detection using noble metal nanoparticles. *Crit. Rev. Anal. Chem.* 50, 97–110. doi:10.1080/10408347.2019.1576496

Zheng, W., Su, R., Lin, X., and Liu, J. (2022). Nanochannel array modified three-dimensional graphene electrode for sensitive electrochemical detection of 2,4,6-trichlorophenol and prochloraz. *Front. Chem.* 10, 954802. doi:10.3389/fchem.2022.954802

Zheng, Y., Lin, J., Xie, L., Tang, H., Wang, K., and Liu, J. (2021). One-step preparation of nitrogen-doped graphene quantum dots with anodic electrochemiluminescence for sensitive detection of hydrogen peroxide and glucose. *Front. Chem.* 9, 688358. doi:10.3389/fchem.2021.688358

Zhou, H., Ding, Y., Su, R., Lu, D., Tang, H., and Xi, F. (2022). Silica nanochannel array film supported by ß-cyclodextrin-functionalized graphene modified gold film electrode for sensitive and direct electroanalysis of acetaminophen. *Front. Chem.* 9, 812086. doi:10.3389/fchem.2021.812086

Zhou, X., Han, Q., Zhou, J., Liu, C., and Liu, J. (2023). Reagentless electrochemical detection of tumor biomarker based on stable confinement of electrochemical probe in bipolar silica nanochannel film. *Nanomaterials* 13, 1645. doi:10.3390/nano13101645

Zhu, D., Tan, Y., Zheng, L., Lao, J., Liu, J., Yu, J., et al. (2023). Microneedle-coupled epidermal sensors for in-situ-multiplexed ion detection in interstitial fluids. *ACS Appl. Mat. Interfaces* 15, 14146–14154. doi:10.1021/acsami.3c00573

Zhu, X., Xuan, L., Gong, J., Liu, J., Wang, X., Xi, F., et al. (2022). Three-dimensional macroscopic graphene supported vertically-ordered mesoporous silica-nanochannel film for direct and ultrasensitive detection of uric acid in serum. *Talanta* 238, 123027. doi:10.1016/j.talanta.2021.123027

Check for updates

Pharmacokinetic and pharmacodynamic studies of nicotine in rat brain: a simultaneous investigation of nicotine metabolites and the release of neurotransmitters *in vivo*

Lulu Guo[1,2,3†], Jian Mao[2,3†], Qidong Zhang[2], Wu Fan[2], Dingzhong Wang[2], Zhonghao Li[2], Jiaqiang Huang[1]* and Jianping Xie[1,2,3]*

[1]Department of Nutrition and Health, Beijing Advanced Innovation Center for Food Nutrition and Human Health, China Agricultural University, Beijing, China, [2]Beijing Life Science Academy, Beijing, China, [3]Food Laboratory of Zhongyuan, Zhengzhou University, Zhengzhou, China

Introduction: The body's ability to metabolize nicotine and the disposition of nicotine in the brain are important determinants of its exposure. Limited knowledge about the near real-time changes of neurochemicals during the brain nicotine metabolic process hinders the recognition of its multiple neuropharmacological effects.

Methods: An online microdialysis coupled with UHPLC-HRMS/MS method for the *in vivo* multi-analysis of nicotine metabolites and several neurotransmitters in rat brain was developed. Whether the systemic modulation of metabolic enzyme CYP2B would modulate nicotine pharmacokinetics and local neurochemical effects was further investigated.

Results: The dynamic profiles of over 10 nicotine metabolites and neurotransmitters were simultaneously obtained after a single injection of nicotine (2 mg·kg^{-1}, i.p.) using the new method. Proadifen pretreatment (50 mg·kg^{-1}·d^{-1}, i.p., 4 days) caused significant inhibition of brain CYP2B1 activity. When exposed to nicotine, the brain C_{max} of nicotine was 1.26 times higher and the levels of nicotine metabolites, nornicotine, and nicotine-*N*-oxide, were decreased by 85.3% and 34.4% in proadifen-pretreated rats. The higher level of brain nicotine induced a greater release of dopamine, serotonin, glutamate, and γ-amino-butyric acid in the nucleus accumbens. The concentrations of nicotine and dopamine were positively correlated, and the average levels of γ-amino-butyric acid and serotonin were 2.7 and 1.2 times higher, respectively, under the inhibition of nicotine metabolism.

Discussion: These results demonstrated that inhibiting nicotine metabolism in rats can enhance the residence of brain nicotine and its local neurotransmitter effects. The metabolic activity of nicotine under different physiological conditions could regulate nicotine's bioavailability and its resulting pharmacology.

1 Introduction

Nicotine (Nic) is a principal bioactive ingredient in cigarettes and the component most associated with tobacco dependence (Tanner et al., 2015; Xiao et al., 2020). The development and persistence of tobacco dependence are due to the reward effect produced by activating nicotine acetylcholine receptors (nAChRs) in the mesolimbic reward circuitry (Tapper et al., 2004; Changeux, 2010; Henderson et al., 2017; Chen et al., 2022). In addition to its strong addictive potential, extensive studies showed that Nic is a potential drug for the amelioration of ulcerative colitis, Alzheimer's disease, and Parkinson's disease (Quik et al., 2012; Quik et al., 2012). A rapid elevation of Nic in the brain may be the first choice for the treatment of Nic dependence; however, for the amelioration of Alzheimer's disease and Parkinson's disease, maintaining an effective Nic level in the brain for a long time may be a better approach (Alsharari et al., 2014). The bioavailability and pharmacokinetics of Nic were found to be affected by its molecular form and metabolic enzyme activity (Hwa Jung et al., 2001). The multiple physiological effects of Nic are mainly because Nic can potently regulates the release of neurochemicals and even the metabolism of neurotransmitters, including dopamine (DA), γ-amino-butyric acid (GABA), glutamate (Glu), serotonin (5-HT), and acetylcholine (Ach), within various mesocorticolimbic structures, such as the ventral tegmental area (VTA), nucleus accumbens (NAc), and prefrontal cortex (Grieder et al., 2019; Vivekanandarajah et al., 2019; Jadzic et al., 2021; Nguyen et al., 2021; Pietilä et al., 1996). Therefore, investigating the release information of neurotransmitters in the brain during Nic exposure is an effective approach to studying the multiple effects of Nic.

The local biodegradation and metabolic process of Nic is an important determinant of its exposure in the brain. Even though peripheral analysis of Nic and its metabolites by the more sensitive method HPLC-MS have been studied extensively in biological fluids, the metabolism of Nic in the central nervous system (CNS) has been given little attention (Rangiah et al., 2011; Piller et al., 2014; Mao et al., 2015). Similar to peripheral system in the liver and blood, Nic has been confirmed to be oxidized, N-demethylated, and hydroxylated in the CNS (Xu et al., 2019), which generates cotinine (Cot), nicotine-N-oxide (NNO), nornicotine (NNic), norcotinine (NCot), trans-3′-hydroxy-cotinine (OH-Cot), 4-oxo-4-(3-pyridyl)-butanoic acid (OxPyBut), and 4-hydroxy-4-(3-pyridyl)-butanoic acid (HyPyBut). Several studies showed that some Nic metabolites also have pharmacological activity and may contribute to the multiple effects of Nic exposure. For example, the main metabolite Cot, which acts as a weak agonist of nAChRs, was considered to actively regulate the cholinergic, DAergic, and 5-HTergic systems, and promote synaptic plasticity and stress resilience (Mendoza et al., 2018; Oliveros-Matus et al., 2020). Other studies have shown that regulation of the Nic metabolism changed its bioavailability and pharmacology. Inhibition of mouse CYP2A5 increased the bioavailability of Nic and prolonged the duration of analgesia and hypothermia induced by Nic (Alsharari et al., 2014). Furthermore, in rats and monkeys, continuous treatment with Nic increased the levels of the Nic metabolizing enzyme CYP2B in the cerebrum, which decreased brain Nic levels, altered the reinforcing effects, and thereby increased withdrawal symptoms (Garcia et al., 2015). However, it is unknown how the changes of physiological effects caused by different brain Nic levels

were clearly related to the release of neurotransmitters. Therefore, it is necessary to synchronously investigate the brain distribution, metabolic characteristics, and the related neurotransmitter effects resulting from Nic exposure in the CNS.

Synchronous investigation of brain Nic pharmacokinetics and the related local changes of neurotransmitters have been given little attention due to the difficulty of obtaining the brain samples *in vivo* and a lack of effective detection methods. The greatest obstacle is that the different polarity, unstable chemical properties, and low concentration in biological matrices hinders the quantitative determination of most neurotransmitters and some Nic metabolites (Jha et al., 2018; Olesti et al., 2019; El-Sherbeni et al., 2020; Zhou et al., 2020). Microdialysis coupled with analytical techniques such as HPLC-MS/MS has become a workhorse and a state-of-the-art technique to assess the *in vivo* changes of extracellular compounds, and has been applied extensively in neuroscience, pharmacokinetics, and pharmacodynamics (Nandi and Lunte, 2009; Zestos et al., 2019; Shi et al., 2014). However, the off-line microdialysis based analytical systems still suffer from some drawbacks, such as unexpected contamination, evaporation, or degradation of the analytes during sample storage and transfer. Online analysis is a better alternative that largely circumvents these problems (Wang et al., 2015). The direct coupling of microdialysis with HPLC-MS/MS enables the integration of *in vivo* minimally invasive sampling with high temporal resolution analysis for continuous monitoring of drug pharmacological effects. Meanwhile, derivatization regents such as benzoyl chloride, N-Boc-l-tryptophan hydroxysuccinimide ester, and (5-N-succinimidoxy-5-oxopentyl) triphenylphosphonium bromide have been employed to improve the separations and increase the detection sensitivity of neurotransmitter by LC-MS (Song et al., 2012; Greco et al., 2013; Zhang et al., 2014). Here, a precolumn "one-step" derivatization-based online microdialysis coupled with ultra-high performance liquid chromatography-high resolution tandem mass spectrometry (UHPLC-HRMS/MS) was developed, which integrated the *in vivo* sampling with online injection for the simultaneous detection of Nic metabolites and several neurochemicals. Relevant information on brain Nic pharmacokinetics and neurotransmitter release was effectively obtained in different rat models (i.e., normal group and enzyme inhibition group), which provided an in-depth understanding of Nic neuropharmacology under different physiological conditions.

2 Materials and methods

2.1 Chemicals and materials

Nicotine and its metabolites standards were purchased from Toronto Research Chemicals (North York, Canada) (−) nicotine (Nic), (−) cotinine (Cot), (R, S)- nornicotine (NNic), (R, S)-norcotinine (NCot), *trans*-3′-hydroxycotinine (OH-Cot), (1′S, 2′S)-nicotine-1′-oxide (NNO), (S)-cotinine-N-oxide (CNO), 4-oxo-4-(3-pyridyl)-butanoic acid (OxPyBut), 4-hydroxy-4-(3-pyridyl)-butanoic acid (HyPyBut), (1′S, 2′S)-nicotine-1′-oxide-d_3 (NNO-d_3), and (R, S)- nornicotine-d_4 (NNic-d_4). Dopamine hydrochloride (DA), 3,4-dihydrophenylacetic acid (DOPAC), homovanillic acid (HVA), serotonin hydrogenoxalate (5-HT),

5-hydroxyindole-3-acetic acid (5-HIAA), γ-amino-butyric acid (GABA), glutamate (Glu), and Acetylcholine chloride (Ach) were purchased from Sigma-Aldrich (St Louis, MO, USA) unless otherwise noted. Distilled deionized water (>18.2 MΩ cm⁻¹ at 25 °C) was obtained from Thermo Scientific GenPure (Thermo-Fisher Scientific, Stockland, Niederelbert, Germany). Isoflurane was purchased from RWD Life Science Co., Ltd. (Shenzhen, China).

The stock solution of $10 \, g \, L^{-1}$ Nic and its metabolites were prepared by HPLC grade acetonitrile. $5 \, g \, L^{-1}$ DA, DOPAC, HVA, 5-HT, 5-HIAA, GABA, Glu, and Ach were prepared with acetonitrile-water 1:1 (v/v) with 1% hydrochloric acid to preserve the stability of neurotransmitters (Saracino et al., 2015; Tufi et al., 2015). The intermediate solution of Nic and its metabolites and neurotransmitters ($1 \, g \, L^{-1}$) were diluted by acetonitrile, respectively. The stock solution and intermediate solution were kept at −80 °C. The series of gradient mixture standard working solutions (0.1, 0.5, 1, 5, 10, 25, 100, 500 µg L⁻¹) and the quality control (5, 25, 100 µg L⁻¹) samples were further prepared using Ringer's solution (147 mM Na⁺; 2.2 mM Ca²⁺; 4 mM K⁺; pH 7.0, Shanghai yuanye Bio-Technology Co., Ltd.) and stored at −20°C.

2.2 Animal and treatment

SPF-grade male Sprague Dawley (SD) rats (220 ± 20) g were purchased from Henan Huaxing Experimental Animal Center (License number SCXY(Yu) 20190002, Zhengzhou, China). All rats were housed under a stable condition with *ad libitum* access to food and water under a 12 h light-dark cycle. Animal studies and experimental procedures were all strictly conducted under the condition of permission and supervision.

To inhibit the main Nic metabolic enzyme CYP2B in the brain, rats received intraperitoneal injections of proadifen (50 mg kg⁻¹·day⁻¹, 4 d) (Song et al., 2012). Control animals were pretreated with saline using the same protocol. All the rats were sacrificed by cardiac perfusion after microdialysis sampling. The brain tissues were separated and divided into four parts (cerebrum, cerebellum, diencephalon, and brainstem). The CYP2B activity in different rat brain regions was determined following the instructions of the GENMED CYP2B1 activity fluorescence quantitative detection kit (GENMED SCIENTIFICS INC. U.S.A, GMS18019.1).

2.3 Microdialysis sampling

Anesthesia was induced with 3% isoflurane in an induction chamber before surgical procedures and was placed in a stereotaxic frame equipped with a rat ear and bite bar. Rat was maintained under anesthesia with 1%–2% isoflurane during operation procedures. And the cranium above the ventral striatum (coordinates relative to bregma: anterior/posterior (*AP*), +1.2 mm; medial/lateral (*ML*), −2.4 mm; dorsal/ventral (*DV*), −6.0 mm) or NAc (coordinates relative to bregma: anterior/posterior (*AP*), +1.7 mm; medial/lateral (*ML*), −1.5 mm; dorsal/ventral (*DV*), −6.5 mm) was exposed to implant the probe guide-cannula (CMA/12), two screws were implanted into the skull to serve as an anchor and dental cement was used as an adhesive to fixed the probe guide-cannula. To avoid the interference of neurotransmitter changes due to physical stimulation of

pain receptors during intraperitoneal injection of Nic, Nic was injected with the aid of an administration catheter (Instech, BTPU-040, 6.35 × 10.16 mm, America), which was implanted in the abdomen, the other end of the catheter was passed under the skin and sent to the back and sealed with a plug (Instech, PNP3M-F22R, America). The rats were housed individually and allowed to recover from surgery for at least 24 h.

For *in vivo* microdialysis sampling, the probe (CMA/12 Elite, membrane parameters: polyarylethersulfone material; 2 mm length; φ 0.5 mm; 20 kDa cut-off) was inserted into the brain through the cannula. After implantation, the probe was perfused with Ringer's solution by the syringe pump (CMA/402, piston propulsion speed: 2.4 µm·min⁻¹–1.2 mm min⁻¹; velocity range: 0.1 µL·min⁻¹–20 µL min⁻¹; precision: −1.5%-1.5%) at fixed flow rates (1.5 µL min⁻¹), and the dialysates were analyzed under the optimized UHPLC-HRMS/MS condition directly. Intraperitoneal administration of $2 \, mg \, kg^{-1}$ Nic was performed until stable levels of neurotransmitters were obtained, which was defined as the mean value of neurotransmitter concentrations in six consecutive samples varied by no more than 10%.

2.4 Chromatographic conditions and mass spectrometry settings

UHPLC-HRMS/MS system was performed on Dionex Ultimate 3000 UHPLC equipped with a Q-Exactive mass spectrometer and electrospray ionization (ESI) interface (Thermo Fisher Scientific, Germany). Chromatographic separation was achieved by the pentafluorophenyl phase column (Discovery® HS F5-3 column, 2.1 × 150 mm, 3 µm) with linear binary gradient elution, at a flow rate of 0.5 mL min⁻¹. Eluent A was 10 mM ammonium acetate with FA (0.1%, v/v) dissolved in water, and eluent B was acetonitrile with 0.1% FA (v/v). The gradient elution was started at 10% B and kept for 1 min, then linearly increased to 45% B over 2 min. From 3 to 6 min, a linear gradient was applied from 45% to 75% B and then return linearly to the initial condition at 9 min and the column was allowed to equilibrate for 1 min.

The mass spectrometer was operated in positive ionization mode. The optimized mass spectrometer parameters were as follows: a resolution of 35000; automatic gain control (AGC) target was 2.0 e⁵; maximum injection time (IT) was 100 m; 3.5 kV for spray voltage; ion transfer tube temperature, 350°C; S-Lens RF level, 60%. The isolation window of the precursor ions was done using a quadrupole with an isolation window of m/z 1. The normalized collision energy was set at 10%. Analytes were determined by a parallel reaction monitoring (PRM) method by acquiring two transitions for each compound. The most specific transition was selected for the quantitative purpose. All data were gathered and analyzed using Xcalibur 2.2 software (Thermo Fisher Scientific, Germany).

3 Results

3.1 Establishing the method for *in vivo* sampling and simultaneous online detection

In order to improve the response of several monoamine derivatives and reduce the differences in properties between Nic

FIGURE 1
Schematic diagram of the precolumn derivatization online microdialysis UHPLC-HRMS/MS system.

FIGURE 2
Representative PRM chromatograms of target analytes.

metabolites and certain neurotransmitters, we modified the conventional microdialysis system by adding a Y-shaped in-house binary static mixer at the outlet of the microdialysis probe to combine the derivatization reagent with dialysate online. The multi-step derivatization reaction condition reported in the literature (Wong et al., 2016) was modified to complete the reaction in one step, which was necessary to realize the *in-situ* derivatization system. The derivatization reagent was composed of 100 mM sodium carbonate and benzoyl chloride (10% (*v/v*) in acetonitrile) at 3:1 (*v/v*), and the pH was adjusted to 9.2 with sodium hydroxide. The system consisted of two syringe pumps

for supplying Ringer's solution at a flow rate of 1.5 μL min^{-1} and the derivatization reagent at a flow rate of 0.5 μL min^{-1}, respectively. The derivatized extracellular fluid from microdialysis was introduced into the UHPLC-HRMS/MS system through an online injector (six-port injection valve) to realize the direct analysis, which minimized the possible contamination and degradation during sample storage and transfer. Specifically, port 1 was used to sample the derivatized dialysate, and port 3 and port 6 were connected through a 20 μL quantitative loop for loading the sample (Figure 1). The mobile phase was pumped into port 5, and port 4 was connected to the chromatographic separation column. The injection time difference between run 1 and run 2 was the separation time of run 1; that is, the solid line in the diagram represents the loading state lasting 10 min, and the dashed lines indicate the injection state for 0.2 min, so that as soon as run 1 ended, run 2 began immediately, and this cycle was repeated to obtain uninterrupted *in vivo* data.

Despite the high specificity of the HRMS/MS detector, the electrospray ionization technique is susceptible to interference by co-eluting compounds; therefore, suitable chromatographic separation and an appropriate retention time were essential to improve the quantitative accuracy. To achieve better separation and sharper peaks of analytes in a short time, different chromatographic columns, mobile phases (acetonitrile-H_2O, methanol-H_2O), and salt concentrations were investigated. The final test results indicated that the pentafluorophenyl phase column was the best choice; that 0.1% formic acid should be added to both phases to provide an acidic environment; and that 10 mM ammonium formate was helpful for improving the peak shape. The gradient elution program was adjusted so that the target compounds were well separated from 2 min to 9 min (Figure 2), and the chromatographic column can completely return to the initial

TABLE 1 Accurate mass and PRM parameters of the analytes.

Analyte	Protonated ion mass		Mass error (ppm)	nCE (%)	Main daughter ion (m/z)[a]	MS species
	Theoretical	Experimental				
Nic	163.1230	163.1231	0.6	55	**130.0652**/132.0808	M + H$^+$
Cot	177.1022	177.1021	−0.5	70	**80.0501**/98.0604	M + H$^+$
mono-Bz-NNic	253.1335	253.1331	−1.5	55	**147.0916**/235.1232	M + H$^+$
mono-Bz-NNic-d_4	257.1587	257.1584	−1.1	30	**105.0338**	M + H$^+$
NCot	163.0866	163.0865	−0.6	70	**80.0500**	M + H$^+$
NNO	179.1179	179.1176	−1.6	55	**132.0807**/130.0650	M + H$^+$
NNO-d_3	182.1367	182.1368	0.5	55	**132.0807**/130.0650	M + H$^+$
CNO	193.0972	193.0971	−0.5	65	**96.0449**/98.0605	M + H$^+$
mono-Bz-OH-Cot	297.1234	297.1235	0.3	25	**175.0864**/279.1121	M + H$^+$
OxPyBut	180.0655	180.0657	1.1	50	**134.0603**	M + H$^+$
HyPyBut	182.0812	182.0811	−0.5	50	**164.0705**/109.0525	M + H$^+$
tri-Bz-DA	466.1649	466.1647	−0.4	15	241.0859/**105.0338**	M + H$^+$
bi-Bz-DOPAC	394.1285	394.1283	−0.5	25	**105.0338**	M + NH$_4^+$
mono-Bz-HVA	304.1179	304.1182	0.9	10	137.0599/**105.0338**	M + NH$_4^+$
bi-Bz-5-HT	385.1547	385.1545	−0.5	25	**264.1018**/105.0338	M + H$^+$
mono-Glu	252.0867	252.0863	−1.6	10	**105.0338**	M + H$^+$
mono-GABA	208.0968	208.0969	0.4	10	**105.0338**	M + H$^+$
mono-Bz-5-HIAA	296.0917	296.0912	−1.6	15	146.0599/**105.0338**	M + H$^+$
Ach	146.1176	146.1175	−0.6	35	**87.0446**	M + H$^+$

[a]Quantification ion transitions are in bold.

pressure at 10 min for the next online injection. The suitable separation conditions and the matched temporal resolution of microdialysis sampling provided an advantage for correlating the relationship between Nic metabolism and its neurochemical effects.

Among the selected compounds, NNic, NCot, OH-Cot, and several neurotransmitters were benzoylated. For the best ion response, MS parameters, including the spray voltage, capillary temperature, vaporizer temperature, sheath gas, auxiliary gas, and S-lens RF level were manually tuned. PRM mode was used to provide the highest specificity and sensitivity. The mass accuracy between theoretical and experimental masses of all analytes was less than 2 ppm (Table 1). Based on the good separation ability of the UHPLC column and high accuracy of the Q-Orbitrap HRMS, the high selectivity of the method was guaranteed.

3.2 Method validation

NNic-d_4 and NNO-d_3 were added to the perfusate and used as internal standards after retrodialysis for derivatized and non-derivatized products, respectively, which eliminated the minor errors caused by instrument analysis and corrected the small deviation of the dialysis rate between samples during the long sampling process of microdialysis. The instrument analytical

performance was investigated in terms of linearity, precision and accuracy, limit of detection (LOD), and limit of quantification (LOQ) under the optimized conditions. The developed method had a wide range for the Nic metabolites and neurotransmitters with the coefficient of determination (R^2) higher than 0.9935 for all analytes. The LOD and LOQ were from 0.003 to 1.0 μg L^{-1} ($S/N = 3$) and from 0.01 to 2.5 μg L^{-1} ($S/N = 10$), respectively. The intra-day precision and accuracy ranged from 1.7% to 8.4% and −2.6% to 6.5%, respectively (Table 2). All these results were within the acceptable criteria, indicating that the established method was reliable and suitable for the simultaneous analysis of Nic metabolites and neurotransmitters in microdialysis samples.

3.3 Determination of Nic metabolites and neurochemicals in rat brain

To demonstrate the utility of the method in monitoring the low concentration analytes in the dialysates, rats were exposed to Nic by single intraperitoneal injection (2 mg kg^{-1}, i. p.), and the brain samples from the ventral striatum were analyzed as extracted ion chromatograms. All the expected Nic metabolites in the dialysate were detected, and NCot was only detected in a few periods. The extracted ion chromatograms of Nic metabolites and classical

TABLE 2 Linearity, accuracy, precision, limits of detection (LODs) and microdialysis recoveries for target analytes.
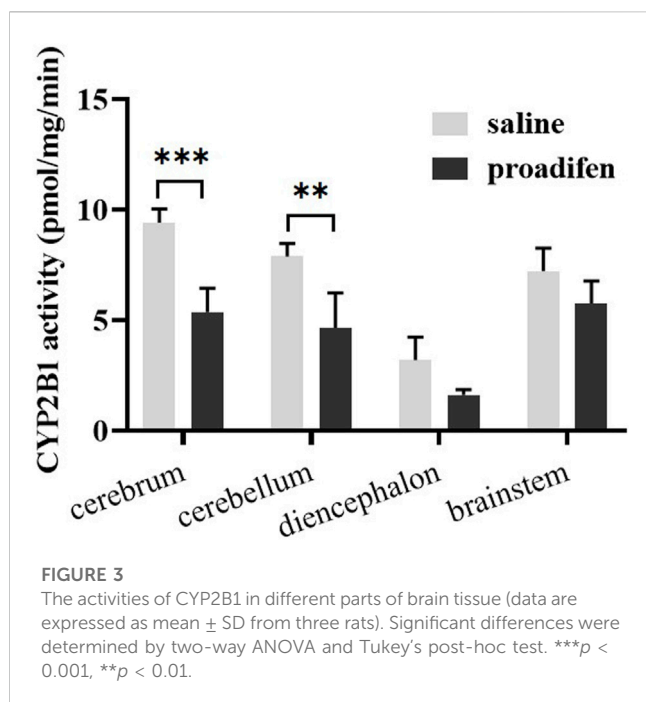
Analyte	LOD ($\mu g \cdot L^{-1}$)	Linear range ($\mu g \cdot L^{-1}$)	R^2	Accuracy (RE, %) (n = 5, $\mu g \cdot L^{-1}$)			Precision (RSD, %) (n = 5, $\mu g \cdot L^{-1}$)			R_{dial} of probe
				5	25	100	5	25	100	
Nic	0.3	1.0–250	0.996	2.5	1.3	3.5	5.3	4.1	3.2	30.0 ± 3.6
Cot	0.003	0.01–250	0.998	1.5	3.2	2.7	2.2	3.0	4.1	21.3 ± 4.7
Bz-NNic	0.03	0.1–250	0.992	2.2	0.5	1.9	3.2	5.7	1.7	18.8 ± 2.5
NCot	0.003	0.01–250	0.998	1.5	1.3	3.0	2.4	2.5	3.7	18.1 ± 3.1
NNO	0.3	1.0–250	0.997	2.1	0.9	1.9	3.7	7.1	4.4	22.8 ± 2.0
CNO	0.015	0.05–250	0.995	2.1	−1.8	0.9	3.6	7.5	5.5	25.8 ± 3.0
Bz-OH-Cot	0.15	0.5–250	0.995	1.2	0.6	1.9	4.2	2.2	3.6	21.3 ± 2.6
OxPyBut	0.03	0.1–250	0.999	2.5	0.8	1.5	2.9	2.7	3.1	23.3 ± 1.6
HyPyBut	0.03	0.1–250	0.999	2.8	3.8	2.1	3.8	4.1	4.2	22.3 ± 2.9
Bz-DA	1.0	2.5–500	0.994	6.5	3.3	2.9	8.4	6.8	7.4	20.7 ± 4.2
Bz-DOPAC	0.3	1.0–500	0.996	4.5	5.8	5.3	5.3	5.3	7.9	31.8 ± 2.5
Bz-HVA	0.3	1.0–500	0.996	6.4	4.0	4.7	7.1	6.2	7.5	18.1 ± 1.1
Bz-5-HT	1.0	2.5–500	0.999	6.1	4.0	3.5	7.0	5.3	6.4	28.0 ± 1.0
Bz-5-HIAA	0.03	0.1–500	0.996	1.4	2.4	3.6	1.9	3.9	4.6	25.3 ± 1.8
Bz-GABA	0.30	1.0–500	0.996	3.7	2.9	1.0	7.0	7.2	2.8	20.4 ± 2.1
Bz-Glu	0.3	1.0–500	0.997	4.3	−2.6	0.8	4.8	3.8	2.7	19.1 ± 3.0
Ach	0.3	1.0–500	0.995	2.6	2.4	0.7	5.7	2.7	4.2	22.1 ± 1.9

neurotransmitters are shown in Supplementary Figure S1. In addition, another six amino acids (aspartic acid, glycine, glutamine, histidine, taurine, and serine) were incidentally extracted, which were confirmed by the precise molecular weight of the derivatized product (238.0710, 180.0655, 251.1026, 260.1029, 230.0482, and 314.1023, respectively) and benzoyl fragment (m/z 105.0338) (Supplementary Figure S2). These results suggested that the developed precolumn derivatization-based online microdialysis coupled with UHPLC-HRMS/MS was not just a proof-of-principle study. It not only fulfilled the need to investigate the release of neurotransmitters during Nic metabolism, but simultaneously also monitored the changes of other neurochemicals, which may shed more light on the neurobiological mechanisms underlying behavioral changes induced by Nic exposure.

We further investigated the time course curves of Nic metabolites and monoamine neurotransmitters in rat striatum after administration of Nic (2 mg kg^{-1}, i. p.) (Supplementary Figure S3). The results showed that the most abundant Nic metabolites in rat striatum were Cot, NNO, and NNic, and the brain metabolic process of Nic was similar to that in the peripheral system. The rapid distribution of Nic in the brain induced a high intensity release of monoamine neurotransmitters. After 3 h of Nic exposure, the average levels of DA and its metabolites DOPAC and HVA, and 5-HT and its metabolite 5-HIAA were 25.1, 99.2, 169.8, 45.9, and 234.4 µg L^{-1}, respectively. It is worth noting that the levels of DA and 5-HT were lower than their metabolites, which showed that neurotransmitters were rapidly metabolized or absorbed after being released into the synaptic space.

3.4 Effect of proadifen pretreatment on the metabolism of Nic in rat brain

CYP2B1, which corresponds to human CYP2B6, plays a major role in the metabolism of Nic in rat (Hammond et al., 1991; Al Koudsi and Tyndale, 2010). Previous studies using rats confirmed that alternating brain CYP2B activity influenced brain Nic levels and Nic-mediated behaviors (Garcia et al., 2015; Garcia et al., 2017). To investigate the effect of CYP2B inhibition on Nic biotransformation and neurotransmitter release in rat brains, another group of rats was pretreated with proadifen (50 mg kg$^{-1}\cdot$d^{-1}, i. p., 4 days) in our research. Compared with the saline-pretreated control group, the activities of CYP2B1 were inhibited in different brain tissues, including the cerebrum, cerebellum, diencephalon, and brainstem (Figure 3). The whole brain CYP2B1 activity decreased by 36.9% on average after proadifen treatment. The brain concentration–time profiles of Nic and its main metabolites Cot, NNO, and NNic were generated using the mean concentration levels of each time bin (Figure 4), and the pharmacokinetic parameters of each analyte estimated by the two-compartment model are listed in Table 3. The concentration of Nic increased rapidly after intraperitoneal injection and then gradually declined. By 360 min, Nic was almost completely cleared from the rat brain. There was no difference in the t_{max} of Nic between the proadifen-pretreated rats and the saline-pretreated group. However, the levels of Nic in the proadifen-pretreated rats were consistently higher than those of the saline group between t_{max} to 360 min. The C_{max} of Nic in the proadifen

FIGURE 3
The activities of CYP2B1 in different parts of brain tissue (data are expressed as mean ± SD from three rats). Significant differences were determined by two-way ANOVA and Tukey's post-hoc test. ***$p <$ 0.001, **$p <$ 0.01.

4 Discussion

As a major reinforcing ingredient of tobacco products that is responsible for addiction in smokers, Nic has multiple and complex effects, such as reward, analgesia, and an improvement in mood or cognitive function. All these effects stem from the presence of Nic in the brain, which triggers a cascade of downstream signaling events by binding to nAChRs, and mainly modulates multiple neurotransmitter systems. The continual neuropharmacological effects of Nic are closely related to the brain tissue distribution and the body's metabolic ability. However, information on the detailed neurotransmitter release induced by Nic during its metabolic process has rarely been reported, which is an obstacle to comprehensively elucidating its complex physiological effects. Even though the peripheral pharmacokinetics of Nic have been extensively studied, these studies cannot truly reflect the local biotransformation of Nic in the brain. Therefore, it is necessary to synchronously investigate the brain disposition, metabolic characteristics, and the related neurotransmitter effects resulting from Nic exposure in the CNS.

Synchronous investigation of brain Nic pharmacokinetics and the changes of various neurotransmitters has been given little attention because of the difficulty of continuously obtaining the brain samples in vivo and the lack of an effective detection method. The local biotransformation of Nic in the brain has been studied in our recent work, and approximately 10 Nic metabolites have been determined by brain microdialysis coupled with UHPLC-HRMS/MS (Xu et al., 2019). Many assays for the detection of classic neurotransmitters from brain samples have been developed, such as electrochemical detection, HPLC-fluorescence detection, and HPLC-MS. Although continuously obtaining the animal brain samples in vivo could be solved by microdialysis techniques, simultaneously determining Nic metabolites and various neurotransmitters using HPLC-MS/MS is challenged by the disparate polarity of the molecules, trace levels in the brain, and the extremely unstable chemical properties of some neurotransmitters (Nandi and Lunte, 2009; Jha et al., 2018; Olesti et al., 2019; Zhou et al., 2020). In this work, precolumn derivatization-based online microdialysis coupled with UHPLC-HRMS/MS was successfully developed to monitor the changes of Nic metabolites and several neurochemicals. This achieved minimally invasive continuous sampling of awake animals and avoided degradation and contamination caused by sample preservation and transfer. Using this approach, Nic and its metabolites, five monoamine neurotransmitters, and eight amino acids were simultaneously obtained in rat striatum dialysate following Nic peripheral exposure (2 mg kg^{-1}, i. p.). Compared with the G-protein coupled receptor-based sensors for imaging neurochemicals developed by Li et al. and in vivo enzymatic electrochemical biosensors for in situ neurochemical measurements in recent years (Liu et al., 2017; Jing et al., 2019; Pan et al., 2020; Sun et al., 2020), although the temporal resolution based on our analysis was poor, it allowed us to achieve long-term and simultaneous monitoring of several compounds, including neurotransmitters. It is not possible with these other novel technologies to investigate the metabolic effects of Nic on multiple neurotransmitter systems.

Variations in both the levels of Nic in the brain (via Nic metabolizing enzymes) and the brain response to Nic (via

group was as high as 1221 μg L^{-1}, which was 1.26 times higher than that in the saline group. The greater $t_{1/2}$ and mean residence time (MRT) values indicated a slower elimination, which could also be explained by the increase of the area under the curve (AUC) and was consistent with Tyndale's study. Compared with the control rats exposed to Nic, the C_{max} of NNic and NNO decreased by 85.3% and 65.6% after CYP2B1 inhibition, respectively.

3.5 The release of neurotransmitters in the NAc under the regulation of Nic metabolism

To eliminate the differences in neurotransmitter levels between each rat, the changes of all neurotransmitter levels were expressed as the relative values of neurotransmitter concentrations for each time bin to baseline values before Nic exposure. Nic yielded a series of complex changes in the classical neurochemicals in the NAc (Figure 5A). It induced an increase in baseline levels of DA, Glu and Ach (Figures 5B–D), but caused almost the opposite change in the inhibitory neurotransmitter GABA (Figure 5E). The peak concentration of the DA metabolites DOPAC and HVA reached nearly 290% and 270% in the saline group, and 340% and 330% of the baseline in the proadifen pretreated group after Nic stimulation (Figures 5F, G), respectively. The peak level of Ach after Nic injection was almost doubled of its baseline levels, but proadifen inhibition did not further increased it. The level of GABA in the proadifen group was 2.7 times higher than that in the saline group on average. The trend of the DA curve appeared to mirror the concentration-time curve of Nic, and the concentration of Nic and DA release was positively correlated (Figure 5H). The levels of 5-HT and its metabolite 5-HIAA in the rat NAc first increased and then decreased slowly after Nic exposure. The C_{max} of 5-HT and 5-HIAA were almost 390% and 240% of baseline in the proadifen pretreatment group, respectively (Figures 5I, J).

FIGURE 4
Time-course curves of Nic (A), Cot (B), NNic (C), and NNO (D) in rat brain after administration of Nic (2 mg kg⁻¹, i. p.) (Each point was expressed as mean ± SD from three rats).
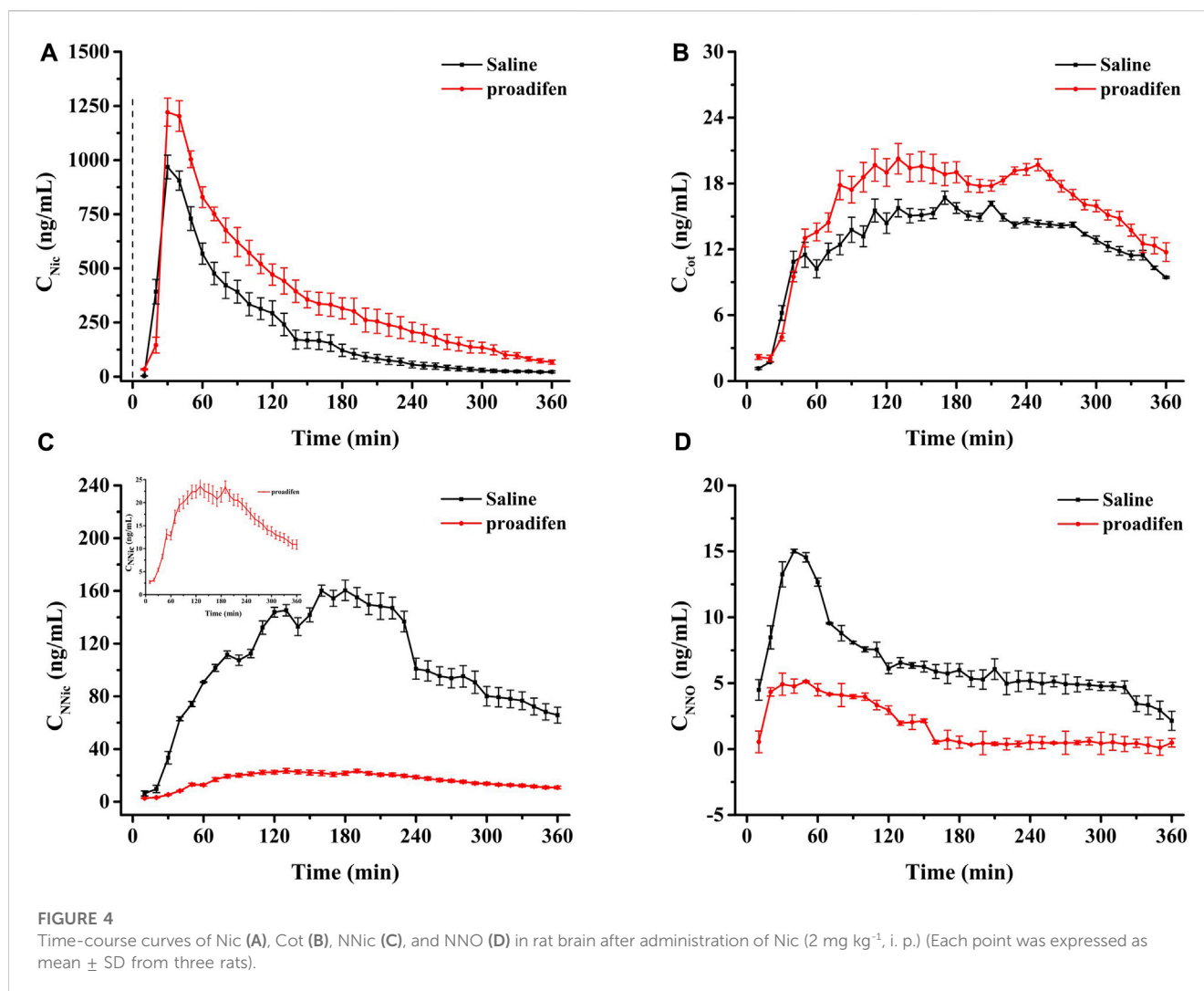
TABLE 3 Estimated pharmacokinetic parameters for Nic and its main metabolites from rat NAc treated with single injection of Nic (2 mg kg⁻¹, ip).

	$AUC_{0-360\ min}$ (mg·min⁻¹·mL⁻¹)		CL/F (mL min⁻¹)		$t_{1/2z}$ (min)		MRT (min)		t_{max} (min)		C_{max} (µg L⁻¹)	
	Saline	Prodifine	Saline	Prodifine	Saline	Prodifine	Saline	Prodifine	Saline	Prodifine	Saline	Prodifine
Nic	75.1	131.5	25.0	14.0	128.8	76.7	85.9	113.5	30	30	968.3	1221.3
Cot	4.6	5.6	9.0	7.0	104.3	131.1	186.7	187.1	160	120	16.7	20.3
NNic	37.4	5.9	2.0	7.0	115.9	166.9	179.9	179.4	170	120	160.4	23.5
NNO	2.3	0.6	5.0	3.2	48.1	53.7	143.3	94.5	30	40	15.1	5.2

nAChRs binding) may influence the multiple pharmacological properties of Nic. To investigate the effect of the Nic metabolic rate on neurotransmitter release in the NAc, which is innervated by DAergic neurons of the mesolimbic reward system, rats were pretreated with proadifen, and the CYP2B activity in the brain decreased by 36.9% compared with the saline group. The N-demethylation and N-oxidation metabolic pathways of Nic were measurably downregulated in the brain compared to the saline-treated control, and the C_{max} and AUC of the C-oxidation product Cot were lower in the saline and proadifen group, indicating

that CYP2B plays a key role in the N-demethylated and N-oxidated biotransformation of Nic in the rat NAc. In addition, proadifen pretreatment showed no effect on the t_{max} of Nic, which indicated that inhibition of CYP2B did not affect the rate of Nic entry into the brain, as studies have shown that the absorption rate of Nic largely depends on the molecular forms of Nic (Hukkanen et al., 2005).

The release and regulation of neurotransmitters between hundreds of millions of neurons play a vital role in maintaining normal physiological functions of the body. Much evidence has indicated that Nic binds to α4β2 and α7 nAChRs located on
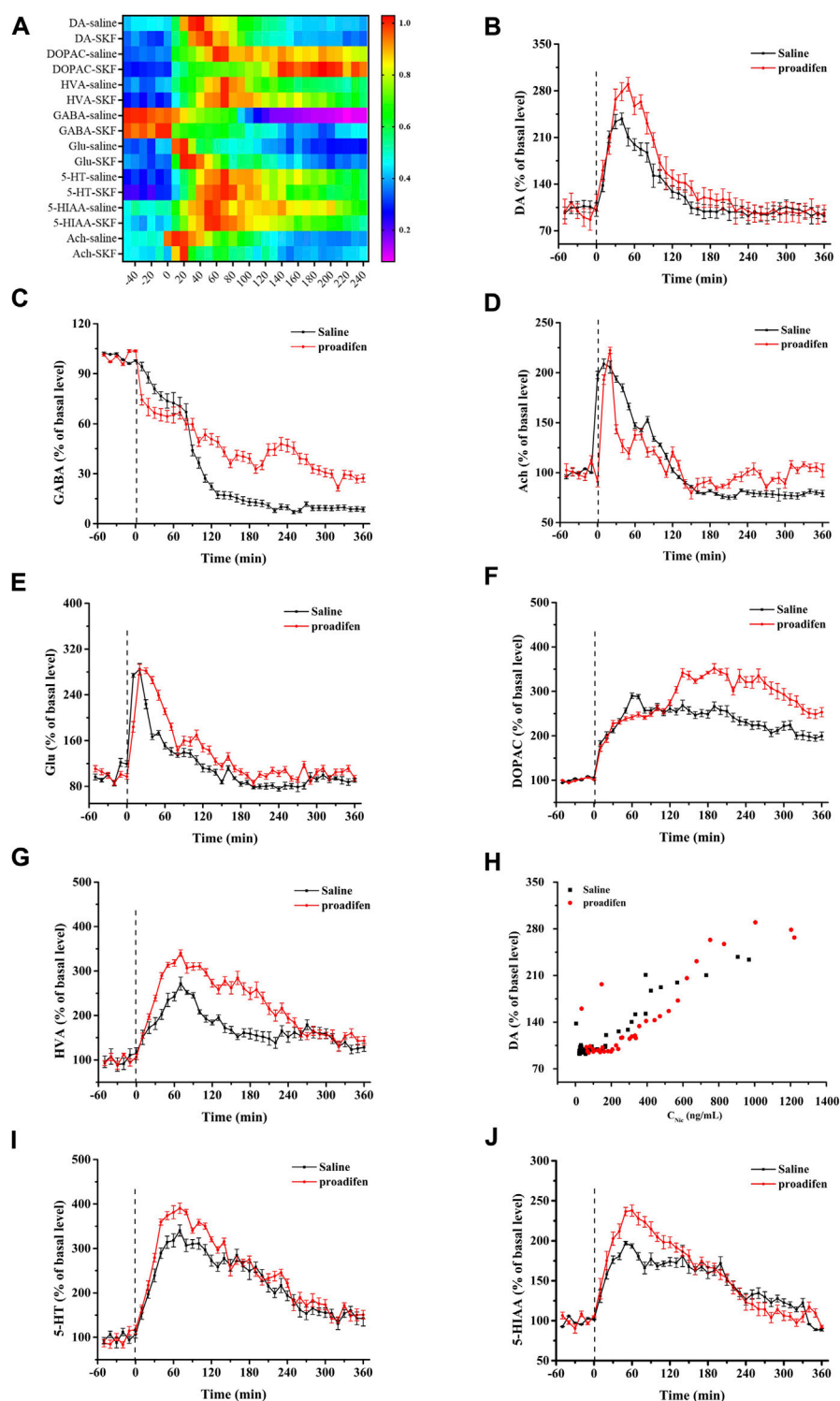
FIGURE 5
(A) The heat map shows all changes of neurotransmitters, where the colors correlated with the changes expressed as percentage of baseline. Time course of Nic exposure evoked DA **(B)**, Glu **(C)**, Ach **(D)**, GABA **(E)**, DOPAC **(F)**, HVA **(H)**, 5-HT **(I)**, and 5-HIAA **(J)** release in the NAc, data were expressed as % of basal release. (Each point was expressed as mean $\pm$ SD from three rats) **(G)** Scatter plot of Nic concentration and DA release level.

DAergic, glutamatergic, and GABAergic neurons in the mesolimbic DA system, which is responsible for the increase in extracellular DA in the NAc (Xi et al., 2009), but as a strong agonist of nAChRs, it is little known about the effects on extracellular Ach release in the

NAc. We found that acute Nic treatment affects the release and metabolism of DA in rat NAc. The levels of DA and its metabolites, such as DOPAC and HVA, were elevated, which was consistent with Pietilä's results that DOPAC and HVA were significantly increased

and 3-MT was decreased after acute Nic administration in striatum (Pietilä et al., 1996). The level of DA in the rat NAc increased after intraperitoneal injection of Nic, and the level of DA metabolites, DOPAC and HVA, were higher than DA, which confirmed that DA was rapidly metabolized after release into the synaptic cleft. The higher concentration of Nic after proadifen inhibition enhanced the spike of DAergic neurons in the VTA, which thereby increased the release of excitatory neurotransmitters in the NAc. Like Nic, Ach is also involved and binds with nAChRs. However, little knowledge about the effects of Nic on extracellular Ach release in the NAc. The basal forebrain contains large number of acetylcholinergic neurons, and the NAc is mainly composed of GABAergic neurons. However, we found that after Nic stimulation, Ach in the NAc also increased sharply, this may be due to the regulation of NAc by cholinergic neurons in the prefrontal cortex (Cooper and Henderson, 2020), and some research has reported that Ach in the NAc is associated with aversive states and satiation (Rada et al., 2001; Hoebel et al., 2007). In addition, Nic acted on the nAChRs on GABAergic neurons in NAc, and nAChRs were desensitized by the high Nic concentration, which decreased the GABAergic effects on DAergic neurons, resulting in the disinhibition of DA neurons (Grieder et al., 2019; Cooper., et al., 2020). These results also speak to the previous report that DAergic neurons in the VTA project to GABAergic and cholinergic interneurons in the NAc, which together with glutamatergic projections from the prefrontal cortex provide a complex regulatory network with multiple effects of Nic (Morozova et al., 2020). Studies have shown that compared with smokers with a normal Nic metabolism ability, individuals lacking full functional CYP2A6 were perceptibly protected against becoming tobacco-dependent smokers (Pianezza et al., 1998). Nic plus methoxsalen given orally inhibits the first-pass metabolism of Nic, and the combination directly reduces the desire to smoke (Sellers et al., 2000). These results indicated that the decrease of Nic metabolism caused by genetic or drug factors can alleviate dependence-related behaviors. Our present results extend these findings, demonstrating that the influence of inadequate Nic metabolism on related behaviors is due to the relatively high level and long residence of Nic in the brain that can trigger a more lasting release of neurotransmitters.

After inhibiting the metabolism of Nic, higher concentrations of Nic in the NAc continued to act on 5-HTergic neurons to exert an analgesic effect. This may be related to the anti-nociception properties of Nic confirmed by extensive and compelling studies that found that peripheral administration of methoxsalen for inhibiting mouse Nic metabolism dramatically prolonged the Nic-induced analgesic effect, which was confirmed by tail-flick and hot-plat tests. In addition, Shen et al. established a rat Nic withdrawal model and founded that after Nic discontinuation, the mechanical withdrawal threshold and thermal withdrawal latency of rats were notably reduced with the decreased level of 5-HT; however, intrathecal injection of 5-HT abolished these differences between the control and Nic withdrawal group (Shen et al., 2021). Based on these related behavioral phenomena reported previously and the results of our analysis, it was further indicated that 5-HTergic neurons may play a key role in the analgesic effect of Nic.

In conclusion, correlating the changes of neurotransmitters with brain Nic levels during its metabolic process in the body can provide more definitive evidence for comprehensively understanding the influence of Nic clearance on its neuropharmacological actions. Our

results indicated that the precolumn derivatization-based online microdialysis coupled with a UHPLC-HRMS/MS system was an efficient and novel technique to synchronously monitor the brain Nic metabolism and neurochemical changes in freely-moving animals. After inhibition of the rat CYP2B activity, the brain Nic pharmacokinetics changed, and the higher concentration of Nic in the brain led to a further release of the excitatory neurotransmitter DA, as well as the release of the inhibitory neurotransmitter GABA, which may be one of the reasons why the high concentration of Nic would produce adverse effects. The increased 5-HT release further confirmed the previously reported phenomenon that the analgesic effect of Nic was prolonged after inhibiting Nic metabolism.

5 Conclusion

We developed a precolumn derivatization-based online microdialysis coupled with UHPLC-HRMS/MS method to achieve continuous sampling and simultaneous investigation of Nic metabolites and several neurochemicals in the brain. The usefulness of this platform was confirmed by monitoring the brain pharmacokinetic profiles of Nic and the associated time-dependent neurotransmitter release following peripheral Nic exposure. The N-demethylation and N-oxidation metabolic pathways of Nic were significantly declined in the brain with the inhibition of rat CYP2B activity, inducing the higher level and longer residence of Nic and the enhanced release of neurotransmitters in the NAc. These results indicated that the disposition and metabolism of Nic was an important determinant of its neurochemical effects in the specific brain regions. To our knowledge, it was the first time to synchronously obtain the cerebral Nic pharmacokinetics and the related changes of neurotransmitters regulated by Nic metabolism. The present study provides a fundamental basis for monitoring the brain metabolic profiles and pharmacodynamics of Nic when developing the Nic delivery systems, Nic replacement therapy, or studying the potential role of Nic in improving depression and other neurological diseases.

Data availability statement

The datasets presented in this study can be found in online repositories. The names of the repository/repositories and accession number(s) can be found in the article/Supplementary Material.

Ethics statement

The animal study was approved by Life Science Ethics Review Committee of Zhengzhou University. The study was conducted in accordance with the local legislation and institutional requirements.

Author contributions

LG: Conceptualization, Data curation, Formal Analysis, Investigation, Methodology, Writing–original draft. JM: Conceptualization, Data curation, Formal Analysis, Investigation,

Methodology, Writing–original draft. QZ: Data curation, Formal Analysis, Methodology, Writing–review and editing. WF: Data curation, Formal Analysis, Methodology, Writing–review and editing. DW: Data curation, Formal Analysis, Methodology, Writing–review and editing. ZL: Data curation, Formal Analysis, Methodology, Writing–review and editing. JH: Writing–review and editing. JX: Conceptualization, Funding acquisition, Project administration, Writing–review and editing.

Funding

Conflict of interest

The authors declare that the research was conducted in the absence of any commercial or financial relationships that could be construed as a potential conflict of interest.

Publisher's note

All claims expressed in this article are solely those of the authors and do not necessarily represent those of their affiliated organizations, or those of the publisher, the editors and the reviewers. Any product that may be evaluated in this article, or claim that may be made by its manufacturer, is not guaranteed or endorsed by the publisher.

Supplementary material

The Supplementary Material for this article can be found online at: https://www.frontiersin.org/articles/10.3389/fchem.2023.1275478/full#supplementary-material

References

Al Koudsi, N., and Tyndale, R. F. (2010). Hepatic CYP2B6 is altered by genetic, physiologic, and environmental factors but plays little role in nicotine metabolism. *Xenobiotica* 40 (6), 381–392. doi:10.3109/00498251003713958

Alsharari, S. D., Siu, E. C. K., Tyndale, R. F., and Damaj, M. I. (2014). Pharmacokinetic and pharmacodynamics studies of nicotine after oral administration in mice: effects of methoxsalen, a CYP2a5/6 inhibitor. *Nicotine Tob. Res.* 16 (1), 18–25. doi:10.1093/ntr/ntt105

Changeux, J. P. (2010). Nicotine addiction and nicotinic receptors: lessons from genetically modified mice. *Nat. Rev. Neurosci.* 11, 389–401. doi:10.1038/nrn2849

Chen, A. J., Kang, Y. Y., Liu, J., Wu, J. R., Feng, X. L., Wang, M. L., et al. (2022). Improvement of synaptic plasticity by nanoparticles and the related mechanisms: applications and prospects. *J. Control Release* 347, 143–163. doi:10.1016/j.jconrel.2022.04.049

Cooper, S. Y., and Henderson, B. J. (2020). The impact of electronic nicotine delivery system (ENDS) flavors on nicotinic acetylcholine receptors and nicotine addiction-related behaviors. *Molecules* 25, 4223. doi:10.3390/molecules25184223

El-Sherbeni, A. A., Stocco, M. R., Wadji, F. B., and Tyndale, R. F. (2020). Addressing the instability issue of dopamine during microdialysis: the determination of dopamine, serotonin, methamphetamine and its metabolites in rat brain. *J. Chromatogr. A* 1627, 461403. doi:10.1016/j.chroma.2020.461403

Garcia, K. L. P., Coen, K., Miksys, S., Lê, A. D., and Tyndale, R. F. (2015). Effect of brain CYP2B inhibition on brain nicotine levels and nicotine self-administration. *Neuropsychopharmacol* 40, 1910–1918. doi:10.1038/npp.2015.40

Garcia, K. L. P., Lê, A. D., and Tyndale, R. F. (2017). Brain CYP2B induction can decrease nicotine levels in the brain. *Addict. Biol.* 22, 1257–1266. doi:10.1111/adb.12411

Greco, S., Danysz, W., Zivkovic, A., Gross, R., and Stark, H. (2013). Microdialysis analysis of monoamine neurotransmitters-A versatile and sensitive LC-MS/MS method. *Anal. Chim. Acta* 771, 65–72. doi:10.1016/j.aca.2013.02.004

Grieder, T. E., Besson, M., Maal-Bared, G., Pons, S., Maskos, U., and van der Kooy, D. (2019). β2* nAChRs on VTA dopamine and GABA neurons separately mediate nicotine aversion and reward. *P Natl. Acad. Sci. U. S. A.* 116, 25968–25973. doi:10.1073/pnas.1908724116

Hammond, D. K., Bjercke, R. J., Langone, J. J., and Strobel, H. W. (1991). Metabolism of nicotine by rat liver cytochromes P-450. Assessment utilizing monoclonal antibodies to nicotine and cotinine. *Drug Metab. Dispos.* 19 (4), 804–808.

Henderson, B. J., Wall, T. R., Henley, B. M., Kim, C. H., Mckinney, S., and Lester, H. A. (2017). Menthol enhances nicotine reward-related behavior by potentiating nicotine-induced changes in nAChR function, nAChR upregulation, and DA neuron excitability. *Neuropsychopharmacol* 42, 2285–2291. doi:10.1038/npp.2017.72

Hoebel, B. G., Avena, N. M., and Rada, P. (2007). Accumbens dopamine-acetylcholine balance in approach and avoidance. *Cuur Opin. Pharmacol.* 7 (6), 617–627. doi:10.1016/j.coph.2007.10.014

Hukkanen, J., Jacob, P., 3rd, and Benowitz, N. L. (2005). Metabolism and disposition kinetics of nicotine. *Pharmacol. Rev.* 57, 79–115. doi:10.1124/pr.57.1.3

Hwa Jung, B., Chul Chung, B., Chung, S. J., and Shim, C. K. (2001). Different pharmacokinetics of nicotine following intravenous administration of nicotine base and nicotine hydrogen tartarate in rats. *J. Control Release* 77, 183–190. doi:10.1016/s0168-3659(01)00452-7

Jadzic, D., Bassareo, V., Carta, A. R., and Carboni, E. (2021). Nicotine, cocaine, amphetamine, morphine, and ethanol increase norepinephrine output in the bed nucleus of stria terminalis of freely moving rats. *Addict. Biol.* 26, e12864. doi:10.1111/adb.12864

Jha, R. R., Singh, C., Pant, A. B., and Patel, D. K. (2018). Ionic liquid based ultrasound assisted dispersive liquid-liquid microextraction for simultaneous determination of 15 neurotransmitters in rat brain, plasma and cell samples. *Anal. Chim. Acta* 100, 43–53. doi:10.1016/j.aca.2017.12.015

Jing, M., Zhang, Y. J., Wang, H., and Li, Y. L. (2019). G-protein coupled receptor-based sensors for imaging neurochemicals with high sensitivity and specificity. *J. Neurochem.* 151, 279–288. doi:10.1111/jnc.14855

Liu, X. M., Xiao, T. F., Wu, F., Shen, M. Y., Zhang, M. N., Yu, H. H., et al. (2017). Ultrathin cell-membrane-mimic phosphorylcholine polymer film coating enables large improvements for *in vivo* electrochemical detection. *Angew. Chem. Int. Ed. Engl.* 56, 11802–11806. doi:10.1002/anie.201705900

Mao, J., Xu, Y., Lu, B. B., Liu, J. H., Hong, G. F., Zhang, Q. D., et al. (2015). Simultaneous determination of nicotine and its nine metabolites in rat blood utilizing microdialysis coupled with UPLC-tandem mass spectrometry for pharmacokinetic application. *Anal. Bioanal. Chem.* 407, 4101–4109. doi:10.1007/s00216-015-8643-0

Mendoza, C., Barreto, G. E., Iarkov, A., Tarasov, V. V., Aliev, G., and Echeverria, V. (2018). Cotinine: a therapy for memory extinction in post-traumatic stress disorder. *Mol. Neurobiol.* 55, 6700–6711. doi:10.1007/s12035-018-0869-3

Morozova, E., Faure, P., Gutkin, B., Lapish, C., and Kuznetsov, A. (2020). Distinct temporal structure of nicotinic ACh receptor activation determines responses of VTA neurons to endogenous ACh and nicotine. *eNeuro* 7, ENEURO.0418–19.2020. doi:10.1523/ENEURO.0418-19.2020

Nandi, P., and Lunte, S. M. (2009). Recent trends in microdialysis sampling integrated with conventional and microanalytical systems for monitoring biological events: a review. *Anal. Chim. Acta* 651, 1–14. doi:10.1016/j.aca.2009.07.064

Nguyen, C., Mondoloni, S., Borgne, T. L., Centeno, I, Come, M., Jehl, J., et al. (2021). Nicotine inhibits the VTA-to-amygdala dopamine pathway to promote anxiety. *Neuron* 109, 2604–2615.e9. doi:10.1016/j.neuron.2021.06.013

Olesti, E., Rodríguez-Morató, J., Gomez-Gomez, A., Ramaekers, J. G., de la Torre, R., and Pozo, O. J. (2019). Quantification of endogenous neurotransmitters and related compounds by liquid chromatography coupled to tandem mass spectrometry. *Talanta* 192, 93–102. doi:10.1016/j.talanta.2018.09.034

Oliveros-Matus, P., Perez-Urrutia, N., Alvarez-Ricartes, N., Echeverria, F., Barreto, G. E., Elliott, J., et al. (2020). Cotinine enhances fear extinction and astrocyte survival by mechanisms involving the nicotinic acetylcholine receptors signaling. *Front. Pharmacol.* 11, 303. doi:10.3389/fphar.2020.00303

Pan, C., Wei, H., Han, Z. J., Wu, F., and Mao, L. Q. (2020). Enzymatic electrochemical biosensors for *in-situ* neurochemical measurement. *Curr. Opin. Electrochem* 19, 162–167. doi:10.1016/j.coelec.2019.12.008

Pianezza, M. L., Sellers, E. M., and Tyndale, R. F. (1998). Nicotine metabolism defect reduces smoking. *Nature* 393, 750. doi:10.1038/31623

Pietilä, K., Salminen, O., Leikola-Pelho, T., and Ahtee, L. (1996). Tolerance to nicotine's effects on striatal dopamine metabolism in nicotine-withdrawn mice. *Eur. J. pharmacol.* 318 (1), 17–22. doi:10.1016/s0014-2999(96)00767-4

Piller, M., Gilch, G., Scherer, G., and Scherer, M. (2014). Simple, fast and sensitive LC–MS/MS analysis for the simultaneous quantification of nicotine and 10 of its major metabolites. *J. Chromatogr. B* 952, 7–15. doi:10.1016/j.jchromb.2014.01.025

Quik, M., Perez, X. A., and Bordia, T. (2012). Nicotine as a potential neuroprotective agent for Parkinson's disease. *Mov. Disord.* 27, 947–957. doi:10.1002/mds.25028

Rada, P., Jensen, K., and Hoebel, B. G. (2001). Effects of nicotine and mecamylamine-induced withdrawal on extracellular dopamine and acetylcholine in the rat nucleus accumbens. *Psychopharcology* 157 (1), 105–110. doi:10.1007/s002130100781

Rangiah, K., Hwang, W. T., Mesaros, C., Vachani, A., and Blair, I. A. (2011). Nicotine exposure and metabolizer phenotypes from analysis of urinary nicotine and its 15 metabolites by LC-MS. *Bioanalysis* 3 (7), 745–761. doi:10.4155/bio.11.42

Saracino, M. A., Santarcangelo, L., Raggi, A. A., and Mercolini, L. (2015). Microextraction by packed sorbent (MEPS) to analyze catecholamines in innovative biological samples. *J. Pharm. Biomed. Anal.* 104, 122–129. doi:10.1016/j.jpba.2014.11.003

Sellers, E. M., Kaplan, H. L., and Tyndale, R. F. (2000). Inhibition of cytochrome P450 2A6 increases nicotine's oral bioavailability and decreases smoking. *Clin. Pharmacol. Ther.* 68, 35–43. doi:10.1067/mcp.2000.107651

Shen, L., Qiu, H. B., Xu, H. H., Wei, K., Zhao, L., Zhu, C. C., et al. (2021). Nicotine withdrawal induces hyperalgesia via downregulation of descending serotonergic pathway in the nucleus raphe magnus. *Neuropharmacology* 189, 108515. doi:10.1016/j.neuropharm.2021.108515

Shi, F., Guo, C. C., Gong, L. P., Li, J., Dong, P., Zhang, J. L., et al. (2014). Application of a high resolution benchtop quadrupole-Orbitrap mass spectrometry for the rapid screening, confirmation and quantification of illegal adulterated phosphodiesterase-5 inhibitors in herbal medicines and dietary supplements. *J. Chromatogr. A* 1344, 91–98. doi:10.1016/j.chroma.2013.12.030

Song, P., Mabrouk, O. S., Hershey, N. D., and Kennedy, R. (2012). *In vivo* neurochemical monitoring using benzoyl chloride derivatization and liquid chromatography-mass spectrometry. *Anal. Chem.* 84, 412–419. doi:10.1021/ac202794q

Sun, F. M., Zhou, J. H., Dai, B., Qian, T. R., Zeng, J. Z., Li, X. L., et al. (2020). Next-generation GRAB sensors for monitoring dopaminergic activity *in vivo*. *Nat. methods* 17, 1156–1166. doi:10.1038/s41592-020-00981-9

Tanner, J. A., Chenoweth, M. J., and Tyndale, R. F. (2015). Pharmacogenetics of nicotine and associated smoking behaviors. *Curr. Top. Behav. Neurosci.* 23, 37–86. doi:10.1007/978-3-319-13665-3_3

Tapper, A. R., McKinney, S. L., Nashmi, R., Schwarz, J., Deshpande, P., Labarca, C., et al. (2004). Nicotine activation of α4* receptors: sufficient for reward, tolerance, and sensitization. *Science* 306, 1029–1032. doi:10.1126/science.1099420

Tufi, S., Lamoree, M., Boer, J., and Leonards, P. (2015). Simultaneous analysis of multiple neurotransmitters by hydrophilic interaction liquid chromatography coupled to tandem mass spectrometry. *J. Chromatogr. A* 1395, 79–87. doi:10.1016/j.chroma.2015.03.056

Vivekanandarajah, A., Waters, K. A., and Machaalani, R. (2019). Cigarette smoke exposure effects on the brainstem expression of nicotinic acetylcholine receptors (nAChRs), and on cardiac, respiratory and sleep physiologies. *Resp. Physiol. Neurobi* 259, 1–15. doi:10.1016/j.resp.2018.07.007

Wang, Q. Q., Zhang, J., Pi, Z. F., Zheng, Z., Xing, J. P., Song, F. R., et al. (2015). Application of online microdialysis coupled with liquid chromatography-tandem mass spectrometry method in assessing neuroprotective effect of Rhizoma coptidis on diabetic rats. *Anal. Methods* 7, 45–52. doi:10.1039/c4ay01809e

Wong, J. M., Malec, P. A., Mabrouk, O. S., Ro, J., Dus, M., and Kennedy, R. T. (2016). Benzoyl chloride derivatization with liquid chromatography-mass spectrometry for targeted metabolomics of neurochemicals in biological samples. *J. Chromatogr. A* 1446, 78–90. doi:10.1016/j.chroma.2016.04.006

Xi, Z. X., Spoller, K., and Gardner, E. L. (2009). Mechanism-based medication development for the treatment of nicotine dependence. *Acta Pharmacol. Sin.* 30, 723–739. doi:10.1038/aps.2009.46

Xiao, C., Zhou, C. Y., Jiang, J. H., and Yin, C. (2020). Neural circuits and nicotinic acetylcholine receptors mediate the cholinergic regulation of midbrain dopaminergic neurons and nicotine dependence. *Acta Pharmacol. Sin.* 41, 1–9. doi:10.1038/s41401-019-0299-4

Xu, Y., Zhang, Q. D., Li, P., Hong, G. F., Wang, D. Z., Liu, J. H., et al. (2019). Nicotine pharmacokinetics in rat brain and blood by simultaneous microdialysis, stable-isotope labeling, and UHPLC-HRMS: determination of nicotine metabolites. *Anal. Chem.* 91, 2916–2922. doi:10.1021/acs.analchem.8b05078

Zestos, A. G., Luna-Munguia, H., Stacey, W. C., and Kennedy, R. T. (2019). Use and future prospects of *in vivo* microdialysis for epilepsy studies. *ACS Chem. Neurosci.* 10, 1875–1883. doi:10.1021/acschemneuro.8b00271

Zhang, M. L., Fang, C. W., and Smagin, G. (2014). Derivatization for the simultaneous LC/MS quantification of multiple neurotransmitters in extracellular fluid from rat brain microdialysis. *J. Pharm. Biomed. Anal.* 100, 357–364. doi:10.1016/j.jpba.2014.08.015

Zhou, G. S., Yuan, Y. C., Yin, Y., Tang, Y. P., Xu, R. J., Liu, Y., et al. (2020). Hydrophilic interaction chromatography combined with ultrasound-assisted ionic liquid dispersive liquid-liquid microextraction for determination of underivatized neurotransmitters in dementia patients' urine samples. *Anal. Chim. Acta* 1107, 74–84. doi:10.1016/j.aca.2020.02.027

Unraveling the potential of breath and sweat VOC capture devices for human disease detection: a systematic-like review of canine olfaction and GC-MS analysis

Laetitia Maidodou[1,2,3], Igor Clarot[2], Michelle Leemans[4], Isabelle Fromantin[4,5], Eric Marchioni[3] and Damien Steyer[1]*

[1]Twistaroma, Illkirch Graffenstaden, France, [2]CITHEFOR, EA 3452, Université de Lorraine, Nancy, France, [3]DSA, IPHC UMR7178, Université de Strasbourg, Strasbourg, France, [4]Clinical Epidemiology and Ageing, IMRB—Paris Est Créteil University /Inserm U955, Créteil, France, [5]Wound Care and Research Unit, Curie Institute, Paris, France

The development of disease screening methods using biomedical detection dogs relies on the collection and analysis of body odors, particularly volatile organic compounds (VOCs) present in body fluids. To capture and analyze odors produced by the human body, numerous protocols and materials are used in forensics or medical studies. This paper provides an overview of sampling devices used to collect VOCs from sweat and exhaled air, for medical diagnostic purposes using canine olfaction and/or Gas Chromatography-Mass spectrometry (GC-MS). Canine olfaction and GC-MS are regarded as complementary tools, holding immense promise for detecting cancers and infectious diseases. However, existing literature lacks guidelines for selecting materials suitable for both canine olfaction and GC-MS. Hence, this review aims to address this gap and pave the way for efficient body odor sampling materials. The first section of the paper describes the materials utilized in training sniffing dogs, while the second section delves into the details of sampling devices and extraction techniques employed for exhaled air and sweat analysis using GC-MS. Finally, the paper proposes the development of an ideal sampling device tailored for detection purposes in the field of odorology. By bridging the knowledge gap, this study seeks to advance disease detection methodologies, harnessing the unique abilities of both dogs and GC-MS analysis in biomedical research.

KEYWORDS

breath, sweat, VOC, canine olfaction, sampling devices, gas chromatography, mass spectrometry

1 Introduction

Human body odors are widely studied to develop non-invasive disease diagnosis methods. A plethora of reviews exist on the subject, encompassing biomedical detection dogs (Gordon et al., 2008; Moser and McCulloch, 2010a; Lippi and Cervellin, 2012a; Pirrone and Albertini, 2017a; Catala et al., 2019) and instrumental analysis (Ligor et al., 2008; Dormont et al., 2013; de Lacy Costello et al., 2014; Monteiro et al., 2014; Prada et al., 2014; Robinson et al., 2018; Lippi and Heaney, 2020; Chai and Chua, 2021; Sinclair et al., 2021). Additionally, alternative systems like electronic noses have emerged since the mid-1980s.

FIGURE 1
Flowchart (created in BioRender.com) illustrating the process for human VOCs sampling, extraction, and analysis by canine olfaction and GC-MS; GC-MS: Gas Chromatography coupled to Mass Spectrometry, SPME: Solid Phase Micro-Extraction, SBSE: Stir Bars Sorptive Extraction.
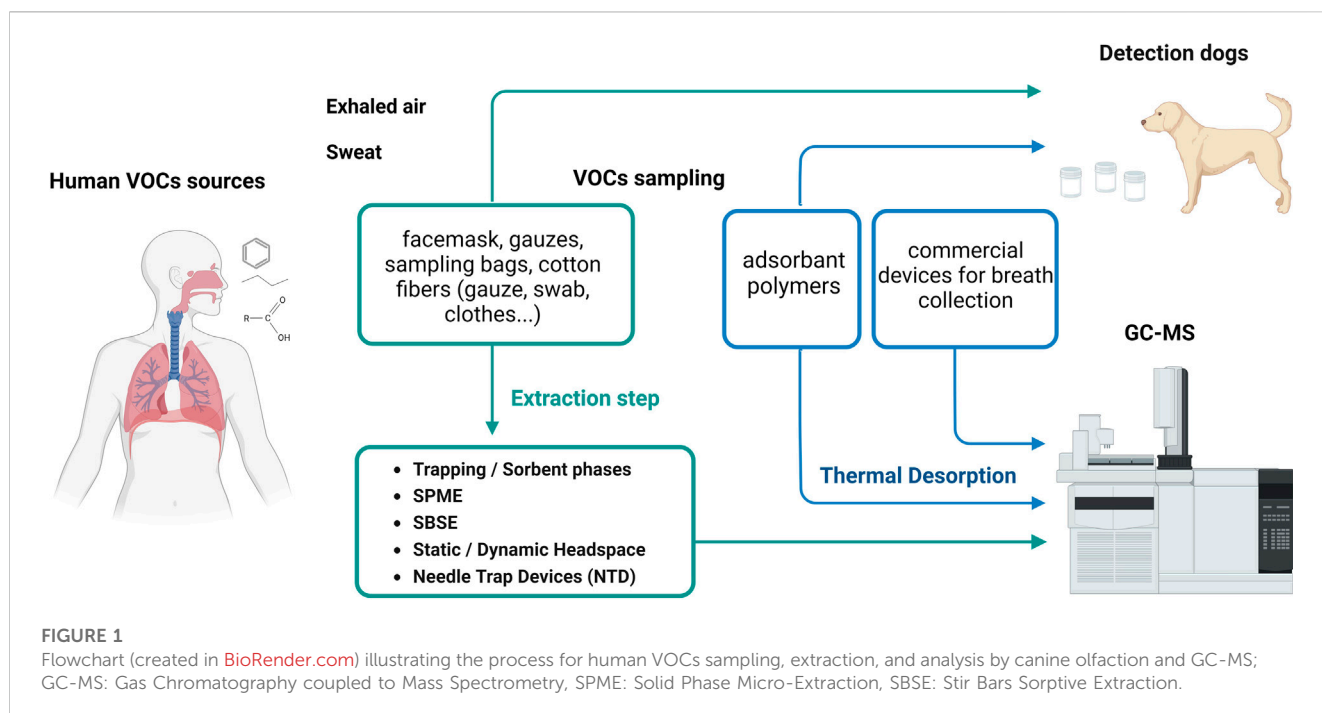
These systems utilize sensors to detect disease-specific biomarkers, offering quick real-time preliminary diagnoses at a lower cost. One of their drawbacks is the lower level of sample discrimination (Wilson and Forse, 2023). Electronic nose systems are less portable than canine olfaction due to potential restrictions posed by power, weight, or space requirements (Wilson and Forse, 2023). Despite this, the use of the dog as a diagnostic tool has not yet been standardized nor validated by health organizations (Bauër et al., 2022a). Therefore, GC-MS is of great interest to identify diseases-specific VOCs, detected by dogs. It can be employed as a complementary tool to validate canine olfaction-based diagnosis methods and to understand how dogs discriminate sick from healthy humans.

The choice of the sampling material plays a critical role in training dogs to recognize a specific pattern of volatile biomarkers. To effectively present the material to the dog, it must be appropriately sized and contained, such as a cloth, cotton gauze, swab, or a facemask capable of absorbing VOCs. The detection of precise odors can be challenging due to the variability in samples and the environment. Therefore, selecting an appropriate material that can collect and diffuse odors efficiently can greatly facilitate the dog's sniffing process, leading to more accurate results during detection exercises.

In the context of instrumental analysis using GC-MS for VOCs detection, it is essential to extract the VOCs from the sampling material and inject them into the analytical system. This paper focuses on discussing specific devices based on adsorbent polymers designed for training detection dogs. Among these devices, the most suitable ones are those that are both dog-compatible and can be directly used with GC-MS systems through thermal desorption, as illustrated in Figure 1.

In addition to the medical context, sniffing dogs find extensive application in forensics. Standardized protocols are used to train these dogs for explosives or illicit substance detection and criminal suspect identification (Lorenzo et al., 2003). Commonly, hands and

feet serve as the VOCs sources for suspect identification, and gauze is often employed for sweat sampling (Cuzuel et al., 2017). Notably, The Scent Transfer Unit or STU100 (odor suction tool) plays a pivotal role in concentrating odors on gauze within this context (Curran et al., 2010a; Degreeff and Furton, 2011). This unit comprises a vacuum pump that actively samples VOCs emitted from any object onto a gauze.

The National Institute of Science and Technology (NIST) has developed a polymer-based adsorption canine training device made of polydimethylsiloxane (PDMS). This device, safe for the dog (non-toxic, non-infectious) (MacCrehan et al., 2020), has been employed in training dogs for explosive detection (MacCrehan et al., 2018a; Simon et al., 2021). Additionally, Getxent® tubes (Biodesiv, France), consisting of a patented adsorbent polymer, have been developed for detection dog training and are utilized in forensics (Simon, 2022).

This comprehensive bibliographic study delves into a thorough examination of the methodologies utilized for comprehending diverse techniques of odor capture. Specifically, the study focuses on canine olfaction and/or Gas Chromatography-Mass Spectrometry (GC-MS) systems within the context of medical odor analysis. By delving into the intricacies of these methodologies, this study aims to shed light on the intricate processes involved in capturing odors, thereby contributing to the advancement of our understanding in the field.

2 Materials and methods

2.1 Literature search

In adherence to the widely recognized Preferred Reporting Items for Systematic Reviews and Meta-Analyses (PRISMA) standards, our search was conducted independently on both Pubmed and Web of Science. PRISMA is the most commonly utilized method for systematic reviews ((Moher et al., 2022).

FIGURE 2
PRISMA flow-chart for canine olfaction and GC-MS analysis.
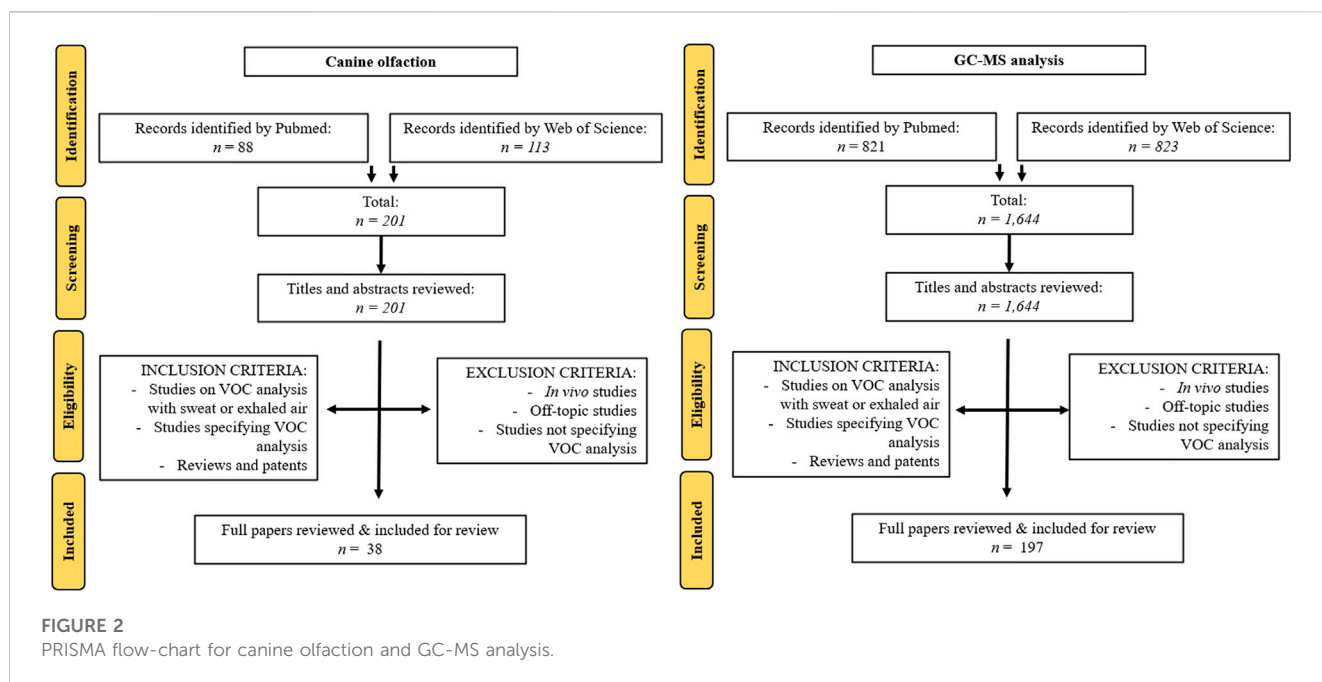
2.1.1 Canine olfaction

In this study, the research is focused on the different scent collection devices related to the analysis of gaseous non-invasive materials: exhaled air, and sweat/body odor, in a medical context. The subsequent sequence is researched in Web of Science and PubMed databases: *((dog) OR(canine)) AND ((odor)OR(odour)OR(smell)OR(sniff)OR(volatile organic compounds)OR(volatile)) AND ((breath)OR(exhaled air) OR(sweat)) AND ((diagnosis)OR(disease)OR(medical)) AND ((human) OR(patient)OR(subject)).* Studies have been selected without date restrictions until March 2023.

2.1.2 GC-MS analysis

The subsequent sequence was researched in Web of Sciences and PubMed databases: *((GC-MS) OR (gas chromatography) OR (volatolomics)) AND ((odor) OR (odour) OR (volatile organic compounds) OR (volatile)) AND ((breath) OR (exhaled air) OR (sweat) OR (body odor)) AND ((diagnosis) OR (disease) OR (medical)) AND ((human) OR (patient) OR (subject)).* Studies have been selected without date restrictions until March 2023.

2.2 Study selection and eligibility criteria

Following the PRISMA standards, data obtained from the independent searches on Pubmed and Web of Science were consolidated into a worksheet file, incorporating essential details such as DOI number, title, publication year, authors, journal, and abstracts. For canine olfaction, the initial search yielded a total of 201 records, with 88 from PubMed and 113 from Web of Science. After a comprehensive evaluation of 201 full-text papers, 163 were excluded based on relevance, resulting in the inclusion of 38 papers in the final systematic review. For GC-MS analysis, a total of 197 papers were included with initially 821 articles from Pubmed and 823 from Web of

Science. After the removal of duplicates, the remaining titles and abstracts were carefully reviewed to identify studies relevant to the topic. To ensure thoroughness, two researchers (L.M. and D.S.) independently assessed the studies, resolving any discrepancies through discussion. Articles were considered if they featured a dedicated "material and methods" section that comprehensively delineated the protocol employed for sampling VOCs. A prerequisite was the presence of at least one sampling material being explicitly cited. Furthermore, the study took into account reviews and patents. Importantly, no differentiation was made based on the level of pathologies, ensuring a broad and inclusive scope. Conversely, articles were excluded if they lacked pertinent information concerning VOCs sampling. Additionally, no *in vivo* studies were included (Figure 2). To ensure a comprehensive overview, reference lists of the included articles were also screened based on their titles and abstracts, enabling the inclusion of further pertinent articles.

2.3 Data extraction

The relevant data were extracted from the selected studies. Standardized tables were designed to abstract the studies of interest. Table 1 highlights instances where PDMS-based sampling devices are employed to capture volatile compounds for medical odor analysis. Table 2 showcases practical scenarios demonstrating the use of fabric-based techniques to capture volatile compounds, contributing to odor analysis. In Table 3, various extraction techniques post-sample collection are illustrated, vital for isolating volatile compounds for subsequent analysis.

In the Supplementary Table S1, a detailed breakdown of sweat analysis using Gas Chromatography-Mass Spectrometry (GC-MS) is provided. Supplementary Table S2 outlines diverse extraction

TABLE 1 Application examples of PDMS-based sampling devices.

Body area	Sampling device	Sampling method	Desorption method	Sample storage conditions	Analysis system	GC-column	Sensibility	Ref.
wrist and ankle	a 25 cm long tube made of medical grade PDMS (0.64 mm OD × 0.3 mm ID, Sil-Tec®).	passive sampling for 1 h	Thermal desorption at 250°C in a splitless mode for 30 s (PDMS sampler is inserted into a glass inlet liner (Agilent)	stored in aluminum foil at 4°C for 48 h	GCxGC-TOFMS	1D column: Rxi-5Sil (Restek) 30 m × 0.25 mm × 0.25 µm. 2D column: Rxi-17Sil (Restek) 1 m × 0.25 mm × 0.25 µm	not specified	Wooding et al. (2020)
forehead	PDMS patch (5 mm × 15 mm x 0.45 mm)	passive sampling for 30 min	Thermal desorption at 180°C for 10 min. Cryo-focusing at −10°C. Injection splitless at 300°C for 5 min	stored into TD-tubes at −80°C for 21 days	GC-MS	DB-5 MS (Agilent) 60 m × 0.25 mm x 0.25 µm	170 to 200 pg/cm	Martin et al. (2016)
forearms and abdomen	PDMS patches (20 mm × 15 mm × 0.45 mm)	passive sampling for 5–120 min	Thermal desorption at 180°C for 5 min. Cryo-focusing at −10°C. Injection splitless at 300°C for 3 min	stored into TD tubes at 4°C for 24 h	GC-MS	DB-5MS (Agilent) 60 m × 0.25 mm x 0.25 µm	50 pg to 100 ng per sample (relative estimation)	Riazanskaia et al. (2008)
upper back, forearm, and back thigh	PDMS round patches (6, 11 and 17 mm diameter, 0.25 mm, thickness)	passive sampling for 60 min	Thermal desorption at 250°C for 3 min. Cryo-focusing at −120°C. Injection splitless at 280°C	stored no longer than 72 h	GC-MS	RK13870 (Restek) 30 m × 0.32 mm x 1.8 µm	not specified	Jiang et al. (2013)
forearms	Twisters (10 mm, 0.5 mm in film thickness, 24 µL PDMS phase volume, Gerstel)	active sampling (Twisters roll on the skin), the sampling time is not specified	Thermal desorption at 280°C for 10 min. Cryo-focusing at −60°C. Injection at 280°C for 10 min	stored at 4°C for 14 days	GC-MS	DB-5MS (Agilent) 20 m × 0.18 mm x 0.18 µm	not specified	Penn et al. (2007)
			Thermal desorption at 250°C for 3 min. Cryo-focusing at −80°C. Injection at 280°C for 10 min	stored at 4°C for 14 days	GC-MS	DB-5MS (Agilent) 20 m × 0.18 mm x 0.18 µm	not specified	Soini et al. (2006)
axilla			Thermal desorption at 250°C for 3 min. Cryo-focusing at −80°C. Injection at 280°C for 10 min	stored at 4°C for 20 days	GC-MS	DB-5MS (Agilent) 20 m × 0.18 mm x 0.18 µm	not specified	Xu et al. (2007)

methods for Gas Chromatography-Mass Spectrometry (GC-MS) analysis of breath samples collected. Supplementary Table S3 offers a comprehensive comparison of odor capture systems, applicable to canine olfaction studies and Gas Chromatography-Mass Spectrometry (GC-MS) analysis.

3 Results

3.1 Canine olfaction

In 1989, a first study suggested the potential of dogs to diagnose cancer (Williams and Pembroke, 1989). Over the next 2 decades, the interest in this area grew exponentially, as evidenced by Moser et al.'s review in 2010, which identified 531 publications on cancer detection by dogs (Moser and McCulloch, 2010a). Among the various reviews (Moser and McCulloch, 2010b; Lippi and

Cervellin, 2012b; Guest et al., 2019; Jendrny et al., 2021a), Jendrny et al.'s recent review (Jendrny et al., 2021a) stands out as it followed strict selection criteria including peer-reviewed studies with reported detection rate and the diagnostic accuracy (sensitivity/specificity) of the diseases under investigation. From the pool of studies, they focused on studies, with a substantial overlap between the selection made by Pirrone et al. (Pirrone and Albertini, 2017b) (17 selected publications) and by Moser et al. (Moser and McCulloch, 2010a) (6 publications retained out of 531). Two key aspects were highlighted in the selected studies: the diseases studied and sampling sources. Notably, odor detection by dogs was predominantly explored for hypoglycemia (25%), epilepsy (10%), and prostate cancer (10%). The primary non-invasive matrices studied included urine (20% of publications), sweat (10%), breath and sweat together (10%), and feces (10%) (Jendrny et al., 2021b). However, this review does not delve into the VOCs sampling from urine, leaving it to be explored in future studies.

TABLE 2 Application examples of sampling protocols using fabrics.

Body area	Sampling device	Sampling method	Extraction method	Adsorbent phase	Sample storage conditions	Analysis method	Ref.
hand	DUKAL brand, sterile, 2 × 2, 8ply, gauze sponges	active sampling in direct contact with the skin (palm hands)	SPME at room temperature for 21 h	CAR/DVB/PDMS	stored at room temperature for 24 h	GC-MS	Curran et al. (2010b)
feet	a strip of cotton wool (3.0 g)	sampling in direct contact with the feet skin (cotton placed in the socks) for 6 h	SPME 10 min at 55°C	polyacrylate (85 mm) 100-mm-long fiber	not specified	GC-MS	Caroprese et al. (2009)
genitourinary area	gauze made of cotton and cellulose, of 20 × 13 cm dimension	sampling in direct skin (genito-urinary area) overnight	Headspace 100°C for 30 min	n/a	not specified	GC-MS	Rodríguez-Esquivel et al. (2018)
palm of hands	gauze	sampling in direct contact with the skin (2 cm square area of the palm is wiped for 1 min with 0.1 g of dry gauze)	SPME at 50°C for 45 min	PDMS/DVB	stored 24 h at 4°C	GC-MS	Saito et al. (2021)
upper back	medical gauze	active sampling by swabbing the gauze on the skin to collect the sebum and the sweat (sampling time not specified)	DHS; incubation for 5 min at 60 °C, trapping by purging 500 mL of the sample headspace at 50 mL/min with dry nitrogen through an adsorbent tube kept at 40°C	Tenax TA	stored at −80°C in inert plastic bags	GC-MS	Trivedi et al. (2019b)
armpit	absorbent pads	passive sampling (pads are attached via stainless steel poppets in pre-cleaned T-shirts)	HSSE in 250 mL Scott-Duran GLS80 bottles with a PDMS stir bar (1 cm long, 1 mm thickness) at 60°C for 2 h	PDMS	stored in bags and vacuum-sealed at −28°C	GCxGC-TOFMS	Smeets et al. (2020)
hand	Sterile cotton gauze pads (100% cotton) Dukal		SPME; equilibration at 50°C for 24 h, extraction for 15 h	2 cm fiber, 50/30 μm DVB/CAR/PDMS	stored in cleaned 10 mL vials, sealed and secured with parafilm around the screw cap opening	GC-MS	Crespo-Cajigas et al. (2023)
palm of hands	Gauze pads were DUKAL brand, 100% cotton, sterile, 2 × 2, 8-ply, gauze sponges	Subjects hold the gauze between the palms of their hands as they walked outdoors for 10 min	SPME at room temperature for 21 h	50/30 μm DVB/CAR/PDMS	stored in a sealed 10 mL glass vial for 24 h prior to extraction at ambient temperature	GC-MS	Curran et al. (2007)
armpit	Gauze pads were Dukal brand, sterile, 2 × 2, 8-ply, gauze sponges	Subjects wiped a gauze on their armpit after 30 min of outdoor physical exercised	SPME at room temperature for 15 h	50/30 μm DVB/CAR/PDMS	stored in a sealed 10 mL glass vial for 24 h prior to extraction at ambient temperature	GC-MS	Curran et al. (2005b)
bust	cotton-shirts	passive sampling: subjects wear the shirt for 3 days; a rectangular piece 20 × 30 cm is cut and stored in a 10 L Tedlar® bag	DHS at 23°C for 18 h, using a sampling pump at a flow rate of 1.8 L/min with purified air	TENAX-TA (GL Science)	stored in a 10 L Tedlar® bag at room temperature in a dark place for no longer than 1 day	GC-MS	Haze et al. (2022).

3.1.1 Human sweat capture for disease detection by dogs

In the realm of disease detection, an intriguing focus emerges in Section 3.1.1, where we delve into the captivating domain of human

sweat capture for canine olfaction. In the case of malaria diagnosis by detection dogs, researchers conducted a randomized and blinded study where children wore socks overnight before being presented to the dogs (Guest et al., 2019). Encouraging results were obtained from

TABLE 3 Application examples of extraction techniques after sample collection.

Source	Sampling device	Extraction method	Adsorbent phase	Protocol	Analysis system	Sensibility	Ref.
Breath	Tedlar® bag, 1 L	NTD	PDMS, Carbopack X, Carboxen 1,000	air pump, 30 mL/min	GC-MS	ppb	Monedeiro et al. (2021)
	sampling bag		Carbotrap-B, Carbopack-X	air pump, 30 mL/min	GC-ToF-MS	ppb	Pizzini et al. (2018)
	sampling bag	SPME	Carboxen, PDMS	25 min at room temperature	GC-MS	ppt	Koureas et al. (2020)
	sampling bag		DVB, Carboxen, PDMS	60 min at 22°C	GCxGC-ToF-MS	ppq (pg/L)	Caldeira et al. (2012)
	Tedlar® bag, 3 L		Carboxen, PDMS	10 min at 40°C	GC-MS	ppb	Mochalski et al. (2014)
	sampling bag	TF-SPME	PDMS Thin film, 5% Carboxen	3 h at 25°C	GC-MS	ppb	Murtada et al. (2021)
	FlexFilm bag, 3 L	Trapping in TD tube	Tenax, Carbograph, Carboxen	air pump, 200 mL/min	GCxGC	ppq (pg/L)	Berna et al. (2021)
					BenchTOF-MS		
	sampling bag		Tenax	air pump, 250 mL/min	GC-MS	ppb	Brinkman et al. (2017)
	sampling bag		Tenax TA	air pump, 100 mL/min	GC-MS	ppb	Broza et al. (2017)
Sweat	gauze	SPME	PDMS/DVB	45 min at 50°C	GC-MS	LOD for 2-nonenal: 2.4 pg/cm²/h	Saito et al. (2021)
	cotton-shirts	DHS	TENAX-TA (GL Science)	at 23°C for 18 h, using a sampling pump at a flow rate of 1.8 L/min with purified air	GC-MS	ppm (concentrations in ng per mg skin surface lipids)	Haze et al. (2022)

the analysis of 175 samples, with detection dogs showing a sensitivity of 72% and a specificity of 91%. For hypoglycemia detection, sniffing dogs are trained (1–2 weeks) to assist diabetic patients by sniffing their blood glucose status without the need for any specific sampling device (Gonder-Frederick et al., 2017; Rooney et al., 2019). However, in two studies investigating blood glucose level recognition in type I diabetes by dogs, sweat was collected on gauze from the arms (Dehlinger et al., 2013) or neck (Hardin et al., 2015) and stored (the storage time is not mentioned) at −18°C before being analyzed by the dogs (Hardin et al., 2015). So far, the results obtained using hypoglycemia sniffing dogs are not as accurate as standard invasive methods for blood glucose determination (ISO15197:2003 standards prescribe a maximal deviation of 20% in 95% of measurements when blood glucose levels are above 75 mg/dL and a deviation of 15 mg/dL when below 75 mg/dL (Eerdeken et al., 2020)). The sensitivity of hypoglycemia sniffing dogs ranged from 50% to 87.5%, and the specificity from 89.6% to 97.9% (Hardin et al., 2015).

In the context of epilepsy diagnosis, a study by Catala et al. (Catala et al., 2019) used a similar protocol to Hardin et al. (Hardin et al., 2015), where patients rubbed gauze on their necks and placed it in a zip lock bag (Catala et al., 2019). Dogs detected epileptic with a sensitivity of 87% and a specificity of 98% in this small cohort study (5 patients). Another epilepsy-related study used gauze to collect sweat from different body parts before storing it in an inert sampling bag (Mylar®) and presenting it to the sniffing dogs (Maa et al., 2021). In this case, dogs were able to alert the subject before a seizure happened with a probability of 82%.

Several studies focused on the detection of COVID-19 by canine olfaction, including the work of Devillier et al. (Grandjean et al., 2020; Devillier et al., 2022). These studies used gauze (no brand name specified, 20 mins of contact to recover up to 76 mg of sweat) and Getxent® tubes to collect sweat from underarms, and the sampling devices were stored at 18°C and 6°C in separate laboratories before being presented to the dogs. Lately, Jendrny et al. conducted a review of 22 studies related to SARS-CoV-2 detection by canine olfaction (Jendrny et al., 2021b), with sweat being the most commonly used VOCs source (11 of 22 studies). Dogs' performances in terms of sensitivity range from 65% to 100% and in specificity from 76% to 99% in these studies (Jendrny et al., 2021b).

Furthermore, one study evaluates the effect of freezing sweat samples collected on gauze between collection and usage (Lenochova et al., 2009), with human panelists evaluating the odors. Interestingly, no differences were observed between fresh and 6 months frozen samples.

3.1.2 Human exhaled air capture for disease detection by dogs

Several systems have been developed to capture VOCs from exhaled air and present them to dogs for evaluation. However, there is currently no standardized method, and different teams employ their approaches to collect odorant compounds. Two main methods are commonly used for collecting odors for dog evaluation: breath sampling tubes and sampling bags.

Breath sampling tubes, often custom-made, are used in some studies on the analysis of exhaled air. These tubes can range from 15 cm tubes (Montes et al., 2017) to 20 cm long (Reeve et al., 2020) and are equipped with materials like cotton balls or two layers of glass wool (one hydrophobic and hydrophilic) to trap the breath samples (McCulloch et al., 2006; Ehmann et al., 2012; Walczak et al., 2012; Montes et al., 2017).

Sampling bags are another approach used to collect exhaled air for dog evaluation. In this method, subjects exhale air into special bags, which are then presented to the dogs for the detection of various conditions, such as colorectal cancer (Sonoda et al., 2011).

More recently, researchers have explored the use of surgical facemasks for COVID-19 detection through canine olfaction (Devillier et al., 2022; Mendel et al., 2021). Mendel et al. (Mendel et al., 2021) pre-tested patients at a healthcare facility for COVID-19 and then asked to wear masks for 30–45 mins. These facemasks were then collected in special bags and transported to the testing laboratory. Masks were exposed to UV light to inactivate the potential virus particles. UV treatment of the facemasks has been tested and does not affect the nature of VOCs (Martin et al., 2020). After, the facemasks were cut into small squares for presentation to the dogs for sniffing tests and instrumental analysis. The study demonstrated promising results, with canine olfaction achieving an accuracy greater than 90% ((Mendel et al., 2021).

However, it is worth noting that using surgical facemasks for breath sampling may introduce additional VOCs from sweat and sebum present on the patient's facial skin. Despite, this potential confounding factor, the study achieved impressive sensitivity and specificity values after 1 month of training dogs for COVID-19 detection (Mendel et al., 2021; Devillier et al., 2022).

Regarding storage of breath samples, different studies have employed varying temperatures, such as in cold storage at 4°C (Sonoda et al., 2011; Devillier et al., 2022) or at room temperature (McCulloch et al., 2006; Ehmann et al., 2012; Walczak et al., 2012; Reeve et al., 2018; Reeve et al., 2020), for varying lengths of time, which strongly depend on the study length. However, justification for these specific storage conditions is not always provided in the literature.

3.2 GC-MS analysis

The analysis of human sweat and breath is highly diverse and varies significantly among different research teams. Each team tends to use distinct odor sampling systems tailored to the specific objectives of their studies. In the subsequent section, we will delve into the description of sweat sampling devices concerning disease diagnosis through GC-MS analysis.

3.2.1 Sweat sampling devices for GC-MS analysis
3.2.1.1 Use of PDMS for body odor sampling

Several devices based on polydimethylsiloxane (PDMS) have been developed to collect sweat from human skin for analysis (Soini et al., 2006; Bicchi et al., 2007; Xu et al., 2007; Riazanskaia et al., 2008; Sgorbini et al., 2010; Jiang et al., 2013; Martin et al., 2016; Roodt et al., 2018; Wooding et al., 2020; Wooding et al., 2021). These Medical-grade PDMS-based materials are often fashioned into small pieces known as "patches" or "skin patches", which can be placed in

direct contact with the skin to allow passive sampling. After sweat collection, these patches are subjected to a thermal desorption process to desorb VOCs. The analytes are then cryo-focused into a cold trap before being injected into the gas chromatography column in a splitless mode for further analysis (details are provided in Table 1).

Researchers choose the size and shape of the PDMS-based skin patch based on the sampling area and specific study requirements. For example, Martin et al. (Martin et al., 2016) used rectangular patches measuring 5 mm × 15 mm patches with a thickness of 0.45 mm, to collect sebum and sweat from the whole forehead of volunteers. Round patches of various diameters (6,11, and 17 mm) and a thickness of 0.25 mm were employed to collect sweat from the upper back, forearm, and back tight (Jiang et al., 2013). The signal intensity obtained through TD-GC-MS increases with the size of the patch (Jiang et al., 2013), indicating its influence on sensitivity. Additionally, Wooding et al. (Wooding et al., 2020) utilized PDMS patches to sample VOCs from the arm and abdomen skin surface for durations ranging from 5 to 120 mins. The results demonstrated a sensitivity increase proportional to the sampling time for most compounds, except for highly volatile ones like 2,4,6-trimethylcarbazole.

In some cases, to prevent the PDMS patch from getting impregnated with skin sweat and sebum, it is placed in a "sandwich" between two stainless steel meshes (Jiang et al., 2013), which additionally aids in reducing background noise. For certain research involving mosquito attractants emitted from the skin of healthy subjects, PDMS-based samplers in the form of bracelets and wristbands have been developed (Wooding et al., 2020). These samplers are made of medical-grade PDMS tubing and are enclosed by Mylar® sheeting (Hydroponic) to avoid contamination from surrounding air. It is recommended to store PDMS-based samplers at 4°C (Riazanskaia et al., 2008; Wooding et al., 2020) for no longer than 24 h (Riazanskaia et al., 2008).

PDMS-based Twisters, commonly used for Stir Bars Sorptive Extraction (SBSE), have also been employed as sampling materials to collect VOCs from skin regions like the arms (Soini et al., 2006; Penn et al., 2007; Xu et al., 2007) and axilla (Xu et al., 2007). These twisters can be rolled on specific areas of the skin, enabling researchers to identify individuals and gender-volatile markers in human body odor (Penn et al., 2007). About 400 compounds are detected and 100 are identified. Twisters were stored for up to 14 or 20 days at 4°C before analysis (Penn et al., 2007; Xu et al., 2007).

PDMS-based samplers offer numerous advantages, including ease of use and reproducibility in the sampling procedure, self-administrability, and portability. These devices can be stored in empty stainless steel thermal desorption tubes, making transportation and storage convenient. Moreover, the size and shape of the patch can be customized for different applications, making them suitable for canine olfaction. In forensics, PDMS has shown relevance in capturing and releasing explosives' odorants for dog sniffing applications (MacCrehan et al., 2018b).

While quantification of VOCs in sweat is infrequently reported. Two studies (Riazanskaia et al., 2008; Martin et al., 2016), shown in Table 1, utilized PDMS skin patches and provided detected and identified VOCs concentration range values.

Overall, PDMS-based sweat sampling devices offer a valuable and versatile tool for capturing volatile compounds from the skin,

with potential applications in various scientific fields and canine olfaction studies.

3.2.1.2 Use of Sorbstar® tubes for body odors sampling

In the thesis work of V. Cuzuel, Sorbstar® tubes demonstrated good efficiency in capturing and releasing VOCs from the palms of hands (Cuzuel, 2022). This sampling approach is akin to SBSE, and active sampling can be holding and rolling the Sorbstar® tubes in the palms of the hands. Despite its promising performance, Sorbstar® tubes are not widely utilized in research studies, as only one paper implementing this sampling device has been identified.

3.2.1.3 Use of gauze, clothes, or cotton for body odors sampling

In numerous experimental studies, gauzes have been utilized for body odor sampling (Curran et al., 2005a; Curran et al., 2010b; Rodríguez-Esquivel et al., 2018; Crespo-Cajigas et al., 2023) (protocols detailed in Table 2). However, the brand and type of gauze used are often not explicitly specified. A comprehensive comparison of nine commercially available gauzes (Dukal, J&J, Nexcare, IMCO, Eckerds, Cotton Roll, King's Cotton, Polish Absorbers, and Hungarian Cotton) was conducted by Furton and Curran in 2006, as published in a patent (The Patent Cooperation Treaty, 2007). Among these gauzes, Nexcare was found to release the highest number of volatile compounds (58 VOCs), while Dukal released the least VOCs (12 VOCs). This variation implies that the choice of gauze can significantly influence GC-MS analysis and dog sniffing results. Proper cleaning of the gauze before sweat sampling is crucial to ensure accurate and reliable sampling. The patent suggests cleaning vials and septa with acetone and then heating them at 210°C for 48 h to remove any residual VOCs traces before SPME GC-MS analysis ((The Patent Cooperation Treaty, 2007)).

In the context of studying the primary odor of subjects and differentiating between volunteers based on their body odor, gauzes have been used (Curran et al., 2010b). A protocol involving a pump and a supercritical fluid extractor is employed to clean the gauze before sweat sampling (Curran et al., 2010b). Cleaned gauze were placed on the subject's hands for 5 mins following a hand-washing protocol and then stored at room temperature for 24 h. VOCs are subsequently extracted using SPME for an extended duration (21 h) at room temperature and analyzed by GC-MS. This study, conducted in 2009, provided the first evidence of the possibility of individual discrimination based on the analysis of VOCs from hands (Curran et al., 2010b).

Trivedi et al. (Trivedi et al., 2019a) conducted a study prompted by the discovery of a "super smeller" named Joy Milne who detects a distinct odor in her Parkinson's disease-afflicted husband. They investigated healthy and Parkinson's disease patients, totaling 64 subjects. Sweat and sebum were collected from their upper backs using gauze which were then stored at −80°C for analysis. The researchers employed DHS (Dynamic Headspace) extraction to extract VOCs from the gauze, followed by GC-MS coupled with an olfactometer. Results revealed that Perillic aldehyde tended to decrease for Parkinson's disease patients, while three other components (Hippuric acid, Eicosan, and Octadecanal) increased. The peer-reviewed publication, originally an application note (Anatune, 2019), presented a solution to analyze the volatile

compounds captured on gauze. In a subsequent study in 2021 (Sinclair et al., 2021) the research team failed to replicate the same biomarkers as in their 2019 study (Trivedi et al., 2019a).

Haze et al. (Haze et al., 2022) conducted a study on the evolution of t-2-nonenal during aging, utilizing T-shirts as sampling devices. Participants wore the T-shirt for 3 days, and a portion of the cloth was placed in a 10 L Tedlar® bag. VOCs were extracted using a sampling pump to mimic dynamic headspace extraction (DHS), with a constant flow rate of 1.8 L/min. To maintain the 10 L capacity in the bag, deodorized air was supplied, and DHS collection was performed at 23°C for 18 h. VOCs were trapped into a Tenax® TA cartridge and later subjected to liquid desorption using 10 mL of diethyl ether. In contrast, results from an American study contradicted these findings, suggesting that trans-2-nonenal is not a volatile biomarker of aging in a non-Japanese population (Gallagher et al., 2008).

More details on analytical methods, including desorption parameters, GC-MS system, and chromatographic columns are provided in Supplementary Table S1.

3.2.2 Exhaled air sampling devices for GC-MS analysis

Diverse sampling systems have been developed with differences in parameters like sample volume and the fraction of exhaled air collected. In adults, each breath typically consists of around 500 mL of air. The initial 150 mL corresponds to the dead space, comprising air from the mouth and the surrounding environment, which is not involved in blood gas exchange. The subsequent 350 mL constitutes the alveolar portion, where the air has come into contact with the blood in the lungs. Capturing the alveolar breath, obtained at the end of exhalation, is more advantageous as it avoids dilution by dead space air (White and Fowler, 2018).

3.2.2.1 Sampling bags

Sampling bags are widely used to collect exhaled air for studying VOCs. Patients are asked to fast for at least 6 h and rest for 10 mins before breathing normally through a filter to purify inhaled air or medical air. Sometimes, patients wear a nose clip to ensure that only oral cavity air is collected. Consistency in respiratory parameters, such as the breathing route, is crucial to avoid bias in the clinical interpretation of exhaled VOCs patterns (Sukul et al., 2017).

Subjects are often asked to hold their breath for 10–30 s and then exhale deeply to fill the sampling bag (Koureas et al., 2020). Different types of bags, including Tedlar® (made of polyvinyl fluoride), Flexfilm® (unknown polymer), and Kynar® (made of polyvinylidene difluoride) have been compared (Mochalski et al., 2013a). A study by Mochalski et al. (Mochalski et al., 2013a) found that Tedlar® bags provide the least background emission, while Flexfilm® bags provide the highest. The authors recommend storing breath samples for up to 6 h at a cold temperature (4°C), in pre-conditioned Tedlar® bags (flushed with an inert gas).

Cleaning the sampling bags with pure nitrogen, (Caldeira et al., 2012; Mochalski et al., 2013a; Amal et al., 2016; Gashimova et al., 2019; Koureas et al., 2020), helium (Murtada et al., 2021) or humidified zero-air (Be et al., 2008). the main drawback of sampling bags is their storage time, with Mochalski et al. (Mochalski et al., 2013a) recommending storing the bags at 4°C and to not extract VOCs from the bags beyond 6 h after sampling.

3.2.2.2 Commercial devices

The Breath Collection Apparatus (BCA, Menssana Research) is a tube-based device where patients blow for 2 min, wearing a nose clip to collect only oral cavity air. Volatile compounds are trapped on activated carbon sorbents inside the tube (Phillips et al., 2019). To our knowledge, published VOCs limits of detection and GC-MS analysis for this system are lacking in the literature.

The Bio-VOC Sampler® (Markes) is designed to collect end-tidal breath, mainly composed of endogenous compounds. The patient blows through a disposable mouthpiece into an inert plastic container with a volume of 175 mL. It samples 88 mL of alveolar air, making it suitable for detecting high-concentration VOCs in the ppm range (Kwak et al., 2014). It has been used for the determining of nitric oxide levels in exhaled air (Henderson and Matthews, 2002). Yet, it is not recommended for identifying unknown biomarkers in low concentrations (<ppb) in breath samples.

The ReCIVA® facemask by Olwstone Medical is an end-tidal breath collection device with an infrared CO_2 sensor and Tenax® adsorbent cartridges. This commercial device has been well thought out for medical research applications (De Vi et al., 2020; Holden et al., 2020). It allows reproducible and precise breath sampling with reduced potential loss of compounds. However, it is an expensive device, and the same facemask cannot be used for multiple patients. One study using a very small cohort (three patients) suggests that the device may be less sensitive than Tedlar® bags (Gilio et al., 2020).

In summary, each commercial device has its advantages and limitations in breath sampling, making them suitable for specific research applications.

3.2.3 Extraction methods for GC-MS analysis

In this section, the main techniques for preparing gaseous samples for VOCs analysis by GC-MS are presented.

3.2.3.1 Solid phase Micro extraction (SPME)

SPME is a well-established technique developed in 1990 by Pawliszyn et al. (Catherine and Janusz, 1990). It is widely used for VOCs analysis. This extraction technique relies on specific polymers like PDMS, Carboxen, and Polyacrylate, which are incorporated into a 1–2 cm long fiber (Reyes-Garcés et al., 2018) with an adsorbent phase ranging from 7 to 100 μm.

SPME protocols involve exposing the fiber to the sample either through immersion for liquid samples or in the headspace of the sample container. After extraction, the VOCs are thermally desorbed from the fiber in the GC-MS inlet for analysis.

A more recent advancement is Thin-Film Solid Phase Microextraction (TF-SPME), developed in 2003 by Bruheim et al. (Bruheim et al., 2003). This technique operates on the same principle as classical SPME but utilizes a thin-film surface, about 200 mm² in size, which is approximately 20 times that of a conventional 100 μm SPME fiber.

Murtada et al. (Murtada et al., 2021), combined TF-SPME with Tedlar® bags for collecting volatile compounds from exhaled air. They introduced a Carboxen/PDMS film into a 1 L Tedlar bag, which was cleaned with helium to eliminate contamination prior to the sample collection. The filled bag was kept for 3 h at 25°C. Subsequently, the fiber was removed and analyzed by thermal desorption and GC-MS.

3.2.3.2 Trapping in the adsorbent phase

Trapping in sorbent phases is a commonly used method for samples collected in sampling bags. A recent review by Westphal et al., 2023 (Westphal et al., 2022) offers valuable guidelines on using sampling bags and adsorbent phase for thermal desorption and GC-MS analysis. These guidelines encompass essential instrumental parameters, ensuring effective and efficient analysis.

3.2.3.3 Needle Trap Device

Needle Trap Device (NTD) is an extraction trap consisting of a sorbent material packed inside a needle, used as an extraction trap (Pizzini et al., 2018; Monedeiro et al., 2021). This principle closely resembles trapping in sorbent phases. VOCs from the sampling bag or device are transferred to the NTD using a sampling pump. Once extracted, the needle is inserted into a thermal desorption unit, such as a thermal desorption tube, for further analysis.

3.2.3.4 Dynamic headspace

Dynamic Headspace (DHS) is a dynamic extraction technique employed for analyzing volatile compounds in a liquid or a solid sample. In this method, the volatile compounds are thermally extracted and trapped in a sorbent phase. The key advantage of DHS is the continuous renewal of analytes to the sorbent phase through an inert gas flow during the extraction process. This ensures that the equilibrium of volatile compounds between the sample and the gas phase (headspace) is never reached.

DHS can be automated or remote and is suitable for various sample types, particularly solid samples with minimal moisture content. For instance, gauze or a Getxent® tubes are suitable sorbent materials for DHS. Notably, DHS was utilized in a volatolomic study to analyze the sebum of patients with Parkinson's disease (Sinclair et al., 2021). Sterile cotton medical gauze was used to collect sebum from patients' upper back. The collected volatile compounds on the gauzes were then extracted by DHS at 80°C for 10 min under nitrogen flow and trapped on a Tenax TA adsorbent cartridge maintained at 40°C. Subsequently, the thermal desorption of the Tenax trap and GC-MS analysis differentiated samples from patients and healthy volunteers.

In a recent systematic review by Mitra et al., 2022 (Mitra et al., 2022), 29 papers were selected, covering diverse sampling devices and extraction techniques for body odor analysis. The number of VOCs detected by GC-MS varied also on the study design, the number of participants, and the analytical instrument used. The sensitivity of the different materials and techniques is challenging to evaluate due to the limited availability of quantification of the VOCs in sweat samples. However, studies providing concentration values demonstrated that 2D-GC with SPME (Caldeira et al., 2012) or Trapping in TD tubes (Berna et al., 2021) allow VOCs detection at very low concentrations (pg/L).

In comparing similar sampling protocols, the sensitivity of the analysis appears to be more influenced by the analytical instrument than the extraction method used.

4 Discussion

Compared to classical extraction methods discussed in this paper (Section 3.2.3), the canine nose is a natural highly efficient

FIGURE 3
Comparison of dog sniffing and dynamic headspace for GC-MS analysis.
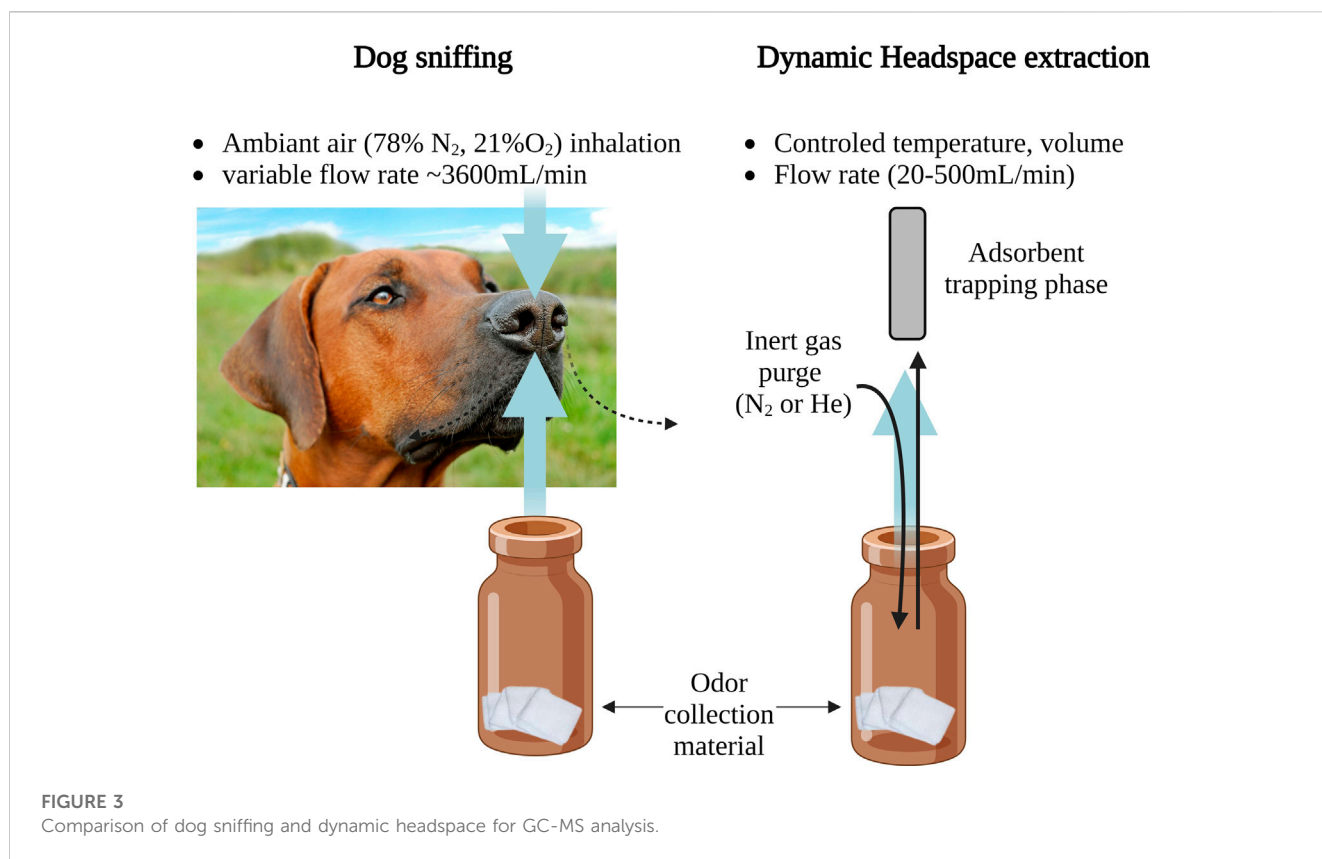
extraction system. The airflow dynamics around a dogs' nostrils are such that the air is inhaled from the front and exhaled to the side resulting in an impressive volume of approximately 30 mL/s/nostril or an approximate airflow of 3,600 mL/min (Kenneth et al., 2017; Kokocińska-Kusiak et al., 2021). This flow rate is over 7 times higher than the typical values used for human exhaled air extraction from sampling bags or gas purge flow used in dynamic headspace to extract sweat-VOCs from materials (ranging from 20 to 500 mL/min) before thermal desorption GC-MS analysis. To better replicate the accuracy of a dog's sniffing process, it is recommended to employ dynamic headspace techniques for VOCs collection instead of using static headspace methods. For instance, using DHS to simulate a 15 s dog sniffing in one nostril, a sample volume of 450 mL has to be extracted at a flow rate of 30 mL/s. Figure 3 illustrates the similarities between dog sniffing and dynamic headspace techniques used in GC-MS analysis.

4.1 Use of the dog as an analytical tool

Canine olfaction as a diagnostic tool offers many advantages. Firstly, it provides a non-invasive, painless, and potentially inexpensive procedure. The use of canine olfaction as a diagnostic tool has shown promise in detecting specific VOCs patterns in sweat or exhaled air associated with infectious diseases like COVID-19, or cancers. Since domestic dogs are familiar with human odors, they need to be trained to differentiate between body odors from multiple healthy subjects and those combined with disease-specific VOCs. The training

process for detection dogs typically involves two steps: generalization, where they are trained to detect specific stimuli, and discrimination: where they learn to differentiate between target odors and distracting samples.

Once properly trained, sniffing dogs, selected based on breed and aptitudes, exhibit remarkable abilities in detecting VOCs at extremely low concentrations, often in the parts per trillion range. Interestingly, the sensitivity of the dog's olfactive system appears to be on par with, if not greater than, the analytical instrument. For instance, when comparing Limit of Detection (LOD) values, butanethiol is estimated to have an LOD of 0.0003 ppb for canine olfaction (Wackermannová et al., 2016) *versus* 0.03 ppb for GC- MS (Muir et al., 2005). On the other hand, certain VOC like Pyrazine are detected at lower LOD by GC-MS (0.4 ppb) (Mochalski et al., 2013b) compared to dog sniffing, which achieves an LOD of 28 ppb (Wackermannová et al., 2016). However, canine olfaction cannot be compared to analytical instruments such as GC-MS systems since these two detection tools are very different. Indeed, canine olfaction is believed to depend on broadly selective receptors and combinatorial signal processing. One crucial factor to consider is that dogs are living beings and exhibit variability in their responses. Interpretation of canine olfaction analyzes must account for the variability among individual animals and among dog's breeds (Bauër et al., 2022b).

Moreover, the complexity of the training exercise can increase this variability. Properly training detection dogs to recognize these disease-specific odorants remain a significant challenge. It is essential to ensure that the dogs do not confuse these odors with

unrelated stimuli, such as contaminants, hospital odors, or even the sampling device or storage conditions.

Therefore, attention must be given to the experimental study's design and the collection and storage of training and test samples. Unfortunately, there is a lack of standardization of canine olfaction training, which is evident in many studies. To address this, a well-defined training protocol should be developed, drawing from experiences acquired in forensic sciences (National Institute of Standards and Technology, 2009).

In a medical context, additional considerations come into play. A study conducted by Elliker *et al.* (Elliker et al., 2014) offers valuable recommendations for experimental studies related to cancer diagnosis using canine olfaction. One of the challenges is that detection dogs can identify samples used in previous training sessions based on individuals' odors or contaminants' odors. To mitigate this issue, it is recommended not to reuse several times training samples from the same individuals but instead to use pooled samples from different donors to create a variety of odor profiles (unfamiliar samples) (Elliker et al., 2014).

The control of VOCs released from the odor capture devices during dog training is also a critical aspect to consider. Forensic experts have developed a standardized procedure called Controlled Odor Mimic Permeation Systems (COMPS) to address this (Kenneth et al., 2008; Kenneth et al., 2017). The diffusion time of a compound within an odor collection material depends on its chemical properties such as vapor pressure and structure, as well as its affinity with the sorbent material. This process involves two distinct physical mechanisms: adsorption, where molecules adhere to the surface of a solid surface, and absorption, where molecules permeate into a porous surface.

Quantifying the amount of VOCs released from odor collection materials under controlled temperature and humidity conditions is essential to determine their suitable usage time based on the nature of the VOCs being studied. For instance, in a study by Simon *et al.* (Simon et al., 2019), headspace concentrations of 12 VOCs were determined using SPME GC-MS. Analytical standards were doped onto cotton gauze (Dukal brand) and placed onto open containers used for dog training. After 1 hour (the estimated time of a canine training session), the diffusion of VOCs from gauze to the surrounding air was measured. SPME fibers (DVB/CAR/PDMS) were placed 5 cm above the gauze, were exposed for 15 s to the odor source, and subsequently analyzed by TD GC-MS. This process was repeated daily for 9 days. The concentrations of VOCs did not significantly decrease for 7 h, allowing the gauzes to be used for up to 7 training sessions (Simon et al., 2019).

4.2 Use of GC-MS as a complementary tool to identify specific-diseases induced VOCs

The analysis of human odor samples by GC-MS applied using untargeted methods allows for the identification of a broad range of volatile molecules. In a first place, to improve the sensibility and the specificity of the analysis, the most relevant materials for sampling and extracting VOCs must be chosen. Commonly used materials like gauze, clothes, and cotton balls cannot be directly used with GC-MS systems and require a preliminary extraction step. The choice of the extraction protocol among various existing headspace

techniques does not significantly impact the analysis's sensitivity. However, it does influence the analysis's selectivity. For example, bipolar sorbents like Tenax TA or Carboxen are capable of trapping both hydrophile and lipophile VOCs, while PDMS favors the extraction of lipophile compounds. To achieve untargeted analyses, essential for detecting and identifying unknown disease biomarkers, it is recommended to use multiple sorbent phases with different properties. This approach allows for the trapping of a wide range of analytes, enhancing the chances of detecting and characterizing diverse compounds during the analysis. Using PDMS-based devices or Sorbstar® tubes for body odors eliminated the need for an extraction step. These materials can be directly used with a GC-MS system through thermal desorption. By applying optimal thermal desorption parameters, a significant portion of the collected analytes on the sorbent surface can be injected for analysis.

After optimizing the parameters for VOCs sampling and extraction, the later step is the analysis. In the field of metabolomics, untargeted GC-MS methods are prevalent. Then the data analysis can be carried out using various methods. The criteria for selecting peak (quality of peak height or range of m/z value), the variables values (peak area, peak height, intensity value of MS or abundance value of TIC) and the choice of data preprocessing method, are key parameters in the data treatment (Md Ghazi et al., 2022). Data preprocessing includes peak detection, baseline correction, chromatographic alignment, deconvolution, feature filtration, missing value replacement, normalization, ratio selection and classification. Typically, when applying metabolomics to disease diagnosis, the primary objective is to predict specific disease classes through the use of multivariate methods (Feizi et al., 2021).

Principal Component Analysis (PCA) is commonly applied in a first place to provide an overview of the data, detect outliers, groups, and patterns. Subsequently, classification can be performed using linear methods such as Partial Least Squares (PLS) and Orthogonal Partial Least-Squares (OPLS), or non-linear methods like Support Vector Machine (SVM) (Feizi et al., 2021). Linear methods are preferred for the analysis of a small sample size relative to a high number of variables, whereas non-linear methods are dedicated to large datasets. For instance, Caldeira *et al.* (Caldeira et al., 2012), applied of GC×GC–ToFMS (Comprehensive Two-Dimensional Gas Chromatography coupled with Time-of-Flight Mass Spectrometry) to the analysis of exhaled air samples from 32 children with allergic asthma (of which 10 also presented with allergic rhinitis) and 27 control children. Subsequently, PLS-Discriminant Analysis in conjunction with Cross Validation, was conducted to identify compounds that might be associated with oxidative stress, inflammatory processes, or other cellular phenomena characteristic of asthma. Following this process, a robust model with a classification rate of 96% is obtained. Within the asthmatic population, a distinctive profile of six VOCs was identified: nonane, 2,2,4,6,6-pentamethylheptane, decane, 3,6-dimethyldecane, dodecane, and tetradecane.

In order to explore potential future clinical applications, targeted methods have also to be developed to reduce the data processing time and enhances the method's suitability for diagnosis purposes. Monedeiro *et al.* (Monedeiro et al., 2021) went in that direction by quantifying 29 target VOCs that have been previously reported as potential biomarkers of lung diseases in breath (lung cancer, chronic
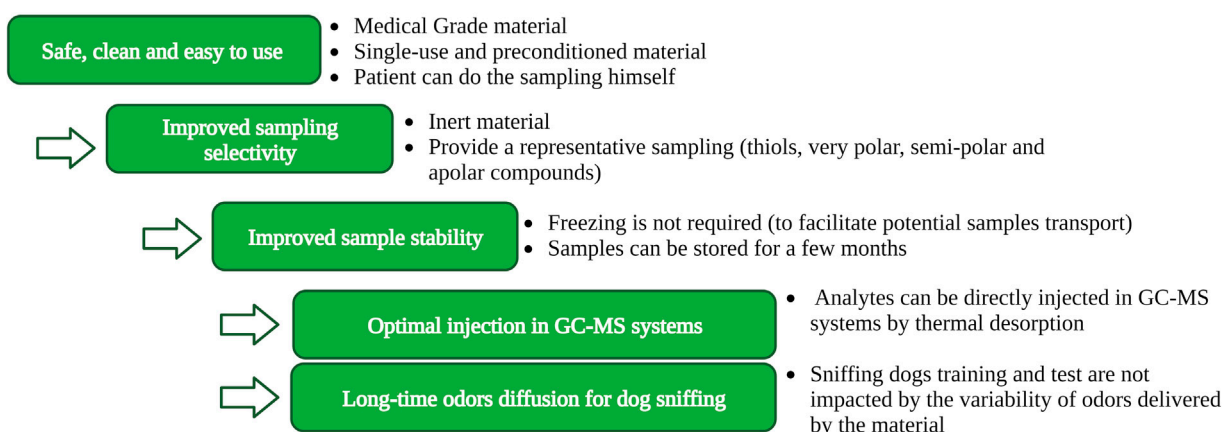
FIGURE 4
A conceptual design for an ideal sampling device enabling for simultaneous analysis of body odors by canine olfaction and GC-MS.

obstructive pulmonary disease, and asthma). Multinomial logistic regression (MLR) has been utilized to assess the relationship between the concentrations of the nine most discriminative targets (2-propanol, 3-methylpentane, (E)-ocimene, limonene, m-cymene, benzonitrile, undecane, terpineol, and phenol) as input variables. This analysis yielded an average overall accuracy of 95.5% for the prediction of multiple classes.

As discussed in Section 3.1, canine olfaction can be employed for simple binary classification of samples. Indeed, it would be intriguing to use GC-MS as an assessment tool for the dog. However, in the current state of our knowledge, we cannot assure what stimuli the dogs are actually responding to. The biomarkers identified by GC-MS might not be the same as those detected by the dogs. Furthermore, it is possible that the LODs of even the most advanced analytical instruments may not allow for the detection of molecules perceived by the dogs.

Nevertheless, studies in the field of analytical chemistry on the olfactory characteristics of pathologies serves as a valuable complement and may contribute to a more comprehensive understanding and standardization of experiments involving detection dogs (Bauër et al., 2022b).

4.3 Design of an ideal device compatible with both canine olfaction and GC-MS analysis

The design of an innovative, ideal device should consider several key elements, as resumed in Figure 4. These elements should be considered as recommendations for future research in the field of medical odor analysis.

1. Practical aspects: To ensure consistency and minimize variability in experimental studies involving numerous subjects, the device should have a user-friendly sampling protocol. An ideal device would come pre-conditioned to be free of contaminants and single-use to avoid cross-contamination. It should be packed in an inert vacuum-sealed individual bag before and after sampling.

2. Sampling selectivity: To improve dogs' performances, the sampling device must be capable of collecting volatile compounds from diverse chemical families with different physicochemical properties. Balancing the ability to trap both apolar and polar compounds is essential, as valuable information could be lost if the collection device favors only one type of compound. Preserving highly reactive compounds like thiol molecules before analysis would be a significant advancement in medical diagnosis applications involving body odors (Schroeder, 2015).

3. Sample stability: Care must be taken when using absorbing materials like cellulose fibers (gauze, surgical facemasks) as they can absorb VOCs, humidity, and non-volatile compounds. Cold storage prior to analysis is necessary to prevent molecule degradation. In contrast, sorbent materials like adsorbent polymers are inert and do not require freezing but should be stored in a cold place to avoid the desorption of volatile compounds prior to analysis. The ideal device should allow long-time storage (several months) to accommodate experimental studies involving patients recruited and sampled over an extended period. Analyzing all samples in the same batch at the end of the study can help reduce instrumental variability.

4. Compatibility with thermal desorption: An ideal material would be compatible with direct thermal desorption prior to GC-MS analysis to enhance the analysis's sensitivity by minimizing VOCs loss from extraction steps.

5. Reproducibility of odor release: Consistency in the amount of odor released from the sampling material throughout the training session or the test time is essential for accurate canine olfaction and GC-MS analysis.

5 Conclusion and perspectives

This bibliographic study explores the tools to comprehend odor capture techniques for both canine olfaction and GC-MS systems. The analysis of odors in a medical context is a relatively recent and diverse field, with numerous proofs of concept utilizing detection dogs or GC-MS. Interestingly, none of the studies reviewed have

been replicated in other laboratories, and their results vary significantly. Notably, the only study on Parkinson's disease was repeated with an increased patient cohort and yielded contradictory results compared to the initial study, serving as a crucial proof of concept odor (Trivedi et al., 2019a; Sinclair et al., 2021).

A key observation is the lack of standardization in sample collection protocols for both dogs and GC-MS studies. Training sniffing dogs necessitates an odor capture device, which can take the form of a sampling bag for patients to blow into, a gauze for sweat collection, or a passive/active polymer-based device to adsorb human VOCs. However, questions arise concerning the preservation and potential reuse of these odor-capturing devices, under specific conditions. Although this review does not offer a definitive answer to this question, it does provide valuable guidelines for consideration in future studies.

To potentially identify volatile biomarkers of pathologies detected by dogs, conducting GC-MS analysis alongside canine olfaction, using replicate samples and direct thermal desorption or multi-sorbent extraction may prove instrumental. This approach could eventually pave the way for significant advancements in the field of medical odor analysis.

Perhaps one of the most conceivable field applications utilizing sniffing dogs, would be the detection of infectious diseases during a pandemic. Indeed, in an observational study related to SARS-CoV-2, Guest et al. (Guest et al., 2022), reported that 2 dogs could screen 300 people in 30 min. This hypothesis makes it possible to imagine using canine olfaction in airports before embarking in a plane. In this scenario, only individuals marked as positive by the dogs would be tested afterwards by PCR tests.

In isolated settings, where access to gold standards diagnosis instruments is difficult, bringing detection dogs appears to be a promising solution for early and rapid detection of pathologies. In our knowledge, there are no established applications using detection dogs in this context. The limitations of this approach are well outlined in the review by Bauer et al. (Bauër et al., 2022b). These drawbacks notably include the associated high costs of employing qualified personnel for such applications, and the challenge of consistently sourcing samples for dogs' trainings, to maintain their performances over time (Bauër et al., 2022b).

Author contributions

LM: Conceptualization, Investigation, Methodology, Validation, Writing–original draft, Writing–review and editing, Data curation.

IC: Validation, Writing–review and editing, Formal Analysis. ML: Formal Analysis, Validation, Methodology, Writing–review and editing. IF: Formal Analysis, Writing–review and editing, Funding acquisition, Project administration, Resources, Supervision. EM: Formal Analysis, Project administration, Resources, Supervision, Validation, Writing–review and editing. DS: Project administration, Supervision, Validation, Conceptualization, Funding acquisition, Investigation, Methodology, Writing–original draft, Writing–review and editing.

Funding

Conflict of interest

The authors declare that the research was conducted in the absence of any commercial or financial relationships that could be construed as a potential conflict of interest.

Publisher's note

All claims expressed in this article are solely those of the authors and do not necessarily represent those of their affiliated organizations, or those of the publisher, the editors and the reviewers. Any product that may be evaluated in this article, or claim that may be made by its manufacturer, is not guaranteed or endorsed by the publisher.

Supplementary material

The Supplementary Material for this article can be found online at: https://www.frontiersin.org/articles/10.3389/fchem.2023.1282450/full#supplementary-material

References

Amal, H., Leja, M., Funka, K., Skapars, R., Sivins, A., Ancans, G., et al. (2016). Detection of precancerous gastric lesions and gastric cancer through exhaled breath. *Gut* 65 (3), 400–407. doi:10.1136/gutjnl-2014-308536

Anatune, (2019). AS184_Sniffing-out-Parkinson-Disease-using-GERSTEL-Dynamic-Headspace-DHS-and-Olfactory-Detection-Port-ODP. https://anatune.co.uk/application-notes/sniffing-out-parkinson-disease-using-gerstel-dynamic-headspace-dhs-and-olfactory-detection-port-odp/.

Bauër, P., Leemans, M., Audureau, E., Gilbert, C., Armal, C., and Fromantin, I. (2022a). Remote medical scent detection of cancer and infectious diseases with dogs and rats: a systematic review. *Integr. Cancer Ther.* 21, 15347354221140516. doi:10.1177/15347354221140516

Bauër, P., Leemans, M., Audureau, E., Gilbert, C., Armal, C., and Fromantin, I. (2022b). Remote medical scent detection of cancer and infectious diseases with dogs and rats: a systematic review. *Integr. Cancer Ther.* 21, 15347354221140516. doi:10.1177/15347354221140516

Beauchamp, J., Herbig, J., Gutmann, R., and Hansel, A. (2008). On the use of Tedlar® bags for breath-gas sampling and analysis. *J. Breath. Res.* 2 (4), 046001. doi:10.1088/1752-7155/2/4/046001

Berna, A. Z., Akaho, E. H., Harris, R. M., Congdon, M., Korn, E., Neher, S., et al. (2021). Reproducible breath metabolite changes in children with SARS-CoV-2 infection. *ACS Infect. Dis.* 7 (9), 2596–2603. doi:10.1021/acsinfecdis.1c00248

Bicchi, C., Cordero, C., Liberto, E., Rubiolo, P., Sgorbini, B., and Sandra, P. (2007). Sorptive tape extraction in the analysis of the volatile fraction emitted from biological solid matrices. *J. Chromatogr. A* 1148 (2), 137–144. doi:10.1016/j.chroma.2007.03.007

Brinkman, P., van de Pol, M. A., Gerritsen, M. G., Bos, L. D., Dekker, T., Smids, B. S., et al. (2017). Exhaled breath profiles in the monitoring of loss of control and clinical recovery in asthma. *Clin. Exp. Allergy* 47 (9), 1159–1169. doi:10.1111/cea.12965

Broza, Y. Y., Har-Shai, L., Jeries, R., Cancilla, J. C., Glass-Marmor, L., Lejbkowicz, I., et al. (2017). Exhaled breath markers for nonimaging and noninvasive Measures for detection of multiple Sclerosis. *ACS Chem. Neurosci.* 8 (11), 2402–2413. doi:10.1021/acschemneuro.7b00181

Bruheim, I., Liu, X., and Pawliszyn, J. (2003). Thin-film microextraction. *Anal. Chem.* 75 (4), 1002–1010. doi:10.1021/ac026162q

Caldeira, M., Perestrelo, R., Barros, A. S., Bilelo, M. J., Morête, A., Câmara, J. S., et al. (2012). Allergic asthma exhaled breath metabolome: a challenge for comprehensive two-dimensional gas chromatography. *J. Chromatogr. A* 1254, 87–97. doi:10.1016/j.chroma.2012.07.023

Caroprese, A., Gabbanini, S., Beltramini, C., Lucchi, E., and Valgimigli, L. (2009). HS-SPME-GC-MS analysis of body odor to test the efficacy of foot deodorant formulations. *Skin Res. Technol.* 15 (4), 503–510. doi:10.1111/j.1600-0846.2009.00399.x

Catala, A., Grandgeorge, M., Schaff, J. L., Cousillas, H., Hausberger, M., and Cattet, J. (2019). Dogs demonstrate the existence of an epileptic seizure odour in humans. *Sci. Rep.* 9 (1), 4103. doi:10.1038/s41598-019-40721-4

Catherine, L. A., and Janusz, P. (1990). Solid phase microextraction with thermal desorption using fused silica optical fibers. *Anal. Chem.* 62 (19), 2145–2148. doi:10.1021/ac00218a019

Chai, H. C., and Chua, K. H. (2021). The potential use of volatile biomarkers for malaria diagnosis. *Diagnostics* 11, 2244. doi:10.3390/diagnostics11122244

Crespo-Cajigas, J., Gokool, V. A., Ramírez Torres, A., Forsythe, L., Abella, B. S., Holness, H. K., et al. (2023). Investigating the use of SARS-CoV-2 (COVID-19) odor expression as a non-invasive diagnostic tool—pilot study. *Diagnostics* 13 (4), 707. doi:10.3390/diagnostics13040707

Curran, A. M., Prada, P. A., and Furton, K. G. (2010a). Canine human scent identifications with post-blast debris collected from improvised explosive devices. *Forensic Sci. Int.* 199 (1–3), 103–108. doi:10.1016/j.forsciint.2010.03.021

Curran, A. M., Prada, P. A., and Furton, K. G. (2010b). The differentiation of the volatile organic signatures of individuals through SPME-GC/ms of characteristic human scent compounds. *J. Forensic Sci.* 55 (1), 50–57. doi:10.1111/j.1556-4029.2009.01236.x

Curran, A. M., Rabin, S. I., Prada, P. A., and Furton, K. G. (2005a). Comparison of the volatile organic compounds present in human odor using SPME-GC/MS. *J. Chem. Ecol.* 31 (7), 1607–1619. doi:10.1007/s10886-005-5801-4

Curran, A. M., Rabin, S. I., Prada, P. A., and Furton, K. G. (2005b). Comparison of the volatile organic compounds present in human odor using SPME-GC/MS. *J. Chem. Ecol.* 31 (7), 1607–1619. doi:10.1007/s10886-005-5801-4

Curran, A. M., Ramirez, C. F., Schoon, A. A., and Furton, K. G. (2007). The frequency of occurrence and discriminatory power of compounds found in human scent across a population determined by SPME-GC/MS. *J. Chromatogr. B Anal. Technol. Biomed. Life Sci.* 846 (1–2), 86–97. doi:10.1016/j.jchromb.2006.08.039

Cuzuel, V. (2022). Développement d'une stratégie de caractérisation chimique de la signature odorante d'individus par l'analyse chimiométrique de données issues de méthodes séparatives multidimensionnelles. Available from: https://tel.archives-ouvertes.fr/tel-01680821v2.

Cuzuel, V., Cognon, G., Rivals, I., Sauleau, C., Heulard, F., Thiébaut, D., et al. (2017). Origin, analytical characterization, and use of human odor in forensics. *J. Forensic Sci.* 62 (2), 330–350. doi:10.1111/1556-4029.13394

De Vietro, N., Aresta, A., Rotelli, M. T., Zambonin, C., Lippolis, C., Picciariello, A., et al. (2020). Relationship between cancer tissue derived and exhaled volatile organic compound from colorectal cancer patients. Preliminary results. *J. Pharm. Biomed. Anal.* 180, 113055. doi:10.1016/j.jpba.2019.113055

Degreeff, L. E., and Furton, K. G. (2011). Collection and identification of human remains volatiles by non-contact, dynamic airflow sampling and SPME-GC/MS using various sorbent materials. *Anal. Bioanal. Chem.* 401 (4), 1295–1307. doi:10.1007/s00216-011-5167-0

Dehlinger, K., Tarnowski, K., House, J. L., Los, E., Hanavan, K., Bustamante, B., et al. (2013). Can trained dogs detect a hypoglycemic scent in patients with type 1 diabetes? *Diabetes Care* 36, e98–e99. doi:10.2337/dc12-2342

de Lacy Costello, B., Amann, A., Al-Kateb, H., Flynn, C., Filipiak, W., Khalid, T., et al. (2014). A review of the volatiles from the healthy human body. *J. Breath Res.* 8, 014001. doi:10.1088/1752-7155/8/1/014001

Devillier, P., Gallet, C., Salvator, H., Lecoq-Julien, C., Naline, E., Roisse, D., et al. (2022). Biomedical detection dogs for the identification of SARS-CoV-2 infections from axillary sweat and breath samples. *J. Breath. Res.* 16 (3), 037101. doi:10.1088/1752-7163/ac5d8c

Dormont, L., Bessière, J. M., and Cohuet, A. (2013). Human skin volatiles: a review. *J. Chem. Ecol.* 39, 569–578. doi:10.1007/s10886-013-0286-z

Eerdekens, G. J., Rex, S., and Mesotten, D. (2020). Accuracy of blood glucose measurement and blood glucose targets. *J. Diabetes Sci. Technol.* 14 (3), 553–559. doi:10.1177/1932296820905581

Ehmann, R., Boedeker, E., Friedrich, U., Sagert, J., Dippon, J., Friedel, G., et al. (2012). Canine scent detection in the diagnosis of lung cancer: revisiting a puzzling phenomenon. *Eur. Respir. J.* 39 (3), 669–676. doi:10.1183/09031936.00051711

Elliker, K. R., Sommerville, B. A., Broom, D. M., Neal, D. E., Armstrong, S., and Williams, H. C. (2014). Key considerations for the experimental training and evaluation of cancer odour detection dogs: lessons learnt from a double-blind, controlled trial of prostate cancer detection. *BMC Urol.* 14 (1), 22. doi:10.1186/1471-2490-14-22

Feizi, N., Hashemi-Nasab, F. S., Golpelichi, F., Sabouruh, N., and Parastar, H. (2021). Recent trends in application of chemometric methods for GC-MS and GC×GC-MS-based metabolomic studies. *TrAC - Trends Anal. Chem.* 138, 116239. doi:10.1016/j.trac.2021.116239

Gallagher, M., Wysocki, C. J., Leyden, J. J., Spielman, A. I., Sun, X., and Preti, G. (2008). Analyses of volatile organic compounds from human skin. *Br. J. Dermatology* 159 (4), 780–791. doi:10.1111/j.1365-2133.2008.08748.x

Gashimova, E. M., Temerdashev, A. Z., Porkhanov, V. A., Polyakov, I. S., Perunov, D. v., Azaryan, A. A., et al. (2019). Evaluation of the possibility of volatile organic compounds determination in exhaled air by gas chromatography for the noninvasive diagnostics of lung cancer. *J. Anal. Chem.* 74 (5), 472–479. doi:10.1134/s1061934819050034

Gilio, A. D., Palmisani, J., Ventrella, G., Facchini, L., Catino, A., Varesano, N., et al. (2020). Breath analysis: comparison among methodological approaches for breath sampling. *Molecules* 25 (24), 5823. doi:10.3390/molecules25245823

Gonder-Frederick, L. A., Grabman, J. H., Shepard, J. A., Tripathi, A. v., Ducar, D. M., and McElgunn, Z. R. (2017). Variability of diabetes alert dog accuracy in a real-world setting. *J. Diabetes Sci. Technol.* 11 (4), 714–719. doi:10.1177/1932296816685580

Gordon, R. T., Schatz, C. B., Myers, L. J., Kosty, M., Gonczy, C., Kroener, J., et al. (2008). The use of canines in the detection of human cancers. *J. Altern. Complementary Med.* 14 (1), 61–67. doi:10.1089/acm.2006.6408

Grandjean, D., Sarkis, R., Lecoq-Julien, C., Benard, A., Roger, V., Levesque, E., et al. (2020). Can the detection dog alert on COVID-19 positive persons by sniffing axillary sweat samples? A proof-of-concept study. *PLoS One* 15 (12), e0243122. doi:10.1371/journal.pone.0243122

Guest, C., Dewhirst, S. Y., Lindsay, S. W., Allen, D. J., Aziz, S., Baerenbold, O., et al. (2022). Using trained dogs and organic semi-conducting sensors to identify asymptomatic and mild SARS-CoV-2 infections: an observational study. *J. Travel Med.* 29 (3), taac043. doi:10.1093/jtm/taac043

Guest, C., Pinder, M., Doggett, M., Squires, C., Affara, M., Kandeh, B., et al. (2019). Trained dogs identify people with malaria parasites by their odour. *Lancet Infect. Dis.* 19, 578–580. doi:10.1016/s1473-3099(19)30220-8

Hardin, D. S., Anderson, W., and Cattet, J. (2015). Dogs can Be successfully trained to alert to hypoglycemia samples from patients with type 1 diabetes. *Diabetes Ther.* 6 (4), 509–517. doi:10.1007/s13300-015-0135-x

Haze, S., Gozu, Y., Nakamura, S., Kohno, Y., Sawano, K., Ohta, H., et al. (2022). 2-Nonenal newly found in human body odor tends to increase with aging. *J. Investigative Dermatology* 116, 520–524. doi:10.1046/j.0022-202x.2001.01287.x

Henderson, K. A., and Matthews, I. P. (2002). Biological monitoring of midwives' exposure to N2O using the Bio-VOC breath sampler. *J. Expo. Anal. Environ. Epidemiol.* 12 (5), 309–312. doi:10.1038/sj.jea.7500231

Holden, K. A., Ibrahim, W., Salman, D., Cordell, R., McNally, T., Patel, B., et al. (2020). Use of the ReCIVA device in breath sampling of patients with acute breathlessness: a feasibility study. *ERJ Open Res.* 6 (4), 00119–02020. doi:10.1183/23120541.00119-2020

Jendrny, P., Twele, F., Meller, S., Osterhaus, ADME, Schalke, E., and Volk, H. A. (2021a). Canine olfactory detection and its relevance to medical detection. *BMC Infect. Dis.* 21, 838. doi:10.1186/s12879-021-06523-8

Jendrny, P., Twele, F., Meller, S., Osterhaus, ADME, Schalke, E., and Volk, H. A. (2021b). Canine olfactory detection and its relevance to medical detection. *BMC Infect. Dis.* 21, 838. doi:10.1186/s12879-021-06523-8

Jiang, R., Cudjoe, E., Bojko, B., Abaffy, T., and Pawliszyn, J. (2013). A non-invasive method for *in vivo* skin volatile compounds sampling. *Anal. Chim. Acta* 804, 111–119. doi:10.1016/j.aca.2013.09.056

Kenneth, G., Furton, M. F., Ross, J., and Harper, S. O. (2008). *Controlled odor mimic permeation system*. US20080295783A1. United States Patent Application Publication.

Kenneth, G., Furton, M. F., Ross, J., and Harper, S. O. (2017). *Controlled odor mimic permeation system*. US20080295783A1. United States Patent Application Publication.

Kokocińska-Kusiak, A., Woszczyło, M., Zybala, M., Maciocha, J., Barłowska, K., and Dzięcioł, M. (2021). Canine olfaction: physiology, behavior, and possibilities for practical applications. *Animals* 11 (8), 2463. doi:10.3390/ani11082463

Koureas, M., Kirgou, P., Amoutzias, G., Hadjichristodoulou, C., Gourgoulianis, K., and Tsakalof, A. (2020). Target analysis of volatile organic compounds in exhaled breath for lung cancer discrimination from other pulmonary diseases and healthy persons. *Metabolites* 10 (8), 317–318. doi:10.3390/metabo10080317

Kwak, J., Fan, M., Harshman, S. W., Garrison, C. E., Dershem, V. L., Phillips, J. B., et al. (2014). Evaluation of Bio-VOC sampler for analysis of volatile organic compounds in exhaled breath. *Metabolites* 4 (4), 879–888. doi:10.3390/metabo4040879

Lenochova, P., Roberts, S. C., and Havlicek, J. (2009). Methods of human body odor sampling: the effect of freezing. *Chem. Senses* 34 (2), 127–138. doi:10.1093/chemse/bjn067

Ligor, T., Ligor, M., Amann, A., Ager, C., Bachler, M., Dzien, A., et al. (2008). The analysis of healthy volunteers' exhaled breath by the use of solid-phase microextraction and GC-MS. *J. Breath. Res.* 2 (4), 046006. doi:10.1088/1752-7155/2/4/046006

Lippi, G., and Cervellin, G. (2012a). Canine olfactory detection of cancer versus laboratory testing: myth or opportunity. *Clin. Chem. Laboratory Med.* 50, 435–439. doi:10.1515/cclm.2011.672

Lippi, G., and Cervellin, G. (2012b). Canine olfactory detection of cancer versus laboratory testing: myth or opportunity. *Clin. Chem. Laboratory Med.* 50, 435–439. doi:10.1515/cclm.2011.672

Lippi, G., and Heaney, L. M. (2020). The "olfactory fingerprint": can diagnostics be improved by combining canine and digital noses? *Clin. Chem. Lab. Med.* 58 (6), 958–967. doi:10.1515/cclm-2019-1269

Lorenzo, N., Wan, T., Harper, R. J., Hsu, Y. L., Chow, M., Rose, S., et al. (2003). Laboratory and field experiments used to identify *Canis lupus* var. familiaris active odor signature chemicals from drugs, explosives, and humans. *Anal. Bioanal. Chem.* 376 (8), 1212–1224. doi:10.1007/s00216-003-2018-7

Maa, E., Arnold, J., Ninedorf, K., and Olsen, H. (2021). Canine detection of volatile organic compounds unique to human epileptic seizure. *Epilepsy Behav.* 115, 107690. doi:10.1016/j.yebeh.2020.107690

MacCrehan, W., Young, M., Schantz, M., Craig Angle, T., Waggoner, P., and Fischer, T. (2020). Two-temperature preparation method for PDMS-based canine training aids for explosives. *Forensic Chem.* 21, 100290. doi:10.1016/j.forc.2020.100290

MacCrehan, W. A., Young, M., and Schantz, M. M. (2018a). Measurements of vapor capture-and-release behavior of PDMS-based canine training aids for explosive odorants. *Forensic Chem.* 11, 58–64. doi:10.1016/j.forc.2018.09.002

MacCrehan, W. A., Young, M., and Schantz, M. M. (2018b). Measurements of vapor capture-and-release behavior of PDMS-based canine training aids for explosive odorants. *Forensic Chem.* 11, 58–64. doi:10.1016/j.forc.2018.09.002

Martin, H., Katharina, H., Petra, V., and Christian, L. (2020). Ultraviolet irradiation doses for coronavirus inactivation-review and analysis of coronavirus photoinactivation studies. *GMS Hyg. Infect. Control* 15, Doc08. doi:10.3205/dgkh000343

Martin, H. J., Turner, M. A., Bandelow, S., Edwards, L., Riazanskaia, S., and Thomas, C. L. P. (2016). Volatile organic compound markers of psychological stress in skin: a pilot study. *J. Breath. Res.* 10 (4), 046012. doi:10.1088/1752-7155/10/4/046012

McCulloch, M., Jezierski, T., Broffman, M., Hubbard, A., Turner, K., and Janecki, T. (2006). Diagnostic accuracy of canine scent detection in early- and late-stage lung and breast cancers. *Integr. Cancer Ther.* 5 (1), 30–39. doi:10.1177/1534735405285096

Md Ghazi, M. G., Lee, L. C., Sino, H., and Abdul Halim, M. I. (2022). Review of contemporary chemometric strategies applied on preparing GC–MS data in forensic analysis. *Microchem. J.* 181, 107732. doi:10.1016/j.microc.2022.107732

Mendel, J., Frank, K., Edlin, L., Hall, K., Webb, D., Mills, J., et al. (2021). Preliminary accuracy of COVID-19 odor detection by canines and HS-SPME-GC-MS using exhaled breath samples. *Forensic Sci. Int.* 3, 100155. doi:10.1016/j.fsisyn.2021.100155

Mitra, A., Choi, S., Boshier, P. R., Razumovskaya-Hough, A., Belluomo, I., Spanel, P., et al. (2022). The human skin volatolome: a systematic review of untargeted mass spectrometry analysis. *Metabolites* 12, 824. doi:10.3390/metabo12090824

Mochalski, P., King, J., Haas, M., Unterkofler, K., Amann, A., and Mayer, G. (2014). Blood and breath profiles of volatile organic compounds in patients with end-stage renal disease. *BMC Nephrol.* 15 (1), 43–14. doi:10.1186/1471-2369-15-43

Mochalski, P., King, J., Klieber, M., Unterkofler, K., Hinterhuber, H., Baumann, M., et al. (2013b). Blood and breath levels of selected volatile organic compounds in healthy volunteers. *Analyst* 138 (7), 2134–2145. doi:10.1039/c3an36756h

Mochalski, P., King, J., Unterkofler, K., and Amann, A. (2013a). Stability of selected volatile breath constituents in Tedlar, Kynar and Flexfilm sampling bags. *Analyst* 138 (5), 1405–1418. doi:10.1039/c2an36193k

Moher, D., Liberati, A., Tetzlaff, J., Altman, D. G., and Group, P. (2022). Preferred reporting Items for systematic reviews and meta-analyses: the PRISMA statement. Available from: www.annals.org.

Monedeiro, F., Monedeiro-Milanowski, M., Ratiu, I. A., Brożek, B., Ligor, T., and Buszewski, B. (2021). Needle trap device-gc-ms for characterization of lung diseases based on breath voc profiles. *Molecules* 26 (6), 1789. doi:10.3390/molecules26061789

Monteiro, M., Carvalho, M., Henrique, R., Jerónimo, C., Moreira, N., de Lourdes Bastos, M., et al. (2014). Analysis of volatile human urinary metabolome by solid-phase microextraction in combination with gas chromatography-mass spectrometry for biomarker discovery: application in a pilot study to discriminate patients with renal cell carcinoma. *Eur. J. Cancer* 50 (11), 1993–2002. doi:10.1016/j.ejca.2014.04.011

Montes, Á. G., López-Rodó, L. M., Rodríguez, I. R., Dequigiovanni, G. S., Segarra, N. V., Sicart, R. M. M., et al. (2017). Lung cancer diagnosis by trained dogs. *Eur. J. Cardio-thoracic Surg.* 52 (6), 1206–1210. doi:10.1093/ejcts/ezx152

Moser, E., and McCulloch, M. (2010a). Canine scent detection of human cancers: a review of methods and accuracy. *J. Veterinary Behav.* 5, 145–152. doi:10.1016/j.jveb.2010.01.002

Moser, E., and McCulloch, M. (2010b). Canine scent detection of human cancers: a review of methods and accuracy. *J. Veterinary Behav.* 5, 145–152. doi:10.1016/j.jveb.2010.01.002

Muir, B., Quick, S., Slater, B. J., Cooper, D. B., Moran, M. C., Timperley, C. M., et al. (2005). Analysis of chemical warfare agents: II. Use of thiols and statistical experimental design for the trace level determination of vesicant compounds in air samples. *J. Chromatogr. A* 1068 (2), 315–326. doi:10.1016/j.chroma.2005.01.094

Murtada, K., Galpin, V., Grandy, J. J., Singh, V., Sanchez, F., and Pawliszyn, J. (2021). Development of porous carbon/polydimethylsiloxane thin-film solid-phase microextraction membranes to facilitate on-site sampling of volatile organic compounds. *Sustain Chem. Pharm.* 21, 100435. doi:10.1016/j.scp.2021.100435

National Institute of Standards and Technology, (2009). SWGDOG SC2-GENERAL GUIDELINES. https://www.nist.gov/system/files/documents/2018/04/25/swgdog_general_guidelines.pdf.

Penn, D. J., Oberzaucher, E., Grammer, K., Fischer, G., Soini, H. A., Wiesler, D., et al. (2007). Individual and gender fingerprints in human body odour. *J. R. Soc. Interface* 4 (13), 331–340. doi:10.1098/rsif.2006.0182

Phillips, M., Bauer, T. L., and Pass, H. I. (2019). A volatile biomarker in breath predicts lung cancer and pulmonary nodules. *J. Breath. Res.* 13 (3), 036013. doi:10.1088/1752-7163/ab21aa

Pirrone, F., and Albertini, M. (2017a). Olfactory detection of cancer by trained sniffer dogs: a systematic review of the literature. *J. Veterinary Behav. Clin. Appl. Res.* 19, 105–117. doi:10.1016/j.jveb.2017.03.004

Pirrone, F., and Albertini, M. (2017b). Olfactory detection of cancer by trained sniffer dogs: a systematic review of the literature. *J. Veterinary Behav. Clin. Appl. Res.* 19, 105–117. doi:10.1016/j.jveb.2017.03.004

Pizzini, A., Filipiak, W., Wille, J., Ager, C., Wiesenhofer, H., Kubinec, R., et al. (2018). Analysis of volatile organic compounds in the breath of patients with stable or acute exacerbation of chronic obstructive pulmonary disease. *J. Breath. Res.* 12 (3), 036002. doi:10.1088/1752-7163/aaa4c5

Prada, P., Curran, A., and Furton, K. (2014). Characteristic human scent compounds trapped on natural and synthetic fabrics as analyzed by SPME-GC/MS. *J. Forensic Sci. Criminol.* 1 (1). doi:10.15744/2348-9804.1.s101

Reeve, C., Cummings, E., McLaughlin, E., Smith, S., and Gadbois, S. (2020). An idiographic investigation of diabetic alert dogs' ability to learn from a small sample of breath samples from people with type 1 diabetes. *Can. J. Diabetes* 44 (1), 37–43.e1. doi:10.1016/j.jcjd.2019.04.020

Reeve, C., Wentzell, P., Wielens, B., Jones, C., Stehouwer, K., and Gadbois, S. (2018). Assessing individual performance and maintaining breath sample integrity in biomedical detection dogs. *Behav. Process.* 155, 8–18. doi:10.1016/j.beproc.2017.08.008

Reyes-Garcés, N., Gionfriddo, E., Gómez-Ríos, G. A., Alam, M. N., Boyacl, E., Bojko, B., et al. (2018). Advances in solid phase microextraction and perspective on future directions. *Anal. Chem.* 90, 302–360. doi:10.1021/acs.analchem.7b04502

Riazanskaia, S., Blackburn, G., Harker, M., Taylor, D., and Thomas, C. L. P. (2008). The analytical utility of thermally desorbed polydimethylsilicone membranes for *in-vivo* sampling of volatile organic compounds in and on human skin. *Analyst* 133 (8), 1020–1027. doi:10.1039/b802515k

Robinson, A., Busula, A. O., Voets, M. A., Beshir, K. B., Caulfield, J. C., Powers, S. J., et al. (2018). Plasmodium-associated changes in human odor attract mosquitoes. *Proc. Natl. Acad. Sci. U. S. A.* 115 (18), E4209-E4218–18. doi:10.1073/pnas.1721610115

Rodríguez-Esquivel, M., Rosales, J., Castro, R., Apresa-García, T., Garay, Ó., Romero-Morelos, P., et al. (2018). Volatolome of the Female genitourinary area: toward the metabolome of cervical cancer. *Arch. Med. Res.* 49 (1), 27–35. doi:10.1016/j.arcmed.2018.04.004

Roodt, A. P., Naudé, Y., Stoltz, A., and Rohwer, E. (2018). Human skin volatiles: passive sampling and GC × GC-ToFMS analysis as a tool to investigate the skin microbiome and interactions with anthropophilic mosquito disease vectors. *J. Chromatogr. B Anal. Technol. Biomed. Life Sci.* 1097–1098, 83–93. doi:10.1016/j.jchromb.2018.09.002

Rooney, N. J., Guest, C. M., Swanson, L. C. M., and Morant, S. (2019). How effective are trained dogs at alerting their owners to changes in blood glycaemic levels? variations in performance of glycaemia alert dogs. *PLoS One* 14 (1), e0210092. doi:10.1371/journal.pone.0210092

Saito, K., Tokorodani, Y., Sakamoto, C., and Kataoka, H. (2021). Headspace solid-phase microextraction/gas chromatography–mass spectrometry for the determination of 2-nonenal and its application to body odor analysis. *Molecules* 26 (19), 5739. doi:10.3390/molecules26195739

Schroeder, W. (2015). Volatile S-nitrosothiols and the typical smell of cancer. *J. Breath. Res.* 9 (1), 016010. doi:10.1088/1752-7155/9/1/016010

Sgorbini, B., Ruosi, M. R., Cordero, C., Liberto, E., Rubiolo, P., and Bicchi, C. (2010). Quantitative determination of some volatile suspected allergens in cosmetic creams spread on skin by direct contact sorptive tape extraction-gas chromatography-mass

spectrometry. *J. Chromatogr. A* 1217 (16), 2599–2605. doi:10.1016/j.chroma.2009.12.052

Simon, A. G. (2022). Analysis of non-hazardous canine training aids for triacetone triperoxide (TATP). *Forensic Chem.* 30, 100440. doi:10.1016/j.forc.2022.100440

Simon, A. G., De Greeff, L. E., Frank, K., Peranich, K., Holness, H., and Furton, K. G. (2019). A method for controlled odor delivery in olfactory field-testing. *Chem. Senses* 44 (6), 399–408. doi:10.1093/chemse/bjz031

Simon, A. G., Van Arsdale, K., Barrow, J., and Wagner, J. (2021). Real-time monitoring of TATP released from PDMS-based canine training aids versus bulk TATP using DART-MS. *Forensic Chem.* 23, 100315. doi:10.1016/j.forc.2021.100315

Sinclair, E., Walton-Doyle, C., Sarkar, D., Hollywood, K. A., Milne, J., Lim, S. H., et al. (2021). Validating differential volatilome profiles in Parkinson's disease. *ACS Cent. Sci.* 7 (2), 300–306. doi:10.1021/acscentsci.0c01028

Smeets, M. A. M., Rosing, E. A. E., Jacobs, D. M., van Velzen, E., Koek, J. H., Blonk, C., et al. (2020). Chemical fingerprints of emotional body odor. *Metabolites* 10 (3), 84. doi:10.3390/metabo10030084

Soini, H. A., Bruce, K. E., Klouckova, I., Brereton, R. G., Penn, D. J., and Novotny, M. (2006). *In situ* surface sampling of biological objects and preconcentration of their volatiles for chromatographic analysis. *Anal. Chem.* 78 (20), 7161–7168. doi:10.1021/ac0606204

Sonoda, H., Kohnoe, S., Yamazato, T., Satoh, Y., Morizono, G., Shikata, K., et al. (2011). Colorectal cancer screening with odour material by canine scent detection. *Gut* 60 (6), 814–819. doi:10.1136/gut.2010.218305

Sukul, P., Oertel, P., Kamysek, S., and Trefz, P. (2017). Oral or nasal breathing? Real-time effects of switching sampling route onto exhaled VOC concentrations. *J. Breath. Res.* 11 (2), 027101. doi:10.1088/1752-7163/aa6368

The Patent Cooperation Treaty, (2007). *Identification of humans through characteristic compounds detected in human scent*. Washington, D C, United States: The Patent Cooperation Treaty.

Trivedi, D. K., Sinclair, E., Xu, Y., Sarkar, D., Walton-Doyle, C., Liscio, C., et al. (2019a). Discovery of volatile biomarkers of Parkinson's disease from sebum. *ACS Cent. Sci.* 5 (4), 599–606. doi:10.1021/acscentsci.8b00879

Trivedi, D. K., Sinclair, E., Xu, Y., Sarkar, D., Walton-Doyle, C., Liscio, C., et al. (2019b). Discovery of volatile biomarkers of Parkinson's disease from sebum. *ACS Cent. Sci.* 5 (4), 599–606. doi:10.1021/acscentsci.8b00879

Wackermannová, M., Pinc, L., and Jebavý, L. (2016). Olfactory sensitivity in mammalian species. *Physiol. Res.* 65 (3), 369–390. doi:10.33549/physiolres.932955

Walczak, M., Jezierski, T., Górecka-Bruzda, A., Sobczyńska, M., and Ensminger, J. (2012). Impact of individual training parameters and manner of taking breath odor samples on the reliability of canines as cancer screeners. *J. Veterinary Behav. Clin. Appl. Res.* 7 (5), 283–294. doi:10.1016/j.jveb.2012.01.001

Westphal, K., Dudzik, D., Waszczuk-Jankowska, M., Graff, B., Narkiewicz, K., and Markuszewski, M. J. (2022). Common strategies and factors affecting off-line breath sampling and volatile organic compounds analysis using thermal desorption-gas chromatography-mass spectrometry (TD-GC-MS). *Metabolites* 13, 8. doi:10.3390/metabo13010008

White, I. R., and Fowler, S. J. (2018). "Capturing and storing exhaled breath for offline analysis," in *Breath analysis* (Amsterdam, Netherlands: Elsevier), 13–31.

Williams, H., and Pembroke, A. (1989). Sniffer dogs in the melanoma clinic? *Lancet* 1, 734. doi:10.1016/s0140-6736(89)92257-5

Wilson, A. D., and Forse, L. B. (2023). Potential for early noninvasive COVID-19 detection using electronic-nose technologies and disease-specific VOC metabolic biomarkers. *Sensors* 23 (6), 2887. doi:10.3390/s23062887

Wooding, M., Dodgen, T., Rohwer, E. R., and Naudé, Y. (2021). Mass spectral studies on the human skin surface for mosquito vector control applications. *J. Mass Spectrom.* 56 (2), e4686. doi:10.1002/jms.4686

Wooding, M., Rohwer, E. R., and Naudé, Y. (2020). Chemical profiling of the human skin surface for malaria vector control via a non-invasive sorptive sampler with GC×GC-TOFMS. *Anal. Bioanal. Chem.* 412 (23), 5759–5777. doi:10.1007/s00216-020-02799-y

Xu, Y., Dixon, S. J., Brereton, R. G., Soini, H. A., Novotny, M. V., Trebesius, K., et al. (2007). Comparison of human axillary odour profiles obtained by gas chromatography/mass spectrometry and skin microbial profiles obtained by denaturing gradient gel electrophoresis using multivariate pattern recognition. *Metabolomics* 3 (4), 427–437. doi:10.1007/s11306-007-0054-6

*CORRESPONDENCE
Qin Yao,
✉ dr_yao@qdu.edu.cn
Pengjiao Zeng,
✉ pjzeng@qdu.edu.cn

HPLC for simultaneous quantification of free mannose and glucose concentrations in serum: use in detection of ovarian cancer

Yulong Chen[1,2], Qin Yao[1,2]*, Lijuan Zhang[3] and Pengjiao Zeng[3]*

[1]Department of Obstetrics and Gynecology, The Affiliated Hospital of Qingdao University, Qingdao, China, [2]Department of Obstetrics and Gynecology, Qingdao University Medical College, Qingdao, China, [3]Medical Research Center, The Affiliated Hospital of Qingdao University, Qingdao, China

Background: Abnormal levels of monosaccharides in blood have been linked to tumorigenesis. In this study, a novel high-performance liquid chromatography (HPLC) method was established for the simultaneous determination of free mannose and glucose in the serum.

Methods: The serum was directly derivatized by 1-phenyl-3-methyl-5-pyrazolone under alkaline conditions using L-rhamnose as an internal standard. The chromatographic separation was then performed on a Poroshell EC-C$_{18}$ chromatographic column (4.6 × 100 mm, particle size 2.7 μm, Agilent) with gradient elution using NH_4Ac-HAc and acetonitrile as the mobile phases. The method was thereafter validated according to international guidelines. The serum samples obtained from 200 healthy individuals and 200 ovarian cancer (OC) patients were analyzed for free mannose and glucose.

Results: The method was found to be reproducible for quantification within 20 min and included online sample purification. The method displayed excellent linearity in the concentration range (for mannose: 0.5–500 μg/mL; glucose: 0.5–1500 μg/mL). The precision, recovery, and stability met the FDA bioanalytical method validation acceptance criteria. Overall, the measurement of glucose content by HPLC correlated well with the different enzymatic methods. Ovarian cancer mannose levels in the serum were significantly higher in the advanced stage (61.22 μmol/L, $p < 0.0001$) than those in healthy volunteers and early-stage patients (44.51 μmol/L *versus* 50.09 μmol/L, $p < 0.0001$). The AUC for the ratio of serum free glucose to mannose (G/M) was 0.98 ($p < 0.0001$), with a sensitivity of 91.46% and a specificity of 98.50%, which served as a biomarker for OC diagnosis.

Conclusion: We report a simple, repeatable, and attractive analytical method by HPLC, which can be used for quantitative estimation of free mannose and glucose simultaneously in human serum. Our results indicate that the serum level of mannose could be used as a potential biomarker of ovarian cancer.

1 Introduction

Ovarian cancer (OC) is one of the most fatal of gynecologic malignancies which can seriously threaten the lives and health of women (Gaona-Luviano et al., 2020). In 2023, 19,710 new diagnoses and 13,270 deaths due to this malignancy have been estimated to occur in the United States (Siegel et al., 2023). Because the ovary is located deep in the pelvic cavity, the early pathological changes are not easy to detect, and about 70%–80% patients are diagnosed at advanced stage (III/IV) and exhibit a poor prognosis (Shulman et al., 2019; Yue et al., 2022). After treatment, the 5-year survival rate has been reported to reach approximately 93% in stage I epithelial OC but only 30% in patients diagnosed with advanced stage tumors (Siegel et al., 2023). Therefore, early diagnosis and treatment remain key to improved survival. Currently, OC is diagnosed primarily through gynecologic pelvic examination, transvaginal ultrasonography, serum carbohydrate antigen 125, human epididymal protein 4, and other markers in combination with different imaging tests, but these methods have relatively low sensitivity and are associated with several limitations (Elias et al., 2018). So, it is essential to develop a simple, non-invasive, and sensitive method for early diagnosis of this malignancy in affected patients (Xiao et al., 2022).

The monosaccharide composition in the biological samples can indicate the health status of individuals (Han et al., 2020). Monosaccharides play a key role in regulating cellular metabolism and can serve as potential biomarkers. Moreover, the quantitative detection of free monosaccharides in the biological fluids is gaining popularity in the medical field (Wang et al., 2022). For instance, it has been previously reported that elevated levels of D-mannose (Man), D-fructose, and threonine in the cerebrospinal fluid have been found in patients with Parkinson's disease (Trezzi et al., 2017). In addition, serum monosaccharide composites demonstrated better early diagnostic efficacy than carcinoembryonic antigen in patients diagnosed with colorectal cancer and can also be used for prognosis (Li et al., 2022). We found in our previous study that the levels of monosaccharides in hydrolyzed serum were significantly increased in patients diagnosed with endometrial cancer (Chen et al., 2022). These monosaccharide profiles indicated that the occurrence of tumors was accompanied by changes in the amount of monosaccharides in the blood and that there was a distinct difference in the metabolism of monosaccharides. These findings could form the basis of further studies for application of monosaccharide markers (Wang et al., 2022).

More importantly, Man is a minor monosaccharide in the blood of animals (Jin et al., 2021), which can be directly used to synthesize glycoproteins and is involved in immune regulation. A number of clinical studies have shown that Man can be used as a marker for early detection to improve the clinical outcome of various diseases. Interestingly, serum Man can serve as an indicator of invasive candidiasis, and its content was related to the degree of infection (Monson and Wilkinson, 1981; Marier et al., 1982). In addition, Man has recently been implicated in regulating cancer metabolism in esophageal carcinoma (Sanchez-Espiridion et al., 2015; Gu et al., 2017; White et al., 2017) and breast cancer (Jobard et al., 2014). Elevated Man levels have been linked to increased risk of chronic disorders, including diabetic individuals with insulin resistance (Amano et al., 2018; Ferrannini et al., 2020), coronary heart disease (Koseler et al., 2020; Koseler et al., 2021), acute respiratory distress syndrome (Wei et al., 2021), and tuberculosis infection (Conde et al., 2022). As a result, Man has been proposed as a novel biomarker of disease risk as well as its associated complications, and its detection may be useful for the development of new therapeutic strategies (Wang et al., 2022). It is exceedingly difficult to understand the condition at the beginning of the disease development or to determine whether there is a residual tumor after the treatment in OC patients. A number of studies have indicated that mannose is a reliable marker for tracking the progression and remission of OC (Gehrke et al., 1979). This is very useful for the clinicians to track the response to chemotherapy, but there are few reports related to the early diagnosis of mannose in OC.

The human serum free monosaccharides contain relatively elevated levels of glucose, a C-2 epimer of Man, which is usually measured by a method based on the enzyme hexokinase in the clinical laboratories (Bietenbeck et al., 2018), but Man levels cannot be estimated. At present, the main techniques for the measurement of Man in plasma or serum include enzymatic (Soyama, 1984; Etchison and Freeze, 1997), GC-MS (Pitkanen, 1996), HPLC (Taguchi et al., 2003; Miwa and Taguchi, 2013), LC-MS (White et al., 2017; Han et al., 2020; Wang et al., 2022), and capillary electrophoresis (Carchon and Jaeken, 2001). However, these methods have been found to be not entirely suitable for routine use for a variety of reasons, as they require time-consuming elimination of ~100 times excess glucose, limited instrument usage, and the need for relatively large sample volumes (Taguchi et al., 2003). Hence, identification of a simple method for the simultaneous determination of serum free Man and glucose has high clinical applications. In this study, we have designed a novel HPLC method for simultaneous detection of serum free Man and glucose, and the performance was verified in accordance with clinical guidance documents. We also validated the linearity, limit of detection (LOD), limit of quantification (LOQ), recovery, intra-day/inter-day precision, and stability. The free Man and glucose in serum were thereafter analyzed using this new method to further validate their potential value as biomarkers for early diagnosis of OC (Figure 1, Research Scheme).

FIGURE 1
A schematic representation of the experimental design.
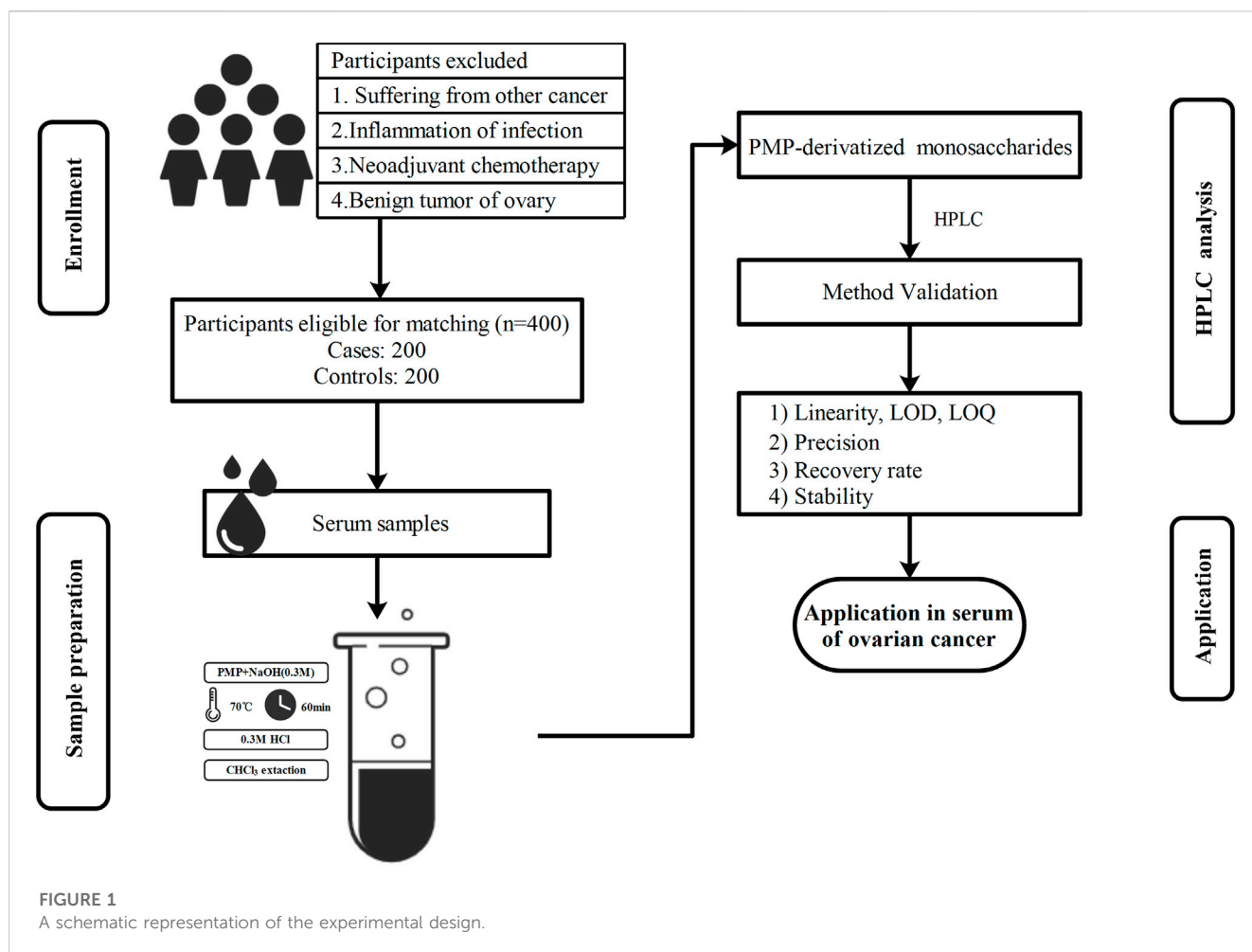
2 Materials and methods

2.1 Reagents and materials

D-mannose (Man), D-Glucose (Glc), L-rhamnose (Rha, internal standard, IS), 1- phenyl-3-methyl-5-pyrazolone (PMP), and bovine serum albumin (BSA, fatty acid and globulin-free) were purchased from Sigma-Aldrich (≥99.5% pure, St. Louis, MO, United States). Hydrochloric acid (HCl), sodium hydroxide (NaOH), ammonium acetate, acetic acid, ammonia, and chloroform ($CHCl_3$) were obtained from Sinopharm Chemical Reagent (Shanghai, China). Phosphate-buffered saline (PBS) was acquired from Biological Industries (Shanghai, China). Acetonitrile and methanol (Merck, Germany) were of HPLC-grade. Ultra-purified water was provided using a MilliQ Direct Water Purification System (MILLIPORE, Germany).

2.2 Preparation of the calibrator and quality control solutions

We first dissolved the monosaccharide standard in ultra-purified water to obtain stock solutions of Man (10 mg/mL), Glc (10 mg/mL), and IS (1 mg/mL) and stored at −20℃. The working solution was obtained by mixing a stock solution of Man and Glc and then diluting it with water to a final concentration of 1 mg/mL. Thereafter, the mixture was diluted with blank serum (4% BSA PBS solution) to prepare different concentrations of calibrators (for Man: 0.5, 1, 2.5, 5, 10, 25, 50, 100, and 500 μg/mL and for Glc: 0.5, 1, 2.5, 5, 10, 25, 50, 100, 250, 500, 1,000, and 1500 μg/mL). Quality control (QC) solutions were prepared at 2.5 (low), 25 (medium), and 250 μg/mL (high) concentration levels in the same way. The IS stock solution was diluted with water to obtain a working solution at 100 μg/mL. The stability QCs were prepared in the mixed human serum. The aforementioned working solutions were briefly stored at 4℃ and then constituted immediately before use.

2.3 Serum samples

We obtained the fasting venous blood from OC patients before surgery in the morning and placed it in the sterile coagulant tubes. After coagulation, the serum samples were collected by centrifugation at 1,000 g for 10 min, and the

FIGURE 2
Derivatization of reducing sugar with PMP in weakly alkaline condition.
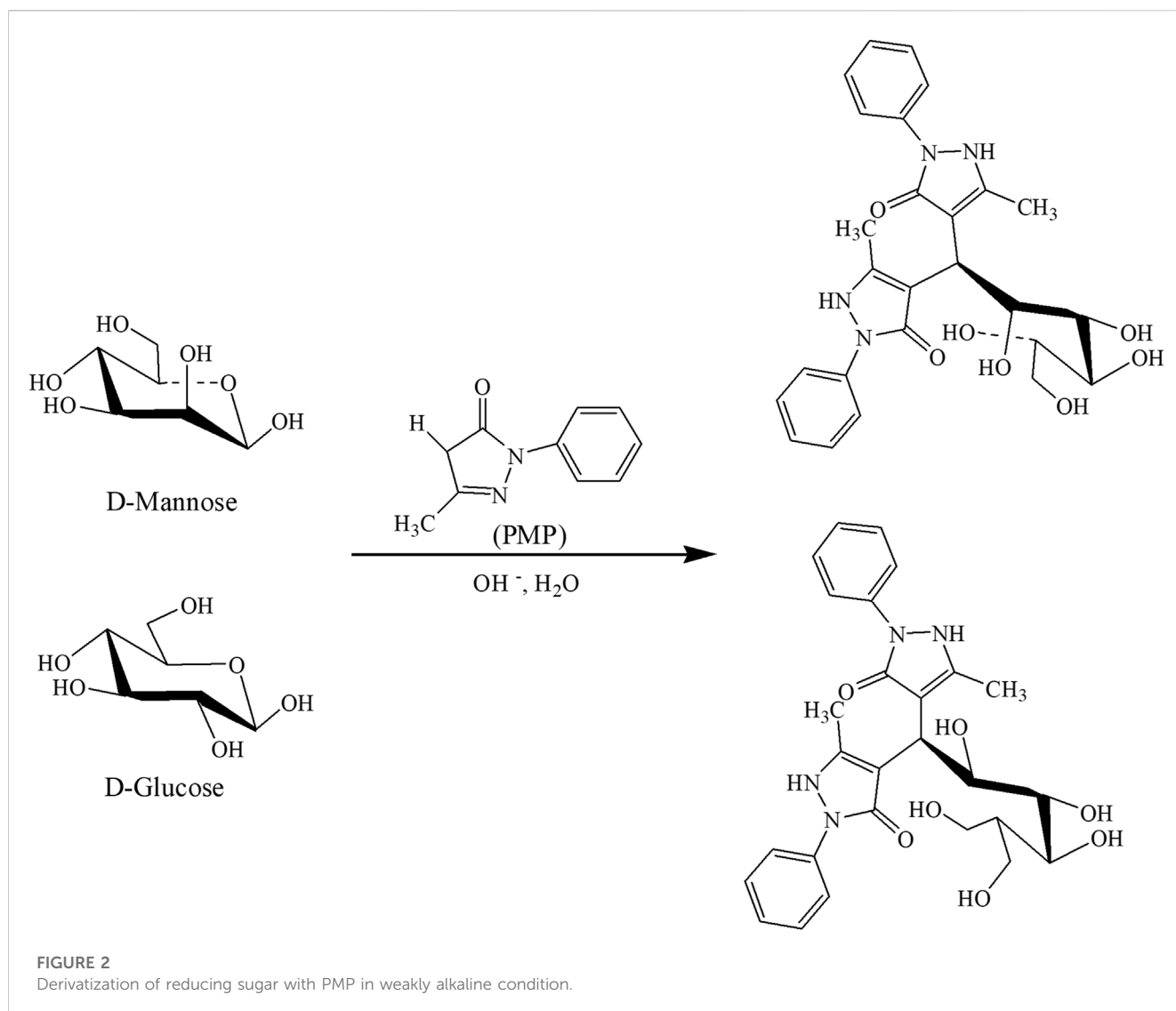
supernatant was stored at −80 °C until use. The serum samples were collected from matched healthy individuals using the same method.

2.4. Extraction of the free monosaccharides

PMP-derivatized free monosaccharides were obtained by the method described previously (Lijiuan and Yong, 2020), with minor modifications (Figure 2). Briefly, 10 μL standards were dissolved in 30 μL IS working solution, and QC or serum sample was treated in a similar fashion. The monosaccharides were derivatized for 60 min at 70°C with the addition of 60 μL PMP solution (0.5 M dissolved in methanol) and 40 μL NaOH (0.3 M). We then added 40 μL HCl (0.3 M) to neutralize the reaction, vortexed for at least 5 s, and then extracted with 500 μL CHCl$_3$. The mixture was then centrifuged at 20,800 g for 10 min in order to discard the lower layer of CHCl$_3$, and the extraction was repeated twice to carefully collect the upper aqueous phase. After filtration with a 0.22-μm filter membrane, the supernatant was transferred for further analysis.

2.5 HPLC conditions

We separated PMP-derivatized monosaccharides by using an Agilent 1260 infinity HPLC system (Quat Pump G7111A, Vial sampler G7129A, thermostatic column compartment G7116A, UV detector DAD, G7115A, Agilent Technologies, Germany) equipped with a Poroshell EC-C18 column (4.6 × 100 mm, 2.7 μm particle size, Agilent). The separation was carried out at 37°C for 20 min at a flow rate of 1 mL/min. The sample injection volume was kept at 20 μL and detected at λ = 254 nm. These parameters are reported in Supplementary Table S1. The mobile phase A was 100 mM NH$_4$Ac-HAc (0.1 mol NH$_4$Ac dissolved in 1 L Milli-Q water, PH = 5.5), and mobile phase B was 100% acetonitrile. A gradient setting has been shown in Supplementary Table S2. The monosaccharide concentrations were calculated by comparing the peak area of PMP-derivatized Man and Glc with those of Rha. Serum Glc concentration was also assessed using the glucose oxidase method (Bietenbeck et al., 2018), and the results were compared with those of our method.

2.6 Method validation

The method was validated in accordance to the Center for Drug Evaluation and Research (CDER) "Bioanalytical Method Validation Guidance for Industry" (FDA, 2018). The validation was conducted with specificity, linearity, LOD, LOQ, recovery, precision, and stability.

2.6.1 Specificity

The specificity of an analytical method depends on its ability to distinguish the analyte from various other components (impurities, degradation products, metabolites, etc.) and thereby generate distinct signals which are free from interference (Ramakrishna et al., 2020). The samples were prepared with surrogate blank serum at a standard concentration of 500 µg/mL, IS, and 10 different samples from mixed OC patients and healthy control serum. These three sets of samples were then analyzed using the method of free monosaccharide extraction, and the resulting chromatograms were compared.

2.6.2 Linearity of calibration curve

The linearity was established to determine the potential relationship between instrument response and known concentrations of the analyte. A calibration curve in the surrogate serum was constructed as usual by using standard solutions at 10 different levels, within the concentration range (for Man: 0.5, 1, 2.5, 5, 10, 25, 50, 100, and 500 µg/mL and for Glc: 0.5, 1, 2.5, 5, 10, 25, 50, 100, 250, 500, 1,000, and 1500 µg/mL). Y represented the ratio of monosaccharide peak area A_i to IS peak area $A_{IS,}$ and X represented the known concentrations of the monosaccharide concentration C_i. Thus, based on the least squares linear regression method, we estimated the slope, intercept, and coefficient of determination using $1/X^2$ weighting.

2.6.3 LOD and LOQ

LOD, which is also known as the selectivity, refers to the minimum quantity of the analyte that can be tested and analyzed at a certain background. LOQ is the smallest amount that can be measured quantitatively by a given method. We determined the LOD and LOQ by using the signal-to-noise ratios (3:1 and 10:1, respectively) within CV < 20%.

2.6.4 Precision and extraction recovery

Intra-day precision was assessed using three different concentrations of the standard solution (2.5, 25, and 250 µg/mL). The samples were analyzed five times in 1 day, and the accuracy was then calculated from the average and % CV. The inter-day accuracy was validated by repeating this assay for 3 consecutive days.

The extraction recovery was also evaluated by comparing the peak areas from three different experiments: a) QC samples (low, medium, and high); b) mixed serum (10 patients and 10 healthy individuals); c) the added QCs with the mixed serum. The extraction recovery was calculated using the following equation:

$$\text{Extraction Recovery} (\%) = c / (a + b) \times 100.$$

2.6.5 Stability

All the samples were prepared in comparison with the freshly prepared samples at the same concentrations. All the stability experiments were repeated thrice. We evaluated the stock solution stability through comparing the freshly prepared one with the stored solution at 4°C for 2 months. Freeze-thaw stability samples were prepared by exposure to three cycles of freezing (−80°C) and thawing (at room temperature). The freshly prepared samples were left on the bench top at room temperature for 24 h to evaluate short-term (bench top) stability. The processed sample stability was measured by comparing the stability of the freshly obtained samples with that of serum extracts remaining in the autosampler for 24 h at the room temperature. The freshly prepared and stored solutions at −80°C were compared for 14 days to assess the long-term storage stability.

2.7 Determination of free monosaccharides in human serum samples

We determined the concentration of the free monosaccharides in the serum of 400 serum samples, including 200 OC patients and 200 healthy controls, by using the established HPLC method. All the subjects were from the Affiliated Hospital of Qingdao University. All OC patients were newly diagnosed, histologically confirmed, and had never received radiotherapy or chemotherapy prior to the surgery in the Department of Gynecology. The healthy individuals who did not suffer from any disease were enrolled from the Physical Examination Center. This study protocol was implemented in accordance with the ethical guidelines of the 2013 Declaration of Helsinki and has been approved by the Ethics Committee of the Affiliated Hospital of Qingdao University. Informed consent forms were filled out for all the subjects.

2.8 Statistical analysis

All the data were analyzed with GraphPad Prism 9.0 (GraphPad Software Inc., San Diego, CA, United States). The structures were created using ChemDraw Ultra 7.0. We used the multi-sample Shapiro–Wilk test to check the normality of continuous variables. The continuous variables have been presented as mean (SDs) or median and interquartile range (IQR). We used Student's t-test (normal distribution) or Mann–Whitney U test (skew distribution) to compare the difference of the continuous variables, and p-values <0.05 were considered statistically significant.

3 Results

3.1 Analytical performance

As depicted in the chromatograms, the PMP-labeled Man, Glc, and Rha could all be absolutely separated within 13 min. The first monosaccharide isolated from the column was Man at 7.36 ± 0.019 min and the last was Glc at 12.32 ± 0.012 min (Figure 3). The reproducibility of the method was excellent. The peaks of each monosaccharide were found to be symmetrical and sharp, and the resolutions were all >1.5, ensuring the specificity of the method. The thin-shell porous chromatographic column used in this method
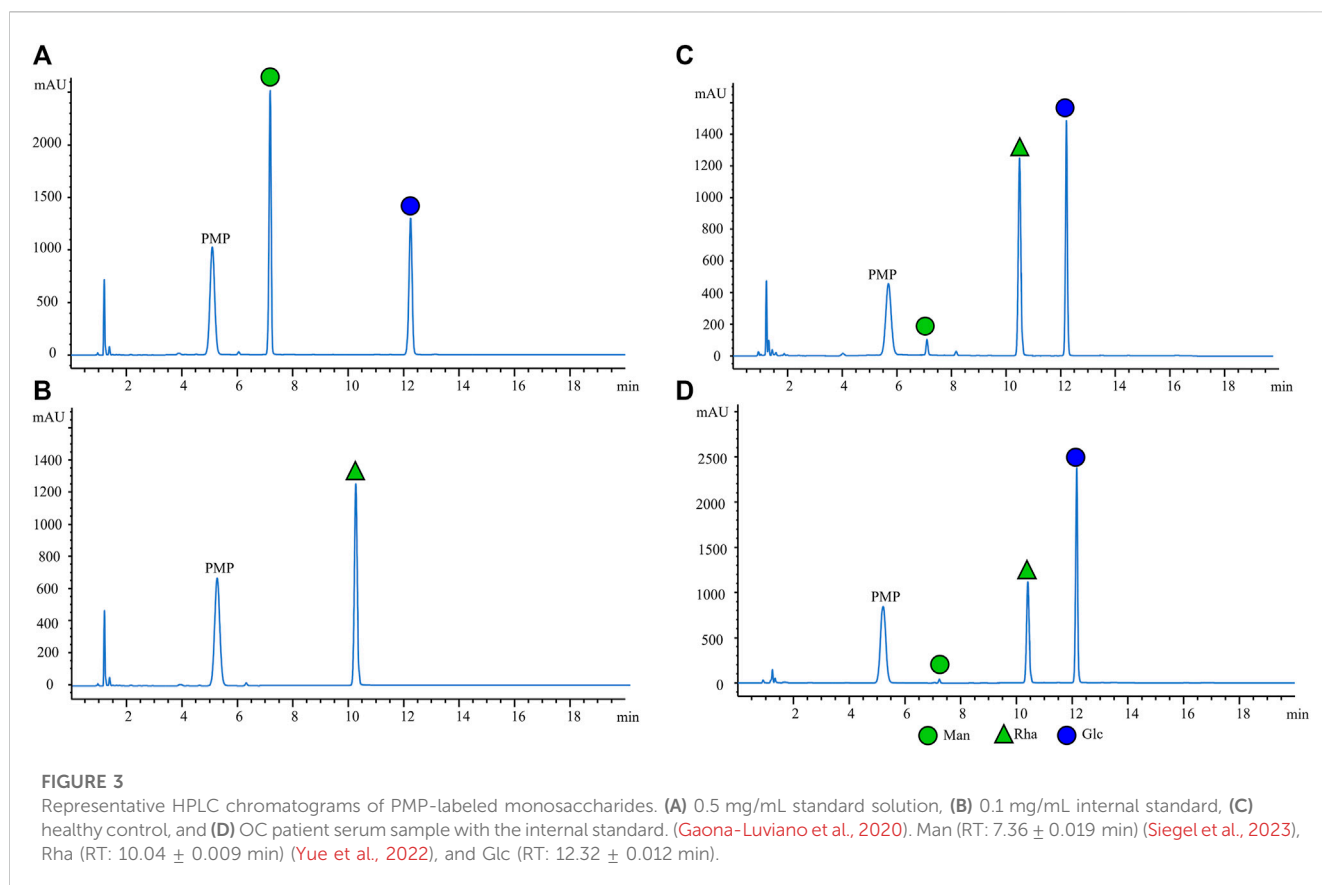
FIGURE 3
Representative HPLC chromatograms of PMP-labeled monosaccharides. **(A)** 0.5 mg/mL standard solution, **(B)** 0.1 mg/mL internal standard, **(C)** healthy control, and **(D)** OC patient serum sample with the internal standard. (Gaona-Luviano et al., 2020). Man (RT: 7.36 ± 0.019 min) (Siegel et al., 2023), Rha (RT: 10.04 ± 0.009 min) (Yue et al., 2022), and Glc (RT: 12.32 ± 0.012 min).

TABLE 1 Analytical performance of the method.

Monosaccharide	Retention time (min)	Correlation coefficient R^2	Concentration range (µg/mL)	LOD (µg/mL)	LOQ (µg/mL)
Man	7.36 ± 0.019	0.9999	0.5–500	0.37	1.26
Glc	12.32 ± 0.012	0.9999	0.5–1,500	0.61	2.07

facilitated monosaccharide analysis in a suitable gradient mode within 20 min, which was superior to the full-porous chromatographic column previously reported (Chen et al., 2022). Figure 3 displays the typical representative chromatograms: A) 0.5 mg/mL standard solution, B) 0.1 mg/mL IS, C) serum obtained from the healthy individual, and D) serum collected from OC patients. The experimental data indicated that our novel method could successfully separate Man and Glc without interference peaks.
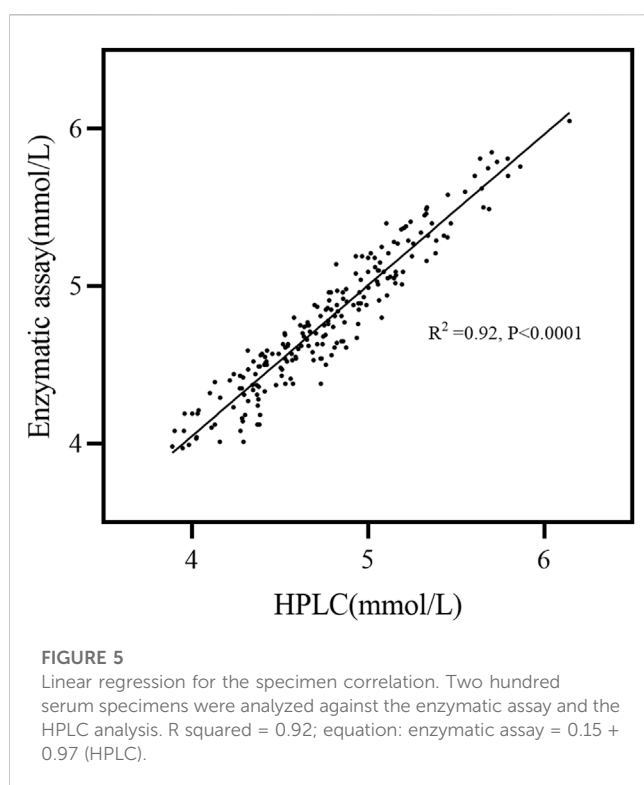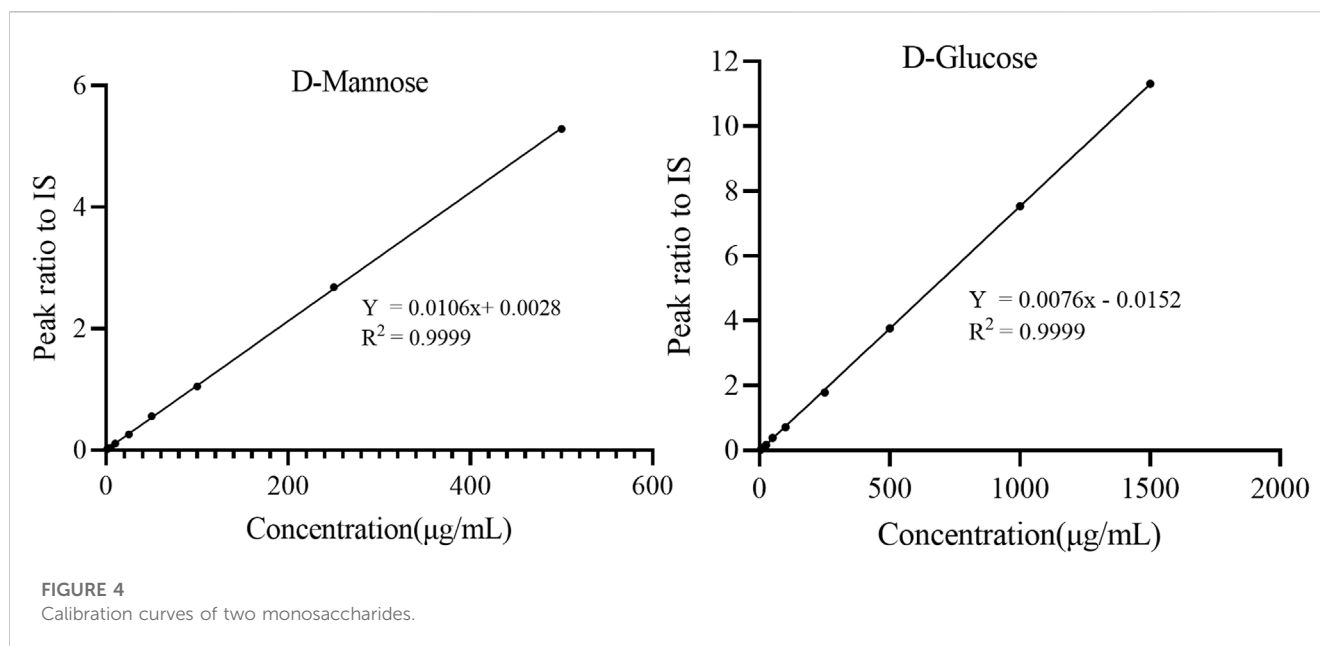
3.2 Method validation

3.2.1 Linearity, LOD, and LOQ

The calibration curve was established by plotting the peak area ratio Y) of the analyte IS and the nominal concentration X) of the analyte, and weighted ($1/X^2$) linear regression was performed. The calibration curve was linear in the obtained concentration range (for Man: 0.50–500.0 µg/mL and for Glc: 0.5–1500 µg/mL), and the correlation coefficients R^2 were observed to be > 0.999. This

finding showed that the method exhibited good linearity in the calibration range (Table 1; Figure 4), sufficient quantitative sensitivity, and good validation results. The LOD and LOQ for Man were 0.37 and 1.26 µg/mL, respectively, which were identical to those found in the previously reported study (Campi et al., 2019). The LOD and LOQ for Glc were 0.61 and 2.07 µg/mL, respectively (Table 1). The concentrations of the serum Glc obtained by our method was consistent with those obtained by the enzymatic method (Figure 5).

3.2.2 Precision and extraction recovery

Both the intra-day/inter-day precision and extraction recoveries (expressed as the relative standard deviations) of the method were found to be within the acceptable range of 15% (results are summarized in Supplementary Table S3). The intra-day precisions of Man and Glc were 0.44%–1.35% and 0.67%–1.56%, respectively. Inter-day precisions were observed to be 0.46%–3.22% and 0.90%–3.70%, respectively. The average extracted recoveries for Man at low, medium, and high QC concentrations were 102.62%, 99.46% and 106.30%, respectively. The recoveries for Glc were

FIGURE 4
Calibration curves of two monosaccharides.

FIGURE 5
Linear regression for the specimen correlation. Two hundred serum specimens were analyzed against the enzymatic assay and the HPLC analysis. R squared = 0.92; equation: enzymatic assay = 0.15 + 0.97 (HPLC).

109.31%, 116.51%, and 104.40%, respectively. These data demonstrated that simple sample preparation methods can effectively yield extremely high and stable extraction recovery.

3.2.3 Stability

The stability test was performed to assess the stability of the free monosaccharides under the expected sample pretreatment and storage conditions. The results of the stability studies have been summarized in Supplementary Table S4 and expressed as the mean

remaining percentage of the nominal concentrations. The stock solution after 2 months of storage at 4°C; the low, medium, and high QC samples after three freeze–thaw cycles at room temperature for 24 h; residual serum extract left in the autosampler at room temperature for 24 h; and stability at −80°C for 14 days were included. The stability of Man was 90.08%–103.74%, and that of Glc was 95.97%–103.49%.

Overall, all the validation results indicated that the established method had sufficient linearity, sensitivity, precision, and stability and could be used for the analysis of target free monosaccharides.
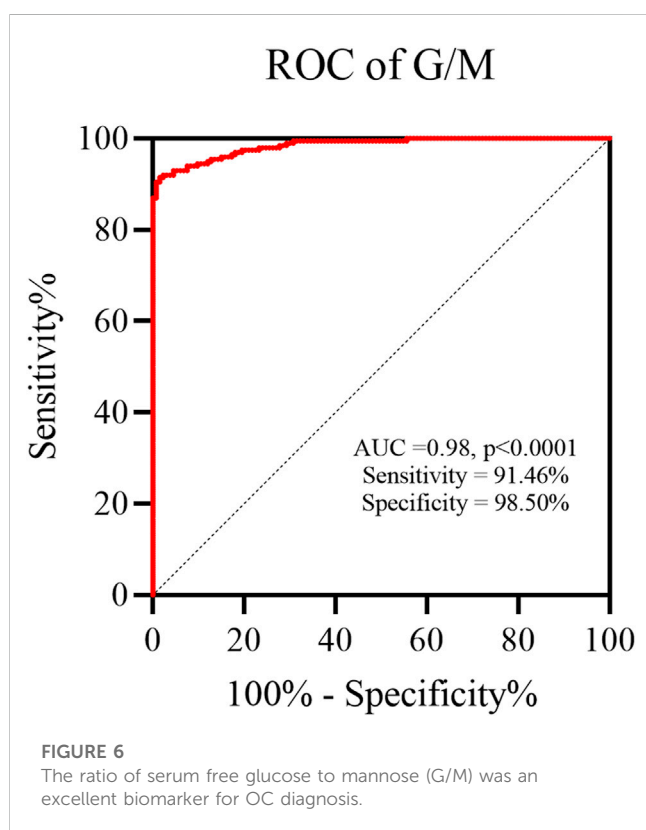
3.3 Quantification of the free monosaccharides in OC serum

In the present study, metabolite levels of the serum free Man and Glc were analyzed using established HPLC methods in 200 OC patients and 200 age-matched healthy controls. A non-parametric multiple comparison Kruskal–Wallis test (a non-parametric ANOVA) was conducted to compare the differences between the two groups. We compared the serum levels of free Man in patients with early-stage OC (FIGO = I+II) and healthy individuals, and significantly higher levels of serum Man were found in the early-stage OC patients than in the healthy individuals (50.09 μmol/L versus 44.51 μmol/L, $p < 0.0001$) as well as in the advanced (FIGO = III+IV) OC patients versus the early-stage OC patients (61.22 μmol/L versus 50.09 μmol/L, $p < 0.0001$). There was no significant difference in the levels of serum free glucose between the early and late-stage OC patients, but they were higher in both than those in the healthy individuals (Table 2).

We next investigated the diagnostic properties of mannose and glucose as potential biomarkers for OC by performing the receiving operator curve (ROC) analysis. The previous study conducted by our research group had reported a potential correlation between the ratio of serum free glucose to mannose (G/M) and the extent of human systemic dysfunction (Lijiuan and Yong, 2020). So, in this

TABLE 2 Levels of mannose in controls, early-stage, and late-stage OC cases.

| | Control/(N = 200) | | Cases | | | | p-value | | |
| | | | Early-stage (N = 80) | | Late-stage (N = 120) | | | | |
	Mean (SD)	RSD/%	Mean (SD)	RSD/%	Mean (SD)	RSD/%	(Early vs. controls)	(Late vs. controls)	(Early vs Late)
Mannose/ μmol/L	44.51 (4.42)	0.98	50.09 (10.69)	1.22	61.22 (21.64)	0.82	<0.0001	<0.0001	<0.001
Glucose/ mmol/L	4.55 (0.46)	0.31	4.99 (0.38)	1.99	4.95 (0.44)	0.75	<0.0001	<0.0001	0.36

FIGURE 6
The ratio of serum free glucose to mannose (G/M) was an excellent biomarker for OC diagnosis.

study, we have introduced the G/M and compared it between the healthy individuals and OC patients. The AUC for G/M as a biomarker for OC diagnosis was 0.98 ($p < 0.0001$), with a sensitivity of 91.46% and a specificity of 98.50% (Figure 6). Thus, our preliminary results suggested that it holds significant promise as a potential biomarker for OC.

4 Discussion

Identification of novel strategies to diagnose OC earlier can dramatically improve the chances of survival for many patients. One way to do this is to discover specific biomarkers that can circulate in blood. However, the quantity of these biomarkers is so low that detecting them has proven to be difficult. With the development of research technology, serum monosaccharides have been considered

potential biomolecules for biomarker discovery (White et al., 2017; Chen et al., 2022; Li et al., 2022; Wang et al., 2022). Interestingly, Man levels have been found to be abnormal in the serum of patients with tumors, but it has not been reported in the serum of OC patients. At present, almost all studies aimed at identifying serum Man as a potential cancer biomarker have emphasized on tedious sample pretreatment process and costly equipment, which makes it relatively difficult to translate the readings rapidly for clinical application. Here, we have developed a novel HPLC analysis method for detection of free Man and Glc simultaneously in a large number of serum samples, which may serve as an effective tool in diagnosing OC patients.

There are several published methods describing the analysis of free Man in body fluids (Table 3), and according to published studies, current methods used for the detection of Man in blood include GC (Monson and Wilkinson, 1979; Pitkanen, 1996), HPLC (Taguchi et al., 2003; Jozwik et al., 2007; Miwa and Taguchi, 2013), capillary electrophoresis (Carchon and Jaeken, 2001), and enzymatic method (Soyama, 1984; Akazawa et al., 1986; Pitkanen et al., 1997; Sone et al., 2003). For example, Etchison et al. analyzed the free Man in 200 μL serum by high-performance anion exchange chromatography with an amperometric detector (Etchison and Freeze, 1997). Carchon et al. examined the levels of serum free Man by capillary electrophoresis using pre-column derivatization. The analysis time for this method was only 8 min (Carchon and Jaeken, 2001). Taguchi et al. determined the free Man in plasma by HPLC equipped with an anion exchange column and a fluorescence detector. In addition, as post-column derivatization was used, a sophisticated equipment was required, and the analysis time of this method was 57 min (Taguchi et al., 2003). However, the aforementioned studies required the removal of the high glucose content by a more complex pre-processing step to detect the Man. Sato et al. used ethyl p-aminobenzoate as a derivative reagent of serum monosaccharides, separated different monosaccharides by HPLC, and detected Glc by using a UV detector and mannose by using a fluorescence detector, thus achieving the first simultaneous quantitative analysis of Glc and Man in serum of dogs and chickens. The serum dosage of the method was 100 μL, but this method has not yet been used for quantitative and qualitative analysis of glucose and mannose in human serum (Sato et al., 2008). Our previous research method was based on hydrolysis of serum samples for degrading the various polysaccharides and glycoproteins into monosaccharide components. Thereafter, eight different monosaccharides were detected by PMP derivations and further

TABLE 3 Detailed comparison of published methods for the analysis of mannose.

Year	Author	Body fluid	Method	Column/Enzyme	Pretreatment	Detector	Analyzing time	linearity range	LOD/LOQ	References
1979	Monson et al.	Serum	GC	Coiled 1.8-m glass column	Aidononitrile acetate derivatives	Flame-ionization	41.0 min	100–900 ng	100 ng	Monson and Wilkinson et al. (1979)
1984	Soyama et al.	Serum	Enzymatic assay	Mannosephosphate isomerase	Elimination of glucose	Spectrophotometer (340 nm)	-	25–1000 μmol/L	-	Soyama (1984)
1986	Akazawa et al.	Plasma/amniotic fluid	Enzymatic assay	PMI/PGI/G6PDH	Elimination of glucose	Spectrophotometer (340 nm)	-	-	-	Akazawa et al. (1986)
1996	Pitkänen et al.	Plasma	GC–MS	-	-	-	-	-	-	Pitkanen (1996)
1997	Etchison et al.	Serum	HPAEC	CarboPac PA-10 column	Elimination of glucose	Amperometric detection	20.0 min	5–200 mmol/L	-	Etchison and Freeze et al. (1997)
1997	Pitkanen et al.	Serum	Enzymatic assay	G6PDH/HK/GPI	Elimination of glucose	-	-	20–220 μmol/L	-	Pitkanen et al. (1997)
2001	Carchon et al.	Serum	CE	Fused-silica capillaries	APTS-derivatives	FLD	8.0 min	5–500 mmol/L	2.5 mmol/L	Carchon and Jaeken (2001)
2003	Taguchi et al.	Plasma	HPLC	Finepak GEL SA-121Anion-exchange column	-	FLD	57.0 min	400 μmol/L	5 μmol/L	Taguchi et al. (2003)
2003	Sone et al.	Plasma	Enzymatic assay	Glucokinase	Elimination of glucose	-	-	0–500 μg/mL	0.5 μg/mL	Sone et al. (2003)
2007	Józwik et al.	Plasma/preovulatory follicular fluid	HPLC	CarboPac MA1 anion-exchange column	-	Amperometric detection	30.0 min	-	-	Jozwik et al. (2007)
2008	Sato et al.	Serum	HPLC	ODS column	ABEE-derivatives	D-mannose: FLD, D-glucose: UV	30.0 min	0.27–320 μmol/L	0.09 μmol/L	Sato et al. (2008)
2013	Miwa et al.	Plasma	HPLC	Develosil ODS-UG-3 column	ABEE-derivatives	FLD	23.0 min	up to 600 μmol/l	5 μmol/L	Miwa and Taguchi (2013)
2015	Sanchez-Espiridion et al.	Serum	LC-MS/MS	Phenomenex Lux 5u Cellulose-1 column	-	-	-	-	-	Sanchez-Espiridion et al. (2015)
2017	White et al.	Serum	LC–MS/MS	SUPELCOGEL™ Pb, 6% Crosslinked HPLC column		-	24.0 min	1–50 μg/mL	LLOQ: 1 μg/mL, ULOQ: 50 μg/mL	White et al. (2017)
2019	Campi et al.	Plasma	LC-MS-MS	Shodex HILICpak VG-50 4E		-	14.0 min	0.31–40 μg/mL	LOD: 0.31 μg/mL, LOQ: 1.25 μg/mL	Campi et al. (2019)
2020	Han et al.	Plasma	UHPLC-HRMS	HILIC amino column	-	-	34.0 min	1–50 μg/mL	LOD : 0.5 μg/mL, LOQ: 1 μg/mL	Han et al. (2020)

analyzed by HPLC. It was observed that compared to the serum before hydrolysis, the composition and properties of the sample were altered significantly. Therefore, this method was not suitable for the direct detection of serum free monosaccharides. In addition, the method used in this approach displayed a long detection time and low efficiency (Chen et al., 2022). Further studies of free monosaccharides in the serum have been hampered by the limitations of detection methods.

The method developed in this study is primarily based on a simplified PMP-derived monosaccharide procedure in an alkaline environment. It comprises a clean chromatogram, all the monosaccharides were completely separated, and the methodological validation met the FDA bioanalytical method validation acceptance criteria (Figure 3; Table 1, Supplementary Table S3, Supplementary Table S4). In addition, the fast HPLC step can be completed within 13 min, thus expanding the capacity of the instrument and matching with a large number of the clinical samples. Our method can obtain both serum free Man and Glc data in a single HPLC profile by using only 10 μL of serum and then effectively generate quantitative data reports. Lastly, this approach can provide a novel method for HPLC analysis of monosaccharides by using Rha, which is not present in the serum, as an internal standard and as a standard sample for the blank substitution of serum. However, the limitation of this study is that all the subjects were recruited from a single center, and hence it is necessary to expand the sample set and validate it in a larger multicenter cohort study in the future, which is currently in progress.

As expected, we employed the HPLC method mentioned previously to analyze serum Man and Glc metabolism levels in OC patients as well as healthy individuals. It was found that the Glc concentration results showed good consistency with the enzymatic method (Figure 5), which is the most routinely used analysis method, but is expensive, while our method is relatively cheaper. We observed that serum levels of Man in patients with advanced (III+IV) OC were 1.37-fold higher and 1.12-fold upregulated in early-stage (I+II) patients in comparison to the healthy controls, which initially suggested that Man metabolism was abnormal in the serum of OC patients (Table 2). These results are consistent with previously observed increase in Man concentrations in patients with advanced-stage esophageal cancer in comparison to early-stage disease (White et al., 2017). The G/M showed potential ability as a diagnostic biomarker for OC (AUC = 0.98, sensitivity = 91.46%, specificity = 98.50%) (Figure 6). This phenomenon may reflect potential changes in metabolism to support the abnormal anabolic needs of the cancer cells and incomplete glycosylation processes, rather than being a predisposition factor. Man, an epimer of Glc, is a monosaccharide constituent present in both glycoproteins and glycolipids, which can be converted into each other *in vivo* (Zhang et al., 2017). It has been found that after entering the tumor cell, Man can effectively accumulate in the form of mannose-6-phosphate, which can block the energy source of tumors by interfering with Glc metabolism and thus inhibiting tumor cell growth. It can also increase the anticancer effect of doxorubicin *in vivo* and significantly prolong the survival time of the mice (Gonzalez et al., 2018). Tumors display a higher need for Glc to sustain their rapid growth than the normal tissues. It has been established that Man efflux from the cells constitutes the main source of free Man in mammalian blood (Sharma and Freeze, 2011). Tumorigenesis can affect changes in the

extracellular matrix or blood monosaccharides that can accurately reflect the pathophysiological state of the cell or person (Wang et al., 2022). Thus, exploring the metabolic levels of serum Man and Glc in OC might lead to the discovery of novel diagnostic markers and aid in further exploring the pathogenesis of OC.

In conclusion, we have developed a method for quantifying the levels of serum free monosaccharide using the HPLC and validated it in this study. This method was found suitable for analysis of the clinical samples and was used for the simultaneous quantification of Man and Glc concentrations in the human serum obtained from OC and healthy subjects. Our preliminary data showed that the Man levels were significantly higher in OC patients as compared to the healthy controls. Although further validation is required in a large multicenter sample, the results clearly indicate that Man levels can serve as a useful biomarker in diagnosis of OC.

Data availability statement

The original contributions presented in the study are included in the article/Supplementary Material; further inquiries can be directed to the corresponding authors.

Ethics statement

The studies involving humans were approved by and this study protocol was implemented in accordance with the ethical guidelines of the 2013 Declaration of Helsinki and has been approved by the Ethics Committee of the Affiliated Hospital of Qingdao University. The studies were conducted in accordance with the local legislation and institutional requirements. The participants provided their written informed consent to participate in this study.

Author contributions

YC: data curation, formal analysis, resources, software, writing–original draft, and investigation. QY: investigation, resources, visualization, writing–original draft, and conceptualization. LZ: data curation, investigation, methodology, validation, and writing–review and editing. PZ: funding acquisition, project administration, supervision, writing–review and editing, and validation.

Funding

Acknowledgments

Conflict of interest

The authors declare that the research was conducted in the absence of any commercial or financial relationships that could be construed as a potential conflict of interest..

Publisher's note

All claims expressed in this article are solely those of the authors and do not necessarily represent those of their affiliated organizations, or those of the publisher, the editors, and the reviewers. Any product that may be evaluated in this article, or claim that may be made by its manufacturer, is not guaranteed or endorsed by the publisher.

Supplementary material

The Supplementary Material for this article can be found online at: https://www.frontiersin.org/articles/10.3389/fchem.2023.1289211/full#supplementary-material

References

Akazawa, S., Metzger, B. E., and Freinkel, N. (1986). Relationships between glucose and mannose during late gestation in normal pregnancy and pregnancy complicated by diabetes mellitus: concurrent concentrations in maternal plasma and amniotic fluid. *J. Clin. Endocrinol. Metab.* 62 (5), 984–989. doi:10.1210/jcem-62-5-984

Amano, E., Funakoshi, S., Yoshimura, K., Hirano, S., Ohmi, S., Takata, H., et al. (2018). Fasting plasma mannose levels are associated with insulin sensitivity independent of BMI in Japanese individuals with diabetes. *Diabetol. Metab. Syndr.* 10, 88. doi:10.1186/s13098-018-0391-9

Bietenbeck, A., Geilenkeuser, W. J., Klawonn, F., Spannagl, M., Nauck, M., Petersmann, A., et al. (2018). External quality assessment schemes for glucose measurements in Germany: factors for successful participation, analytical performance and medical impact. *Clin. Chem. Lab. Med.* 56 (8), 1238–1250. doi:10.1515/cclm-2017-1142

Campi, B., Codini, S., Bisoli, N., Baldi, S., Zucchi, R., Ferrannini, E., et al. (2019). Quantification of d-mannose in plasma: development and validation of a reliable and accurate HPLC-MS-MS method. *Clin. Chim. Acta* 493, 31–35. doi:10.1016/j.cca.2019.02.024

Carchon, H. A., and Jaeken, J. (2001). Determination of D-mannose in serum by capillary electrophoresis. *Clin. Chem.* 47 (7), 1319–1321. doi:10.1093/clinchem/47.7.1319

Chen, Y., Yao, Q., Zeng, X., Hao, C., Li, X., Zhang, L., et al. (2022). Determination of monosaccharide composition in human serum by an improved HPLC method and its application as candidate biomarkers for endometrial cancer. *Front. Oncol.* 12, 1014159. doi:10.3389/fonc.2022.1014159

Conde, R., Laires, R., Goncalves, L. G., Rizvi, A., Barroso, C., Villar, M., et al. (2022). Discovery of serum biomarkers for diagnosis of tuberculosis by NMR metabolomics including cross-validation with a second cohort. *Biomed. J.* 45 (4), 654–664. doi:10.1016/j.bj.2021.07.006

Elias, K. M., Guo, J., and Bast, R. C., Jr (2018). Early detection of ovarian cancer. *Hematol. Oncol. Clin. North Am.* 32 (6), 903–914. doi:10.1016/j.hoc.2018.07.003

Etchison, J. R., and Freeze, H. H. (1997). Enzymatic assay of D-mannose in serum. *Clin. Chem.* 43 (3), 533–538. doi:10.1093/clinchem/43.3.533

FDA (2018). *Bioanalytical method validation guidance for Industry.*

Ferrannini, E., Bokarewa, M., Brembeck, P., Baboota, R., Hedjazifar, S., Andersson, K., et al. (2020). Mannose is an insulin-regulated metabolite reflecting whole-body insulin sensitivity in man. *Metabolism* 102, 153974. doi:10.1016/j.metabol.2019.153974

Gaona-Luviano, P., Medina-Gaona, L. A., and Magana-Perez, K. (2020). Epidemiology of ovarian cancer. *Chin. Clin. Oncol.* 9 (4), 47. doi:10.21037/cco-20-34

Gehrke, C. W., Waalkes, T. P., Borek, E., Swartz, W. F., Cole, T. F., Kuo, K. C., et al. (1979). Quantitative gas—liquid chromatography of neutral sugars in human serum glycoproteins. *J. Chromatogr.* 162 (4), 507–528. doi:10.1016/s0378-4347(00)81831-9

Gonzalez, P. S., O'Prey, J., Cardaci, S., Barthet, V. J. A., Sakamaki, J. I., Beaumatin, F., et al. (2018). Mannose impairs tumour growth and enhances chemotherapy. *Nature* 563 (7733), 719–723. doi:10.1038/s41586-018-0729-3

Gu, J., Liang, D., Pierzynski, J. A., Zheng, L., Ye, Y., Zhang, J., et al. (2017). D-mannose: a novel prognostic biomarker for patients with esophageal adenocarcinoma. *Carcinogenesis* 38 (2), 162–167. doi:10.1093/carcin/bgw207

Han, B., Park, J. W., Kang, M., Kim, B., Jeong, J. S., Kwon, O. S., et al. (2020). Simultaneous analysis of monosaccharides using ultra high performance liquid chromatography-high resolution mass spectrometry without derivatization for validation of certified reference materials. *J. Chromatogr. B Anal. Technol. Biomed. Life Sci.* 1160, 122370. doi:10.1016/j.jchromb.2020.122370

Jin, P., Wang, Y. Y., Liang, Z. G., Yuan, M., Li, H., and Du, Q. Z. (2021). Efficient bioconversion of high-concentration d-fructose into d-mannose by a novel N-acyl-d-glucosamine 2-epimerase from Thermobifida halotolerans. *Catal. Sci. Technol.* 11 (5), 1922–1930. doi:10.1039/d0cy01915a

Jobard, E., Pontoizeau, C., Blaise, B. J., Bachelot, T., Elena-Herrmann, B., and Tredan, O. (2014). A serum nuclear magnetic resonance-based metabolomic signature of advanced metastatic human breast cancer. *Cancer Lett.* 343 (1), 33–41. doi:10.1016/j.canlet.2013.09.011

Jozwik, M., Jozwik, M., Teng, C., and Battaglia, F. C. (2007). Concentrations of monosaccharides and their amino and alcohol derivatives in human preovulatory follicular fluid. *Mol. Hum. Reprod.* 13 (11), 791–796. doi:10.1093/molehr/gam060

Koseler, A., Arslan, I., Sabirli, R., Zeytunluoglu, A., Kilic, O., and Kilic, I. D. (2020). Molecular and biochemical parameters related to plasma mannose levels in coronary artery disease among nondiabetic patients. *Genet. Test. Mol. Biomarkers* 24 (9), 562–568. doi:10.1089/gtmb.2020.0095

Koseler, A., Arslan, I., Sabirli, R., Zeytunluoglu, A., Kilic, O., and Kilic, I. D. (2021). Associations between serum lipids and mannose levels in coronary artery disease among nondiabetic patients. *Biomark. Med.* 15 (12), 1035–1042. doi:10.2217/bmm-2020-0468

Li, H. R., Wang, X. L., Huang, X. D., He, Y. L., Zhang, Y. R., Hao, C., et al. (2022). Circulating glycan monosaccharide composite-based biomarker diagnoses colorectal cancer at early stages and predicts prognosis. *Front. Oncol.* 12, 852044. doi:10.3389/fonc.2022.852044

Lijiuan, Z., and Yong, L. (2020). *Detection of serum free mannose and glucose by HPLC.* patent, CN108956792B.

Marier, R. L., Milligan, E., and Fan, Y. D. (1982). Elevated mannose levels detected by gas-liquid chromatography in hydrolysates of serum from rats and humans with candidiasis. *J. Clin. Microbiol.* 16 (1), 123–128. doi:10.1128/jcm.16.1.123-128.1982

Miwa, I., and Taguchi, T. (2013). A simple HPLC assay for plasma D-mannose. *Clin. Chim. Acta* 422, 42–43. doi:10.1016/j.cca.2013.04.005

Monson, T. P., and Wilkinson, K. P. (1979). D-Mannose in human serum, measured as its aldononitrile acetate derivative. *Clin. Chem.* 25 (8), 1384–1387. doi:10.1093/clinchem/25.8.1384

Monson, T. P., and Wilkinson, K. P. (1981). Mannose in body fluids as an indicator of invasive candidiasis. *J. Clin. Microbiol.* 14 (5), 557–562. doi:10.1128/jcm.14.5.557-562.1981

Pitkanen, E. (1996). Mannose, mannitol, fructose and 1,5-anhydroglucitol concentrations measured by gas chromatography/mass spectrometry in blood plasma of diabetic patients. *Clin. Chim. Acta* 251 (1), 91–103. doi:10.1016/0009-8981(96)06284-5

Pitkanen, E., Pitkanen, O., and Uotila, L. (1997). Enzymatic determination of unbound D-mannose in serum. *Eur. J. Clin. Chem. Clin. Biochem.* 35 (10), 761–766. doi:10.1515/cclm.1997.35.10.761

Ramakrishna, V. R., Shyam Sunder, R., Kumar, K. R., and Narayan Sinha, S. (2020). Method development and validation for rapid identification of epigallocatechin gallate using ultra-high performance liquid chromatography. *PLoS One* 15 (1), e0227569. doi:10.1371/journal.pone.0227569

Sanchez-Espiridion, B., Liang, D., Ajani, J. A., Liang, S., Ye, Y., Hildebrandt, M. A., et al. (2015). Identification of serum markers of esophageal adenocarcinoma by global and targeted metabolic profiling. *Clin. Gastroenterol. Hepatol.* 13 (10), 1730–1737.e9. doi:10.1016/j.cgh.2015.05.023

Sato, T., Katayama, K., Arai, T., Sako, T., and Tazaki, H. (2008). Simultaneous determination of serum mannose and glucose concentrations in dog serum using high performance liquid chromatography. *Res. Vet. Sci.* 84 (1), 26–29. doi:10.1016/j.rvsc.2007.03.002

Sharma, V., and Freeze, H. H. (2011). Mannose efflux from the cells: a potential source of mannose in blood. *J. Biol. Chem.* 286 (12), 10193–10200. doi:10.1074/jbc.m110.194241

Shulman, L. P., Francis, M., Bullock, R., and Pappas, T. (2019). Clinical performance comparison of two in-vitro diagnostic multivariate index assays (IVDMIAs) for

presurgical assessment for ovarian cancer risk. *Adv. Ther.* 36 (9), 2402–2413. doi:10.1007/s12325-019-01010-8

Siegel, R. L., Miller, K. D., Wagle, N. S., and Jemal, A. (2023). Cancer statistics, 2023. *CA Cancer J. Clin.* 73 (1), 17–48. doi:10.3322/caac.21763

Sone, H., Shimano, H., Ebinuma, H., Takahashi, A., Yano, Y., Iida, K. T., et al. (2003). Physiological changes in circulating mannose levels in normal, glucose-intolerant, and diabetic subjects. *Metabolism* 52 (8), 1019–1027. doi:10.1016/s0026-0495(03)00153-7

Soyama, K. (1984). Enzymatic determination of D-mannose in serum. *Clin. Chem.* 30 (2), 293–294. doi:10.1093/clinchem/30.2.293

Taguchi, T., Miwa, I., Mizutani, T., Nakajima, H., Fukumura, Y., Kobayashi, I., et al. (2003). Determination of D-mannose in plasma by HPLC. *Clin. Chem.* 49 (1), 181–183. doi:10.1373/49.1.181

Trezzi, J. P., Galozzi, S., Jaeger, C., Barkovits, K., Brockmann, K., Maetzler, W., et al. (2017). Distinct metabolomic signature in cerebrospinal fluid in early Parkinson's disease. *Mov. Disord.* 32 (10), 1401–1408. doi:10.1002/mds.27132

Wang, H., Zhang, X., Peng, Y., Pan, B., Wang, B., Peng, D. H., et al. (2022). A LC-MS/MS method to simultaneously profile 14 free monosaccharides in biofluids.

J. Chromatogr. B Anal. Technol. Biomed. Life Sci. 1192, 123086. doi:10.1016/j.jchromb.2021.123086

Wei, Y., Huang, H., Zhang, R., Zhu, Z., Zhu, Y., Lin, L., et al. (2021). Association of serum mannose with acute respiratory distress syndrome risk and survival. *JAMA Netw. Open* 4 (1), e2034569. doi:10.1001/jamanetworkopen.2020.34569

White, L., Ma, J., Liang, S., Sanchez-Espiridion, B., and Liang, D. (2017). LC-MS/MS determination of d-mannose in human serum as a potential cancer biomarker. *J. Pharm. Biomed. Anal.* 137, 54–59. doi:10.1016/j.jpba.2016.12.017

Xiao, Y., Bi, M., Guo, H., and Li, M. (2022). Multi-omics approaches for biomarker discovery in early ovarian cancer diagnosis. *EBioMedicine* 79, 104001. doi:10.1016/j.ebiom.2022.104001

Yue, X., Zhong, L. L., Wang, Y. S., Zhang, C. Y., Chen, X. F., Wang, S., et al. (2022). Value of assessment of different neoplasias in the adnexa in the differential diagnosis of malignant ovarian tumor and benign ovarian tumor: a meta-analysis. *Ultrasound Med. Biol.* 48 (5), 730–742. doi:10.1016/j.ultrasmedbio.2022.02.001

Zhang, D., Chia, C., Jiao, X., Jin, W., Kasagi, S., Wu, R., et al. (2017). D-mannose induces regulatory T cells and suppresses immunopathology. *Nat. Med.* 23 (9), 1036–1045. doi:10.1038/nm.4375

PAS-based analysis of natural gas samples

Marc-Simon Bahr[1,2]* and Marcus Wolff[1]

[1]Heinrich Blasius Institute of Physical Technologies, Hamburg University of Applied Sciences, Hamburg, Germany, [2]School of Computing, Engineering and Physical Sciences, University of the West of Scotland, Paisley, United Kingdom

Photoacoustic spectroscopy (PAS) is well known for the detection of short-chain hydrocarbons, such as methane, ethane and propane, in the ppm (parts per million) or ppb (parts per billion) range. However, in the production process of natural gas and its combustion in gas-fired devices the composition, especially the concentrations of the main alkanes, plays a decisive role. Gas chromatography (GC) is considered the gold standard for natural gas analysis. We present a method to analyze natural gas samples by PAS. Furthermore, we describe a method to prepare storage gas samples, which are usually under atmospheric pressure, for PAS analysis. All measurements are validated by means of GC. The investigation allows conclusions to be drawn to what extent PAS is suitable for the investigation of natural gas samples.

KEYWORDS

photoacoustic spectroscopy, main alkanes, interband cascade laser, natural gas, hydrocarbons

1 Introduction

Natural gas is one of the most important energy sources of our time and plays a significant role in the global energy supply. It consists of 75%–99% methane, 1%–15% ethane and 1%–10% propane as well as other small amounts of longer-chain hydrocarbons such as butane and pentane, but also of small amounts of nitrogen, carbon dioxide and noble gases (Hammer et al., 2003). The exact composition of natural gas is strongly dependent on its origin (Decourt et al., 2014).

When drilling for gas production, gas samples are taken at various drilling depths. These samples have a composition similar to commercial natural gas and, based on the compositions of the samples, allow geological conclusions regarding the surrounding rock but also about the expected gas deposit (Wiersberg and Erzinger, 2007).

Furthermore, the knowledge of composition of natural gas is extremely important for an effective combustion. The proportions of the individual hydrocarbons determine the energy content of the natural gas and thus its calorific value. In a mixture the different components contribute according to their concentrations (Leicher et al., 2017; Park et al., 2021).

Optimal operating parameters of gas-fired devices depend on the composition because methane, ethane and propane require different amounts of oxygen for a complete (stoichiometric) combustion (Demoulin et al., 2008). If the ratio of oxygen to gas components is not correct, incomplete combustion can occur, reducing energy efficiency and potentially causing harmful emissions. The knowledge of the composition helps to set the right combustion conditions to ensure optimal and environmentally friendly combustion (Wei et al., 2021).

In addition, the composition of natural gas has a significant influence on the monetary value of the natural gas. Both, industrial and private customers of natural gas receive bills

based on average values of the natural gas composition and thus the energy content. The actual energy content sometimes varies significantly from the values used for billing, which often results in financial disadvantages for the customer. Knowing the actual composition of the natural gas purchased would make it possible to create correct bills regarding the energy content (Paulus and Lemort, 2023).

The knowledge of the exact composition of natural gas is of utmost importance in many aspects. Several methods exist for determining the natural gas composition regarding the individual hydrocarbons.

Gas chromatography (GC) is considered the gold standard of natural gas analysis. The individual natural gas components are separated in a separation column and then quantitatively detected, for example, with a flame ionization detector (FID) (Rhoderick, 2003; Brown et al., 2004). The advantage of GC is the high accuracy and the high dynamic range regarding the concentrations. With a gas chromatograph, measurements with deviations of 1%–2% are possible in a dynamic range starting in the ppb range up to 100%. The flame of the FID can be problematic in places with a high risk of explosion, for example, at drilling sites. Furthermore, a variety of operating gases are required, such as helium as carrier gas, synthetic air and hydrogen as combustion gas for the FID. Additionally, the analysis time can be up to 45 min depending on the selected analysis parameters (Poole, 2021).

A number of spectroscopic methods have been tried out for natural gas analysis, which have both advantages and disadvantages compared to the established GC.

Infrared spectroscopy in various forms was tested. The wavelength range was typically 1,000–2,000 nm.

A variety of measuring instruments exist which can detect methane, the main component of natural gas, by means of infrared absorption spectroscopy (Compur Monitors, 2021; Mueller-Elektronik AG, 2023). These devices are very compact and thus allow field measurements with very short measuring times. The disadvantage of this type of measurement devices, however, is that they cannot perform a natural gas analysis and thus only provide an indication of natural gas leakage.

Infrared absorption spectroscopy can also be performed from higher altitudes. Unmanned flying objects (drones) and satellites are used for this purpose (Iwaszenko et al., 2021; Pandey et al., 2023). Their emitted laser radiation is reflected at the Earth's surface and thus also allows conclusions to be drawn about the presence of methane in the atmosphere. The advantage of these methods is the large measurement area that can be covered. Since the reflectivity depends on the existing topography of the reflecting point and the interaction path is large due to the measurement height, cross-sensitivities causing larger deviations are to be expected with this measurement method.

Fourier transform near-infrared (FTNIR) spectroscopy is a well-known embodiment of infrared spectroscopy (Haghi et al., 2017). Based on a Michelson interferometer, an absorption spectrum is generated in conjunction with the Fourier transform, from which the proportions of the individual components of the gas sample can be determined.

Another method of infrared spectroscopy is transmission spectroscopy based on hollow-core photonic bandgap fibers (Li et al., 2012). The gas mixture to be analyzed flows into the fiber,

where the interaction between the laser radiation and the natural gas occurs. By tuning the laser, an absorption spectrum can be recorded by means of an intensity detector. The resulting spectra can also be used to quantify the individual gas components.

The advantage of both methods is the comparatively short measurement time in the range of seconds compared to gas chromatography. Water exhibits strong absorption lines in the spectral range mentioned, so that large cross-sensitivities can occur, which leads to considerable measurement deviations. Furthermore, there is a temperature dependency for both methods, which negatively influences the accuracy. For these reasons, field measurements are hardly possible.

A further spectroscopy method, which enables the detection of almost all natural gas components, is Raman spectroscopy (Kiefer et al., 2008; Dąbrowski et al., 2019; Petrov et al., 2022). This measurement technique based on the Raman Effect requires laser power in the Watt range, which makes it expensive and eye safety becomes an important issue. Furthermore, a set of calibration measurements are prerequisite to obtain reliable results under a wide range of measurement conditions.

One of the most recently published spectroscopic technologies for natural gas analysis is based on proton Nuclear Magnetic Resonance (NMR) spectroscopy (Duchowny et al., 2022). The advantage of this method is the high accuracy of the results, the relative error is less than 1% in relation to the GC reference. Measurements under different temperature and pressure conditions are also possible. Nevertheless, field measurements are hardly possible since a benchtop NMR, such as the Spinsolve 60 ULTRA NMR spectrometer from Magritek (Aachen, Germany), weighs 60 kg and measures 58 × 43 × 40 cm.

Recently, a sensor based on light-induced thermoelastic spectroscopy (LITES) was presented, that is capable of detecting natural gas main components. However, the measurements were limited to synthetic gas mixtures consisting of methane, ethane and nitrogen. The maximum methane share investigated was 10% (Zifarelli et al., 2023).

Photoacoustic spectroscopy is well known as an analytical method for the detection of trace gases in the sub-ppt to ppm range (Sigrist, 1995; Wang et al., 2022). The main advantage over purely optical absorption spectroscopy is that photoacoustic spectroscopy is an offset-free technique.

When modulated laser radiation hits molecules, which absorb the energy of the photons, complex intermolecular relaxation processes can occur. Subsequently, a thermal wave is generated, which leads to a pressure wave. This phenomenon is well known as the photoacoustic effect which is applied in photoacoustic spectroscopy. The resulting sound wave is typically amplified by means of an acoustic resonator and detected by a microphone (Palzer, 2020).

QEPAS (Quartz Enhanced Photoacoustic Spectroscopy) represents a special embodiment of PAS. In this case, the microphone is replaced by a quartz tuning fork, which typically has a Q-factor greater than 10,000 (Sampaolo et al., 2022). QEPAS has already been successfully used to study the relaxation processes of gas mixtures consisting of methane, ethane and propane, each with fractions in the lower percentage range (Menduni et al., 2022). First QEPAS measurements involving the simultaneous detection of synthetic natural gas-like mixtures consisting of methane, ethane, and propane under laboratory conditions were presented (Luo et al.,
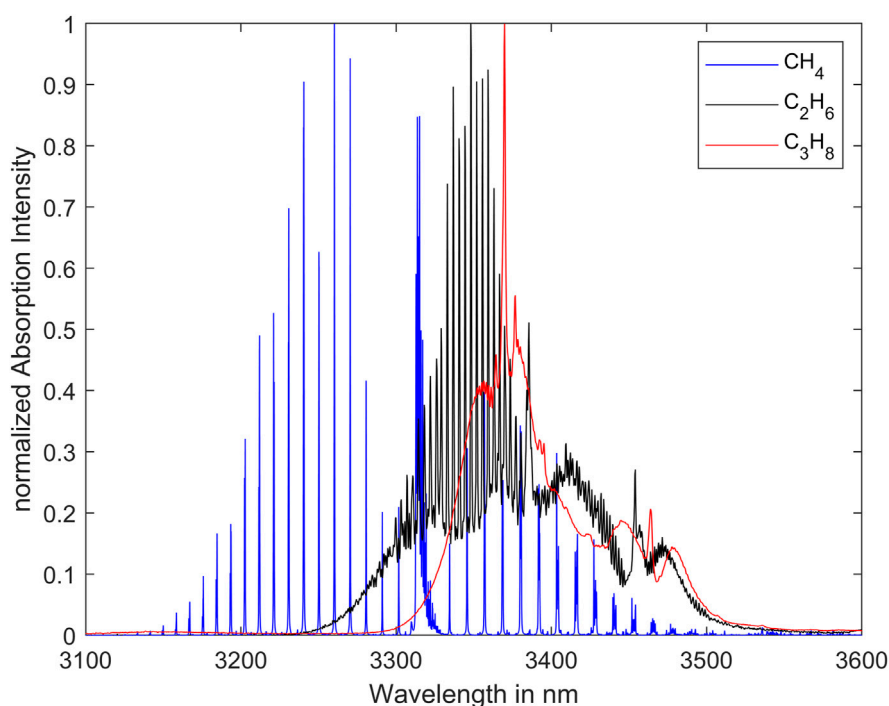
FIGURE 1
Absorption spectra of methane, ethane and propane (GEISA, 2022; Gordon et al., 2022).

2022). The evaluation is based on the signal amplitude at discrete wavelengths. The measurements are so far limited to synthetic mixtures.

To the best of our knowledge, we developed the first photoacoustic analyzer that can determine the concentrations of methane, ethane and propane of real natural gas samples. The investigated natural gas originates from the house supply of Hamburg University of Applied Sciences (Hamburg, Germany). Furthermore, we have investigated a gas sample originating from a German natural gas storage. In this regard we also present a method for preparing gas samples of atmospheric pressure for the photoacoustic measurement.

Chapter 2 provides the relevant short-chain hydrocarbons absorption spectra and describes the measurement setup and the respective measurement procedure. The third chapter presents the measurement results, which are subsequently discussed in Chapter 4.

2 Methods and material

2.1 Methane, ethane and propane absorption spectra

The analyzer is based on an interband cascade laser (ICL) emitting in the mid-infrared range. Figure 1 shows the normalized absorption spectra of methane, ethane and propane at room temperature (296 K) and atmospheric pressure (1013.25 hPa). The absorption cross-section coefficient of methane, ethane and propane are all of a similar order of magnitude in this spectral range. The center wavelength of the laser has been empirically selected to be 3324.15 nm and is displayed by the vertical dark line in the yellow box in Figure 2. To clearly identify several

components of a gas mixture, it is necessary to analyze the spectrum in a specific range. For this purpose, the laser is spectrally tuned. The yellow box represents the laser tuning range whose spectral bandwidth is approximately 5.3 nm.

2.2 Measurement setup

The measurement setup is schematically shown in Figure 3. The ICL 3272 manufactured by nanoplus GmbH (Gerbrunn, Germany) emits radiation around 3323 nm with a spectral linewidth smaller than 20 MHz. The laser chip temperature can be varied between 20 and 30°C. Laser operating currents between 19 and 120 mA allow stimulated emission. For the operation of the ICL the Thorlabs (Newton, MA/USA) laser diode driver TLD001 and the temperature controller TTC001 are used. The TLD001 allows to set the laser current with an accuracy of 10 μA with a noise level below 3 μA rms. Installed in a TO66 housing, the ICL chip temperature is controlled using a temperature sensor and a Peltier element. The single-mode emission can be continuously tuned between 3318.41 nm and 3330.64 nm. Approximately 25 mW output power can be reached at maximum. The cylindrically symmetrical photoacoustic measurement cell, that the laser beam centrally passes, is designed according to the established H geometry boasting a longitudinal resonance around 3 kHz (Nodov, 1978). The photoacoustic signal is detected with the analog microphone ROM-2235P-HD-R from PUI Audio (Fairborn, OH/USA) which is mounted in the center of the cell, membrane flush with the wall. The microphone exhibits a diameter of 5.8 mm and a detection sensitivity of −35 ± 3 dB at 1 kHz and 50 cm distance. The
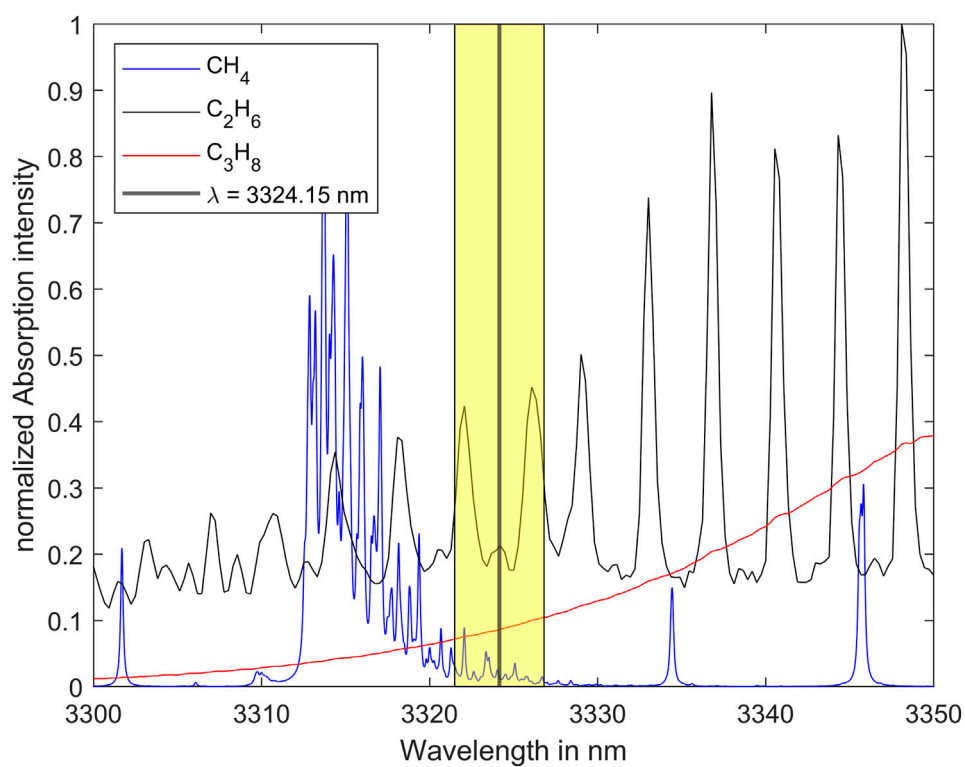
FIGURE 2
Absorption spectra of methane, ethane and propane together with the laser tuning range (yellow box) and the laser center wavelength (GEISA, 2022; Gordon et al., 2022).
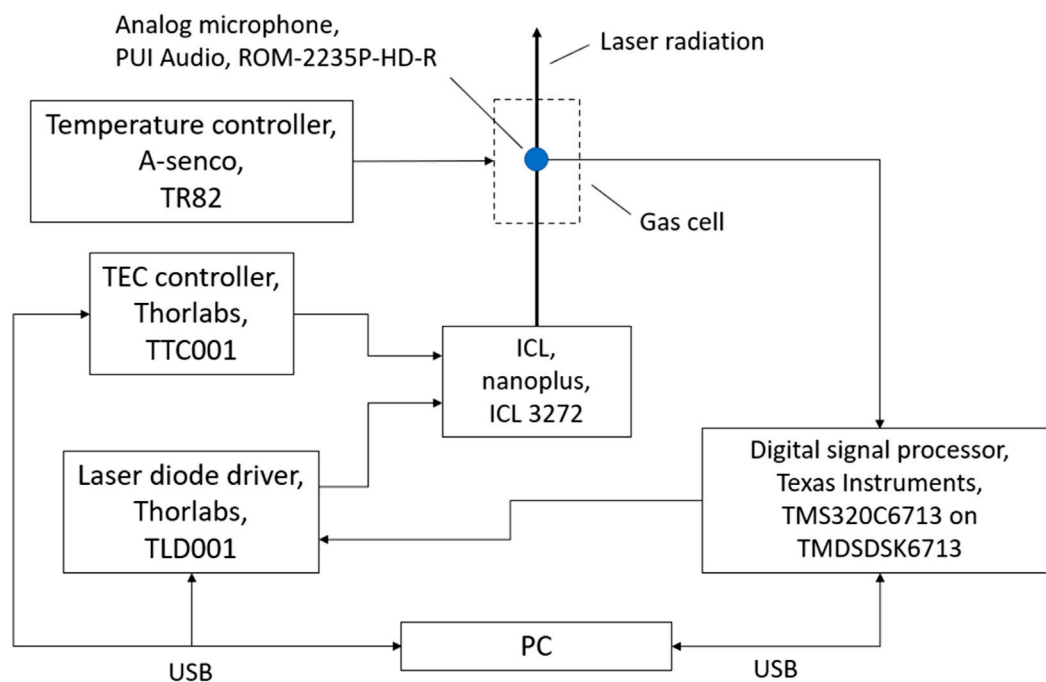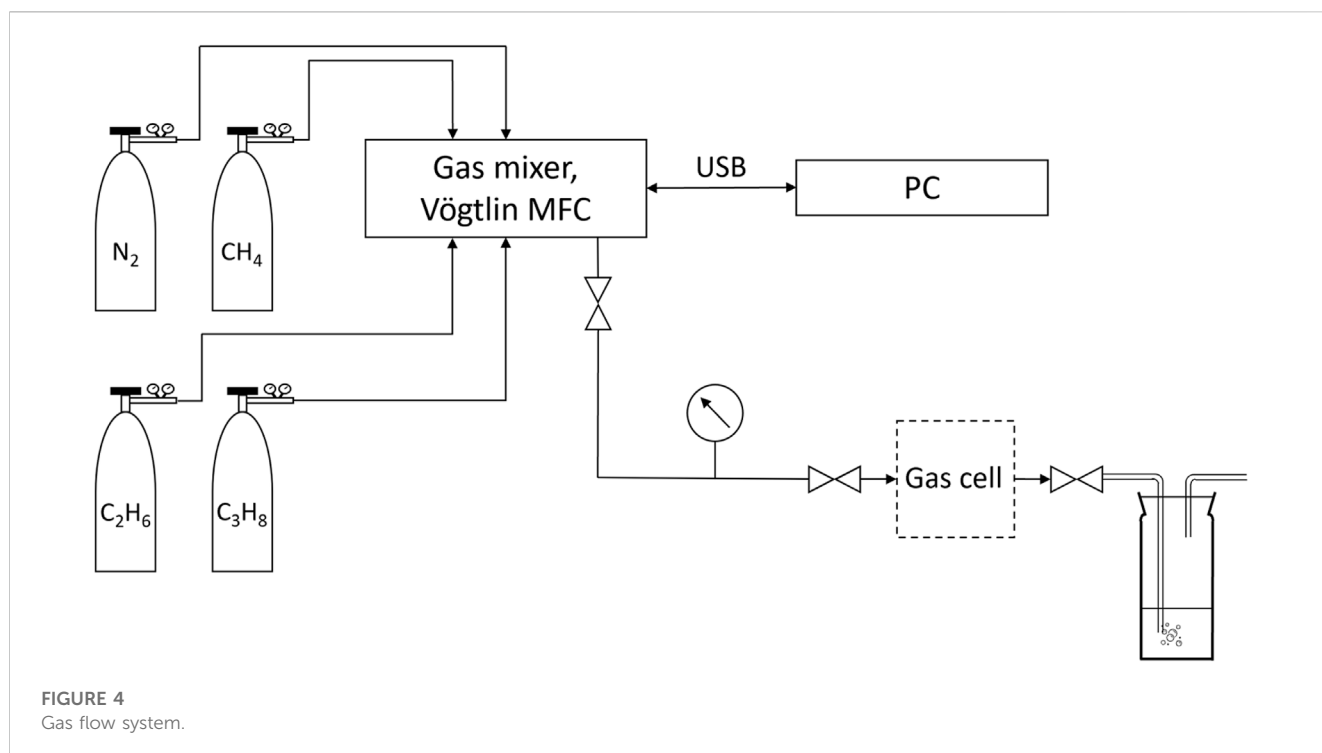

FIGURE 3
Experimental setup.

FIGURE 4
Gas flow system.

temperature of the measurement cell is controlled by the A-senco (Aalen, Germany) temperature controller, which heats the cell to a constant temperature above the ambient temperature by means of two heating mats. The maximum heating power is 30 W. The demodulation is performed on a Texas Instruments (Dallas, TX/USA) TMS320C6713 digital signal processor (DSP) which is mounted on the Texas Instruments TMDSDSK6713 evaluation board. The laser current modulation is controlled by the digital signal processor as well. A PC is used to control laser diode driver, TEC controller and DSP. The photoacoustic signals calculated by the DSP are recorded by the PC as function of the average current. These spectra of known mixtures serve as basis for a PLSR model based on a MATLAB script, which can subsequently be used to calculate the concentrations of the single components of unknown mixtures.

The gas flow system for the generation of the calibration mixtures is schematically shown in Figure 4. The gas is provided in four containers:

- CH_4: 10 L geometric volume, 200 bar filling pressure, purity: 2.5, distributor: Westfalen AG,
- C_2H_6: 1 L geometric volume, 12 bar filling pressure, purity: 2.0, distributor: Westfalen AG,
- C_3H_8: 1 L geometric volume, 7.3 bar filling pressure, purity: 2.5, distributor: Westfalen AG,
- N_2: 10 L geometric volume, 200 bar filling pressure, purity: 5.0, distributor: Westfalen AG.

All gas mixtures for calibration are generated using the 4-channel gas mixer based on Vögtlin Instruments GmbH (Muttenz, Swiss) mass flow controllers (MFC), which are distributed by HTK Hamburg GmbH (Hamburg, Germany). The maximum relative error of a single MFC is specified to be up to 1%.

The validation measurements of the natural gas samples were carried out using the Shimadzu (Kyōto, Japan) GC 2014, which is equipped with an FID and a thermal conductivity detector (TCD). The relative measurement error is specified to be up to 2%.

The storage gas sample was provided by GEO-data (Garbsen, Germany) in a gas collection tube with a geometric volume of about 350 mL. The storage gas originates from a natural gas storage facility within Germany. Its preparation has been performed using the setup shown in Figure 5. A lecture bottle (geometric volume approximately 400 mL) was evacuated by the VACUUBRAND GmbH and Co. KG (Wertheim, Germany) Chemistry-HYBRID pump down to 0.1 mbar absolute pressure.

The natural gas samples used are from Hamburger Energiewerke GmbH (Hamburg, Germany) and were obtained from the house gas connection of the Hamburg University of Applied Sciences.

2.3 Measurement procedure

At a constant temperature of 20°C, the ICL applied in this investigation is operated in the injection-current modulation mode. The injection-current consists of two parts. One part is continuously tuned between 66.00 and 120.12 mA covering a spectral range of approximately 5.3 nm. The other part is sinusoidally modulated with an amplitude of 1.18 mA which corresponds to a spectral range of approximately 0.1 nm.

The temperature of the measurement cell is set and controlled to constant 30°C by the temperature controller.

The microphone signal is sampled at a sampling rate of 44.1 kHz. The recorded spectra consist of 315 points, with each spectral component calculated from 1,500 samples. The demodulation of the microphone signal on the DSP, based on the Goertzel
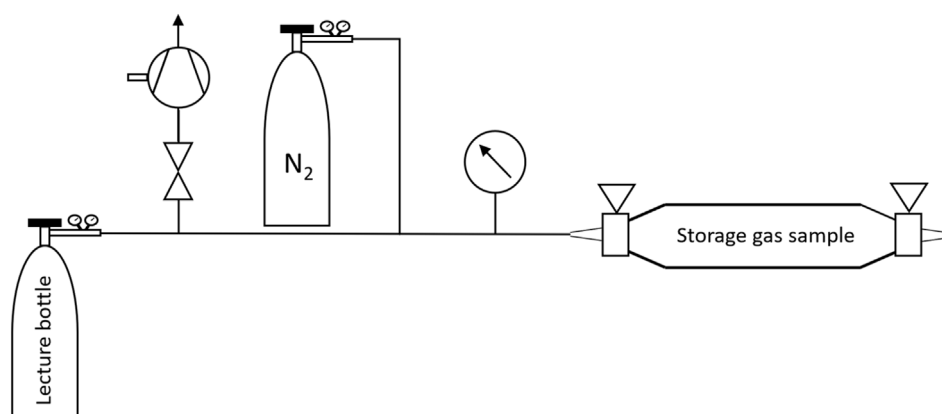
FIGURE 5
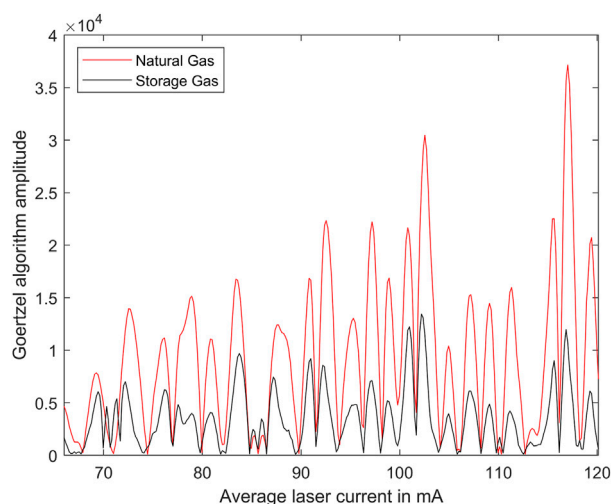Storage gas preparation system.

FIGURE 6
Exemplary photoacoustic spectra of natural gas and storage gas measured on 28 June 2023 and 29 June 2023, respectively.

TABLE 1 Analysis results.

Sample type	Date	PAS			GC		
		Methane (%)	Ethane (%)	Propane (%)	Methane (%)	Ethane (%)	Propane (%)
Natural gas	26 May 2023	86.11	4.98	0.92	85.23	4.70	0.96
	28 June 2023	85.03	4.95	0.67	85.10	4.96	0.87
	2 August 2023	82.35	4.60	0.62	84.33	4.41	0.77
Storage gas	29 June 2023	6.79	0.41	-	6.78	0.48	<0.1

algorithm, is performed at the injection-current modulation frequency at 3,528 Hz (Engelberg, 2008). The resulting spectra correspond approximately to the first derivative of the absorption spectra, which emphasizes the changes in the absorption coefficient, induced by changes in the single gas concentrations.

Figure 6 shows exemplary photoacoustic spectra, i.e., the PA signals as function of the average laser current after the Goertzel algorithm based demodulation on the DSP. All measurements were taken at a sample (cell) temperature of 30°C and a pressure of 1,013 hPa.
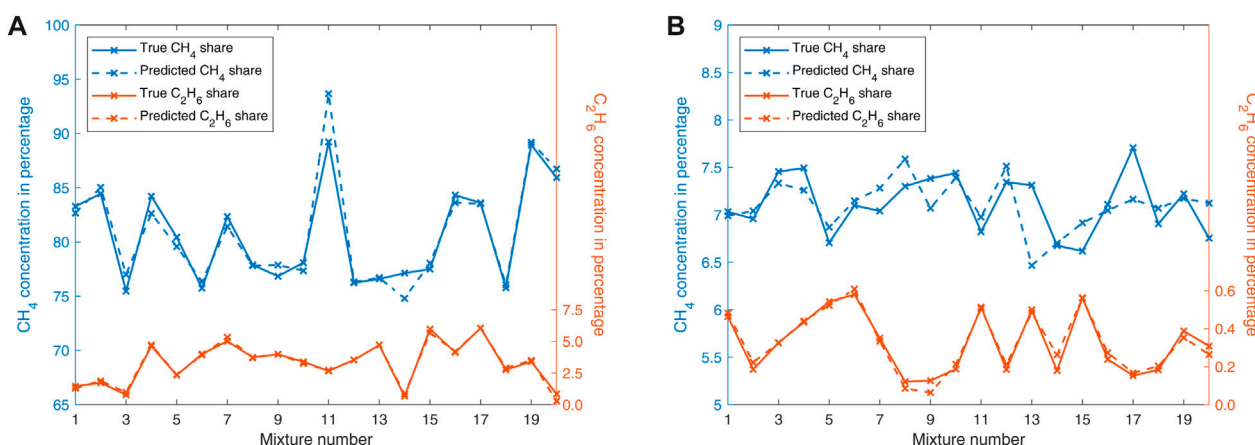
FIGURE 7
(A) Results of the leave-one-out cross-validation of natural gas (propane is hidden for clarity). **(B)** Results of the leave-one-out cross-validation of storage gas.
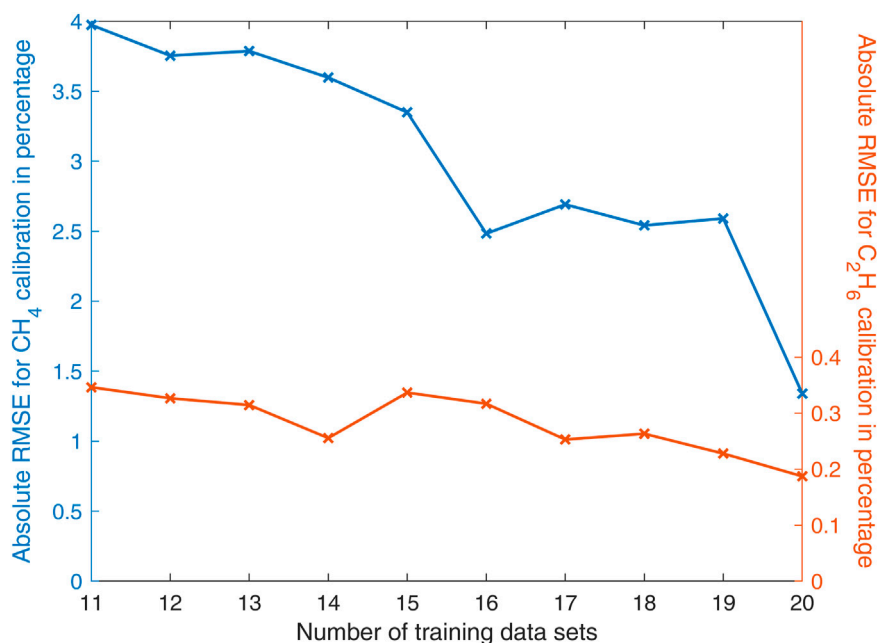

FIGURE 8
Absolute RMSE as function of the number of training data sets.

The investigation of complex gas mixtures such as natural gas requires a multivariate approach to determine the methane, ethane and propane shares. As shown in previous investigations, Partial Least Squares Regression (PLSR) proved to be suitable for this task (Menduni et al., 2022). Reference calibration measurements of the photoacoustic sensor are required to predict the individual shares of the natural gas samples with a high precision and reliability. A training data set of 20 different mixtures has been used, all concentrations are uniform distributed. All calibration gas mixtures consist of methane,

ethane and propane. The calculation of the PLSR model is performed on the PC. The magnitudes of the spectrum represent the predictor scores and the corresponding known concentrations provide the response scores. The beta-parameters are the result of the PLSR model calculation, which are the basis for the prediction of gas mixture compositions. By multiplication and summation operations of the beta-parameters with the spectra of unknown mixtures, the concentrations of its hydrocarbon components are calculated (Rosipal and Krämer, 2006).

A complete measurement run including calculation of the unknown hydrocarbon concentrations of a gas mixture requires approximately 12 s.

The filling and purging of the measuring cell are carried out as shown in Figure 4 using gas samples with overpressure relative to the atmosphere. If the gas samples do not have an overpressure, they must be prepared according to Figure 5. In this case, a lecture bottle is evacuated. The pressure in the system is less than 0.5 mbar absolute pressure when evacuated. The valve of the gas collection tube is subsequently opened and a constant pressure lower than the ambient pressure is established in the system. To generate the necessary overpressure relative to the atmosphere, the lecture bottle is then filled with nitrogen up to 4 bar above atmospheric pressure. This procedure allows a sample preparation adequate for the measurement cell. The concentration ratios of the single hydrocarbons, except for nitrogen, remain unchanged.

For GC analysis, the samples are injected into the GC by means of a dosing loop which, in conjunction with a valve circuit, dispenses the analyte onto the packed column. After 12 min retention time the measuring results of the TCD and the FID are available. The evaluation of the chromatograms is based on calibration curves, which were measured using the following calibration gases:

- Methane: 2.5%, 50%, 100%
- Ethane: 0.85%, 1%, 100%
- Propane: 0.85%, 100%
- Nitrogen: 100%

The residual gases are in all cases nitrogen.

3 Results

Table 1 lists all gas samples that were investigated. The natural gas samples of the supplier Hamburger Energiewerke GmbH have been investigated at three different times. Due to the ambient pressure of the storage gas sample, it had to be prepared and diluted as described in Section 2.3 using the setup shown in Figure 5. PAS did not detect any propane in this sample and the GC result was "less than 1‰".

Figures 7A, B show the true and the predicted shares for methane and ethane exemplarily. The absolute root mean square errors (RMSE) for the methane, ethane and propane concentrations in Figure 7A are 1.34%, 0.19% and 0.13%, respectively. The absolute RMSE for methane and ethane concentrations in Figure 7B are 0.29% and 0.03%, respectively.

The number of training data sets significantly influences the absolute RMSE. Figure 8 illustrates this relationship.

4 Discussion

Figure 6 shows an exemplary photoacoustic spectrum. It does not perfectly correspond to the derivative of the absorption spectrum, due to the nonlinear spectral behavior of the injection-current modulation and the missing normalization regarding the laser output power.

As shown in Tab. 1, the PAS results are in good agreement with the GC results. If we consider that the GC exhibits a relative error of up to 2%, the agreement can be described as excellent.

As displayed in Figure 8, an increase of the number of training data sets leads to a significantly decreasing absolute RMSE. Notwithstanding only a relatively low number of 20 training data sets were used for this investigation, accurate results could be achieved. A further increase of the number of training data sets would further decrease the error.

The natural gas analysis on 28 June 2023 delivered a methane concentration of 85.03% (PAS) and 85.10% (GC), respectively (see Tab. 1). Both values do not agree with the 91.95% officially published by Gasnetz Hamburg GmbH (Hamburg, Germany) for this month (Gasnetz Hamburg GmbH, 2023). The true value is almost 7% smaller than the value used for invoicing.

In conclusion it can be stated that, photoacoustic spectroscopy in combination with PLSR is a suitable method for analyzing natural gas samples as well as storage gas samples in a wide dynamic range. Due to the short analysis time of approximately 12 s and the absence of any operating gases, the presented PAS-based sensor could be further developed into an alternative to GC that is attractive in terms of price and performance.

Data availability statement

The original contributions presented in the study are included in the article/Supplementary material, further inquiries can be directed to the corresponding author.

Author contributions

M-SB: Writing–original draft. MW: Writing–review and editing.

Funding

Conflict of interest

The authors declare that the research was conducted in the absence of any commercial or financial relationships that could be construed as a potential conflict of interest.

Publisher's note

References

Brown, A. S., Milton, M. J. T., Cowper, C. J., Squire, G. D., Bremser, W., and Branch, R. W. (2004). Analysis of natural gas by gas chromatography. *J. Chromatogr. A* 1040 (2), 215–225. doi:10.1016/j.chroma.2004.04.007

Compur Monitors (2021). Infrared gas detectorStatox 501 LC IR und MC IR for combustible gases. Available at: https://www.compur.com/en/stationary-gas-detectors/combustible-gas-detector-statox-501-lc-and-mc-ir/ (Accessed October 24, 2023).

Dąbrowski, K. M., Kuczyński, S., Barbacki, J., Włodek, T., Smulski, R., and Nagy, S. (2019). Downhole measurements and determination of natural gas composition using Raman spectroscopy. *J. Nat. Gas Sci. Eng.* 65, 25–31. doi:10.1016/j.jngse.2019.02.003

Decourt, B., Debarre, R., and Alias, S. (2014) Introduction to natural gas. Available at: https://www.energy-transition-institute.com/documents/17779499/17781903/Introduction+to+Natural+Gas_FactBook.pdf/cb59da84-42b6-936b-83dc-7f04688654e4?t=1561052377799 (Accessed 11 August 2023).

Demoulin, O., Le Clef, B., Navez, M., and Ruiz, P. (2008). Combustion of methane, ethane and propane and of mixtures of methane with ethane or propane on Pd/γ-Al2O3 catalysts. *Appl. Catal. A General* 344 (1-2), 1–9. doi:10.1016/j.apcata.2008.03.026

Duchowny, A., Mohnke, O., Thern, H., Dupuy, P. M., Widerøe, H. C., Faanes, A., et al. (2022). Composition analysis of natural gas by combined benchtop NMR spectroscopy and mechanistical multivariate regression. *Energy Rep.* 8, 3661–3670. doi:10.1016/j.egyr.2022.02.289

Engelberg, S. (2008). *Digital signal processing: an experimental approach.* London: Springer.

Gasnetz Hamburg GmbH (2023). Hamburg gas analysis 06/2023. Available at: https://filehub.admiralcloud.com/v5/deliverFile/f319f405-f8bf-411d-aa1f-93de20f26b9d?download=true (Accessed October 24, 2023).

GEISA (2022). geisa. Available at: https://geisa.aeris-data.fr/(Accessed August 16, 2023).

Gordon, I. E., Rothman, L. S., Hargreaves, R. J., Hashemi, R., Karlovets, E. V., Skinner, F. M., et al. (2022). The HITRAN2020 molecular spectroscopic database. *J. Quantitative Spectrosc. Radiat. Transf.* 277, 107949. doi:10.1016/j.jqsrt.2021.107949

Haghi, R. K., Yang, J., and Tohidi, B. (2017). Fourier transform near-infrared (FTNIR) spectroscopy and partial least-squares (PLS) algorithm for monitoring compositional changes in hydrocarbon gases under *in situ* pressure. *Energy and Fuels* 31 (9), 10245–10259. doi:10.1021/acs.energyfuels.7b01677

Hammer, G., Lübcke, T., Kettner, R., Pillarella, M. R., Recknagel, H., Commichau, A., et al. (2003). Natural gas, in *Ullmann's encyclopedia of industrial chemistry*. Editors M. Bohnet and F. Ullmann 6th edn (Weinheim: Wiley VCH).

Iwaszenko, S., Kalisz, P., Slota, M., and Rudzki, A. (2021). Detection of natural gas leakages using a laser-based methane sensor and UAV. *Remote Sens.* 13 (3), 510. doi:10.3390/rs13030510

Kiefer, J., Seeger, T., Steuer, S., Schorsch, S., Weikl, M. C., and Leipertz, A. (2008). Design and characterization of a Raman-scattering-based sensor system for temporally resolved gas analysis and its application in a gas turbine power plant. *Meas. Sci. Technol.* 19 (8), 085408. doi:10.1088/0957-0233/19/8/085408

Leicher, J., Giese, A., Görner, K., Werschy, M., Krause, H., and Dörr, H. (2017). Natural gas quality fluctuations – surveys and statistics on the situation in Germany. *Energy Procedia* 120, 165–172. doi:10.1016/j.egypro.2017.07.161

Li, X., Liang, J., Lin, S., Zimin, Y., Zhang, Y., and Ueda, T. (2012). NIR spectrum analysis of natural gas based on hollow-core photonic bandgap fiber. *IEEE Sensors J.* 12 (7), 2362–2367. doi:10.1109/jsen.2012.2188099

Luo, P., Harrist, J., Menduni, G., Mesdour, R., StMichel, N., and Sampaolo, A. (2022). Simultaneous detection of methane, ethane, and propane by QEPAS sensors for on-site hydrocarbon characterization and production monitoring. *ACS Omega* 7 (4), 3395–3406. doi:10.1021/acsomega.1c05645

Menduni, G., Zifarelli, A., Sampaolo, A., Patimisco, P., Giglio, M., Amoroso, N., et al. (2022). High-concentration methane and ethane QEPAS detection employing partial least squares regression to filter out energy relaxation dependence on gas matrix composition. *Photoacoustics* 26, 100349. doi:10.1016/j.pacs.2022.100349

Mueller-Elektronik, A. G. (2023) Gas sensor methane (IR). Available at: https://www.mueller-elektronik.ch/en/gas-warning-systems/gas-sensors/me-1250/flammable-gases/methane/methane-ir/(Accessed 24 October 2023).

Nodov, E. (1978). Optimization of resonant cell design for optoacoustic gas spectroscopy (H-type). *Appl. Opt.* 17 (7), 1110–1119. doi:10.1364/ao.17.001110

Palzer, S. (2020). Photoacoustic-based gas sensing: a review. *Sensors (Basel, Switz.* 20, 2745–2749. doi:10.3390/s20092745

Pandey, S., van Nistelrooij, M., Maasakkers, J. D., Sutar, P., Houweling, S., Varon, D. J., et al. (2023). Daily detection and quantification of methane leaks using Sentinel-3: a tiered satellite observation approach with Sentinel-2 and Sentinel-5p. *Remote Sens. Environ.* 296, 113716. doi:10.1016/j.rse.2023.113716

Park, C., Oh, S., Kim, C., Choi, Y., and Ha, Y. (2021). Effect of natural gas composition and gas interchangeability on performance and emission characteristics in an air–fuel controlled natural gas engine. *Fuel* 287, 119501. doi:10.1016/j.fuel.2020.119501

Paulus, N., and Lemort, V. (2023). Establishing the energy content of natural gas residential consumption: example with Belgian field-test applications. *IOP Conf. Ser. Earth Environ. Sci.* 1185 (1), 012013. doi:10.1088/1755-1315/1185/1/012013

Petrov, D. V., Matrosov, I. I., Zaripov, A. R., and Tanichev, A. S. (2022). Raman natural gas analyzer: effects of composition on measurement precision. *Sensors* 22 (9), 3492. doi:10.3390/s22093492

C. Poole (Editor) (2021). *Gas chromatography*. Second Edition (Amsterdam, Elsevier). Available at: https://www.sciencedirect.com/science/book/9780128206751.

Rhoderick, G. C. (2003). Analysis of natural gas: the necessity of multiple standards for calibration. *J. Chromatogr. A* 1017 (1-2), 131–139. doi:10.1016/j.chroma.2003.08.002

Rosipal, R., and Krämer, N. (2006). Overview and recent advances in partial least squares, *Lecture Notes in Computer Science* 3940 34–51. doi:10.1007/11752790_2

Sampaolo, A., Patimisco, P., Giglio, M., Zifarelli, A., Wu, H., Dong, L., et al. (2022). Quartz-enhanced photoacoustic spectroscopy for multi-gas detection: a review. *Anal. Chim. Acta* 1202, 338894. doi:10.1016/j.aca.2021.338894

Sigrist, M. W. (1995). Trace gas monitoring by laser-photoacoustic spectroscopy. *Infrared Phys. Technol.* 36 (1), 415–425. doi:10.1016/1350-4495(94)00093-Z

Wang, Z., Wang, Q., Zhang, H., Borri, S., Galli, I., Sampaolo, A., et al. (2022). Doubly resonant sub-ppt photoacoustic gas detection with eight decades dynamic range. *Photoacoustics* 27, 100387. doi:10.1016/j.pacs.2022.100387

Wei, Z., Li, M., Li, S., Wang, R., and Wang, C. (2021). Development of natural gas chemical kinetic mechanisms and application in engines: a review. *ACS Omega* 6 (37), 23643–23653. doi:10.1021/acsomega.1c03197

Wiersberg, T., and Erzinger, J. (2007). Real-time mud gas monitoring: a technique to obtain information on the composition and distribution of gases at depth while drilling. Sci. Drill. *Spec. Spec.* 1, 71–72. doi:10.5194/sd-specialissue-71-2007

Zifarelli, A., Sampaolo, A., Patimisco, P., Giglio, M., Gonzalez, M., Wu, H., et al. (2023). Methane and ethane detection from natural gas level down to trace concentrations using a compact mid-IR LITES sensor based on univariate calibration. *Photoacoustics* 29, 100448. doi:10.1016/j.pacs.2023.100448

Check for updates

Identification of *Bletilla striata* and related decoction pieces: a data fusion method combining electronic nose, electronic tongue, electronic eye, and high-performance liquid chromatography data

Han Li[1†], Pan-Pan Wang[2†], Zhao-Zhou Lin[3], Yan-Li Wang[2], Xin-Jing Gui[2], Xue-Hua Fan[1], Feng-Yu Dong[1], Pan-Pan Zhang[1], Xue-Lin Li[2,4,5,6]* and Rui-Xin Liu[2,4,5,6,7]*

[1]School of Pharmacy, Henan University of Chinese Medicine, Zhengzhou, China, [2]Department of Pharmacy, The First Affiliated Hospital of Henan University of Chinese Medicine, Zhengzhou, China, [3]Beijing Zhongyan Tongrentang Medicine R&D Co., Ltd., Beijing, China, [4]Henan Province Engineering Research Center for Clinical Application, Evaluation and Transformation of Traditional Chinese Medicine, Zhengzhou, China, [5]Co-construction Collaborative Innovation Center for Chinese Medicine and Respiratory Diseases by Henan and Education Ministry of China, Henan University of Chinese Medicine, Zhengzhou, China, [6]Henan Provincial Key Laboratory for Clinical Pharmacy of Traditional Chinese Medicine, Zhengzhou, China, [7]Engineering Research Center for Pharmaceutics of Chinese Materia Medica and New Drug Development, Ministry of Education, Beijing, China

Introduction: We here describe a new method for distinguishing authentic *Bletilla striata* from similar decoctions (namely, *Gastrodia elata*, *Polygonatum odoratum*, and *Bletilla ochracea schltr*).

Methods: Preliminary identification and analysis of four types of decoction pieces were conducted following the *Chinese Pharmacopoeia* and local standards. Intelligent sensory data were then collected using an electronic nose, an electronic tongue, and an electronic eye, and chromatography data were obtained via high-performance liquid chromatography (HPLC). Partial least squares discriminant analysis (PLS-DA), support vector machines (SVM), and back propagation neural network (BP-NN) models were built using each set of single-source data for authenticity identification (binary classification of *B. striata* vs. other samples) and for species determination (multi-class sample identification). Features were extracted from all datasets using an unsupervised approach [principal component analysis (PCA)] and a supervised approach (PLS-DA). Mid-level data fusion was then used to combine features from the four datasets and the effects of feature extraction methods on model performance were compared.

Results and Discussion: Gas chromatography−ion mobility spectrometry (GC-IMS) showed significant differences in the types and abundances of volatile organic compounds between the four sample types. In authenticity determination, the PLS-DA and SVM models based on fused latent variables (LVs) performed the best, with 100% accuracy in both the calibration and validation sets. In species identification, the PLS-DA model built with fused

principal components (PCs) or fused LVs had the best performance, with 100% accuracy in the calibration set and just one misclassification in the validation set. In the PLS-DA and SVM authenticity identification models, fused LVs performed better than fused PCs. Model analysis was used to identify PCs that strongly contributed to accurate sample classification, and a PC factor loading matrix was used to assess the correlation between PCs and the original variables. This study serves as a reference for future efforts to accurately evaluate the quality of Chinese medicine decoction pieces, promoting medicinal formulation safety.

1 Introduction

Bletillae Rhizoma refers to the dried tuber of the plant *Bletilla striata*. It has a long history of use in medicines due to its pharmacological activities, which include hemostatic, gastric mucosal protective, anti-ulcer, antibacterial, anti-inflammatory, and wound healing functions (Li et al., 2014; Posocco et al., 2015; Zhou et al., 2023). Bletillae Rhizoma is also commonly used as a biomedical or cosmetic raw material (Luo et al., 2010; Ding et al., 2016; Jiang et al., 2017; Zhang et al., 2019b), a pharmaceutical excipient (Feng et al., 1995), and a component of industrial glue (Cui et al., 2017; Liao et al., 2019). Continuous discovery of Bletillae Rhizoma functions has gradually expanded its application scope and the market demand. However, *B. striata* plants are fastidious, and their reproductive rates are low under natural conditions (Jiang et al., 2022). Due to excessive collection by humans, wild *B. striata* resources are decreasing every year (Jin et al., 2017). As a result, *B. striata* is now listed as a second-class protected plant in the List of National Key Protected Wild Plants in China (Batch 2) (Zhang et al., 2019a). In recent years, due to high demand and limited availability of high-quality resources, raw *B. striata* materials and decoctions pieces on the market have become heterogeneous in quality. For example, *B. striata* materials are often mixed with the plants *Bletilla ochracea schltr* (Li et al., 2023), *Gastrodia elata*, or *Polygonatum odoratum*, which have some similar characteristics but differ in medicinal value from *B. striata* (Zhai et al., 2012). Thus, circulation of counterfeit *B. striata* products affects the clinical efficacy of *B. striata* decoction pieces and can compromise drug safety. It is therefore necessary to develop efficient, rapid, sensitive detection techniques to measure decoction piece quality.

At present, the primary methods of identifying *B. striata* include traditional manual identification, microscopic analysis, thin-layer chromatography (TLC), near-infrared spectroscopy, and DNA barcoding technology (Cai et al., 2020; Niu et al., 2020). These detection methods are based on modern analysis technologies and exhibit high accuracy, strong reliability, and precise detection. However, some such methods require complex pretreatments and can be prohibitively time-consuming and costly.

Artificial intelligence sensory technologies can be used to quantify multiple quality signals, including sensory information obtained from bionic sensory systems, and to perform pattern recognition for sample classification. This approach provides fast, accurate, comprehensive sample data, and has been widely used in detection and analysis of drugs and foods in the past (Lu et al., 2022; Gui et al., 2023). Data fusion technology consists in merging complementary information to obtain more data points; this technology was originally used in the military, but has gradually been applied in various types of quality evaluation of traditional Chinese medicine such as origin identification (Ru et al., 2019; Wang et al., 2021), species identification (Lan et al., 2020; Sun et al., 2020), quality control of production process (Zhang et al., 2022), and evaluation of preparation quality (Wang et al., 2017; Yan and Sun, 2018). Traditional Chinese medicines are complex in composition and the matrix elements utilized are diverse. Data fusion can organically integrate these types of multi-dimensional data. Furthermore, multi-class intelligent sensory data fusion can simulate traditional manual evaluations by combining visual, auditory, taste, and scent-based data, integrating complementary sensory information to improve identification accuracy. Indeed, several studies have clearly demonstrated the advantages of multi-intelligent sensory data fusion (Zhang et al., 2021b; Li et al., 2022; Hou et al., 2023; Wang et al., 2023).

Data fusion approaches include multiple levels: low, mid, and high. Mid-level fusion can avoid the disadvantages of the large data volumes used in low-level fusion algorithms, effectively reducing data dimensionality (Wang et al., 2019) to highlight key information and facilitate rapid modeling. There are many methods used for feature extraction in mid-level data fusion. In the present study, principal components (PCs) and latent variables (LVs) were used as feature variables and extracted with an unsupervised algorithm [principal component analysis (PCA)] and a supervised algorithm [partial least squares discriminant analysis (PLS-DA)]. Most previous studies have extracted PCs through whole-sample joint dimensionality reduction. However, that dimensionality reduction method reveals information about the validation dataset, jeopardizing accurate analysis of model generalizability. An improved dimensionality reduction method has therefore been developed based on the principle of PCA, enabling isolated dimensionality reduction in the calibration dataset and the validation dataset. This method uses a dimensionality reduction framework (standard deviation and variable boundary) that is consistent between the validation and calibration datasets. Some studies have found that features extracted by supervised algorithms are related to classification labels, which improves identification performance (Xue-Mei et al., 2018; Zhang et al., 2021a). We therefore compared classification results obtained from fused PCA and PLS-DA features.

Here, a mid-level data fusion strategy based on feature extraction was used to identify *B. striata* and related decoction pieces. First, four types of decoction pieces were manually identified based on the *Chinese Pharmacopoeia* and local standards. Differences in the volatile substances present in each type of decoction pieces were analyzed
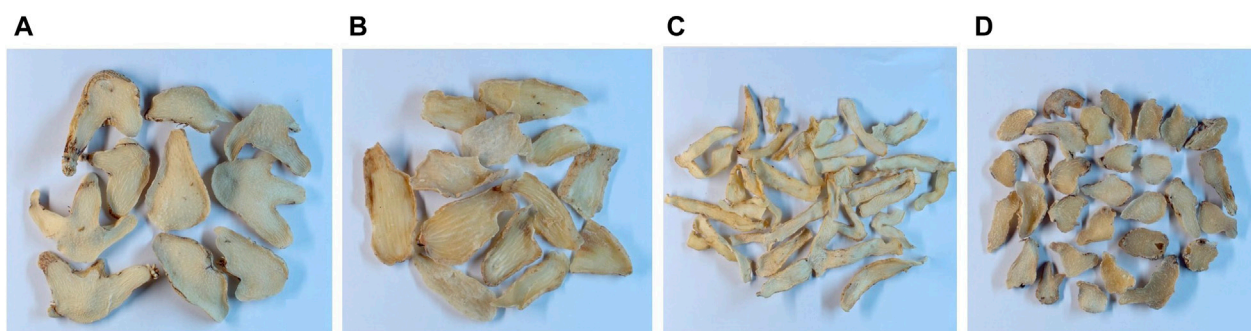
FIGURE 1
Samples of **(A)** *Bletilla striata*, **(B)** *Gastrodia elata*, **(C)** *Polygonatum odoratum*, and **(D)** *Bletilla ochracea schltr*.

with gas chromatography (GC)–ion mobility spectrometry (IMS). Similarities in high-performance liquid chromatography (HPLC) fingerprints were calculated and response values from an electronic nose, eye, and tongue were analyzed. Using single-source data, models were constructed for authenticity and species identification using PLS-DA, support vector machines (SVM), and back propagation (BP)–neural network (NN) models. Features (PCs and LVs) were extracted using PCA and PLS-DA, respectively. Finally, using the feature fusion data, authenticity and species identification were conducted. Classification performance was compared between the two feature extraction methods and the contribution of each PC to sample identification was analyzed. Finally, the factor loading matrix was calculated for the PCs to explore the feature elements that most strongly influenced sample identification. Overall, our study provides a flexible and accurate method for quality evaluation of *B. striata* and other decoction pieces, promoting medicinal formulation safety.

2 Materials and methods

2.1 Samples

Samples of dried tubers were collected from the Chengdu lotus pond Chinese medicine market and from seven hospitals, including Zhengzhou Hospital of Chinese Medicine, the First Affiliated Hospital of Henan University of Chinese Medicine, the Henan Hospital of Chinese Medicine, and the Zhang Zhongjing Pharmacy. The samples comprised 45 batches of *B. striata* (BS), 30 batches of *G. elata* (GE), 30 batches of *P. odoratum* (PO), and 29 batches of *B. ochracea schltr* (BOS). Each batch consisted of 100 g of material (Figure 1).

2.2 Sample identification

2.2.1 Pharmacopoeia- and local standard-based identification

A total of 134 samples were identified with the following methods: appearance analysis; microscopic identification; thin-layer chromatography (TLC) identification; moisture content; and ash content. These detection items were conducted as described in the BS section of the *Chinese Pharmacopoeia* (2020) and the BOS sections of the *Sichuan Provincial Standards for Processing Chinese*

Herbal Pieces (2015), the *Gansu Provincial Standards for Processing Chinese Herbal Pieces* (2009), and the *Gansu Provincial Standards for Chinese Medicinal Materials* (2009).

2.2.2 GC-IMS identification

GC-IMS was performed with a FlavourSpec® flavor analyzer (GAS, Germany) equipped with analytical software including Laboratory Analytical Viewer (LAV), Reporter, Gallery Plot, and GC × IMS Library Search. For each sample, 1.0 g of crude powder was accurately weighed and placed in a 20-mL headspace bottle. The powder was incubated at 80°C for 20 min before injection into the flavor analyzer. Each sample was injected twice in parallel. The headspace injection conditions were as follows: incubation temperature, 80°C; incubation time, 20 min; incubation speed, 500 rpm; injection needle temperature, 85°C; injection volume, 500 μL. For GC, an FS-SE-54-CB-1 chromatographic column of 15 m in length was used; the column temperature was 60°C. The carrier gas flow volume was as follows: 0–2 min, 2 mL·min^{-1}; 2–20 min, 2–100 mL·min^{-1}; and 20–30 min, 100 mL·min^{-1}. For IMS conditions, the carrier and drift gas were N$_2$, the temperature was 45°C, and the drift gas flow rate was 150 mL·min^{-1}. The NIST and IMS databases included with the instrument software were used to identify the volatile organic compounds present in the samples, then the abundances of the volatile organic compounds were analyzed with the Reporter and Gallery Plot functions.

2.3 HPLC

Reference standards of militarine and gastrodin (both with purity ≥98%) were obtained from Shanghai Yuanye Biotechnology Co., Ltd (catalog number K18O9B72711) and the National Institute for Food and Drug Control (batch number 110807—201809), respectively. *B. striata* reference medicinal materials were obtained from the National Institute for Food and Drug Control (batch number 121261—201706). Ethanol (Tianjin Yongda Chemical Reagent Co., Ltd.), methanol (Merck KGaA, 64271 Darmstadt, Germany), acetonitrile (Merck KGaA, 64271 Darmstadt, Germany), and phosphoric acid (Beijing DiKMA Technology Co., Ltd.) was chromatographic pure.

For each of the 134 samples, a sufficient volume was crushed through a No. 4 sieve to produce at least 2.0 g powder, which was accurately weighed and placed in a 50-mL stoppered bottle. 40 mL

dilute ethanol (concentration: 52.9%) was added to each sample. The total mass was weighed, then ultrasonic extraction was performed for 30 min at 200 W and 40 kHz. Samples were filtered and the filtrate was concentrated until the ethanol was not detectable by taste. The residue was dissolved in 3% acetonitrile in water, centrifuged for 10 min, then filtered through a 0.45 μm microporous membrane. The resulting filtrates were used in HPLC fingerprint analysis, which was performed on UltiMate-3000 HPLC instrument [Thermo Fisher Scientific (ChinaCo., Ltd.] equipped with an ultraviolet detector. The chromatographic column was a Shim-pack GIST C18-AQ (250 mm × 4.6 mm, 5 μm). Mobile phase A was 0.1% aqueous phosphoric acid solution and mobile phase B was acetonitrile. Before use, the mobile phases were degassed and filtered through a 0.2 μm microporous filter membrane. The gradient elution program was as follows: 0–5 min, 5%–20% A; 5–10 min, 20%–24% A; 10–20 min, 24%–31.5% A; 20–25 min, 31.5%–35% A; 25–30 min, 35%–42% A; 30–45 min, 42%–60% A. The flow rate was 1.0 mL/min, the column temperature was 30°C, the injection volume was 10 μL, and the detection wavelength was 280 nm.

2.4 Electronic sensory signal acquisition

2.4.1 Electronic nose

Olfactory information was collected using 10 types of metal oxide sensors (W1C, W5S, W3C, W6S, W5C, W1S, W1W, W2S, W2W, and W3S) in a PEN3 portable electronic nose (AIRSENSE, Germany). For each of the 134 samples, there were three replicates of 2 g of powder each. Based on data from our pre-experimental results, the samples were tested after incubating at room temperature in a covered container for 30 min. The sampling time was 80 s, the cleaning time was 80 s, the sensor zeroing time was 5 s, the sample preparation time was 5 s, and the air intake flow rate was 400 mL·min^{-1}. The resulting olfactory data were used to construct the olfactory information matrix $X1$ (134 × 10).

2.4.2 Electronic eye

The IRIS VA400 electronic eye was used to collect visual data from the samples. Samples of an area of about 10 × 10 cm^2 were randomly selected and placed on A4 white paper. Top lighting conditions were selected based on pre-experimental results. A 24-color plate was used for color correction. The electronic eye used a 5-mm aperture and the upper and lower backlights were used simultaneously to eliminate the background. Three separate images were taken of each sample with the position of the slices changed between images. The resulting visual data, obtained with 85 sensors, were used to construct the visual information matrix $X2$ (134 × 85).

2.4.3 Electronic tongue

Taste information was collected from each of the 134 samples using the TS-5000Z Insent electronic tongue (Ensoul Technology LTD. Electronic tongue sensors include Sourness, Bitterness, Astringency, Aftertaste-B, Aftertaste-A, Umami, Richness and Saltiness.). For each sample, 2 g was weighed out and crushed in an electric homogenizer for 15 s. The resulting powder was placed in a 100-mL beaker with an appropriate volume of purified water. After

stirring, samples were incubated at room temperature without perturbation for 5 min. The samples were subsequently filtered, sterilized and poured into a special cup to be tested by the electronic tongue. The electronic tongue sensor was cleaned in a cleaning solution for 90 s, in a reference solution for 120 s, and in a different reference solution for 120 s. The sensor started to collect sample information after the response value stabilized at 0 for 30 s. The acquisition time of the beforetaste value of each sample was 30 s, the sensors were then cleaned for 3 s in the two reference solutions. Finally, the sensors were inserted into the new reference solution to collect data for 30 s and the aftertaste value was exported. This cycle was repeated four times; data from the first cycle were removed and the average value was calculated from the last three cycles. The resulting taste data, obtained from eight sensors, were used to construct the taste information matrix $X3$ (134 × 8).

2.5 Construction of authenticity and species identification models based on single-source data

To eliminate randomness and ensure model stability, the Kennard-Stone algorithm was used to divide samples of the four species into a calibration set (100 samples) and a validation set (34 samples). The linear classifier PLS-DA, the nonlinear classifier SVM, and BP-NN were used to establish authenticity identification (binary classification) models based on data from the electronic nose, electronic tongue, electronic eye, and HPLC. Model performance was evaluated in terms of accuracy in the calibration set with cross-validation and accuracy in the validation set. Because the program used for SVM could not be used for multi-classification problems, only the PLS-DA and BP-NN algorithms were used to establish multi-class species identification models. The performances of these models were evaluated as described for the authenticity identification model.

PLS-DA is a discriminant method based on partial least squares regression that can be used for dimensionality reduction, classification, and prediction. The algorithm allows determination of whether a given sample belongs to a specific predefined category (Ballabio and Consonni, 2013; Borraz-Martínez et al., 2019). It can transform input data into a set of linear latent variables for classification problems. SVM and BP-NN are nonlinear classifiers based on a kernel function and a large number of neurons, respectively. Both algorithms are widely used in the field of machine learning. SVM is used to identify an optimal decision boundary (a classification hyperplane) and uses a kernel function to map input samples to high-dimensional space for linear separable or non-separable problems (Chauhan et al., 2019). Because the radial basis kernel function of SVM has the advantages of local feature expression and strong learning abilities (Gao et al., 2008), we selected this kernel function. BP-NN is based on abstraction and simulation of the basic characteristics of the human brain or a natural neural network. It includes input, output, and hidden layers. The addition of a momentum term can accelerate the algorithm's learning speed and avoid the oscillation caused by a high convergence speed (Zheng, 2005). The number of hidden-layer neurons is determined by the specific problem to which it is applied. A greater number of hidden-layer neurons is associated with higher accuracy but reduced generalizability. Furthermore, a
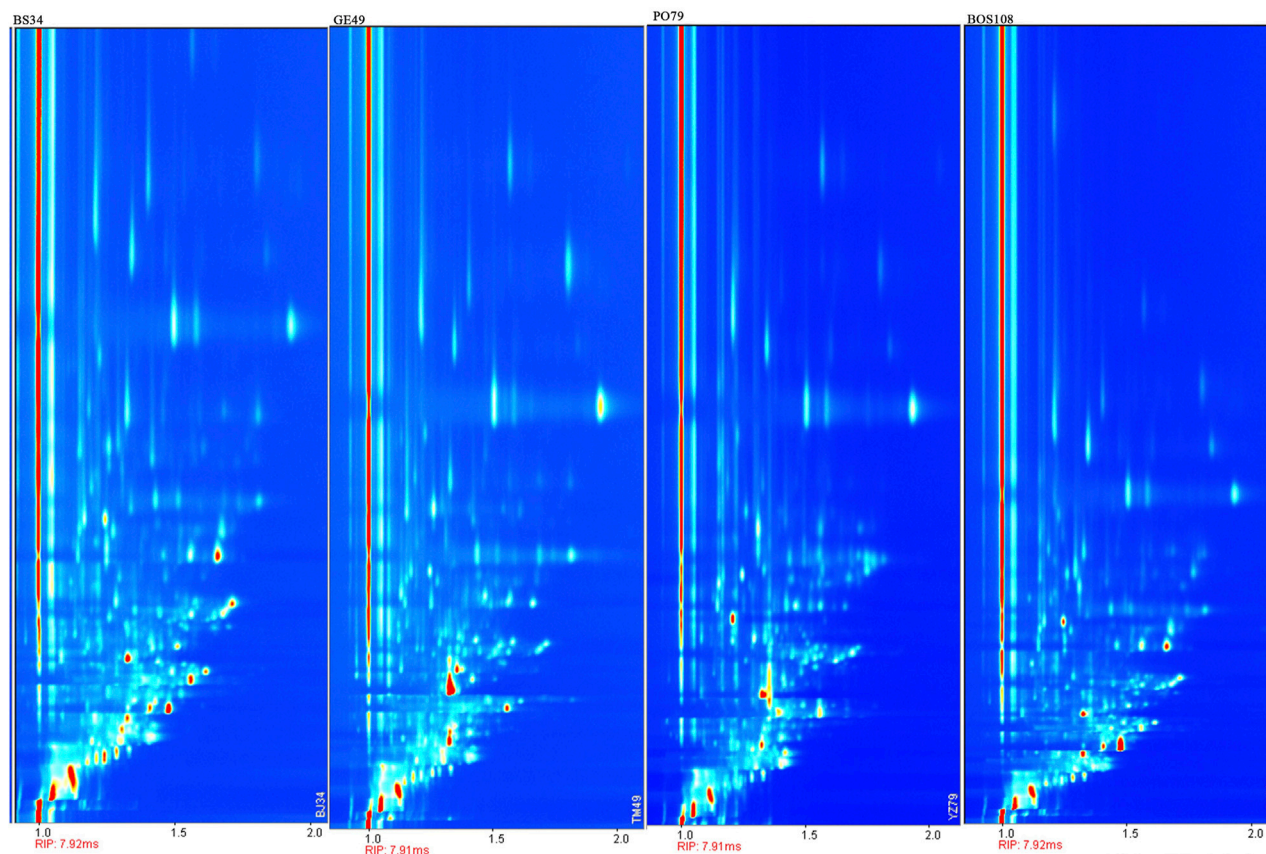
FIGURE 2
Vertical view plot of four types of decoction pieces [BS, GE, PO, and BOS] based on GC-IMS.

smaller number of neurons can reduce the network cost. These parameters usually require a series of repeated tests for optimization.

2.6 Feature extraction

Feature extraction was carried out with both PCA and PLS-DA. Improved PCA-based feature extraction was performed in a home-made program designed in MATLAB. First, the PC scores of the calibration samples from each data source were extracted. The validation set was then added to the calibration set for simultaneous standardization of the entire dataset. Standardization was performed with the z-score method (Formula 1):

$$X'_{ij} = \frac{X_{ij} - \overline{X_j}}{S_j}, \ j = 1, 2, 3, \ldots, m \qquad (1)$$

X_{ij} refers to the number in the ith row and the jth column. X'_{ij} refers to the number after standardization in the ith row and the jth column; $\overline{X_j}$ refers to the average value of the number in jth column; S_j refers to the standard deviation of the number in jth column.

The standardized data in the validation set were then inserted into the linear expression of each PC (Formula 2) to obtain the PC scores of the validation set:

$$Z_i = a_{i1}X'_1 + a_{i2}X'_2 + \ldots + a_{im}X'_m \quad i = 1, 2, \ldots, m \qquad (2)$$

Z_i refers to the scores of ith principal component; a_{i1}, a_{i2}, ..., a_{im} refers to eigenvector; X'_1, X'_2, ..., X'_m refers to the number value of the sample in the first, second, ..., mth original variables.

For feature extraction based on PLS-DA, the latent variable scores of the calibration set and the validation set were obtained in the process of algorithm operation.

PCA can be used to transform multiple variables into a small number of comprehensive variables, represented by PCs, through dimensionality reduction. The PCs are linear combinations of the original variables that collectively reflect most of the information contained in the original variables. LVs can likewise explain most of the variance of the original data. Here, the PCs selection principle was explanation of more than 90% of the variance in the original data; the selection principle of LVs was determined with leave-one-out cross-validation. The PC and LV scores were used as the input variables for subsequent data analysis.

2.7 Construction of authenticity and species identification models with fused data

Using the sample identification results and the features extracted as described in Section 2.6, PLS-DA, SVM, and BP-NN authenticity
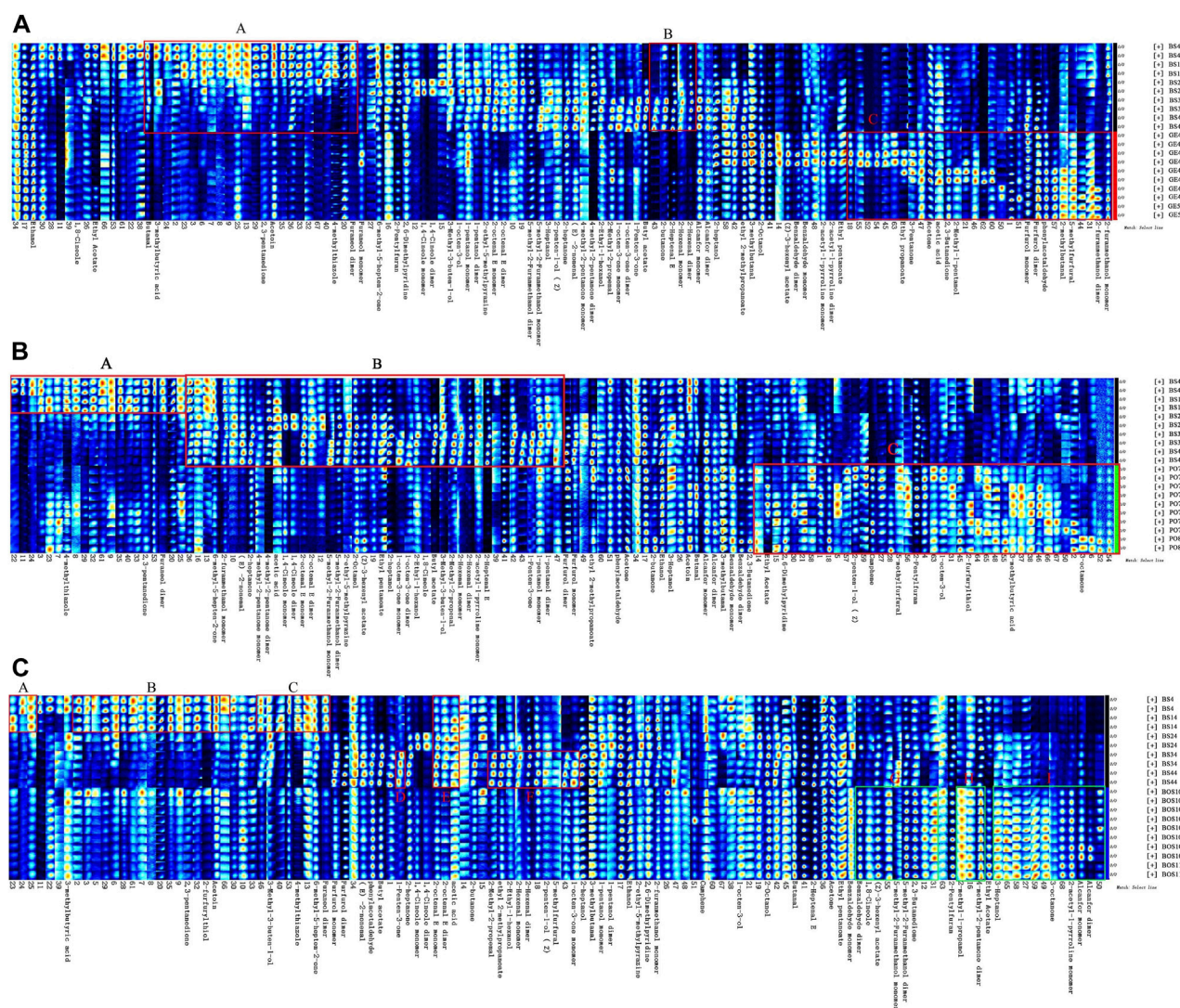
FIGURE 3
GC-IMS fingerprints of BS compared to **(A)** GE, **(B)** PO, and **(C)** BOS.

identification fusion models and PLS-DA and BP-NN species identification fusion models were constructed. Model performance was evaluated as described in Section 2.5.

2.8 Model analysis

Wilk's lambda value represents the ratio of intra-group variation to inter-group variation in a calibration dataset (Yue et al., 2019). A smaller value corresponds to a stronger discriminant ability in a given variable. The factor loading represents the correlation coefficient between PCs and original variables, reflecting the closeness and direction of the relationship between the types of data. Thus, the correlation between each PC and each original variable can be understood through the factor loading matrix. Here, using Wilk's lambda value, we identified PCs with large contributions to classification in the fusion models. The factor loading of each feature was calculated as follows to analyze the key features affecting sample identification (Formula 3):

$$q_{ij} = \sqrt{\lambda_i} a_{ij} \qquad (3)$$

where λ_i is the eigenvalue of the ith PC and a_{ij} is the coefficient of the original variable X_j.

3 Results and discussion

3.1 Sample identification

3.1.1 Identification based on the pharmacopoeia and local standards

We first analyzed 134 dried tuber samples as set forth in the Pharmacopoeia and with microscopic, TLC, moisture content, and ash content analysis. Based on these analyses combined, 45 batches of *B. striata* decoction pieces met the standards for classification as BS on the *Chinese Pharmacopoeia* (Part I) and did not meet the standards for classification as BOS based on the *Sichuan Provincial Standards for Processing Chinese Herbal Pieces*, the *Gansu Provincial Standards for Processing Chinese Herbal Pieces*, or the *Gansu Provincial Standards*

FIGURE 4
HPLC fingerprints of 134 batches of decoction pieces. Data are shown for **(A)** BA, **(B)** GE, **(C)** PO, and **(D)** BOS.
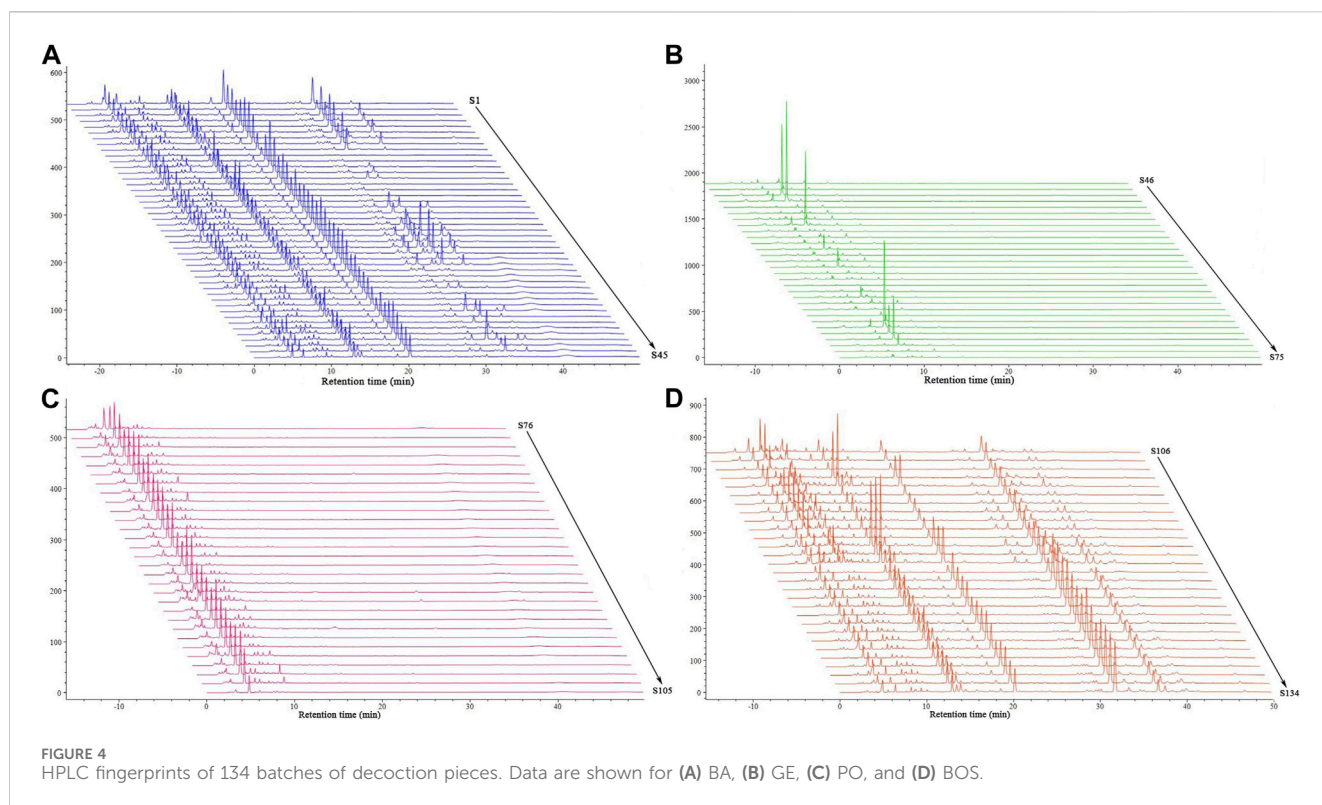
for Chinese Medicinal Materials. Similarly, 30 samples each of GE and PO decoction pieces did not meet the standards for classification as BS; they were positively identified as authentic GE and PO, respectively. However, many of the 29 batches of BOS not only met the standards for classification as BOS, but also met the standards for classification as BS. Specifically, the traits of BOS samples 106–120 were essentially identical to those of BS. However, samples 121–134 were highly wooded and had a significantly different texture than BS, thus meeting local standards for classification as BOS. There was extremely high similarity in TLC results between the 29 BOS batches and the control medicinal samples of BS, making it difficult to distinguish between the two sample types. Microscopic characteristics were consistent between the 29 BOS batches and the BS samples, displaying the characteristic "epidermal cells with wavy curved walls, calcium oxalate needle crystal bundles, catheters, fiber bundles and gelatinized starch granules" described in Pharmacopoeia. However, the microscopic background was more turbid in BOS than in BS samples. Overall, the moisture contents of 134 samples ranged from 6.10% to 12.75% and the ash contents ranged from 1.22% to 4.39%, consistent with expectations based on the Pharmacopoeia.

3.1.2 GC-IMS identification

We next analyzed the levels of volatile organic compounds in each sample with GC-IMS. Sample 34 (BS), sample 49 (GE), sample 79 (PO), and sample 108 (BOS) were randomly selected for comparison of the two-dimension vertical view plot of BS with the vertical view plots of the other sample types (Figure 2). In Figure 2, the ordinate represents the GC retention time and the abscissa represents the normalized ion draft time. The red vertical

line at abscissa = 1.0 is the normalized reactive ion peak (RIP). Each point on the right side of the RIP peak represents one type of volatile organic compound. Concentrations are indicated with color depth. The results clearly showed significant differences in both the types and abundances of volatile organic compounds between BS and other three types of decoction pieces.

We first compared the fingerprints of BS and GE (Figure 3A). In regions A and B, levels of volatile compounds were higher in BS. Specifically, BS had an increased abundance of butyraldehyde, 3-methylbutyric acid, 2,3-pentanedione, 4-methylthiazole, 2-butanone, 2-heptenal, 2-hexenal (monomer), 2-hexenal (polymer), and several unknown compounds compared to GE. Region C shows volatile compounds that were more abundant in GE than in BS, namely, ethyl propionate, 3-pentanone, acetone, acetic acid, 2,3-butanedione, 2-methyl-1-pentanol, furfural (monomer and dimer), phenylacetaldehyde, 2-methylbutanal, 5-methylfurfural, and 2-furanmethanol (monomer and dimer).

Comparison of fingerprints between BS and PO (Figure 3B) showed numerous volatile compounds that were more abundant in BS (regions A and B): 2,3-pentanedione, 4-hydroxy-2,5-dimethyl-3(2H) furanone (dimer), methylheptenone, furfuryl alcohol (monomer), trans-2-nonenal, 2-heptanone, 4-methyl-2-pentanone (dimer), and some unknown compounds. However, compounds including 1-octen-3-ol, furfuryl mercaptan, cis-2-penten-1-ol, isovaleric acid, 3-octanone, 5-methylfuranaldehyde, camphene, and ethyl acetate were more abundant in PO (region C). Finally, the fingerprints of BS and BOS were compared (Figure 3C). Overall, the volatile organic compounds were similar in both identity and abundance between the two types of decoction pieces, although there were subtle differences. Regions A–F show compounds
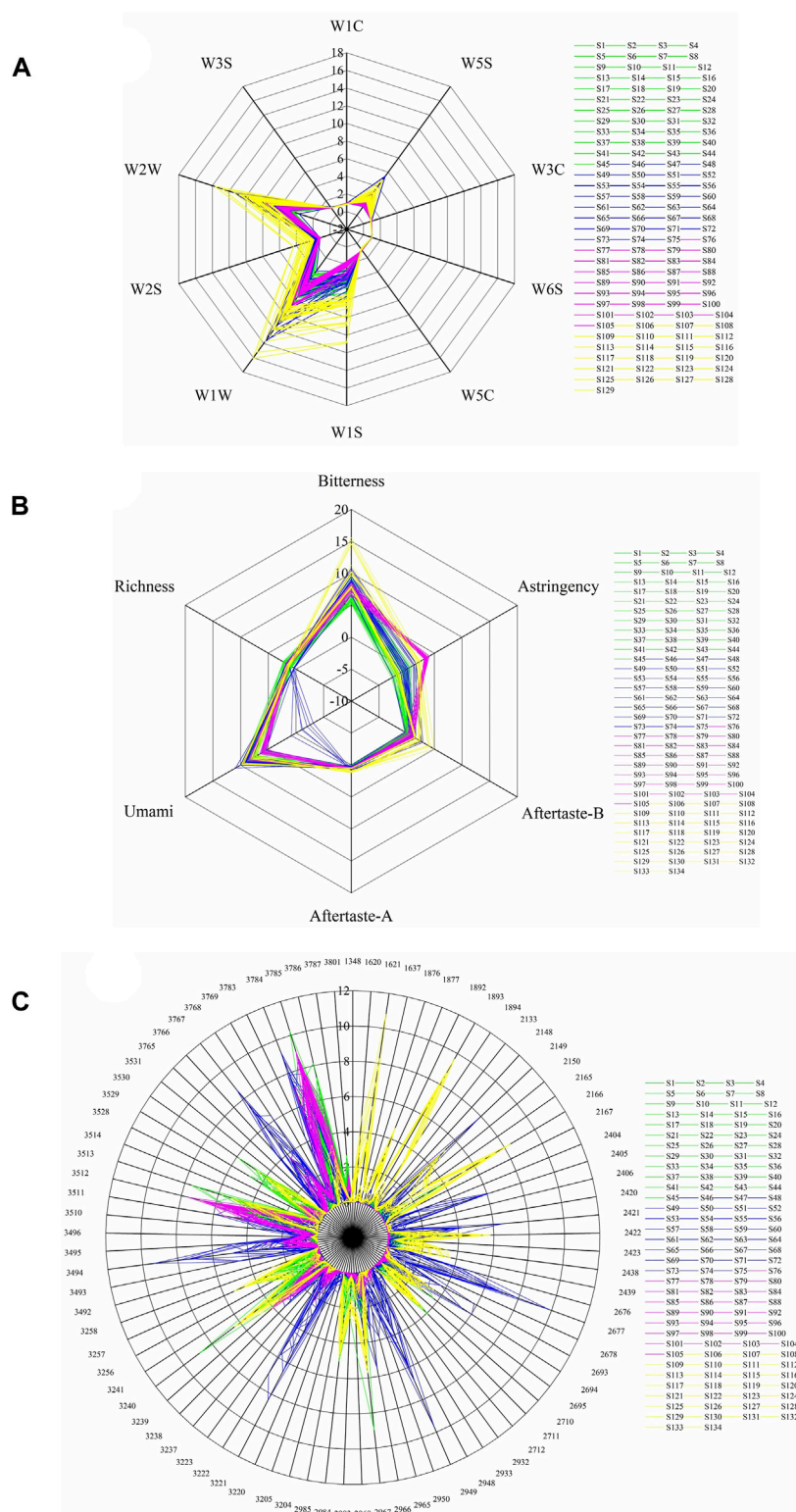
FIGURE 5
Response values of the electronic **(A)** nose, **(B)** tongue, and **(C)** eye devices for samples of BS (S1–S45), GE (S46–S75), PO (S76–S105), and BOS (S106–S134).

(including 2,3-pentanedione, furfuryl mercaptan, 3-hydroxy-2-butanone, 3-methyl-3-buten-1-ol, 4-methylthiazole, methylheptenone, 4-hydroxy-2,5-dimethyl-3 (2H) furanone [dimer],

and 1-penten-3-one) that were more abundant in BS than in BOS. Regions G–I show compounds that were significantly more abundant in BOS than in BS, including benzaldehyde (dimer), eucalyptol, ethenyl
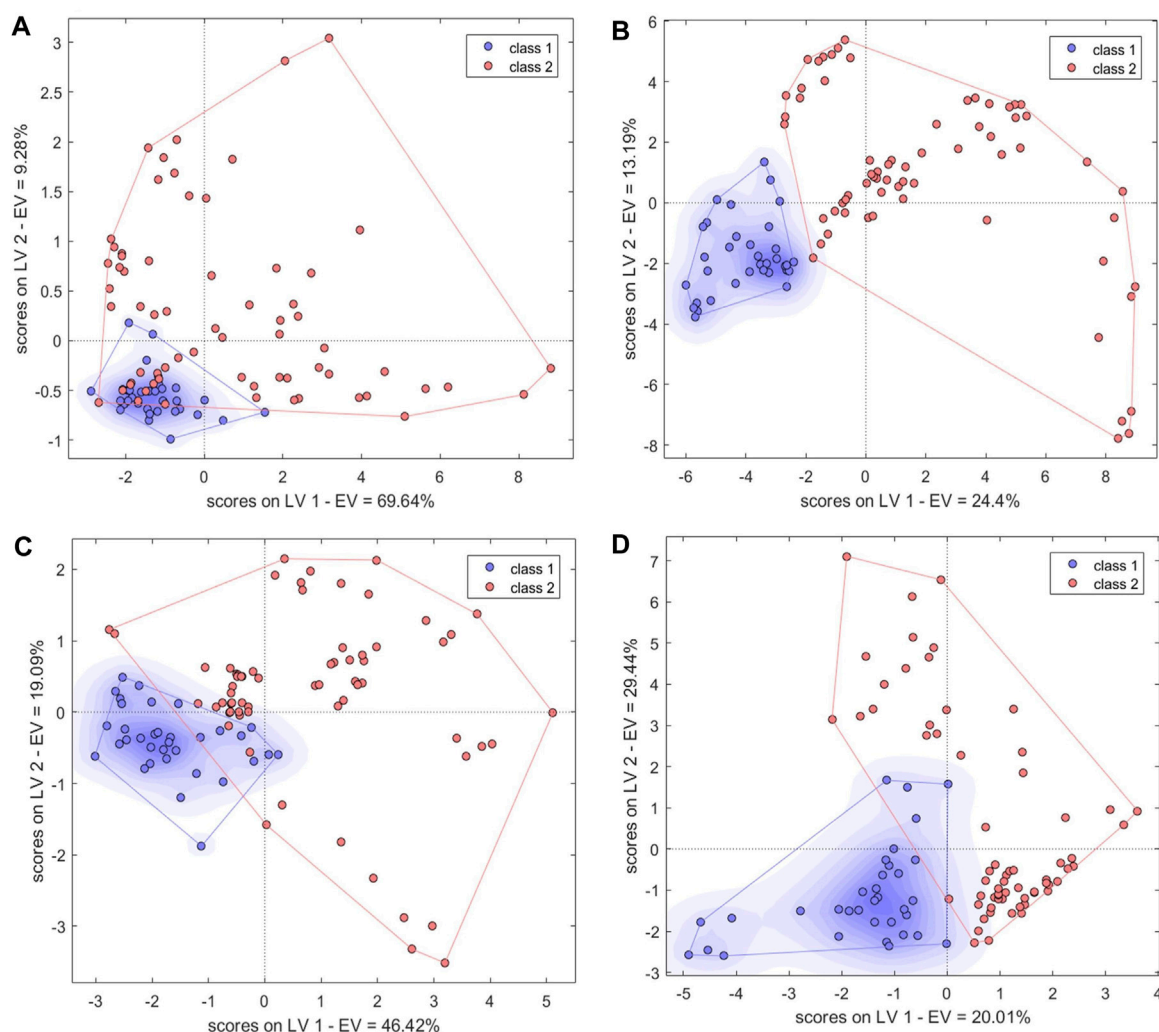
FIGURE 6
Score plots of single-source PLS-DA authenticity and counterfeit identification model based on **(A)** electronic nose, **(B)** electronic tongue, **(C)** electronic eye and **(D)** high-performance liquid chromatography. Class1, BS; class2, counterfeit species (GE, PO, and BOS).

acetate, 5-methyl-2-furanmethanol (monomer and dimer), 2,3-butanedione, isobutanol, and 4-methyl-2-pentanone (monomer). Thus, the integrated results of the Pharmacopoeia, local standards, and GC-IMS positively identified samples 1–45 as BS, samples 46–75 as GE, samples 76–105 as PO, and samples 106–134 as BOS, consistent with the known identities of the samples.

3.2 HPLC fingerprinting

Each sample was next analyzed with HPLC fingerprinting (Figure 4). Based on reference samples, peak 3 in the control fingerprint (Supplementary Figure S1) of BS was gastrodin and peak 14 was militarine. There were significant differences in the fingerprints of BS, GE, and PO samples. The 45 batches of BS were used as representative samples to generate a control fingerprint. Using the control fingerprint as a reference, the similarities of the 134 batches of decoction pieces were

calculated with the common peak weighting method; militarine and other components were weighted as 2.5 and 1, respectively. The fingerprints of the 45 BS, 30 GE, 30 PO, and 29 BOS batches showed similarities of 0.88–0.98, 0.2–0.34, 0.1–0.2, and 0.7–0.88, respectively. Thus, the fingerprint similarities differed considerably between the four types of decoction pieces. Precision: S14 solution was continually injected 6 times according to the above chromatographic conditions. The RSD of relative retention time and relative peak area of 8 common peaks measured with militarine as the reference peak was both ≤0.1%. Repeatability: 6 batches of identical S14 solution were injected according to the above chromatographic conditions. The RSD of relative retention time and relative peak area of 8 common peaks measured by militarine as reference peak were ≤0.1% and ≤2.3%, respectively. Stability: S2 solution was injected at 0, 2, 4, 8, 12 and 24 h after preparation according to the above chromatographic conditions. The RSD of relative retention time and relative peak area of

TABLE 1 Authenticity identification results and model parameters [*Se* = TP/(TP + FN); *Sp* = TN/(TN + FP); *Ac* = TP/(TP + FP); TP: true positive; FP: false positive; TN: true negative; FN: false negative].

Model	Data matrix	Calibration set					Validation set	
		Misclassified samples	Not-assigned samples	Se	Sp	Ac	Misclassified or not-assigned samples	Ac
PLS-DA	EN	3	0	0.9400	0.9800	0.9700	1	0.9706
	EE	2	0	1.0000	0.9700	0.9800	1	0.9706
	ET	1	0	0.9700	1.0000	0.9900	1	0.9706
	HPLC	2	0	0.9700	0.9800	0.9800	0	1.0000
	Data fusion by PCs	**0**	**0**	**1.0000**	**1.0000**	**1.0000**	**1**	**0.9706**
	Data fusion by LVs	**0**	**0**	**1.0000**	**1.0000**	**1.0000**	**0**	**1.0000**
SVM	EN	8	0	0.9100	0.9200	0.9200	4	0.8824
	EE	1	0	1.0000	0.9800	0.9900	1	0.9706
	ET	10	0	1.0000	0.9800	0.9000	2	0.9412
	HPLC	6	0	0.8500	0.9800	0.9400	0	1.0000
	Data fusion by PCs	**0**	**0**	**1.0000**	**1.0000**	**1.0000**	**1**	**0.9706**
	Data fusion by LVs	**0**	**0**	**1.0000**	**1.0000**	**1.0000**	**0**	**1.0000**
BP-NN	EN	2	0	0.9400	1.0000	0.9800	1	0.9706
	EE	**1**	**0**	**1.0000**	**0.9800**	**0.9900**	**1**	**0.9706**
	ET	1	1	1.0000	0.9800	0.9800	1	0.9706
	HPLC	5	0	0.9100	0.9700	0.9500	0	1.0000
	Data fusion by PCs	**1**	**0**	**1.0000**	**0.9800**	**0.9900**	**1**	**0.9706**
	Data fusion by LVs	**1**	**0**	**1.0000**	**0.9800**	**0.9900**	**1**	**0.9706**

The bold values indicate the optimal model.

8 common peaks measured with militarine as the reference peak was 0.1% and 0.3%, respectively, indicating that the sample solution was stable within 24 h.

3.3 Electronic sense signals

All 134 samples were analyzed with an electronic nose, an electronic tongue, and an electronic eye. Most of the samples had the highest response for the electronic nose sensors W1W, W2W, and W1S, followed by W5S and W2S (Figure 5A). Notably, the response values at sensors W5S and W2S were significantly higher for BOS than for BS samples. Most of the samples had low response values at sensors detecting alkanes and hydrogen gases (e.g., W3S and W6S) and aromatic compounds (e.g., W1C, W5C, and W3C). In the electronic tongue sensor detection, Bitterness, Astringency, Aftertaste-B, and Umami showed the greatest differences between sample types (Figure 5B). The bitterness and astringency response values were relatively low in BS samples but very large in some BOS samples. Other BOS samples showed high similarity to BS samples, indicating extensive heterogeneity among the 29 BOS batches. The results also showed significantly stronger astringency in PO compared to BS samples. Across all samples, the electronic eye

detected the strongest color values at numbers 3784, 3785, 3786, 3767, 3494, 3512, 3513, 2677, 3221, 3222, 2949, 2967, and 3240 (Figure 5C). These corresponded to moderate yellow and light yellowish brown sample colors.

3.4 Authenticity identification models

3.4.1 Models built with electronic nose data

The PLS algorithm was used to convert the electronic nose data into linear LVs. Six LVs were then used to establish a PLS-DA model with good performance. These first six LVs explained 99% of the total variance among the samples. For the first two LVs, there were some similarities between BS and counterfeit samples (Figure 6A). In the calibration set, the BS samples S34 and S44 were misclassified, and S76 (PO) was misclassified as BS (Table 1). In the validation set, S57 (GE) was misclassified as BS. Misclassification of the samples may have been due to differences in volatile components compared to other samples resulting from changes in temperature and humidity during transportation and storage. Overall, the model accuracy was 97% in the calibration set and 97.06% in the validation set. The model sensitivity (*Se*) and specificity (*Sp*) were 0.94 and 0.98, respectively. This indicated that electronic nose data could be used to accurately distinguish between BS and similar decoction pieces.
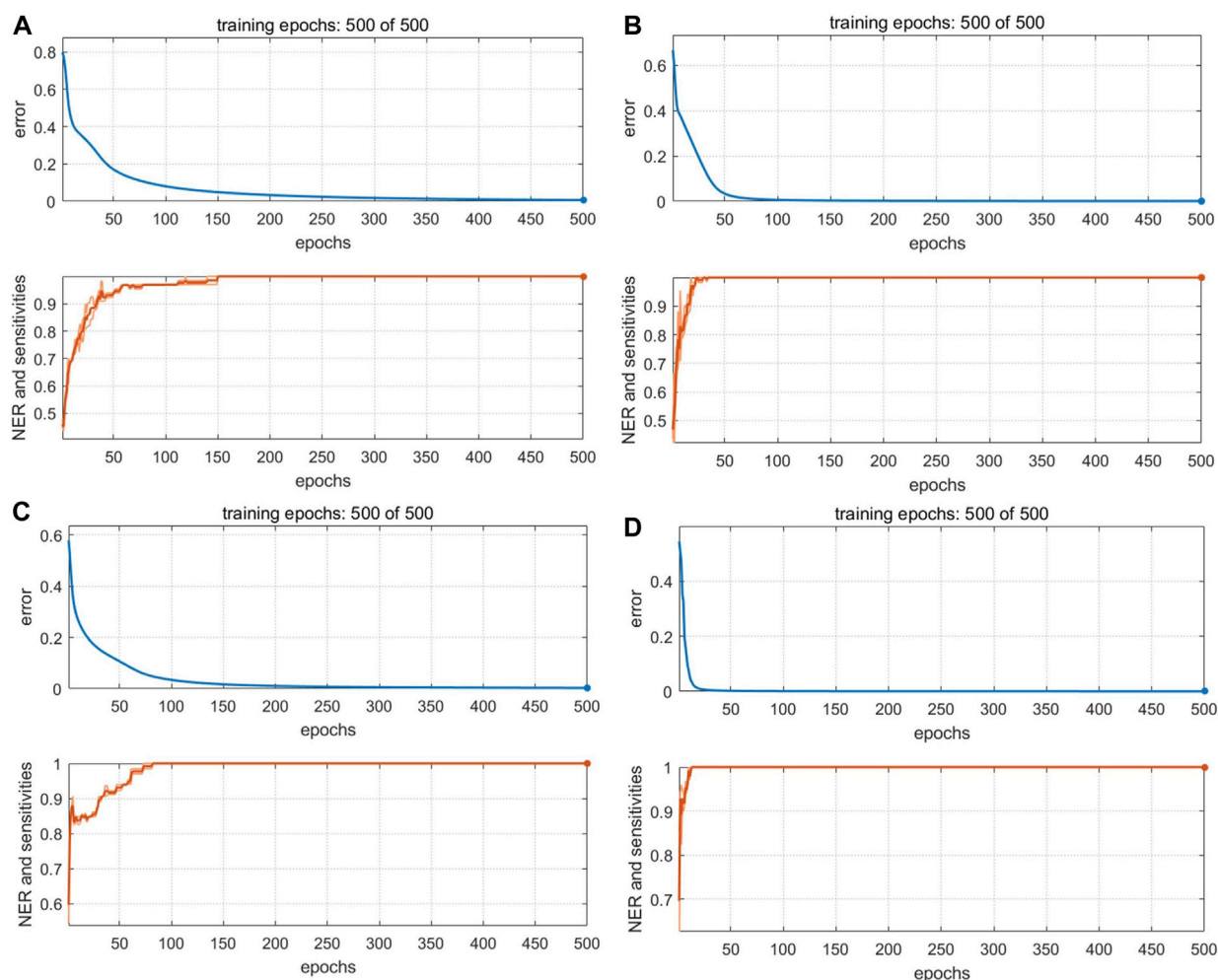
FIGURE 7
Training iterations and error rates of BP-NN authenticity and counterfeit model. Models were built with data from **(A)** an electronic nose, **(B)** an electronic eye, **(C)** an electronic tongue, and **(D)** HPLC.

We next optimized the kernel parameter and cost values, which were initially 0.05 and 0.1, respectively (Supplementary Figure S2). The error rate in cross-validation changed along with the kernel parameters and cost values, and we selected the combination that produced the lowest error rate and highest accuracy (kernel parameter = 1.13, cost value = 10). The model was run again with the optimized parameters. In the calibration set, S28, S34, and S44 (BS) were misclassified, whereas S64 (GE), S83, S86, and S101 (PO), and S121 (BOS) were misclassified as BS; in the validation set, S30, S81, S82, and S128 were misclassified. Thus, the accuracy was 92% and 88.24% in the calibration and validation sets, respectively. The model Se and Sp were 0.91 and 0.92, respectively. Visualization of the SVM classification hyperplane and decision boundaries (Supplementary Figure S3A) indicated that the performance of the model built with electronic nose data required improvement.

The optimized BP-NN model parameters were as follows: two hidden layers; 10 neurons per layer; learning rate = 0.01; momentum term = 0.5; 500 iterations. After 500 iterations of training, the model error rate was 0 (Figure 7A). In the calibration set, the BS samples

S28 and S44 were misclassified; in the validation set, S82 was unassigned. Notably, these three samples were also misclassified or unclassified in the PLS-DA and SVM models, presumably due to differences in sample quality. The accuracy was 98% and 97.06% in the calibration and validation sets, respectively, and the Se and Sp were 0.94 and 1.0, respectively. Thus, the BP-NN model built with electronic nose data could be used to accurately distinguish between BS and related decoction pieces.

3.4.2 Models built with electronic eye data

In leave-one-out cross-validation, the PLS-DA model performed best when using the first three LVs, which together explained 63% of the sample variance. The two types of samples (BS and others) had good aggregation in the first two LVs (Figure 6B). S84, S91, and S5 were misclassified. Analysis of the original samples suggested that they may have been misclassified because they had slightly different surface color characteristics compared with other samples. The accuracy was 98% and 97.06% in the calibration and validation sets, respectively, and the Se and Sp were 1.0 and 0.97, respectively.
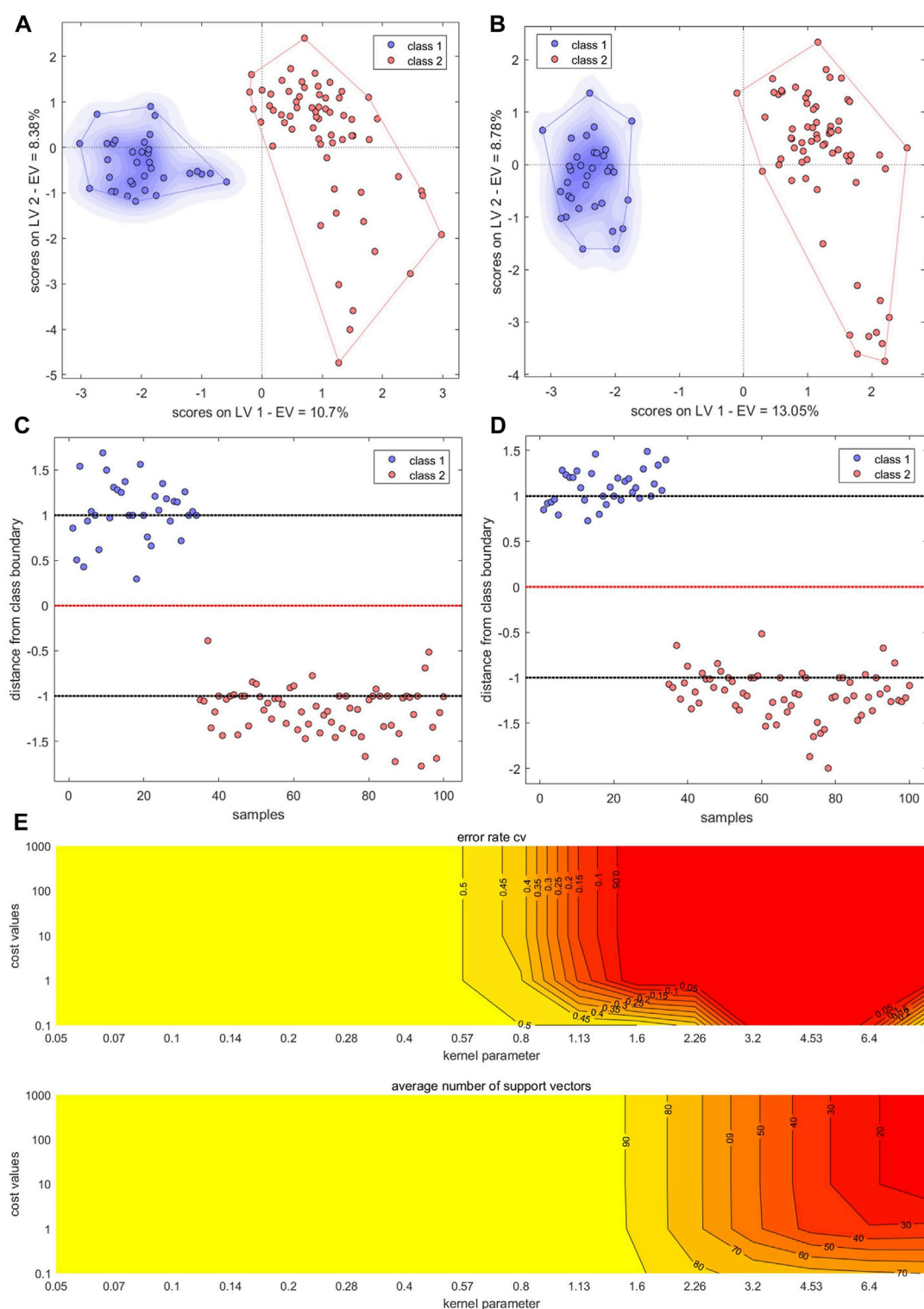
FIGURE 8
Results of models built with fused data. **(A,B)** PLS-DA score plots. **(C,D)** SVM classification hyperplanes and support vectors. **(E)** SVM parameter optimization. Models shown in **(A,C)** were built with fused PCs; models shown in **(B,D,E)** were built with fused LVs.

The SVM model had the lowest error rates when the kernel parameter was 1.6, 2.26, 3.2, or 4.53 and the corresponding cost value was 1, 1, 1, or 0.1, respectively; these parameter combinations produced accuracies of 96%, 99%, 99%, and 96%, respectively.

Larger kernel parameter and cost values were associated with smaller numbers of support vectors (Supplementary Figure S4). The role of a support vector is to determine the optimal classification hyperplane. The number of support vectors is affected by both the
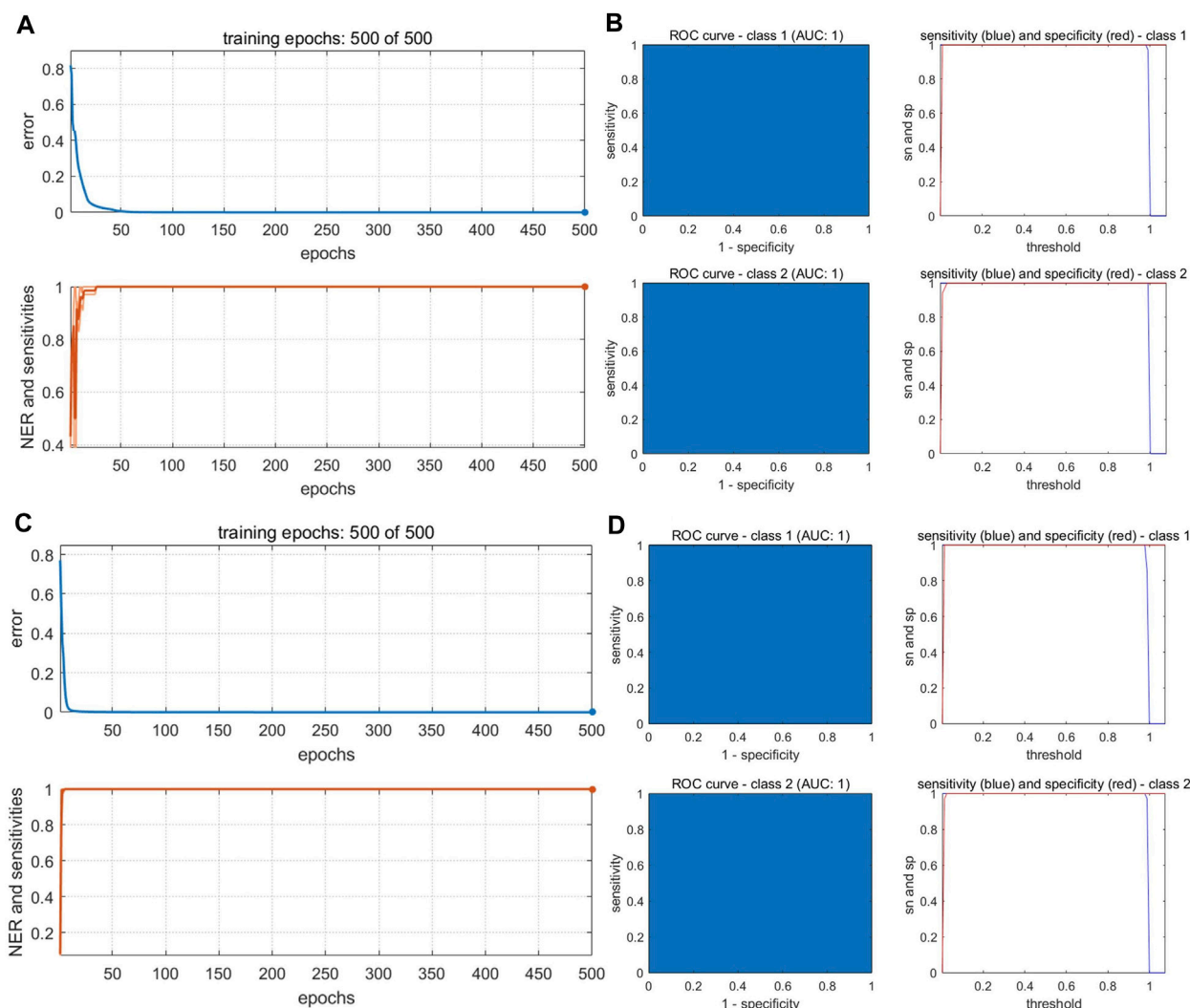
FIGURE 9
Performance of BP-NN authenticity and counterfeit model. **(A)** Training iterations and error rates for a model built with fused PCs. **(B)** Receiver operating characteristic (ROC) curves (left), sensitivity, and specificity (right) for a model built with fused PCs. **(C)** Training iterations and error rates for a model built with fused LVs. **(D)** ROC curves (left), sensitivity, and specificity (right) for a model built with fused LVs.

penalty parameter *c* and the kernel parameter *g* (Yang and Gao, 2020). A larger *c* corresponds to fewer support vectors, higher model accuracy, a smaller occupied network space, and faster prediction speeds. The number of support vectors was smallest (51) when the kernel parameter was 3.2 and the cost value was 1. This model was therefore selected for further analysis. Using these parameters, S91 and S5 were misclassified in the calibration and validation sets, respectively; *Ac* was 99% and 97.06% in the calibration and validation sets, respectively; *Se* and *Sp* were 1.0 and 0.98, respectively.

Because there were 85 color values detected by the electronic eye and the input variables were large, the number of hidden-layer neurons in the BP-NN model needed to be optimized for these data. Too many hidden-layer neurons will weaken model generalizability and increase network operation costs. After optimization, the parameters were as follows: three hidden layers; 10 neurons per layer; learning rate = 0.01; momentum term = 0.5; 500 iterations. When the number of training

iterations was 500, the model error rate was 0 (Figure 7B). However, S5 was still misclassified in the validation set. This sample comprised irregular thick slices with sections of white, gray-white, and brown; thus, the sample characteristics were different from the irregular thin slices and white color of the 44 other BS samples. In the validation set, S116 was misclassified. *Ac* was 99% and 97.06% in the calibration and validation sets, respectively and the model *Se* and *Sp* were 1.0 and 0.98, respectively.

3.4.3 Models built with electronic tongue data

The PLS-DA model performed best when it was built with four LVs that explained 83% of the sample variance (Figure 6C). S3 and S60 were misclassified in the calibration and validation sets, respectively. BS and non-BS samples showed some similarities in the variance of the first two LVs. The *Se* and *Sp* of the model were 0.97 and 1, respectively, and the classification performance was good.
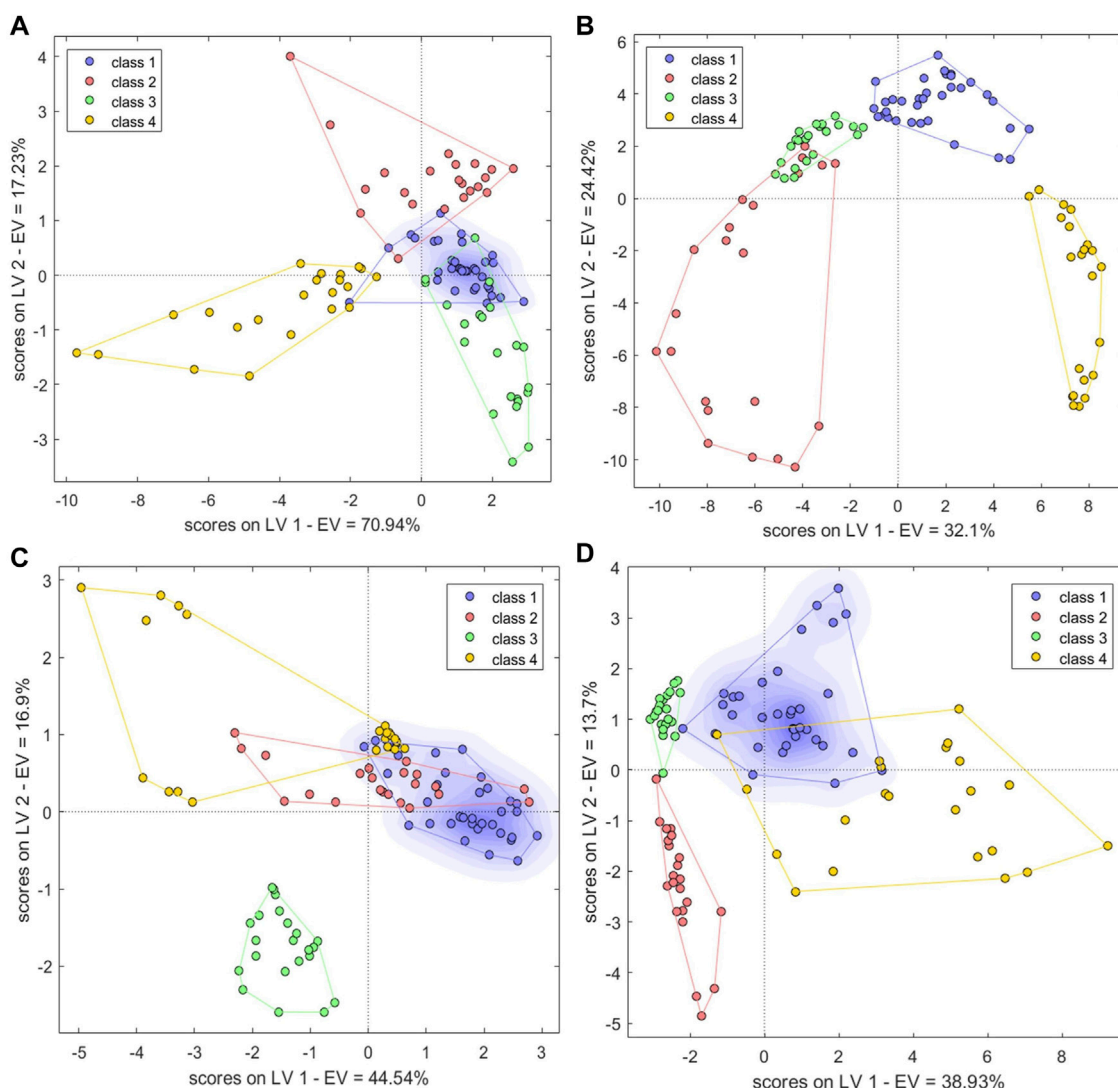
FIGURE 10
Single-source PLS-DA score plots of species identification model based on **(A)** electronic nose, **(B)** electronic tongue, **(C)** electronic eye and **(D)** HPLC. Class1, BS; class2, GE; class3, PO; class4, BOS.

In cross-validation, the SVM model error rate was smallest when the kernel parameter was 0.4, 0.57, 0.8, 1.6, or 3.2, and the corresponding cost value was 1, 1, 1, 10, or 1, respectively. Model accuracy was highest (90% and 94.12% for the calibration and training sets, respectively) at kernel parameter = 0.57 and cost value = 1. Using this model, there were seven and three misclassified BS and GE samples, respectively, in the calibration set. In the validation set, S10 and S67 were misclassified. *Se* and *Sp* were 1.0 and 0.98, respectively. The classification result showed that when the SVM classifier performed pattern recognition on the electronic tongue data, the relationship between the recognition mechanism and the differences in electronic tongue data demonstrated a need for further optimization.

The optimal BP-NN model contained two hidden layers and five neurons per layer; it had a learning rate of 0.01, a momentum term of 0.3, and was trained for 500 iterations. In the calibration set, the accuracy was 98%, S15 was unassigned, and S53 was misclassified. S48 was misclassified in the validation set (*Ac*: 97.06%). After

500 iterations of training, the error rate was 0 (Figure 7C). Model accuracy increased the most when the momentum term was gradually increased from 0.2 to 0.5 while other parameters were unchanged. However, when the momentum term was increased from 0.4 to 0.5, the accuracy decreased due to an increase in the number of unclassified samples. This indicated that a larger momentum term was not well suited for model classification and that parameters in the BP-NN model should be further optimized. The model *Se* and *Sp* were 1.0 and 0.98, respectively.

3.4.4 Models built with HPLC data

The first 12 LVs, which could explain 89% of the sample variance, were selected to construct a PLS-DA model. In the calibration set, S41 and S119 were misclassified, but the accuracy in the validation set was 100% (Figure 6D). The model *Se* and *Sp* were 0.97 and 0.98, respectively, and the classification performance was good. For the SVM model (Supplementary Figure S3D), accuracy was highest (94% and 100% in the calibration and

TABLE 2 Species identification results and model parameters.

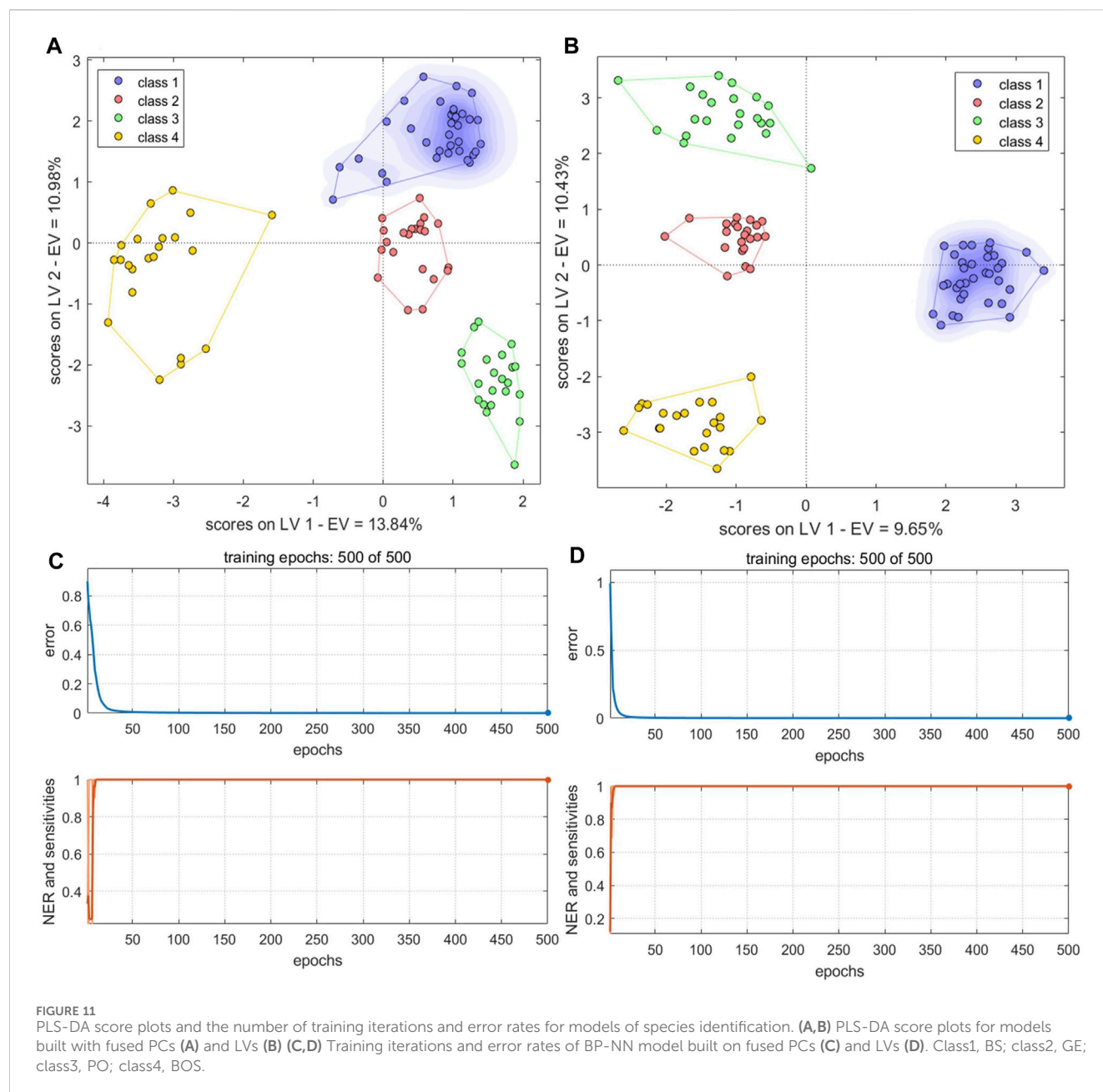| Model	Data matrix	Calibration set					Validation set	
		Misclassified samples	Not assigned samples	Se	Sp	Ac	Misclassified or not-assigned samples	Ac
PLS-DA	EN	2	6	0.9400	1.0000	0.9200	4	0.8824
	EE	3	7	1.0000	0.9800	0.9000	5	0.8529
	ET	0	3	1.0000	1.0000	0.9700	0	1.0000
	HPLC	4	4	0.9400	0.9800	0.9200	0	1.0000
	Data fusion by PCs	**0**	**0**	**1.0000**	**1.0000**	**1.0000**	**1**	**0.9706**
	Data fusion by LVs	**0**	**0**	**1.0000**	**1.0000**	**1.0000**	**1**	**0.9706**
BP-NN	EN	1	2	0.9700	1.0000	0.9700	2	0.9412
	EE	1	1	1.0000	1.0000	0.9800	3	0.9118
	ET	2	3	0.9700	0.9800	0.9500	1	0.9706
	HPLC	4	5	0.9400	0.9700	0.9100	0	1.0000
	Data fusion by PCs	**0**	**2**	**1.0000**	**1.0000**	**0.9800**	**1**	**0.9706**
	Data fusion by LVs	1	2	1.0000	1.0000	0.9700	2	0.9412

The bold values indicate the optimal model.

validation sets, respectively) when the kernel parameter was 9 and the cost value was 1. The model *Se* and *Sp* were 0.85, 0.98, respectively. The optimized BP-NN model contained two hidden layers and 10 neurons per layer; the learning rate was 0.1, the momentum term was 0.5, and it was trained for 500 iterations, producing an error rate of 0 (Figure 7D). There were five misclassified samples in the calibration set with *Ac* of 95%, but the validation set accuracy was 100%. The model *Se* and *Sp* were 0.91, 0.97, respectively. The high accuracy in the validation set may have been because there were extensive differences in the HPLC data between the four types of decoction pieces; especially when the sample size was small, this could correspond to clear difference between sample types. Thus, for the HPLC data, the accuracies of both the linear and nonlinear classifiers were 100% on the validation set.

3.4.5 Models built with mid-level fused data

The PC scores of the electronic sensor and HPLC data were fused and models were built as described above. The accuracy of the resulting PLS-DA model was 100% for the calibration set, which was superior to the performance of the PLS-DA models constructed with single-source data. In the validation set, only S5 was misclassified (*Ac*: 97.06%). *Se* and *Sp* were 1.0, 1.0, respectively. The two sample types could be completely divided into two categories based on the first two LVs (Figure 8A); the aggregation trend was also superior compared to the models built with single-source data. This indicated that fused PCs (each explaining more than 90% of sample variance in the single-source data) could be used to accurately identify the two sample types while reducing the algorithm running speed. The optimal SVM model had a kernel parameter of 6.4 and cost value of 1; this produced a classification prediction probability of 1 for both sample types (Supplementary Figure S5), which was better than the corresponding SVM model for each single-data source. Model accuracy was also 100% when the kernel parameter was 2.26 or

9 and the cost value was 1, but the number of support vectors was larger in the former case and the classification prediction probability was lower in the latter case. Thus, a kernel parameter/cost value combination of 6.4/1 was selected. The classification hyperplane and support vectors of SVM model was shown in Figure 8C. In the validation set, S5 was misclassified (*Ac*: 97.06%). *Se* and *Sp* were 1.00, 1.00, respectively. The optimal BP-NN model built with the fusion data contained two hidden layers and 10 neurons per layer with a learning rate of 0.1, a momentum term of 0.4. It was trained for 500 iterations, producing a final error rate of 0 (Figure 9A). The area under the curve (AUC) of the receiver operating characteristic (ROC) was 1 (Figure 9B). In the calibration set, S120 was misclassified with *Ac* of 99.00%; S5 remained misclassified in the validation set with *Ac* of 97.06%. The model *Se* and *Sp* were 1.00, 0.98, respectively.

After fusing the LVs from each data source, all three model types could discriminate between samples better than the corresponding models trained on single-source data and performed comparably to or better than the models built with PC fusion data. The PLS-DA model showed 100% accuracy in both the calibration and validation sets, and *Se* and *Sp* were both 1. The two sample types could be completely separated on the first two LVs, and samples clustered together better than in the results of the models built with PC fusion data (Figure 8B). For SVM, the optimal parameter combination was kernel parameter = 9 and cost value = 1 (Figure 8E); this model had 33 support vectors (Figure 8D) and accuracy was 100% on both the calibration and validation sets. *Se* and *Sp* were 1.00, 1.00, respectively. The optimized BP-NN model had two hidden layers, 10 neurons per layer, a learning rate of 0.1, a momentum term of 0.3, and 500 iterations (final error rate = 0) (Figure 9C). Using this parameter combination, only S76 was misclassified. The AUC of ROC was 1, and the *Se* and *Sp* values at varying prediction probability thresholds showed that the *Sp* value increases when it is close to 0 and the *Se* value decreases when it is close to 1 and the

FIGURE 11
PLS-DA score plots and the number of training iterations and error rates for models of species identification. **(A,B)** PLS-DA score plots for models built with fused PCs **(A)** and LVs **(B) (C,D)** Training iterations and error rates of BP-NN model built on fused PCs **(C)** and LVs **(D)**. Class1, BS; class2, GE; class3, PO; class4, BOS.

area surrounded by the red and blue lines is also large, which indicated that the model had good classification performance (Figure 9D). The accuracy of the final model was 99%, with only one sample misclassified in the validation set and the model *Se* and *Sp* were 1.00, 0.98, respectively; this was superior to the classification results based on electronic nose or electronic tongue data alone.

3.5 Species identification

3.5.1 Models built with electronic nose data

Six LVs which can explain 99% of the sample variance were selected for construction of an optimal PLS-DA species identification model. The four sample types showed similarities in the variance represented by the first two latent variables

(Figure 10A). S28 and S34 were misclassified in the calibration set. Because PLS-DA can divide samples only into predefined categories, this model was unable to identify specific samples; one, one, and four BS, GE, and PO samples, respectively, were unassigned. The accuracy was 92% in the calibration set, and *Se* and *Sp* were 0.94 and 1, respectively. There were four unassigned samples in the validation set. This indicated a need for further improvement of this model.

The model identification criteria were strict in the BP-NN model because the samples were divided into four categories. This necessitated an appropriate increase in the number of hidden layers and the number of neurons in each layer. The final model contained three hidden layers with 10 neurons per layer and had a learning rate of 0.1, a momentum term of 0.3, and was trained for 500 iterations. In the calibration set, S28 was misclassified and
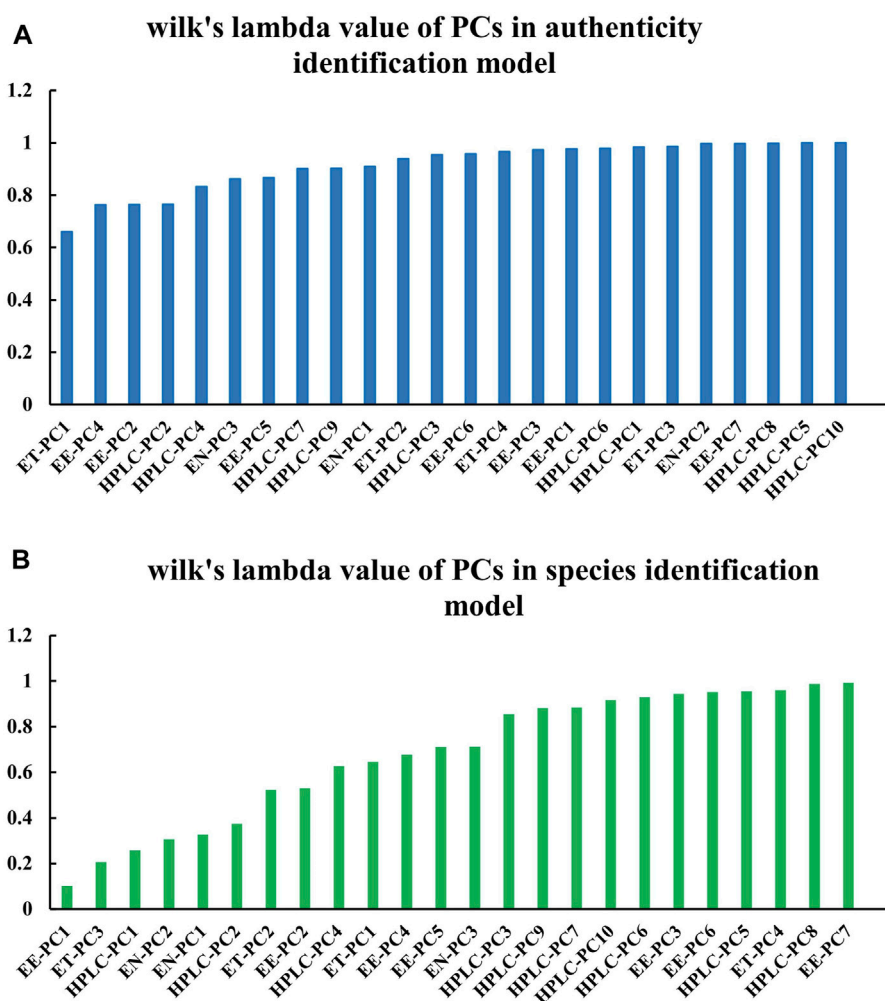
FIGURE 12
Wilk's lambda values of variables in the PCs-based data fusion models. Data are shown for the **(A)** sample authenticity binary classification model and the **(B)** species identification multi-class model.

TABLE 3 Original variables with larger factor loading values of highly contributing principal components.

Problems of classification	PCs	Original variables
Authenticity identification	ET-PC1	Sourness
	EE-PC4	Color number value 1621
	EE-PC2	Color number value 1621
	HPLC-PC2	Peak 4
Species identification	EE-PC1	Color number value 1621
	ET-PC3	Sourness
	HPLC-PC1	Peak 5
	EN-PC2	W1C

S80 and S83 were unclassified and Ac was 97.00%. The model Se and Sp were 0.97, 1.00, respectively. In the validation set, two samples were misclassified and the overall accuracy was 94.12%.

3.5.2 Models built with electronic eye data

The first 13 LVs, which explained 95% of the sample variance, were selected to establish a PLS-DA model. The four sample types could be clearly distinguished in the two-dimensional plot, with GE and PO clustering relatively close to one another and BS and BOS samples also clustering near one another (Figure 10B). In the calibration set, S52, S63, and S91 were misclassified and seven samples were unclassified (Ac: 90%). In the validation set, S5, S11, and S48 were unassigned and S67 and S93 were misclassified (Ac: 85.29%). Se and Sp were 1.00, 0.98, respectively.

For the BP-NN model, the optimal parameter combination was two hidden layers, 15 neurons per layer, a learning rate of 0.1, a momentum term of 0.3, and 500 training iterations. In the calibration set, the accuracy was 98%; S23 was unclassified and S69 was misclassified. The model Se and Sp were 1.00, 1.00, respectively. The AUC-ROC was 1, indicating good parameter optimization (Supplementary Figure S6). Increasing the number of hidden layers from two to three while keeping the other parameters unchanged led to a sudden increase in the number of unclassified samples. This suggested that the multi-classification

ability of the model could not be improved overall by only increasing the number of hidden layers.

3.5.3 Models built with electronic tongue data

To some extent, taste responses reflected the chemical composition of each sample. The electronic tongue data could therefore theoretically characterize the differences between the four types of decoction pieces better than the other sensory data types. Seven LVs accounting for a full 100% of the sample variance were used to build a PLS-DA model. Compared to the other two sensory data types, the number of unassigned samples decreased to one GE and two PO samples. There were no misclassified samples. *Ac* was 97.00% and 100% in the calibration and validation sets, respectively and *Se* and *Sp* were 1.0 and 1.0, respectively. Clustering based on just the first two LVs also showed good sample separation (Figure 10C); PO samples clustered far away from the other three sample types. BS, GE, and some BOS samples clustered close together, indicating that their tastes were similar. The clear distinction of the latter three sample types from PO was likely because PO is a member of the family *Liliaceae*, whereas the other three belong to the family *Orchidaceae*.

The optimal BP-NN model contained two hidden layers with five neurons per layer; the learning rate was 0.1, the momentum term was 0.4, and there were 500 iterations. In the calibration set, S29 and S53 were misclassified and S24, S79, S114 were unclassified (*Ac*: 95%). In the validation set, the accuracy was 97.06% and there was only one unassigned sample. The model *Se* and *Sp* were 0.97, 0.98, respectively. The error rate reached 0 after 500 iterations and the AUC-ROC was 1 (Supplementary Figure S7). This indicated that the selected parameters were appropriate for distinction between the four sample types.

3.5.4 Models built with HPLC data

A PLS-DA model was constructed from the first nine LVs, which explained 84% of the sample variance. There were four misclassified and four unclassified samples in the calibration set (*Ac*: 92%); in the validation set, the accuracy was 100%. *Se* and *Sp* were 0.94, 0.98, respectively. In the two-dimensional plot, the BS and BOS samples overlapped, whereas GE and PO samples could be clearly classified into two separate categories, distinct from the BS and BOS samples (Figure 10D). This was consistent with the high similarity between BS and BOS samples in the HPLC fingerprint data. The optimal BP-NN model built on these data had two hidden layers, 10 neurons per layer, a learning rate of 0.1, a momentum term of 0.5, and 500 iterations. There were nine misclassified samples in the calibration set, but the accuracy was 100% in the validation set. The model *Se* and *Sp* were 0.94, 0.97, respectively.

3.5.5 Models built with mid-level fused data

The PCs from the electronic sensor data were next fused with the PCs from HPLC data (Table 2). PLS-DA and BN-NN models built with the fused data had improved classification abilities compared to the corresponding models built with single-source data. The PLS-DA model was constructed with the first five LVs. The accuracy in the calibration set was 100%; in the validation set, S5 was still misclassified (*Ac*: 97.06%). *Se* and *Sp* were 1.00, 1.00, respectively. In the variance represented by the first two LVs, the four sample types could be clearly distinguished, although BS and GE were close together (Figure 11A). The optimal BP-NN model had three

hidden layers, 10 neurons per layer, a learning rate of 0.1, a momentum term of 0.4, and 500 iterations. After data fusion, there were two unassigned samples in the calibration set (*Ac*: 97.00%); *Se* and *Sp* were 1.0 and 1.0, respectively; the error rate decreased consistently as the training iteration number increased (Figure 11C). The AUC-ROC was 1 for the four sample types (Supplementary Figure S8), indicating that appropriate parameters had been selected.

The LVs were then fused for the electronic sensor and HPLC data. The classification results of a PLS-DA model built with the fused LV data were the same as the results of the model built with the fused PC data: no unclassified or misclassified samples in the calibration set; 100% accuracy; and only S5 unclassified in the validation set. *Se* and *Sp* were 1.00, 1.00, respectively. The four sample types were fully separated based on the first two LVs (Figure 11B), and the model performed better than it did with the fused PCs. However, the classification performance of a BP-NN model built with the fused LV data was not significantly improved compared to models built with single-source data. The optimal model had two hidden layers, 15 neurons per layer, a learning rate of 0.1, a momentum term of 0.4, and was trained for 500 iterations. In the calibration set, this model misclassified one sample and two others were unassigned (*Ac*: 97%); there was one unassigned and one misclassified sample in the validation set (*Ac*: 94.12%). *Se* and *Sp* were 1.00, 1.00, respectively. After 500 training iterations, the error rate was 0 (Figure 11D).

3.6 Highly contributing feature analysis

In classifying sample authenticity, the PCs with relatively small Wilk's lambda values were electronic tongue (ET)-PC1, electronic eye (EE)-PC4, EE-PC2, and HPLC-PC2 (Figure 12A). In species identification, the PCs with small Wilk's lambda values included EE-PC1, ET-PC3, HPLC-PC1, and electronic nose (EN)-PC2 (Figure 12B). These PCs contributed greatly to the classification model. Notably, the results indicated that it was not only the first three PCs that played major roles in classification with each data type; other PCs also represented a great deal of variance.

We next constructed a factor loading matrix of the four types of data sources (Supplementary Table S1). Some of the original variables (Table 3) had larger factor loading values of the highly contributing PCs. These original variables were highly correlated with the PCs, and changes in these values would be expected to have a strong impact on the classification performance of the model.

4 Conclusion

In this study, a preliminary identification of *B. striata* and similar decoction pieces was firstly conducted based on the classification scheme in the *Chinese Pharmacopoeia* and local standards. Samples were then analyzed with GC-IMS, an electronic nose, an electronic eye, an electronic tongue, and HPLC. Classical machine learning and deep learning algorithms were used to classify samples based on each type of data. Furthermore, using improved data fusion technology, highly effective models were constructed to accurately distinguish between *B. striata* and similar decoction pieces. In the sample

authenticity binary classification model (*B. striata* vs. other samples), the PLS-DA and SVM models built with fused LV data had the best performance, with an accuracy of 100% after cross-validation of the calibration dataset and only one misclassified sample in the validation set. In the multi-class species identification model, the PLS-DA model built with fused PCs and the PLS-DA model generated with fused LVs performed the best, with accuracies of 100% and just one misclassified sample each in the validation set. The results of feature extraction were compared between a supervised and an unsupervised algorithm; overall, fused LVs performed better than fused PCs in the PLS-DA and SVM authenticity identification models, whereas fused PCs performed comparably to or better than fused LVs fusion in the BP-NN authenticity and species identification models. PCs beyond the first three components can make large contributions to sample classification, sometimes playing key roles in model identification. Factor loading values indicated that some original variables had higher values of the highest-contributing PCs, demonstrating the importance of specific original variables in accurately classifying samples. These variables included the Sourness sensor in the ET, the W1C sensor in the EN (aromatic organic compounds), color number 1621 in the EE (dark reddish gray), and peaks 4 and 5 in the HPLC data. In summary, our study provides a highly feasible method of accurately evaluating putative *B. striata* and related samples, promoting quality evaluation and control in Chinese decoction pieces.

Data availability statement

The original contributions presented in the study are included in the article/Supplementary Material, further inquiries can be directed to the corresponding authors.

Author contributions

HL: Writing–original draft, Writing–review and editing. P-PW: Writing–original draft, Writing–review and editing. Z-ZL: Methodology, Software, Writing–review and editing. Y-LW: Writing–review and editing. X-JG: Writing–review and editing. X-HF: Writing–review and editing. F-YD: Writing–review and editing. P-PZ: Writing–review and editing. X-LL: Writing–review and editing. RL: Writing–review and editing.

Conflict of interest

Author Z-ZL was employed by Beijing Zhongyan Tongrentang Medicine R&D Co., Ltd.

The remaining authors declare that the research was conducted in the absence of any commercial or financial relationships that could be construed as a potential conflict of interest.

Publisher's note

All claims expressed in this article are solely those of the authors and do not necessarily represent those of their affiliated organizations, or those of the publisher, the editors and the reviewers. Any product that may be evaluated in this article, or claim that may be made by its manufacturer, is not guaranteed or endorsed by the publisher.

Supplementary material

The Supplementary Material for this article can be found online at: https://www.frontiersin.org/articles/10.3389/fchem.2023.1342311/full#supplementary-material

References

Ballabio, D., and Consonni, V. (2013). Classification tools in chemistry. Part 1: linear models. PLS-DA. *Anal. Methods* 5 (16), 3790–3798. doi:10.1039/c3ay40582f

Borraz-Martínez, S., Boqué, R., Simó, J., Mestre, M., and Gras, A. (2019). Development of a methodology to analyze leaves from Prunus dulcis varieties using near infrared spectroscopy. *Talanta* 204, 320–328. doi:10.1016/j.talanta.2019.05.105

Cai, Z., Wang, H., and Wang, G. (2020). Complete chloroplast genome sequence of Bletilla striata (Thunb.) Reichb. f., a Chinese folk medicinal plant. *Mitochondrial DNA B Resour.* 5 (3), 2239–2240. doi:10.1080/23802359.2020.1770138

Chauhan, V. K., Dahiya, K., and Sharma, A. (2019). Problem formulations and solvers in linear SVM: a review. *Artif. Intell. Rev.* 52 (2), 803–855. doi:10.1007/s10462-018-9614-6

Cui, X., Zhang, X., Yang, Y., Wang, C., Zhang, C., and Peng, G. (2017). Preparation and evaluation of novel hydrogel based on polysaccharide isolated from Bletilla striata. *Pharm. Dev. Technol.* 22 (8), 1001–1011. doi:10.1080/10837450.2016.1221422

Ding, L., Shan, X., Zhao, X., Zha, H., Chen, X., Wang, J., et al. (2016). Spongy bilayer dressing composed of chitosan-Ag nanoparticles and chitosan-Bletilla striata polysaccharide for wound healing applications. *Carbohydr. Polym.* 157, 1538–1547. doi:10.1016/j.carbpol.2016.11.040

Feng, X. S., Qiu, F. Z., and Xu, Z. (1995). Experimental studies of embolization of different hepatotropic blood vessels using Bletilla striata in dogs. *J. Tongji Med. Univ.* 15 (1), 45–49. doi:10.1007/bf02887885

Gao, H. S., Guo, A. L., Yu, X. D., and Li, C. C. (2008). "RBF-SVM and its application on network security risk evaluation," in 2008 4th International Conference on Wireless Communications, Networking and Mobile Computing, Dalian, China, 12-14 Oct. 2008 (IEEE), 1–4. doi:10.1109/WiCom.2008.1110

Gui, X. J., Li, H., Ma, R., Tian, L. Y., Hou, F. G., Li, H. Y., et al. (2023). Authenticity and species identification of Fritillariae cirrhosae: a data fusion method combining electronic nose, electronic tongue, electronic eye and near infrared spectroscopy. *Front. Chem.* 11, 1179039. doi:10.3389/fchem.2023.1179039

Hou, F., Fan, X., Gui, X., Li, H., Li, H., Wang, Y., et al. (2023). Development of a variety and quality evaluation method for Amomi fructus using GC, electronic tongue, and electronic nose. *Front. Chem.* 11, 1188219. doi:10.3389/fchem.2023.1188219

Jiang, J., Chen, H., Tang, X., and Zhou, Y. (2017). Consideration on development of Bletillae striata based on whitenino theory in traditional Chinese medicine. *Chin. Tradit. Herb. Drugs* 48 (11), 2313–2320. doi:10.7501/i.issn.0253-2670.2017.11.027

Jiang, L., Lin, M., Wang, H., Song, H., Zhang, L., Huang, Q., et al. (2022). Haplotype-resolved genome assembly of Bletilla striata (Thunb.) Reichb.f. to elucidate medicinal value. *Plant J.* 111 (5), 1340–1353. doi:10.1111/tpj.15892

Jin, C., Kankan, Y., Zhiwei, W., Feiying, Z., Zhongliang, Q., Aiguo, H., et al. (2017). Study on genetic diversity of bletilla striata germplasm resources using RAPD and ISSR markers. *Chin. Agric. Sci. Bull.* 33 (12), 137–142. doi:10.11924/j.issn.1000-6850.casb17010097

Lan, Z., Zhang, Y., Sun, Y., Ji, D., Wang, S., Lu, T., et al. (2020). A mid-level data fusion approach for evaluating the internal and external changes determined by FT-NIR, electronic nose and colorimeter in Curcumae Rhizoma processing. *J. Pharm. Biomed. Anal.* 188, 113387. doi:10.1016/j.jpba.2020.113387

Li, H., WangYue, Y. Y., Hou, F., and Li, H. (2023). Study on the difference of volatile organic compounds between bletilla striata decoction pieces and Bletilla ochracea decoction pieces based on GC-IMS. *J. Chin. Pharm. Sci.* 58 (12), 1074–1083. doi:10.11669/cpj.2023.12.003

Li, Q., Li, K., Huang, S. S., Zhang, H. L., and Diao, Y. P. (2014). Optimization of extraction process and antibacterial activity of bletilla striata polysaccharides. *Asian J. Chem.* 26 (12), 3574–3580. doi:10.14233/ajchem.2014.16500

Li, X., Yang, Y., Zhu, Y., Ben, A., and Qi, J. (2022). A novel strategy for discriminating different cultivation and screening odor and taste flavor compounds in Xinhui tangerine peel using E-nose, E-tongue, and chemometrics. *Food Chem.* 384, 132519. doi:10.1016/j.foodchem.2022.132519

Liao, Z., Zeng, R., Hu, L., Maffucci, K. G., and Qu, Y. (2019). Polysaccharides from tubers of Bletilla striata: physicochemical characterization, formulation of buccoadhesive wafers and preliminary study on treating oral ulcer. *Int. J. Biol. Macromol.* 122, 1035–1045. doi:10.1016/j.ijbiomac.2018.09.050

Lu, L., Hu, Z., Hu, X., Li, D., and Tian, S. (2022). Electronic tongue and electronic nose for food quality and safety. *Food Res. Int.* 162, 112214. doi:10.1016/j.foodres.2022.112214

Luo, Y., Diao, H., Xia, S., Dong, L., Chen, J., and Zhang, J. (2010). A physiologically active polysaccharide hydrogel promotes wound healing. *J. Biomed. Mater. Res. Part A* 94 (1), 193–204. doi:10.1002/jbm.a.32711

Niu, J., Zhao, G., Mi, Z., Chen, L., Liu, S., Wang, S., et al. (2020). *De novo* sequencing of Bletilla striata (Orchidaceae) transcriptome and identification of genes involved in polysaccharide biosynthesis. *Genet. Mol. Biol.* 43 (3), e20190417. doi:10.1590/1678-4685-gmb-2019-0417

Posocco, B., Dreussi, E., De Santa, J., Toffoli, G., Abrami, M., Musiani, F., et al. (2015). Polysaccharides for the delivery of antitumor drugs. *Materials* 8 (5), 2569–2615. doi:10.3390/ma8052569

Ru, C., Li, Z., and Tang, R. (2019). A hyperspectral imaging approach for classifying geographical origins of rhizoma atractylodis macrocephalae using the fusion of spectrum-image in VNIR and SWIR ranges (VNIR-SWIR-FuSI). *Sensors (Basel)* 19 (9), 2045. doi:10.3390/s19092045

Sun, F., Chen, Y., Wang, K. Y., Wang, S. M., and Liang, S. W. (2020). Identification of genuine and adulterated pinellia ternata by mid-infrared (MIR) and near-infrared (NIR) spectroscopy with partial least squares - discriminant analysis (PLS-DA). *Anal. Lett.* 53, 937–959. doi:10.1080/00032719.2019.1687507

Wang, L., Wang, Q., Wang, Y., and Wang, Y. (2021). Comparison of geographical traceability of wild and cultivated macrohyporia cocos with different data fusion approaches. *J. Anal. Methods Chem.* 2021, 1–13. doi:10.1155/2021/5818999

Wang, Q. Q., Huang, H. Y., and Wang, Y. Z. (2019). Geographical authentication of macrohyporia cocos by a data fusion method combining ultra-fast liquid chromatography and fourier transform infrared spectroscopy. *Molecules* 24 (7), 1320. doi:10.3390/molecules24071320

Wang, S. C., Zhang, Q., Liu, C. Z., Wang, Z. Q., Gao, J. Y., Yang, X. J., et al. (2023). Synergetic application of an E-tongue, E-nose and E-eye combined with CNN models and an attention mechanism to detect the origin of black pepper. *Sensors Actuators a-Physical* 357, 114417. doi:10.1016/j.sna.2023.114417

Wang, Y., Sun, G., Jin, Y., Zhang, J., Gao, J., and Sabi-Mouka, E. M. B. (2017). A comprehensive strategy to quantify the complex system by ultraviolet and infrared spectra analyses coupled with combustion heat for recognizing the quality consistency of san-huang tablets. *Am. J. Anal. Chem.* 8 (10), 13. doi:10.4236/ajac.2017.810049

Wu, X.-M., Zuo, Z.-T., Zhang, Q.-Z., Wang, Y.-Z., et al. (2018). FT-MIR and UV-vis data fusion strategy for origins discrimination of wild Paris Polyphylla Smith var. yunnanensis. *Vib. Spectrosc.* 96, 125–136. doi:10.1016/j.vibspec.2018.04.001

Yan, B., and Sun, G. (2018). Monitoring quality consistency of Liuwei Dihuang Pill by integrating the ultraviolet spectroscopic fingerprint, a multi-wavelength fusion fingerprint method, and antioxidant activities. *J. Sep. Sci.* 41 (6), 1182–1191. doi:10.1002/jssc.201700620

Yang, J., and Gao, H. (2020). Cultural emperor penguin optimizer and its application for face recognition. *Math. Problems Eng.* 2020, 1–16. doi:10.1155/2020/9579538

Yue, H., Li, M., Wang, C., and An, J. (2019). Maize drought statistic discriminant model based on color and texture features. *J. Agric. Sci. Technol.* 21 (05), 62–73. doi:10.13304/j.nykjdb.2018.0256

Zhai, M., Ma, Y., Zheng, G., and Jin, L. (2012). Comparative identification between commercial Bletilla Striata and three kinds of counterfeits. *J. Chengdu Univ. Tradit. Chin. Med.* 35 (03), 53–56. doi:10.13593/j.cnki.51-1501/r.2012.03.023

Zhang, J., Wang, Y., Yang, Z., and Zhang, J. (2021a). Data fusion of ATR-FTIR and UV-vis to identify the origin of Polygonatum kingianum. *Spectrosc. Spect. Anal.* 41 (05), 1410–1416. doi:10.3964/j.issn.1000-0593(2021)05-1410-07

Zhang, J., Xu, X., Li, L., Li, H., Gao, L., Yuan, X., et al. (2022). Multi critical quality attributes monitoring of Chinese oral liquid extraction process with a spectral sensor fusion strategy. *Spectrochim. Acta A Mol. Biomol. Spectrosc.* 278, 121317. doi:10.1016/j.saa.2022.121317

Zhang, M., Han, T., Hu, C., Bai, Y., Fan, Z., and Hong, L. (2019a). Industrialization condition and sustainable development strategies of Bletillae Rhizoma. *Chin. Tradit. Herb. Drugs* 50 (20), 5103–5108. doi:10.7501/j.issn.0253-2670.2019.20.037

Zhang, Q., Qi, C., Wang, H., Xiao, X., Xu, W., Gu, S., et al. (2019b). Biocompatible and degradable bletilla striata polysaccharide hemostasis sponges constructed from natural medicinal herb bletilla striata. *Carbohydr. Polym.* 226, 115304. doi:10.1016/j.carbpol.2019.115304

Zhang, X., Wu, H., Lin, L., Du, X., Tang, S., Liu, H., et al. (2021b). The qualitative and quantitative assessment of xiaochaihu granules based on e-eye, e-nose, e-tongue and chemometrics. *J. Pharm. Biomed. Anal.* 205, 114298. doi:10.1016/j.jpba.2021.114298

Zheng, G. (2005). *Convergence analysis of BP neural network with momentum term*. Dalian: Dalian University of Technology.

Zhou, M., Yuan, F., Ruan, H. L., Li, J., Huang, J. F., Liu, S., et al. (2023). Neuroprotective neolignan glycosides from the pseudobulbs of Bletilla striata. *Fitoterapia* 171, 105691. doi:10.1016/j.fitote.2023.105691

Construction of porphyrinic manganese-organic frameworks based on structural regulation for electrochemical determination of nitrobenzene in water and vegetable samples

Li Wang, Mengjie Zhang, Yuanyuan Li, Xiumei Chen, Hao Qin, Jin Yang, Suhua Fan* and Hai Wu*

Anhui Province Key Laboratory for Degradation and Monitoring of Pollution of the Environment, Anhui Province Key Laboratory of Environmental Hormone and Reproduction, Fuyang Normal University, Fuyang, China

Nitrobenzene (NB) is one of the major organic pollutants that has seriously endangered human health and the environment even in trace amounts. Therefore, it is of great significance to detect trace NB efficiently and sensitively. Herein, a porphyrinic metal-organic framework (MOF) of Mn-PCN-222 (PCN, porous coordination network) was first synthesized by the coordination between Zr_6 cluster and tetrakis (4-carboxyphenyl)-porphyrin-Mn (III) (MnTCPPCl) ligand. To regulate its structure and the electrochemical properties, a phenyl group was inserted in each branched chain of TCPP to form the TCBPP organic ligand. Then, we used Zr_6 clusters and manganese metalloporphyrin (MnTCBPPCl) to synthesize a new porphyrin-based MOF (Mn-CPM-99, CPM, crystalline porous material). Due to the extended chains of TCPP, the rod-shaped structure of Mn-PCN-222 was switched to concave quadrangular bipyramid of Mn-CPM-99. Mn-CPM-99 exhibited higher porosity, larger specific surface area, better electrochemical performances than those of Mn-PCN-222. By using modular assembly technique, Mn-CPM-99 film was sequentially assembled on the surface of indium-tin-oxide (ITO) to prepare an electrochemical sensor (Mn-CPM-99/ITO). The proposed sensor showed excellent electrochemical reduction of NB and displayed three linear response ranges in the wide concentration ranges. The obtained low limit of detection (LOD, 1.3 nM), high sensitivity and selectivity, and good reproducibility of the sensor for NB detection fully illustrate that Mn-CPM-99 is an excellent candidate for electrochemical sensor interface material. Moreover, the sensor was successfully applied to the detection of NB in lake water and vegetable samples showing satisfactory recovery of 98.9%–101.8%.

1 Introduction

Nitrobenzene (NB) and its compounds play crucial roles in the synthesis of dyes, pesticides, and explosives, moreover, they serve as solvents during petroleum refining processes (Li et al., 2022). NB contamination in the environment is mainly from the discharge of industrial waste by chemical plants and dyestuff factories (Wang et al., 2023). Due to its moderate water solubility and higher density relative to water, NB compounds tend to sink to the bottom of water and persist for a prolonged period, resulting in severe and persistent pollution of natural water resources (Lu et al., 2023; Wang et al., 2024). When NB enter into the human body, it can lead to a serious problem of methemoglobinemia and liver cancer and remain carcinogenic activities even at trace level (Fang et al., 2021; Li et al., 2021). Moreover, the presence of a nitro group in NB compounds contributes to their poor biodegradability in electron-deficient environments. The allowable level of NB in all types of water is regulated no more than 2 mg·L^{-1} (16.25 μM) by the World Health Organization (WHO) and American Public Health Association (APHA) (Li et al., 2023). It is therefore imperative to enhance environmental monitoring and research on nitrobenzene compounds, implement stricter emission controls, mitigate environmental pollution, and safeguard human health (Seal et al., 2022; Chellappa et al., 2024).

Various analytical methods including gas chromatography-mass spectrometry (GC-MS) (Zhang et al., 2014), high performance liquid chromatography (HPLC) (Wang and Chen, 2002), spectrophotometry (Rafique et al., 2023; Rahman and Ahmad, 2024) and electrochemical techniques have been used for the detection of NB (Koohfar et al., 2023; Wang et al., 2023; Papavasileiou et al., 2024). Among them, electrochemical techniques have received widespread attention due to their simple operation, high sensitivity, and low cost for detecting nitrobenzene. However, the key of electrochemical sensors is to prepare the interface materials with excellent selectivity and good catalytic performance. Metal-organic frameworks (MOFs) are hybrid materials composed of both organic linkers and inorganic metal nodes, and have been extensively used to construct electrochemical sensors (Kajal et al., 2022). MOFs possess special active sites and many advantages due to their controllable structure, high specific surface area, good stability, and tailored functionalities (Zhang et al., 2023; Junior et al., 2024). The composition of organic and inorganic components can be adjusted to control the structure and performances of MOFs, enhancing their sensing capabilities, e.
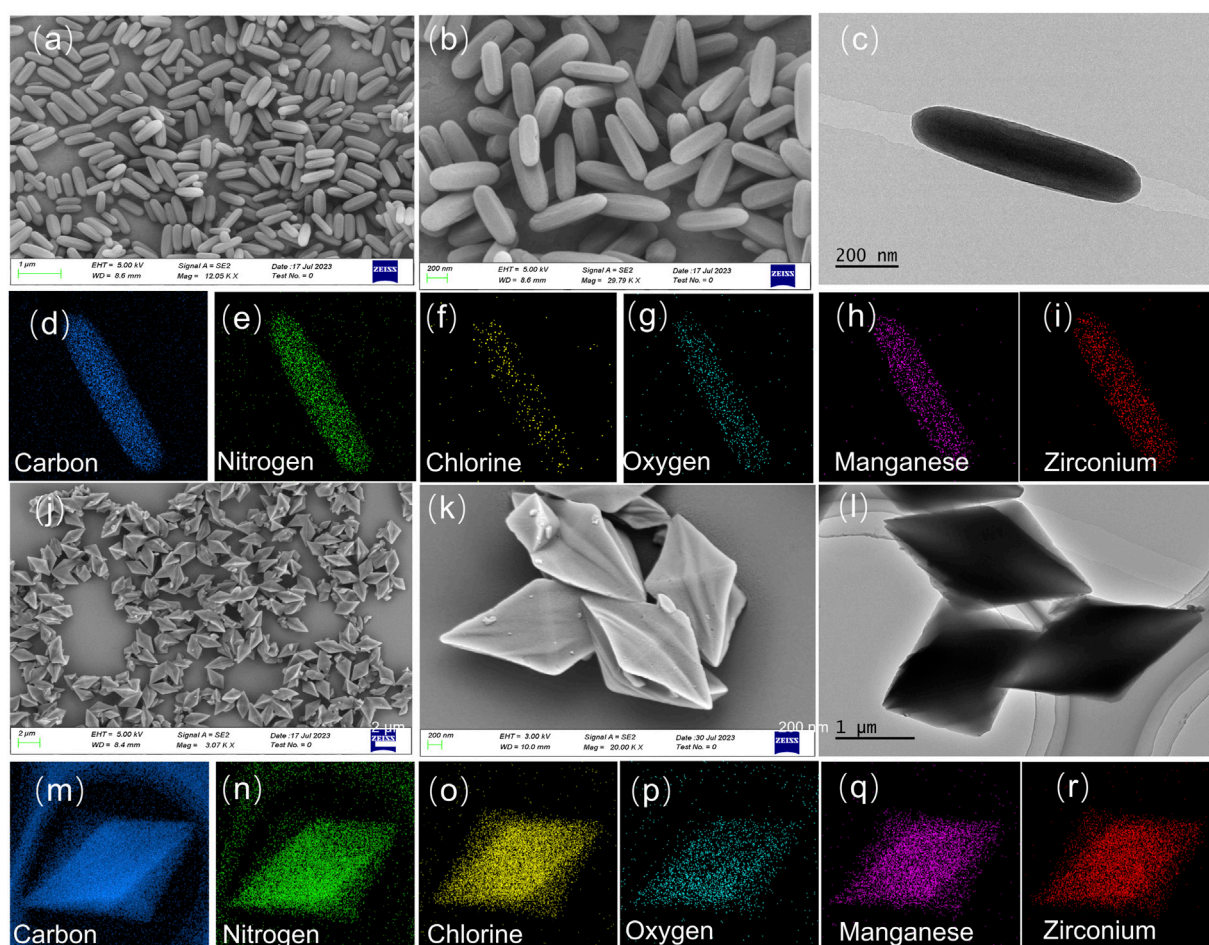

FIGURE 1
SEM images of Mn-PCN-222 (A,B) and Mn-CPM-99 (J,K). TEM images of Mn-PCN-222 (C) and Mn-CPM-99 (L), respectively. Element mapping images of Mn-PCN-222 (D−I) and Mn-CPM-99 (M−R), respectively.
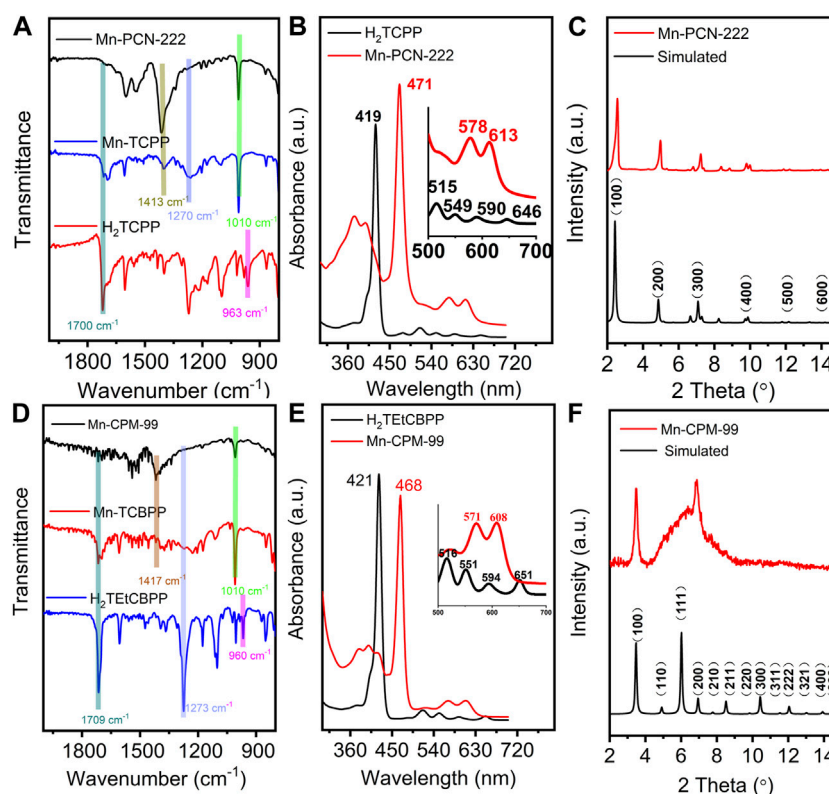
FIGURE 2
(A,D) ATR-IR spectra of free H₂TCPP ligand, MnTCPPCl ligand, Mn-PCN-222, free H₂TEtCBPP ligand, MnTCBPPCl ligand, and Mn-CPM-99. **(B,E)** UV-Vis spectra of free H₂TCPP ligand and Mn-PCN-222 and free H₂TEtCBPP ligand and Mn-CPM-99 (Inset presents a zoomed view of the enlarged Q-band region for clarity). **(C,F)** PXRD patterns of the simulated (red curves) and prepared (blue curves) Mn-PCN-222 and Mn-CPM-99, respectively.

g., by incorporating specific functional groups for target recognition to realize selective detection of target analytes (Liu et al., 2020; Chang et al., 2022). Therefore, several electrochemical sensors based on MOFs have been developed including Cu-MOF (Xin et al., 2023), PCN-222(Fe) (Li et al., 2023), Fe-MOF (Dhayanithi et al., 2023) and showed outstanding sensitivity for the detection of analytes. The adjustable structure and chemical properties make MOFs and their derived materials promising candidates for the development of advanced electrochemical sensors.

Porphyrin-based MOFs can selectively response to NB compounds due to the inherent porphyrin recognition sites in MOFs, exhibiting rapid and selective detection of NB compounds, even in the presence of other interfering compounds (Yang et al., 2015; Zhang et al., 2021). A Zr (IV)-porphyrin MOF PCN-224 (PCN, porous coordination network) was used as fluorescent sensor for rapid detection of 2,4,6-trinitrotoluene (TNT) in aqueous solution (Yang et al., 2015). Fischer et al. proposed an electrochemical sensor using a porphyrin-based MOF (Mn-PCN-222) modified on a conductive indium-tin-oxide (ITO) surface for a variety of electrochemical applications, including nitroaromatics, phenolic and quinone-hydroquinone toxins, heavy metal ions, and biological species (Zhou et al., 2021). The excellent features were attributed to their well-defined porous structures, good electron transfer, and selective reaction between tetra(4-carboxyphenyl)porphyrin (TCPP) and nitroaromatics through hydrogen bonding and π−π stacking interaction.

In this research, to utilize the advantages of porphyrin-based MOFs, we employed Zr₆ clusters as nodes and manganese metalloporphyrin as ligand to prepare a new porphyrin-based MOF (Mn-CPM-99, CPM, crystalline porous material). As shown in Scheme 1A, Zr₆ cluster and Mn-TCPP were first coordinated to construct Mn-PCN-222, containing one of the 1D hexagonal mesoporous channels (Feng et al., 2012; Zhou et al., 2021). To regulate its structure, a phenyl group was inserted in each branched chain of Mn-TCPP to form the Mn-TCBPP ligand, and then, Mn-CPM-99 was prepared. Due to the extended chains of TCPP, the rod-shaped structure of Mn-PCN-222 was switched to quadrangular bipyramid of Mn-CPM-99. Their chemical structures, morphologies, electrochemical behavior, and electrocatalytic abilities were compared in this study. The results showed that the Mn-CPM-99 based electrochemical sensor exhibited high sensitivity and good performances for detection of NB in water and vegetable.

2 Experiments

2.1 Chemicals and reagents

All chemicals and reagents including N,N-Dimethylformamide (DMF), N,N-Diethylformamide (DEF), tetrahydrofuran (THF), were purchased from Energy Chemical (Shanghai, China) and Aladdin Reagent Shanghai Co. Ltd. (China), and directly utilized

SCHEME 1
(A) Synthesis routs and structures of Mn-PCN-222 and Mn-CPM-99. **(B)** Schematic diagram for the processes of modular assembly of Mn-PCN-222 and Mn-CPM-99 on the ITO electrodes.
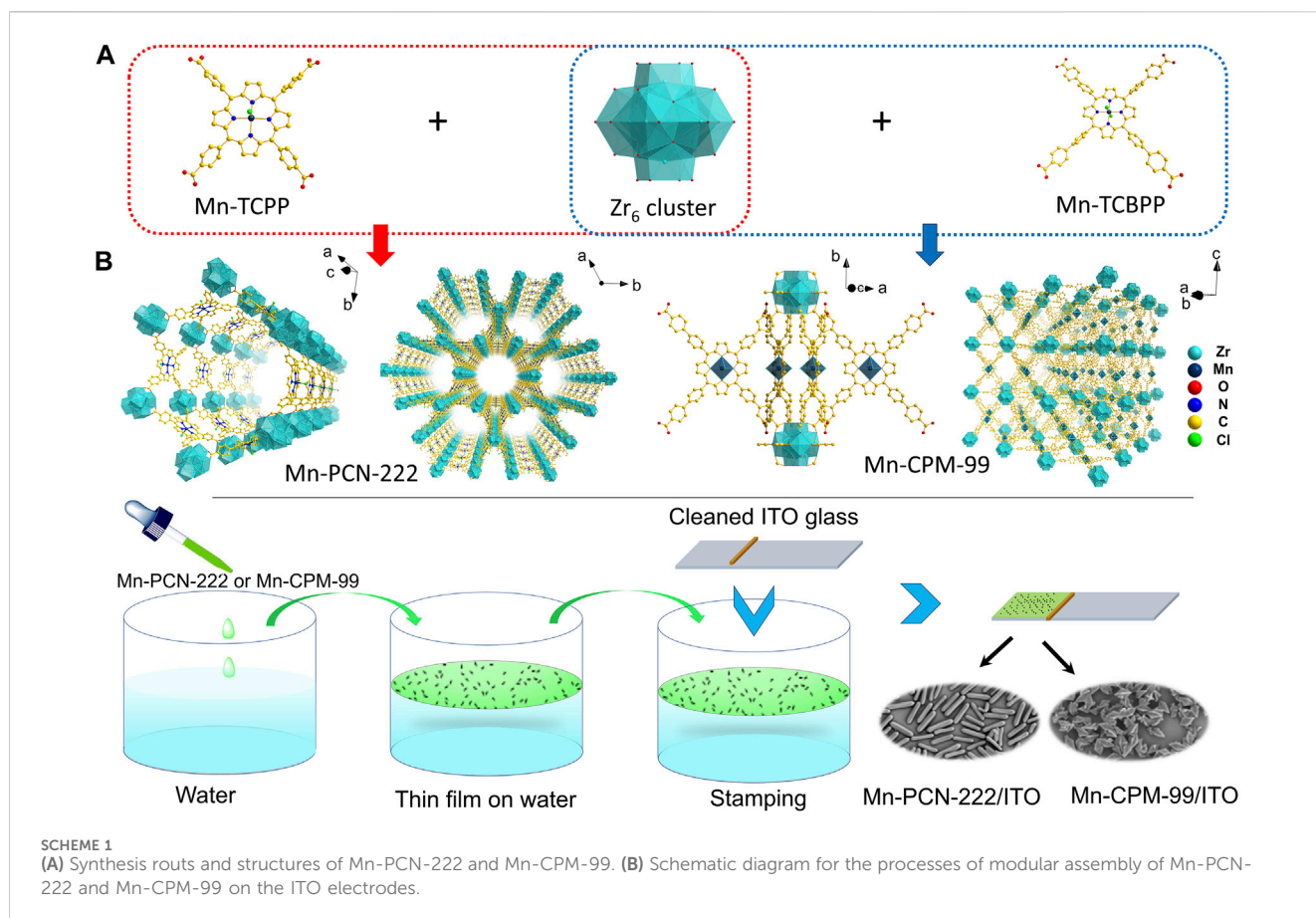
without further purification. The synthesis processes and structural characterizations for the Manganese porphyrin Lingands of MnTCPPCl and MnTCBPPCl Ligands were provided in Supplementary Scheme S1; Supplementary Figures S1–S3). Purification of synthesized products was performed on silica gel (300–400 mesh) and self-prepared PTLC (GF254 silica gel).

2.2 Synthesis of Mn-PCN-222 and Mn-CPM-99 MOFs

Mn-PCN-222 was synthesized by a simple one-step solvothermal method (Zhou et al., 2021). ZrOCl$_2$-8H$_2$O (26 mg), MnTCPPCl (12 mg), and benzoic acid (225 mg) were dissolved in 2 mL of DMF, and ultrasonically dispersed for 10 min. The reaction was then heated with stirring at 80°C and kept for 24 h. When the reaction was cooled to room temperature, the resulting Mn-PCN-222 were rinsed and centrifuged by DMF and ethanol, respectively, and finally dried under vacuum. In the similar way, Mn-CPM-99 were synthesized in DEF solvent at 120°C using 12 mg of MnTCBPPCl ligand.

2.3 Preparation of MOFs film modified ITO electrodes

Mn-PCN-222 and Mn-CPM-99 films was modified on the surface of conductive indium-tin-oxide (ITO) via the modular assembly method. As shown in Scheme 1B, before the modification, the ITO glass was cleaned in ultrasonic baths of acetone, ethanol, and water for 20 min, respectively. Then cleaned ITO was immersed in a solution of (1:1 v/v) ethanol/NaOH (1 M) and was activated for 15 min. Finally, it was rinsed with pure water and dried by N$_2$. The synthesized Mn-PCN-222 or Mn-CPM-99 were homogeneously dispersed in ethanol with ultrasonication to obtain a colloidal suspension of 1.0 mg·mL^{-1}, which was dropped onto the water surface in a beaker and then spread out to form a thin film. The film was then transferred onto the cleaned ITO glass by stamping (1 cm × 1 cm). The assembled film was immersed in ultrapure water to remove the un-deposited Mn-PCN-222 or Mn-CPM-99 and then dried by using N$_2$, Finally, the Mn-PCN-222/ITO and Mn-CPM-99/ITO modified electrodes were obtained.

2.4 Apparatus and measurements

Cyclic voltammetry (CV), chronoamperometric technique (i–t), and electrochemical impedance spectroscopy (EIS) were performed on a CHI660E electrochemical workstation (Chenhua, Shanghai, China). A three-electrode system was used and consisted of a modified ITO electrode as the working electrode (1 cm × 1 cm), a platinum wire served as the auxiliary electrode and an Ag/AgCl electrode (3 M KCl) used as the reference electrode, respectively.
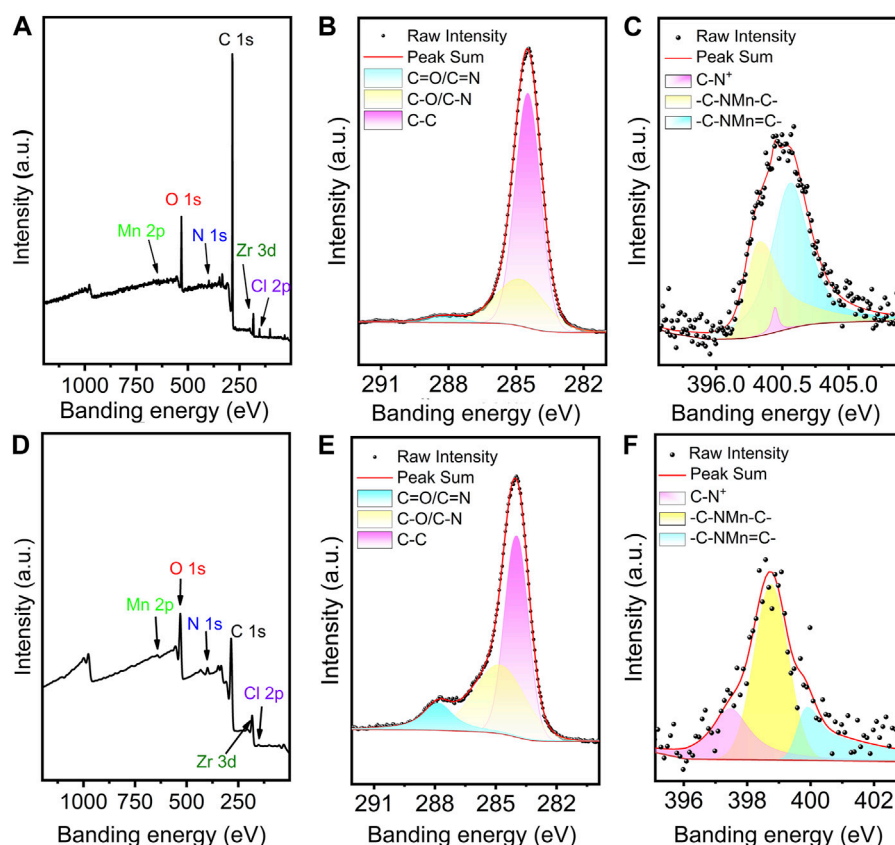
FIGURE 3
Full XPS profiles of Mn-PCN-222 **(A)** and Mn-CPM-99 **(D)**. The high-resolution XPS spectra of C 1s **(B,E)** and N 1s **(C,F)** in Mn-PCN-222 and Mn-PCN-222, respectively.

The morphology, composition, elements, and chemical structure of Mn-PCN-222 and Mn-CPM-99 were characterized by Scanning electron microscope (SEM, Sigma 500, Carl Zeiss, Germany), Transmission electron microscope (TEM, Tecnai G2 F30, FEI, USA), powder X-ray diffraction (XRD, SmartLab SE, Rigaku, Japan), X-ray photoelectron spectroscopy (XPS, K-Alpha, Thermo Scientific, USA), Attenuated total reflectance Infrared spectroscopy (ATR-IR, Nicolet iS50, Thermo Fisher, USA), and UV-Vis spectroscopy (UV-2700i spectrometer, Shimadzu, Japan). ^{1}H NMR spectra for the characterization of the Mn-PCN-222 and Mn-CPM-99 structures in Supplementary Material were measured on a Bruker Ascend 400 MHz instrument (NMR, Ascend 400, BRUKER, Switzerland).

3 Results and discussion

3.1 Characterization of Mn-PCN-222 and Mn-CPM-99

As described in Supplementary Scheme S1, the intermediates of TPPCOOMe and H$_2$TEtCBPP were synthesized and characterized by ^{1}H NMR spectra, and they were further coordinated with manganese metal ions to obtain MnTCPPCl and MnTCBPPCl ligands, respectively (Supplementary Figures S1–S3). MnTCPPCl

and MnTCBPPCl were then hydrolyzed to produce side-chain ester groups, which were then reacted with Zr$_6$ clusters by solvothermal synthesis method to get the Mn-PCN-222 and Mn-CPM-99 MOFs, respectively. The sizes and morphologies of MnTCPPCl and MnTCBPPCl were observed by SEM and TEM measurements, respectively.

As shown in Figures 1A–C, Mn-PCN-222 presents regular rod shape with an average diameter of 165 nm. However, Mn-CPM-99 exhibits the structure of concave quadrangular bipyramid with uniform distribution (about 700–850 nm long, Figures 1J–L). The Energy-dispersive X-ray spectroscope (EDS) elemental mapping of Mn-PCN-222 and Mn-CPM-99 MOFs were performed to reveal the element distribution. The EDS spectra presented in Supplementary Figure S4 confirm the presence of C, N, Cl, O, Mn, and Zr elements in the samples. We can find that all the measured elements (C, N, Cl, O, Mn, Zr) in the elemental maps are uniformly distributed in the samples (Figures 1D–I; Figures 1M–R). The clean and homogeneous surfaces of Mn-PCN-222 and Mn-CPM-99 MOFs indicate that the synthesis was successful and could obtain relatively pure compounds.

The compositions of Mn-PCN-222 and Mn-CPM-99 were analyzed by attenuated total reflection infrared spectroscopy (ATR-IR) and UV-Vis spectroscopy. As shown in Figure 2A, compared with the free H$_2$TCPP ligand, MnTCPPCl ligand exhibits a new peak at 1010 cm^{-1} assigned to Mn-N bonds with
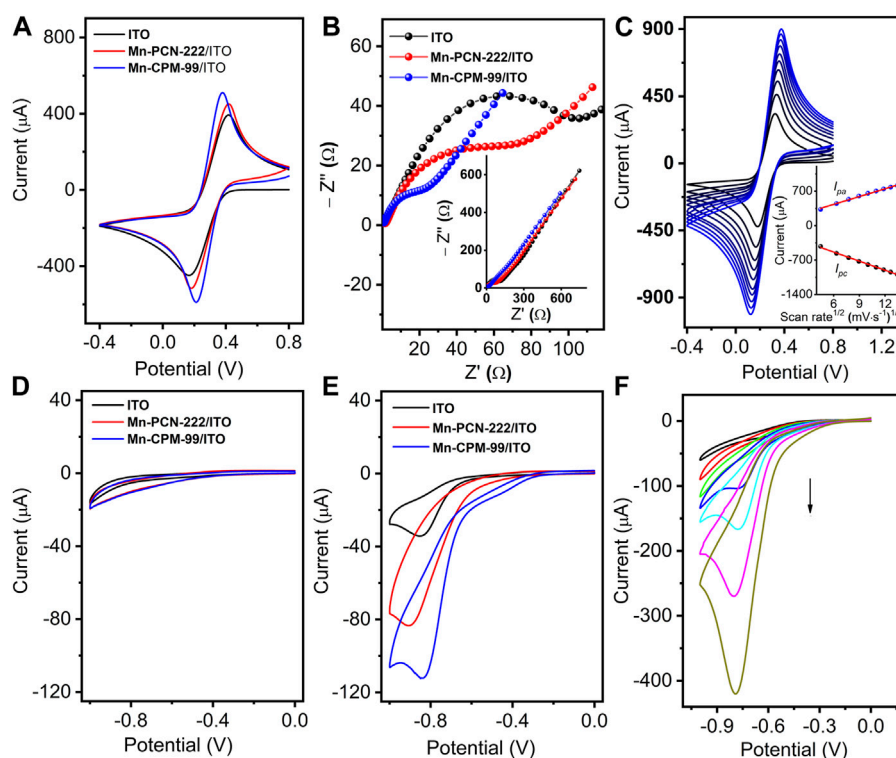
FIGURE 4
(A) CV and **(B)** EIS of ITO, Mn-PCN-222/ITO, and Mn-CPM-99/ITO in 5 mM [Fe(CN)$_6$]$^{3-/4-}$ solution with 0.1 M KCl (scan rate: 50 mV·s^{-1}). **(C)** CVs of Mn-CPM-99/ITO at different scan rates from 20 to 200 mV·s^{-1} (Inset: The linear relationship between redox peak currents (I_{pa} and I_{pc}) and the square root of the scan rates). **(D,E)** CVs of different modified electrodes in 0.4 M NaCl (pH 7.0) without and with 40 μM NB, respectively. **(F)** CV response of the Mn-CPM-99/ITO sensor in 0.4 M NaCl toward various concentration of NB (0.06, 0.3, 3, 24, 60, 150, and 300 μM).
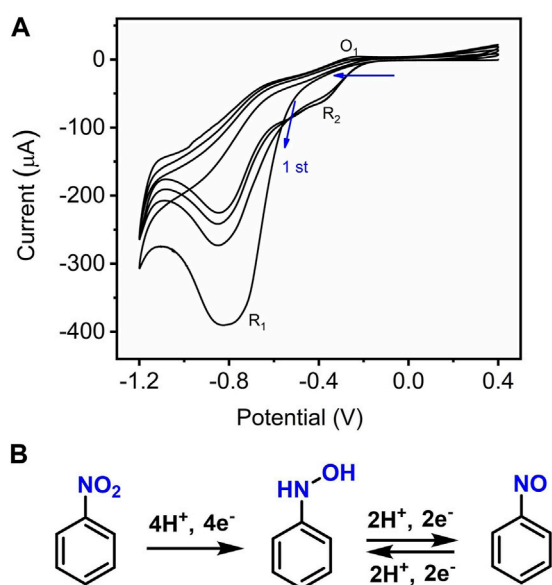
FIGURE 5
(A) CVs of Mn-CPM-99/ITO in 0.4 M NaCl (pH 7.0) containing 0.3 mM NB for four potential cycle scans; **(B)** Electrochemical redox processes of NB on the interface of Mn-CPM-99/ITO.

the disappearance of the N-H stretching vibration peak at 963 cm^{-1}, indicating the coordination of Mn to porphyrin ring in MnTCPPCl (Yu et al., 2020; Xu et al., 2021; Zhou et al., 2021). The signature of Mn-N bonds is also observed in the Mn-PCN-222 film. In contrast to MnTCPPCl, Mn-PCN-222 does not show the characteristic peaks of C=O bonds (1700 cm^{-1}) and C−O bonds (1270 cm^{-1}) whereas exhibits strong peak of −COO symmetric stretch bonds (1413 cm^{-1}), suggesting the carboxyl group coordinating to the Zr$_6$ centers in MnTCPPCl (Figure 2D). The results are agreement with those in the literature and which suggested the Mn-PCN-222 material was prepared successfully (Zhou et al., 2021). Similarly, the ATR-IR spectra of Mn-CPM-99 does not show the characteristic peaks near 1709 cm^{-1} (C=O bond) and 1273 cm^{-1} (C-O bond) of MnTCBPPCl and H$_2$TEtCBPP, while the emergence of a strong peak at 1417 cm^{-1} (COO symmetric stretching bond) reflects the carboxyl group coordinated to the Zr$_6$ cluster in MnTCBPPCl (Zhou et al., 2021; Zhu et al., 2021; Kaur et al., 2023). In addition, the metallation of the MnTCBPPCl ligand can be proved by the disappearance of the N-H stretching vibration at 960 cm^{-1} and the appearance of a new peak for the Mn-N bond at 1010 cm^{-1}. The UV-Vis spectra of both H$_2$TCPP and H$_2$TEtCBPP ligands present a strong Soret band and four Q-bands (Figures 2B, E). Furthermore, the Soret bands of Mn-PCN-222 and MnTCBPPCl films are noticed to undergo red shifts about
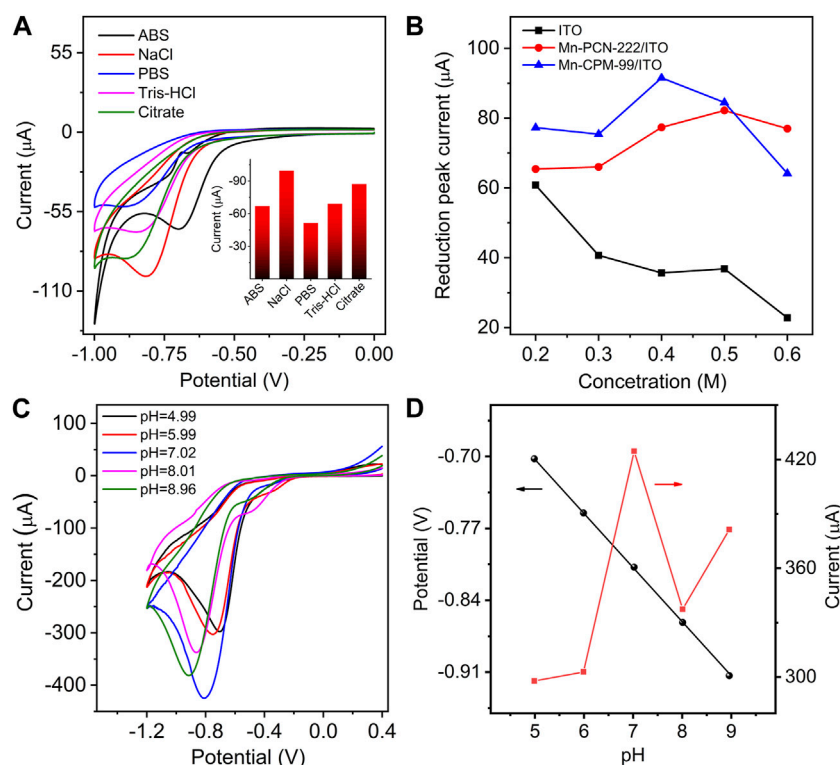
FIGURE 6
(A) CVs of Mn-CPM-99/ITO in different electrolyte solutions in the presence of 40.0 µM NB. (ABS: acetic acid buffer solution, PBS: phosphoric acid buffer solution, Tris-HCl: Tris (hydroxymethyl) aminomethane hydrochloride, Citate: Sodium citrate-citric acid buffer solutions; Concentration of every solution: 0.4 M). Inset: The reduction peak current in different electrolyte solutions. **(B)** The reduction peak currents of NB at different electrodes in NaCl solution with various concentration from 0.20 to 0.60 M **(C)** CVs of Mn-CPM-99/ITO toward 0.30 mM NB of in 0.40 mM NaCl with different pH. **(D)** Change in the reduction peak potential and current at different pH obtained from **(C)**.
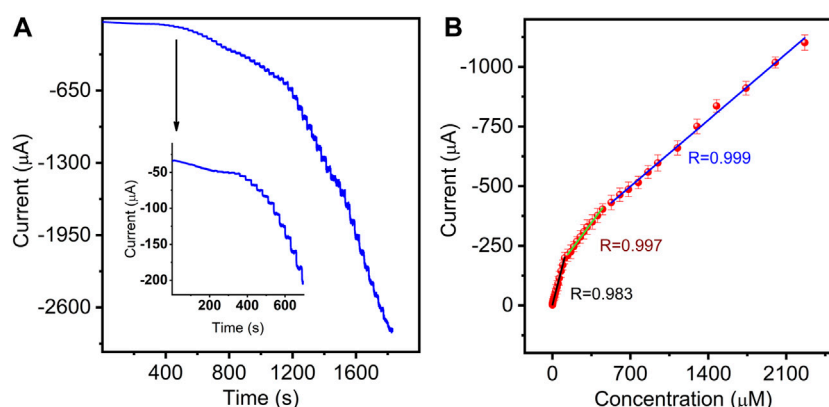
FIGURE 7
(A) Amperometric responses of the sensor in 3.0 mL stirring 0.4 M NaCl aqueous solution with successive additions of NB (0.005−2266 µM). **(B)** Corresponding calibration curves between electrocatalytic currents and NB concentrations (error bars represent standard deviations for three tests).

50 nm, and only two Q bands can be observed, confirming the metalation of porphyrin rings by Mn(III) in the Mn-PCN-222 films. Moreover, there is no characteristic peak of the free TCPP or other new metallized TCPP, indicating the absence of Mn leaching and substitution by other metal ions during the synthesis of Mn-PCN-222 films.

Powder X-ray diffraction (PXRD) patterns of Mn-PCN-222 and Mn-CPM-99 were recorded in Figures 2C, F. The results show that the intense diffraction peaks of Mn-PCN-222 are in good agreement with the simulated XRD profile, which indicate that the three-dimensional Mn-PCN-222 has been successfully prepared. Figure 2F displays the XRD patterns of Mn-CPM-99 which the
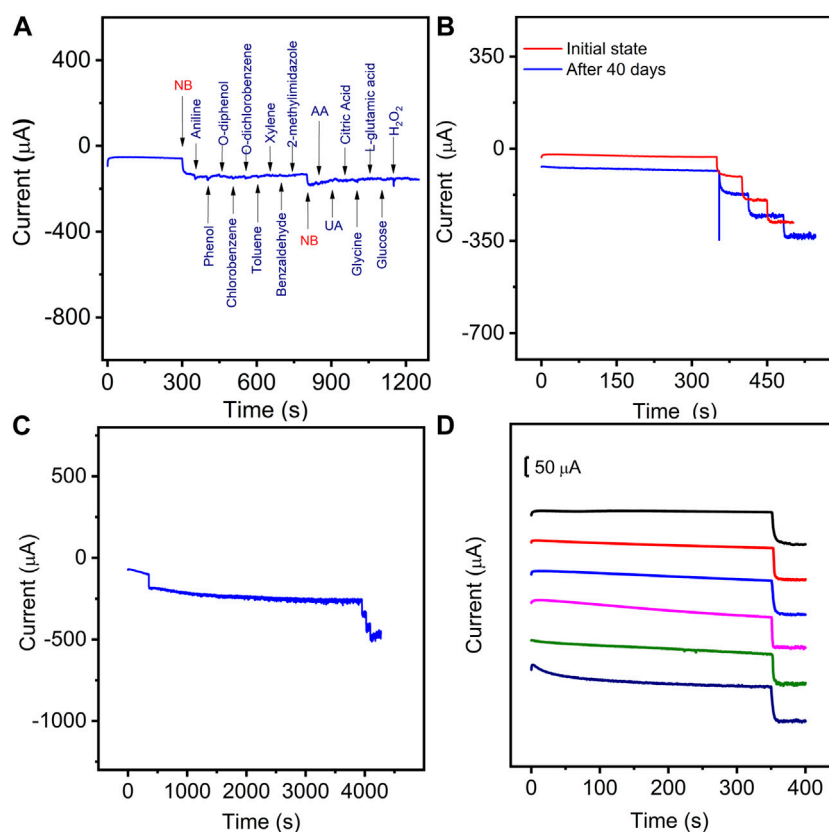
FIGURE 8
(A) Amperometric responses of the Mn-CPM-99/ITO sensor in 3.0 mL stirring 0.4 M NaCl aqueous solution with successive additions of 50.0 µM NB, 200 µM Aniline, phenol, o-diphenol, chlorobenzene, o-dichlorobenzene, Toluene, xylene, benzaldehyde, 2-Methylimidazole, AA, UA, citric acid, Glycine, L-glutamic acid, glucose, and H₂O₂ at the applied potential of −0.8V. **(B)** Storage stability of the Mn-CPM-99/ITO sensor in response to 50.0 µM NB after 40 days. **(C)** Successive current response of the sensor toward 50.0 µM NB before and after 4000 s response. **(D)** The current-time curves of six Mn-CPM-99/ITO electrodes toward 50 µM NB.

TABLE 1 Detection of NB in the real samples.

| Samples	Added (µM)	Average detected value (µM)	Average recovery (%)	Mean relative standard deviation (%)
River water	–[a]	–	–	–
	3.00	3.01	100.2	3.17
	6.00	5.93	98.9	3.70
Pakchoi vegetable	–	0.85	–	4.39
	5.00	5.87	100.4	1.16
	10.00	11.03	101.8	0.70

[a]NB, could not be detected.

plane of (100) is located at 2θ of 3.5°. Meanwhile, the broad peak around 2θ of 7° is attributed to the X-ray diffraction peak broadening by amorphization effect. These results indicate the existence of nanocrystals with tiny size in the structure of Mn-CPM-99. More evidences in Supplementary Figure S5 exhibit that Mn-CPM-99 are combined by the nanocrystals sizing of ca. 5.9 nm and organic ligands with disordered structures. Further, the calculated interplanar spacing of the nanocrystals is about 1.28 nm which is corresponding to the plane of (200) locates at 6.94° (Kollias et al.,

2022; Xu et al., 2022). Then, the highly dispersed diffraction ring in Supplementary Figure S6 of the selected electron diffraction pattern confirms Mn-CPM-99 possess typical amorphous structure. The abovementioned results are identical to the conclusion of the XRD pattern for Mn-CPM-99.

The elemental valence states of Mn-PCN-222 and Mn-CPM-99 materials were investigated using XPS analysis, respectively. The full XPS survey spectra are shown in Figures 3A, D and demonstrate the presence of the C, N, Cl, O, Mn, and Zr elements in the

Mn-PCN-222 and Mn-CPM-99 materials, which are in good agreement with the above-mentioned results of the EDX energy spectra. In Figure 3B, the three peaks at 288.07 eV, 284.80 eV, and 284.48 eV in the C 1s spectra are attributed to the C-O/C-N, C-C, C=O/C=N valence bonding structure of the TCPP framework, respectively. Correspondingly, the three resolved peaks from the C 1s spectra at 287.81 eV, 284.80 eV and 283.96 eV are attributed to the C-O/C-N, C-C, C=O/C=N valence bond structures of the TCBPP framework, respectively (Figure 3E). Figures 3C, F show the peaks at 399.98, 398.98 and 401.18 eV in Mn-PCN-222 and 397.47, 398.75, and 399.89 eV in Mn-CPM-99 for the N 1s, corresponding to C-N, C-N-Mn-C, and C-N-Mn=C, respectively. Both of the Mn 2P XPS spectra of the Mn-PCN-222 (Supplementary Figure S7A) and Mn-CPM-99 (Supplementary Figure S7B) show four peaks for two oxidation states of Mn(III) and Mn(II) in $2P_{1/2}$ and $2P_{3/2}$ bimodal states, respectively. The amplified spectrum of O 1s (Supplementary Figure S7C, D) can be deconvoluted into three peaks (531.06, 532.3 and 529.65 eV in Mn-PCN-222; 532.5, 531.9 and 530.37 eV in Mn-CPM-99), which are attributed to the C=O, Zr-O, and C-O valence bond structures, respectively. These results confirm the successful preparation of Mn-PCN-222 and Mn-CPM-99.

3.2 Electrochemical properties of the different modified electrodes

Mn-PCN-222 and Mn-CPM-99 were rapidly integrated on ITO glass by modular assembly method to obtain the Mn-PCN-222/ITO and Mn-CPM-99/ITO modified electrodes, which were characterized by CV technology and electrochemical impedance method. The CV curves of the ITO, Mn-PCN-222/ITO, and Mn-CPM-99/ITO electrodes were recorded in 5 mM $[Fe(CN)_6]^{3-/4-}$ solution with 0.1 M KCl at a scan rate of 50 mV·s^{-1} (Figure 4A). Compared to the ITO and Mn-PCN-222/ITO electrodes, the Mn-CPM-99/ITO electrode shows the best reversible redox peaks and largest peak currents. All their corresponding Nyquist plots in 5 mM $[Fe(CN)_6]^{3-/4-}$ solution Figure 4B show very small resistivity (R_{ct}). But the R_{ct} value of the Mn-CPM-99/ITO electrode (34 Ω) is significantly lower than those of Mn-PCN-222/ITO (86 Ω) and ITO (124 Ω). The results can be attributed to the strong synergistic effect between the organic ligand and the zirconium clusters after ring extension, resulting in more active sites, lower charge transfer resistance, and a larger contact area between the electrode and electrolyte. The CV curves of the Mn-CPM-99/ITO, ITO, and Mn-PCN-222/ITO electrodes at different scan rates (20–200 mV·s^{-1}) are shown in Figure 4C and Supplementary Figure S8. There are good linear relationships between the redox peak currents and the square root of the scan rates. The good linearity indicates that the redox process of the $[Fe(CN)_6]^{3-/4-}$ probe is a diffusion-controlled process at the modified electrodes. According to the Randles-Sevcik equation (Supplementary Figure S8), the electrochemically active surface areas of ITO, Mn-PCN-222/ITO and Mn-CPM-99/ITO were calculated to be 0.353, 0.497, and 0.558 cm^2, respectively, and therefore, the significantly larger active surface area of Mn-CPM-99/ITO provides obvious advantages for NB detection.

To investigate the catalytic activities, the CV responses of the modified electrodes were recorded in 0.4 M NaCl. As shown in Figure 4D, in the absence of NB, three different electrodes do not show obvious reduction peaks, but show different capacitive characteristics from ITO, Mn-PCN-222/ITO, and Mn-CPM-99/ITO modified electrodes due to their porosity and specific surface area. In the presence of NB, Mn-CPM-99/ITO shows sharp and well-defined reduction peak with the highest peak currents and more positive reduction potentials compared to other modified and unmodified electrodes (Figure 4E). Based on the special structure of the manganese metal porphyrin-based MOFs, the higher electrocatalytic activity for NB can be ascribed to reasons as follows: Firstly, the highly conjugated porphyrin ring (π–π stacking interaction with the NB molecules) and the large specific surface of Mn-PCN-222 and Mn-CPM-99 as the porous substrates enable the sensor interface to effectively trap NB molecules; Secondly, the inherent redox activity of the organic ligands TCPP and TCBPP, and the reduction of the electron intermediate of Mn(III) to Mn(II) state in the center of Mn-PCN-222 and Mn-CPM-99 structure contribute to the acceleration of electron transport, which were confirmed by the electrocatalysis of NB on TCPP/ITO, TCBPP/ITO, MnTCPP/ITO, and MnTCBPP/ITO electrodes (Supplementary Figure S9). In addition, the strong electron-withdrawing property of NB itself leads to the formation of an electron donor-acceptor (EDA) system between the porphyrin centers, which facilitates the transfer of electrons to the nitrobenzene, causing its protonation and ultimately leading to the reduction of NB (Zhou et al., 2021).

Figure 4F shows a typical CV response of the Mn-CPM-99/ITO sensor upon continuous addition of NB in 0.4 M NaCl solution. The dramatic increase in the reduction peak currents of NB suggested that the presented sensor showed typical electrocatalytic reduction of NB. In order to study the electrochemical process, CV of 0.5 mM NB was continuously scanned with a wider potential range between 0.4 V and −1.2 V (Figure 5A). During the first sweep, CV of NB at Mn-CPM-99/ITO presents only an irreversible cathodic peak (R_1) at −0.8 V, which is related to the 4H$^+$/4e$^-$ reduction of the nitro group (−NO$_2$) in NB to phenylhydroxylamine. Starting from the second cycle scan, the reduction peak at −0.83 V gradually decreases, and a pair of new redox peaks (O_1/R_2) gradually appear and increase between −0.2 V and −0.4 V, which corresponds to is the 2H$^+$/2e$^-$ redox process between phenylhydroxylamine and nitrosobenzene (Li et al., 2023; Yuan et al., 2023). The results suggested that phenylhydroxylamine was gradually produced by electrochemical reduction of NB, and then was oxidized to nitrosobenzene, appearing a new reduction peak (R_2). The overall redox mechanism of NB is summarized in Figure 5B.

3.3 Effect of the electrolyte solutions and pH

To achieve the best electrochemical response, the effects of different electrolyte solutions, electrolyte concentration, and pH of the solution on the electrocatalysis of the sensor toward NB were investigated (Sang et al., 2014; Stergiou et al., 2022). In different electrolyte and buffer solutions, the best response of the Mn-CPM-99/ITO electrode toward NB was obtained in NaCl solution (Figure 6A and inset). Figure 6B and Supplementary

Figure S10 show the electrochemical reduction of 40 μM NB in NaCl solution with various concentrations from 0.2 M to 0.6 M. Obviously, the maximum current of NB could be obtained in 0.4 M NaCl solution. Therefore, 0.4 M NaCl solution was chose as an electrolyte concentration in the following study.

Figure 6C shows the dependence of the sensor on pH. The reduction peak potential shifted negatively with increasing pH. The maximum electrocatalytic current was observed at pH seven and a good linear relationship between peak potential and pH was obtained: Ep (V) = −0.0529 pH−0.438 (Figure 6D). The slope of −0.0529 V/pH is very close to the theoretical value of 0.059 V/pH. The result indicates that an equal number of electrons and protons is involved in the NB electrochemical reduction process (Yuan et al., 2023), which is consistent with the proposed redox mechanism of NB in Figure 5B. All the electrochemical results suggest that Mn-CPM-99/ITO has better response sensitivity to NB and it is more suitable as an electrochemical sensor for detecting NB in aqueous solution.

3.4 Amperometric (i-t) determination of NB on Mn-CPM-99/ITO

To obtain higher response sensitivity, the chronoamperometric technique was performed. As shown in Figure 7A, upon successive addition of different concentrations of NB into stirred solution, the sensor exhibited rapid and typical amperometric current response to NB at the applied potential of −0.77 V. The inset of Figure 7A shows a magnified plot of the reduced current response at low NB concentration. The reduction peak currents grew linearly with the increase in three NB concentration ranges from 5 nM to 109.5 μM, 136.7–450.2 μM, and 527.5–2266 μM (Figure 7B) with the corresponding sensitivities of 1.817 (R = 0.983), 0.621 (R = 0.997), and 0.398 μA μM^{-1} (R = 0.999), respectively. Obviously, at low concentration, the sensor showed higher sensitivity for NB determination due to more available catalytic sites. The limit of detection (LOD) was calculated as low as 1.3 nM (Wu et al., 2018), which is lower than the permissible limit in water (16.25 μM) regulated by APHA (Li et al., 2023). The analytical performances are comparable with those in previously reported NB sensors (Supplementary Table S1).

3.5 Analytical performance of the proposed sensor

The selectivity of the presented sensor towards Nb was first evaluated by adding 4-fold interfering substances using the amperometric (i-t) method. As shown in Figure 8A, the current responses on NB were not interfered by the injection of the common organics (aniline, phenol, o-diphenol, chlorobenzene, o-dichlorobenzene, toluene, xylene, benzaldehyde, 2-methylimidazole), biomolecules (ascorbic acid (AA), uric acid (UA), citric acid, glycine (Gly), L-glutamic acid (L-GAA), glucose (Glu), and hydrogen peroxide (H$_2$O$_2$). Some common cations in aqueous solution were also evaluated including K$^+$, Na$^+$, Ca^{2+}, Mg^{2+}, Fe^{2+}, Ni^{2+}, Fe^{3+}, and Cr^{3+} (Supplementary Figure S11). The current response of the interfering metal cations is obviously lower than that

of NB at the same concentration level. These results indicate that the proposed sensor has good selectivity for NB detection.

The repeatability and stability reveal the potential capabilities of the proposed method for practical applications. The long-term storage stability of the sensor was evaluated by measuring the response currents of NB for 40 days of storage (Figure 8B), which showed that all the current responses towards three concentrations of NB retained over 97% of their original currents. In Figure 8C, the catalytic current of 50 μM NB does not decay for 4000 s of successive response, furthermore, the sensor still shows a sensitive response to NB, indicating good operational stability. The reproducibility of the sensor was evaluated by utilizing six modified electrodes on different GCEs. As shown in Figure 8D, the relative standard deviations were calculated to be 3.4%, indicating high reproducibility. Therefore, the satisfactory stability and reproducibility suggest that Mn-CPM-99/ITO is potentially applicable as a reliable sensor for the determination of NB in real water samples.

3.6 Analysis of real samples

The practicality of the Mn-CPM-99/ITO electrode was verified by the determination of NB in river water and vegetable (Pakchoi) samples. The Pakchoi vegetable was sprayed with 5 mL 20 mM NB solution. After 1 day, 3 g of fresh leaves were grinded and dissolved in 10 mL ethanol, which was then centrifuged at 6000 rpm. The obtained supernatant of vegetable and river water were filtered through 0.22 μm membrane filter and used directly for the actual sample analysis by standard addition method (Supplementary Figure S12). As shown in Table 1, NB in river water could not be detected while an average of 0.85 μM NB could be detected in the NB-pretreated vegetable samples. All of the recoveries with the added NB standard solution ranged from 98.8% to 101.8%, indicating that the electrochemical sensor based on Mn-CPM-99 MOF has good utility for the determination of NB content in real water or vegetables.

4 Conclusion

In conclusion, a concave quadrangular bipyramidal Mn-CPM-99 MOF was successfully designed based on the coordination reaction between MnTCBPPCl organic ligands and Zr$_6$ clusters. The structure and electrochemical properties of Mn-CPM-99 MOF were compared with those of Mn-PCN-222 MOF with rod-shaped structure (constructed form TCPP and Zr$_6$). Due to the broadened chain of TCPP organic ligands by the phenyl group, Mn-CPM-99 MOF shows the bipyramidal structure with higher porosity and larger specific surface area than those of Mn-PCN-222. After comparing their morphology, electrochemical behavior, and electrocatalytic ability, it is found that Mn-CPM-99 modified ITO electrode has better electrocatalytic performances towards NB reduction. The high sensitivity and selectivity, low LOD, wide linear concentration range, and good reproducibility make the presented sensor (Mn-CPM-99/ITO) successfully applied to the detection of NB in river water and vegetable samples. Therefore, the strategy based on the structural design will broaden the

application of the porphyrin-based MOF materials and provide a new platform to study the relationship between structural improvement and its function.

Data availability statement

The original contributions presented in the study are included in the article/Supplementary Material, further inquiries can be directed to the corresponding authors.

Author contributions

LW: Formal Analysis, Investigation, Writing–original draft. Mengjie Zhang: Formal Analysis, Investigation, Writing–original draft. YL: Formal Analysis, Investigation, Writing–original draft. XC: Formal Analysis, Investigation, Writing–original draft. HQ: Formal Analysis, Resources, Writing–review and editing. JY: Investigation, Resources, Writing–review and editing. SF: Conceptualization, Funding acquisition, Software, Writing–review and editing. HW: Funding acquisition, Writing–original draft, Writing–review and editing.

Funding

Conflict of interest

The authors declare that the research was conducted in the absence of any commercial or financial relationships that could be construed as a potential conflict of interest.

Publisher's note

All claims expressed in this article are solely those of the authors and do not necessarily represent those of their affiliated organizations, or those of the publisher, the editors and the reviewers. Any product that may be evaluated in this article, or claim that may be made by its manufacturer, is not guaranteed or endorsed by the publisher.

Supplementary material

The Supplementary Material for this article can be found online at: https://www.frontiersin.org/articles/10.3389/fchem.2024.1380551/full#supplementary-material

References

Bindu, P., and Thomas, S. (2014). Estimation of lattice strain in ZnO nanoparticles: X-ray peak profile analysis. J. Theor. 8, 123–134. doi:10.1007/s40094-014-0141-9

Chang, Y., Lou, J. X., Yang, L. Y., Liu, M. M., Xia, N., and Liu, L. (2022). Design and application of electrochemical sensors with metal–organic frameworks as the electrode materials or signal tags. Nanomater 12, 3248. doi:10.3390/nano12183248

Chellappa, V., Meenakshisundaram, N., Annaraj, J., and Sagadevan, S. (2024). Hydrothermal synthesis of MnO₂ nanorods for efficient electrochemical detection of environmental anthropogenic pollutants and nitrobenzene. Inorg. Chem. Commun. 160, 112015. doi:10.1016/j.inoche.2023.112015

Chen, X., Feng, X. Z., Zhan, T., Xue, Y. T., Li, H. X., Han, G. C., et al. (2023). Construction of a portable enzyme-free electrochemical glucose detection system based on the synergistic interaction of Cu-MOF and PtNPs. Sens. Actuators B Chem. 395, 134498. doi:10.1016/j.snb.2023.134498

Dhayanithi, C. A., Palpandi, K., Raman, N., and Babu, S. G. (2023). Development of amine-based transition metal MOFs as efficient electrochemical sensors for the detection of chloramphenicol in food and pharmaceutical samples. Electrochim. Acta 470, 143358. doi:10.1016/j.electacta.2023.143358

Fang, Y., Wang, D., Lv, X., Xu, X., Zhou, H., Liu, P., et al. (2021). Simultaneous electrochemical determination of nitrophenol isomers Based on spirofluorene - based microporous polymer film modified electrodes through one-step electropolymerization strategy. Sens. Actuators B Chem. 333, 129568. doi:10.1016/j.snb.2021.129568

Feng, D., Gu, Z., Li, J., Jiang, H., Wei, Z., and Zhou, H. (2012). Zirconium-metalloporphyrin PCN-222: mesoporous metal-organic frameworks with ultrahigh stability as biomimetic catalysts. Angew. Chem. Int. Ed. 124, 10453–10456. doi:10.1002/ange.201204475

Junior, D. W., Hryniewicz, B. M., and Kubota, L. T. (2024). Advanced hybrid materials in electrochemical sensors: combining MOFs and conducting polymers for environmental monitoring. Chemosphere 352, 141479. doi:10.1016/j.chemosphere.2024.141479

Kajal, N., Singh, V., Gupta, R., and Gautam, S. (2022). Metal organic frameworks for electrochemical sensor applications: a review. Environ. Res. 204, 112320. doi:10.1016/j.envres.2021.112320

Kaur, G., Anthwal, A., Kandwal, P., and Sud, D. (2023). Mechanochemical synthesis and theoretical investigations of Fe (II) based MOF containing 4, 4′-bipyridine with ordained intercalated p-aminobenzoic acid: application as fluoroprobe for detection of carbonyl group. Inorg. Chim. Acta 545, 121248. doi:10.1016/j.ica.2022.121248

Kollias, L., Rousseau, R., Glezakou, V. A., and Salvalaglio, M. (2022). Understanding metal–organic framework nucleation from a solution with evolving graphs. J. Am. Chem. Soc. 144, 11099–11109. doi:10.1021/jacs.1c13508

Koohfar, S., Ghasemi, M., Hafen, T., Dimitrakopoulos, G., Kim, D., Pike, J., et al. (2023). Improvement of oxygen reduction activity and stability on a perovskite oxide surface by electrochemical potential. Nat. Commun. 14, 7203. doi:10.1038/s41467-023-42462-5

Li, S., Fang, J., Li, L., Zhu, M., Zhang, F., Zhang, B., et al. (2021). An ultra-sensitive electrochemical sensor of Ni/Fe-LDH toward nitrobenzene with the assistance of surface functionalization engineering. Talanta 225, 122087. doi:10.1016/j.talanta.2021.122087

Li, W., Zhao, J., Yan, C., Dong, B., Zhang, Y., Li, W., et al. (2022). Asymmetric activation of the nitro group over a Ag/graphene heterointerface to boost highly selective electrocatalytic reduction of nitrobenzene. ACS Appl. Mat. Interfaces 14, 25478–25489. doi:10.1021/acsami.2c04533

Li, Y., Zhuge, R., and Zhang, T. (2023). MOF-conductive polymer composite electrode as electrochemical sensor of nitrobenzene. Inorg. Chem. Commun. 154, 110904. doi:10.1016/j.inoche.2023.110904

Lin, Q., Bu, X., Kong, A., Mao, C., Zhao, X., Bu, F., et al. (2015). New heterometallic zirconium metalloporphyrin frameworks and their heteroatom-activated high-surface-area carbon derivatives. *J. Am. Chem. Soc.* 137, 2235–2238. doi:10.1021/jacs.5b00076

Liu, C. S., Li, J. J., and Pang, H. (2020). Metal-organic framework-based materials as an emerging platform for advanced electrochemical sensing. *Coord. Chem. Rev.* 410, 213222. doi:10.1016/j.ccr.2020.213222

Lu, A., Xiang, X., Lei, M., Huang, S., Liang, B., Zhao, S., et al. (2023). Highly efficient catalytic transfer hydrogenation for the conversion of nitrobenzene to aniline over PdO/TiO$_2$: the key role of *in situ* switching from PdO to Pd. *J. Environ. Sci.* 148, 515–528. doi:10.1016/j.jes.2023.10.010

Papavasileiou, A. V., Antonatos, N., Luxa, J., Dekanovský, L., Ashtiani, S., Fomekong, R. L., et al. (2024). Two-dimensional VSe$_2$ nanoflakes as a promising sensing electrocatalyst for nitrobenzene determination in water samples. *Electrochim. Acta* 475, 143653. doi:10.1016/j.electacta.2023.143653

Rafique, S., Irshad, H., Majeed, S., Rubab, R., Imran, M., Khan, A. M., et al. (2023). AIEE active stilbene based fluorescent sensor with red-shifted emission for vapor phase detection of nitrobenzene and moisture sensing. *J. Photochem. Photobiol. A* 437, 114459. doi:10.1016/j.jphotochem.2022.114459

Rahman, N., and Ahmad, I. (2024). Coordination polymer gel mediated spectrophotometric, ICP-AES and spectrofluorimetric methods for trace As(III) determination in water and food samples. *Chemosphere* 351, 141272. doi:10.1016/j.chemosphere.2024.141272

Sang, Y. T., Wang, B. Y., Wang, Q. C., Zhao, G., and Guo, P. Z. (2014). Insights into the electrocatalysis of nitrobenzene using chemically-modified carbon nanotube electrodes. *Sci. Rep.* 4, 6321. doi:10.1038/srep06321

Seal, K., Chaudhuri, H., Pal, S., Srivastava, R. R., and Soldatova, E. (2022). A study on water pollution scenario of the Damodar river basin, India: assessment of potential health risk using long term database (1980–2019) and statistical analysis. *Environ. Sci. Pollut. Res.* 29, 53320–53352. doi:10.1007/s11356-022-19402-9

Stergiou, A. D., Broadhurst, D. H., and Symes, M. D. (2022). Electrochemical reduction of nitrobenzene via redox-mediated chronoamperometry. *Star. Protoc.* 3, 101817. doi:10.1016/j.xpro.2022.101817

Wang, K., Zhao, J., Zhang, X., Jiang, L., Zhou, X., Xie, C., et al. (2023). Fluorescent noncovalent organic framework for supporting gold nanoparticles as heterogeneous catalyst with merits of easy detection and recycle. *Small* 20, e2303834. doi:10.1002/smll.202303834

Wang, S., and Chen, H. (2002). Separation and determination of nitrobenzenes by micellar electrokinetic chromatography and high-performance liquid chromatography. *J. Chromatogr. A* 979, 439–446. doi:10.1016/s0021-9673(02)01435-8

Wang, W., Wang, Y., Zhao, X., Li, Y., He, H., Lian, L., et al. (2024). Surface oxygen vacancies of TiO$_2$–x enabled water transfer photocatalytic hydrogenation of nitrobenzene to aniline without use of co-catalyst. *Chem. Eng. Sci.* 285, 119645. doi:10.1016/j.ces.2023.119645

Wang, X., Guo, A., Fu, Y., Tan, M., Luo, W., and Yang, W. (2023). Porphyrin-conjugated microporous polymer nanospheres as electrocatalysts for nitrobenzene

detection and oxygen evolution reaction. *ACS Appl. Nano Mat.* 6, 3226–3235. doi:10.1021/acsanm.2c04811

Weidenthaler, C. (2011). Pitfalls in the characterization of nanoporous and nanosized materials. *Nanoscale* 3, 792–810. doi:10.1039/c0nr00561d

Wu, H., Li, X., Chen, M., Wang, C., Wei, T., Zhang, H., et al. (2018). A nanohybrid based on porphyrin dye functionalized graphene oxide for the application in non-enzymatic electrochemical sensor. *Electrochim. Acta* 259, 355–364. doi:10.1016/j.electacta.2017.10.122

Xu, J., Li, W., Liu, W., Jing, J., Zhang, K., Liu, L., et al. (2022). Efficient photocatalytic hydrogen and oxygen evolution by side-group engineered benzodiimidazole oligomers with strong built-in electric fields and short-range crystallinity. *Angew. Chem. Int. Ed.* 61, e202212243. doi:10.1002/anie.202212243

Xu, Q. B., Zhan, G. T., Zhang, Z. L., Yong, T. Y., Yang, X. L., and Gan, L. (2021). Manganese porphyrin-based metal-organic framework for synergistic sonodynamic therapy and ferroptosis in hypoxic tumors. *Theranostics* 11, 1937–1952. doi:10.7150/thno.45511

Yang, J., Wang, Z., Hu, K. L., Li, Y. S., Feng, J. F., Shi, J. L., et al. (2015). Rapid and specific aqueous-phase detection of nitroaromatic explosives with inherent porphyrin recognition sites in metal–organic frameworks. *ACS Appl. Mat. Interfaces* 7, 11956–11964. doi:10.1021/acsami.5b01946

Yu, K., Puthiaraj, P., and Ahn, W. S. (2020). One-pot catalytic transformation of olefins into cyclic carbonates over an imidazolium bromide-functionalized Mn(III)-porphyrin metal–organic framework. *Appl. Catal. B Environ.* 273, 119059. doi:10.1016/j.apcatb.2020.119059

Yuan, C., Li, N., Zhang, X., Wang, Y., Zhou, S., Zhang, L., et al. (2023). Flower-like copper sulfide-decorated boron-nitrogen co-doped carbon-modified glassy carbon electrode for selective and sensitive electrochemical detection of nitrobenzene in natural water. *Colloids Surf. A-Physicochem. Eng. Asp.* 675, 132011. doi:10.1016/j.colsurfa.2023.132011

Zhang, G., Zhou, X., Zang, X., Li, Z., Wang, C., and Wang, Z. (2014). Analysis of nitrobenzene compounds in water and soil samples by graphene composite-based solid-phase microextraction coupled with gas chromatography–mass spectrometry. *Chin. Chem. Lett.* 25, 1449–1454. doi:10.1016/j.cclet.2014.05.049

Zhang, W. Q., Li, X. J., Ding, X. M., Hua, K., Sun, A., Hu, X. X., et al. (2023). Progress and opportunities for metal–organic framework composites in electrochemical sensors. *RSC Adv.* 13, 10800–10817. doi:10.1039/d3ra00966a

Zhang, X., Wasson, M. C., Shayan, M., Berdichevsky, E. K., Ricardo-Noordberg, J., Singh, Z., et al. (2021). A historical perspective on porphyrin-based metal–organic frameworks and their applications. *Coord. Chem. Rev.* 429, 213615. doi:10.1016/j.ccr.2020.213615

Zhou, Z. Y., Mukherjee, S., Hou, S. J., Li, W. J., Elsner, M., and Fischer, R. (2021). Porphyrinic MOF film for multifaceted electrochemical sensing. *Angew. Chem. Int. Ed.* 60, 20551–20557. doi:10.1002/anie.202107860

Zhu, Y., Zhang, Z., Cheng, J., Guo, H., and Yang, W. J. (2021). Ni-BTC metal-organic framework loaded on MCM-41 to promote hydrodeoxygenation and hydrocracking in jet biofuel production. *J. Hydrogen Energy* 46, 3898–3908. doi:10.1016/j.ijhydene.2020.10.216

Deep eutectic solvent-based shaking-assisted extraction for determination of bioactive compounds from Norway spruce roots

Alina Kalyniukova[1]*, Alica Várfalvyová[2], Justyna Płotka-Wasylka[3],
Tomasz Majchrzak[3], Patrycja Makoś-Chełstowska[4],
Ivana Tomášková[1], Vítězslava Pešková[1], Filip Pastierovič[1],
Anna Jirošová[1] and Vasil Andruch[2]

[1]Faculty of Forestry and Wood Sciences, Czech University of Life Sciences Prague, Prague, Czechia,
[2]Department of Analytical Chemistry, Institute of Chemistry, Faculty of Science, P. J. Šafárik University,
Košice, Slovakia, [3]Department of Analytical Chemistry, Faculty of Chemistry, Gdańsk University of
Technology, Gdańsk, Poland, [4]Department of Process Engineering and Chemical Technology, Faculty of
Chemistry, Gdańsk University of Technology, Gdańsk, Poland

Polyphenolic compounds play an essential role in plant growth, reproduction,
and defense mechanisms against pathogens and environmental stresses.
Extracting these compounds is the initial step in assessing phytochemical
changes, where the choice of extraction method significantly influences the
extracted analytes. However, due to environmental factors, analyzing numerous
samples is necessary for statistically significant results, often leading to the use of
harmful organic solvents for extraction. Therefore, in this study, a novel DES-
based shaking-assisted extraction procedure for the separation of polyphenolic
compounds from plant samples followed by LC-ESI-QTOF-MS analysis was
developed. The DES was prepared from choline chloride (ChCl) as the
hydrogen bond acceptor (HBA) and fructose (Fru) as the hydrogen bond
donor (HBD) at various molar ratios with the addition of 30% water to reduce
viscosity. Several experimental variables affecting extraction efficiency were
studied and optimized using one-variable-at-a-time (OVAT) and confirmed by
response surface design (RS). Nearly the same experimental conditions were
obtained using both optimization methods and were set as follows: 30 mg of
sample, 300 mg of ChCl:Fru 1:2 DES containing 30% w/w of water, 500 rpm
shaking speed, 30 min extraction time, 10°C extraction temperature. The results
were compared with those obtained using conventional solvents, such as
ethanol, methanol and water, whereby the DES-based shaking-assisted
extraction method showed a higher efficiency than the classical procedures.
The greenness of the developed method was compared with the greenness of
existing procedures for the extraction of polyphenolic substances from solid

---

Abbreviations: ABS, aqueous biphasic systems; CD, cyclodextrin; BAGI, blue applicability grade index;
ChCl, choline chloride; ComplexGAPI, complementary green analytical procedure index; DES, deep
eutectic solvents; Fru, fructose; HBA, hydrogen bond acceptor; HBD, hydrogen bond donor; NADES,
natural deep eutectic solvent; OVAT, one variable-at-a-time method; RS, response surface design; UAE,
ultrasound-assisted extraction; MAHD, microwave-assisted hydrodistillation; LoF, lack of fit; WAC, White
Analytical Chemistry.

plant samples using the complementary green analytical procedure index (ComplexGAPI) approach, while the results for the developed method were better or comparable to the existing ones. In addition, the practicability of the developed procedure was evaluated by application of the blue applicability grade index (BAGI) metric. The developed procedure was applied to the determination of spruce root samples with satisfactory results and has the potential for use in the analysis of similar plant samples.

1 Introduction

Secondary plant metabolites, mainly polyphenolic compounds, play an important role in the processes of growth, reproduction and the defense mechanisms of plants against pathogens and environmental stresses (Hartmann and Trumbore, 2016; Pang et al., 2021). They possess adaptive traits that have undergone natural selection through evolution or climate change. The extraction of secondary plant metabolites is the first step in evaluating phytochemical changes in plants. However, it should be noted that the extracted substances may depend on the extraction method chosen (Bentley et al., 2020). Due to the various environmental factors affecting the synthesis of certain compounds in plants, it is necessary to analyze a large number of samples to obtain statistically significant results, leading to the need to use a large amount of harmful organic solvents for extraction.

In line with the requirements of green chemistry, the current trend is to replace dangerous solvents with less harmful and environmentally friendly alternatives, as well as to reduce the total amount of solvents used. One possibility is the use of deep eutectic solvents (DES), which can be considered as promising green solvents for the extraction of bioactive compounds from complex matrix samples, such as fruits, vegetables and plants (Duan et al., 2016; Shishov et al., 2017; Vieira et al., 2018; Cai et al., 2019; El Kantar et al., 2019; Skarpalezos and Detsi, 2019; Bajkacz et al., 2020; Chen et al., 2020; Ivanović et al., 2020; Koel et al., 2020; Hikmawanti et al., 2021; Kalyniukova et al., 2021; Chen et al., 2022; Mansour et al., 2024). However, the high viscosity of most DESs is a fundamental limitation that can affect the extraction efficiency of the target compounds and subsequently complicate the quantification of analytes by instrumental methods. The addition of water can reduce the viscosity of DESs and thus increase the extraction efficiency (El Achkar et al., 2019; Rozas et al., 2021).

One of the most commonly used types of DES involves systems based on choline chloride as a hydrogen bond acceptor (HBA) in combination with various hydrogen bond donors (HBD), such as organic acids, urea or sugars. Recently, articles have been published devoted to DESs prepared from choline chloride and sugars to the study of the influence of the nature of the HBD (sucrose, glucose, fructose, and xylose) on the distribution behavior of selected compounds in a two-phase liquid–liquid system (Liu et al., 2022); to the use in an ultrasound-assisted dispersive liquid–liquid microextraction procedure for the extraction of aflatoxin M_1 in milk samples prior to its determination by UV–VIS spectrophotometry (Gürsoy et al., 2022); and as potential absorbents for NH_3 capture (Li et al., 2020). DESs based on choline chloride and d-fructose in different ratios were prepared, and their

physical properties, such as density, viscosity, surface tension, refractive index and pH, were investigated at different temperatures (25°C–85°C). The measured physical properties indicated that DESs have the potential to be used for various applications, including extraction processes (Hayyan et al., 2012).

In the extraction of bioactive compounds from solid plant samples, the mass transfer is usually supported by some auxiliary energy, for example, by ultrasound or shaking. Here are a few examples of using choline chloride-fructose DES for plant sample analysis: Razboršek et al. investigated different natural deep eutectic solvents (NADESs) based on choline chloride for the ultrasound-assisted extraction (UAE) of phenolic compounds from dried chokeberries and found that the highest values of total phenolics and total flavonoids were obtained using the choline chloride-fructose system. Additionally, the results were compared with those obtained using conventional methanol extraction, and their high extraction efficiency was demonstrated (Razboršek et al., 2020). Takla et al. presented a comparison of the potential of NADES and nonionic surfactants with conventional solvents (methanol, ethanol and water) for the ultrasound extraction of alkaloids from plant material. High-performance thin-layer chromatography was used for quantification. The highest extraction yields were obtained using a DES consisting of choline chloride:fructose (5:2) with 35% water. The results showed that a NADES and surfactants were much more efficient in extracting alkaloids than previous methods (Takla et al., 2018). NADESs prepared from choline chloride (ChCl) and sucrose, fructose, glucose and xylose were used for ultrasound-assisted extraction of antioxidants from the halophyte *Polygonum maritimum* L. (sea knotgrass) and compared with conventional solvents, such as ethanol and acetone. The obtained extracts were evaluated for *in vitro* antioxidant properties and profiled using liquid chromatography analysis. The results indicate that a NADES containing ChCl and sucrose/fructose can replace conventional solvents in the extraction of antioxidants from sea knotgrass (Rukavina et al., 2021).

Zhang et al. developed a selective shaking-assisted extraction of astaxanthin ester and free astaxanthin from *Haematococcus pluvialis* by aqueous biphasic systems (ABS) composed of ionic liquids and deep eutectic solutions. ABS composed of tributyloctylphosphine chloride and choline chloride:D-fructose performed the best. The results was compared with organic solvent extraction and prior methods (Zhang et al., 2024). A DES-based pretreatment followed by microwave-assisted hydrodistillation (MAHD) for the extraction of essential oil from dry fruits of white and black peppers was developed. The DES comprised of choline chloride and fructose at a molar ratio of 3:1 was used. The obtained essential oils were analyzed using gas chromatography-mass spectrometry (GC-MS), identifying more compounds than

TABLE 1 List of compounds monitored by LC-ESI-QTOF-MS/MS.

Compound	Formula	Retention time, min	Theoretical mass	Extracted mass	m/z	Fragments	Mass error, ppm
Taxifolin	$C_{15}H_{12}O_7$	2.96	304.0583	304.0596	303.0499	285.0404	−0.13
						177.0195	
						125.0245	
Catechin	$C_{15}H_{14}O_6$	1.21	290.0789	290.0783	289.0715	245.0819	0.44
						203.0716	
						151.0402	
						125.0244	
						109.0296	
Procyanidin B1	$C_{30}H_{26}O_{12}$	1.03	578.1419	578.1429	577.1350	451.1019	0.86
						425.0876	
						289.0713	
						161.0243	
						125.0242	
Epigallocatechin	$C_{15}H_{14}O_7$	1.06	306.0740	306.0742	305.0671	261.0788	0.78
						219.0651	
						167.0350	
						125.0242	
4-Coumaric acid	$C_9H_8O_3$	1.95	164.0474	164.0474	163.0401	119.0504	0.08
						91.0550	
Epicatechin	$C_{15}H_{14}O_6$	1.93	290.0790	290.0794	289.0721	245.0824	1.30
						174.9566	
						125.0243	
Piceatannol	$C_{14}H_{12}O_4$	3.41	244.0738	244.0736	243.0664	201.0554	−0.01
						130.9660	
Isorhapontin	$C_{21}H_{24}O_9$	3.54	420.1417	420.1420	419.1288	257.0819	1.01
						241.0521	
						178.9524	

hydrodistillation (Yu et al., 2017). García et al. developed an electrokinetic chromatography method enabling separation of the four stereoisomers of the acetamide herbicide dimethenamid. They tested different anionic cyclodextrins (CDs) based on the use of single and dual CD systems with the addition of ionic liquids and DESs and found that choline chloride-D-fructose, when added to the CDs dual system, enabled separating the four stereoisomers of dimethenamid (Angeles Garcia et al., 2022).

The aim of this work was to develop a novel shaking-assisted extraction method for phenolic compounds from plant samples using a green extraction solvent, a DES based on choline chloride as the HBA and fructose as the HBD. Despite the popularity of ChCl-based DES for analytical purposes, the mixtures of ChCl with Fru are less investigated, especially for plant analysis. That is why we focused on this combination. The parameters influencing the extraction efficiency were investigated by the one variable-at-a-time method (OVAT) and a response surface design (RS) based on face-centered central composite design. The method was subsequently applied to the analysis of Norway spruce root samples in conjunction with LC-ESI-QTOF-MS quantification of polyphenolic compounds.

2 Methods

2.1 Chemicals

The DES was composed of choline chloride (ChCl) (purity ≥99%) obtained from Gentham Life Science, UK, and D (−)fructose (Fru) (purity ≥99%) purchased from Acros Organics, United States. The solvents, such as methanol (purity ≥99.9%), acetonitrile (purity ≥99.9%)

and water (LC-MS grade), were obtained from Honeywell, Germany. The chemical standards were obtained as follows: piceatannol (purity ≥98%), epicatechin (purity ≥98%), procyanidin B1 (purity ≥98%), (−)-epigallocatechin (purity ≥98%) and taxifolin (purity ≥98%) from Chem Faces, China; isorhapontin (purity ≥98%) from Toronto Research Chemicals, Canada; 4-coumaric acid (purity ≥98%) and (+)-catechin (purity ≥98%) from Extrasynthese, France. Ultra-pure water was obtained using a Millipore Milli-Q Plus water treatment system (Millipore Bedford Corp., Bedford, MA).

2.2 LC-ESI-QTOF-MS/MS analysis

LC-ESI-QTOF-MS/MS analysis was carried out using an Agilent 1,290 Infinity II system coupled to an Agilent 6546 LC/MS QTOF mass spectrometer (Agilent, United States). The LC separation was conducted using a Zorbax Eclipse Plus C18 column (2.1 × 50 mm, 1.8 μm), (Agilent, United States). The optimal conditions were as follows: mobile phase A consisted of water containing 0.05% formic acid, and mobile phase B consisted of acetonitrile; flow rate, 1.1 mL min^{-1}; injection volume, 1 μL; and column temperature, 35°C. For separation of polyphenolic compounds, the gradient elution was set as follows: 0–0.1 min, 95% A; 0.one to eight min, 72% A; 8–9.1 min, 25% A; 9.1–11 min, 95% A.

The determination of polyphenolic compounds (Table 1) was carried out by LC-MS/MS in negative ionization mode. The QTOF parameters were optimized using the standards and were set as follows: scan range 100–1,000 m/z; drying gas temperature, 350°C; sheath gas flow rate, 12.0 L/min; sheath gas temperature, 400°C; capillary voltage, 5.0 kV; nozzle voltage 0.9 kV; fragmentor, 140 V; collision energy at 10, 20 and 40 eV. MS/MS data were acquired at a scan range of 50–800 m/z; retention time window, 0.5 min; isolation window, 1.3 amu and an acquisition rate of two spectra s^{-1}. During the analysis, two reference masses (112.9855 and 966.0007 m/z) were continuously measured to mass correction. The data collection was carried out using the Agilent Mass Hunter Acquisition software, and data analysis was performed using Mass Hunter Qualitative Analysis 10.0 and Q-TOF Quantitative analysis (Agilent, United States).

2.3 Sample collection

Norway spruce root samples (*Picea abies* L.) were collected from a depth of 15 cm approximately 1 m from the stem base in the Ore Mts (GPS coordinates 50.65 lat and 13.63 long). The roots were rinsed from the soil, inserted into conical tubes and placed into liquid nitrogen immediately. Samples were freeze-dried, homogenized, passed through 50 μm analytical sieve, and stored at −80°C before LC-ESI-QTOF-MS analysis.

2.4 Preparation of the deep eutectic solvents

Choline chloride (HBA) was mixed with fructose (HBD) in different molar ratios (1:1, 1:2, 2:1 and 5:2) with the addition of 30% water w/w to reduce the viscosity, and the mixtures were stirred at 350 rpm at 60°C on a heating magnetic stirrer (Witeg MSH-20D, Germany) until a transparent liquid was formed.

2.5 General extraction procedure

A 30 mg sample was precisely weighed in 2-mL test tube and 300 mg of DES was added. Then, 200 μL of water was added, and the sample was vortexed and placed into the thermoshaker (Bioer, China) for 30 min at 500 rpm. After extraction, the sample was centrifuged at 13,000 rpm for 5 min; 200 μL of collected supernatant was transferred to a new dry test tube, diluted with 800 μL of methanol, filtered through a 0.22 μm PTFE filter and injected into the LC system.

2.6 Response surface design

In order to validate findings from OVAT optimization, the response surface design was performed. The selected face-centered central composite design with five replicates on the center point was used to find optimal values of shaking speed, extraction time and extraction temperature. The outcome of the RS was a maximizing of the area under the peak of procyanidin B1, catechin, epicatechin and taxifolin. The RS was performed using Minitab v. 17.1.0 (LEAD Technologies, Inc.), and surface plots were generated using in-house Python code. The residues distribution of the obtained models were checked to determine their close to normal distribution characteristics. The residues distribution for catechin and procyanidin B1 were found to be asymmetric; thus Box-Cox transformation of the model input data for those compounds was proposed (the 'find optimal λ' option was implemented) giving satisfactory results. The RS is presented in detail in the Supplementary Materials.

2.7 Green assessment tools

The complementary green analytical procedure index (ComplexGAPI) (Płotka-Wasylka and Wojnowski, 2021) was used as the green assessment tool. In addition to the green character evaluation, an assessment of the method practicality was performed. For this purpose, the blue applicability grade index (BAGI) (Manousi et al., 2023) was applied.

3 Results and discussion

Parameters affecting the extraction efficiency, such as the choline chloride and fructose molar ratio, shaking speed, extraction time, extraction temperature and addition of water, were investigated.

3.1 Effect of choline chloride and fructose molar ratio

In general, we can consider DESs as promising solvents in extraction and separation processes (Zainal-Abidin et al., 2017). However, the ability of a DES to extract bioactive compounds from plant samples depends on various factors, such as the type of HBA and HBD used as well as their molar ratio. Therefore, ChCl:Fru DESs with various molar ratios were tested for the extraction of polyphenolic compounds from spruce roots. Supplementary Figure S1 shows that the highest extraction yield was obtained for the DES

FIGURE 1
Comparison of DES extraction ability with conventional solvent. Extraction conditions: sample amount, 30 mg; DES amount, 300 mg; solvent amount, 500 μL, water volume, 200 μL (in the case of DES); extraction temperature, 10°C; shaking speed, 500 rpm, extraction time, 5 min.
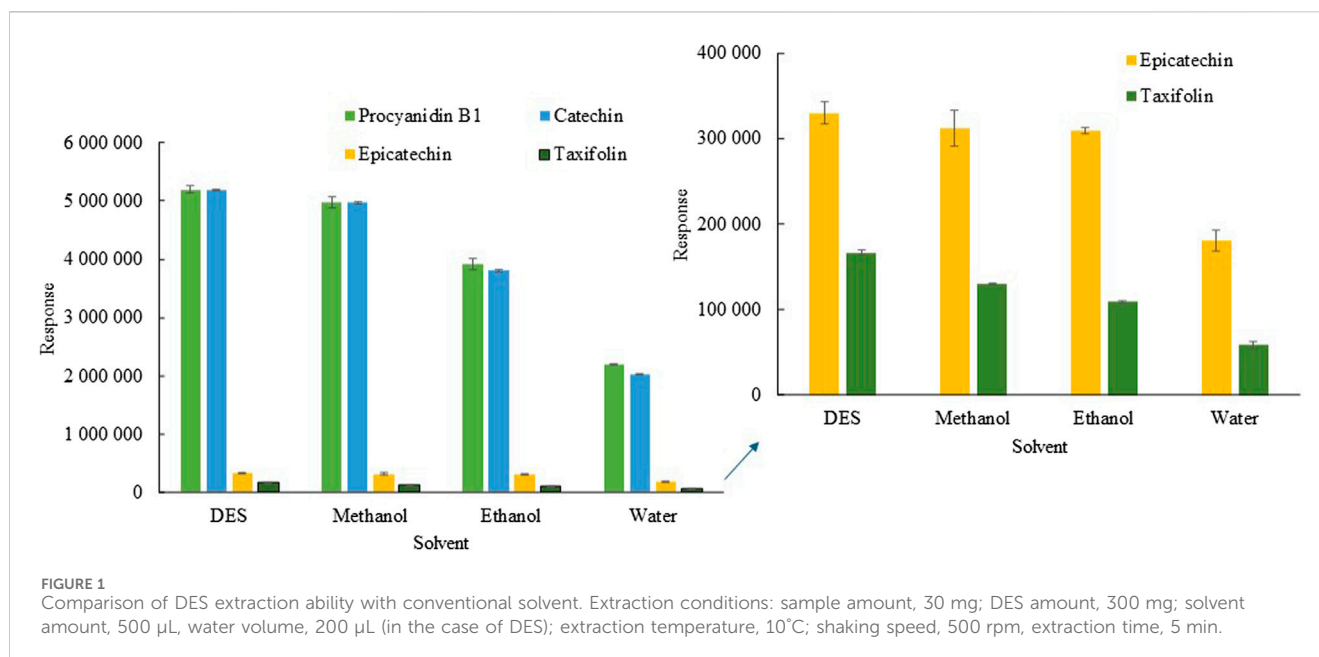
at a 1:2 M ratio; therefore, this ratio was selected for further studies. The results indicate that an increase in the fructose content within the DES structure correlates with enhanced extraction efficiency. This can be attributed to the presence of active groups in the fructose structure, notably five -OH groups and one = O group, capable of forming robust hydrogen bonds with bioactive substances. In contrast, the ChCl structure possesses only one hydroxyl group, leading to a reduction in extraction efficiency. Another influential factor affecting extraction efficiency is dynamic viscosity, impacting the mass transfer process. With an elevation in the concentration of ChCl, the viscosity of the DES increases, consequently leading to a decrease in extraction efficiency. The extraction efficiency of DES was compared with conventional solvents, such as methanol, ethanol and water. Figure 1 shows that the extraction efficiency of DES is higher compared to methanol at 4%–22%, at ethanol 15%–25%, at 42%–58%, depending on bioactive compounds.

3.2 Effect of shaking speed

Another parameter that influences the extraction yield is shaking speed, which ensures the rate of mass transfer from solid phase into the DES phase. The shaking speed was examined in the range from 100 to 1,500 rpm. From Supplementary Figure S2 is evident that the shaking speed has no significant effect on the extraction efficiency; however, a slight increase was observed at 500 rpm which then remains stable up to 1,500 rpm. Therefore, 500 rpm was selected for further optimization steps.

3.3 Effect of extraction time

The effect of extraction time was examined in the range of 5–60 min. Supplementary Figure S3 reveals that the extraction yield slowly but gradually and clearly increases with time, reaching a maximum value at 30 min, then remains stable. This can be attributed to the heightened solubility of bioactive compounds in the DES during agitation, thereby facilitating the efficient mass transfer of bioactive compounds from the spruce roots to the DES phase. To ensure high extraction yield in the shortest possible analysis time, 30 min was chosen as the optimum value.

3.4 Effect of extraction temperature

Temperature can affect the extraction efficiency; therefore, its influence was studied in a wide range from 5°C to 90°C. In principle, elevating the extraction temperature is expected to decrease the dynamic viscosity of DES, thereby enhancing the efficiency of the mass exchange process. However, excessively high temperatures are undesirable, because the interactions between the DES and bioactive compounds involve an exothermic reaction, in accordance with Van 't Hoff's law. This law asserts that in an exothermic reaction heat is liberated, resulting in a negative net enthalpy change. This, in turn, directly affects the partition coefficient value between the DES and bioactive compounds (Tellinghuisen, 2006). Furthermore, heightened temperatures can lead to the degradation of D-fructose. This degradation may manifest as caramelization followed by pyrolysis of the sugars (Woo et al., 2011).

As can be seen from Supplementary Figure S4, the efficiency of catechin extraction clearly increases with increasing temperature up to 30°C and subsequently decreases. In the case of procyanidin B1, the extraction efficiency is highest and stable up to 20°C; with a further increase in temperature, a lowering of the inter-sample repeatability is observed (30°C–60°C) and at temperatures above 60°C, the extraction efficiency decreases. The extraction efficiency of epicatechin is highest at lower temperatures up to 20°C, and from 30°C it gradually decreases. The extraction efficiency of taxifolin is less affected by temperature, but even in this case we can observe a gentle and slow increase to a maximum of 30°C, followed by a slow

FIGURE 2
RS surface plots for catechin peak area optimization. Factors taken for optimization: extraction time (15−45 min), extraction temperature (10°C−50°C) and shaking speed (300−1,000 rpm).
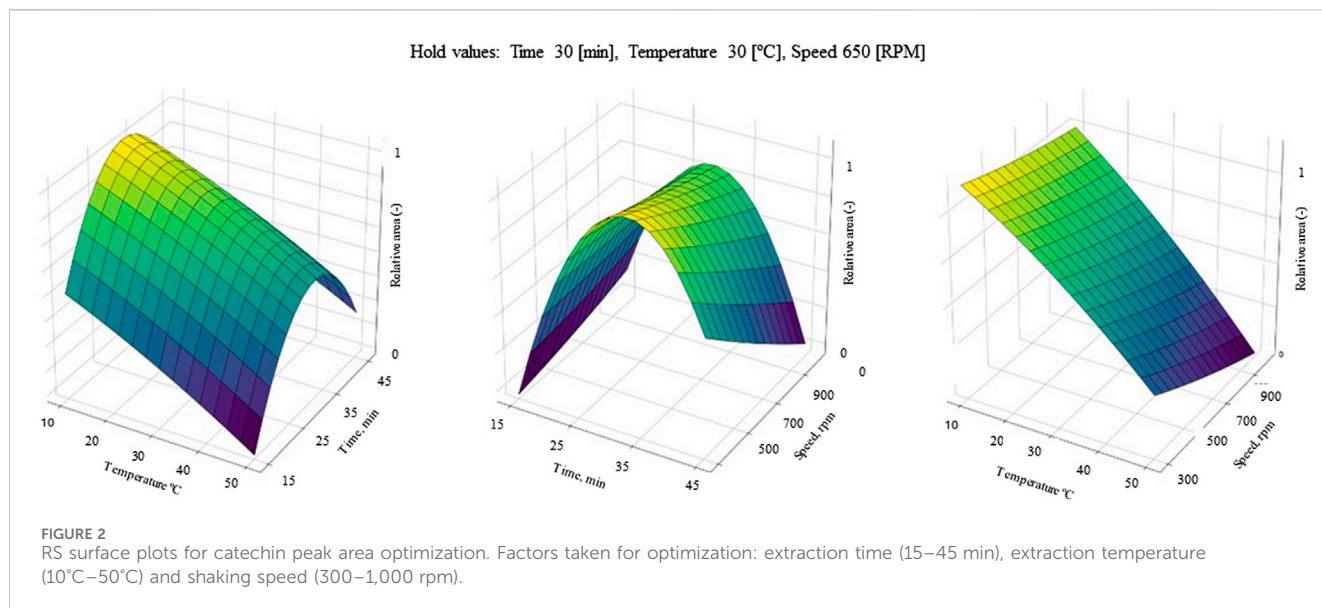
but clear decrease. Therefore, choosing the optimal extraction temperature is difficult, and it was necessary to choose a temperature that would provide the best results for the maximum number of analytes. Therefore 10°C was selected for further analysis.

3.5 Effect of water volume

In general, DESs are viscous, which complicates their use for the extraction of substances from solid samples such as plants. The addition of a small amount of water can affect the viscosity, but also the density and polarity of the DES, which can lead to improved extraction properties (El Achkar et al., 2019). On the other hand, an excessive amount of water can weaken the interactions between the DES and the target compounds, as well as the interactions between the DES components, which can lead to disruption of the DES supramolecular structure (El Achkar et al., 2019; Vilková et al., 2020). Therefore, the effect of adding water up to 600 µL was investigated and based on the obtained results (Supplementary Figure S5), 200 µL was selected for further experiments.

3.6 Results of experimental design

In order to confirm the optimal conditions, experimental design was applied. Parameters such as extraction time, extraction temperature and shaking speed were selected for optimization, since the results obtained with OVAT did not include interactions between each optimized factor; thus, it needed to be investigated. In Figure 2 the surface plots of catechin RS optimization are depicted (for others, see Supplementary Materials). Based on the calculations, optimal conditions for catechin determination are a shaking time of 32.5 min, a temperature of 10°C and a shaking speed of 300 rpm. These results are very close to the OVAT optimization. However, for all other optimized compounds strong saddle-shape surface plots were obtained. This can justify findings from OVAT optimization, where the

impact of shaking speed and time was insignificant. The insignificance of some factors used for RS also results in a low lack of fit (LoF), where only the RS model for catechin (LoF 0.1 > 0.05) and taxifolin (LoF 0.09 > 0.05) were valid. Therefore, the authors decided to rely on the OVAT results and keep shaking for 30 min at 500 rpm in 10°C.

3.7 Application to real samples

To show the applicability of the developed method for the extraction of bioactive compounds, a series of experiments was performed by analyzing Norway root samples spiked with standard solutions at a concentration level of 5 µg g^{-1}. The precision and trueness were evaluated by inter-day and intra-day (five consecutive days) measurements. The results are given in Table 2. The recoveries were between 83% and 117%, with RSD less than 9.9% for inter-day and between 93% and 111% with RSD less than 14% for intra-day experiments, respectively.

3.8 Assessment of greenness

The ComplexGAPI tool was applied for the evaluation of the green character of the developed procedure. This metric not only allows the evaluation of the analytical protocol in terms of its environmental friendliness but also those processes which precede the analytical procedure itself (Płotka-Wasylka and Wojnowski, 2021; Locatelli et al., 2023). And so, the greenness aspect of the following parameters was evaluated: yield, conditions, reagents and solvents, instrumentation and workup, and purification which may occur before analytical protocol. Considering the generated waste, E-factor is calculated and presented in the middle of the lower part of the pictogram. As these elements can be applied to assess the synthesis of NADES, ComplexGAPI seems be perfect for use in the evaluation of the developed procedure.

Looking at the generated ComplexGAPI (Figure 3A) pictogram it can be concluded that the DES-based shaking-assisted extraction

TABLE 2 Inter- and intra-day precision and accuracy of phenolic compounds determination in Norway spruce roots (n = 5).

Compound	Added, µg/g	Inter-day			Intra-day		
		Found, µg/g	R, %	RSD, %	Found, µg/g	R, %	RSD, %
Procyanidin B1	0	84.2 ± 0.1		0.2	84.0 ± 2.8		3.3
	5	89.8 ± 1.9	117	2.1	88.7 ± 2.2	94.0	2.5
Epicatechin	0	2.75 ± 0.10		3.6	2.71 ± 0.2		7.3
	5	8.12 ± 0.07	107	0.8	8.27 ± 0.50	111	5.9
Catechin	0	60.8 ± 0.3		0.4	59.8 ± 2.1		3.6
	5	64.9 ± 0.8	82.8	1.2	65.3 ± 2.8	110	4.2
4-Coumaric acid	0	3.23 ± 0.05		1.6	3.22 ± 0.42		13
	5	8.23 ± 0.01	100	0.1	8.46 ± 0.45	105	5.3
Taxifolin	0	0.29 ± 0.03		9.9	0.35 ± 0.05		12
	5	5.28 ± 0.03	99.8	0.5	5.40 ± 0.49	101	9.1
Piceatannol	0	0.19 ± 0.01		7.7	0.21 ± 0.03		14
	5	5.68 ± 0.01	110	0.3	5.23 ± 0.43	100	8.3
Isorhapontin	0	897 ± 3		0.3	895 ± 3		0.1
	5	901 ± 1	80.0	0.1	900 ± 1	100	0.1
Epigallocatechin	0	2.77 ± 0.12		4.5	2.71 ± 0.14		5.3
	5	7.04 ± 0.08	85.1	1.1	7.54 ± 0.44	96.6	5.8
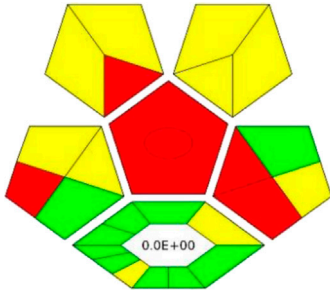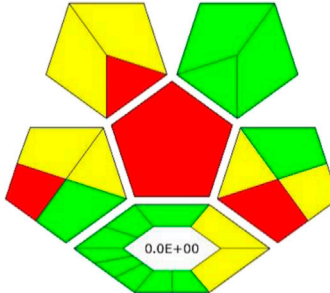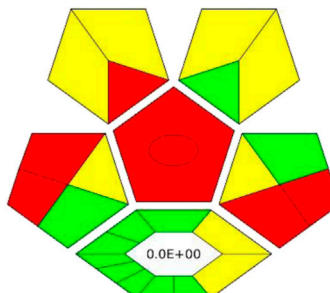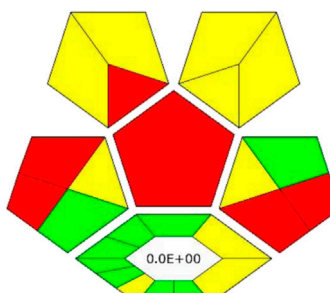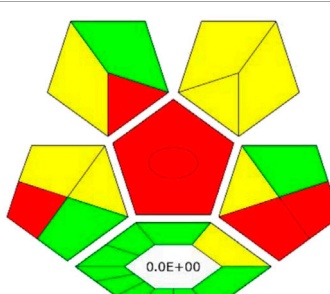
R, recovery; RSD, relative standard deviation.

FIGURE 3
The pictograms of ComplexGAPI **(A)** and BAGI **(B)** generated for the DES-based shaking-assisted extraction coupled to LC-ESI-QTOF-MS for determination of bioactive compounds from Norway spruce roots.
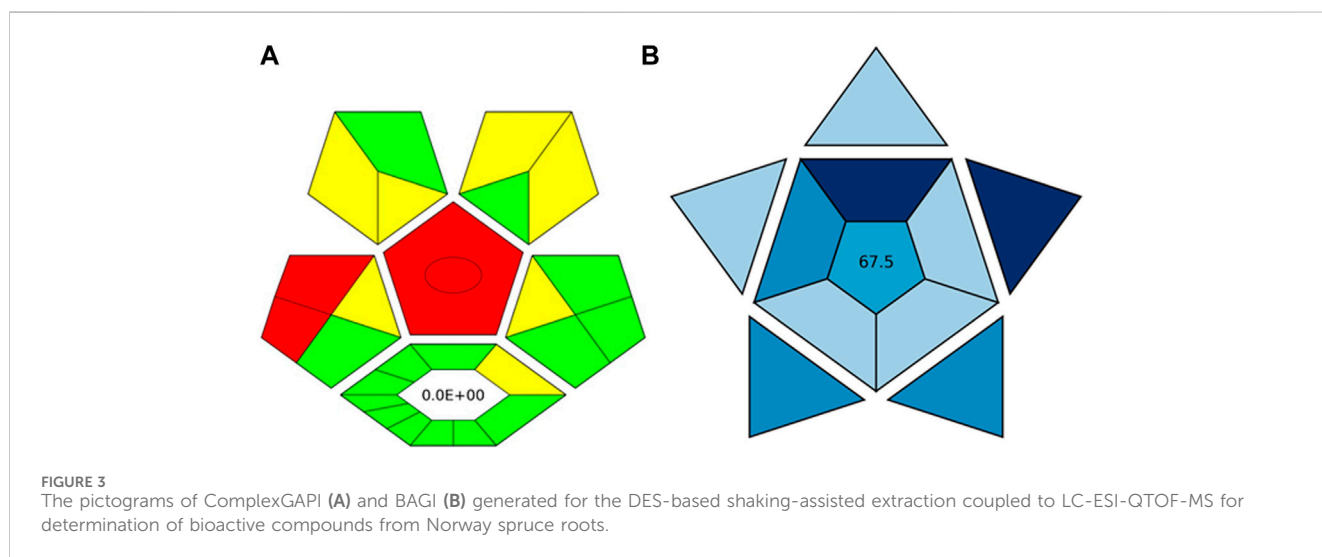
procedure coupled to LC-ESI-QTOF-MS for determination of bioactive compounds from Norway spruce roots can be considered green. This is mainly because the processes related to the synthesis of the DES are based on non-hazardous reagents. In fact, DES synthesis is a very simple process. The synthesis occurs in a 100% yield and no waste is generated during this process (E-factor = 0). The procedure requires small amounts of reagents for the analytical separation; however, what needs to be noted is that moderate toxic solvents (methanol and acetonitrile) are used here. In addition, a few milliliters of waste per sample are generated. The critical point of the procedure is the necessity to transport and store the sample. In order to show the potential of the developed protocol, the greenness of the developed method was compared with that of existing procedures for the extraction of polyphenolic substances from solid plant samples using the ComplexGAPI approach, and the results for the developed method were better or comparable to existing ones (Table 3).
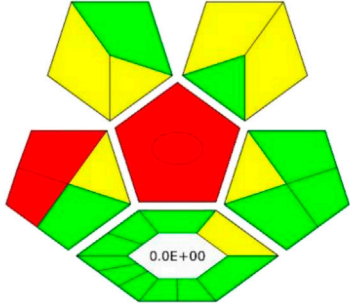
TABLE 3 Comparison of the greenness of the developed method with other reported methods for the extraction of phenolic compounds by means of ComplexGAPI analysis.

Analytes	Sample	Extraction conditions	Detection	ComplexGAPI	Ref.
Catechins	Tea	SLE Sample amount: 150 mg DES: Malic acid–Girard's reagent T 2:1, 30% water; 1.5 mL Time: 50 min Temperature: 50 °C	UHPLC-UV		Bajkacz et al. (2020)
Quercetin	Onion	UAE Sample amount: 50 mg DES: Citric acid–glucose–water 1:1:2; 1 mL Time: 30 min	CSPE		Gomez et al. (2016)
Phenolic compounds	Olive leaf	MAE Sample amount: 200 mg DES: Choline chloride–ethylene glycol 1:2, 43.3% water; 1.5 mL Time: 16.7 min Temperature: 79.6°C	HPLC-DAD-ESI-TOF-MS		Alañón et al. (2020)
Quercetin and myricetin	*Ginkgo biloba* leaves	HRE Sample amount: 1 g DES: Choline chloride–oxalic acid–ethylene glycol 1:1:3, 50% water; 10 mL Temperature: 60 °C Time: 30 min	HPLC-PDA		Tang et al. (2017)
Quercetin, naringenin, kaempferol, isorhamnetin	*Pollen Typhae*	UAE Sample amount: 50 mg DES: Choline chloride–1,2-propanediol 1:4, 30% water; 1 mL Time: 35 min	HPLC-UV		Meng et al. (2018)

(Continued on following page)

TABLE 3 (*Continued*) Comparison of the greenness of the developed method with other reported methods for the extraction of phenolic compounds by means of ComplexGAPI analysis.

Analytes	Sample	Extraction conditions	Detection	ComplexGAPI	Ref.
Polyphenolic compounds	Norway spruce roots	Shaking-assisted	LC-ESI-QTOF-MS	0.0E+00	This work
		Sample amount: 30 mg			
		DES: Choline chloride–fructose 1:2, 30% water; 300 g			
		Temperature: 10°C			
		Time: 30 min			

SLE, Solid–liquid extraction; UAE, Ultrasound-assisted extraction; MAE, Microwave-assisted extraction; HRE, heat reflux extraction; CSPE, Carbon screen-printed electrode; UHPLC-UV, ultra-high-performance liquid chromatography with ultraviolet detector; HPLC-DAD-ESI-TOF-MS, High-performance liquid chromatography with photodiode array detector with electrospray quadrupole time-of-flight tandem mass spectrometry; HPLC-PDA, High-performance liquid chromatography with photodiode array detector; HPLC-UV, high-performance liquid chromatography with an ultraviolet detector; LC-ESI-QTOF-MS, liquid chromatography coupled with electrospray ionization quadrupole time-of-flight mass spectrometry.

In addition to the green character evaluation, an assessment of method's applicability was performed. For this purposes, blue applicability grade index (BAGI) was applied. This metric can be considered complementary to the ComplexGAPI (and other metrics), and it is mainly focused on the practical aspects of White Analytical Chemistry (WAC) (Manousi et al., 2023). Two different types of results can be obtained using the BAGI metric tool and they are correlated to the obtained pictogram and the obtained score as is visible in Figure 3B. In order to be considered practical, it is recommended that the method attains at least 60 points.

Looking at the BAGI pictogram, a great deal of information can be found at first glance. First of all, the information of the analysis was both quantitative and confirmatory due to the employment of the MS detector. The determination enabled the quantification of eight compounds belonging to two different classes (polyphenols and acids). Since the DES needs to be synthesized in the lab in a relatively simple and straightforward way using simple equipment, the procedure lost few points. Regarding the instrumentation, sophisticated equipment was employed. The simultaneous sample preparation can be easily performed using a multichannel pipet. As demonstrated by the results, a one-step preconcentration was needed. The autosampler of LC was used to inject the samples. As for the sample preparation, miniaturized extraction was employed, and the sample volume for the plant matrix was 30 mg. Thus, a BAGI score of 67.5 is attained for the method and the whole protocol shows good applicability potential.

4 Conclusion

In conclusion, this study introduced an environmentally friendly shaking-assisted extraction procedure utilizing a deep eutectic solvent based on choline chloride and fructose for the efficient extraction of polyphenolic compounds from Norway root samples coupled with LC-ESI-QTOF-MS detection. For the optimization of extraction efficiency, two optimization approaches were utilized: one-variable-at-a-time and confirmed by response surface design. Almost identical experimental conditions were achieved using both optimization techniques, as follows: 30 mg of the sample, 300 mg of ChCl:Fru 1:2 DES

with 30% w/w water content, shaking speed set at 500 rpm, extraction time of 30 min, and an extraction temperature of 10°C. The DES was compared with conventional solvents and the results showed that the extraction efficiency of DES is higher compared to methanol, ethanol, and water. The environmental sustainability of the developed method was evaluated using the ComplexGAPI, while the practicality of the developed procedure was assessed through the blue applicability grade index. Furthermore, the method was successfully applied to the analysis of spruce root samples, yielding satisfactory results. We can assume that the suggested approach can (of course, after appropriate validation) also be used for samples of other plants with a similar structure or for the roots of other plants.

Data availability statement

The raw data supporting the conclusion of this article will be made available by the authors, without undue reservation.

Author contributions

AK: Conceptualization, Formal Analysis, Investigation, Supervision, Validation, Visualization, Writing–original draft, Writing–review and editing. AV: Writing–review and editing, Investigation. JP-W: Formal Analysis, Writing–original draft. TM: Formal Analysis, Writing–original draft. PM-C: Writing–original draft. IT: Resources, Writing–review and editing. VP: Resources, Writing–review and editing. FP: Resources, Writing–review and editing. AJ: Resources, Writing–review and editing. VA: Conceptualization, Supervision, Writing–original draft, Writing–review and editing.

Funding

Conflict of interest

The authors declare that the research was conducted in the absence of any commercial or financial relationships that could be construed as a potential conflict of interest.

Publisher's note

All claims expressed in this article are solely those of the authors and do not necessarily represent those of their affiliated organizations, or those of the publisher, the editors and the reviewers. Any product that may be evaluated in this article, or claim that may be made by its manufacturer, is not guaranteed or endorsed by the publisher.

Supplementary material

The Supplementary Material for this article can be found online at: https://www.frontiersin.org/articles/10.3389/fchem.2024.1385844/full#supplementary-material

References

Alañón, M. E., Ivanović, M., Gómez-Caravaca, A. M., Arráez-Román, D., and Segura-Carretero, A. (2020). Choline chloride derivative-based deep eutectic liquids as novel green alternative solvents for extraction of phenolic compounds from olive leaf. *Arabian J. Chem.* 13, 1685–1701. doi:10.1016/j.arabjc.2018.01.003

Angeles Garcia, M., Jimenez-Jimenez, S., and Marina, M. L. (2022). Stereoselective separation of dimethenamid by cyclodextrin electrokinetic chromatography using deep eutectic solvents. *J. Chromatogr. A* 1673, 463114. doi:10.1016/j.chroma.2022.463114

Bajkacz, S., Adamek, J., and Sobska, A. (2020). Application of deep eutectic solvents and ionic liquids in the extraction of catechins from tea. *Molecules* 25, 3216. doi:10.3390/molecules25143216

Bentley, J., Olsen, E. K., Moore, J. P., and Farrant, J. M. (2020). The phenolic profile extracted from the desiccation-tolerant medicinal shrub Myrothamnus flabellifolia using Natural Deep Eutectic Solvents varies according to the solvation conditions. *Phytochemistry* 173, 112323. doi:10.1016/j.phytochem.2020.112323

Cai, C., Li, F., Liu, L., and Tan, Z. (2019). Deep eutectic solvents used as the green media for the efficient extraction of caffeine from Chinese dark tea. *Sep. Purif. Technol.* 227, 115723. doi:10.1016/j.seppur.2019.115723

Chen, Y., Dang, J., Yan, X., Lu, F., and Li, D. (2020). Optimization studies on the extraction of flavone di-C-glycosides from *Premna fulva* craib by deep eutectic solvents. *J. Chem.* 2020, 1–9. doi:10.1155/2020/7240535

Chen, Z., Wu, K., Zhu, W., Wang, Y., Su, C., and Yi, F. (2022). Chemical compositions and bioactivities of essential oil from perilla leaf (Perillae Folium) obtained by ultrasonic-assisted hydro-distillation with natural deep eutectic solvents. *Food Chem.* 375, 131834. doi:10.1016/j.foodchem.2021.131834

Duan, L., Dou, L. L., Guo, L., Li, P., and Liu, E. H. (2016). Comprehensive evaluation of deep eutectic solvents in extraction of bioactive natural products. *ACS Sustain. Chem. Eng.* 4, 2405–2411. doi:10.1021/acssuschemeng.6b00091

el Achkar, T., Fourmentin, S., and Greige-Gerges, H. (2019). Deep eutectic solvents: an overview on their interactions with water and biochemical compounds. *J. Mol. Liq.* 288, 111028. doi:10.1016/j.molliq.2019.111028

el Kantar, S., Rajha, H. N., Boussetta, N., Vorobiev, E., Maroun, R. G., and Louka, N. (2019). Green extraction of polyphenols from grapefruit peels using high voltage electrical discharges, deep eutectic solvents and aqueous glycerol. *Food Chem.* 295, 165–171. doi:10.1016/j.foodchem.2019.05.111

Gomez, F. J. V., Espino, M., de Los Angeles Fernandez, M., Raba, J., and Silva, M. F. (2016). Enhanced electrochemical detection of quercetin by natural deep eutectic solvents. *Anal. Chim. Acta* 936, 91–96. doi:10.1016/j.aca.2016.07.022

Gürsoy, N., SırtBAŞı, B., Şimşek, S., Elik, A., and Altunay, N. (2022). Optimization and application of ultrasound-assisted sugar based deep eutectic solvent dispersive liquid–liquid microextraction for the determination and extraction of aflatoxin M1 in milk samples. *Microchem. J.* 172, 106974. doi:10.1016/j.microc.2021.106974

Hartmann, H., and Trumbore, S. (2016). Understanding the roles of nonstructural carbohydrates in forest trees - from what we can measure to what we want to know. *New phytologist* 211, 386–403. doi:10.1111/nph.13955

Hayyan, A., Mjalli, F. S., Alnashef, I. M., al-Wahaibi, T., al-Wahaibi, and Hashim, M. A. (2012). Fruit sugar-based deep eutectic solvents and their physical properties. *Thermochim. Acta* 541, 70–75. doi:10.1016/j.tca.2012.04.030

Hikmawanti, N. P. E., Ramadon, D., Jantan, I., and Mun'Im, A. (2021). Natural deep eutectic solvents (Nades): phytochemical extraction performance enhancer for pharmaceutical and nutraceutical product development. *Plants* 10, 2091. doi:10.3390/plants10102091

Ivanović, M., Razboršek, M. I., and Kolar, M. (2020). Innovative extraction techniques using deep eutectic solvents and analytical methods for the isolation and characterization of natural bioactive compounds from plant material. *Plants* 9, 1–29. doi:10.3390/plants9111428

Kalyniukova, A., Holuša, J., Musiolek, D., Sedlakova-Kadukova, J., Płotka-Wasylka, J., and Andruch, V. (2021). Application of deep eutectic solvents for separation and determination of bioactive compounds in medicinal plants. *Industrial Crops Prod.* 172, 114047. doi:10.1016/j.indcrop.2021.114047

Koel, M., Kuhtinskaja, M., and Vaher, M. (2020). Extraction of bioactive compounds from Catharanthus roseus and Vinca minor. *Sep. Purif. Technol.*, 252. doi:10.1016/j.seppur.2020.117438

Li, Z. L., Zhong, F. Y., Huang, J. Y., Peng, H. L., and Huang, K. (2020). Sugar-based natural deep eutectic solvents as potential absorbents for NH3 capture at elevated temperatures and reduced pressures. *J. Mol. Liq.*, 317. doi:10.1016/j.molliq.2020.113992

Liu, F., Chen, L., Yin, K., Fan, T., and Yan, Z. (2022). Sugars as hydrogen-bond donors tune the phase behavior in a novel liquid–liquid biphasic system formed by hydrophilic deep eutectic solvents and n-propanol. *Fluid Phase Equilibria* 556, 113393. doi:10.1016/j.fluid.2022.113393

Locatelli, M., Kabir, A., Perrucci, M., Ulusoy, S., Ulusoy, H. I., and Ali, I. (2023). Green profile tools: current status and future perspectives. *Adv. Sample Prep.* 6, 100068. doi:10.1016/j.sampre.2023.100068

Manousi, N., Wojnowski, W., Płotka-Wasylka, J., and Samanidou, V. (2023). Blue applicability grade index (BAGI) and software: a new tool for the evaluation of method practicality. *Green Chem.* 25, 7598–7604. doi:10.1039/d3gc02347h

Mansour, F. R., Bedair, A., Hamed, M., Magdy, G., Ali, I., and Locatelli, M. (2024). Applications of (natural) deep eutectic solvents in liquid phase microextraction: a review. *Microchem. J.* 198, 110178. doi:10.1016/j.microc.2024.110178

Meng, Z., Zhao, J., Duan, H., Guan, Y., and Zhao, L. (2018). Green and efficient extraction of four bioactive flavonoids from Pollen Typhae by ultrasound-assisted deep eutectic solvents extraction. *J. Pharm. Biomed. Analysis* 161, 246–253. doi:10.1016/j.jpba.2018.08.048

Pang, Z., Chen, J., Wang, T., Gao, C., Li, Z., Guo, L., et al. (2021). Linking plant secondary metabolites and plant microbiomes: a review. *Front. Plant Sci.* 12, 621276. doi:10.3389/fpls.2021.621276

Płotka-Wasylka, J., and Wojnowski, W. (2021). Complementary green analytical procedure index (ComplexGAPI) and software. *Green Chem.* 23, 8657–8665. doi:10.1039/d1gc02318g

Razboršek, M. I., Ivanović, M., Krajnc, P., and Kolar, M. (2020). Choline chloride based natural deep eutectic solvents as extraction media for extracting phenolic compounds from chokeberry (Aronia melanocarpa). *Molecules* 25, 1619. doi:10.3390/molecules25071619

Rozas, S., Benito, C., Alcalde, R., Atilhan, M., and Aparicio, S. (2021). Insights on the water effect on deep eutectic solvents properties and structuring: the archetypical case of choline chloride + ethylene glycol. *J. Mol. Liq.*, 344. doi:10.1016/j.molliq.2021.117717

Rukavina, I., Rodrigues, M. J., Pereira, C. G., Mansinhos, I., Romano, A., Ślusarczyk, S., et al. (2021). Greener is better: first approach for the use of natural deep eutectic solvents (nades) to extract antioxidants from the medicinal halophyte polygonum maritimum l. *Molecules* 26, 6136. doi:10.3390/molecules26206136

Shishov, A., Bulatov, A., Locatelli, M., Carradori, S., and Andruch, V. (2017). Application of deep eutectic solvents in analytical chemistry. A review. *Microchem. J.* 135, 33–38. doi:10.1016/j.microc.2017.07.015

Skarpalezos, D., and Detsi, A. (2019). *Deep eutectic solvents as extraction media for valuable flavonoids from natural sources*, 9. Switzerland: Applied Sciences.

Takla, S. S., Shawky, E., Hammoda, H. M., and Darwish, F. A. (2018). Green techniques in comparison to conventional ones in the extraction of Amaryllidaceae alkaloids: best solvents selection and parameters optimization. *J. Chromatogr. A* 1567, 99–110. doi:10.1016/j.chroma.2018.07.009

Tang, W., Li, G., Chen, B., Zhu, T., and Row, K. H. (2017). Evaluating ternary deep eutectic solvents as novel media for extraction of flavonoids from Ginkgo biloba. *Sep. Sci. Technol. Phila.* 52, 91–99. doi:10.1080/01496395.2016.1247864

Tellinghuisen, J. (2006). Van't Hoff analysis of K° (T): how good.or bad? *Biophys. Chem.* 120, 114–120. doi:10.1016/j.bpc.2005.10.012

Vieira, V., Prieto, M. A., Barros, L., Coutinho, J. A. P., Ferreira, I. C. F. R., and Ferreira, O. (2018). Enhanced extraction of phenolic compounds using choline chloride based deep eutectic solvents from Juglans regia L. *Industrial Crops Prod.* 115, 261–271. doi:10.1016/j.indcrop.2018.02.029

Vilková, M., Płotka-Wasylka, J., and Andruch, V. (2020). The role of water in deep eutectic solvent-base extraction. *J. Mol. Liq.* 304, 112747. doi:10.1016/j.molliq.2020.112747

Woo, K. S., Hwang, I. G., Kim, H. Y., Jang, K. I., Lee, J., Kang, T. S., et al. (2011). Thermal degradation characteristics and antioxidant activity of fructose solution with heating temperature and time. *J. Med. Food* 14, 167–172. doi:10.1089/jmf.2010.1166

Yu, G. W., Cheng, Q., Nie, J., Wang, P., Wang, X. J., Li, Z. G., et al. (2017). DES-based microwave hydrodistillation coupled with GC-MS for analysis of essential oil from black pepper (Piper nigrum) and white pepper. *Anal. Methods* 9, 6777–6784. doi:10.1039/c7ay02072d

Zainal-Abidin, M. H., Hayyan, M., Hayyan, A., and Jayakumar, N. S. (2017). New horizons in the extraction of bioactive compounds using deep eutectic solvents: a review. *Anal. Chim. Acta* 979, 1–23. doi:10.1016/j.aca.2017.05.012

Zhang, L., Li, Y., and Gao, J. (2024). Selectively extraction of astaxanthin from Haematococcus pluvialis by aqueous biphasic systems composed of ionic liquids and deep eutectic solutions. *Food Chem.* 434, 137399. doi:10.1016/j.foodchem.2023.137399

Check for updates

Analytical methods and experimental quality in studies targeting carbonyls in electronic cigarette aerosols

Roberto A. Sussman[1], Federica Maria Sipala[2]*,
Simone Ronsisvalle[2,3] and Sebastien Soulet[4]

[1]Institute of Nuclear Sciences, National Autonomous University of Mexico, Mexico City, Mexico,
[2]Department of Drug and Health Sciences, University of Catania, Catania, Italy, [3]Center of Excellence for
the Acceleration of HArm Reduction (CoEHAR), University of Catania, Catania, Italy, [4]Ingesciences,
Cestas, France

We provide an extensive review of 14 studies (11 independent and three industry-funded) on emissions generated by Electronic Cigarettes (ECs), specifically focusing on the evaluation of carbonyls present in these emissions and emphasizing a meticulous evaluation of their analytical methods and experimental procedures. Since the presence of carbonyl by-products in EC aerosol is concerning, it is important to evaluate the reliability of emission studies quantifying these compounds by verifying their compliance with the following criteria of experimental quality: authors must 1) supply sufficient information on the devices and experimental procedures to allow for potentially reproducing or replicating the experiments, 2) use of appropriate puffing protocols that approach consumer usage as best as possible, 3) use of appropriate analytical methods and 4) usage of blank samples to avoid false positive detection. Outcomes were classified in terms of the fulfilment of these conditions as reliable in seven studies, partially reliable in five studies, and unreliable in two studies. However, only five studies used blank samples and six studies failed the reproducibility criterion. Carbonyl yields were far below their yields in tobacco smoke in all reproducible studies, even in the partially reliable ones, thus supporting the role of ECs (when properly tested and operated) as harm reduction products. This review highlights the necessity to evaluate the quality of laboratory standards in testing EC emissions to achieve an objective assessment of the risk profile of ECs.

1 Introduction

Cigarette smoking is responsible for seven million premature deaths each year, including non-smokers passively exposed to exhaled tobacco smoke (Centers for Disease Control and Protection CDC, 2020; World Health Organization WHO, 2023). A global institutional effort has been deployed to address and contain this major health problem, including interventions to prevent smoking initiation and to induce smoking cessation (Athyros et al., 2013; Caponnetto et al., 2013; Kotz et al., 2020). Tobacco Harm Reduction (THR) provides an important and valuable complement to this effort through the substitution of tobacco cigarettes with much safer consumer products such as processed oral smokeless tobacco and Electronic Nicotine Delivery Systems (ENDS) (Amos et al.,

2016; Abrams et al., 2018). The latter is a large class of products comprising Electronic Cigarettes (ECs) and heated tobacco products (HTPs), both delivering nicotine through an aerosol generated electronically without combustion. ECs generate an aerosol by condensing vapor produced by heating a liquid solution (the "e-liquid") with power supplied by an electric battery at temperatures of 180°C–270°C well below tobacco ignition (McNeill et al., 2018; National Academies of Sciences Engineering and Medicine et al., 2018) (HTPs generate a similar aerosol from specially reconstituted tobacco elements). While usage of both types of ENDS is endorsed by several public health experts (Balfour et al., 2021) and has been incorporated in tobacco control policies in the United Kingdom (Office for Health Improvement and Disparities (formerly Public Health England)., 2022) and New Zealand (Ministry of Health NZG, 2024), there are objections to their implementation in public health policies (Ministry of Health NZG, 2024; Pisinger and Døssing, 2014; World Health Organization, 2022), making their usage a controversial issue. However, there is a widespread consensus sustaining that ENDS aerosols expose smokers and bystanders to a significantly reduced level of Hazardous and Potentially Hazardous Compounds (HPHCs) in comparison with cigarette smoke (Amos et al., 2016; Ministry of Health NZG, 2024; U.S. Food and Drug Administration, 2023).

Tobacco smoke is a highly complex set of combustion-originated aerosols, with mainstream emissions inhaled and exhaled by smokers and sidestream emissions emerging from the burning/smouldering tip of cigarettes. Both emissions are generated by the ignition of tobacco biomass at 800°C–950°C, while sidestream emission occurs at 400°C–660°C at the smouldering cigarette tip when the smoker is not puffing (Baker et al., 2004). Environmental tobacco smoke (ETS) is a third aerosol formed by the diluting mixture of mainstream and sidestream emissions in interaction with exogenous environmental pollutants. These emissions expose smokers (and bystanders) to a wide variety of toxicologically relevant HPHCs responsible for multiple adverse health effects (Centers for Disease Control and Prevention et al., 2010). In contrast, aerosols generated by ECs necessarily avoid much of the physicochemical complexity of tobacco smoke, since there is no sidestream emission and their mainstream emission does not contain 97%–99% of compounds (including HPHCs) in tobacco smoke. Emission studies have revealed that carbonyls (specially aldehydes such as formaldehyde, acetaldehyde, and acrolein) are the most abundant (or less negligible) by-products (McNeill et al., 2018; National Academies of Sciences Engineering and Medicine et al., 2018; Office for Health Improvement and Disparities (formerly Public Health England)., 2022), originating from the aerosol formation process from thermal degradation (low-energy pyrolysis or torrefaction) of the ingredients in e-liquids, propylene glycol (PG), and glycerol or vegetable glycerine (VG), which are decomposed into carbonyl compounds, while flavour chemicals also produce by-products (some of which are toxic) from their degradation. Further concerns have been raised for the possible presence of trace levels of metals in the e-liquids and aerosols of ECs, likely leached or transported from the metal components of ECs (McNeill et al., 2018; National Academies of Sciences Engineering and Medicine et al., 2018; Office for Health Improvement and Disparities (formerly Public Health England)., 2022). Carbonyls are particularly concerning because of their association with

deleterious health effects. The International Agency for Research on Cancer (IARC) classifies formaldehyde as a human carcinogen (Group 1) (International Agency for Research on Cancer IARC, 2006). Acetaldehyde is possibly carcinogenic to humans (Group 2 B) according to IARC, and acrolein is probably carcinogenic to humans (Group 2A) (Cogliano et al., 2005; International Agency for Research on Cancer IARC, 2021).

To assess health risks in users, quantification of the contents of HPHCs in EC aerosols is essential. This can be achieved by laboratory emission studies in which the devices are puffed with machines simulating user inhalation. Although these tests rely on standardized and regimented puffing protocols that (evidently) do not accurately reproduce real usage, their outcomes might provide the most basic estimation of potential health risks to users. However, given the wide diversity of ECs (devices, coils, e-liquids, nicotine levels, and flavours), there is also a wide diversity of outcomes in the literature on emissions. Hence, to navigate this complexity and to best interpret the objectivity and reliability of these outcomes (and the inferred risk assessment), it is necessary and important to verify (acknowledging limitations) whether the studies comply with basic criteria of experimental quality. Specifically, emission studies must comply with the following requirements: 1) provide sufficient information on the devices and experimental procedures to allow for a potential reproducibility of outcomes; 2) set up appropriate puffing parameters that are as close as possible to the design of the devices and their usage by consumer; 3) use appropriate analytical methods; and 4) use blank samples to control sample contamination. We consider that the degree of fulfilment of these quality criteria is a necessary condition for assessing the reliability of their experimental outcomes.

Two previous review articles (Soulet and Sussman, 2022b; Soulet and Sussman, 2022a) examined 48 emission studies published after 2018 (12 studies on metals and 36 on organic by-products), evaluating the reliability of their outcomes by verifying the fulfilment of the experimental quality requirements listed above. In the present review, we examine 14 studies (Van Leeuwen et al., 2004; Conklin et al., 2018; El Mubarak et al., 2018; Stephens et al., 2019; Gillman et al., 2020; Nicol et al., 2020; Talih et al., 2020a; Rajapaksha et al., 2021; Son and Khlystov, 2021; El-Hellani et al., 2022; Lalonde et al., 2022; McGuigan et al., 2022; Pinto et al., 2022; Talih et al., 2022) not previously considered in (Soulet and Sussman, 2022a), providing a strong emphasis on the detailed critique of the analytical methods. While more than half of the studies reviewed in (Soulet and Sussman, 2022b; 2022a) generated emissions by puffing sub-ohm high-power devices (power settings above 40 W, resistances below 1 Ω) under conditions that favour overheating (see details in (Soulet and Sussman, 2022b; 2022a)), in the present review all 14 studies (except one) examined low-powered devices under appropriate puffing protocols associated with the CORESTA Recommended Method (CRM) 81 (Cooperation Centre for Scientific Research Relative to Tobacco CORESTA, 2015; International Organization for Standardization ISO, 2018c): 3 s puffs, 30 s inter-puff lapse, 55 mL puff volume and 1 L/min airflow rate, or slight variations of these puffing parameters. In addition, most studies used standard appropriate analytical methods, but only six used blank samples, and one-third of the studies (6 out of 14) failed to provide sufficient information to potentially reproduce or replicate the experiments.

FIGURE 1
PRISMA-recommended workflow.
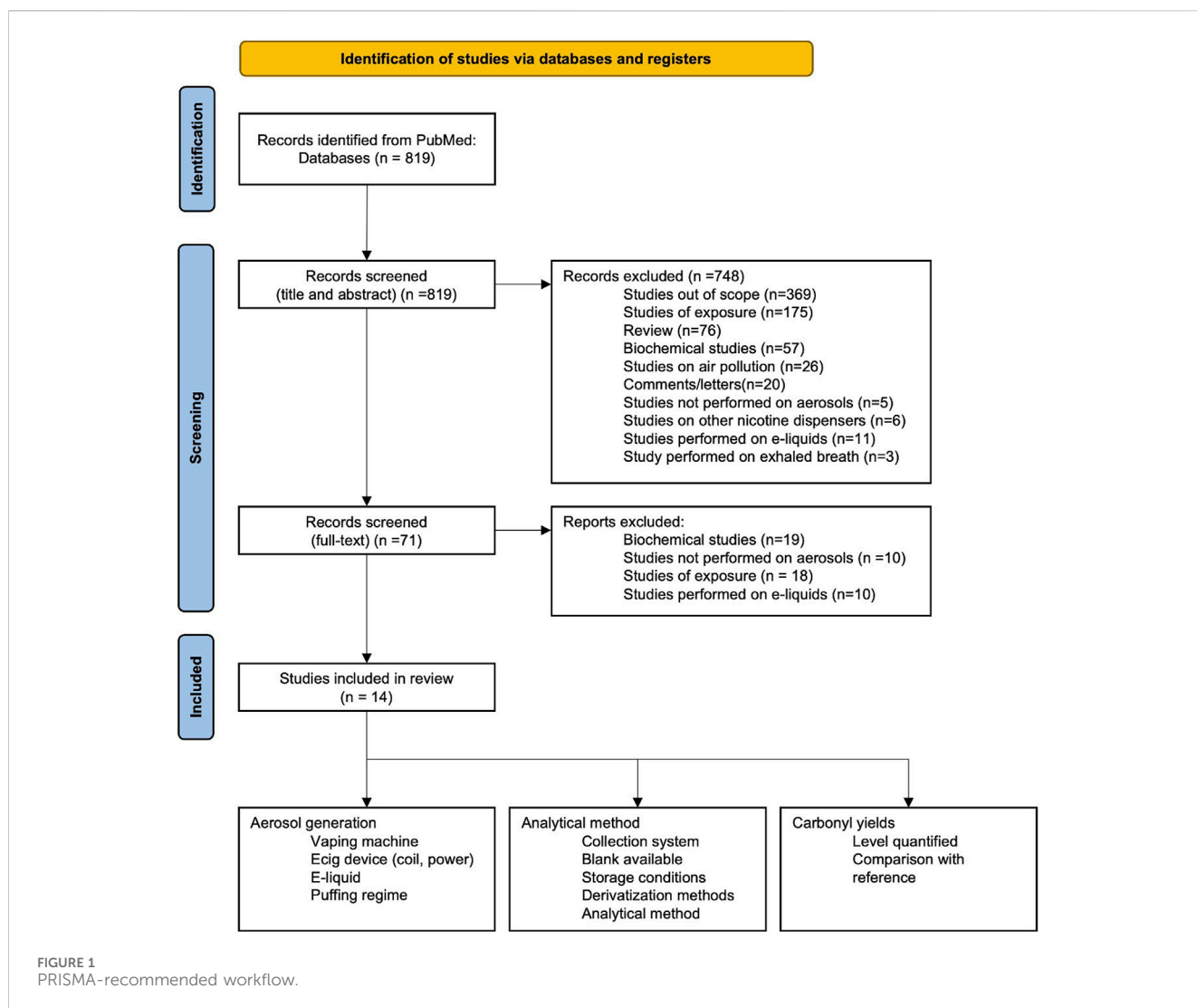
This work aims to provide a comprehensive review of emission studies conducted on ECs, with a particular focus on the assessment of the analytical methods employed in measuring carbonyls. Our section-by-section content is as follows. In Section 2, we describe the PRISMA search process for selecting the studies that we revised. Previous reviews are summarized in Section 3, while in Section 4, we present reviews of the 14 studies. A comprehensive discussion and summary of the revised studies are presented in Section 5, and our conclusions are presented in Section 6.

2 Methods

We performed a search of the PubMed database of articles on carbonyls in aerosol emissions of conventional cigarettes, electronic cigarettes, and heated tobacco products (see the PRISMA-recommended workflow displayed in Figure 1) (Page et al., 2021). The searched keywords were: {carbonyl OR aldehyde OR formaldehyde OR acetaldehyde OR acrolein} AND {e-cig aerosol OR electronic cigarette aerosol}. The searched terms used to locate articles did not include "HPHCs" or "Toxicants", which may have

resulted in relevant studies that included carbonyls being overlooked.

The initial search was performed on titles and abstracts, excluding articles published before 2018, considering that such studies were revised in the review of carbonyls by Farsalinos and Gillman and published in 2018 (Farsalinos and Gillman, 2018). We also excluded the studies reviewed by Soulet and Sussman (Soulet and Sussman, 2022b). Subsequently, a full-text search was performed by two independent reviewers to exclude articles that did not meet our purposes, such as reviews, exposure studies, biochemical studies, studies not focusing on carbonyls and studies that were not performed on aerosols. No language restriction was applied. We critically analysed the papers that were not excluded to highlight the limitations of the analytical methods, and puffing regimes, and to capture protocols used in the carbonyl analysis of, and ECs aerosols. In particular, we examined the fulfilment of the following criteria of experimental quality:

- Studies conducted on aerosols collected according to the standardized or recommended puffing protocol of the

Cooperation Centre for Scientific Research Relative to Tobacco (CORESTA).

- Aerosols were adequately treated for carbonyl entrapment.
- Analytical methods were adequate and reproducible, with particular attention to blank analyses.
- Samples were stored adequately prior to analysis.

The reproducibility criterion follows from demanding that authors provide in their methods section, main manuscript and/ or supplementary material, full information of all pertinent parameters, variables and outcomes in their experimental procedures, which makes it possible for other researchers, in principle, to reproduce or replicate the experiments. The following items were assessed to determine reproducibility: operating parameters and characteristics of the devices, e-liquid composition and nicotine concentration, protocols for aerosol generation, sample treatment and analytical method outcomes obtained in all performed repetitions of the experiments that were performed and all data from statistical analyses. If full information was supplied on these items, then the study is considered reproducible (Resnik and Shamoo, 2017; Laraway et al., 2019).

The search resulted in 14 studies, which we review in this article by placing a stronger emphasis on analytical methods, thus providing a more detailed examination of the processes of carbonyl analysis, the derivatization procedure, and the analytical method used for quantitative analysis. The PRISMA-recommended workflow was used (Figure 1).

3 Previously published review articles on EC carbonyl emissions

Farsalinos and Gillman published in 2018 (Farsalinos and Gillman, 2018) an outstanding landmark review of 32 studies on the emission of carbonyls from e-cigarette aerosols. Their revision elucidated methodological concerns on laboratory testing of EC emission that were discussed later in (Visser et al., 2021) and in (Soulet and Sussman, 2022a; Soulet and Sussman, 2022b), providing also relevant context for the present review article.

In their discussion section Farsalinos and Gillman provide a detailed description and discussion of the "Dry puff" phenomenon, an organoleptic (sensorially perceived) effect that users of ECs identify with a repellent burning taste in the aerosol. Farsalinos and Guillman explain how this phenomenon occurs when the balance of thermal energy on EC operation is disrupted by supplying excessive power, which produces conditions for a sufficiently rapid e-liquid consumption and its subsequent depletion in the tank, facilitating the pyrolization of the organic material in the wick by the heated coil, hence the users' perception of a "burning" taste.

While there was already evidence before 2018 that rising supplied power increases aldehyde yields (Geiss et al., 2015; Gillman et al., 2016), Farsalinos and Gillman showed that, besides their organoleptic effect, dry puff conditions prompt a more significant rise of carbonyl yields in the emissions (even surpassing those of cigarette smoke in extreme cases). Farsalinos and Guillman cited and commented previous studies (Farsalinos

et al., 2017a; Farsalinos et al., 2017b; Farsalinos et al., 2015; Farsalinos et al., 2018; Geiss et al., 2015) that not only verified users' recognition of the organoleptic effect of dry puffs (burning repellent taste), but also verified the increase in carbonyl yields by programing their vaping machines to reproduce (as close as possible) the puffing parameters specifically reported by users as associated with a dry puff sensation. The studies cited before (Farsalinos et al., 2017a; Farsalinos et al., 2017b; Farsalinos et al., 2015; Farsalinos et al., 2018; Geiss et al., 2015) were updated more recently by (Visser et al., 2021) in a detailed observational study complemented with analytic quantification of aldehyde levels in the specific puffing parameters that recruited vapers reported as dry puffs sensations.

Farsalinos and Gillman also focused on replications (Farsalinos et al., 2017a; Farsalinos et al., 2017b; Farsalinos et al., 2018) of three studies that had reported excessively high aldehyde yields (surpassing in two of them levels found in tobacco smoke). The replications proved that such excessive yields occurred under dry puff conditions, but aldehydes remained well below their level in tobacco smoke when the devices were tested under lesser power levels in agreement with normal consumer usage.

Since older EC devices lacked power control, users risked being surprised by the sudden emergence of a dry puff, which would evidently cause them to discontinue further puffing, but vaping machines used in the laboratory continue operating. Since only four of the 32 reviewed studies explicitly verified the occurrence of dry puff conditions, Farsalinos and Gillman suggested that several of the remaining 28 reviewed studies might have been conducted without awareness of these conditions, which do not represent normal conditions of realistic consumer usage. This observation prompted them to recommend that emission studies must consider beforehand puffing parameters that avoid these conditions.

The review of 36 emission studies focused on organic by-products by (Soulet and Sussman, 2022b) updated and extended key issues on carbonyls in EC emissions examined by Farsalinos and Gillman 4 years before. Soulet and Sussman also presented an important result previously reported by Talih et al. (Talih et al., 2020b), namely, the existence of a threshold of supplied power that triggers the onset of the exponential increase in the reaction pathways of carbonyl production. Moreover, they provided also a connection between this exponential increase, key puffing parameters (supplied power and airflow rate) and thermodynamical efficiency of the vaping process. They also re-examined the "Dry Puff" phenomenon discussed by Farsalinos and Gillman, showing that this phenomenon might occur along an abrupt process in low-powered devices (as in devices tested before 2018), but might occur gradually in high-power devices whose operational power range is much wider. Soulet and Sussman evaluated the 36 revised studies in terms of quality criteria of experimental design, criteria that we have adopted and adapted to evaluate the 14 emission studies considered in the present review.

4 Carbonyls in EC emission studies

In what follows we provide an extensive review of emission studies that have not been previously reviewed. The studies are

TABLE 1 Summary of analytical methods used in reviewed papers on carbonyls in emissions from e-cigarettes. Information on the usage of blank samples and other method validation is provided in Table 2.

First author	Funding	EC device	Coil and power	Puffing regime	Analytical method	Derivatization method
Conklin et al	Independent	Vaping robot blu cartridges3R4F	1.8 Ω	4 s puff 91 mL puff volume, 2 puffs/min, ISO 3308:2012	GC-MS/FT-ICR-MS	AMAH solution
El Mubarak et al	Independent	EC Nautilus	0.7 Ω 3.7 V, 19 W	30 puffs 3 s inter-puff	UHPLC-UV	DNPH solution
Lee et al	Independent	Not specified	Not specified	10, 20, 30 s puff 10 inter-puff	HPLC-UV	DNPH solution
Stephens et al	Independent	Kanger-tech CE4, EVOD	1.5 Ω	CRM 81 ISO, 20768:2018	CRM 74 ISO 21160:2018	DNPH solution
Gillman et al	Enthalpy Analytical	Innokin iSub	1.2 Ω	CRM 81 ISO 20768:2018	CRM 74 ISO 21160:2018	DNPH solution
Nicol et al	Industry BAT	Vype ePen	Not specified	CRM 81 ISO, 20768:2018 ISO 20778:2018	GS-MS	PFBHA solution
Talih et al	Independent	Juul	1.7 Ω 1.8 Ω	4 s puff, 10 s inter-puff 1 L/min	HPLC-UV	DNPH-cartridges
Rajapaksha et al	Independent	Juul	1.7 Ω 1.8 Ω	CRM 81 ISO, 20768:2018	rtCRDS	No derivatization
Son et al	Independent	ReuLeaux RX200 Aspire Cleito atomizer	50 W, coil resistance not specified	4 s puff 100 mL puff volume, 30 s inter-puff	HPLC-UV	DNPH solution
El-Hellani et al	Independent	Kangertech Subox Mini	Not specified	4 s puff, 10 s inter-puff 8 L/min	HPLC-UV	DNPH-cartridges
Lalonde et al	Industry Juul Labs	Juul	1.8 Ω	CRM 81 ISO, 20768:2018	UHPLC-MS/MS	DNPH solution
McGuigan et al	Independent	Customized vaping machine	Not specified	CRM 81 ISO, 20768:2018	HPLC-MS/MS	PFBHA solution
Pinto et al	Industry BAT	Vype ePod1.0, 1R6F	Not specified	CRM 81 ISO, 20768:2018	GC-MS	DNPH-cartridges
Talih et al	Independent	Juul and 5 disposables	1.64–1.9 Ω	15 puff 4 s puff 1 L/min	HPLC-UV	DNPH-cartridges

summarized in Tables 1, 2, and their evaluations are summarized in Table 3.

Devices and aerosol generation. The authors used a software-controlled (FlexiWare) cigarette-smoking robot (CSR) (SCIREQ; Montreal, CAN), with e-liquids and carrier solutions PG or VG (or mix of PG: VG) from cartridges of commercial blu® EC, loaded into a refillable, clear tank (0.5 mL) atomizer with a coil resistance of 1.8 Ω coupled with a rechargeable blu PLUS + TM (3.7 V) battery (power output 7.6 W) (Conklin et al., 2018). Puffing regime: 4 s puff, 91 mL puff volume, and two puffs/min.

Analytical methods. The authors aimed to study urine biomarkers from whole-body exposure of 12–20-week-old mice to EC aerosols and 3R4F smoke. The levels of carbonyls emitted by the loaded e-liquids with various flavors were quantified. Ten

puffs were collected in Tedlar bags. A silicon microreactor coated with 4-(2-aminooxyethyl)-morpholin-4-ium chloride (AMAH) was used to trap carbonyl compounds via oxidation reactions. The analysis was performed using gas chromatography-mass spectrometry (GC-MS) or Fourier transform ion cyclotron resonance mass spectrometry (FT-ICR-MS). Analyses were performed on aerosols from liquids containing only PG, VG, or mixtures at different ratios of 25/75 (PG/VG), 50/50 (PG/VG), and 75/25 (PG/VG). The analysis was carried out by derivatizing the carbonyls with AMAH. This method derivatizes carbonyls by forming oximes using AMAH. The latter must be synthesized, and this can lead to increased error in the reaction with carbonyls if byproducts can be formed in the AMAH synthesis reaction or if it is not purified properly. In addition, before

TABLE 2 Summary of method validation used in reviewed papers. √ represents the presence of analysis blanks. In contrast, x represents the flawed or lack of blank samples.

First author	Method validation	Blank analysis
Conklin et al	*p*-values calculated based on Oneway ANOVA with Tukey adjustment	x
El Mubarak et al	LOD was calculated based on the signal-to-noise ratios of 3 LOQ was calculated using a signal-to-noise ratio of 10	√
Lee et al	The precision of the analytical method was calculated and reported as the mean value ±SD.	x
Stephens et al	FDA guidelines for bioanalytical method validation	x
Gillman et al	LOD was calculated based on the signal-to-noise ratios of 3 LOQ was calculated using a signal-to-noise ratio of 10	x
Nicol et al	LOD was calculated based on the signal-to-noise ratios of 3 LOQ was calculated using a signal-to-noise ratio of 10	√
Talih et al	*p*-values calculated based on Oneway ANOVA with Tukey adjustment	x
Rajapaksha et al	Not provided	x
Son et al	LOD was calculated based on the signal-to-noise ratios of 3 LOQ was calculated using a signal-to-noise ratio of 10	√
El-Hellani et al	The precision of the analytical method was calculated and reported as the mean value ±SD.	x
Lalonde et al	The precision of the analytical method was calculated and reported as the mean value ±SD.	x
McGuigan et al	The precision of the analytical method was calculated and reported as the mean value ±SD.	√
Pinto et al	LOD was calculated based on the signal-to-noise ratios of 3 LOQ was calculated using a signal-to-noise ratio of 10	√
Talih et al	The precision of the analytical method was calculated and reported as the mean value ±SD.	x

TABLE 3 Evaluation of the revised studies in terms of fulfilment of the four conditions of experimental quality. We used the symbols √ and x to denote one and zero score points, while "1/2" denotes half a point when a condition was partially fulfilled. Reliability is given in a "traffic light" coloring, with "Reliable" (green) for a score 3.0 and above, "Partially Reliable" (yellow) for a score between 2.0 and 3.0, and "Unreliable" (red) for a score below 2.0.

First author	Provided sufficient information to reproduce results?	Adequate Puffing regime	Adequate Analytical methods	Blanks	Score and Comments
Conklin et al	√	√	√	x	3.0 Reliable
El Mubarak et al	√	√	√	√	4.0 Reliable
Lee et al	Computerize system. Ω NOT disclosed.	?	√	x	1.5 Unreliable
Stephens et al	Ω NOT disclosed	√	√	x	2.5 Partially Reliable
Gillman et al	√	√	√	x	3.0 Reliable
Nicol et al	√	√	√	√	4.0 Reliable
Talih et al	√	Unrealistic puffing regime	√	x	2.5 Partially Reliable
Rajapaksha et al	(1/2) Some results not quantifiable	√	√	x	2.5 Partially Reliable
Son et al	(1/2) Ω of sub-ohm coil not disclosed	(1/2)	√	√	2.0 Partially Reliable
El-Hellani et al	"do-it-yourself" e-liquids, W not disclosed	Unrealistic puffing regime	√	x	1.0 Unreliable
Lalonde et al	√	√	√	x	3.0 Reliable
McGuigan et al	Devices not disclosed	?	√	√	2.0 Partially Reliable
Pinto et al	√	√	√	√	3.0 Reliable
Talih et al	√	√	√	x	3.0 Reliable

performing GC-MS analysis, the oximes synthesized with carbonyls must be treated with poly-4-vinylpyridine to convert positively charged AMAH adducts to neutral AMA adducts.

Carbonyl yields. formaldehyde 0.25 ± 0.12 µg/puff, acetaldehyde 1.01 ± 0.34 µg/puff, acetone 0.11 ± 0.007 µg/puff, and low levels of crotonaldehyde $0.25 \pm 0.12 \times 10^{-3}$ µg/puff were found in the emissions of liquids containing only PG. Acrolein levels were below the detection limit. in VG-only emissions, formaldehyde was 0.59 ± 0.11 µg/puff, acetaldehyde 0.70 ± 0.03 µg/puff, acetone 0.11 ± 0.01 µg/puff and acrolein 0.08 ± 0.002 µg/puff, but crotonaldehyde was below the LOD. The 3R4F cigarette was puffed with 2 s puff, 35 mL puff volume, one puff/min (International Organization for Standardization ISO, 2012). Although the authors made no explicit comparison, aldehydes in EC emissions resulted in significantly lower yields than those in the smoke of the reference cigarette 3R4F.

Device and aerosol generation. A Nautilus atomizer with a 0.7 Ω resistance and supplied voltage of 3.7 V (19.5 W) and a VTC EC were used for sample production (El Mubarak et al., 2018). Thirty puffs were smoked at 3s intervals (El Mubarak et al., 2018).

Analytical methods. This study aims at quantifying the carbonyl compounds in e-cigarette emissions, as they are produced by the decomposition of VG and PG contained in e-liquids. Carbonyls were derivatized with DNPH, by reacting the aerosol sample with a solution of acetonitrile, water, and H_3PO_4. Aerosols were collected from the impingers containing a solution of DNPH, water H_3PO_4, and acetonitrile. The reaction was run for 30 min, and NaOH was used to alkalize the pH of the solution, allowing it to pass through the chromatography columns. Aerosols were collected from two impingers that contained a solution of DNPH and acetonitrile. Analyses were performed using UHPLC-UV. The method of analysis used is adequate, although the authors state that ultra-performance liquid chromatography coupled with mass spectrometry is more sensitive but still uses UV as the detector.

Carbonyl yields. The results of this study were expressed as carbonyls emitted by e-liquids in µg/puff or µg/mL. In particular, for the carbonyl compounds analyzed, an e-liquid made of 100% PG produced a smaller quantity of carbonyls than that made of 100% VG and the same from e-liquids with VG/PG ratios of 50/50 (PG/VG) and 70/30 (PG/VG). The yields in µg/puff were 0.004 ± 0.0003 (pure PG) and 0.079 ± 0.008 (pure VG) for formaldehyde and 0.011 ± 0.001 (pure PG), 0.053 ± 0.0008 (pure VG) for acetaldehyde.

Device and aerosol generation. The EC device consisted of a mouthpiece, an atomizer to vaporize e-solution at a fixed voltage of 4.2 V, a 2-mL cartridge for storing the EC liquid, and a 900-mAh rechargeable battery. A computerized vaping machine was used with the following puffing protocol: 2 s puff duration and 10 s inter-puff duration, with 5, 10, and 15 puffs in each session. The authors did not specify the percentages of PG and VG contained in the e-liquid, which is particularly relevant because different percentages of these two compounds affect the emission of carbonyl compounds.

Analytical methods. Carbonyl compounds in the EC aerosols were analyzed by derivatization using DNPH and HPLC-UV analysis (Lee et al., 2018). The obtained samples were entrained through an impinger filled with a derivatization solution of acetonitrile and DNPH acidified with H_3PO_4, and then analyzed using the HPLC-UV method. It is conceivable that the duration of the reaction is reported for the analysis of carbonyl compounds in e-liquids and, therefore, performed correctly for 30 min. However, it was not possible to precisely determine this, and it was not possible to determine whether the reaction was quenched with a base, as it was not reported by the authors. This could promote secondary condensation reactions and prevent proper quantitative analysis of carbonyls.

Carbonyl yields. Seven carbonyl compounds were analyzed: formaldehyde, acetaldehyde, acrolein, propionaldehyde, butyraldehyde, isovaleraldehyde, and valeraldehyde. In general, formaldehyde was always detected in samples at higher concentrations than those of all other carbonyl compounds. For example, in sample R-2D, the concentration of formaldehyde in µg/mL was 3.2 ± 0.41, while that of acetaldehyde was 0.3 ± 0.01 and acrolein was 0.0002.

Device and aerosol generation. Three generations of EC devices (Kanger-tech CE4, EVOD, and Kanger-tech CE4) and e-liquid formulations with different PV/VG ratios were used. Coils with 1.8 Ω resistance were used for the CE4 and EVOD devices, and power was supplied by an external controllable power supply. The Subox Mini-C includes a 1.5 Ω SSOCC atomizer powered by its battery. Although some characteristics of EC were explained, the author did not state the power setting (in Watts) at which the tests were performed. Aerosols were produced by vaping 50–55 mL puffs for 4 s at intervals of 30 s (CRM 81, ISO 20768:2018) (International Organization for Standardization ISO, 2018c).

Analytical methods. This study aimed to quantify the carbonyls in the emissions from these ECs using a method to trap aerosols consisting of amorphous silica into a syringe for later extraction (Stephens et al., 2019). The aerosols were trapped as droplets on the syringe walls and silica wool threads. The aerosol was recovered from a silica syringe, placed in a centrifuge tube, and centrifuged again. It was then stored at −20°C until analysis. The authors stated that silica wool retained approximately 94 percent of its vaporized liquid mass. Analyses were performed using the CRM 74 method (International Organization for Standardization ISO, 2018a; Cooperation Centre for Scientific Research Relative to Tobacco CORESTA, 2019). The samples were reacted with DNPH for 25 min and then stabilized with Trizma base solution. The derivatized carbonyls were studied using HPLC-DAD and HPLC-MS/MS. Separation was achieved using a C18 column, water, and a mixture of acetonitrile and methanol (1:14) as the mobile phases. The analysis was performed on samples stored at room temperature and −20°C to limit the loss of volatiles. No significant differences were observed among the samples. The recovery of carbonyls by centrifugation was also tested, and the results showed good recovery for all carbonyls, except formaldehyde.

Carbonyl yields. In general, the results for the carbonyls are in agreement with the literature, showing that the use of silica fibers allows for an accurate analysis of carbonyl emissions. In particular, formaldehyde ranged from 0.182 ± 0.023 to 9.896 ± 0.709 µg/puff, and acetaldehyde ranged from 0.059 ± 0.005 to 0.791 ± 0.073 µg/puff. The high upper-end yields of formaldehyde are likely associated with excessive supplied power (a valid assumption since the author did not reveal the power levels used for the aerosol production).

Device and aerosol generation. Aerosols were generated by ten Innokin iSub EC devices (two of which were eliminated from the study) equipped with 1.2 Ω coils powered at 12 W by an Evolv DNA

200 battery unit (Gillman et al., 2020). The devices were tested with four flavored and one non-flavored e-liquids. Puffs were generated by a Cerulean SM450e equipment with the puffing regime of CRM 81 (Cooperation Centre for Scientific Research Relative to Tobacco CORESTA, 2015; International Organization for Standardization ISO, 2018b).

Analytical methods. Highlight differences in carbonyl emission as a function of degradation of the main components of e-liquids, PV, and VG. The unflavoured formulation was homemade to match the PG/VG ratio and nicotine content of the four flavored formulations. The flavored formulations contained a 2/1 ratio of PG/VG and 1.8% nicotine. The unflavored formulation was prepared using a 2/1 ratio of PG/VG and 1.8% nicotine. Tanks and coils were reused for all formulations, emptied, washed with methanol, and air-dried overnight before they were filled with the next formulation. Three replicates were collected for each formulation from 10 ECs, for a total of 30 samples per formulation. Aerosol samples were collected in impingers using a DNPH trapping solution prepared using acetonitrile and H_3PO_4, and then quenched with pyridine. The samples were then analyzed using HPLC-UV (Gillman et al., 2016). Separation was achieved using a C18 column and solvent mixture as the mobile phase, as indicated by CRM 74 (Cooperation Centre for Scientific Research Relative to Tobacco CORESTA, 2019; International Organization for Standardization ISO, 2018a).

Carbonyl yields. The flavored formulations tested resulted in a 150%–200% increase in acetaldehyde, no increase or decrease in acrolein, and, depending on the flavored formulation, an increase, decrease, or no change in formaldehyde levels. The methodology of this study was comprehensive and well applied.

Device and aerosol generation. The purpose of this study was to characterize EC emissions using stainless-steel mesh fabric-free distillation plate technology that heats and aerosolizes e-liquid in a single process (Nicol et al., 2020). Carbonyl emissions were compared with those of a reference cigarette, 1R6F, and an EC device EC(BT) Vype ePen. Having ascertained that the device plays an important role, especially regarding the wick and heating coil, the authors developed a novel device that takes advantage of distillation plate technology. IS1.0 (TT) comprises a stainless-steel wire pressed into a mesh structure. It did not contain a wick or a heating coil. According to the authors, this would result in lower levels of carbon emissions. The EC used to compare carbonyl emission levels had the following characteristics: a rechargeable battery section, a replaceable e-liquid-containing cartridge, and a nichrome wire coil heater wrapped around the wick, with a power output of 4.6 W at 3.6 V. The smoking regimen for the reference cigarette, 1R6F, was Health Canada (HCI) (ISO 20778:2018) (International Organization for Standardization ISO, 2018a), while the CRM 81 (ISO 20768:2018) (Cooperation Centre for Scientific Research Relative to Tobacco CORESTA, 2015; International Organization for Standardization ISO, 2018b) was chosen for e-cigarettes.

Analytical methods. The analytical method used for the detection of carbonyls is described in the Supplementary Material. The authors used a non-standardized and unconventional method for the detection of carbonyls. Aerosols collected in the impingers were extracted with water, derivatized with PFBHA, and analyzed using GC-MS. Furthermore, the authors compared the results obtained with the blank sample, which was

optimal; however, they used different reference values for IS1.0 (TT) (referred to as IS2.0), 1R6F, and EC(BT): micrograms per 50 puffs, micrograms per cigarette, and micrograms per 100 puffs, respectively.

Carbonyl yields. When the results are compared, it is not clear why the authors maintained different ratios and did not report all the results to one universal unit of measure for all three devices used.

Device and aerosol generation. The authors analyzed the emissions of American and British Juul pods, including their electrical power, total and free nicotine, PG/VG ratio, carbonyls, and reactive oxygen species (Talih et al., 2020a). Liquids and aerosols were analyzed by GC-MS, HPLC, and fluorescence. In particular, aerosols were generated using the AUB Aerosol Lab Vaping Instrument, programmed to perform 15 puffs of 4-s duration, a 10-s interval between puffs, and a flow rate of 1 L/min.

Analytical methods. Carbonyl compounds were trapped on the DNPH cartridges, eluted with 90/10 (v/v) ethanol/acetonitrile, and quantified using HPLC-UV. Gradient elution was performed using a C18 column. The solvents used were water/acetonitrile/THF (60/30/10, v/v/v), water/acetonitrile (20/30, v/v), and acetonitrile.

Carbonyl yields. Compared with the U.S. version, the Juul UK version had approximately one-third the concentration of nicotine in liquids and aerosols. In this case, the authors used an unusual puffing regime, and the final volume of aerosols collected was not reported. Regarding carbonyl compounds, differences were found regarding formaldehyde emissions 4.07 (0.24) (μg)/15 puffs in Juul USA and 3.66 (0.14) in Juul UK, while very similar results were found for acetaldehyde, acetone, and acrolein.

Device and aerosol generation. This paper aimed at analyzing three flavors of Juul pods with 3.7 V and 1.6 Ω coil using a new analytical approach: runtime cavity ringdown spectroscopy (rtCRDS) (Rajapaksha et al., 2021). Aerosols were generated using a peristaltic pump following the ISO 20768:2018 (International Organization for Standardization ISO, 2018d) vaping pattern, but with a higher puff volume to compensate for the relatively weak aerosol generation observed in the Juul device compared with the previous generation devices. The puff duration was 4 s, with a 30 s interval between puffs and a volume of 73.33 mL per puff.

Analytical methods. Aerosols were collected in Tedlar gas bags and analyzed using rtCRDS immediately after aerosol collection. The authors used a fairly novel and highly sensitive technique to identify trace levels of chemicals in air. Specifically, it was used to characterize aerosols with a resolution of a single puff. The technique is based on quantum cascade lasers, which, unlike typical IR, provide low energy to allow the analytes to be excited in their vibrational state, thus allowing for the selective identification of molecules through their molecular fingerprints.

Carbonyl yields. Five spectral datasets were acquired for each sample and the average was used to plot the IR spectra of each sample. The authors claimed that PG oxidation is one of the main sources of acetaldehyde in Juul aerosols. However, the results of the analysis only show the presence or absence of carbonyl analytes; in fact, the analysis is not quantitative, and the results reported are not quantifiable.

Device and aerosol generation. The purpose of this study was to develop a method for producing aerosols from ECs (Son and Khlystov, 2021). The authors developed a vaping machine (E-ACES), analyzed

the aerosols produced, and compared them with aerosols produced using conventional smoking machines. An EC "mod" type ReuLeaux RX200 and an Aspire Cleito atomizer were used to produce aerosols. The authors used a puff duration of 4 s, vapor volume of 100 mL vaping interval of 30 s, tobacco-flavored e-liquid (30/70 PG/VG), and 6 mg/mL nicotine at 50 W power output. The puffing parameters lead to an airflow rate of 25 mL/s = 1.5 L/min, but coil resistance was not specified, so it is not possible to determine if this airflow was appropriate for a device powered at 50 W.

Analytical methods. Aerosols were passed through glass wool and beads soaked in an acidic solution of DNPH in acetonitrile. Five aerosol puffs were collected and extracted with acetonitrile. For carbonyl analysis using the conventional puffing method, aerosols were passed through DNPH cartridges and extracted with acetonitrile. All samples were analyzed using an HPLC-UV system using acetonitrile and ultrapure water to separate the carbonyl compounds. However, the chromatographic columns used were not described.

Carbonyl yields. The carbonyl levels measured using the DNPH filter/cartridge method and E-ACES were not significantly different, except for benzaldehyde levels determined using the conventional method, which were significantly higher than those determined using the E-ACES method (0.219 ± 0.008 μg/puff vs 0.111 ± 0.026 μg/puff).

Device and aerosol generation. This study analyzed aerosols from "do-it-yourself" e-cigarette liquids (El-Hellani et al., 2022). Aerosols were produced using the AUB Aerosol Lab22 with a puffing regime of 10 puffs for 4s, an interval between puffs of 10s, and a flow rate of 8 L/min.

Analytical methods. A 1 L/min branch was used for carbonyl quantification using DNPH cartridges. There was missing information in this study, which was not found in the Supplementary files. In fact, the characteristics of the ECs are not explained; for example, the coil resistance or supplied power is a significant flaw because this lack of information makes it impossible to reproduce and assess the results of the analysis.

Carbonyl yields. The carbonyl emissions of DIY concentrates, or menthol and tobacco flavorings mixed with DIY additives were comparable to those of commercially flavored e-liquids. The addition of sucralose to PG/VG resulted in a significant decrease in acetone and crotonaldehyde but a significant increase in propionaldehyde. The addition of ethylmaltol resulted in increased acetaldehyde levels. However, these outcomes might vary with alternative "do-it-yourself" e-liquids.

Device and aerosol generation. The authors aimed at testing a "triple puff" method to perform aerosol collection faster and compare it with the traditional method (Lalonde et al., 2022). Juul e-cigs were vaped according to the ISO 20768:2018 regimen (Cooperation Centre for Scientific Research Relative to Tobacco CORESTA, 2015; International Organization for Standardization ISO, 2018b) (55 mL, 3 s, and 30 s between puffs). Single-puff aerosols were produced using linear smoking machines and triple-puff aerosols were produced using rotary smoking machines.

Analytical methods. Carbonyl concentrations were measured by Enthalpy Analytical by Enthalpy's SOP AM-244. An aliquot of the aerosol condensate was derivatized using DNPH. The analyses were performed by UHPLC-MS/MS. The results of the carbonyl analysis

collected using these two methods were then compared with those of the 1R6F reference cigarette.

Carbonyl yields. Acrolein and acetaldehyde were found to be different from the triple puff and single puff methods, which the authors attributed to the degradation of acetaldehyde. To achieve these considerations, the authors failed to accurately describe the analytical method, which rendered it impossible to reproduce (a serious flaw).

Device and aerosol generation. The purpose of this study was to develop a quantitative method for measuring four harmful carbonyls (acetaldehyde, acrolein, crotonaldehyde, and formaldehyde) in aerosols generated by ECs (McGuigan et al., 2022). Aerosols were formed using a CETI-8 vaping machine following the CRM 81 method (ISO 20768:2018) (Cooperation Centre for Scientific Research Relative to Tobacco CORESTA, 2015; International Organization for Standardization ISO, 2018b). The authors did not provide a description of EC devices.

Analytical methods. The tested method used a commercially available sorbent bed treated with a derivatization solution to trap and stabilize the carbonyls. Analytes were extracted from the sorbent material using acetonitrile and analyzed using HPLC-MS/MS. Separation was performed using a C18 column equipped with a precolumn. Water with ammonium acetate and acetonitrile were used as the mobile phase.

Carbonyl yields. The devices produced aerosols containing the following ranges of carbonyls: acetaldehyde (0.0856–5.59 μg), acrolein (0.00646–1.05 μg), crotonaldehyde (0.00168–0.108 μg) and formaldehyde (0.0533–12.6 μg). The study reported that the method blank samples collected and analyzed daily showed no residual carbonyl content in solvents, cartridges, or vaping. The authors did not describe the EC devices used for aerosol generation, which is a serious shortcoming that prevents assessing the study outcomes on the formation of carbonyl byproducts.

Device and aerosol generation. In this study, aerosols emitted from fourth generation "pod" EC devices Vype ePod1.0 using microporous ceramic as the wicking material were compared with those emitted from the conventional reference 1R6F cigarette (Pinto et al., 2022). The EC operates within a range from non-adjustable 2.2–3.1 V non-adjustable, a power of 6.5 W, resistance NiCr, 0.8–1.4 Ω. Conventional cigarettes were smoked according to the ISO intense smoking regime typically using 9–10 puffs. EC aerosols were generated according to ISO 20768: 2018 (International Organization for Standardization ISO, 2018d) using a rotary or linear puffing machine. Cigarette and EC emissions were sampled and analyzed in five independent replicates.

Analytical methods. Determination of selected carbonyls in E-liquids, EC aerosols, and mainstream tobacco smoke using PFBHA derivatization and gas chromatography/mass spectrometry analysis. The Pads were extracted using an acetonitrile impinger solution. A portion was diluted with Type I water and derivatized with PFBHA, followed by extraction in toluene. The samples were analyzed using GC-MS.

Carbonyl yields. The results showed that carbonyl levels were significantly reduced compared with those in other studies on e-cigarettes and 1R6F cigarettes.

Device and aerosol generation. The purpose of this study was to analyze aerosol emissions from various disposable ECs and compare

them with those from Juul devices (Talih et al., 2022). The vaping pattern was performed with the AUB Aerosol Lab Vaping Instrument consisting of 15 puffs for 4 s at a flow rate of 1 L/min.

Analytical methods. The aerosols were passed through a DNPH cartridge, washed with a 90/10 (v/v) ethanol/acetonitrile solution, and quantified using ultraviolet high-performance liquid chromatography (HPLC-UV). Gradient elution was performed using a C18 column. The solvents used were water/acetonitrile/THF (60/30/10, v/v/v), water/acetonitrile (20/30, v/v), and acetonitrile.

Carbonyl yields. Except for the SEA device, the single-use products generated significantly more toxicants than the Juul.

5 Discussion

Low-molecular-weight carbonyl compounds such as acetaldehyde, acrolein, and formaldehyde are among the most toxic compounds in cigarette smoke. The main sources of these aldehydes are carbohydrates found naturally in tobacco or in the components of e-liquids that undergo thermal degradation, resulting in the emission of carbonyl compounds (Baker et al., 2005).

Consequently, the amount of these aldehydes in the emissions generated by various tobacco products needs to be examined and determined to best assess the potential toxicity of these compounds in EC aerosol. In the 14 studies considered in the present review the detected levels of the main aldehydes (formaldehyde, acetaldehyde and acrolein) cluster below 1 mg/puff. These are considerably lower values than the levels of same compounds found in the smoke of cigarettes used in laboratory tests (Counts et al., 2005): 7.5–12.5 mg/puff (formaldehyde), 50–150 mg/puff (acetaldehyde), 7.5–15 mg/puff (acrolein), where we assume 10 puffs per cigarette to obtain these values.

5.1 Derivatization methods

Several analytical methods for the derivatization of carbonyl compounds are described in this review. However, most studies, particularly 10 papers, reported the use of 2,4-DNPH for the formation of hydrazones, that is, adducts between carbonyl compounds and DNPH (Cox et al., 2016), as recommended by CRM 74 (Cooperation Centre for Scientific Research Relative to Tobacco CORESTA, 2019; International Organization for Standardization ISO, 2018a). The reaction of a carbonyl compound with DNPH is an addition-elimination reaction catalyzed by an acidic environment. The acid activates the carbonyl group via the formation of a carbocation. This is more easily attacked by a nucleophile consisting of the amine of DNPH through nucleophilic addition. A tetrahedral intermediate was then formed. The elimination of water then occurs, resulting in the formation of 2,4-dinitrophenyl hydrazone. The pH of the solution should be adequately controlled to prevent excessively acidic conditions that could lead to the condensation of carbonyl compounds and the consequent inability to quantify them. Furthermore, the optimal reaction time for carbonyl compounds with DNPH was estimated to be 30 min, which allowed the derivatization of all carbonyls in the solution and prevented the

formation of polyderivative compounds. The reaction is usually quenched with a pyridine solution to basify the solution and prevent polyderivatization reactions. In particular, six studies reported the use of an acidic solution of DNPH in acetonitrile, and four used a DNPH cartridge or DNPH silica. Compared to impingers containing an acidic solution of DNPH in acetonitrile, DNPH cartridges exhibit limitations. The first can be saturation, which could occur during the same analysis and may also depend on the volume of aerosol passing through the cartridge. Condensates can be deposited on cartridges, which can impair their ability to retain carbonyls. Additionally, oxidants in the air may cause secondary reactions with DNPH and interfere with the study of carbonyls (Uchiyama et al., 2011). Furthermore, with unsaturated carbonyls (such as acrolein), the possibility of the formation of polymerization byproducts has been demonstrated, preventing the proper analytical identification of unsaturated carbonyl compounds (Van Leeuwen et al., 2004).

Two studies (Nicol et al., 2020; McGuigan et al., 2022) used the PFBHA derivatization technique. Derivatization with PFBHA is the second most widely used reaction following derivatization with DNPH (Szulejko and Kim, 2015). The reaction occurs through nucleophilic addition of PFBHA to the carbonyl, with the formation of an intermediate. Finally, following the removal of a water molecule, a derived oxime was formed (Bao et al., 2014). Conklin et al. used a derivatization reaction with a silicon microreactor coated with 4-(2-aminooxyethyl)-morpholin-4-ium chloride AMAH (Conklin et al., 2018). Rajapaksha et al. collected the aerosols in a Tedlar bag and analyzed them directly in a gas chromatograph coupled to a mass spectrometer and rtCRDS, without derivatizing them (Rajapaksha et al., 2021). The numerous derivatization methods employed pose a challenge in making direct comparisons between study values owing to the diverse parameters utilized.

5.2 Analytical methods

Although several analytical methods have been reported for the quantification of carbonyls, eight studies have used the HPLC-UV method. The HPLC-UV method is the most widely recognized method recommended by CORESTA, although the protocol recommended by CORESTA was not followed by all the authors. The CORESTA recommended methods for HPLC analysis are CRM 74 and CRM 96. CRM 74 outlines the procedures for quantifying all carbonyls in conventional cigarette smoke through derivatization with DNPH and subsequent HPLC-UV or HPLC-DAD analysis (International Organization for Standardization ISO, 2018a). On the other hand, CRM 96 describes procedures for quantifying formaldehyde and acetaldehyde in e-cigarette aerosols using the same methods of derivatization with DNPH and HPLC-UV or HPLC-DAD analysis (Cooperation Centre for Scientific Research Relative to Tobacco, 2024).

In the reviewed studies, chromatographic separation was performed using a reversed-phase C18 column as the stationary phase. Notably, reversed-phase columns retain less polar compounds than more polar compounds. The use of a C18 column increases selectivity because of its high surface coverage. In addition, gradient separation was performed in all

the studies using liquid chromatography. This is because the analytes have different hydrophobicities, and gradient elution allows for rapid analysis. Moreover, all studies that used a UV spectrometer as a detector used a wavelength of 360 nm, which prevents the detection of extraneous peaks with higher absorbance at shorter wavelengths. Despite the widespread use of liquid chromatography coupled with ultraviolet spectrophotometry, there are some issues related to the fact that this methodology was developed for conventional cigarettes and then applied to ECs. Therefore, it would be more appropriate to apply CRM 96, although it outlines operational procedures for the analysis of formaldehyde and acetaldehyde only. Flavors contained in e-liquids have been shown to cause analytical interference in the HPLC-UV method. In addition, mass spectrometry coupled with liquid chromatography (LC-MS) is an analytical technique with better selectivity and sensitivity. This technique, applied to the study of aerosols from ENDS, allows a more accurate quantification of low-concentration carbonyls (mainly medium- and high-molecular-weight carbonyls) and more adequately quantifies these molecules (Flora et al., 2017; Zhu et al., 2020).

Finally, one technique that was not identified in the studies was Gas Chromatography coupled with two-dimensional separation (GCxGC) and various detection methods like Time-of-Flight Mass Spectrometry (TOFMS) and Flame Ionization Detection (FID). Despite its limited use in detecting carbonyls, this technique is considered valuable for identifying volatile organic compounds (VOCs) because of its enhanced selectivity.

In addition to capture and analysis techniques, the composition of e-liquids must also be well-characterized, as they can affect the emission of carbonyls (Qu et al., 2018). The PV/VG ratio and the presence of flavoring agents influence the production of carbonyls. In fact, all the studies examined in this review have well-characterized the characteristics of e-liquids before performing the analysis (Van Leeuwen et al., 2004; Uchiyama et al., 2011).

5.3 Blank analysis and sample storage

Only five of the 14 revised studies used blank samples (Table 2). The blank method involves the analysis of an analyte-free matrix processed using the same method as that used for the analysis. Blank analysis plays a key role in quantitative investigation because it excludes contamination from the results of the analysis. Among the studies reviewed, only six performed or presented a blank analysis of the air. The handling of blank samples is a critical component of chemical analysis. It is essential to closely monitor the results of blank samples during the analysis process to identify anomalies that may suggest issues with collection or analysis procedures. Furthermore, it is crucial to incorporate the results of blank samples into reports or publications to ensure transparency and enable others to comprehend the data more effectively. The results of the blank samples should be presented clearly and concisely alongside those of the other samples. It is important to verify whether the data are derived only from the sample and not from contamination outside the sample (Cantwell, 2019).

This represents a serious shortcoming in the accuracy, treatment, and interpretation of the analyzed data. Table 2 illustrates that the above-mentioned studies utilized a range of

alternative methods to validate the analytical techniques in question. Generally, the limits of detection and quantification are determined by considering the signal in relation to the background noise. Other studies have employed varying numbers of analyses and have reported results in terms of standard deviation.

Furthermore, almost none of the reviewed studies reported how the samples, e-liquids and devices were stored before the analysis. To understand and reproduce these results, it is necessary to know how the devices were maintained, to rule out any form of instrument spoilage or deterioration, and whether the e-liquids of electronic cigarettes were maintained under appropriate temperature and light conditions to exclude the formation of internal secondary reactions. According to the guidelines outlined in the CRM Method 18, devices and aerosols are recommended to be stored at room temperature. This applies specifically to e-liquids, which should be kept in hermetic containers to prevent the accidental ingestion of water. These conditions are necessary when devices and aerosols are used within a short period of aerosol production. However, if these conditions are not applicable, both e-liquids and cartomizers should be stored at a temperature of at least −10 °C. Furthermore, Jităreanu et al. (2022) recently showed that the storage period of e-liquids, storage temperature, and type of cartomizer can strongly influence the concentrations of metals within the liquids (Jităreanu et al., 2022). In addition, for studies comparing the emissions of ECs with those of conventional cigarettes, it is necessary to determine whether the latter has been maintained at an optimal level of temperature and humidity. Similarly, the atmospheric conditions during the analysis are significant for ruling out any kind of analytical interference. Moreover, it is important to know the storage conditions of the collected aerosol samples if they are not analyzed immediately after collection.

5.4 Puffing regimes

The puffing regime in laboratory testing strongly influences the production of carbonyls from e-cigarette emissions. A puffing regime is characterized by four basic parameters: puff duration, puff volume, intervals between puffs, and the airflow rate. There is evidence that variation in even one of these parameters can change the quantity of carbonyls emitted (Bao et al., 2014; Cooperation Centre for Scientific Research Relative to Tobacco CORESTA, 2015). Laboratory emission studies are essential to evaluate quality control and compare EC devices, hence vaping machines require to puff the devices with a protocol of regimented puffs which should (ideally) be systematized within a recognized standard. So far, most emission studies rely on the ISO 20768:2018 CORESTA standard (Cooperation Centre for Scientific Research Relative to Tobacco CORESTA, 2015; International Organization for Standardization ISO, 2018b) (3 s puff, 30 s inter-puff, 55 mL puff volume, airflow 1.1 L/min), or minor variation of these parameters. Evidently, no regimented puffing will reproduce inhalation patterns of the widely varying patterns of consumer usage, but puffing protocols can provide a reasonable proxy of human exposure if they approximate as best as possible consumer puffing patterns for specific devices and vaping styles. In particular, the puffing parameters of the ISO 20768:2018 CORESTA standard were conceived to test low-powered devices, mostly manufactured by

the tobacco industry; hence, they provide a reasonable proxy approximation to puffing patterns of generic low-powered devices (<20 W) used for the mouth-to-lung style (see Section 3). In the present review (see Sections 6 and 7), 24 of the 30 revised studies tested low-powered devices, mostly cartridge-based pods, using the CORESTA standard or minor variations, which are adequate for these devices.

The reviews by Soulet and Sussman, examined several studies in which emissions were generated by puffing various brands of high-powered sub-ohm devices with the CORESTA protocol (or close deviations of it). This combination of high supplied power and low airflow favors overheating conditions that might lead in extreme cases to a dry puff. However, these conditions do not apply to the studies examined in the present review and will not be discussed any further (for details on the problems found in high powered devices see (Soulet and Sussman, 2022b; Soulet and Sussman, 2022a)).

5.5 Evaluation of the studies

In Table 3, we display our evaluation of the reliability of the 14 revised studies in terms of fulfilment of the four criteria of experimental quality: reproducibility, adequacy of puffing regime and analytical methods, and usage of blank samples. We used a "traffic light" coloring of scores, with "Reliable" (green) for scores 3.0 and above, "Partially Reliable" (yellow) for scores between 2.0 and 3.0, and "Unreliable" (red) for scores below 2.0. We assigned a score of 1/2 to studies that partially complied with a given condition or studies that tested both low and high-powered devices, with the latter ones with inappropriate airflow.

Table 3 shows seven studies that are "Reliable", 5 "Partially Reliable" and 2 "Unreliable". It is interesting to see cross references between the different quality conditions. Surprisingly, only one of the 7 Reliable studies used blank samples (only three studies used blank samples). Six studies failed the reproducibility criterion. As described in the reviews of Section 4, practically all studies used reasonable values of puff duration (around 3s) and inter-puff intervals (30s and 60s).

6 Conclusion

Since the introduction of ECs into global markets as safer substitutes for tobacco cigarettes, hundreds of studies have been undertaken to examine the chemical contents of their aerosol emissions as an essential part of the process to fully understand and evaluate their toxicity and risk profile, a process whose outcomes are crucial to inform and guide all stakeholders (consumers, health professionals, regulators, and industries).

Emission studies are the ground-level stage in the evaluation of the risk profile of ECs, followed by preclinical and clinical studies. Reviews of these studies fulfil the important task of collecting and revising the "state of the art" research in each topic, but to be useful they must go beyond merely citing the studies and listing their outcomes; they must also provide detailed and critical assessments of the involved methodology and the consistency of experimental outcomes. With this purpose in mind and considering that carbonyls (especially aldehydes) are the most frequent and

abundant toxic byproducts found in EC emissions, we have presented in this review a detailed and critical examination of the experimental procedures, analytical methods, and outcomes of 14 recently published emission studies focusing on carbonyls (the studies are summarized in Tables 1 and 2). Our review complements two of our own recently published reviews of emission studies targeting toxic byproducts (metals (Soulet and Sussman, 2022a) or organic byproducts (Soulet and Sussman, 2022b)) published after 2018 (we omitted studies published before 2018, as they tested devices that are currently obsolete or of marginal use).

To evaluate the reliability of the studies in our review we examined compliance with (what we regard) as the minimal requirement of experimental quality stated in Section 2, namely, authors must provide: 1) sufficient information on the devices and on all experimental procedures to be reproducible, 2) use of appropriate puffing parameters to generate aerosols, 3) use appropriate analytic methods and 4) use blank samples. From the detailed reviews in Section 4 we defined a gradation system in terms of a "traffic light" point classification given in terms of their degree of compliance with the four quality conditions. The details of this evaluation are displayed in Table 3, showing that seven studies were Reliable, 5 Partially Reliable and 2 Unreliable. Most studies used appropriate analytical methods (although some failed to provide sufficient information on various issues), and most obtained aldehyde yields that are negligible or well below yields in cigarette smoke. However, the studies exhibited the following experimental flaws:

- Although only five of the 14 studies used blank samples, alternative validation methods have been employed.
- six studies failed the replicability condition by not disclosing sufficient information on the devices and experimental procedures.

The issues listed above are serious methodological flaws that occur also in many emission studies (see (Soulet and Sussman, 2022a; Soulet and Sussman, 2022b)). Evidently, these flaws need to be corrected to improve the quality of emission testing, which suggests the need to update and improve the standards of laboratory emissions testing. Testing standards (as well as the peer review process evaluating emission studies) must incorporate and demand the usage of blank samples and that authors supply all relevant information for potentially reproducing or replicating the experiments. In addition, testing standards must overcome the rigidity of considering only the CORESTA airflows (or minor variations) for testing all devices, including high-powered ones used for Direct to Lung style (see criticism on this point in (Soulet and Sussman, 2022a; Soulet and Sussman, 2022b)). As we have suggested in previous reviews, it is also important to incorporate EC users within the experimental logistics, since after all the devices are aimed for consumers. Unfortunately, many emission studies simply ignore the peculiarities of consumer patterns.

Updating and improving testing standards to incorporate basic conditions of experimental quality is necessary to achieve a more objective evaluation of the risk profile of ECs, which will provide valuable information to all stakeholders (consumers, health professionals, regulators, and the industries themselves). We will continue to review emission studies, and in future research we will

conduct our own laboratory studies based on the quality conditions we have indicated in our literature review.

Author contributions

RS: Writing–original draft, Writing–review and editing. FS: Writing–original draft, Writing–review and editing. SR: Writing–review and editing. SS: Writing–review and editing.

Funding

The author(s) declare financial support was received for the research, authorship, and/or publication of this article. Publication fees were covered by Ingesciences.

Conflict of interest

Author SS was employed by Ingésciences.

The remaining authors declare that the research was conducted in the absence of any commercial or financial relationships that could be construed as a potential conflict of interest.

Publisher's note

All claims expressed in this article are solely those of the authors and do not necessarily represent those of their affiliated organizations, or those of the publisher, the editors and the reviewers. Any product that may be evaluated in this article, or claim that may be made by its manufacturer, is not guaranteed or endorsed by the publisher.

References

Abrams, D. B., Glasser, A. M., Pearson, J. L., Villanti, A. C., Collins, L. K., and Niaura, R. S. (2018). Harm minimization and tobacco control: reframing societal views of nicotine use to rapidly save lives. *Annu. Rev. Public Health* 39 (1), 193–213. doi:10.1146/annurev-publhealth-040617-013849

Amos, A., Arnott, D., Aveyard, P., Bauld, L., Bogdanovica, I., Britton, J., et al. (2016). *Nicotine without smoke: tobacco harm reduction*. [place unknown].

Athyros, V. G., Katsiki, N., Doumas, M., Karagiannis, A., and Mikhailidis, D. P. (2013). Effect of tobacco smoking and smoking cessation on plasma lipoproteins and associated major cardiovascular risk factors: a narrative review. *Curr. Med. Res. Opin.* 29 (10), 1263–1274. doi:10.1185/03007995.2013.827566

Baker, R. R., Coburn, S., Liu, C., and Tetteh, J. (2005). Pyrolysis of saccharide tobacco ingredients: a TGA–FTIR investigation. *J. Anal. Appl. Pyrolysis* 74 (1–2), 171–180. doi:10.1016/j.jaap.2004.09.005

Baker, R. R., Massey, E. D., and Smith, G. (2004). An overview of the effects of tobacco ingredients on smoke chemistry and toxicity. *Food Chem. Toxicol.* 42, 53–83. doi:10.1016/j.fct.2004.01.001

Balfour, D. J. K., Benowitz, N. L., Colby, S. M., Hatsukami, D. K., Lando, H. A., Leischow, S. J., et al. (2021). Balancing consideration of the risks and benefits of E-cigarettes. *Am. J. Public Health* 111 (9), 1661–1672. doi:10.2105/AJPH.2021.306416

Bao, M., Joza, P. J., Masters, A., and Rickert, W. S. (2014). Analysis of selected carbonyl compounds in tobacco samples by using Pentafluorobenzylhydroxylamine derivatization and gas chromatography-mass spectrometry. *Beitrage zur Tabakforschung International/Contributions Tob. Res.* 26 (3), 86–97. doi:10.2478/cttr-2014-0017

Cantwell, H. (2019). Blanks in method validation - supplement to eurachem guide the fitness for purpose of analytical methods. Available at: http://www.eurachem.org.

Caponnetto, P., Keller, E., Bruno, C. M., and Polosa, R. (2013). Handling relapse in smoking cessation: strategies and recommendations. *Intern Emerg. Med.* 8 (1), 7–12. doi:10.1007/s11739-012-0864-z

Centers for Disease Control and Prevention (US) (2010). *How tobacco smoke causes Disease: the biology and behavioral basis for smoking-attributable Disease: a report of the surgeon general*. [place unknown].

Centers for Disease Control and Protection CDC (2020). *Health effects smoking and tobacco use*.

Cogliano, V. J., Grosse, Y., Baan, R. A., Straif, K., Secretan, M. B., El Ghissassi, F., et al. (2005). Meeting report: summary of IARC monographs on formaldehyde, 2-butoxyethanol, and 1-tert-butoxy-2-propanol. *Environ. Health Perspect.* 113 (9), 1205–1208. doi:10.1289/ehp.7542

Conklin, D. J., Ogunwale, M. A., Chen, Y., Theis, W. S., Nantz, M. H., Fu, X. A., et al. (2018). Electronic cigarette-generated aldehydes: the contribution of e-liquid components to their formation and the use of urinary aldehyde metabolites as biomarkers of exposure. *Aerosol Sci. Technol.* 52 (11), 1219–1232. doi:10.1080/02786826.2018.1500013

Cooperation Centre for Scientific Research Relative to Tobacco (2024). *CORESTA recommended method No. 96 determination of formaldehyde and acetaldehyde in E-VAPOUR product aerosol*.

Cooperation Centre for Scientific Research Relative to Tobacco CORESTA (2015). No. 81 - routine analytical machine for E-cigarette aerosol generation and collection - definitions and standard conditions. Available at: https://www.coresta.org/routine-analytical-machine-e-cigarette-aerosol-generation-and-collection-definitions-and-standard.

Cooperation Centre for Scientific Research Relative to Tobacco CORESTA (2019). No. 74 - determination of selected carbonyls in mainstream cigarette smoke by high performance liquid chromatography (HPLC). Available at: https://www.coresta.org/determination-selected-carbonyls-mainstream-cigarette-smoke-high-performance-liquid-chromatography.

Counts, M. E., Morton, M. J., Laffoon, S. W., Cox, R. H., and Lipowicz, P. J. (2005). Smoke composition and predicting relationships for international commercial cigarettes smoked with three machine-smoking conditions. *Regul. Toxicol. Pharmacol.* 41 (3), 185–227. doi:10.1016/j.yrtph.2004.12.002

Cox, S., Kośmider, L., McRobbie, H., Goniewicz, M., Kimber, C., Doig, M., et al. (2016). E-cigarette puffing patterns associated with high and low nicotine e-liquid strength: effects on toxicant and carcinogen exposure. *BMC Public Health* 16 (1), 999. doi:10.1186/s12889-016-3653-1

El-Hellani, A., Soule, E. K., Daoud, M., Salman, R., El Hage, R., Ardati, O., et al. (2022). Assessing toxicant emissions from e-liquids with DIY additives used in response to a potential flavour ban in e-cigarettes. *Tob. Control* 31 (Suppl. 3), s245–s248. doi:10.1136/tc-2022-057505

El Mubarak, M. A., Danika, C., Vlachos, N. S., Farsalinos, K., Poulas, K., and Sivolapenko, G. (2018). Development and validation of analytical methodology for the quantification of aldehydes in e-cigarette aerosols using UHPLC-UV. *Food Chem. Toxicol.* 116, 147–151. doi:10.1016/j.fct.2018.04.021

Farsalinos, K., Gillman, G., Kistler, K., and Yannovits, N. (2017a). Comment on "flavoring compounds dominate toxic aldehyde production during E cigarette vaping.". *Environ. Sci. Technol.* 51 (4), 2491–2492. doi:10.1021/acs.est.6b06030

Farsalinos, K. E., and Gillman, G. (2018). Carbonyl emissions in e-cigarette aerosol: a systematic review and methodological considerations. *Front. Physiol.* 8 (JAN), 1119. doi:10.3389/fphys.2017.01119

Farsalinos, K. E., Kistler, K. A., Pennington, A., Spyrou, A., Kouretas, D., and Gillman, G. (2018). Aldehyde levels in e-cigarette aerosol: findings from a replication study and from use of a new-generation device. *Food Chem. Toxicol.* 111, 64–70. doi:10.1016/j.fct.2017.11.002

Farsalinos, K. E., Voudris, V., and Poulas, K. (2015). E-cigarettes generate high levels of aldehydes only in 'dry puff' conditions. *Addiction* 110 (8), 1352–1356. doi:10.1111/add.12942

Farsalinos, K. E., Voudris, V., Spyrou, A., and Poulas, K. (2017b). E-cigarettes emit very high formaldehyde levels only in conditions that are aversive to users: a replication study under verified realistic use conditions. *Food Chem. Toxicol.* 109, 90–94. doi:10.1016/j.fct.2017.08.044

Flora, J. W., Wilkinson, C. T., Wilkinson, J. W., Lipowicz, P. J., Skapars, J. A., Anderson, A., et al. (2017). Method for the determination of carbonyl compounds in E-cigarette aerosols. *J. Chromatogr. Sci.* 55 (2), 142–148. doi:10.1093/chromsci/bmw157

Geiss, O., Bianchi, I., Barahona, F., and Barrero-Moreno, J. (2015). Characterisation of mainstream and passive vapours emitted by selected electronic cigarettes. *Int. J. Hyg. Environ. Health* 218 (1), 169–180. doi:10.1016/j.ijheh.2014.10.001

Gillman, I. G., Kistler, K. A., Stewart, E. W., and Paolantonio, A. R. (2016). Effect of variable power levels on the yield of total aerosol mass and formation of aldehydes in e-cigarette aerosols. *Regul. Toxicol. Pharmacol.* 75, 58–65. doi:10.1016/j.yrtph.2015.12.019

Gillman, I. G., Pennington, A. S. C., Humphries, K. E., and Oldham, M. J. (2020). Determining the impact of flavored e-liquids on aldehyde production during Vaping. *Regul. Toxicol. Pharmacol.* 112, 104588. doi:10.1016/j.yrtph.2020.104588

International Agency for Research on Cancer IARC (2006). Formaldehyde, 2-butoxyethanol and 1-tert-Butoxypropan-2-ol. *IARC Monogr. Eval. Carcinog. Risks Humans* 88, 1–478.

International Agency for Research on Cancer IARC (2021). Acrolein, crotonaldehyde, and arecoline. *IARC Monogr. Identif. Carcinog. Hazards Hum.* 128, 1–335.

International Organization for Standardization ISO (2012). *ISO 3308:2012 Routine analytical cigarette-smoking machine Definitions and standard conditions.*

International Organization for Standardization ISO (2018a). *ISO 20768:2018 Vapour products Routine analytical vaping machine Definitions and standard conditions.*

International Organization for Standardization ISO (2018b). *ISO 20778: 2018 Cigarettes Routine analytical cigarette smoking machine Definitions and standard conditions with an intense smoking regime.*

International Organization for Standardization ISO (2018c). *ISO 21160: 2018 Cigarettes Determination of selected carbonyls in the mainstream smoke of cigarettes Method using high performance liquid chromatography.*

International Organization for Standardization ISO (2018d). Vapour products — routine analytical vaping machine — definitions and standard conditions. Available at: https://www.iso.org/obp/ui/en/#iso:std:iso:20768:ed-1:v1:en.

Jităreanu, A., Cara, I. G., Sava, A., Mârțu, I., Caba, I. C., and Agoroaei, L. (2022). The impact of the storage conditions and type of clearomizers on the increase of heavy metal levels in electronic cigarette liquids retailed in Romania. *Toxics* 10 (3), 126. doi:10.3390/toxics10030126

Kotz, D., Batra, A., and Kastaun, S. (2020). Smoking cessation attempts and common strategies employed: a Germany-wide representative survey conducted in 19 waves from 2016 to 2019 (The DEBRA Study) and analyzed by socioeconomic status. *Dtsch. Arztebl Int.* 117 (1), 7–13. doi:10.3238/ARZTEBL.2020.0007

Lalonde, G., Demir, K., Yao, J., Wolz, R. L., Kosachevsky, P., Gillman, I. G., et al. (2022). Characterization of a rapid condensate collection apparatus for *in vitro* assays of electronic nicotine delivery systems. *Toxicol. Vitro* 84, 105434. doi:10.1016/j.tiv.2022.105434

Laraway, S., Snycerski, S., Pradhan, S., and Huitema, B. E. (2019). An overview of scientific reproducibility: consideration of relevant issues for behavior science/analysis. *Perspect. Behav. Sci.* 42 (1), 33–57. doi:10.1007/s40614-019-00193-3

Lee, M. H., Szulejko, J. E., and Kim, K. H. (2018). Determination of carbonyl compounds in electronic cigarette refill solutions and aerosols through liquid-phase dinitrophenyl hydrazine derivatization. *Environ. Monit. Assess.* 190 (4), 200. doi:10.1007/s10661-018-6553-2

McGuigan, M., Chapman, G., Lewis, E., Watson, C. H., Blount, B. C., and Valentin-Blasini, L. (2022). High-performance liquid chromatography-tandem mass spectrometry analysis of carbonyl emissions from E-cigarette, or vaping, products. *ACS Omega* 7 (9), 7655–7661. doi:10.1021/acsomega.1c06321

McNeill, A., Brose, L. S., Calder, R., Bauld, L., and Robson, D. (2018). *Evidence review of e-cigarettes and heated tobacco products 2018 A report commissioned by Public Health England.* London.

Ministry of Health NZG (2024). Position statement on vaping. Available at: https://www.health.govt.nz/our-work/preventative-health-wellness/tobacco-control/vaping-smokefree-environments-and-regulated-products/position-statement-vaping.

National Academies of Sciences Engineering and Medicine (2018). *Public health consequences of E-cigarettes.* Editors K. Stratton, L. Y. Kwan, and D. L. Eaton (Washington, D.C.: National Academies Press). doi:10.17226/24952

Nicol, J., Fraser, R., Walker, L., Liu, C., Murphy, J., and Proctor, C. J. (2020). Comprehensive chemical characterization of the aerosol emissions of a vaping product based on a new technology. *Chem. Res. Toxicol.* 33 (3), 789–799. doi:10.1021/acs.chemrestox.9b00442

Office for Health Improvement and Disparities (formerly Public Health England) (2022). Nicotine vaping in England: 2022 evidence update main findings. Available at: https://www.gov.uk/government/publications/nicotine-vaping-in-england-2022-evidence-update/nicotine-vaping-in-england-2022-evidence-update-main-findings.

Page, M. J., McKenzie, J. E., Bossuyt, P. M., Boutron, I., Hoffmann, T. C., Mulrow, C. D., et al. (2021). The PRISMA 2020 statement: an updated guideline for reporting systematic reviews. *BMJ* n71, n71. doi:10.1136/bmj.n71

Pinto, M. I., Thissen, J., Hermes, N., Cunningham, A., Digard, H., and Murphy, J. (2022). Chemical characterisation of the vapour emitted by an e-cigarette using a ceramic wick-based technology. *Sci. Rep.* 12 (1), 16497. doi:10.1038/s41598-022-19761-w

Pisinger, C., and Døssing, M. (2014). A systematic review of health effects of electronic cigarettes. *Prev. Med. Balt.* 69, 248–260. doi:10.1016/j.ypmed.2014.10.009

Qu, Y., Kim, K. H., and Szulejko, J. E. (2018). The effect of flavor content in e-liquids on e-cigarette emissions of carbonyl compounds. *Environ. Res.* 166, 324–333. doi:10.1016/j.envres.2018.06.013

Rajapaksha, R. D., Tehrani, M. W., Rule, A. M., and Harb, C. C. (2021). A rapid and sensitive chemical screening method for E-cigarette aerosols based on runtime cavity ringdown spectroscopy. *Environ. Sci. Technol.* 55 (12), 8090–8096. doi:10.1021/acs.est.0c07325

Resnik, D. B., and Shamoo, A. E. (2017). Reproducibility and research integrity. *Account. Res.* 24 (2), 116–123. doi:10.1080/08989621.2016.1257387

Son, Y., and Khlystov, A. (2021). An automated aerosol collection and extraction system to characterize electronic cigarette aerosols. *Front. Chem.* 9, 764730. doi:10.3389/fchem.2021.764730

Soulet, S., and Sussman, R. A. (2022a). Critical review of the recent literature on organic byproducts in E-cigarette aerosol emissions. *Toxics* 10 (12), 714. doi:10.3390/toxics10120714

Soulet, S., and Sussman, R. A. (2022b). A critical review of recent literature on metal contents in E-cigarette aerosol. *Toxics* 10 (9), 510. doi:10.3390/toxics10090510

Stephens, W. E., de Falco, B., and Fiore, A. (2019). A strategy for efficiently collecting aerosol condensate using silica fibers: application to carbonyl emissions from E-cigarettes. *Chem. Res. Toxicol.* 32 (10), 2053–2062. doi:10.1021/acs.chemrestox.9b00214

Szulejko, J. E., and Kim, K. H. (2015). Derivatization techniques for determination of carbonyls in air. *TrAC - Trends Anal. Chem.* 64, 29–41. doi:10.1016/j.trac.2014.08.010

Talih, S., Salman, R., El-Hage, R., Karam, E., Salam, S., Karaoghlanian, N., et al. (2020a). A comparison of the electrical characteristics, liquid composition, and toxicant emissions of JUUL USA and JUUL UK e-cigarettes. *Sci. Rep.* 10 (1), 7322. doi:10.1038/s41598-020-64414-5

Talih, S., Salman, R., Karam, E., El-Hourani, M., El-Hage, R., Karaoghlanian, N., et al. (2020b). Hot wires and film boiling: another look at carbonyl formation in electronic cigarettes. *Chem. Res. Toxicol.* 33 (8), 2172–2180. doi:10.1021/acs.chemrestox.0c00196

Talih, S., Salman, R., Soule, E., El-Hage, R., Karam, E., Karaoghlanian, N., et al. (2022). Electrical features, liquid composition and toxicant emissions from 'pod-mod'-like disposable electronic cigarettes. *Tob. Control* 31 (5), 667–670. doi:10.1136/tobaccocontrol-2020-056362

Uchiyama, S., Inaba, Y., and Kunugita, N. (2011). Derivatization of carbonyl compounds with 2,4-dinitrophenylhydrazine and their subsequent determination by high-performance liquid chromatography. *J. Chromatogr. B Anal. Technol. Biomed. Life Sci.* 879 (17–18), 1282–1289. doi:10.1016/j.jchromb.2010.09.028

U.S. Food and Drug Administration (2023). E-cigarettes, vapes, and other electronic nicotine delivery systems (ENDS). Available at: https://www.fda.gov/tobacco-products/products-ingredients-components/e-cigarettes-vapes-and-other-electronic-nicotine-delivery-systems-ends.

Van Leeuwen, S. M., Hendriksen, L., and Karst, U. (2004). Determination of aldehydes and ketones using derivatization with 2,4-dinitrophenylhydrazine and liquid chromatography-atmospheric pressure photoionization-mass spectrometry. *J. Chromatogr. A* 1058 (1–2), 107–112. doi:10.1016/j.chroma.2004.08.149

Visser, W. F., Krüsemann, E. J. Z., Klerx, W. N. M., Boer, K., Weibolt, N., and Talhout, R. (2021). Improving the analysis of E-cigarette emissions: detecting human "dry puff" conditions in a laboratory as validated by a panel of experienced vapers. *Int. J. Environ. Res. Public Health* 18 (21), 11520. doi:10.3390/ijerph182111520

World Health Organization (2022). Tobacco: E-cigarettes. Available at: https://www.who.int/news-room/questions-and-answers/item/tobacco-e-cigarettes.

World Health Organization WHO (2023). *Tobacco.*

Zhu, J., Heredia, A., Tweedy, J., and Tayyarah, R. (2020). "Method development for the analysis of mono-carbonyl compounds in e-vapor products by LC-MS," in *Integrated science: opportunities and challenges.* [place unknown]: CORESTA.

Glossary

AMAH	4-(2-aminooxyethyl)-morpholin-4-ium chloride
CO	Carbon Monoxide
CORESTA	Cooperation Centre for Scientific Research Relative to Tobacco
CRM	CORESTA Recommended Method
CSR	cigarette-smoking robot
DIY	Do It Yourself
DNPH	2,4-Dinitrophenylhydrazine
DTL	Direct To Lung
EC	Electronic Cigarette
ENDS	Electronic Nicotine Delivery Systems
ETS	Environmental tobacco smoke
FDA US	Food and Drug Administration
FID	Flame Ionization Detection
GCxGC	Gas Chromatography x Gas Chromatography
GC-MS	Gas Chromatography–Mass Spectrometry
FT-ICR-MS	Fourier transformation cyclotron resonance mass spectrometry
HCI	Health Canada Intense
HPHC	Hazardous and Potentially Hazardous Compounds
HPLC-DAD	High-Performance Liquid Chromatography Diode Array Detector
HPLC-MS/MS	
HPLC-UV	High-Performance Liquid Chromatography Ultraviolet
HTP	Heated Tobacco Products
ISO	20778:2018 CORESTA FTC puffing regime (2 s puff 60 s inter-puff 35 mL puff volume)
IARC	International Agency for Research on Cancer
IR	infrared spectroscopy
ISO	20778:2018 HCI puffing regime (2 s puff 30 s inter-puff 55 mL puff volume)
ISO	International Organization for Standardization
LOD	Limit Of Detection
LOQ	Limit Of Quantitation
MEV	mass of e-liquid vaporized
NaOH	Sodium hydroxide
PG	Propylene Glycol
rtCRDS	runtime cavity ringdown spectroscopy
SD	Standard Deviation
PFBHA	o-(2,3,4,5,6-Pentafluorobenzyl)hydroxylamine
THF	Tetrahydrofuran
TOFMS	Time of Flight Mass Spectrometry
UV	Ultraviolet
UHPLC-MS/MS	Ultra-High-Performance Liquid Chromatography Mass Spectrometry
UHPLC-UV	Ultra-High-Performance Liquid Chromatography Ultraviolet
VG	Vegetable Glycerin or Glycerol
WHO	World Health Organization

Check for updates

One of the major challenges of masking the bitter taste in medications: an overview of quantitative methods for bitterness

Panpan Wang[1†], Haiyang Li[2†], Yanli Wang[1], Fengyu Dong[2], Han Li[2], Xinjing Gui[1,3,4], Yanna Ren[2], Xiaojie Gao[5], Xuelin Li[1,2,3,4,6]* and Ruixin Liu[1,2,3,4,6]*

[1]Department of Pharmacy, The First Affiliated Hospital of Henan University of Chinese Medicine, Zhengzhou, China, [2]School of Pharmacy, Henan University of Chinese Medicine, Zhengzhou, China, [3]Henan Province Engineering Research Center for Clinical Application, Evaluation and Transformation of Traditional Chinese Medicine, Henan Province Engineering Laboratory for Clinical Evaluation Technology of Chinese Medicine, Zhengzhou, China, [4]Collaborative Innovation Center for Chinese Medicine and Respiratory Diseases Co-Constructed by Henan Province, Education Ministry of China, Henan University of Chinese Medicine, Zhengzhou, China, [5]Zhengzhou Traditional Chinese Medicine Hospital, Zhengzhou, China, [6]Third Level Laboratory of Traditional Chinese Medicine Preparations of the State Administration of Traditional Chinese Medicine, Zhengzhou, China

Objective: The aim of the present study was to carry out a systematic research on bitterness quantification to provide a reference for scholars and pharmaceutical developers to carry out drug taste masking research. Significance: The bitterness of medications poses a significant concern for clinicians and patients. Scientifically measuring the intensity of drug bitterness is pivotal for enhancing drug palatability and broadening their clinical utility.

Methods: The current study was carried out by conducting a systematic literature review that identified relevant papers from indexed databases. Numerous studies and research are cited and quoted in this article to summarize the features, strengths, and applicability of quantitative bitterness assessment methods.

Results: In our research, we systematically outlined the classification and key advancements in quantitative research methods for assessing drug bitterness, including *in vivo* quantification techniques such as traditional human taste panel methods, as well as *in vitro* quantification methods such as electronic tongue analysis. It focused on the quantitative methods and difficulties of bitterness of natural drugs with complex system characteristics and their difficulties in quantification, and proposes possible future research directions.

Conclusion: The quantitative methods of bitterness were summarized, which laid an important foundation for the construction of a comprehensive bitterness quantification standard system and the formulation of accurate, efficient and rich taste masking strategies.

KEYWORDS

bitterness, quantitative method, traditional human taste panel method, active pharmaceuticals ingredients, traditional Chinese medicine

1 Introduction

As widely recognized, the axiom "good medicine tastes bitter" epitomizes a fundamental attribute of pharmaceuticals, with many drugs exhibiting a bitter taste (Bahia et al., 2018). Our investigation revealed that bitter herbs or decoction pieces constituted 49.0% of the 2020 edition of the "Chinese Pharmacopoeia" (Lin et al., 2016), while 66% of compounds cataloged in the Drug Bank library were projected to possess a bitter taste (Dagan-Wiener et al., 2017). The Bitter DB database archives over 1,000 bitter molecules. Humans and animals exhibit heightened sensitivity to bitterness perception, capable of discerning bitterness even at lower concentrations (Aliani and Eskin, 2017). The intrinsic aversion to bitterness among humans significantly impacts patient medication adherence (Beauchamp, 2016; Boesveldt and de Graaf, 2017), thereby influencing clinical efficacy (Amin et al., 2018; Zheng et al., 2018). The prevalent distaste for medications is frequently cited as a primary reason for patient non-compliance, particularly among children (Clapham et al., 2023). Surveys indicate that over 90% of pediatricians identify drug taste and palatability as major barriers to completing clinical treatments (Milne and Bruss, 2008). In a survey involving nearly 700 European children, 63.7% of respondents attributed difficulty in medication intake to dislike for the drug's taste (Nordenmalm et al., 2019). Peter Drucker, often regarded as the father of modern management, emphasized the necessity of objective and accurate quantitative evaluation of drug bitterness as a crucial prerequisite for understanding its taste patterns and enhancing palatability.

Bitterness primarily arises from the activation of TAS2R (also referred to as bitter receptors). Upon binding of the bitter compound to the receptor, located prominently on taste receptor cells (TRCs), a signal transduction cascade ensues. This activation prompts TAS2R to catalyze the dissociation and liberation of Gβ3/Gγ13 subunits from the Gβ3/Gγ13 heterotrimeric receptor, thereby activating phospholipase C (PLCβ2). Subsequently, PLCβ2 catalyzes the breakdown of phospholipid PIP2, yielding inositol-1,4,5-phosphate (IP3). IP3, in turn, binds to IP3 receptors on the endoplasmic reticulum, eliciting the release of intracellularly stored calcium ions (Ca^{2+}). The elevated intracellular Ca^{2+} concentration ($[Ca^{2+}]i$) prompts the opening of membrane-associated TRPM5 channels, facilitating the influx of sodium ions (Na^+). This ion exchange initiates receptor cell membrane depolarization, triggering the release of adenosine triphosphate (ATP) through calcium homeostasis regulator one and 3 (CALHM1 and CALHM3) channels. Ultimately, the liberated ATP activates purinergic receptors on afferent nerve fibers, converting the chemical signals of bitter compounds into electrical signals, which are relayed to the taste nucleus of the brainstem. Subsequently, these signals are transmitted to the thalamus and eventually to the taste cortex of the cerebral cortex, culminating in the perception of bitterness (Finger et al., 2005; Roper, 2007; Ma et al., 2018), as shown in Figure 1.

According to the law of taste and bitter perception, the factors affecting drug bitterness are affected by the difference of genes and receptors. Single nucleotide polymorphisms (SNPs) in genes encoding bitter taste receptors (TAS2R) leading to varied responses to bitter stimuli. Consequently, individuals with one gene form may perceive strong bitterness, while those with another gene form may not perceive bitterness at all (Hayes et al., 2011; Mennella et al., 2011; Roudnitzky et al., 2011; Roudnitzky et al., 2015; Nolden and Feeney, 2020). The heterologous functional expression experiments have revealed that 25 TAS2Rs exhibit varying degrees of regulation characteristics as bitter taste receptors (Meyerhof et al., 2010). The ability of bitter compounds to stimulate TAS2Rs varies. Compared to the activation of a single receptor, simultaneous

FIGURE 1
Activation mechanism of human TAS2R and signal transduction pathway of bitterness stimulation.
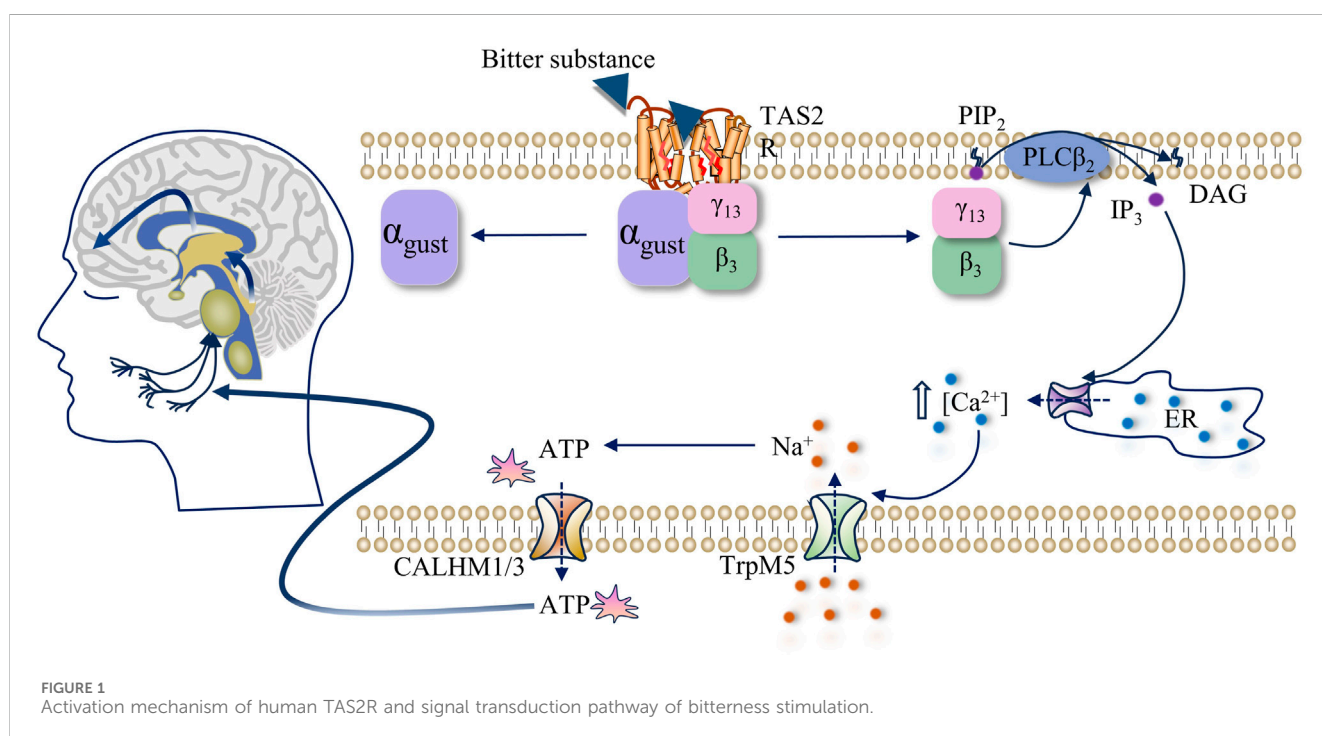
activation of multiple receptors by a compound can elicit a larger cellular or neural response, thereby increasing bitterness. Additionally, the factors that affect the bitterness also include the following: (1) Chemical structure. According to the three-point contact theory of bitterness formation, bitter molecules can be categorized into two groups (Hans-Dieter et al., 1985; Meyerhof, 2005): one consisting of hydrophobic lipophilic compounds with limited water solubility, such as olefins and terpenoids; the other comprising highly polar compounds capable of forming robust hydrophobic interactions, exemplified by alkaloids (Zeng, 1990). (2) Substance concentration. Within a specific concentration range of the same drug, bitterness demonstrates a positive correlation with concentration. Studies have shown that a logarithmic relationship between human sensory intensity and stimulus physical quantity under moderate intensity stimula56tion conditions (S = KlgR) (Omür-Ozbek and Dietrich, 2008; Li et al., 2016). (3) Interaction between substances. The bitterness between substances can be affected by electrostatic interaction (Schalk et al., 2018), hydrophobic interaction (Ogi et al., 2015), covalent bonding (Bohin et al., 2013), and inclusion interaction (Shah and Mashru, 2008). (4) pH. It is established that certain acidic peptides can mitigate bitterness (Sakurai et al., 2009). Bitterness inhibition of sesquiterpene lactone can be achieved by pH control (Yanagisawa and Misaka, 2021). (5) Solution viscosity. Studies have found that an increase in the viscosity of the resulting aqueous solvent leads to a reduction in taste intensity. Additionally, studies have indicated that emulsions demonstrate bitterness inhibition effects on KCl and/or caffeine compared to aqueous solutions (Torrico et al., 2015).

In the realm of food taste assessment, extensive studies have focused on quantitatively evaluating taste attributes. For instance, the bitterness of beer is commonly assessed based on the concentration of isomerized α-acids, the primary source of beer bitterness. Methods such as European Bitterness Units (EBU) (Polshin et al., 2010; Rudnitskaya et al., 2010), International Bitterness Units (IBU) (Howard, 1968; Donley and Anheuser, 1992; Christensen et al., 2005), E.B.C. Bitterness Units (Bishop, 2013), and Bitterness Units (BU) (Tomlinson et al., 2013) are utilized for this purpose. Caffeine, containing numerous bitter compounds, undergoes bitterness intensity evaluation using Sensory Lexicon (Shibamoto et al., 1981; Ginz and Engelhardt, 2000; Aree, 2019). These established quantification methods in the field of food taste can serve as valuable references for assessing drug bitterness. While the bitterness of chemical drugs can be accurately measured based on the content of bitter compounds due to their clear and singular composition, natural drugs encompass a multitude of bitter substances, intricate substance interactions, and a diverse array of taste components. These complexities confer inherent bitterness to natural drugs, emphasizing the importance of elucidating the mechanisms underlying their bitter taste and exploring tailored quantification methodologies.

As research into drug palatability continues to evolve, investigators have undertaken studies on the measurement and quantitative assessment of drug bitterness (Gaudette and Pickering, 2013). These studies primarily encompass *in vivo* and *in vitro* methods. *In vivo* evaluation methods include the traditional human taste panel method (THTPM) (Miyanaga et al., 2003; Rudnitskaya et al., 2013), taste strips test method (Liu et al.,

2020), animal behavior tests (Lemon et al., 2019), and facial expression analysis (Lemon et al., 2019), with THTPM recognized as the gold standard for taste assessment (Gunaratne et al., 2019). *In vitro* bitterness detection methods mainly consist of electronic tongue methods (ETM) (Hui et al., 2014; Immohr et al., 2017), and cell-based evaluations (Qingjun and Ping, 2009), among others. Following an understanding of drug bitterness, researchers have employed taste-masking techniques utilizing flavoring agents, bitterness inhibitors, cyclodextrins, and nanoemulsions (Hu et al., 2023). These methods have contributed positively to advancing the objective measurement and precise control of bitterness, thereby enhancing clinical drug compliance. Nonetheless, despite these advancements, there remains a lack of systematic summarization of research methods for bitterness quantification, as each method possesses unique characteristics and applications. This article seeks to analyze the research progress in drug bitterness quantification, delineate the primary factors influencing drug bitterness, and compile the methodologies for bitterness quantification. The aim is to foster a systematic comprehension of the principles, methodologies, and attributes of bitterness quantification, thereby offering insights for research endeavors in areas such as drug bitterness intensity evaluation, taste masking, and related fields.

2 Quantitative methods for bitterness

In light of the various factors influencing drug bitterness as outlined above, researchers are continuously innovating quantitative methods for assessing drug bitterness. Broadly, these methods can be categorized into two types: one involves quantifying the bitterness of drugs by measuring bitter molecules, while the other quantifies drug bitterness based on the intensity of taste stimulation. The results of both methods are elaborated upon below.

2.1 THTPM

THTPM is a method used to assess the taste of drugs or food, relying on specific technical specifications and processes and utilizing the taste sense of the evaluation group (Medicine, 2024). This method falls under the category of quantifying bitterness based on the intensity of human taste stimulus. The main methods were illustrated in Figure 2. Currently, a range of internationally recognized standards for quantitative sensory evaluation have been established (Clapham et al., 2023), paving the way for researchers to conduct various explorations into quantitative bitterness assessment.

2.1.1 Quantitative description analysis (QDA)
QDA is a method used to characterize the sensory properties and intensity of drugs. Within QDA, standard reference materials provide the bitterness value against which samples are compared for evaluation. For instance, when assessing the bitterness of Huanglian Jiedu Decoction (HLJDD), scholars provide a reference standard of 0.2 g/mL HLJDD with a bitterness value of 10. Evaluators use this reference standard to assess the bitterness of HLJDD after masking with [mPEG2000-PLLA2000, γ-CD, and neotame], revealing a reduction in HLJDD bitterness (Ke et al., 2022).
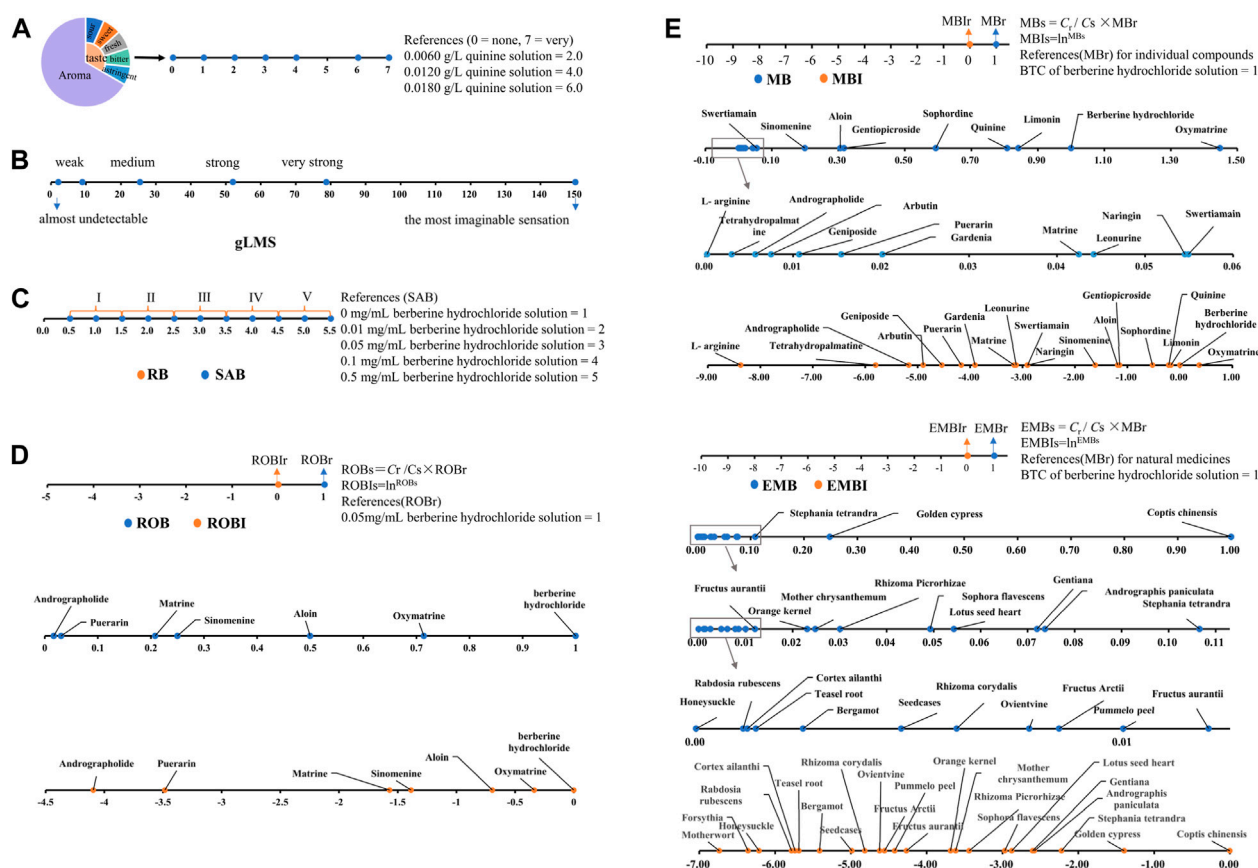
FIGURE 2
Quantitative research method of bitterness based on the THTPM. **(A)** Schematic representation of the quantitative description analysis (QDA). Based on Huan-Huan Li, 2019 (Li et al., 2019). **(B)** Schematic representation of the general labeled magnitude Scale (gLMS) (Deng et al., 2022) **(C)** Schematic representation of Rank bitterness intensity (RB) and standard apparent bitterness (SAB). Representative images were our own work (Li et al., 2023). **(D)** Schematic representation of Ratio of bitterness (ROB). Representative images were our own work (Gao et al., 2022). **(E)** chematic representation of Molecular bitterness (MB) and equivalent molecular bitterness (EMB). Representative images were our own work (Wang et al., 2022).

However, the methods mentioned above lack the ability to provide information on the temporal aspects of bitterness perception. Bitterness exhibits unique temporal characteristics, taking more time to reach peak intensity in the mouth and longer to return to baseline (Guinard et al., 2010). Additionally, with repeated intake, the perceived intensity of bitterness tends to increase (Guinard et al., 1986). The presence of polyphenols (in red wine) and isohumulone (in beer) may amplify the bitterness of these beverages during consumption (Guinard et al., 1994; Noble, 1994). Hence, some scholars employ the time-intensity method to dynamically assess bitterness throughout the entire perception period. In a study evaluating the bitterness of berberine hydrochloride orally disintegrating tablets, researchers instructed subjects to record bitterness intensity levels at various intervals (30 s, 1 min, 2 min, 5 min, 10 min) within a span of 10 min. Bitterness intensity was rated on a scale from 0 to 3. The findings indicated that when the ratio of the drug to the pH-dependent polymer Eudragit E100 increased from 1:0 to 1:0.8, the bitterness of the drug microcapsules significantly decreased, reaching zero bitterness by the second minute (Hu et al., 2013).

Quantitative descriptive analysis also encompasses the evaluation of bitterness across different taste categories. Some

researchers (Sook Chung and Lee, 2012) categorized bitterness into distinct types such as alcohol bitterness, coffee bitterness, grapefruit pith bitterness, medicinal bitterness, and cocoa bitterness. Each type of bitterness corresponds to unique definitions and references, posing higher demands on the evaluator's assessment skills.

2.1.2 General labeled magnitude scale (gLMS)

The gLMS is a psychophysical scale used for sensory testing to evaluate the taste and aftertaste of various stimuli. It comprises a 150 mm line spanning from the bottom to the top of the vertical axis. The scale includes descriptors such as "almost undetectable" (2.1 mm; 1.4 units), "weak" (9 mm; 6 units), "medium" (25.5 mm; 17 units), "strong" (52.05 mm; 34.7 units), "very strong" (78.75 mm; 52.5 units), and "the most imaginable sensation" (150 mm; 100 units). The scale presents adjectives to evaluators without numerical values. Experimenters place the adjectives on the scale in a semi-logarithmic manner based on determined intervals to generate data equivalent to magnitude estimation (Green et al., 1993; Green et al., 1996). Subsequently, numerical data are calculated based on the scale. Using the gLMS method, the intensity of different bitter substances can be directly

TABLE 1 Bitterness ranking and concentration of corresponding reference samples.

No.	Description of bitterness intensity	RB	Corresponding scale	Conc. Of reference samples	SRB
1	Imperceptible	I	[0.5, 1.5)	0 mg/mL (0 mM)	1
2	Slight	II	[1.5, 2.5)	0.01 mg/mL (0.027 mM)	2
3	Moderate	III	[2.5, 3.5)	0.05 mg/mL (0.134 mM)	3
4	High (but still acceptable)	IV	[3.5, 4.5)	0.1 mg/mL (0.269 mM)	4
5	Extreme (almost unacceptable)	V	[4.5, 5.5)	0.5 mg/mL (1.344 mM)	5

compared. For instance, Deng (Deng et al., 2022) employed the gLMS to conduct sensory tests on adults, comparing the bitterness intensity of prednisolone solution with that of quinine. The results indicated that the bitterness level of prednisolone saturated solution (average gLMS score: 46.8) was similar to that of a 1 mM quinine solution (average gLMS score: 40.1). However, substantial individual differences may exist in gLMS assessment. For example, researchers measured the minimum and maximum values of 1 mM quinine as 8.7 and 90.0, respectively (Deng et al., 2022). Furthermore, variations in sensory test data among different researchers also occur. While one study (Deng et al., 2022) reported the average gLMS score of 1 mM quinine as 40.1, another study (Cruickshanks et al., 2009) documented a gLMS score of 50 at the same concentration. Hence, stringent and standardized conditions are necessary for bitterness evaluation using this method.

2.1.3 Rank bitterness intensity (RB) and standard apparent bitterness (SAB)

In bitterness evaluation, descriptions like "unbearable bitterness," "a little bitterness," and "almost no bitterness" often arise, necessitating a method for grading bitterness. In a study on chlorphenamine maleate bitterness, researchers categorized bitterness into five levels: (A) 5: very strong bitterness, (B) 4: strong bitterness, (C) 3: medium bitterness, (D) 2: slightly bitter, and (E) 1: tasteless. Using the uncomplexed pure drug as a control with an average bitterness value of 5, subjects were instructed to compare the bitterness of different drug resin complexes (DRC) with the control and express the perceived bitterness level. The findings revealed that Indion-234, Tulsion-343, and Tulsion-344 effectively masked the bitterness of chlorphenamine maleate, with the bitterness of the drug in DRC decreasing as the ratio of drug to resin increased (Yewale et al., 2013).

Inspired by this approach, some scholars introduced the concept of "RB" (Wang et al., 2021), using berberine (BBR) as a reference. After volunteers pre-tested multiple concentrations, different concentrations of BBR corresponding to each bitterness level were determined (Table 1). The practical application of graded bitterness involves evaluating unknown bitterness samples by referencing the bitterness level and value range of the reference sample group. Once graded, the specific bitterness value is assigned according to the corresponding bitterness range of each grade. Bitterness determined for the reference material in the solution state is termed "Standard Reference Bitterness (SRB)" (Liu et al., 2019; Zhang et al., 2021). Bitterness of other drugs established based on SRB as a reference in the solution state is referred to as "Standard Apparent Bitterness (SAB)", and the level of standard apparent

bitterness is known as "Standard Apparent Rank Bitterness (SARB)". Employing these methods enables us to comprehend the bitterness levels and bitterness profiles of different bitter substances.

Shi et al. (2013) utilized a berberine hydrochloride aqueous solution as the reference solution and applied the THTPM method to assess the bitterness grade of six notable bitter Chinese herbal decoction pieces, including Cortex Phellodendri, Radix Gentianae, Herba Andrographis, Radix Ginseng, and Nelumbinis Plumulae. They investigated the taste-masking effect of β-CD at various mass fractions. Results indicated that the taste-masking effect improved with increasing β-CD concentration. With the exception of Cortex Phellodendri, the bitterness of the liquid after adding 3% β-CD was within a low range (0.65 ± 0.05), all falling into the almost no bitterness grade. This suggested that β-CD could effectively mask the bitter taste of traditional Chinese medicine. (Li et al., 2011). employed the THTPM method to assess the water decoction of 35 different single Chinese medicine decoction pieces with varying bitterness, using berberine hydrochloride as a reference. They preliminarily obtained the bitterness value and distribution characteristics of the water decoction of Chinese medicine decoction pieces, providing a crucial foundation for subsequent taste-masking research (Liu et al., 2012; Liu et al., 2013). conducted research on matrine at different concentrations, with 20 evaluators assessing its bitterness level and specific standard apparent bitterness value. They evaluated sample bitterness using three methods: the order evaluation method (OEM ranking method), score evaluation method (SEM), and integrated score evaluation method (ISEM). Ultimately, the three methods were comprehensively analyzed based on sorting accuracy, judgment sensitivity, assignment precision, and fitting degree, with the ISEM taste evaluation method proving to be the most effective. In order to further explore the bitterness superposition rules of different bitter substances (Zhang et al., 2021), selected nine types of Chinese medicinal slices as research carriers. On the basis of establishing a predictive model between the quality concentration of the monomer slice carrier and the bitterness tasted by mouth, they explored the relationship between the bitterness tasted by mouth when measuring the superposition of binary and ternary systems and the bitterness and quality concentration of the monomer slice. The research found that the quality concentration of the monomer slice can be well fitted to the predictive equation of the bitterness of the superimposed slices, and the contribution rate of Huanglian to the superimposed bitterness is often greater than that of the other components, fully confirming a Chinese saying, "A mute eats Huanglian, and the bitterness is unspeakable."

The bitterness determination method based on RB and SAB offers a direct approach to determining the bitterness of various substances, including monomeric compounds, decoction pieces, and compound decoctions. However, the measurement process may be influenced by the intrinsic structure, concentration, and temperature of the molecule. Therefore, controlling appropriate external conditions during the measurement process is essential.

2.1.4 Ratio of bitterness (ROB)

In the sweetness evaluation method, there exists a calculation method known as "the relative sweetness value (RS)", utilized for comparing different sweeteners. Researchers established the sweetness (Sr) of a 5% sucrose solution (Cr) as one and determined the mass concentration of other sweet substances equivalent to their sweetness. The RS of the sweet compound was then calculated using the formula RSs = Cr/Cs × Sr (Park et al., 2017). Building upon this concept, researchers proposed a method for determining the "Ratio of Bitterness (ROB)" of bitter substances (Li et al., 2023). Specifically, they determined the specific bitterness (ROBr) of a BBR solution with a mass concentration of 0.05 mg/mL (Cr) as one and obtained the mass concentration of other bitter substances equivalent to their bitterness. The ROB of the bitter compound was then calculated using the formula "ROBs = Cr/Cs × ROBr". Due to the significant variance in their values, their natural logarithm is termed the ROB-index (ROBI). Serving as an absolute quantitative index, ROB reflects a fundamental attribute of bitter substances, facilitating a straightforward comparison of bitterness among different bitter substances. Following these principles, researchers successfully determined the ROB of six bitter drug monomers, offering a new bitterness scale for comparing bitterness across various bitter drug monomers and enhancing the scope of research on drug bitterness comparison scales (Li et al., 2023).

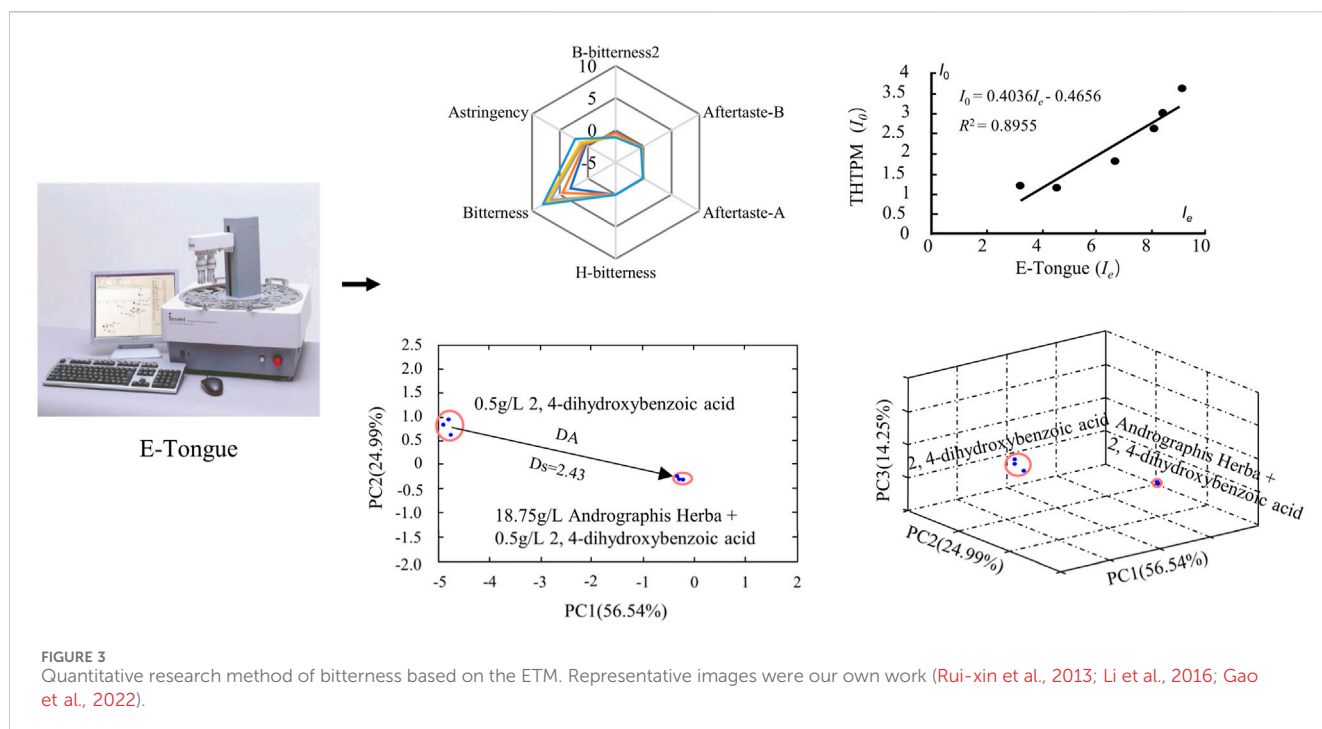## 2.1.5 Molecular bitterness (MB) and equivalent molecular bitterness (EMB)

Many drugs exhibit a bitter taste despite having different chemical structures. The emergence of bitterness is linked to factors such as the shape, size, and properties of functional groups within the molecule, as well as their positions. Eitan Margulis et al (Margulis et al., 2021) successfully constructed a machine learning tool, termed "BitterIntense," based on the chemical structural features of molecules. By calculating molecular descriptors, the tool classifies them into categories of "very bitter" or "not very bitter" with an accuracy rate of over 80%. This is significant for the early stages of drug development, as it allows for the rapid identification of compounds with intense bitterness. However, this method is a simple binary classification of bitterness intensity. How to establish a more precise bitterness intensity prediction algorithm based on molecular structural features remains a question that scholars are currently exploring. Liu et al., 2012 addressed the influence of concentration on the bitterness of bitter substances and introduced the concept of "molecular bitterness," which pertains solely to the properties of drug molecules. The bitterness threshold concentration (BTC) of both the standard bitterness substance and the compound under examination was determined using the "minimum limit method," representing the lowest concentration at which bitterness is detected

by half of the volunteers. The Molecular Bitterness (MB) under the standard bitterness substance BTC was set as 1 (typically using berberine hydrochloride as the reference bitter substance, with an MB of one under BTC). Calculating the MB of the test compounds involved the formula "MBs = Cr/Cs × MBr" (where Cr signifies the BTC of the standard bitter molecule; MBr denotes the MB of standard bitter molecules; Cs represents the BTC of unknown bitter molecules; MBs represents the MB of unknown bitter molecules (Heath et al., 2006; Bora et al., 2008; Li Xuelin et al., 2013; Jelvehgari et al., 2014; Gao et al., 2022)). Given the substantial variance in BTC among different bitter molecules, MB values differ significantly across substances. Therefore, the introduction of the "molecular bitterness index" (MB-Index, MBI) involves taking the natural logarithm of MB to normalize the magnitude difference, facilitating a more straightforward comparison of bitterness across different substances. Using this method, (Gao et al., 2022) calculated the MB of 19 bitter monomer components such as quinine (alkaloids), naringin (glycosides), andrographolide (terpenes), and L-arginine (peptides) to be 0.8398, 0.0551, 0.0058, and 0.0002, respectively. The corresponding MBI values were −0.1746, −2.8982, −5.1447, and −8.3669, respectively, effectively illustrating the bitterness characteristics of various bitter components in a simple and intuitive manner.

The introduction and application of the MB concept addressed the comparison of bitterness between compounds. However, for natural medicine decoction pieces, and even compounds composed of multiple natural medicine decoction pieces, the evaluation extends beyond a single compound to encompass the combination of various bitter compounds. The change in bitterness value within such complex systems after combination is intricate. With numerous types of natural medicines, there's an urgent need to establish an objective and appropriate bitterness evaluation method. Taking bitter natural medicines as an example, the current 2020 edition of the "Chinese Pharmacopoeia" includes a total of 2,711 natural medicines. Among them, 133 natural medicines exhibit a single bitter taste, comprising one very bitter, 14 extremely bitter, 47 bitter, one slightly bitter, and 70 slightly bitter (Supplementary Table S1). Additionally, 180 natural medicines possess not only a bitter taste but also other flavors (Supplementary Table S2). There are also nuanced differences in the taste descriptions of various natural medicines; for instance, Gentiana is described as "very bitter," Sophorae Tonkinensis as "extremely bitter," Bletilla as "bitter," Eucommia as "slightly bitter," and Lily bulb as "a little bitter" However, the distinction in bitterness between each description remains unknown. Furthermore, natural drugs described as 'extremely bitter,' such as Sophora flavescens and Aloe vera, pose the question: is their bitterness identical? Drawing from the MB calculation principle and bitterness measurement, Liu et al. (Gao et al., 2022) introduced the concept of "Equivalent Molecular Bitterness (EMB)" for complex systems. This involves determining the BTC of standard bitter substances and unknown complex systems using the "minimum limit method." The MBr under the standard bitter substance BTC is defined as 1 (typically using berberine hydrochloride as the reference bitter substance, with an MBr of one under BTC). Subsequently, the EMB calculation formula for other bitter Chinese herbal decoction pieces is "EMBs = Cr/Cs × MBr," where Cr represents the BTC of berberine hydrochloride, and Cs denotes the BTC of unknown Chinese

TABLE 2 Analysis of the characteristics of various evaluation indexes of bitterness based on THTPM measurements.

Name	Quantitative description analysis	gLMS score	Rank bitterness intensity	Standard apparent bitterness	Ratio of bitterness	Molecular bitterness	Equivalent molecular bitterness
Abbreviation	QDA	gLMS	RB	SAB	ROB	MB/MBI (Index)	EMB/EMBI (Index)
Reference	Each has different	General Psychophysical Scale	Five specific concentrations of BBR (across low/medium/high bitterness)	Five specific concentrations of BBR (across low/medium/high bitterness)	0.05 mg · mL-1 BBR (SAB = 3, medium bitterness)	Bitterness threshold concentration (9.947×10^{-6} M/L, very low bitterness) of BBR	Bitterness threshold concentration (9.947×10^{-6} M/L, very low bitterness) of BBR
Relationship with concentration	Related (Logarithm/Weibull)	Related (Logarithm/Weibull)	Related (Logarithm/Weibull)	Related (Logarithm/Weibull)	Independence	Independence	Independence
Data characteristics	Relative value	Absolute value	Absolute value	Relative value	Absolute value	Absolute value	Absolute value
Advantages	Most of the bitter substance solution can be measured; suitable for monomer, decoction pieces, and compound decoctions	The evaluation process is simple, and suitability is the same as "QDA"	The same as "QDA"	The same as "QDA"	It has nothing to do with the concentration; it can be directly used to compare the intensity of bitterness; suitable for bitter monomer compounds	The same as "ROB"	It has nothing to do with the concentration; it can be directly used to compare the intensity of bitterness; it is suitable for the bitterness of decoction pieces, and compound decoctions
Disadvantages	Affected by the evaluator's own factors; affected by factors such as the concentration of bitter substances and the determination temperature; the test methods of each research institution are different; it is difficult to make a direct horizontal comparison of the values due to the different participating carriers	Affected by the evaluator's own factors; affected by the concentration of bitter substances, determination temperature and other factors; the test methods of each research institution are different	Affected by the evaluator's own factors; affected by factors such as the concentration of bitter substances and the determination temperature; the test methods of each research institution are different; it is difficult to make a direct horizontal comparison of the values due to the different participating carriers	The same as "RB"	It is not suitable for the evaluation of low bitterness level at high concentration	Applicable to the bitterness evaluation of bitter monomers; bitterness prediction suitable for low bitterness of multiple monomers	Applicable to the bitterness evaluation of bitter decoction pieces; it is suitable for the bitterness prediction of low bitterness aqueous solutions of compound decoction pieces
Applicable conditions	It is widely used to evaluate the bitterness of most bitter substance solutions	It is widely used to evaluate the bitterness of most bitter substance solutions	Bitterness evaluation of most bitter substance solutions; prediction of bitterness under different concentrations of the same carrier	Bitterness evaluation of most bitter substance solutions; prediction of bitterness under different concentrations of the same carrier; it can directly compare and predict the low, medium, and high bitterness of the carrier; prediction of bitterness under different concentrations of the same carrier	Evaluation and comparison of ROB bitterness of bitter monomer compounds; bitterness prediction of medium bitterness aqueous solutions	Evaluation and comparison of MB bitterness of bitter monomer compounds; bitterness prediction of low bitterness solutions	Evaluation and comparison of MB bitterness of bitter decoction pieces; bitterness prediction of low bitterness compound solutions

FIGURE 3
Quantitative research method of bitterness based on the ETM. Representative images were our own work (Rui-xin et al., 2013; Li et al., 2016; Gao et al., 2022).

herbal pieces. The natural logarithm of this ratio is termed the EMB-index (EMBI) (Wang et al., 2022). measured the EMB and EMBI of 23 kinds of bitter Chinese herbal pieces using the aforementioned methods and established a quantitative method for determining the bitterness of bitter Chinese herbal pieces. This comparative analysis of the bitterness characteristics of different types of Chinese herbal pieces offers valuable insights, laying a robust foundation for the accurate masking of natural drugs within complex systems.

The comprehensive review reveals that researchers approach quantitative analysis of bitterness from diverse perspectives and levels using THTPM as a foundation. Each method presents distinct advantages, limitations, and applicability (Table 2). When embarking on quantitative investigations into bitterness, it is crucial to select appropriate methodologies tailored to the study's objectives and the nature of the research subject.

2.2 ETM

Sensory group evaluation poses significant challenges due to medical ethics considerations, associated health risks, and the substantial costs of personnel training. Moreover, the inherent subjectivity among individuals can lead to fatigue, slow evaluation speeds, and a limited sample size. Throughout the evaluation process, there is a risk of sample perception migration and perception saturation, thereby imposing constraints on the assessment of taste within the general population (Legin et al., 2004). The Gustation Analytical Fingerprint Technique (GFAT) represents a recent development in taste recognition and detection technology, relying on taste sensors and chemical information processing methods. These taste sensors function as intelligent recognition electronic systems, emulating the human taste mechanism to generate signals (optical, electrochemical,

electrophysiological). They possess the capability to discern subtle differences in basic tastes, such as lingering or transient tastes. Notably, GFAT offers advantages such as rapid analysis, low cost, minimal sample preparation, and automation of analysis (Rudnitskaya et al., 2010; Podrażka et al., 2017). Scholars have conducted a systematic evaluation of the application of ETM and sensory groups in taste assessments of pediatric drugs. The findings reveal that sensory tests for children are infrequent (10.3%), with ETM predominating in pediatric drug taste evaluations (57.5%), highlighting the efficacy of ETM (Guedes et al., 2021). Over the past few decades, leveraging electronic tongue technology, researchers have successfully employed methods such as the conversion of electronic tongue taste information value (Zeng et al., 2015; Li et al., 2016), bitter distance calculation, and the establishment of relationships between electronic tongue information and human sensory evaluation (Ito et al., 1998; Uchida et al., 2001). These advancements have facilitated the quantitative analysis and prediction of various drug tastes, as shown in Figure 3.

2.2.1 Electronic tongue converts taste information value

Using the TS-5000Z multi-channel taste sensor as an illustration, it employs an artificial lipid membrane sensor technology akin to the functioning principle of human tongue taste cells. This sensor has the capability to objectively and digitally detect five basic tastes as well as flavor attributes such as "sharpness" and "richness." In the TS-5000Z taste analysis system, Relative value (R) and Change of Membrane Potential caused by Adsorption (CPA) are commonly utilized (Li et al., 2020). To initiate taste analysis, the taste sensor is immersed in a reference solution comprising a mixture of KCl and tartaric acid at a predetermined concentration, yielding the corresponding membrane potential, denoted as Vr. This reference solution is essentially tasteless.

Subsequently, the sensor is submerged in the sample solution to determine the potential difference value of the solution potential (Vs.), which is then subtracted from Vr, termed as the first taste (R). Following a gentle cleanse of the taste sensor with the reference solution, it is re-immersed to detect the potential Vr'. The disparity between Vr' and Vr is referred to as aftertaste (CPA), indicating the potential change induced by chemical adsorption.

The first taste and aftertaste can be calculated by Equations 1, 2:

$$R = Vs\text{-}Vr \tag{1}$$

$$CPA = Vr'\text{-}Vr \tag{2}$$

Based on the initial taste and aftertaste values, a specific mathematical conversion is performed to derive the electronic tongue conversion taste information value (I.e.,), serving as a metric for quantitative bitterness evaluation (Zeng et al., 2015). employed the electronic tongue technology-based taste analysis method to quantify the characteristics of Scutellaria baicalensis from various sources. By establishing a positive correlation between the bitterness, astringency, bitter aftertaste, astringency aftertaste, sour taste information of Scutellaria baicalensis, and the baicalin content, it was possible to infer the baicalin content in Scutellaria baicalensis. In a similar vein (Jing et al., 2022), utilized electronic tongue technology to quantify the taste of 20 batches of Magnolia officinalis, assessing the taste of six monomer compounds. Pearson correlation analysis was employed to ascertain the correlation between eight chemical components and the taste sensor response value. The investigation revealed a significant positive correlation between honokiol, magnolol, and spicy menthol magnolol in Magnolia officinalis, and the bitter taste and bitter aftertaste detected by the electronic tongue.

2.2.2 Distance of bitterness
2.2.2.1 Distance of bitterness in multidimensional space

Using the French ASTREE electronic tongue method as a case study, the quantification of bitterness index relies on data gathered from seven sensors within the electronic tongue apparatus. Through meticulous data processing, a numerical value is derived, providing a quantitative or semi-quantitative representation of the drug's bitterness. This value is termed the Bitterness Distance (D). Utilizing chemometric techniques such as PCA, the spatial disparity between the sample under examination and a reference solution is computed. This approach mirrors principles found in cluster analysis and other methodologies, where the distance between samples is evaluated within a multidimensional space comprising various variables.

Distance serves as a metric to gauge the spatial separation between two entities. Common distance metrics encompass Euclidean distance, Mahalanobis distance, Ming's distance, among others. The Euclidean distance (EUCLID), or Euclidean metric, stands out as a prevalent distance measure, delineating the true geometric distance between two points within an m-dimensional space. Its applicability is underscored by its capacity to be expressed in a unified recursive formula, making it the most frequently utilized distance metric.

The Euclid and Standardized Euclid can be calculated by Equations 3, 4:

$$Euclid = \sqrt{\sum_{i=1}^{k}(x_i\text{-}y_i)^2} \tag{3}$$

$$Standardized\ Euclid = \sqrt{\sum_{i=1}^{k}\left(\frac{x_i\text{-}y_i}{S_i}\right)^2} \tag{4}$$

Where k represents the number of variables each sample possesses, with x_i indicating the value of the first sample on the i-th variable, and y_i representing the value of the second sample on the same variable. In the context of bitter samples, the Euclidean distance between samples exhibiting varying degrees of bitterness serves as a measure of the disparity in bitterness levels.

For instance, consider the compound BBR, which was formulated into samples of varying concentrations. Each sample, along with purified water, underwent analysis using an electronic tongue. The resulting dataset facilitated the direct calculation of its Euclidean distance, effectively quantifying the multidimensional space between them. Notably, a larger Euclidean distance between the sample and purified water signifies a higher bitterness level in the sample, and conversely, a smaller distance indicates lower bitterness.

2.2.2.2 Distance of bitterness in reduced-dimensional space

The data collected by the electronic tongue underwent reduction via Principal Component Analysis (PCA) and similar techniques. Subsequently, based on these findings, the distance between each sample and the reference solution within the principal component space (whether in two-dimensional, three-dimensional, or other dimensions) was computed to determine the relative bitterness of each sample.

In a two-dimensional or three-dimensional space, the Euclidean distance serves as the measure of separation between two points, delineating the extent of spatial disparity, as shown in Equations 5, 6:

$$EUCLID_{(2D)} = \sqrt{(x_1\text{-}x_2)^2 + (y_1\text{-}y_2)^2} \tag{5}$$

$$EUCLID_{(3D)} = \sqrt{(x_1\text{-}x_2)^2 + (y_1\text{-}y_2)^2 + (z_1\text{-}z_2)^2} \tag{6}$$

When employing PCA for dimensionality reduction analysis, we can compare the bitterness differences among samples by assessing the distance from each sample to the reference solution in both two-dimensional and three-dimensional spaces. Nakamura *et al.* conducted a study to assess the taste of orally disintegrating tablets (ODT) containing famotidine and amlodipine besylate using the Astree electronic tongue and THTPM. The palatability of the tablets was further evaluated using a 100 mm VAS scale. The findings indicated that both physical masking and organoleptic masking could enhance the palatability of famotidine and amlodipine. In the electronic tongue analysis, the Euclidean distance of samples subjected to physical masking, organoleptic masking alone, and in combination, was found to be smaller compared to unmasked drugs (Nakamura et al., 2015). Liu *et al.* investigated bitter drug carriers employing BBR and Andrographis paniculata decoction, screening taste masking agents by assessing bitterness reduction values in reduced-dimensional or multi-dimensional space (Liu et al., 2013; Rui-xin et al., 2013). Li et al. (2011) assessed the masking effect of various agents on berberine

hydrochloride using bitterness distance, D, and bitterness reduction distance, ΔD (Li et al., 2013).

While the results derived from PCA analysis slightly underperform compared to multi-dimensional space distance, they offer a more intuitive representation through two-dimensional or three-dimensional maps, overcoming the graphical limitations of multi-dimensional spaces. Moreover, data standardization aids in further reducing system errors. However, it is important to note that this method is only applicable to distinguishing bitterness within the same component.

2.2.3 The relationship between electronic tongue taste information value and THTPM

The electronic tongue taste information is typically expressed through relative response values or bitterness values. Establishing the relationship between electronic tongue taste information and THTPM involves data-driven modeling and prediction, relying on experimental data and mathematical methods. Several studies have demonstrated a strong correlation between taste assessed by electronic tongue and human taste perception (Ito et al., 2013; Wang et al., 2013; Maniruzzaman et al., 2014; Maniruzzaman and Douroumis, 2015). In recent years, there has been a proliferation of applications for quantitatively predicting bitterness using electronic tongue. For instance, Li (Li et al., 2016) utilized berberine hydrochloride as a reference and matrine and oxymatrine as model drugs to establish a bitterness prediction model (BPM) based on THTPM bitterness ratings and data from the TS-5000Z electronic tongue sensor. The results indicated a significant correlation between taste bitterness and electronic tongue bitterness ($R^2_{matrine}$ = 0.8955, $R^2_{oxymatrine}$ = 0.9793). The electronic tongue-based bitterness prediction model for matrine and oxymatrine exhibited high accuracy ($R^2_{matrine}$ = 0.9639, $R^2_{oxymatrine}$ = 0.9535). (Liu et al., 2014a) developed a BPM for berberine hydrochloride using a genetic algorithm-back propagation neural network (GA-BP), incorporating bitterness intensity evaluated by sensory groups and data provided by electronic tongue. The model demonstrated excellent fitting (R^2 = 0.99965) and could effectively predict the bitterness of berberine hydrochloride across different concentrations, serving as a reference for developing BPMs for other drugs. Chen (Chen et al., 2020) presented a biosensor utilizing *Drosophila* odorant binding protein (OBP) as a biosensitive material. This biosensor was employed to study typical bitter molecules such as denatonium, quinine, and berberine using electrochemical impedance spectroscopy. The findings revealed significant binding properties between the bitter molecules and OBP, displaying a linear response within the concentration range of 10-9-10-6 mg/mL, indicating broad application prospects for the OBP-based biosensor. (Xue, 2022) employed Weibull curve fitting to evaluate the taste of oseltamivir phosphate and ginkgo leaves, along with electronic tongue data, enabling quantitative description of bitterness. The prediction model's accuracy and superiority were assessed through cross-validation. Additionally, the electronic tongue method's ability to predict the bitterness of bitter substances was validated against THTPM results.

In general, there exists a certain correlation between the taste information provided by the electronic tongue and the outcomes from THTPM, although this correlation may not always be consistent. Numerous factors contribute to this, including the type of electronic tongue, sensor selection, signal processing methods, data analysis techniques, standardization of tasting methods, and the training of evaluators. Due to variations in perception mechanisms and sensitivity between electronic tongues and human taste, the electronic tongue may not fully capture the nuanced characteristics of individual taste perception (Uchida et al., 2001). Consequently, the relationship between electronic tongue taste information and taste assessment methods requires calibration and validation specific to the samples and conditions at hand and cannot be generalized.

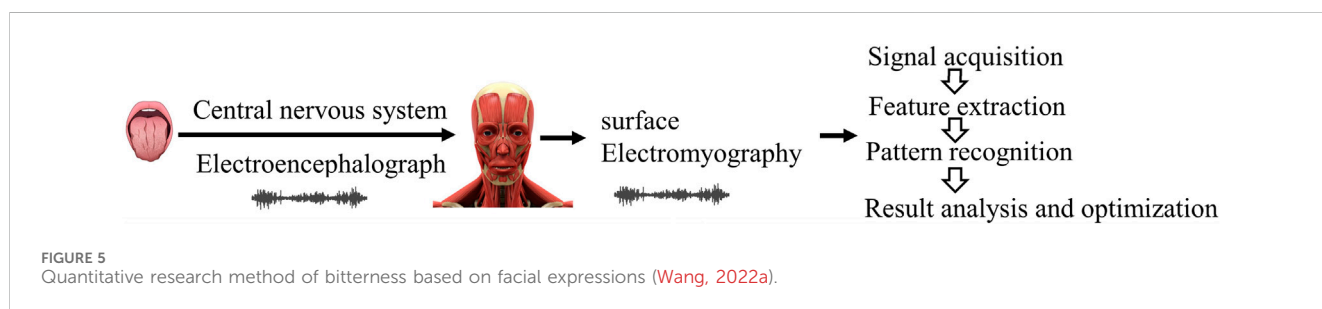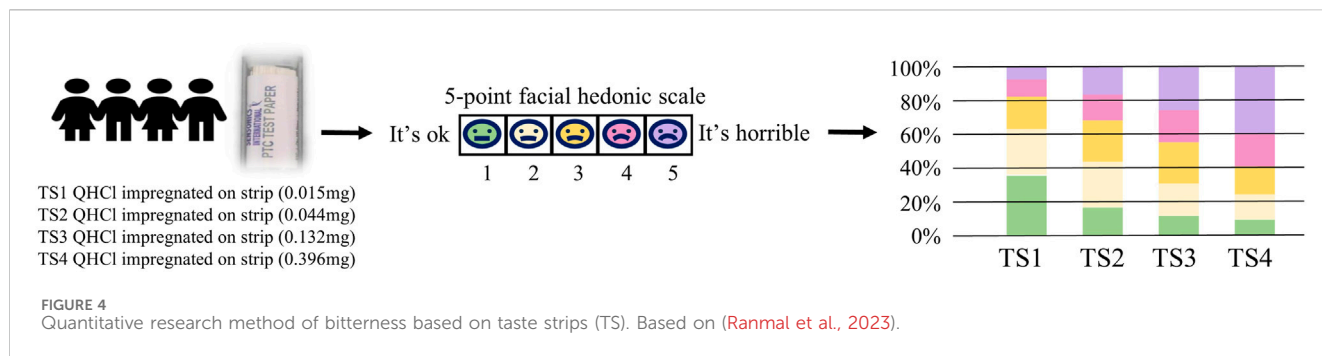## 2.3 Taste strips and filter paper disc method

Taste strips (TS) consist of filter paper infused with taste substances. When evaluating, the evaluator places the TS on the tongue's center, closes the mouth, and gradually moves the tongue, allowing saliva to dissolve the taste enhancer on the strip. After a designated period, the strip is removed for taste assessment, as shown in Figure 4. Ranmal (Ranmal et al., 2023) examined subjects' hedonistic responses to bitter stimuli from TS. Findings revealed that as the concentration of quinine hydrochloride (QHCl) on TS increased, both children and adults showed heightened aversion to bitterness. Similarly, Schienle (Schienle and Schlintl, 2020) utilized QHCl TS to gauge taste intensity, ranging from no sensation to "the strongest imaginable sensation of any kind." Green (Green et al., 2022) employed TS containing high and low concentrations of four tastes (sour, sweet, bitter, and salty) to assess taste function in healthy participants. Results indicated elevated recognition levels among participants exposed to high-concentration taste strips in laboratory settings.

Another bitterness measurement method akin to the TS method is the filter paper disc method (FPD). KATARINA(Berling et al., 2011) employed FPD to assess evaluators' perception thresholds for various flavors. Each flavor agent comprised five different concentrations. Using a scoring system from one to 6, where one indicates the lowest threshold, five represents the highest measurable threshold, and six signifies an unmeasurable high threshold, evaluators progressed from low to high concentrations until they correctly identified the taste, thus determining the recognition threshold. Results indicated standard thresholds for four flavors: bitter 1.9 ± 1.30, acid 2.3 ± 1.09, salty 2.5 ± 1.53, and sweet 2.6 ± 1.37, respectively, with bitterness identified at a lower concentration than other flavors.

The TS and FPD methods offer a straightforward, rapid, safe, and effective out-of-laboratory (OOL) sensory evaluation approach for assessing bitterness perception. Nonetheless, further research is warranted to establish a stronger correlation between the "local stimulation" method and the "full mouth" method based on the classical population taste evaluation method.

2.4 Facial expression analysis

Facial expressions serve as a rich source of emotional information. When individuals taste different flavors of medications, their facial expressions vary accordingly. For

FIGURE 4
Quantitative research method of bitterness based on taste strips (TS). Based on (Ranmal et al., 2023).

FIGURE 5
Quantitative research method of bitterness based on facial expressions (Wang, 2022a).

instance, tasting non-bitter Chinese medicine may elicit "neutral" expressions, whereas tasting bitter Chinese medicine may provoke expressions of "disgust," characterized by tight frowns and clenched teeth. Facial expression recognition technology leverages facial expression data to objectively analyze human emotional responses. Utilizing this technology, we can extract facial expression features of individuals and employ suitable expression classification methods to objectively assess taste perception, as shown in Figure 5.

Wang (2022a) utilized taste stimulation to perceive potential signals from nerve-related facial muscles and gland-related muscles, converting them into digital signals to acquire taste information, thus enabling the acquisition of taste information from electric potential signals. Furthermore, variations in the intensity of expression responses may occur when evaluators taste natural medicines with differing levels of bitterness (Zhi et al., 2017). observed that facial expression intensity can indicate the degree of taste stimulation across various concentrations and levels. Most participants displayed pronounced aversion to medium and high concentrations of bitterness, manifesting as expressions of disgust. With the rapid advancement of deep learning, facial expression recognition technology has progressed from simple classification to intensity level analysis. Yang et al., 2010 introduced a novel technique for facial expression analysis based on a ranking model. They transformed the task of expression intensity analysis into a ranking problem and employed RankBoost modeling. The resulting ranking score can directly estimate intensity and demonstrated good performance on the Cohn-Kanade dataset. As facial expression recognition technology continues to evolve, researchers have established datasets such as JAFFE, FER 2013, and CK + for facial expression analysis. However, an exclusive dataset for bitterness evaluation is yet to be established. Developing

such a dataset is crucial to advancing the intelligent and accurate quantification of bitterness.

2.5 Animal behavior test

When one animal is attracted to a stimulus while another avoids it, it suggests that the compound may possess distinct perceptual characteristics for different tasters, leading to varied evaluations (Loney et al., 2012). The two-bottle preference test (TBP) (Yoneda et al., 2007) is employed to assess the aversive taste of food or beverages, utilizing the preference index (PI) as the evaluation metric (Loney et al., 2011). Rodents are commonly chosen as experimental subjects due to their highly homologous bitter taste receptors to humans, thus exhibiting similar taste perceptions (Noorjahan et al., 2014). Han (Han et al., 2018) established the relationship between quinine concentration and animal PI. Subsequently, the PI of 12 bitter Traditional Chinese herbal (TCH) compounds was determined using TBP, and the bitterness results were standardized into a unified numerical system based on the concentration-PI relationship. This standardization offers a methodological framework for sensory evaluation of natural medicines, as shown in Figure 6.

Magdalena Münster (Münster et al., 2017) assessed the palatability of the bitter compound praziquantel using the rodent transient contact taste aversion (BATA) model and calculated the IC_{50} value, representing the concentration of praziquantel inhibiting 50% of the maximum licking response. The findings revealed a decrease in licking frequency with increasing praziquantel concentration, with an IC_{50} value of 0.06 mg/mL (95% CI 0.049-0.082). Comparative analysis indicated that praziquantel elicited a stronger aversive response compared to other bitter compounds
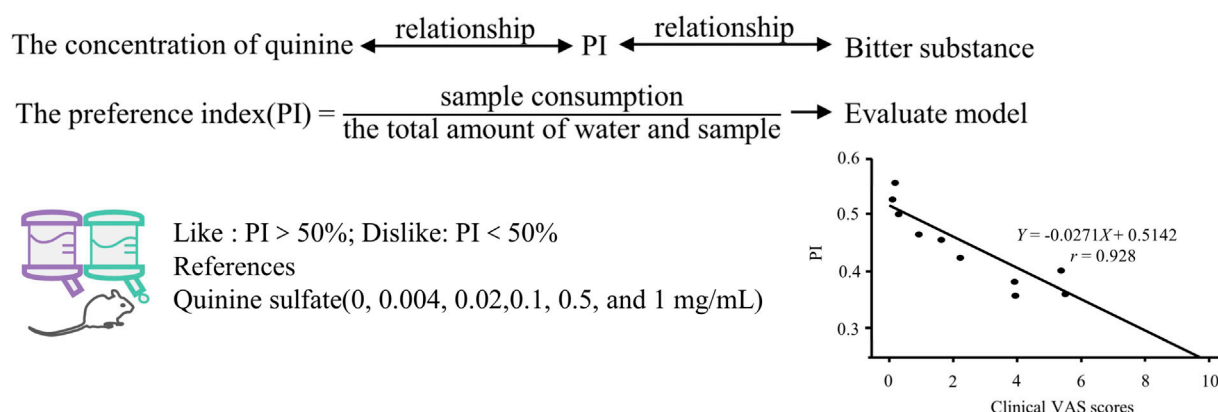
FIGURE 6
Quantitative research method of bitterness based on animal behavior test. Based on (Han et al., 2018).
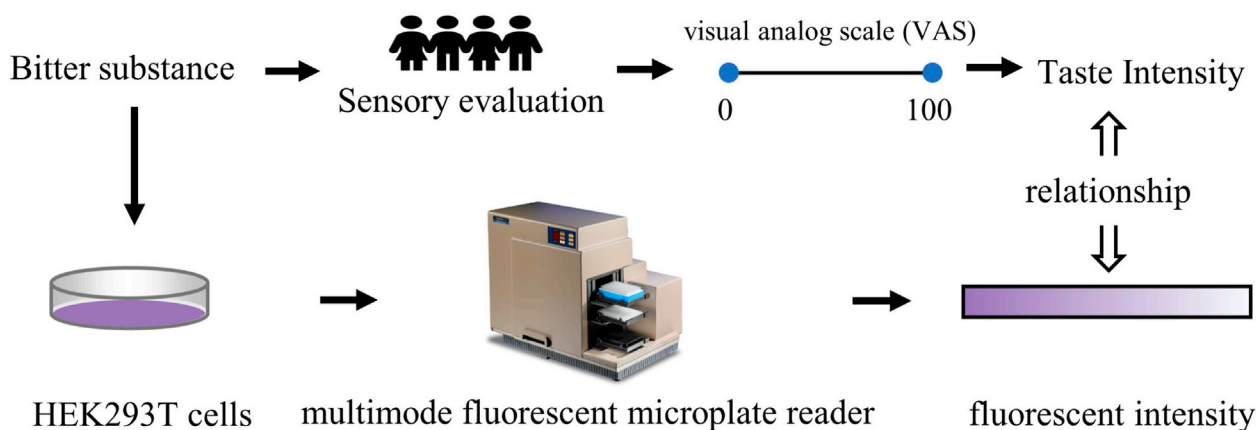

FIGURE 7
Quantitative research method of bitterness based on animal behavior test. Based on (Narukawa et al., 2011).

such as sildenafil citrate, caffeine citrate, diclofenac, or paracetamol (Soto, 2016).

It is important to note that the outcomes of animal studies are influenced by species-specific expression of bitter taste receptors, resulting in bitter taste responses that may differ from those in humans (Dong et al., 2009). Future research endeavors should focus on refining methodologies to achieve more accurate quantitative assessments of bitter taste.

2.6 Cell-based assessment methods

Bitter substances, serving as flavoring agents, can stimulate certain taste bud cells. By describing the interaction strength between them, it is possible to achieve an objective measurement for the quantification of bitterness (Narukawa et al., 2011), as shown in Figure 7. (Hui et al., 2012) utilized human intestinal endocrine STC-1 cells expressing G protein-coupled receptors and bitter receptors (type 2 members) as sensing devices to conduct specific detection of bitter substances. The findings demonstrated that the sensor utilizing STC-1 cells selectively

responded to bitter agents and mixtures, with the type and concentration of bitter agents determinable via signal-to-noise ratio parameters. This approach offers a valuable avenue for investigating taste mechanisms and evaluating bitterness intensity. Nakamura (Nakamura et al., 2003) investigated the effect of quinine on $[Ca^{2+}]i$ levels in cultured nerve-2a cells, exploring the potential of $[Ca^{2+}]i$ levels to predict the bitterness of quinine solutions. Following quinine stimulation, $[Ca^{2+}]i$ levels in nerve-2a cells increased in a concentration-dependent manner.

However, the cell-based biosensor evaluation method also has certain limitations, as cells may not be able to detect all bitter substances. For instance, Thomas (Delompré et al., 2022) demonstrated the bitterness of vitamins B2 and B3 in sensory analysis, where cell-based assays failed to yield any information. This may be attributed to the inherent fluorescence characteristics of the two vitamins at high concentrations (Chen and Chung, 2022). Additionally, current taste cell culture methods are susceptible to the influence of pseudo-taste cells, potentially leading to overinterpretation. Therefore, caution must be exercised when employing this method.
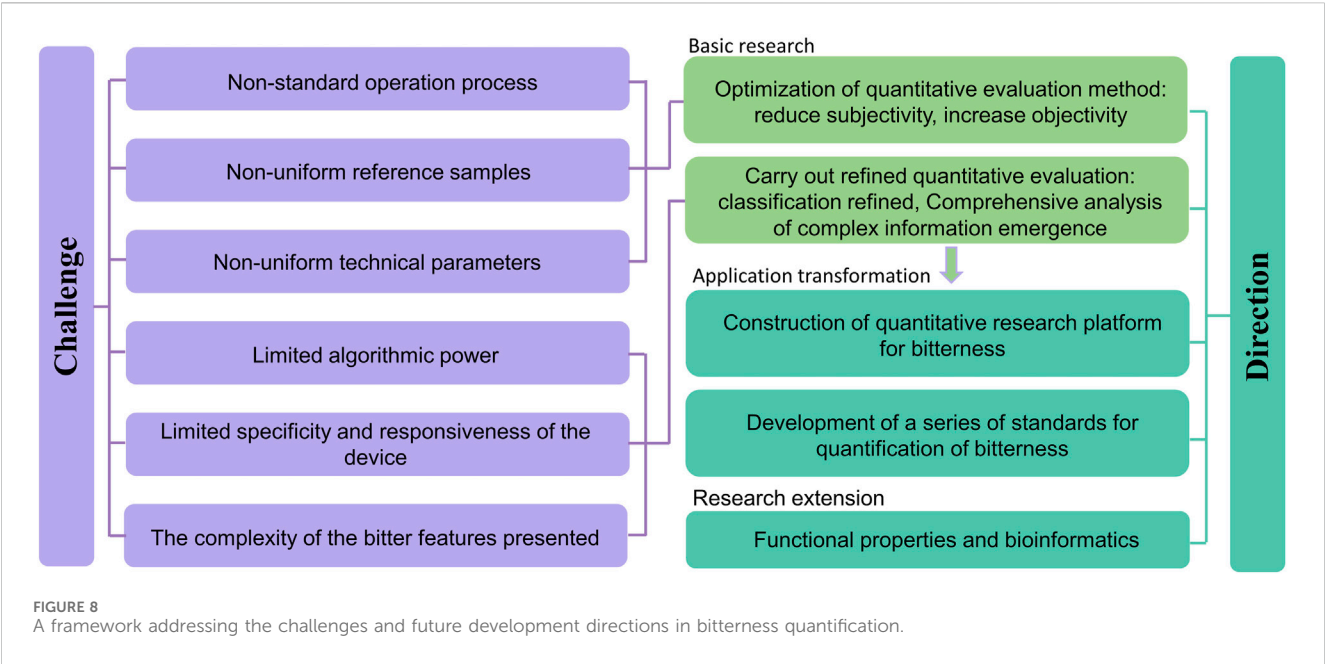
FIGURE 8
A framework addressing the challenges and future development directions in bitterness quantification.

TABLE 3 Analysis of the advantages and disadvantages of various bitterness quantitative methods.

Name	THTPM	Taste strips and filter paper disc method	ETM	Facial expression analysis	Animal behavior test	Cell-based assessment methods
Advantages	It can intuitively give the taste of bitter substances	It can intuitively give the taste of bitter substances	It can objectively collect the taste data information of bitter substances; it is easy to operate, has low cost, has high sensitivity, and has a low detection threshold; it exhibits good repeatability and does not need ethical approval	It can be used for people who cannot express their evaluations through language	The taste of the sample can be judged by the number of animal intakes of the experimental sample or some escape reactions, such as shaking of the head or agitation; results are relatively intuitive	It is helpful for understanding the mechanism and characteristics of bitter substances
Disadvantages	Strong subjectivity, easy fatigue, poor repeatability, and limitations for toxic substances; the requirements for taste sensitivity of the evaluators are high; it is time-consuming and laborious; the number of samples for a single test is small and the operation is cumbersome, so it is not suitable for rapid taste evaluation of a large number of samples	The bitterness characteristics obtained by "local stimulation" are limited	The results are not intuitive enough, and further processing and analysis is needed through model algorithms; the sensor richness and detection limits need to be improved	It is susceptible to factors such as occlusion, illumination, and local changes in subtle expressions	The properties of the test samples cannot be obtained; can only be used as a supplement to the taste evaluation of the population; generally applicable for comparisons of bitterness intensity between compounds with known bitterness	Limited access to information; easy to be affected by the fluorescent cells; pseudo-flavor cells, resulting in negative results or over-interpretation

In summary, researchers have conducted numerous quantitative studies on bitterness using both *in vivo* and *in vitro* methods. Throughout this process, researchers have identified various dimensions of bitterness quantification, including local and overall characteristics, static and dynamic features, and external macro performance and internal micro mechanisms. Each method possesses its own advantages and disadvantages (Table 3). When evaluating drug development, taste masking, and palatability,

researchers can select appropriate methods based on research objectives, cost, time constraints, and other factors. However, it is important to note that bitterness research methods are still evolving. In the future, researchers need to continue exploring quantitative evaluation methods for bitterness, standardizing the evaluation process to facilitate the high-quality development of bitterness quantification.

3 Future research directions

Due to the influence of ethical reviews, the complexity of the regularity of bitter substance structural characteristics, the significant differences in the activation capacity of bitter taste receptors, and the surrounding environment of bitter substances, the quantitative research methods for bitterness are still actively being explored. The current research method system for bitterness, which is primarily based on THTPM and supplemented by other research methods, still requires further improvement to meet basic research needs. The main aspects which is shown in Figure 8 include: (1) Optimizing the quantification and evaluation methods for bitterness. By strictly selecting the evaluation population, establishing standardized operating procedures, and developing methods for handling outliers, the subjectivity of direct bitterness evaluation methods is reduced (Medicine, 2024); by strengthening the basic research on the structural characteristics of bitter substances, the characteristics of activating ligands, and the mechanisms of bitterness presentation, the relationship between concentration-structure-function-bitterness is explored, as well as the relationship between key chromatographic information/ electrical signals/fluorescent signals and bitterness. This provides foundational support for optimizing indirect bitterness evaluation methods and actively utilizes machine learning algorithms to enhance the objectivity, accuracy, speed, and transparency of indirect bitterness evaluation methods. (2) Conduct refined quantification of bitterness and explore new methods for bitterness quantification research. Since there is a subtle relationship between people's preferences or aversions to bitterness (Mura et al., 2018), research methods from the food field can be referenced to make refined distinctions in bitterness, such as good bitterness and bad bitterness, and to carry out refined quantitative evaluation of different types of bitterness in drugs (Sook Chung and Lee, 2012; Araujo et al., 2021). At the same time, closely focus on the taste-affecting factors that influence the bitterness of drugs and construct new methods for bitterness quantification and evaluation. For example, based on methods such as virtual screening, biofishing, and physicochemical detection, establish the relationship between key parameters of the above methods and bitterness, and systematically analyze the comprehensive impact of structural characteristics, concentration, and external environmental factors of bitter substances on bitterness. (3) Construct a quantitative research platform for bitterness. Currently, researchers often reveal the mechanisms of bitterness from a mesoscopic or microscopic perspective, and the bitterness platforms constructed are mostly centered around qualitative identification (determining whether it is bitter or not) (Chu et al., 2024). On this basis, there is an urgent need to build a quantitative research platform and equipment for bitterness, and to

integrate different types of data in multiple dimensions, to promote the transformation of basic research on bitterness quantification to applied research. (4) Improve and establish a series of standards for quantitative research on bitterness. In order to achieve scientific measurement and effective evaluation of senses, a series of international documents have been issued for sensory analysis. For the sensory evaluation of bitterness, some scholars have already conducted research on the technical specifications for sensory evaluation based on the characteristics of natural medicines (Medicine, 2024). In the future, it is still necessary to formulate industry, national, and global standards around the research design and plan framework guidelines, statistical analysis plans, methodological validation, data processing, etc., of bitterness quantification, to promote the standardization, scientification, and systematization of quantitative research on drug bitterness. (5) Research Extension. Bitter substances possess a variety of physiological activities (Zuluaga, 2024). In traditional Chinese medicine theory, bitterness is believed to have effects such as " downbearing and discharging, drying dampness, and consolidating Yin " Advancing the research on the functional attributes of bitterness and its extension into the field of bioinformatics, including the relationships between bitterness and efficacy, and bitterness and receptors, can provide support for accelerating the development of target drugs.

In the process of exploring the quantification of bitterness, we also face many challenges. On one hand, there are issues such as non-standardized operating procedures and inconsistent technical parameters. These mainly include the lack of uniformity in scales, reference solutions, the volume of samples evaluated at one time, temperature, evaluation time and intervals, and limited instrument stability, which hampers the comparability of results between different studies (Zuluaga, 2024). On the other hand, the complexity of bitter taste presentation makes the quantification of bitterness very difficult, especially for the measurement of the comprehensive bitterness in complex systems, where it is urgent to explore the taste rules in the independent state of substances and under the state of complex systems (Zhang et al., 2021; Gao et al., 2023). In addition, the flexibility of virtual screening methods, the specificity and sensitivity of indirect measurement methods, and the computational power of different machine algorithms also affect the accuracy of bitterness quantification. In the future, researchers urgently need to further enrich the database of bitter substances, establish standardized and unified operating standards, and by improving detection technology and optimizing algorithm capabilities, jointly explore and mutually verify the characteristics of bitterness from macroscopic, mesoscopic, or microscopic perspectives (Li et al., 2024).

4 Conclusion and foresight

In nature, various taste substances exist alongside intricate taste mechanisms, and numerous factors influence the quantification of drug bitterness to varying extents. In light of this, different quantitative evaluation methods for bitterness have been established, each possessing its own merits. Presently. Currently, an increasing number of researchers are leveraging column chromatography, HPLC, HPLC/ESI-MS, LC/ESI-MS/MS, UPLC-

Q-TOF/MS, and nontargeted LC/MS flavoromics analysis to separate and identify the bitter compounds (Suryawanshi et al., 2006; Mustafa et al., 2015; Höhme et al., 2023). They also combine methods such as sensory-guided, virtual screening, and chromatography-taste association to improve the efficiency of discovering bitter components (Yu et al., 2020; Yang et al., 2023). This signifies that the study of bitterness in natural medicines is steadily advancing. However, the identification of bitter components represents merely the initial phase. A precise, dependable, and straightforward method for evaluating drug bitterness is required to investigate bitterness masking strategies for medications. Similar to the measurement of length using the international unit "meter" and temperature using the "degree Celsius," bitterness should also be subject to standardized, objective quantitative methods and parameters. This review scrutinizes research on bitterness quantification, delineates factors influencing drug bitterness, and acknowledges the role of material, human, and environmental factors in affecting bitterness perception. Consequently, in the quantitative exploration of drug bitterness, it is imperative to identify and regulate these factors to ensure the reliability of outcomes. Furthermore, this paper consolidates the characteristics of various bitterness quantification methods, systematically categorizes the quantitative approaches for representative drugs, and emphasizes the challenges associated with quantifying bitterness in natural drugs characterized by complex systems. It also elucidates the future research directions that urgently need to be undertaken. This is of significant guiding importance for our continued in-depth focus on the research of quantitative bitterness methods and lays an important foundation for the development of precise, efficient, and rich taste-masking strategies. Such efforts aim to foster research into taste masking optimization and palatability enhancement, thereby laying a crucial groundwork for enhancing the clinical acceptance of natural medications.

Author contributions

PW: Writing–original draft. HL: Writing–original draft. YW: Investigation, Writing–review and editing. FD: Investigation, Writing–review and editing. HL: Writing–review and editing. XG: Investigation, Writing–review and editing. YR: Writing–original draft. XG: Investigation, Writing–review and editing. XL: Funding acquisition, Project administration, Writing–review and editing. RL: Funding acquisition, Project administration, Writing–review and editing.

Funding

Conflict of interest

The authors declare that the research was conducted in the absence of any commercial or financial relationships that could be construed as a potential conflict of interest.

Publisher's note

All claims expressed in this article are solely those of the authors and do not necessarily represent those of their affiliated organizations, or those of the publisher, the editors and the reviewers. Any product that may be evaluated in this article, or claim that may be made by its manufacturer, is not guaranteed or endorsed by the publisher.

Supplementary material

The Supplementary Material for this article can be found online at: https://www.frontiersin.org/articles/10.3389/fchem.2024.1449536/full#supplementary-material

References

Aliani, M., and Eskin, M. N. A. (2017). Bitterness: perception. *Chem. Food Process.*, 239–243. doi:10.1002/9781118590263

Amin, F., Khan, S., Shah, S. M. H., Rahim, H., Hussain, Z., Sohail, M., et al. (2018). A new strategy for taste masking of azithromycin antibiotic: development, characterization, and evaluation of azithromycin titanium nanohybrid for masking of bitter taste using physisorption and panel testing studies. *Drug Des. Devel Ther.* 12, 3855–3866. doi:10.2147/dddt.S183534

Araujo, L. D., Parr, W. V., Grose, C., Hedderley, D., Masters, O., Kilmartin, P. A., et al. (2021). In-mouth attributes driving perceived quality of Pinot noir wines: sensory and chemical characterisation. *Food Res. Int.* 149, 110665. doi:10.1016/j.foodres.2021.110665

Aree, T. (2019). Understanding structures and thermodynamics of β-cyclodextrin encapsulation of chlorogenic, caffeic and quinic acids: implications for enriching antioxidant capacity and masking bitterness in coffee. *Food Chem.* 293, 550–560. doi:10.1016/j.foodchem.2019.04.084

Bahia, M. S., Nissim, I., and Niv, M. Y. (2018). Bitterness prediction in-silico: a step towards better drugs. *Int. J. Pharm.* 536 (2), 526–529. doi:10.1016/j.ijpharm.2017.03.076

Beauchamp, G. K. (2016). Why do we like sweet taste: a bitter tale? *Physiol. Behav.* 164 (Pt B), 432–437. doi:10.1016/j.physbeh.2016.05.007

Berling, K., Knutsson, J., Rosenblad, A., and von Unge, M. (2011). Evaluation of electrogustometry and the filter paper disc method for taste assessment. *Acta Otolaryngol.* 131 (5), 488–493. doi:10.3109/00016489.2010.535850

Bishop, L. R. (2013). EUROPEAN BREWERY CONVENTION THE E.B.C. SCALE OF BITTERNESS. *J. Inst. Brew.* 73 (6), 525–527. doi:10.1002/j.2050-0416.1967.tb03078.x

Boesveldt, S., and de Graaf, K. (2017). The differential role of smell and taste for eating behavior. *Perception* 46 (3-4), 307–319. doi:10.1177/0301006616685576

Bohin, M. C., Roland, W. S., Gruppen, H., Gouka, R. J., van der Hijden, H. T., Dekker, P., et al. (2013). Evaluation of the bitter-masking potential of food proteins for EGCG by

a cell-based human bitter taste receptor assay and binding studies. *J. Agric. Food Chem.* 61 (42), 10010–10017. doi:10.1021/jf4030823

Bora, D., Borude, P., and Bhise, K. (2008). Taste masking by spray-drying technique. *AAPS PharmSciTech* 9 (4), 1159–1164. doi:10.1208/s12249-008-9154-5

Chen, Z., and Chung, H. Y. (2022). Pseudo-taste cells derived from rat taste and non-taste tissues: implications for cultured taste cell-based biosensors. *J. Agric. Food Chem.* 70 (35), 10826–10835. doi:10.1021/acs.jafc.2c04934

Chen, Z., Zhang, Q., Shan, J., Lu, Y., and Liu, Q. (2020). Detection of bitter taste molecules based on odorant-binding protein-modified screen-printed electrodes. *ACS Omega* 5 (42), 27536–27545. doi:10.1021/acsomega.0c04089

Christensen, J., Ladefoged, A. M., and Nrgaard, L. (2005). Rapid determination of bitterness in beer using fluorescence spectroscopy and chemometrics. *J. Inst. Brew.* 111 (1), 3–10. doi:10.1002/j.2050-0416.2005.tb00642.x

Chu, X., Zhu, W., Li, X., Su, E., and Wang, J. (2024). Bitter flavors and bitter compounds in foods: identification, perception, and reduction techniques. *Food Res. Int.* 183, 114234. doi:10.1016/j.foodres.2024.114234

Clapham, D., Belissa, E., Inghelbrecht, S., Pensé-Lhéritier, A. M., Ruiz, F., Sheehan, L., et al. (2023). A guide to best practice in sensory analysis of pharmaceutical formulations. *Pharmaceutics* 15 (9), 2319. doi:10.3390/pharmaceutics15092319

Cruickshanks, K. J., Schubert, C. R., Snyder, D. J., Bartoshuk, L. M., Huang, G. H., Klein, B. E., et al. (2009). Measuring taste impairment in epidemiologic studies: the beaver dam offspring study. *Ann. N. Y. Acad. Sci.* 1170, 543–552. doi:10.1111/j.1749-6632.2009.04103.x

Dagan-Wiener, A., Nissim, I., Ben Abu, N., Borgonovo, G., Bassoli, A., and Niv, M. Y. (2017). Bitter or not? BitterPredict, a tool for predicting taste from chemical structure. *Rep* 7 (1), 12074. doi:10.1038/s41598-017-12359-7

Delompré, T., Belloir, C., Martin, C., Salles, C., and Briand, L. (2022). Detection of bitterness in vitamins is mediated by the activation of bitter taste receptors. *Nutrients* 14 (19), 4141. doi:10.3390/nu14194141

Deng, M., Hida, N., Yamazaki, T., Morishima, R., Kato, Y., Fujita, Y., et al. (2022). Comparison of bitterness intensity between prednisolone and quinine in a human sensory test indicated individual differences in bitter-taste perception. *Pharmaceutics* 14 (11), 2454. doi:10.3390/pharmaceutics14112454

Dong, D., Jones, G., and Zhang, S. (2009). Dynamic evolution of bitter taste receptor genes in vertebrates. *BMC Evol. Biol.* 9, 12. doi:10.1186/1471-2148-9-12

Donley, J. R. (1992). Solid-phase extraction of hop acids from beer or wort for subsequent analysis. *J. Am. Soc. Brew. Chem.* 50 (3), 89–93.

Finger, T. E., Danilova, V., Barrows, J., Bartel, D. L., Vigers, A. J., Stone, L., et al. (2005). ATP signaling is crucial for communication from taste buds to gustatory nerves. *Science* 310 (5753), 1495–1499. doi:10.1126/science.1118435

Gao, C., Tello, E., and Peterson, D. G. (2023). Identification of compounds that enhance bitterness of coffee brew. *Food Chem.* 415, 135674. doi:10.1016/j.foodchem.2023.135674

Gao, X., Bai, X., Gui, X., Wang, Y., Wang, J., Yao, J., et al. (2022). Study on quantitative method of drug's molecular bitterness based on bitterness threshold concentration. *Chin. Traditional Herb. Drugs* 53 (3), 8. doi:10.7501/j.issn.0253-2670.2022.03.007

Gaudette, N. J., and Pickering, G. J. (2013). Modifying bitterness in functional food systems. *Crit. Rev. Food Sci. Nutr.* 53 (5), 464–481. doi:10.1080/10408398.2010.542511

Ginz, M., and Engelhardt, U. H. (2000). Identification of proline-based diketopiperazines in roasted coffee. *J. Agric. Food Chem.* 48 (8), 3528–3532. doi:10.1021/jf991256v

Green, B. G., Dalton, P., Cowart, B., Shaffer, G., Rankin, K., and Higgins, J. (1996). Evaluating the 'Labeled Magnitude Scale' for measuring sensations of taste and smell. *Chem. Senses* 21 (3), 323–334. doi:10.1093/chemse/21.3.323

Green, B. G., Shaffer, G. S., and Gilmore, M. M. (1993). Derivation and evaluation of a semantic scale of oral sensation magnitude with apparent ratio properties. *Chem. Senses* 18 (6), 683–702. doi:10.1093/chemse/18.6.683

Green, T., Wolf, A., Oleszkiewicz, A., Aronis, A., Hummel, T., Pepino, M., et al. (2022). Subjective assessment and taste strips testing of gustatory function, at home, and in the lab. *bioRxiv*, 507407. doi:10.1101/2022.09.11.507407

Guedes, M. D. V., Marques, M. S., Guedes, P. C., Contri, R. V., and Kulkamp Guerreiro, I. C. (2021). The use of electronic tongue and sensory panel on taste evaluation of pediatric medicines: a systematic review. *Pharm. Dev. Technol.* 26 (2), 119–137. doi:10.1080/10837450.2020.1860088

Guinard, J. X., Hong, D. Y., and Budwig, C. (2010). TIME-INTENSITY PROPERTIES OF SWEET AND BITTER STIMULI: IMPLICATIONS FOR SWEET AND BITTER TASTE CHEMORECEPTION. *J. Sens. Stud.* 10 (1), 45–71. doi:10.1111/j.1745-459x.1995.tb00004.x

Guinard, J. X., Hong, D. Y., Zoumas-Morse, C., Budwig, C., and Russell, G. F. (1994). Chemoreception and perception of the bitterness of isohumulones. *Physiol. Behav.* 56 (6), 1257–1263. doi:10.1016/0031-9384(94)90374-3

Guinard, J. X., Pangborn, R. M., and Lewis, M. J. (1986). Effect of repeated ingestion on temporal perception of bitterness in beer. *J. Am. Soc. Brew. Chem.* 44 (1), 28–32. doi:10.1094/asbcj-44-0028

Gunaratne, T. M., Fuentes, S., Gunaratne, N. M., Torrico, D. D., Gonzalez Viejo, C., and Dunshea, F. R. (2019). Physiological responses to basic tastes for sensory evaluation of chocolate using biometric techniques. *Foods* 8 (7), 243. doi:10.3390/foods8070243

Han, X., Jiang, H., Han, L., Xiong, X., He, Y., Fu, C., et al. (2018). A novel quantified bitterness evaluation model for traditional Chinese herbs based on an animal ethology principle. *Acta Pharm. Sin. B* 8 (2), 209–217. doi:10.1016/j.apsb.2017.08.001

Hans-Dieter, B., and Herbert, W. (1985). Bitter compounds: occurrence and structure activity relationships. *Food Rev. Int.* 2, 271–354. doi:10.1080/87559128509540773

Hayes, J. E., Wallace, M. R., Knopik, V. S., Herbstman, D. M., Bartoshuk, L. M., and Duffy, V. B. (2011). Allelic variation in TAS2R bitter receptor genes associates with variation in sensations from and ingestive behaviors toward common bitter beverages in adults. *Chem. Senses* 36 (3), 311–319. doi:10.1093/chemse/bjq132

Heath, T. P., Melichar, J. K., Nutt, D. J., and Donaldson, L. F. (2006). Human taste thresholds are modulated by serotonin and noradrenaline. *J. Neurosci.* 26 (49), 12664–12671. doi:10.1523/JNEUROSCI.3459-06.2006

Höhme, L., Fischer, C., and Kleinschmidt, T. (2023). Characterization of bitter peptides in casein hydrolysates using comprehensive two-dimensional liquid chromatography. *Food Chem.* 404 (Pt A), 134527. doi:10.1016/j.foodchem.2022.134527

Howard, G. A. (1968). Institute of brewing analysis committee estimation of the bitterness of beer. *J. Inst. Brew.* 74 (3), 249–251. doi:10.1002/j.2050-0416.1968.tb03121.x

Hu, S., Liu, X., Zhang, S., and Quan, D. (2023). An overview of taste-masking technologies: approaches, application, and assessment methods. *AAPS PharmSciTech* 24 (2), 67. doi:10.1208/s12249-023-02520-z

Hu, X., Li, Y., Zhang, E., Wang, X., Xing, M., Wang, Q., et al. (2013). Preparation and evaluation of orally disintegrating tablets containing taste-masked microcapsules of berberine hydrochloride. *AAPS PharmSciTech* 14 (1), 29–37. doi:10.1208/s12249-012-9880-6

Hui, G., Mi, S., Ye, S., Jin, J., Chen, Q., and Yu, Z. (2014). Tastant quantitative analysis from complex mixtures using taste cell-based sensor and double-layered cascaded series stochastic resonance. *Electrochimica Acta* 136, 75–88. doi:10.1016/j.electacta.2014.05.060

Hui, G. H., Mi, S. S., and Deng, S. P. (2012). Sweet and bitter tastants specific detection by the taste cell-based sensor. *Biosens. Bioelectron.* 35 (1), 429–438. doi:10.1016/j.bios.2012.02.028

Immohr, L. I., Dischinger, A., Kühl, P., Kletzl, H., Sturm, S., Günther, A., et al. (2017). Early pediatric formulation development with new chemical entities: opportunities of e-tongue besides human taste assessment. *Int. J. Pharm.* 530 (1-2), 201–212. doi:10.1016/j.ijpharm.2017.07.069

Ito, M., Ikehama, K., Yoshida, K., Haraguchi, T., Yoshida, M., Wada, K., et al. (2013). Bitterness prediction of H1-antihistamines and prediction of masking effects of artificial sweeteners using an electronic tongue. *Int. J. Pharm.* 441 (1-2), 121–127. doi:10.1016/j.ijpharm.2012.11.047

Ito, T., Radecka, H., Tohda, K., Odashima, K., and Umezawa, Y. (1998). On the mechanism of unexpected potentiometric response to neutral phenols by liquid membranes based on quaternary ammonium SaltsSystematic experimental and theoretical approaches. *J. Am. Chem. Soc.* 120 (13), 3049–3059. doi:10.1021/ja973179v

Jelvehgari, M., Barghi, L., and Barghi, F. (2014). Preparation of chlorpheniramine maleate-loaded alginate/chitosan particulate systems by the ionic gelation method for taste masking. *Jundishapur J. Nat. Pharm. Prod.* 9 (1), 39–48. doi:10.17795/jjnpp-12530

Jing, W., Zhao, X., Zhang, Q., Cheng, X., Ma, S., and Wei, F. (2022). Material basis of"Bitterness"Medicinal properties of magnoliae officinalis cortex based on electronic tongue and multi-component quantitative technology. *Mod. Chin. Med.* 24 (002), 258. 264Xue, W. (2022). *Study on the taste masking of two bitter substances based on the combination of taste method and electronic tongue technology.* master.

Ke, X., Ma, H., Yang, J., Qiu, M., Wang, J., Han, L., et al. (2022). New strategies for identifying and masking the bitter taste in traditional herbal medicines: the example of Huanglian Jiedu Decoction. *Front. Pharmacol.* 13, 843821. doi:10.3389/fphar.2022.843821

Legin, A., Rudnitskaya, A., Clapham, D., Seleznev, B., Lord, K., and Vlasov, Y. (2004). Electronic tongue for pharmaceutical analytics: quantification of tastes and masking effects. *Anal. Bioanal. Chem.* 380 (1), 36–45. doi:10.1007/s00216-004-2738-3

Lemon, C. H., Norris, J. E., and Heldmann, B. A. (2019). The TRPA1 ion channel contributes to sensory-guided avoidance of menthol in mice. *eNeuro* 6 (6), ENEURO.0304-19.2019. doi:10.1523/eneuro.0304-19.2019

Li, C., Ren, Y., Yao, J., Wang, Y., Gao, X., Han, Li, et al. (2023). Study on quantitative method of specific bitterness of bitter compounds based on traditional human taste panel method. *Chin. Traditional Herb. Drugs* 54 (09), 2758–2764.

Li, C., Ren, Y., Yao, J., Wang, Y., Gao, X., Li, H., et al. (2023). Study on quantitative method of specific bitterness of bitter compounds based on traditional human taste panel method. *Chin. Traditional Herb. Drugs* 54 (09), 2758–2764.

Li, C., Yao, J., Zhang, P., Dai, X., Hou, F., Shi, J., et al. (2024). Application of computer simulation in the taste-masking of traditional Chinese medicine decoction. *Her. Med.* 43 (07), 1107–1111. doi:10.3870/j.issn.1004-0781.2024.07.015

Li, H. H., Luo, L. Y., Wang, J., Fu, D. H., and Zeng, L. (2019). Lexicon development and quantitative descriptive analysis of Hunan fuzhuan brick tea infusion. *Food Res. Int.* 120, 275–284. doi:10.1016/j.foodres.2019.02.047

Li, S., Zhang, Y., Khan, A. R., He, S., Wang, Y., Xu, J., et al. (2020). Quantitative prediction of the bitterness of atomoxetine hydrochloride and taste-masked using hydroxypropyl-β-cyclodextrin: a biosensor evaluation and interaction study. *Asian J. Pharm. Sci.* 15 (4), 492–505. doi:10.1016/j.ajps.2019.11.001

Li, X., Gui, X., Liu, R., Gao, X., Meng, X., Chen, P., et al. (2016). Bitterness intensity prediction of bitter compounds of traditional Chinese medicine based on an electronic tongue. *Chin. J. New Drugs* 25 (11), 1307–1314.

Li, X., Li, H., Liu, R., Zhang, X., Qiu, J., and Wu, Z. (2013). Study on the evaluation of drug taste masking effect by electronic tongue. *Mod. Traditional Chin. Med. Materia Medica-World Sci. Technol.* 15 (7), 1532–1537. doi:10.11842/wst.2013.07.008

Li, X., Wu, Z., Liu, R., Xu, Z., Shi, J., and Li, H. (2011). *Study on bitterness evaluation of Chinese.*

Li, X., Wu, Z., Liu, R., Xu, Z., Shi, J., and Li, H. (2011). Study on bitterness evaluation of Chinese Herbal Decoction by THTPM. *Chin. J. Exp. Traditional Med. Formulae* 17 (23), 11–13. doi:10.13422/j.cnki.syfjx.2011.23.017.%W.CNKI

Lin, Z., Zhang, Q., Liu, R., Gao, X., Zhang, L., Kang, B., et al. (2016). Evaluation of the bitterness of traditional Chinese medicines using an E-tongue coupled with a robust partial least squares regression method. *Sensors (Basel)* 16 (2), 151. doi:10.3390/s16020151

Liu, D. T., Besser, G., Oeller, F., Mueller, C. A., and Renner, B. (2020). Bitter taste perception of the human tongue mediated by quinine and caffeine impregnated taste strips. *Ann. Otol. Rhinol. Laryngol.* 129 (8), 813–820. doi:10.1177/0003489420906187

Liu, R., Zhang, X., Li, X., Shi, J., Li, H., and Qiu, J. (2013). Drug evaluation of bitterness intensity by three kinds of THTPM. *Chin. J. Exp. Tradit. Med. Formulae* 19 (20), 118–122. doi:10.7501/j.issn.0253-2670.2013.16.009

Liu, R., Li, X., Yao, j., Gui, x., Wang, Q., Shi, J., et al. (2012). *A drug bitterness measurement method based on bitterness threshold concentration.*

Liu, R., Wang, Y., Tian, L., Gui, X., Shi, J., Zhang, L., et al. (2019). Masking efficiency and regularity of bitterness suppressants to berberine hydrochloride based on tongue taste and electronic tongue taste. *Chin. Pharm. J.* 54 (03), 208–218. doi:10.11669/cpj.2019.03.008

Liu, R., Zhang, X., Li, X., Shi, J., Li, H., and Qiu, J. (2013). Drug evaluation of bitterness intensity by three kinds of THTPM. *Chin. J. Exp. Traditional Med. Formulae* 19 (20), 118–122.

Liu, R., Zhang, X., Zhang, L., Gao, X., Li, H., Shi, J., et al. (2014a). Bitterness intensity prediction of berberine hydrochloride using an electronic tongue and a GA-BP neural network. *Exp. Ther. Med.* 7 (6), 1696–1702. doi:10.3892/etm.2014.1614

Li Xuelin, Z. X., Liu, R., Huiling, Li, Jixi, Q., and Wu, Z. (2013). Study on quantitation of bitterness intensity and relationship between bitterness intensity and concentration of bitter drug. *World Sci. Technology/Modernization Traditional Chin. Med. Materia Medica* (04), 667–671.

Loney, G. C., Blonde, G. D., Eckel, L. A., and Spector, A. C. (2012). Determinants of taste preference and acceptability: quality versus hedonics. *J. Neurosci.* 32 (29), 10086–10092. doi:10.1523/jneurosci.6036-11.2012

Loney, G. C., Torregrossa, A. M., Smith, J. C., Sclafani, A., and Eckel, L. A. (2011). Rats display a robust bimodal preference profile for sucralose. *Chem. Senses* 36 (8), 733–745. doi:10.1093/chemse/bjr048

Ma, Z., Taruno, A., Ohmoto, M., Jyotaki, M., Lim, J. C., Miyazaki, H., et al. (2018). CALHM3 is essential for rapid ion channel-mediated purinergic neurotransmission of GPCR-mediated tastes. *Neuron* 98 (3), 547–561.e10. doi:10.1016/j.neuron.2018.03.043

Maniruzzaman, M., Bonnefille, M., Aranyos, A., Snowden, M. J., and Douroumis, D. (2014). An in-vivo and in-vitro taste masking evaluation of bitter melt-extruded drugs. *J. Pharm. Pharmacol.* 66 (2), 323–337. doi:10.1111/jphp.12169

Maniruzzaman, M., and Douroumis, D. (2015). An in-vitro-in-vivo taste assessment of bitter drug: comparative electronic tongues study. *J. Pharm. Pharmacol.* 67 (1), 43–55. doi:10.1111/jphp.12319

Margulis, E., Dagan-Wiener, A., Ives, R. S., Jaffari, S., Siems, K., and Niv, M. Y. (2021). Intense bitterness of molecules: machine learning for expediting drug discovery. *Comput. Struct. Biotechnol. J.* 19, 568–576. doi:10.1016/j.csbj.2020.12.030

Medicine, C. A. o.C. (2024). Technical specification for sensory evaluation of bitterness of oral liquid preparation of traditional Chinese medicine. *T/CACM 1574—2024.*

Mennella, J. A., Pepino, M. Y., Duke, F. F., and Reed, D. R. (2011). Psychophysical dissection of genotype effects on human bitter perception. *Chem. Senses* 36 (2), 161–167. doi:10.1093/chemse/bjq106

Meyerhof, W. (2005). Elucidation of mammalian bitter taste. *Rev. Physiol. Biochem. Pharmacol.* 154, 37–72. doi:10.1007/s10254-005-0041-0

Meyerhof, W., Batram, C., Kuhn, C., Brockhoff, A., Chudoba, E., Bufe, B., et al. (2010). The molecular receptive ranges of human TAS2R bitter taste receptors. *Chem. Senses* 35 (2), 157–170. doi:10.1093/chemse/bjp092

Milne, C. P., and Bruss, J. B. (2008). The economics of pediatric formulation development for off-patent drugs. *Clin. Ther.* 30 (11), 2133–2145. doi:10.1016/j.clinthera.2008.11.019

Miyanaga, Y., Inoue, N., Ohnishi, A., Fujisawa, E., Yamaguchi, M., and Uchida, T. (2003). Quantitative prediction of the bitterness suppression of elemental diets by

various flavors using a taste sensor. *Pharm. Res.* 20 (12), 1932–1938. doi:10.1023/b:pham.0000008039.59875.4f

Münster, M., Mohamed-Ahmed, A. H. A., Immohr, L. I., Schoch, C., Schmidt, C., Tuleu, C., et al. (2017). Comparative *in vitro* and *in vivo* taste assessment of liquid praziquantel formulations. *Int. J. Pharm.* 529 (1-2), 310–318. doi:10.1016/j.ijpharm.2017.06.084

Mura, E., Yagi, M., Yokota, K., Seto, E., Matsumiya, K., Matsumura, Y., et al. (2018). Tolerance of bitter stimuli and attenuation/accumulation of their bitterness in humans. *Biosci. Biotechnol. Biochem.* 82 (9), 1539–1549. doi:10.1080/09168451.2018.1484273

Mustafa, A. M., Caprioli, G., Ricciutelli, M., Maggi, F., Marín, R., Vittori, S., et al. (2015). Comparative HPLC/ESI-MS and HPLC/DAD study of different populations of cultivated, wild and commercial Gentiana lutea L. *Food Chem.* 174, 426–433. doi:10.1016/j.foodchem.2014.11.089

Nakamura, H., Uchida, S., Sugiura, T., and Namiki, N. (2015). The prediction of the palatability of orally disintegrating tablets by an electronic gustatory system. *Int. J. Pharm.* 493 (1-2), 305–312. doi:10.1016/j.ijpharm.2015.07.056

Nakamura, T., Akiyoshi, T., Tanaka, N., Shinozuka, K., Matzno, S., Nakabayashi, T., et al. (2003). Effect of quinine solutions on intracellular Ca2+ levels in neuro-2a cells--conventional physiological method for the evaluation of bitterness. *Biol. Pharm. Bull.* 26 (11), 1637–1640. doi:10.1248/bpb.26.1637

Narukawa, M., Noga, C., Ueno, Y., Sato, T., Misaka, T., and Watanabe, T. (2011). Evaluation of the bitterness of green tea catechins by a cell-based assay with the human bitter taste receptor hTAS2R39. *Biochem. Biophys. Res. Commun.* 405 (4), 620–625. doi:10.1016/j.bbrc.2011.01.079

Noble, A. C. (1994). Bitterness in wine. *Physiol. Behav.* 56 (6), 1251–1255. doi:10.1016/0031-9384(94)90373-5

Nolden, A. A., and Feeney, E. L. (2020). Genetic differences in taste receptors: implications for the food industry. *Annu. Rev. Food Sci. Technol.* 11, 183–204. doi:10.1146/annurev-food-032519-051653

Noorjahan, A., Amrita, B., and Kavita, S. (2014). *In vivo* evaluation of taste masking for developed chewable and orodispersible tablets in humans and rats. *Pharm. Dev. Technol.* 19 (3), 290–295. doi:10.3109/10837450.2013.778870

Nordenmalm, S., Kimland, E., Ligas, F., Lehmann, B., Pelle, B., Nafria, B., et al. (2019). Children's views on taking medicines and participating in clinical trials. *Archives Dis. Child.* 104 (9), 900–905. doi:10.1136/archdischild-2018-316511

Ogi, K., Yamashita, H., Terada, T., Homma, R., Shimizu-Ibuka, A., Yoshimura, E., et al. (2015). Long-chain fatty acids elicit a bitterness-masking effect on quinine and other nitrogenous bitter substances by formation of insoluble binary complexes. *J. Agric. Food Chem.* 63, 8493–8500. doi:10.1021/acs.jafc.5b03193

Omür-Ozbek, P., and Dietrich, A. M. (2008). Developing hexanal as an odor reference standard for sensory analysis of drinking water. *Water Res.* 42 (10-11), 2598–2604. doi:10.1016/j.watres.2008.01.010

Park, H.-W., Kim, M.-J., Seo, S., Yoo, S., and Hong, J.-H. (2017). Relative sweetness and sweetness quality of Xylobiose. *Food Sci. Biotechnol.* 26 (3), 689–696. doi:10.1007/s10068-017-0109-z

Podrażka, M., Bączyńska, E., Kundys, M., Jeleń, P. S., and Witkowska Nery, E. (2017). Electronic tongue-A tool for all tastes? *Biosens. (Basel)* 8 (1), 3. doi:10.3390/bios8010003

Polshin, E., Rudnitskaya, A., Kirsanov, D., Legin, A., Saison, D., Delvaux, F., et al. (2010). Electronic tongue as a screening tool for rapid analysis of beer. *Talanta* 81 (1-2), 88–94. doi:10.1016/j.talanta.2009.11.041

Qingjun, L., and Ping, W. (2009). *Cell-based biosensors: principles and applications.* Boston, London: Artech.

Ranmal, S. R., Nhouchi, Z., Keeley, A., Adler, L., Lavarde, M., Pensé-Lhéritier, A. M., et al. (2023). Taste assessment for paediatric drug Development: a comparison of bitterness taste aversion in children versus Naïve and expert young adult assessors. *Int. J. Pharm.* 647, 123494. doi:10.1016/j.ijpharm.2023.123494

Roper, S. D. (2007). Signal transduction and information processing in mammalian taste buds. *Pflugers Arch.* 454 (5), 759–776. doi:10.1007/s00424-007-0247-x

Roudnitzky, N., Behrens, M., Engel, A., Kohl, S., Thalmann, S., Hübner, S., et al. (2015). Receptor polymorphism and genomic structure interact to shape bitter taste perception. *PLoS Genet.* 11 (9), e1005530. doi:10.1371/journal.pgen.1005530

Roudnitzky, N., Bufe, B., Thalmann, S., Kuhn, C., Gunn, H. C., Xing, C., et al. (2011). Genomic, genetic and functional dissection of bitter taste responses to artificial sweeteners. *Hum. Mol. Genet.* 20 (17), 3437–3449. doi:10.1093/hmg/ddr252

Rudnitskaya, A., Kirsanov, D., Blinova, Y., Legin, E., Seleznev, B., Clapham, D., et al. (2013). Assessment of bitter taste of pharmaceuticals with multisensor system employing 3 way PLS regression. *Anal. Chim. Acta* 770, 45–52. doi:10.1016/j.aca.2013.02.006

Rudnitskaya, A., Nieuwoudt, H. H., Muller, N., Legin, A., du Toit, M., and Bauer, F. F. (2010). Instrumental measurement of bitter taste in red wine using an electronic tongue. *Anal. Bioanal. Chem.* 397 (7), 3051–3060. doi:10.1007/s00216-010-3885-3

Ruixin, L., Huiling, L., Xuelin, L., Xingfen, Z., and Jixi, Q. (2013). Evaluation on taste-masking effect of Andrographis Herba by electronic tongue. *Chin. Traditional Herb. Drugs* 44 (16), 2240–2245. doi:10.7501/j.issn.0253-2670.2013.16.009

Sakurai, T., Misaka, T., Nagai, T., Ishimaru, Y., Matsuo, S., Asakura, T., et al. (2009). pH-Dependent inhibition of the human bitter taste receptor hTAS2R16 by a variety of acidic substances. *J. Agric. Food Chem.* 57 (6), 2508–2514. doi:10.1021/jf8040148

Schalk, P., Kohl, M., Herrmann, H. J., Schwappacher, R., Rimmele, M. E., Buettner, A., et al. (2018). Influence of cancer and acute inflammatory disease on taste perception: a clinical pilot study. *Support Care Cancer* 26 (3), 843–851. doi:10.1007/s00520-017-3898-y

Schienle, A., and Schlintl, C. (2020). The association between quinine hydrochloride sensitivity and disgust proneness in children and adults. *Springer U. S.* 13 (1), 78–83. doi:10.1007/s12078-019-09268-6

Shah, P. P., and Mashru, R. C. (2008). Formulation and evaluation of taste masked oral reconstitutable suspension of primaquine phosphate. *AAPS PharmSciTech* 9 (3), 1025–1030. doi:10.1208/s12249-008-9137-6

Shi, J., Zhang, X., Qiu, J., Li, X., and Liu, R. (2013). Investigation of bitter masking mechanism of β-cyclodextrin to several traditional Chinese medicines. *Chin. J. Exp. Traditional Med. Formulae* 19 (12). doi:10.11653/syfj2013120001

Shibamoto, T., Harada, K., Mihara, S., Nishimura, O., Yamaguchi, K., Aitoku, A., et al. (1981). APPLICATION OF HPLC FOR EVALUATION OF COFFEE FLAVOR QUALITY. *Qual. Foods and Beverages*, 311–334. doi:10.1016/b978-0-12-169102-8.50028-3

Sook Chung, H., and Lee, S. Y. (2012). Modification of ginseng flavors by bitter compounds found in chocolate and coffee. *J. Food Sci.* 77 (6), S202–S210. doi:10.1111/j.1750-3841.2012.02716.x

Soto, J. (2016). "Assessing the feasibility of using an animal model for *in vivo* taste assessment of pharmaceutical compounds and formulations," in *Ucl.*

Suryawanshi, S., Mehrotra, N., Asthana, R. K., and Gupta, R. C. (2006). Liquid chromatography/tandem mass spectrometric study and analysis of xanthone and secoiridoid glycoside composition of Swertia chirata, a potent antidiabetic. *Rapid Commun. Mass Spectrom.* 20 (24), 3761–3768. doi:10.1002/rcm.2795

Tomlinson, J. B., Ormrod, I. H. L., and Sharpe, F. R. (2013). A NOVEL METHOD FOR BITTERNESS DETERMINATION IN BEER USING A DELAYED FLUORESCENCE TECHNIQUE. *J. Inst. Brew.* 101 (2), 113–118. doi:10.1002/j.2050-0416.1995.tb00855.x

Torrico, D. D., Sae-Eaw, A., Sriwattana, S., Boeneke, C., and Prinyawiwatkul, W. (2015). Oil-in-Water emulsion exhibits bitterness-suppressing effects in a sensory threshold study. *J. Food Sci.* 80 (6), S1404–S1411. doi:10.1111/1750-3841.12901

Uchida, T., Kobayashi, Y., Miyanaga, Y., Toukubo, R., Ikezaki, H., Taniguchi, A., et al. (2001). A new method for evaluating the bitterness of medicines by semi-continuous measurement of adsorption using a taste sensor. *Chem. Pharm. Bull. (Tokyo)* 49 (10), 1336–1339. doi:10.1248/cpb.49.1336

Wang, H. (2022a). Research on basic taste perception recognition based on physiological electrical signals. *Doctor.*

Wang, Q., Gao, X., Gui, X., Wang, Y., Wang, J., Li, C., et al. (2022). Study on quantitative method of equivalent molecular bitterness of traditional Chinese medicines based on bitterness threshold concentration. *Chin. Traditional Herb. Drugs* 53 (21), 6698–6705. doi:10.7501/j.issn.0253-2670.2022.21.006

Wang, Y., Chen, P., Gui, X., Yao, J., Zhang, L., Shi, J., et al. (2021). Study on four kinds of taste classification and identification of natural medicines based on electronic tongue. *China J. Traditional Chin. Med. Pharm.* 36 (01), 423–433.

Wang, Y., Feng, Y., Wu, Y., Liang, S., and Xu, D. (2013). Sensory evaluation of the taste of berberine hydrochloride using an Electronic Tongue. *Fitoterapia* 86, 137–143. doi:10.1016/j.fitote.2013.02.010

Yanagisawa, T., and Misaka, T. (2021). Characterization of the human bitter taste receptor response to sesquiterpene lactones from edible asteraceae species and suppression of bitterness through pH control. *ACS Omega* 6 (6), 4401–4407. doi:10.1021/acsomega.0c05599

Yang, J., Qiu, M., Lu, T., Yang, S., Yu, J., Lin, J., et al. (2023). Discovery and verification of bitter components in Panax notoginseng based on the integrated strategy of pharmacophore model, system separation and bitter tracing technology. *Food Chem.* 428, 136716. doi:10.1016/j.foodchem.2023.136716

Yang, P., Liu, Q., and Metaxas, D. N. (2010). "RankBoost with l1 regularization for facial expression recognition and intensity estimation," in IEEE International Conference on Computer Vision.

Yang, Z. xin, Meng, Y., Wang, Q., Yang, B., and Kuang, H. (2011). Substance basis of bitter resolution and composition from fructus evodiae. *Chin. J. Exp. Traditional Med. Formulae* 17 (021), 74–77. doi:10.13422/j.cnki.syfjx.2011.21.029

Yewale, C. P., Rathi, M. N., Kore, G. G., Jadhav, G. V., and Wagh, M. P. (2013). Formulation and development of taste masked fast-disintegrating tablets (FDTs) of Chlorpheniramine maleate using ion-exchange resins. *Pharm. Dev. Technol.* 18 (2), 367–376. doi:10.3109/10837450.2011.627870

Yoneda, T., Saitou, K., Mizushige, T., Matsumura, S., Manabe, Y., Tsuzuki, S., et al. (2007). The palatability of corn oil and linoleic acid to mice as measured by short-term two-bottle choice and licking tests. *Physiol. Behav.* 91 (2-3), 304–309. doi:10.1016/j.physbeh.2007.03.006

Yu, M., Li, T., Raza, A., Wang, L., Song, H., Zhang, Y., et al. (2020). Sensory-guided identification of bitter compounds in hangbaizhi (angelica dahurica). *Food Res. Int.* 129, 108880. doi:10.1016/j.foodres.2019.108880

Zeng, G. (1990). The taste change trend when the molecular structure of the flavor is changed. *Chin. J. Nat.* 13 (2), 70–75.

Zeng, Y., Guo, L., Wang, J., Huang, L., Tian, Z., Jiao, L., et al. (2015). Study on taste information of different Scutellaria baicalensis georgi and correlation between taste information and main chemical compositions based on technology of electronic-tongue. *Mod. Chin. Med.* 17(11), 1139–1147. doi:10.13313/j.issn.1673-4890.2015.11.007

Zhang, Pu, Zhang, Y., Gui, X., Shi, J., Zhang, H., Feng, W., et al. (2021). Study on superposition rule of bitterness of decoction of Chinese materia medica based on traditional human taste panel method and electronic tongue method. *Chin. Traditional Herb. Drugs* 52 (3), 653–668. doi:10.7501/j.issn.0253-2670.2021.03.007

Zheng, X., Wu, F., Hong, Y., Shen, L., Lin, X., and Feng, Y. (2018). Developments in taste-masking techniques for traditional Chinese medicines. *Pharmaceutics* 10 (3), 157. doi:10.3390/pharmaceutics10030157

Zhi, R., Cao, L., and Cao, G. (2017). Asians' facial responsiveness to basic tastes by automated facial expression analysis system. *J. Food Sci.* 82 (3), 794–806. doi:10.1111/1750-3841.13611

Zuluaga, G. (2024). Potential of bitter medicinal plants: a review of flavor physiology. *Pharm. (Basel)* 17 (6), 722. doi:10.3390/ph17060722

Development and validation of a novel high-performance liquid chromatography (HPLC) method for the detection of related substances of pralsetinib, a new anti-lung cancer drug

Yonghong Zhu[1], Jisu Qin[2], Wenyi Wu[3] and Liangliang Cai[2]*

[1]Department of Pharmacy, Affiliated Nantong Hospital of Shanghai University (The Sixth People's Hospital of Nantong), Nantong, Jiangsu, China, [2]Department of Pharmacy, Affiliated Hospital of Nantong University, Pharmacy School of Nantong University, Nantong, China, [3]Department of Quality Inspection, Sinopharm Holding Nantong Ltd., Nantong, China

Background: Pralsetinib, a targeted inhibitor of the RET enzyme, plays a critical role in the treatment of adult patients with locally advanced or metastatic non-small cell lung cancer (NSCLC) characterized by RET gene fusion mutations following platinum-based chemotherapy. Nevertheless, impurities resulting from the manufacturing and degradation of pralsetinib have the potential to impact its therapeutic effectiveness and safety profile.

Methods: To address this issue, a liquid chromatography method was developed and validated for the specific identification of pralsetinib and its related impurities. The separation of pralsetinib and its related impurities was achieved via a Waters X Bridge C_{18} column with dimensions of 4.6 mm × 250 mm and a particle size of 5 µm. Mobile phase A was composed of 20 mmol/L potassium dihydrogen phosphate (KH_2PO4) and acetonitrile (ACN) at a volume ratio of 19:1, while mobile phase B consisted solely of ACN, utilizing a gradient elution technique. Detection was performed at a wavelength of 260 nm, with an injection volume of 10 µL and a flow rate of 1.0 mL/min.

Results: The chromatographic method established in this study was validated according to the ICH Q2 (R1) guidelines. The method demonstrated excellent linearity over a specific concentration range (imp-A: 0.035–10.21 µg/mL; imp-B: 0.09–10.16 µg/mL; imp-C: 0.15–10.19 µg/mL; pralsetinib: 0.04–10.32 µg/mL). Additionally, the method possesses high sensitivity, with detection limits for impurities A, B, C, and pralsetinib of 0.01, 0.03, 0.015, and 0.013 µg/mL, respectively, and quantification limits of 0.035, 0.09, 0.05, and 0.04 µg/mL, respectively. In terms of specificity, stability, repeatability, accuracy, and robustness, the method met the validation acceptance criteria. Overall, the chromatographic technique established in this study can effectively separate pralsetinib and its impurities, providing reliable assurance for the accurate detection and quantification of impurities.

Conclusion: The chromatographic method developed in this study can be utilized for the detection of pralsetinib and its impurities, offering a crucial reference for research on the quality of pralsetinib.

1 Introduction

Non-small cell lung cancer (NSCLC) is the most common type of lung cancer, accounting for approximately 85%–90% of all lung cancer cases (Chen et al., 2022; Melosky et al., 2022). Unlike other types of lung cancer, NSCLC usually does not exhibit symptoms in the early stages, which leads to delayed diagnosis and often results in its discovery in the later stages (Du et al., 2022; Spagnuolo and Gridelli, 2023). To improve the treatment outcomes of NSCLC, scientists have conducted extensive research aiming to identify specific therapeutic targets for interventional treatment. Currently, the clinically targeted therapeutic drugs for non-small cell lung cancer mainly include epidermal growth factor receptor (EGFR) inhibitors (Yu et al., 2020; Cheng et al., 2021), kirsten rat sarcoma viral oncogene homologue (KRAS) inhibitors (Sidaway, 2021; Nakajima et al., 2022; Ou et al., 2022), anaplastic lymphoma kinase (ALK) inhibitors (Frampton, 2013; Camidge et al., 2019; Shaw et al., 2020), and (rearranged during transfection) RET inhibitors (Huang et al., 2023; Zhou et al., 2023).

RET is a transmembrane glycoprotein receptor tyrosine kinase encoded by the RET proto-oncogene, which is located on chromosome 10q11.2 and plays a pivotal role in the embryonic development of the kidney and enteric nervous system (Yadav et al., 2020; Buchholz et al., 2021). The presence of RET fusion, an oncogenic driver, is observed in approximately 1%–2% of individuals with NSCLC (Lin et al., 2020). Targeted therapies directed at RET have demonstrated notable efficacy in NSCLC, leading to enhanced response rates and extended disease-free survival for patients.

Pralsetinib, chemically known as (((R)-3-(6-(4-fluoro-1H-pyrazol-1-yl)pyridin-3-yl)-1-((1s,4S)-1-methoxy-4-(4-methyl-6-((5-methyl-1H-pyrazol-3-yl)amino)pyrimidin-2-yl) cyclohexyl) butan-1-one--(S)-1-(6-(4-fluoro-1H-pyrazol-1-yl)pyridin-3-yl) ethan-1-amine), a highly selective RET inhibitor (Griesinger et al., 2022), was approved by the China National Medical Products Administration in March 2021 for the treatment of locally advanced or metastatic non-small cell lung cancer in adult patients with RET gene fusion who previously received platinum-based chemotherapy.

Current research on pralsetinib primarily focuses on its clinical effectiveness and safety in treating NSCLC (Gainor et al., 2021; Griesinger et al., 2022). Meanwhile, studies have employed HPLC-MS/MS technology to detect drug concentrations in the plasma of patients taking pralsetinib (Gulikers et al., 2023). However, it is noteworthy that no literature has yet reported the use of high-performance liquid chromatography (HPLC) to detect related substances in pralsetinib's bulk drug. The process impurities and degradation impurities that may be generated during the synthesis and storage of pralsetinib may affect its safety and efficacy. Therefore, developing a detection method for pralsetinib and its impurities.

The high-performance liquid chromatography (HPLC) technique, characterised by its convenience, simplicity, stability, and cost-effectiveness, remains the most ideal separation technique for determining active ingredients and related substances in pharmaceutical samples in the pharmaceutical industry (Zhao et al., 2022). Furthermore, the majority of bulk medications included in the United States Pharmacopeia (USP) and the European Pharmacopeia (EP) utilize HPLC to detect related substances (Agtas et al., 2024; Gondhale-Karpe and Manwatkar, 2023; Zhao and Rustum, 2024). Currently, there is a scarcity of documented literature on techniques for detecting related substances in pralsetinib's bulk drug. Considering the potential impact of impurities on pralsetinib's efficacy and safety, it is crucial to develop an HPLC method for detecting relevant substances in pralsetinib's bulk drug.

This research presents the successful development and implementation of a RP-HPLC method for detecting impurities in pralsetinib. This method is distinguished by its simplicity, sensitivity, accuracy, and durability. In particular, this approach can efficiently separate pralsetinib-related substances, including some unknown impurities and known impurities. Furthermore, the specificity, accuracy, stability, and robustness of the method were assessed. The RP-HPLC method was assessed for its limit of quantitation (LOQ), limit of detection (LOD), linearity, and recovery rate simultaneously. In conclusion, the established RP-HPLC method offers a novel approach for the advancement of process development and quality assessment of pralsetinib.

2 Materials and methods

2.1 Chemicals and reagents

Pralsetinib and its known impurities (named imp-A, imp-B, and imp-C) were acquired from Beijing Bailingwei Technology Co., Ltd. (Beijing, China). Merck (Darmstadt, Germany) provided HPLC-grade ACN and methanol (MeOH). Other analytical grade chemical reagents were purchased from China National Pharmaceutical Group Chemical Reagent Co., Ltd. (Beijing, China).

2.2 Instruments

An Agilent 1200 HPLC system, which was outfitted with an ultraviolet (UV) detector, and a Shimadzu LC-20AD system, which was equipped with a photodiode array detector, were used for method development and validation.

2.3 HPLC conditions

A chromatographic column (4.6 mm × 250 mm, 5 μm) was used to separate pralsetinib and its impurities at a flow rate of

Time (min)	Mobile phase A (%)	Mobile phase B (%)
0	92	8
2	92	8
18	62	38
28	60	40
35	40	60
40	40	60
41	92	8
50	92	8

1.0 mL/min. Mobile phase A is composed of a 20 mmol/L aqueous solution of potassium dihydrogen phosphate (KH_2PO_4) and acetonitrile (ACN) at a volume ratio of 19:1, whereas mobile phase B is composed solely of acetonitrile (ACN). Table 1

presents a thorough explanation of the gradient elution procedure. UV analysis was conducted at a wavelength of 260 nm, with an injection volume of 10 μL.

2.4 Preparation of stock solutions

2.4.1 Preparation of pralsetinib stock solutions

Approximately 25 mg of pralsetinib was precisely weighed and transferred to a 50 mL volumetric flask. Next, a suitable volume of 50% methanol-water mixture was added, and the mixture was sonicated for dissolution. The volume was subsequently adjusted to the mark value to obtain the pralsetinib stock solution.

2.4.2 Preparation of pralsetinib-related substance stock solutions

The impurities (imp-A, imp-B, and imp-C) were measured at approximately 10 mg each and transferred individually to 20 mL volumetric flasks. The impurities were subsequently dissolved in a 50% methanol solution using ultrasonication and diluted to the
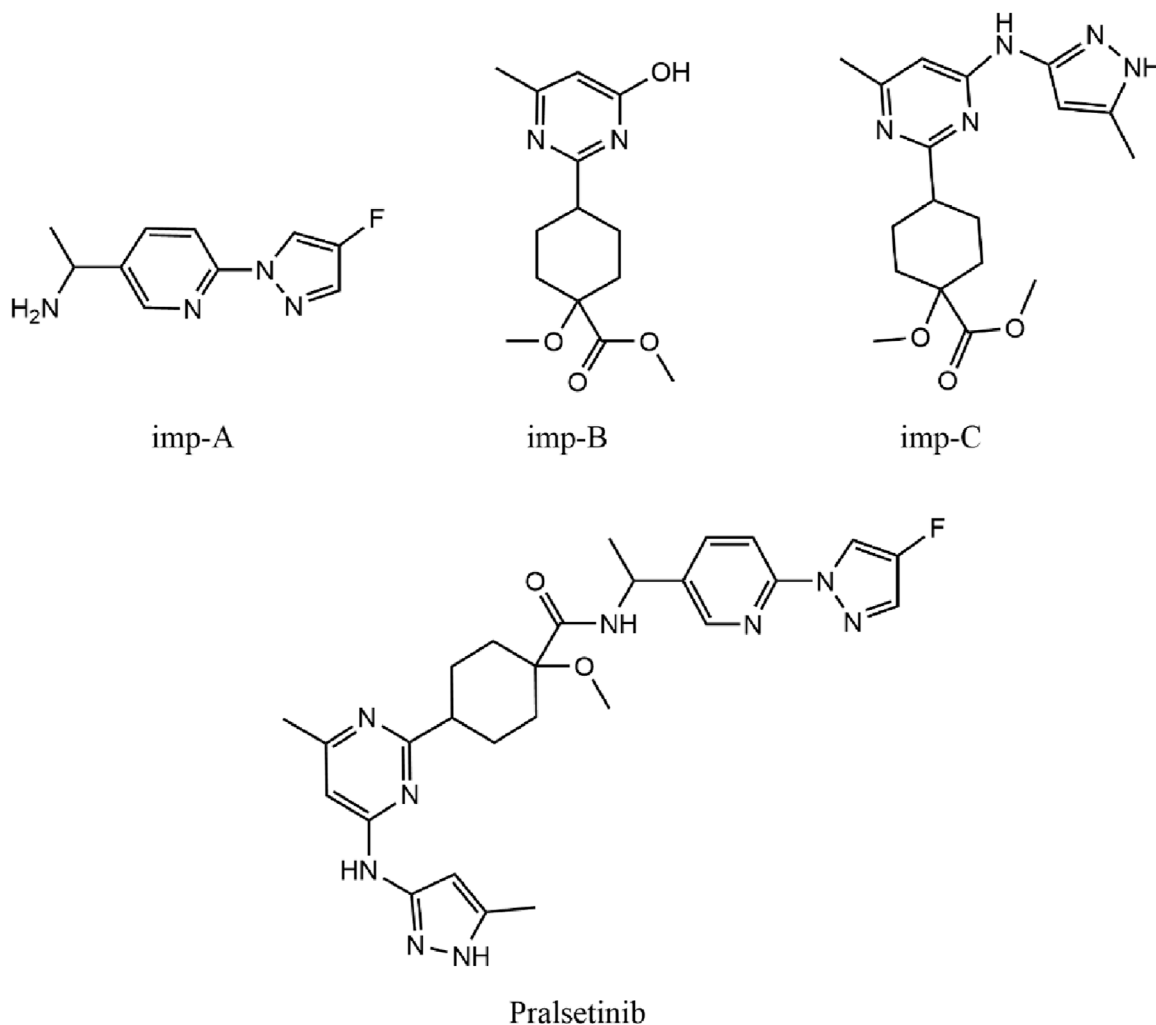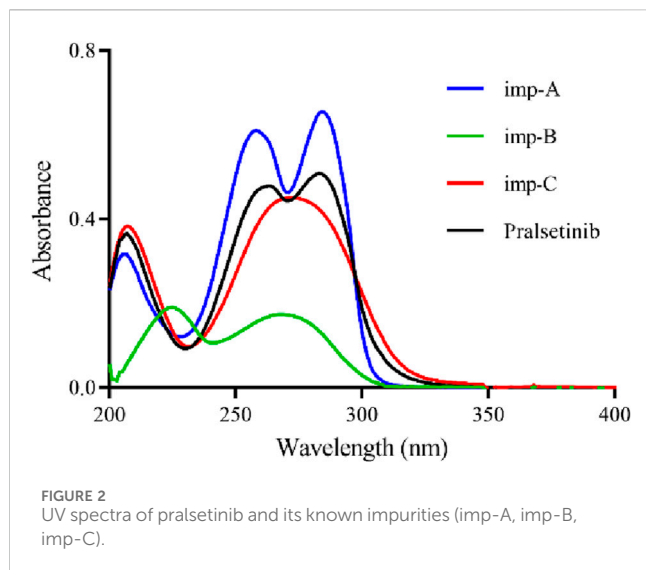

FIGURE 1
Chemical structures of pralsetinib, imp-A, imp-B and imp-C.

FIGURE 2
UV spectra of pralsetinib and its known impurities (imp-A, imp-B, imp-C).

calibration mark, yielding a stock solution of impurities with a concentration of 0.5 mg/mL.

2.5 Preparation of mixed solutions and system suitability solutions

A total of 10 mg of pralsetinib was accurately weighed and transferred to 20 mL volumetric flask. The compounds were subsequently dissolved in 10 mL of methanol, and 5 mL of a 1 mol/L hydrochloric acid (HCl) solution was added. The resulting mixture was heated at 75°C for 48 h. Upon completion of the reaction, the mixture was neutralised with a 1 mol/L sodium hydroxide (NaOH) solution. Next, the mixture was diluted with a 50% methanol aqueous solution to a total volume of 20 mL to obtain the acidic degradation product.

In a comparable manner, 10 mg of pralsetinib should be accurately weighed and transferred into a 20 mL volumetric flask, followed by the addition of 10 mL of methanol for sonication to facilitate dissolution. Subsequently, 10 mL of a 3% hydrogen peroxide solution was added, and the reaction was allowed to proceed at ambient temperature for a duration of 1.5 h. Following the completion of the reaction, it was suggested to that the reaction be terminated with manganese dioxide, followed by filtration to separate the manganese dioxide and collect the resulting solution containing the oxidative degradation product. Finally, the acidic degradation product and the oxidative degradation product should be combined at a ratio of 3:1 to generate a system suitable solution.

2.6 Preparation of the sample solution

For sample solution preparation, approximately 10 mg of pralsetinib bulk drug were precisely measured and then dissolved in a mixture of methanol and water mixture (50/50, volume/volume) until a concentration of approximately 0.5 mg per milliliter was reached.

3 Results and discussion

3.1 Method development

The synthesis of the RET inhibitor pralsetinib was conducted according to the synthetic pathway outlined in Supplementary Figure S1 of the US patent US20170121312A1. The synthesis of pralsetinib consists of seven steps and uses various reagents and intermediates. Figure 1 depicts the chemical structures of three known impurities and pralsetinib studied. Imp-B and imp-C are impurities not only from photodegradation, but also from the manufacturing process.

The current preliminary research on pralsetinib primarily encompasses two significant aspects: evaluating the efficacy and safety of pralsetinib in treating NSCLC, as well as monitoring and analyzing its serum drug concentration. Notably, no studies have been reported thus far regarding the detection of pralsetinib-related substances.

To optimise the detection method, an investigation was conducted on the impact of the solvent, detection wavelength, mobile phase composition, and elution method on sample separation. The selection of an appropriate solvent involved dissolving pralsetinib in both methanol (MeOH) and acetonitrile (ACN). The results of the experiments indicated that pralsetinib was less soluble in acetonitrile than in methanol, which completely dissolved the sample. Owing to the volatile nature of methanol, a 50% methanol-water mixture was also tested as a solvent, revealing that the sample could still be fully dissolved at a concentration of 0.5 mg/mL. Following the solution stability study, it was determined that there was no notable alteration in related substances within the sample when a 50% methanol-water mixture was used as the solvent within a period of 48 h. Consequently, the selected solvent for this investigation was ultimately a 50% methanol-water mixture. To identify the most suitable detection wavelength, pralsetinib and its known impurities (imp-A, imp-B, imp-C) were diluted with a 50% methanol-water mixture to a concentration of 10 μg/mL and subjected to UV-VIS scanning analysis within the wavelength range of 200–400 nm. The UV spectrum, depicted in Figure 2, revealed prominent absorption peaks near 260 nm for both pralsetinib and its impurities. Consequently, the detection wavelength for this study was 260 nm.

When developing the analytical method, the system suitability solution was selected because of the presence of a large number of impurities and difficult-to-separate chromatographic peak pairs. The peak shape, retention time, and peak resolution was used as evaluation criteria. During the development of the analytical methodology, the system suitability solution was chosen because of its complexity, containing numerous impurities and challenging chromatographic peak pairs. The evaluation process emphasized three key metrics: peak symmetry, retention time, and peak resolution. We preferred to utilize high-performance liquid chromatography (HPLC) with an isocratic elution strategy, emphasizing the simplicity of the mobile phase composition. The inclusion of buffer salts was minimized when possible. Our initial experiments involved the use of a mobile phase ratio of ACN-H_2O (70:30, v/v). Despite the primary peak having a retention time of 2.271 min, overlap among impurity peaks was observed, leading to a compromise in separation efficiency, as illustrated in Figure 3A.
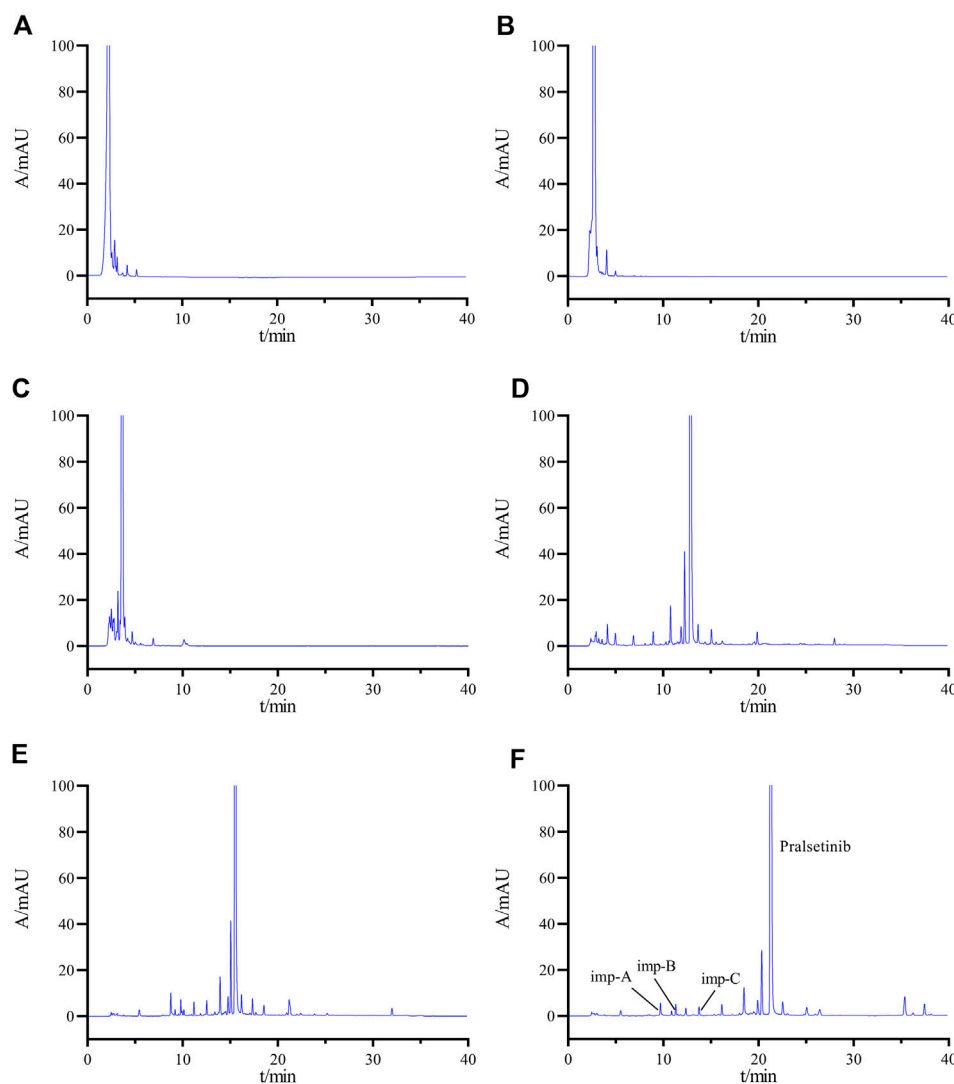
FIGURE 3
Chromatogram obtained by optimizing the HPLC conditions **(A)** ACN-H$_2$O (70:30); **(B)** ACN-20 mM KH$_2$PO4 solution (70:30); **(C)** ACN-20 mM KH$_2$PO4 solution (50:50); **(D)** gradient elution Condition 1; **(E)** gradient elution Condition 2; **(F)** final determined gradient elution condition.

Owing to the weak basic characteristics of pralsetinib, the incorporation of buffer salts to improve chromatographic separation was explored. Specifically, we utilized acetonitrile and 20 mM potassium dihydrogen phosphate (KH$_2$PO$_4$) as mobile phase components, and evaluated two ratios: 70:30 and 50:50 (v/v). However, the experimental results (depicted in Figures 3B, C) revealed limited improvement in peak resolution between the main peak and impurities.

Subsequently, an investigation was conducted on the impact of gradient elution. The established gradient elution condition 1 (0–2 min, 20% B →20% B; 2–20 min, 20% B → 70% B; 20–30 min, 70% B → 70% B; 30–31 min, 70% B → 20% B; 31–40 min, 20% B → 20% B) revealed a minimum separation of 1.08 (<1.2) between adjacent impurity peaks and a separation of 3.96 between the main peak and the impurity peaks (Figure 3D), failing to meet the specified criteria. Therefore, the initial organic phase ratio of the gradient was reduced, and the gradient change rate

was adjusted to establish gradient elution condition 2. (0–2 min, 8% B→8% B; 2–20 min, 8% B →70% B; 20–30 min, 70% B→70% B; 30–31 min, 70% B→8% B; 31–40 min, 8% B →8% B). Under these conditions, the separations between the main peak and adjacent impurities and between impurities improved, but still did not meet the experimental requirements (Figure 3E). After multiple adjustments, we finally determined the gradient elution conditions as described in Section 2.3 (Figure 3F).

3.2 Method validation

Validation of the HPLC method for detecting related substances in the receptor tyrosine kinase inhibitor pralsetinib was carried out as per the guidelines set by the International Council for Harmonization of Technical Requirements for Pharmaceuticals for Human Use (ICH) Guideline Q2 (R1) (Guideline, 2005). This
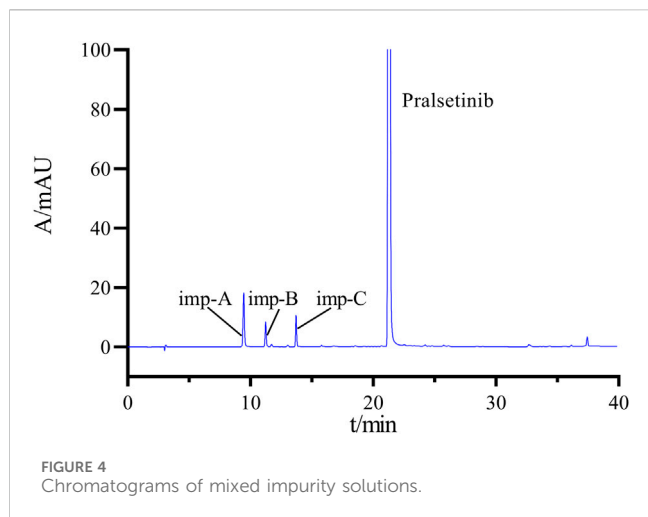
FIGURE 4
Chromatograms of mixed impurity solutions.

validation encompasses specificity, sensitivity, solution stability, linearity, precision, accuracy, and robustness.

3.2.1 Specificity

Following the chromatographic parameters outlined in Section 2.3, the solvent, mixed impurities, and system suitability solution were injected to assess the specificity of the detection method. Figure 4 shows the chromatogram of the mixed impurity solution, where Peaks one to four are identified as imp-A, imp-B, imp-C, and pralsetinib, respectively. The retention time (RT), relative retention time (RRT), and resolution values can be found in Supplementary Table S1. The minimum resolution between these impurities and pralsetinib is calculated to be 4.98 (>1.5), satisfying the experimental requirements.

Additionally, the chromatogram of the system suitability solution is depicted in Figure 3F, revealing resolutions of 5.01 and 6.15 between the main peak and adjacent impurity peaks, surpassing the threshold of 1.5. Moreover, the minimum resolution between impurity peaks is 1.49, exceeding the threshold of 1.2. Collectively, these findings indicate that the method displays favorable specificity.

3.2.2 Forced degradation experiments

For the forced degradation study, approximately 10 mg of pralsetinib was weighed and transferred to a 20 mL volumetric flask. The compound was then dissolved in methanol and subjected to a range of degradation conditions, such as acid and alkali hydrolysis, oxidation, photolysis, and heat degradation.

To simulate acid-induced stress, the pralsetinib solution was subjected to treatment with 1 mol/L HCl at a temperature of 75°C for 48 h. The process of alkaline degradation involved the use of a 1 mol/L NaOH solution at a temperature of 75°C for 72 h, followed by the application of a 10% H_2O_2 solution for 1.5 h. These conditions were used to mimic the degradation effects of alkali and oxidation. The pralsetinib sample was subjected to thermal degradation at 100°C for a period of 30 days, and photodegradation was induced by exposure to an LED tube with an intensity of 4,500 lx for a duration of 30 days. The sample was subsequently diluted to 0.5 mg/mL via a mixture of methanol and water (v/v 1:1) and analyzed according to the procedure specified in Section 2.3.

Figure 5 shows the chromatographic results obtained from the forced degradation study of pralsetinib. Supplementary Table S2 presents an evaluation of the compound's stability when subjected to different forced degradation conditions, considering the number of impurities, main peak content, minimum separation between principal components and impurities, minimum separation between impurities, and equilibrium rate. Pralsetinib is notably stable under conditions of elevated temperature, exposure to light, and alkaline environments, although it is susceptible to degradation under acidic and oxidative conditions. Importantly, despite differing degradation conditions, the minimum resolution difference between the main peak and impurities exceeds 1.5, whereas the minimum resolution difference among impurities surpasses 1.2, thereby meeting the specified criteria. Additionally, the equilibrium rate falls within the range of 95%–105%. This range is commonly accepted as a critical criterion for achieving equilibrium in material balance.

3.2.3 LODs and LOQs

The sensitivity of the detection method was assessed by determining the limit of detection (LOD) and limit of quantification (LOQ) through stepwise dilution of stock solutions of pralsetinib and its identified impurities (imp-A, imp-B, imp-C), followed by computation of signal-to-noise ratio. The concentrations corresponding to signal-to-noise (S/N) ratios of 3:1 and 10:1 were designated the LOD and LOQ, respectively. The detailed results can be found in Table 2.

3.2.4 Stability of the solution

A thorough stability assessment was conducted on the pralsetinib sample solution by analyzing it at different time points (0, 1, 2, 4, 6, 8, 12, and 24 h) to determine its stability. This assessment included monitoring changes in the number of impurities, maximum content of individual impurities, and overall impurity content. The results of these analyses are detailed in Supplementary Table S3. Additionally, after being exposed to room temperature for 24 h, the sample mixture presented minimal alterations in the three parameters, indicating its stability at room temperature for a period of 24 h.

To evaluate the stability of solutions containing known impurities, a mixed impurity solution was prepared and analysed via injection at various time points over a 24-h period using the chromatographic parameters specified in Section 2.3. The results indicated that the relative standard deviations of the peak areas for pralsetinib and impurities A, B, and C were 1.35%, 1.27%, 1.39% and 1.73%, respectively, which are all below the predetermined 2% threshold. These findings suggest that solutions containing these impurities remain stable for 24 h.

3.2.5 Linearity

This study presents an investigation of the linear relationship between pralsetinib and its related substances at concentrations ranging from the LOD to 2.0% of the desired concentration (approximately 0.5 mg/mL).

To conduct the analysis, multiple concentrations of detection solutions were prepared by diluting the prasetinib standard stock solution and the impurity (imp-A, -B, and -C) standard stock solutions with a MeOH/H_2O mixture (50/50, v/v). The linearity

FIGURE 5
HPLC chromatograms of undegraded **(A)**, acid-degraded **(B)**, base-degraded **(C)**, oxidatively degraded **(D)**, heat-degraded **(E)**, and photolytically degraded **(F)** samples.
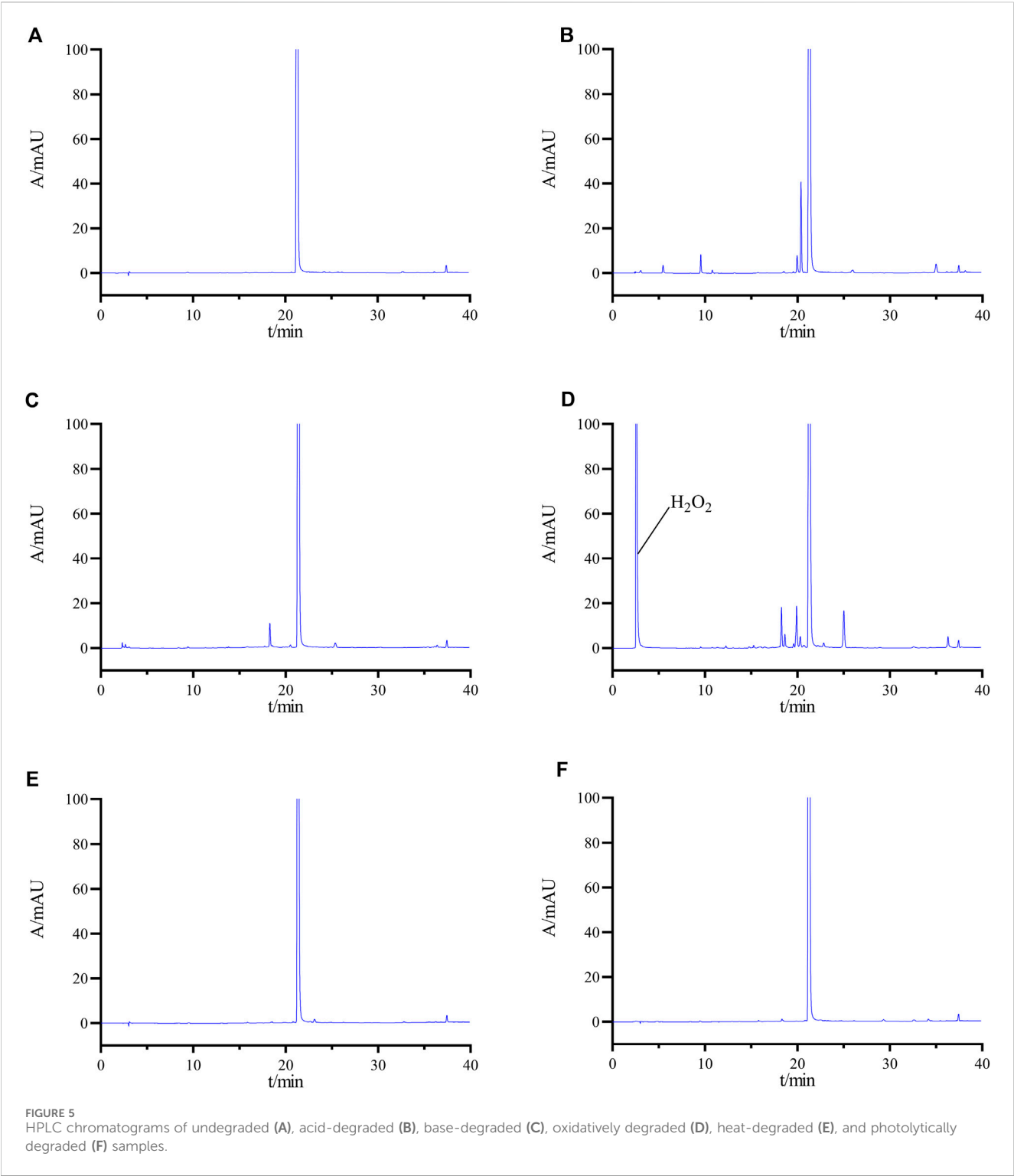
TABLE 2 Linearity, LODs and LOQs of pralsetinib and known impurities (imp-A, imp-B, imp-C).

Substance	Standard calibration curves	Correlation coefficient (r)	LOD (µg/mL)	LOQ (µg/mL)
Pralsetinib	y = 22.04x + 2.767	0.9991	0.013	0.04
imp-A	y = 27.37x − 1.107	0.9989	0.010	0.035
imp-B	y = 10.86x − 1.204	0.9993	0.030	0.09
imp-C	y = 11.64x − 1.536	0.9990	0.015	0.05

TABLE 3 Recovery of known impurities (imp-A, imp-B, imp-C) in pralsetinib.

Substance	Target Level (%)	Spiked Conc. (µg/mL)	Determined Conc. (µg/mL)	Recovery (%)	Average recovery (%)	RSD (%)
imp-A	50	0.511	0.502	98.33	101.01	1.56
		0.511	0.513	100.49		
		0.511	0.527	103.23		
	100	1.021	1.042	102.06		
		1.021	1.028	100.69		
		1.021	1.035	101.37		
	150	1.532	1.542	100.69		
		1.532	1.575	102.84		
		1.532	1.522	99.38		
imp-B	50	0.508	0.501	98.62	99.03	1.89
		0.508	0.492	96.85		
		0.508	0.497	97.83		
	100	1.016	1.008	99.21		
		1.016	1.002	98.62		
		1.016	0.997	98.13		
	150	1.524	1.535	100.72		
		1.524	1.496	98.16		
		1.524	1.572	103.15		
imp-C	50	0.510	0.489	95.98	99.13	1.78
		0.510	0.495	97.15		
		0.510	0.503	98.72		
	100	1.019	1.035	101.57		
		1.019	1.025	100.59		
		1.019	1.009	99.02		
	150	1.529	1.539	100.69		
		1.529	1.512	98.92		
		1.529	1.522	99.57		

TABLE 4 Test conditions of robustness.

Chromatogram conditions	The variation range of parameters
The initial proportion of mobile phases A-B (%)	94:6; 92:8; 90:10
Wavelength (nm)	255, 260, 265
Column temperature (°C)	35, 40, 45
Flow rate (mL/min)	0.9, 1.0, 1.1
Chromatographic column	Waters-C_{18}, Agilent-5HC-C_{18}, Luna-C_{18}

of the method was assessed through chromatographic analysis. The regression curve for pralsetinib and its related substances is shown in Supplementary Figure S2, while Table 2 presents the calibration curve and correlation coefficient. Across the analytical concentration range of the LOD to 2.0% of the target concentration (~0.5 mg/mL), all correlation coefficients surpassed 0.99.

3.2.6 Precision

The precision of the instrument was assessed by performing six consecutive injections of the mixed solution described in Item 2.5 under the specific HPLC conditions outlined in Item 2.3. Chromatographs were subsequently generated to quantify both the relative retention time and peak area. The relative standard deviations (RSDs) for pralsetinib and its impurities (imp-A, -B, and -C) were found to be 0.04%, 0.06%, and 0.08%, respectively. Similarly, the RSDs for the peak areas were determined to be 0.85%, 0.65%, 1.21% and 0.75%, respectively. Notably, all RSD values were less than 2%, indicating a high level of precision in the instrument.

3.2.7 Repeatability

To evaluate the reproducibility of the method, six samples with known impurities were prepared and subsequently analysed under the conditions outlined in Section 2.3. The RSD for impurities A, B, and C were calculated to be 0.57%, 0.79%, and 1.32%, respectively. These findings, which all fall below the 2% threshold, suggest that the method has satisfactory reproducibility.

3.2.8 Recovery

This study tested the recovery rates of known impurities (imp-A, imp-B, and imp-C) from pralsetinib at three different concentrations, 50%, 100%, and 150%, with a concentration of approximately 1 μg/mL used as the reference concentration at the 100% level. To achieve these concentrations, different volumes of impurity stock solutions were added to the pralsetinib sample solution. Each concentration of the sample was prepared in triplicate and injected, and the recovery rate was calculated. The findings depicted in Table 3 indicate that the recoveries of all known impurities ranged from 50% to 150%, with RSD values for these compounds below 2.0%. These findings suggest that the method demonstrates a high level of accuracy.

3.2.9 Durability

To assess the durability of the method, we determined the optimal parameters for the system under various chromatographic conditions. These conditions included variations in the initial ratio of mobile phases A-B, wavelength, column temperature, flow rate, and column type. A comprehensive overview of the conditions for durability can be found in Table 4.

The resolution between pralatinib and its adjacent impurity peaks was greater than 1.5 under various acceptable conditions, with the minimum resolution between impurity peaks exceeding 1.2. There were no notable changes observed in the quantity and composition of impurities. Furthermore, adjustments to the column temperature and wavelength did not affect the detection of related substances. However, variations in the flow rate, column type, and initial mobile phase ratio had minimal effects on the retention time and resolution. Fortunately, minor modifications to these parameters did not substantially impact the detection results, effectively highlighting the robustness of the methodology.

3.2.10 Sample detection

Accurately weigh 10 mg of pralsetinib's bulk drug from each of the three different batches and place them individually in 20 mL volumetric flasks. Subsequently, dissolve the samples using a 50% methanol-water solution and dilute to the volumetric flask's mark. Afterward, perform the detection according to the chromatographic conditions outlined in "Item 2.3." The results of the detection are presented in Table 5.

4 Conclusion

This study aimed to develop an analytical method for detecting process impurities generated during the synthesis of pralsetinib and degradation impurities resulting from forced degradation experiments. Based on the characteristics of these impurities, a new RP-HPLC-UV method was developed for the quantitative analysis of pralsetinib and its related substances. The method involved evaluating factors critical to separation efficiency,

TABLE 5 Results of related substances in three batches of pralsetinib samples.

Batch number	Related substances (%)				
	imp-A	imp-B	imp-C	Other single maximum impurity	Total impurities
20230821	0.08	0.05	0.09	0.09	0.38
20231215	0.06	0.07	0.10	0.13	0.49
20240301	0.11	0.06	0.07	0.11	0.42

including solvents, detection wavelength, mobile phase composition, elution methods, and chromatographic columns. The method was validated in accordance with ICH guidelines, exhibiting satisfactory sensitivity, specificity, accuracy, linearity, repeatability, and robustness, thereby meeting the criteria for method validation. Consequently, this research offers valuable insights for the quality assurance of pralsetinib.

Data availability statement

The original contributions presented in the study are included in the article/Supplementary Material, further inquiries can be directed to the corresponding author.

Author contributions

YZ: Conceptualization, Validation, Writing–original draft. JQ: Investigation, Visualization, Writing–original draft. WW: Investigation, Resources, Visualization, Writing–original draft. LC: Funding acquisition, Visualization, Writing–original draft, Writing–review and editing.

Funding

Conflict of interest

Author WW was employed by Sinopharm Holding Nantong Ltd.

The remaining authors declare that the research was conducted in the absence of any commercial or financial relationships that could be construed as a potential conflict of interest.

Publisher's note

All claims expressed in this article are solely those of the authors and do not necessarily represent those of their affiliated organizations, or those of the publisher, the editors and the reviewers. Any product that may be evaluated in this article, or claim that may be made by its manufacturer, is not guaranteed or endorsed by the publisher.

Supplementary material

The Supplementary Material for this article can be found online at: https://www.frontiersin.org/articles/10.3389/fchem.2024.1450692/full#supplementary-material

References

Agtas, C., Bellur Atici, E., Ayaz Seyhan, S., and Bilgic Alkaya, D. (2024). Development and validation of stability indicating UPLC methods for related substances and assay analyses of ricobendazole hydrochloride. *J. Pharm. Biomed. Anal.* 237, 115761. doi:10.1016/j.jpba.2023.115761

Buchholz, K., Antosik, P., Grzanka, D., Gagat, M., Smolinska, M., Grzanka, A., et al. (2021). Expression of the body-weight signaling players: GDF15, GFRAL and RET and their clinical relevance in gastric cancer. *J. Cancer* 12 (15), 4698–4709. doi:10.7150/jca.55511

Camidge, D. R., Dziadziuszko, R., Peters, S., Mok, T., Noe, J., Nowicka, M., et al. (2019). Updated efficacy and safety data and impact of the EML4-ALK fusion variant on the efficacy of alectinib in untreated ALK-positive advanced non-small cell lung cancer in the global phase III ALEX study. *J. Thorac. Oncol.* 14 (7), 1233–1243. doi:10.1016/j.jtho.2019.03.007

Chen, B., Zhao, H., Li, M., She, Q., Liu, W., Zhang, J., et al. (2022). SHANK1 facilitates non-small cell lung cancer processes through modulating the ubiquitination of Klotho by interacting with MDM2. *Cell Death Dis.* 13 (4), 403. doi:10.1038/s41419-022-04860-3

Cheng, F. J., Chen, C. H., Tsai, W. C., Wang, B. W., Yu, M. C., Hsia, T. C., et al. (2021). Cigarette smoke-induced LKB1/AMPK pathway deficiency reduces EGFR TKI sensitivity in NSCLC. *Oncogene* 40 (6), 1162–1175. doi:10.1038/s41388-020-01597-1

Du, W., He, B., Luo, X., and Chen, M. (2022). Diagnostic value of artificial intelligence based on CT image in benign and malignant pulmonary nodules. *J. Oncol.* 2022, 1–6. doi:10.1155/2022/5818423

Frampton, J. E. (2013). Crizotinib: a review of its use in the treatment of anaplastic lymphoma kinase-positive, advanced non-small cell lung cancer. *Drugs* 73 (18), 2031–2051. doi:10.1007/s40265-013-0142-z

Gainor, J. F., Curigliano, G., Kim, D. W., Lee, D. H., Besse, B., Baik, C. S., et al. (2021). Pralsetinib for RET fusion-positive non-small-cell lung cancer (ARROW): a multi-cohort, open-label, phase 1/2 study. *Lancet Oncol.* 22 (7), 959–969. doi:10.1016/S1470-2045(21)00247-3

Gondhale-Karpe, P., and Manwatkar, S. (2023). Quantitative determination of related substances for Lamotrigine extended release tablet by RP-HPLC. *Heliyon* 9 (5), e15732. doi:10.1016/j.heliyon.2023.e15732

Griesinger, F., Curigliano, G., Thomas, M., Subbiah, V., Baik, C. S., Tan, D. S. W., et al. (2022). Safety and efficacy of pralsetinib in RET fusion-positive non-small-cell lung cancer including as first-line therapy: update from the ARROW trial. *Ann. Oncol.* 33 (11), 1168–1178. doi:10.1016/j.annonc.2022.08.002

Guideline, I. H. T. J. Q. (2005). Validation of analytical procedures: text and methodology. *ICH Harmon. Tripart. Guidel.* 1 (20), 05.

Gulikers, J. L., van Veelen, A. J., Sinkiewicz, E. M. J., de Beer, Y. M., Slikkerveer, M., Stolk, L. M. L., et al. (2023). Development and validation of an HPLC-MS/MS method to simultaneously quantify brigatinib, lorlatinib, pralsetinib and selpercatinib in human K2-EDTA plasma. *Biomed. Chromatogr.* 37 (6), e5628. doi:10.1002/bmc.5628

Huang, Y., Dai, S., Yin, W., Luo, F., and Li, Y. (2023). Sustained clinical response to 4th-line therapy with selpercatinib in RET fusion-positive combined small cell lung cancer. *Onco Targets Ther.* 16, 1015–1020. doi:10.2147/OTT.S440610

Lin, J. J., Liu, S. V., McCoach, C. E., Zhu, V. W., Tan, A. C., Yoda, S., et al. (2020). Mechanisms of resistance to selective RET tyrosine kinase inhibitors in RET fusion-positive non-small-cell lung cancer. *Ann. Oncol.* 31 (12), 1725–1733. doi:10.1016/j.annonc.2020.09.015

Melosky, B., Kambartel, K., Hantschel, M., Bennetts, M., Nickens, D. J., Brinkmann, J., et al. (2022). Worldwide prevalence of epidermal growth factor receptor mutations in non-small cell lung cancer: a meta-analysis. *Mol. Diagn Ther.* 26 (1), 7–18. doi:10.1007/s40291-021-00563-1

Nakajima, E. C., Drezner, N., Li, X., Mishra-Kalyani, P. S., Liu, Y., Zhao, H., et al. (2022). FDA approval summary: sotorasib for KRAS G12C-mutated metastatic NSCLC. *Clin. Cancer Res.* 28 (8), 1482–1486. doi:10.1158/1078-0432.CCR-21-3074

Ou, S. I., Janne, P. A., Leal, T. A., Rybkin, I. I., Sabari, J. K., Barve, M. A., et al. (2022). First-in-Human phase I/IB dose-finding study of adagrasib (MRTX849) in patients with

advanced *KRAS*[G12C] solid tumors (KRYSTAL-1). *J. Clin. Oncol.* 40 (23), 2530–2538. doi:10.1200/JCO.21.02752

Shaw, A. T., Bauer, T. M., de Marinis, F., Felip, E., Goto, Y., Liu, G., et al. (2020). First-Line lorlatinib or crizotinib in advanced ALK-positive lung cancer. *N. Engl. J. Med.* 383 (21), 2018–2029. doi:10.1056/NEJMoa2027187

Sidaway, P. (2021). Sotorasib effective in KRAS-mutant NSCLC. *Nat. Rev. Clin. Oncol.* 18 (8), 470. doi:10.1038/s41571-021-00533-w

Spagnuolo, A., and Gridelli, C. (2023). The role of immunotherapy in the first-line treatment of elderly advanced non-small cell lung cancer. *Cancers (Basel)* 15 (8), 2319. doi:10.3390/cancers15082319

Yadav, L., Pietila, E., Ohman, T., Liu, X., Mahato, A. K., Sidorova, Y., et al. (2020). PTPRA phosphatase regulates GDNF-dependent RET signaling and inhibits the RET mutant MEN2A oncogenic potential. *iScience* 23 (2), 100871. doi:10.1016/j.isci.2020.100871

Yu, J. J., Zhou, D. D., Yang, X. X., Cui, B., Tan, F. W., Wang, J., et al. (2020). TRIB3-EGFR interaction promotes lung cancer progression and defines a therapeutic target. *Nat. Commun.* 11 (1), 3660. doi:10.1038/s41467-020-17385-0

Zhao, D., and Rustum, A. M. (2024). Determination of Clorsulon and its related substances in commercial bulk drug substance batches by a rapid ion-pair UPLC method. *J. Pharm. Biomed. Anal.* 239, 115896. doi:10.1016/j.jpba.2023.115896

Zhao, D., Wimalasinghe, R. M., Wang, L., and Rustum, A. M. (2022). Development and validation of a reversed-phase high-performance liquid chromatography (RP-HPLC) method for identification, assay and estimation of related substances of ivermectin in bulk drug batches of ivermectin drug substance. *J. Chromatogr. Sci.* 60 (7), 620–632. doi:10.1093/chromsci/bmab112

Zhou, Q., Zhao, J., Chang, J., Wang, H., Fan, Y., Wang, K., et al. (2023). Efficacy and safety of pralsetinib in patients with advanced RET fusion-positive non-small cell lung cancer. *Cancer* 129 (20), 3239–3251. doi:10.1002/cncr.34897

Frontiers in
Chemistry

Explores all fields of chemical science across the periodic table

Advances our understanding of how atoms, ions, and molecules come together and come apart. It explores the role of chemistry in our everyday lives - from electronic devices to health and wellbeing.

Discover the latest Research Topics

See more →

frontiers

Frontiers in
Chemistry

frontiers | Research Topics